

DOE FILE COPY

STMPO-078

SAN/1109-8/2

**SOLAR PILOT PLANT, PHASE 1
PRELIMINARY DESIGN REPORT**

Volume 2

System Description and System Analysis (CDRL Item 2)

May 1, 1977

Work Performed Under Contract No. EY-76-C-03-1109

**Honeywell, Incorporated
Energy Resources Center
Minneapolis, Minnesota**



U.S. Department of Energy



Solar Energy

NOTICE

This report was prepared as an account of work sponsored by the United States Government. Neither the United States nor the United States Department of Energy, nor any of their employees, nor any of their contractors, subcontractors, or their employees, makes any warranty, express or implied, or assumes any legal liability or responsibility for the accuracy, completeness or usefulness of any information, apparatus, product or process disclosed, or represents that its use would not infringe privately owned rights.

This report has been reproduced directly from the best available copy.

Available from the National Technical Information Service, U. S. Department of Commerce, Springfield, Virginia 22161.

Price: Paper Copy \$19.00
Microfiche \$3.00

Honeywell

ERDA Contract No. E(04-3)-1109

1 MAY 1977

SOLAR PILOT PLANT
PHASE I

PRELIMINARY DESIGN REPORT

VOLUME II

SYSTEM DESCRIPTION AND SYSTEM ANALYSIS

CDRL Item 2



C. J. Bunnell
Contract Administrator

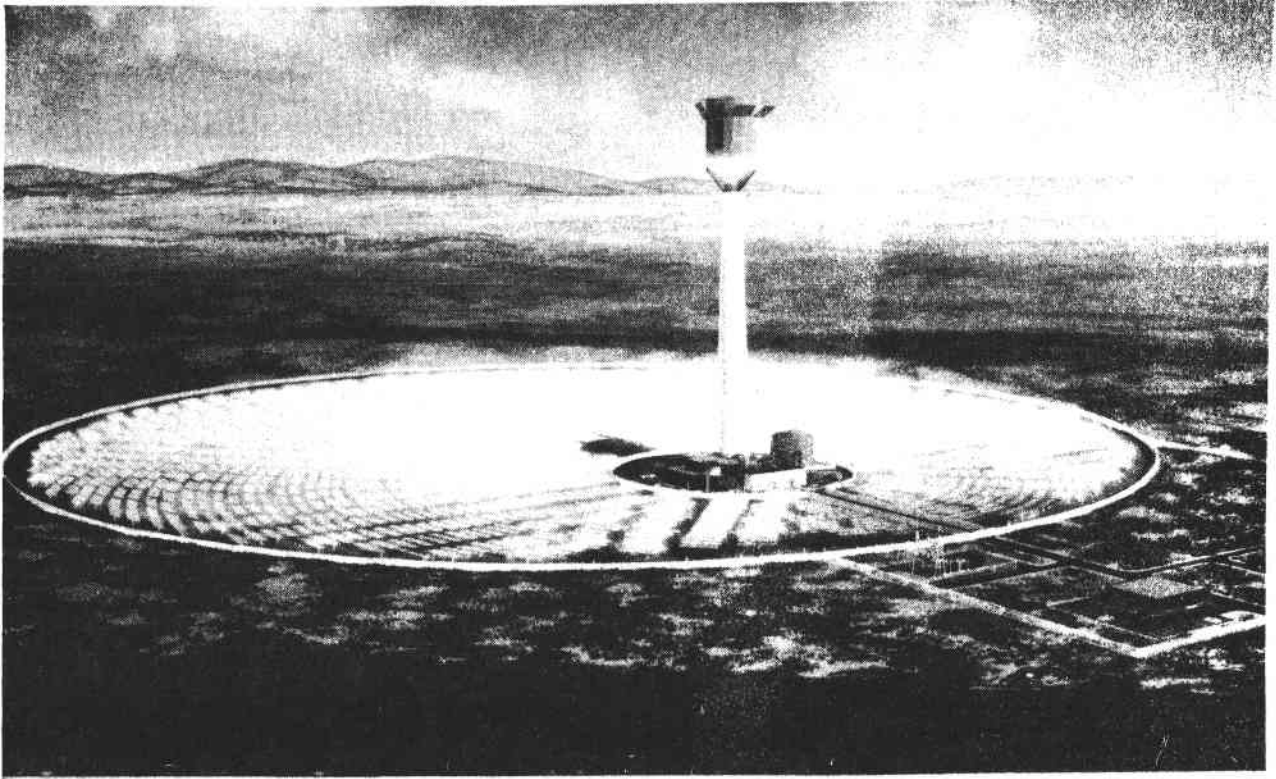


J. C. Powell
Program Manager

Energy Resources Center
2600 RIDGWAY PARKWAY,
MINNEAPOLIS, MINNESOTA 55413

FOREWORD

This is the initial submittal of the Solar Pilot Plant Preliminary Design Report per Contract Data Requirement List Item 2 of ERDA Contract E(04-3)-1109. The report is submitted for review and approval by ERDA. This is Volume II of seven volumes.



10 MEGAWATT SOLAR PILOT PLANT
ENERGY RESEARCH AND DEVELOPMENT ADMINISTRATION

ABSTRACT

Honeywell conducted a parametric analysis of the 10-MW(e) solar pilot plant requirements and expected performance and established an optimum system design. The main analytical simulation tools were the optical (ray trace) and the dynamic simulation models. These are described in detail in Books 2 and 3 of this volume under separate cover. In making design decisions, available performance and cost data were used to provide a design reflecting the overall requirements and economics of a commercial-scale plant. This volume contains a description of this analysis/design process and resultant system/subsystem design and performance.

CONTENTS

	<u>Page</u>	
SECTION 1	INTRODUCTION	1-1
	Background	1-1
	Phase I Program Scope	1-1
	Organization of the Preliminary Design Report	1-4
	Abstracts	1-5
	Vol. III - Collector Subsystem	1-5
	Vol. IV - Receiver Subsystem	1-5
	Vol. V - Thermal Storage Subsystem	1-6
	Vol. VI - Electrical Power Generation Subsystem, Controls, and Balance-of-Plant	1-6
SECTION 2	SUMMARY SYSTEM DESCRIPTION	2-1
	Background	2-1
	Phase I Goals and Requirements	2-3
	Central Receiver Solar Thermal Power Plant Concept	2-4
	Pilot Plant Preliminary Design	2-6
	Commercial Plant Preliminary Design	2-11
	Design Requirements	2-11
	Pilot Plant Subsystem Descriptions	2-14
	Collector Subsystem Description	2-14
	Receiver Subsystem Description	2-25
	Thermal Storage Subsystem Description	2-34
	Electrical Power Generation Subsystem Description	2-39
	Plant Control	2-44
	Hierarchy of Control	2-44
	Coordinated Master Control	2-46
	Pilot Plant Performance	2-48
	Heliostat Field Performance	2-48
	Incident Flux Map	2-53
	Cavity/Steam Generator Performance	2-55
	Thermal Storage Subsystem Performance	2-62
	EPGS/Balance-of-Plant Performance	2-63
	Pilot Plant Design Point Performance	2-70
	Net Annual Energy Performance	2-74
	Commercial Plant Description	2-83
	Field Plant Layout	2-83
	Tower Receiver Design	2-87
	Storage System	2-92
	Balance of Plant	2-92

	Commercial Plant Performance	2-105
	Collector System Performance	2-105
	Receiver Optical and Thermal Losses	2-105
	Gross Cycle Efficiency	2-112
	Auxiliary Power Losses	2-112
	Performance Results	2-114
SECTION 3	DESIGN TRADEOFF ANALYSIS	3-1
	Approach	3-1
	Heliostat Subsystem Tradeoffs	3-9
	Heliostat Configuration Tradeoff	3-10
	Receiver Effects	3-12
	Heliostat Size Effects	3-15
	Tracking Error Effects	3-16
	Field Heliostat Packing Effects	3-19
	Heliostat Configuration Selection	3-22
	Field Analysis	3-24
	Facet Focusing and Toe-In	3-53
	Receiver Subsystem Tradeoff	3-62
	Aperture Analysis	3-66
	Steam Generator Configuration	3-79
	Electrical Generation Subsystem Tradeoffs	3-81
	Storage Subsystem Tradeoffs	3-85
	Commercial Plant Design Tradeoffs	3-98
	Design Guidelines	3-98
	Design Alternatives	3-100
	Electrical Power Generation Subsystem Requirements	3-109
	Cost Tradeoffs	3-111
	Design Selection	3-112
SECTION 4	PILOT PLANT OPERATION	4-1
	Modes of Pilot Plant Operation	4-1
	Operator Sequences for Startup and Shutdown	4-12
	Analysis of Pilot Plant Transient Performance	4-12
	Transient Analysis Study Results	4-18
	Conclusions of Transient Analysis Study	4-89
SECTION 5	SUPPORTING DATA	5-1
	Pilot Plant Safety Considerations	5-1
	Inherent Hazards	5-1
	Collector Subsystem Criteria	5-12
	Receiver Subsystem Criteria	5-14
	Thermal Storage Subsystem Criteria	5-15
	Electric Power Generating System Criteria	5-16
	Existing Applicable Codes and Standards	5-17

	Solar Pilot Plant Availability Analysis	5-18
	Summary	5-18
	Analysis Detail	5-20
	Plant Support Equipment	5-44
	General Site Area	5-46
	Collector Subsystem	5-47
	Receiver Subsystem	5-51
	Thermal Storage Subsystem	5-51
	Electrical Power Generation Subsystem	5-52
	Recommendations	5-57
	Preliminary System Test and Evaluation	5-57
	General	5-58
	Shop Testing	5-59
	Construction Testing	5-61
	Preoperational Testing	5-66
	Initial Operation Testing	5-72
	Normal Operation Testing	5-75
	References	5-82
SECTION 6	SRE TEST SUMMARY	6-1
	Heliostat Test Setup	6-1
	Data Collection	6-6
	Subassembly Tests	6-8
	Contour Errors	6-8
	Tracking Errors	6-9
	Reflectance Measurements	6-14
	Power Balance	6-15
	Image Characteristics	6-21
SECTION 7	ANALYTICAL MODELS	7-1
	Central Receiver Optical Model	7-1
	Analytic Description	7-5
	Methodology	7-7
	Input/Output	7-9
	Single-Heliostat Optical Model	7-12
	Cavity Reradiation Model	7-25
	Cavity Heat-Transfer Analysis	7-26
	View Factor Analysis	7-35
	Sensitivity Analysis	7-42
	Atmospheric Attenuation Loss Model	7-44
	Analysis Model	7-48
	Example Calculations	7-52
	Net Annual Energy Model	7-59
	Dynamic Simulation Model	7-64
	Solar Pilot Plant Dynamic Simulation	7-68
	Description	

Collector Subsystem Model Overview	7-70
Steam Generator Subsystem Model Overview	7-76
Electrical Power Generation Subsystem Model Overview	7-80
Thermal Storage Subsystem Model Overview	7-82
Master Controller Subsystem Model Overview	7-84

APPENDIX A IDENTIFICATION OF DATA

APPENDIX B SYSTEM CHARACTERISTICS AND REQUIREMENT
COMPLIANCE

ILLUSTRATIONS

<u>Figure</u>		<u>Page</u>
1-1	Honeywell Team for Phase I Solar Pilot Plant Program	1-2
1-2	Chronology of Phase I Solar Pilot Plant Program	1-3
2-1	Central Receiver Solar Thermal Power Plant Concept	2-5
2-2	Pilot Plant Schematic	2-7
2-3	Pilot Plan	2-8
2-4	Plant Arrangement	2-9
2-5	Collector/Receiver Interface	2-10
2-6	Commercial Plant Conceptual Design	2-12
2-7	Site Plan	2-13
2-8	Pilot Plant Heliostat	2-17
2-9	Collector Subsystem Tower One-Half South Field Layout	2-19
2-10	Control Scheme	2-21
2-11	Pilot Plant Collector Subsystem Block Diagram	2-23
2-12	Receiver Tower and Foundation	2-26
2-13	Receiver Housing	2-27
2-14	Steam Generator Subsystem Flow Circuit	2-29
2-15	Receiver/Cavity Configuration	2-31
2-16	Pilot Plant Steam Generator Arrangement	2-35
2-17	Sensible Heat Storage Subsystem	2-37
2-18	Pilot Plant Storage Subsystem Arrangement	2-38
2-19	Electrical Power Generation Subsystem Schematic Diagram	2-41
2-20	Functional Block Diagram of the Master Control	2-47

2-21	Field Efficiency at Equinox Day	2-49
2-22	Cosine-Only Field Geometry	2-51
2-23	Redirected Field Efficiency	2-51
2-24	Power Into Cavity Field Efficiency	2-52
2-25	Cavity Wall Incident Flux Map for Noon on Equinox Day	2-54
2-26	Cavity Efficiency versus Power Into Cavity at Various Windspeeds	2-56
2-27	Absorbed/Incident Radiation versus Cavity Position for 3/21 Noon	2-58
2-28	Absorbed/Incident Radiation versus Cavity Position for 3/21 7 a. m.	2-58
2-29	Convection Heat Loss Vertical Distribution	2-61
2-30	Pilot Plant Design Heat Balance Schematic	2-65
2-31	Pilot Plant Gross Efficiency	2-66
2-32	Wet Cooling Tower with Steam Surface Condenser	2-68
2-33	Condenser Pressure versus Wet-Bulb Temperature at Various Throttle Steam Flows	2-69
2-34	Correction Curve for Various Condenser Pressures	2-69
2-35	Pilot Plant Design Point Power Stair Step - 12/21 p. m.	2-72
2-36	Pilot Plant Net Annual Energy Stair Step (Receiver-Only Operation)	2-76
2-37	Pilot Plant Net Annual Energy Stair Step (Diurnal Charge and Discharge at Storage Operation)	2-77
2-38	Field - Plant Layout	2-85
2-39	Steam Line Piping Layout	2-86
2-40	Tower Design	2-89
2-41	Receiver and Supports	2-90

2-42	Commercial Plant Receiver Configuration	2-91
2-43	Storage System Schematic	2-93
2-44	Schematic of the 100-MW(e) Electrical Power Generation Subsystem	2-95
2-45	Utility Cycle Tray Deaerating Heater for 100-MW(e) Commercial Pilot Plant	2-98
2-46	Turbine Building Ground Floor Plan	2-100
2-47	Turbine Building Mezzanine Floor Plan	2-101
2-48	Turbine Building Operating Floor Plan	2-102
2-49	Turbine Building Deaerator Platform	2-103
2-50	Collector System Efficiencies for Various Times of the Year	2-106
2-51	Commercial Plant Estimate of Receiver Steam Total Piping Heat Loss from Receiver to Turbine Building	2-111
2-52	Commercial Plant Design Point Performance	2-115
3-1	Weather Data Model Differences	3-6
3-2	Az-El and Tilt-Tilt Heliostat Configurations	3-11
3-3	Net MWh(th) versus Aperture Area for 45 Percent Ground Cover	3-13
3-4	Aperture Upper and Lower Boundary Determination Methodology	3-14
3-5	Heliostat Size versus Performance for the Az-El Configuration	3-16
3-6	Tracking Error Variations	3-17
3-7	Heliostat Performance versus Size	3-18
3-8	Field Packing Geometries	3-21
3-9	Ground Coverage Determination	3-22
3-10	Selected Heliostat Configuration	3-23

3-11	Tilt-Tilt Summary	3-25
3-12	Ray Trace Energy Path	3-27
3-13	Cosine Definition	3-28
3-14	Cosine-Only, Annual Tracking Efficiency	3-29
3-15	Cosine Performance for Various Fields	3-30
3-16	Shading and Blocking Simulation Parameters	3-34
3-17	Annual Shading and Blocking Energy Losses versus Field Position	3-35
3-18	Annual Shading and Blocking Energy Losses versus Radial Distance from the North Field	3-36
3-19	Maximum Ground Cover Ratio versus Field Position	3-37
3-20	Cosine Only, Annual Average Tracking Efficiency	3-39
3-21	Cosine-Only, Percentage Loss versus Tower Angle	3-41
3-22	Shading and Blocking Loss versus Tower Height	3-41
3-23	Tower Shadow Loss versus Tower Height	3-42
3-24	Overall Receiver Loss versus Tower Height	3-43
3-25	Annual Tracking Efficiency versus Tower Height	3-45
3-26	Cost Per Unit Energy versus Tower Height	3-46
3-27	Radial Spacing versus Distance from Tower	3-48
3-28	Nonuniform Heliostat Packing Density Field Zones	3-49
3-29	Annual Tracking Efficiency versus Tower Location	3-51
3-30	Heliostat Optical Modeling	3-54
3-31	Sensitivity to Toe-In and Focus Strategies	3-56
3-32	Single-Heliostat Ray Trace Model	3-32
3-33	Heliostat Toe-In	3-60

3-34	Aiming Accuracy for a Heliostat Directly East of Tower	3-61
3-35	RMS Dispersion Over the Day for Various Toe-In Times - East Field	3-63
3-36	RMS Dispersion Over the Day for Various Toe-In Times - South Field	3-64
3-37	RMS Dispersion Over the Day for Various Toe-In Times - North Field	3-65
3-38	Tilted-Cone Aperture	3-67
3-39	Energy versus Aim Circle Radius	3-71
3-40	Flux into Aperture in Polar Zones	3-72
3-41	Tilted-Cone Aperture and Receiver Geometry	3-75
3-42	Cavity Wall Incident Flux Map	2-75
3-43	Rerad Cavity/Aperture Models	3-76
3-44	Power Loss versus Shield Length	3-77
3-45	Baseline Aperture Configuration	3-78
3-46	Steam Generator Configuration	3-80
3-47	Comparison of Oil and Salt Storage Annual Energy Cost versus Cycle Pressure	3-83
3-48	Relative Energy Cost versus Pressure Ratio for the Two Turbine Types a 9997 kPa Receiver Pressure with Latent Heat Storage	3-84
3-49	Comparison of Annual Energy Cost for Sensible Oil and Latent Salt Storage Systems	3-87
3-50	Expansion Line Matching	3-89
3-51	Temperature/Enthalpy Diagram for Storage	3-90
3-52	Sensible Heat Storage Subsystem	3-92
3-53	Storage Temperatures versus Turbine Admission Pressure	3-93
3-54	Turbine Efficiency and Thermal Storage Capacity versus Turbine Admission Pressure	3-95

3-55	Oil Quantity versus Storage Discharge Pressure	3-95
3-56	Cost Optimization of Storage Discharge Pressure	3-97
3-57	Commercial Plant Module	3-101
3-58	Commercial Plant Design Computer Results--Power versus Aperture Area for Four-Tower Concept Tower Height / 720 ft	3-103
3-59	Commercial Plant Design--Power versus Aperture Area for Single-Tower Concept, Tower Height = 1440 ft	3-104
3-60	Commercial Plant Modular Field Layout (12 Powers)	3-113
3-61	Commercial Plant Modular Field Layout (Four Towers)	3-114
3-62	Single-Tower Design	3-115
4-1	Basic Electrical Generation Subsystem Working Fluid Flow Diagram	4-3
4-2	Electrical Generation Subsystem Fluid Flow Diagram Operating Mode A	4-6
4-3	Electrical Generation Subsystem Working Fluid Flow Diagram for Operating Mode B	4-7
4-4	Electrical Generation Subsystem Working Fluid Flow Diagram for Operating Mode C	4-8
4-5	Electrical Generation Subsystem Working Fluid Flow Diagram for Operating Mode D	4-9
4-6	Electrical Generation Subsystem Working Fluid Flow Diagram for Operating Mode E	4-10
4-7	Electrical Generation Subsystem Working Fluid Flow Diagram for Operating Mode F	4-11
4-8	Plant Startup Time Line for Transient Analysis Studies	4-23
4-9	Direct Normal Intensity versus Time for Run No. 300	4-26
4-10	Plant Startup Results for Transient Analysis Studies	4-28
4-11	Various Solar Power Parameter Variations with Time for Variable-Pressure Startup	4-31

4-12	Redirected and Incident Solar Power Variations for Variable-Pressure Startup	4-32
4-13	Steam Generator Metal and Steam Temperatures for Variable-Pressure Startup	4-35
4-14	Steam Generator Metal Temperature Rates for Variable-Pressure Startup	4-36
4-15	Heliostat Field Location Effects on Steam Generator for Transient Analysis Studies	4-40
4-16	Cloud Scenario for Transient Analysis Studies	4-45
4-17	Effect of Cloud Traveling to East, Covering North Field Half on Steam Generator Subsystem Absorbed Power Levels	4-47
4-18	Effect of Cloud Traveling to East, Covering North Field Half on Steam Generator Subsystem Absorbed Power Ratios	4-48
4-19	Effect of Cloud Traveling to East, Covering North Field Half on Various Solar Power Parameters	4-51
4-20	Effect of Cloud Traveling to East, Covering North Field Half on Steam Generator Subsystem Metal Temperature Rates and Drum Level	4-52
4-21	Effect of Cloud Traveling to East, Covering North Field Half on Steam Generator Subsystem Steam and Metal Temperatures	4-53
4-22	Effect of Cloud Traveling to East, Covering North Field Half on Various Steam Generator Subsystem Flow and Pressure Parameters	4-56
4-23	Cloud Transient Effects on Plant for Transient Analysis Studies	4-58
4-24	Turbine Valve and Inlet Flow Parameters for Cloud Transient Run No. 303	4-60
4-25	Pressure, Temperature, Steam Flow Parameters for Cloud Transient Run No. 303	4-61
4-26	Master Controller Operation During Cloud Transient Run No. 303	4-62

4-27	Megawatt Demand and Steam Generator Subsystem Power, Energy-Delivered Variations for Cloud Transient Run No. 303	4-64
4-28	Various Energy and Power Parameters for Cloud Transient Run No. 303	4-65
4-29	Peak Steam Generator Subsystem Metal Temperature Changes and Rates of Change, Absorbed Power Rates of Change for Various Cloud Conditions	4-68
4-30	Peak Steam Generator Subsystem Metal Temperature Change (From Average) versus Rate of Change for Various Cloud Conditions	4-70
4-31	Peak Steam Generator Subsystem Metal Temperature Rates of Change and Temperature Change versus Cloud Cover	4-73
4-32	Insolation Data Segment Used for Simulation Run No. 317	4-74
4-33	Solar Power Parameters versus Time for Cloud Transient Run No. 317	4-75
4-34	Steam Generator Subsystem Steam and Metal Temperature Variations for Cloud Transient Run No. 317	4-76
4-35	Steam Generator Subsystem Outlet Conditions for Cloud Transient Run No. 317	4-78
4-36	Turbine Inlet Valve for Flow Parameters for Cloud Transient Run No. 317	4-79
4-37	Various Power and Energy Parameters for Cloud Transient Run No. 317	4-80
4-38	Plant Response to Load Demand Changes for Transient Analysis Studies	4-82
4-39	Steam Generator Subsystem Metal Temperature Rates and Drum Level Change Due to Simulated Recirculating Pump Failure	4-84
4-40	Steam Generator Drum Pressure and Various Flows for Simulated HP Heater Failure (Run No. 315)	4-86
4-41	Steam Generator Metal and Steam Temperature Changes Due to Simulated HP Heater Failure (Run No. 315)	4-87

4-42	Steam Generator Outlet Flow, Pressure, and Temperature for Simulated HP Heater Failure (Run No. 315)	4-88
4-43	Steam Generator Drum Pressure and Steam/Water Flows for Simulated Collector Field Failure (Run No. 316)	4-90
4-44	Steam Generator Metal and Temperature Variations After Simulated Partial Collector Field Failure (Run No. 316)	4-91
5-1	Single-Facet Curved Mirror	5-5
5-2	Four-Facet Mirror	5-8
5-3	One-Sum Intensity Limit	5-9
5-4	Flux versus Distance	5-9
5-5	Barrier Concept	5-11
5-6	Aircraft Restricted Zone	5-12
5-7	Solar Pilot Plant System Availability Model	5-24
5-8	Collector Subsystem Availability Model	5-26
5-9	Thermal Storage Subsystem Availability Model	5-29
5-10	Coordinated Master Control Availability Model	5-39
5-11	Preoperational Function and Operational Testing Sequence	5-67
6-1	Collector SRE Site Plan	6-3
6-2	Heliostat, Stowed Position	6-4
6-3	Heliostat, Operational Position	6-4
6-4	Calibration Array Facing North, 9/27/76, Engineering Engineering Model Image	6-5
6-5	Engineering Model Open-Loop Tracking Results	6-7
6-6	Mirror Contour Data	6-9
6-7	Heliostat Assembly	6-11
6-8	Image Horizontal Centroid Track, South Site	6-13

6-9	Image Vertical Centroid Track, South Site	6-13
6-10	Calibration Array Output	6-16
6-11	Photocell Off-Axis Correction Curve	6-18
6-12	Predicted Atmospheric Attenuation Losses versus Range	6-20
6-13	Flux Density Measured on the Calibration Array	6-23
6-14	Optical Model Predicted Flux Density	6-24
6-15	Comparison of Predicted and Measured Flux Distribution	6-26
6-16	Comparison of Test Data with Optical Model - North Site	6-27
6-17	Comparison of Test Data with Optical Model - South Site	6-28
6-18	Comparison of Test Data with Optical Model - East Site	6-29
7-1	Solar Pilot Plant	7-2
7-2	Experimental Heliostat Assembly	7-3
7-3	Central Receiver	7-4
7-4	Ray Trace Flow Chart	7-10
7-5	Single-Heliostat Model	7-13
7-6	Basic Vector Triad	7-14
7-7	Single-Heliostat Model Program Flow Chart	7-16
7-8	Heliostat Vector Triads	7-18
7-9	Toe-In Strategy	7-19
7-10	Facet Surface Vectors	7-20
7-11	Final Mirror Normal Perturbation	7-21
7-12	Target Triad Definition	7-22
7-13	Vectors Necessary to Determine Target Hitpoint	7-24
7-14	Rerad Model Node Numbering	7-27

7-15	Rubber Model View Factor Algebra	7-37
7-16	Cavity Geometry for Shielded Cavity Case	7-37
7-17	Rerad Model Software Costs	7-38
7-18	Proof of Relationship Between View Factors	7-38
7-19	Spectral Distribution Curves Related to Sun	7-45
7-20	Pilot Plant Design Time Atmospheric Attenuation Losses	7-47
7-21	Wavelength Windows Relative to Solar Spectrum	7-50
7-22	Water Vapor Transmission	7-53
7-23	Heliostat Field Cells	7-56
7-24	Atmospheric Attenuation Losses for the Pilot Plant	7-58
7-25	Radiation Intensity Attenuation from Mirror to Target	7-58
7-26	Pilot Plant Model Flow Chart	7-60
7-27	Pilot Plant Distribution Flows for Transient Analysis Studies	7-65
7-28	Time-Dependent Factors in Pilot Plant Operations	7-66
7-29	Solar Pilot Plant Dynamic Simulation Functional Diagram	7-69
7-30	Collector Subsystem Model Flow Relationships	7-71
7-31	Solar Intensity versus Time Plots for Days 1 and 2 for Collector Subsystem Model	7-72
7-32	Solar Intensity versus Time Plots for Days 3 and 4 for Collector Subsystem Model	7-73
7-33	Typical Scenario for Transient Analysis Studies	7-75
7-34	Steam Generator Subsystem Concept Model Elements	7-77
7-35	Steam Generator Subsystem Controller Block Diagram	7-79
7-36	Functional Schematic of Electrical Generation Subsystem	7-81

7-37	Thermal Storage Subsystem Discharge Configuration	7-83
7-38	Master Control Subsystem Block Diagram	7-85
7-39	Power Flows Under Master Controller Direction	7-86

TABLES

<u>Table</u>		<u>Page</u>
2-1	Design Point Specifications	2-15
2-2	System Performance Requirements	2-15
2-3	Environmental Design Constraints	2-16
2-4	Pilot Plant Baseline Collector Subsystem Characteristics	2-24
2-5	Pilot Plant Receiver Tower Characteristics	2-28
2-6	Steam Generator Physical Characteristics	2-36
2-7	Pilot Plant Thermal Storage Subsystem Characteristics	2-40
2-8	Electrical Power Generation Subsystem Characteristics	2-43
2-9	Attemperator Flows and Outlet Steam Temperatures for Different Convection Loss Models	2-60
2-10	Thermal Storage Subsystem Heat Losses (100-Hour basis)	2-64
2-11	Thermal Storage Subsystem Baseline Characteristics Performance	2-64
2-12	Electrical Power Generation Subsystem Parameters	2-67
2-13	Pilot Plant Auxiliary Power Requirements	2-71
2-14	Pilot Plant Net Annual Energy Results	2-78
2-15	Pilot Plant Storage Losses	2-82
2-16	Field Layout Parameters	2-84
2-17	Feedwater and Steam Pipe Sizes and Materials	2-88
2-18	Tower Dimensions	2-88
2-19	Thermal Storage Design Parameters	2-94
2-20	Heater Design Data	2-97
2-21	100 MW(e) Cooling Tower Design Data (Marley Company)	2-104

2-22	Collector System Performance	2-107
2-23	Receiver Optical Losses	2-108
2-24	Receiver Thermal Losses	2-110
2-25	Auxiliary Power Requirements	2-114
3-1	Annual Performance Sensitivity to Insolation Model	3-5
3-2	Selected Field Layouts	3-20
3-3	Effect of Tower Location on Performance	3-51
3-4	Computer Results for Cone Mapping Runs	3-70
3-5	Four-Tower Design (TH = 219 m)	3-108
3-6	One-Tower Design (TH = 439 m)	3-108
3-7	12-Tower Design (Pilot Plant) (TH = 126 m)	3-108
3-8	Thermal Loss Due to Piping Lengths	3-109
3-9	Auxiliary Power Requirements	3-110
3-10	Commercial Plant Design Cost	3-111
3-11	Comparison of Performance Characteristics and Cost	3-117
4-1	Pilot Plant Operating Modes	4-4
4-2	Pilot Plant Cold Startup Sequence	4-13
4-3	Pilot Plant Diurnal (or Warm) Startup Sequence	4-14
4-4	Pilot Plant Storage Charge Startup Sequence	4-15
4-5	Pilot Plant Storage Discharge Startup Sequence	4-16
4-6	Pilot Plant Shutdown Sequence	4-17
4-7	Run Schedule for Solar Pilot Plant Dynamic Simulation Computer Results	4-19
4-8	Plant Startup Summary Results for Transient Analysis	4-29
4-9	Various Statistics for Metal and Steam Temperatures for Cloud Transient Run No. 303	4-54

5-1	Single- and Four-Facet Mirror Characteristics	5-7
5-2	Flux versus Slant Range for Four Facets	5-10
5-3	Thermal Storage Subsystem Component Failure Rates	5-31
5-4	Typical Power Plant Component Failure Rates	5-34
5-5	SGS and EGS Forced Outage Predictions	5-37
5-6	Solar Pilot Plant Scheduled Maintenance Requirements	5-40
5-7	Collector Subsystem Long-Life Support Equipment	5-48
5-8	Collector Subsystem Short-Life Support Equipment	5-49
5-9	Collector Subsystem Construction Equipment	5-50
5-10	Electrical Generation Subsystem Electrical Support Equipment	5-54
5-11	Electrical Generation Subsystem Control Support Equipment	5-55
5-12	Industry Codes and Standards	5-60
5-13	Leak Tightness Tests for Major Systems	5-63
5-14	Typical Electrical Construction Checks	5-65
5-15	Typical Electrical Preoperational Checks	5-69
5-16	Typical Electrical Initial Operation Checks	5-73
5-17	Preliminary Collector Subsystem Instrumentation List	5-82
6-1	Heliostat Location	6-2
6-2	Maximum Tracking Errors	6-12
6-3	Reflectances at Various Wavelengths for Two Samples of Mirror Obtained from Honeywell Avionics Division, St. Petersburg, Fla.	6-14
6-4	Power Balance Comparison	6-21

7-1	Error* in Net Cavity Efficiency Due to the Rubber Model (3/21 Noon)	7-40
7-2	Sensitivity Analysis Variables	7-43
7-3	Sensitivity Analysis Results for 3/21 Noon	7-44
7-4	Window Limits and Constants	7-52
7-5	Atmospheric Transmission Calculation	7-54

GLOSSARY

- Average cavity efficiency: The integrated annual absorbed energy including radiation, conduction, convection, and startup losses divided by the integrated annual energy into the cavity
- Average collection efficiency: The integrated annual energy into the cavity, including mirror reflectance and atmospheric attenuation divided by the usable energy
- Average net cycle efficiency: The integrated annual net electrical output divided by the integrated annual energy into the turbine
- Cosine-only field efficiency: The power which could be redirected after cosine losses divided by the total available power
- CS: Collector subsystem
- DNI: Direct normal intensity. Refers to solar radiation available at the ground.
- EGS or EPGS: Electric generation subsystem or electric power generation subsystem
- Facet or MM: Mirror module
- LOS: Line of sight
- PPPD: Pilot plant preliminary design
- Power into the cavity efficiency or overall tracking efficiency: The power into the cavity divided by the total available power
- SG or SGS: Steam generator or steam generator subsystem
- SPP: Solar pilot plant
- SRE: Subsystem Research Experiment
- Total available power: The total heliostat mirror surface area times the DNI

Tracking efficiency or redirected field efficiency: The redirected power divided by the total available power

TS or TSS: Thermal storage or thermal storage subsystem

Usable energy: Energy that is usable by the pilot plant (i. e. , that energy available after scheduled maintenance, high-wind tracking, and shut-down losses).

SECTION 1 INTRODUCTION

BACKGROUND

Supplies of most conventional fuels are being depleted rapidly. Consequently, it is necessary to identify alternate sources of energy and to develop the most promising to ensure availability when needed.

An alternative with great potential is the conversion of sunlight to energy. One aspect of this usage is generating electricity through solar energy. A goal of the national energy program is to demonstrate the technical and economic feasibility of a central receiver solar power plant for generating electricity. Pursuant to that goal, the Energy Research and Development Administration (ERDA), on 1 July 1975, awarded Honeywell Inc. a two-year contract for Phase I of such a program.

The initial program phase, which is the subject of this report, consisted of developing a preliminary design for a 10 MW(e) proof-of-concept solar pilot plant. The second phase will consist of building and operating the pilot plant and projecting the information gained to larger-scale plants. This phase is scheduled to be completed in the early 1980's. The third phase will consist of designing, building, and operating two 50-100 MW(e) demonstration plants. The final phase will consist of building and operating plants in the 100-300 MW(e) range.

PHASE I PROGRAM SCOPE

The Phase I program consisted of developing a pilot plant preliminary design by first developing a preliminary baseline design to meet specified

and assumed performance requirements. The baseline was then refined through analysis and experimentation, and evaluated by testing key subsystems, i. e., collector, steam generator, and thermal energy storage.

The complexity of the undertaking dictated a team approach to provide the technical and managerial skills required. The Honeywell team is identified in Figure 1-1.

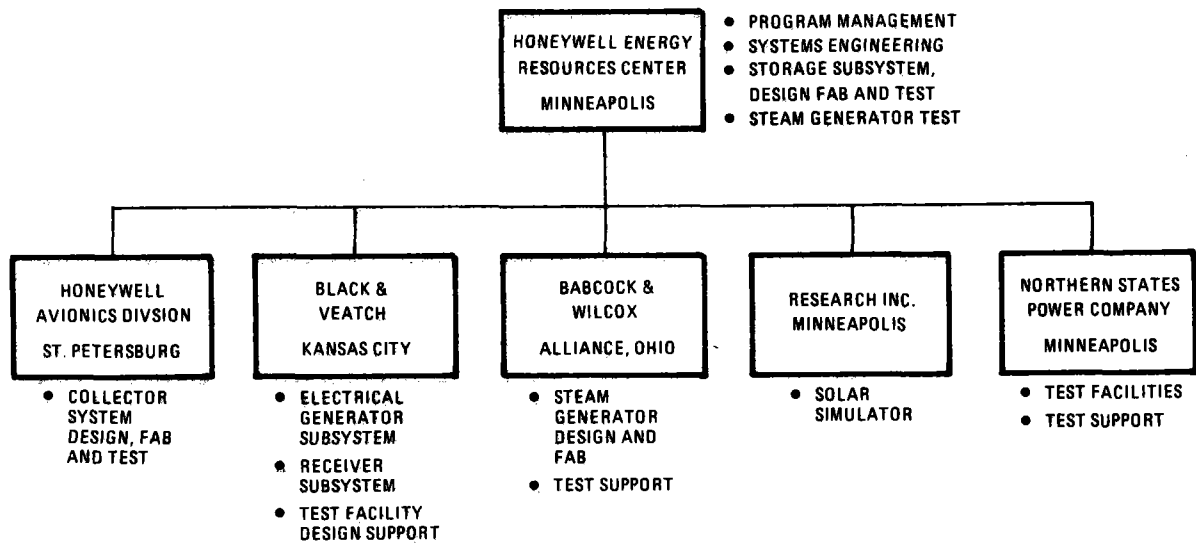


Figure 1-1. Honeywell Team for Phase I Solar Pilot Plant Program.

A unique feature of the test plan was the use of selected facilities of an operating power plant, Northern States Power's Riverside Plant in Minneapolis, Minnesota, to test the steam generator and thermal energy storage subsystems. An ERDA-directed change from latent heat (phase change) storage to sensible heat storage cancelled the storage portion of the test

plan. The steam generator was tested using a solar array to simulate the insolation required to generate steam. The collector subsystem hardware, one mobile and three stationary, full-scale, four-mirror units, was field tested for performance and reaction to operating environments at Honeywell's Avionics Division facility in St. Petersburg, Florida.

The information obtained from the subsystems tests was used to complete the pilot plant preliminary design, and to project performance and cost of a 100 MW(e) plant to facilitate long-range planning.

The chronology of the work done in Phase I is summarized in Figure 1-2.

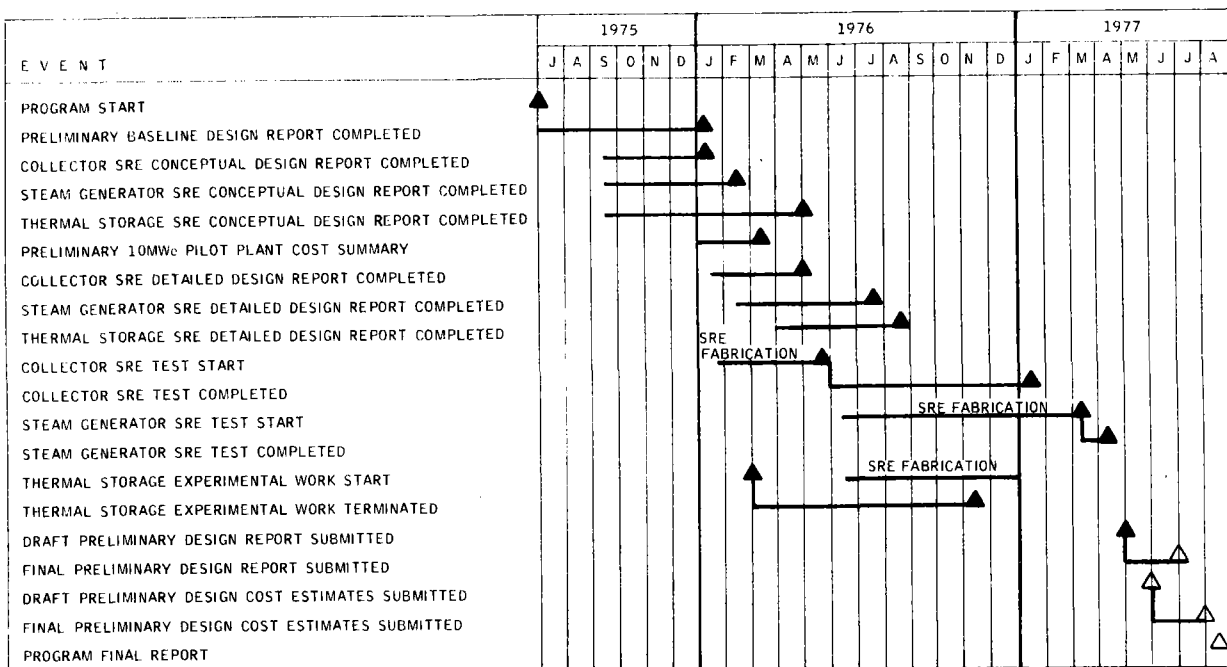


Figure 1-2. Chronology of Phase I Solar Pilot Plant Program

ORGANIZATION OF THE PRELIMINARY DESIGN REPORT

The preliminary design and supportive data resulting from the Phase I work are presented in seven volumes:

- I - Executive Overview
- II - System Description and System Analysis (3 books)*
- III - Collector Subsystem
- IV - Receiver Subsystem
- V - Thermal Storage Subsystem
- VI - Electrical Power Generation/Master Control Subsystems and Balance of Plant
- VII - Pilot Plant Cost/Commercial Plant Cost and Performance

Abstracts of volumes other than the one in hand and Volumes I and VII are on the following pages.

- *Book 2 is Central Receiver Optical Model Users Manual
- Book 3 is Dynamic Simulation Model and Computer Program Descriptions

ABSTRACTS

Vol. III - COLLECTOR SUBSYSTEM

The Honeywell collector subsystem features a low-profile, multifaceted heliostat designed to provide high reflectivity and accurate angular and spatial positioning of the redirected solar energy under all conditions of wind load and mirror attitude within the design operational envelope. The heliostats are arranged in a circular field around a cavity receiver on a tower halfway south of the field center. A calibration array mounted on the receiver tower provides capability to measure individual heliostat beam location and energy periodically. This information and weather data from the collector field are transmitted to a computerized control subsystem that addresses the individual heliostat to correct pointing errors and determine when the mirrors need cleaning. This volume contains a detailed subsystem design description, a presentation of the design process, and the results of the SRE heliostat test program.

Vol. IV - RECEIVER SUBSYSTEM

The Honeywell receiver subsystem design uses well established fossil technology and consists of a cavity receiver housing, a steam generator, a cavity barrier, piping, and a support tower. The steam generator absorbs the redirected solar energy from the collector subsystem and converts it to superheated steam which drives the turbine. The receiver is adequately shielded to protect personnel and equipment.

A cavity barrier is lowered at night to conserve heat and expedite startup the following day. This volume contains the subsystem design and methodology and the correlation with the design and performance characteristics of the SRE steam generator which was fabricated and successfully tested during the program.

Vol. V - THERMAL STORAGE SUBSYSTEM

The Honeywell thermal storage subsystem design features a sensible heat storage arrangement using proven equipment and materials. The subsystem consists of a main storage containing oil and rock, two buried superheater tanks containing inorganic salts (Hitec), and the necessary piping, instrumentation, controls, and safety devices. The subsystem can provide 7 MW (e) for three hours after twenty hours of hold. It can be charged in approximately four hours. Storage for the commercial-scale plant consists of the same elements appropriately scaled up. This volume contains a description of the subsystem design methodology and evolution and the subsystem operation and performance.

Vol. VI - ELECTRICAL POWER GENERATION SUBSYSTEM, CONTROLS, AND BALANCE-OF-PLANT

The Honeywell electrical power generation subsystem centers on a General Electric dual admission, triple extraction turbine generator sized to the output requirements of the Pilot Plant. The turbine receives steam from the receiver subsystem

and/or the thermal storage subsystem and supplies those subsystems with feedwater. The turbine condenser is wet cooled. The plant control system consists of a coordinated digital master and subsystem digital/analog controls. The remainder of the plant, work spaces, maintenance areas, roads, and reception area are laid out to provide maximum convenience compatible with utility and safety. Most of the activities are housed in a complex around the base of the receiver tower. This volume contains a description of the relationship of the electrical power generation subsystem to the rest of the plant, the design methodology and evolution, the interface integration and control, and the operation and maintenance procedures.

SECTION 2

SUMMARY SYSTEM DESCRIPTION

BACKGROUND

Historically, the socio-economic pressures of exponentially growing energy demand in a closed ecosystem have been alleviated through technological breakthroughs. As it stands, the present energy situation appears to have the basic dimensions of an ecocrisis; exponentially growing demand and diminishing returns. To this problem, the national response has been along four fronts:

- Energy conservation to slow down the exponential curve
- Increased use of base load coal and nuclear fission power plants to stabilize the supply
- Accelerated pursuit of technological breakthroughs in nuclear fusion to fundamentally change the nature of the ecosystem from one with finite resources to one with essentially infinite fuel
- Research and development of alternate energy sources such as solar thermal, solar electric, wind, ocean, and geothermal.

Studies in the early 1970s showed one of these alternate sources, namely, solar thermal to electric, to be feasible with present-day technology, thus avoiding a prolonged search for a breakthrough. The studies investigated a variety of concept configurations, such as distributed and central receiver systems using thermodynamic cycles from organic Rankine to closed-helium Brayton. For larger-scale, utility level, generation capacity of the central receiver system coupled to a water/steam Rankine-cycle conventional

turbogenerator emerged as the most promising concept primarily for the following two reasons:

- The high-temperature/pressure capabilities of the concept promised high conversion efficiencies at conventional power plant sizes without the piping cost penalties of the distributed concepts
- Preliminary cost estimates promised eventual economic viability as compared with conventional power sources for intermediate and peak load applications

The federal central receiver program that was initiated on the basis of the concept investigation studies is a multiphased effort that attempts to lead the technology from concept to commercialization. These phases are:

- Phase I - Pilot Plant Preliminary Design
Commercial Plant Conceptual Design
Subsystem Research Experiments
- Phase II - Pilot Plant Detailed Design
Commercial Plant Preliminary Design
Subsystem In-Situ Tests
- Phase III - Pilot Plant Build and Operate
Commercial Plant Detailed Design
- Phase IV - First Commercial Plant Build and Operate.

This volume of the final report contains the results of Honeywell's effort to perform the system definition for Phase I of the Central Receiver Program.

PHASE I GOALS AND REQUIREMENTS

The Phase I project goals must be understood within the framework of the total program and its final objective: commercial solar electric power. Each major Phase I project effort attempts to establish the fundamental technical and economic operative factors and relationships between the pilot plant and the first commercial plant as well as the nth solar power generating unit within a conventional network.

In detail, the pilot plant preliminary design effort had as its goal the specification of a plant that will demonstrate in operation the technical feasibility of a large-scale application. Furthermore, the pilot plant design must be such as to allow scaling up to the first commercial plant that has as its goal the demonstration of economic viability under utility operation.

Therefore, the pilot plant preliminary design has to be closely coupled to the commercial plant design, since their goals complement each other. In addition, the Subsystem Research Experiments (SREs) design, build, and test efforts of Phase I have to relate directly to the pilot plant goal of demonstrating technical feasibility. In a hierarchy of goals, the efforts then would appear as:

- Subsystem Research Experiments - Demonstrate technical feasibility at the subsystem level
- Pilot Plant - Demonstrate technical feasibility at the system level
- First Commercial Plant - Demonstrate economic viability at the utility network level

Within the overall effort constraint of using conventional hardware as much as possible, the pilot plant preliminary design effort attempts to synthesize

a configuration that, once implemented, will demonstrate technical feasibility and operating capability within the following envelope:

- Transient and periodic environmental conditions such as the solar insolation variation, the vagaries of weather, and earthquake disturbances
- Varying operational modes under different storage utilization strategies
- Emergency plant or network conditions

Within this framework, the design must attempt to resolve, upon implementation, such issues as diurnal startup and shutdown, response to cloud transients, overnight standby losses, scalability, safety, expected life time performance, grid interface, as well as maintenance and repair requirements. Furthermore, the design must be such as to allow the identification of the primary economic factors: capital investment requirements and bus bar costs as related to annual performance under different operating strategies.

CENTRAL RECEIVER SOLAR THERMAL POWER PLANT CONCEPT

The concept to be developed consists of four subsystems as shown in Figure 2-1. The collector subsystem consists of a field of heliostats and the control necessary to redirect the solar insolation onto the receiver. The receiver subsystem consists of heat-transfer surfaces for transferring the reflected incident energy to a heat-transfer fluid; a tower to support the heat-transfer surfaces at an elevated position; heat-transfer fluid plumbing for accepting low-temperature fluid from and transporting high-temperature fluid to the heat engine in the electric power generation subsystem or the thermal storage subsystem; necessary environmental protection; and the control elements necessary for efficient operation. The

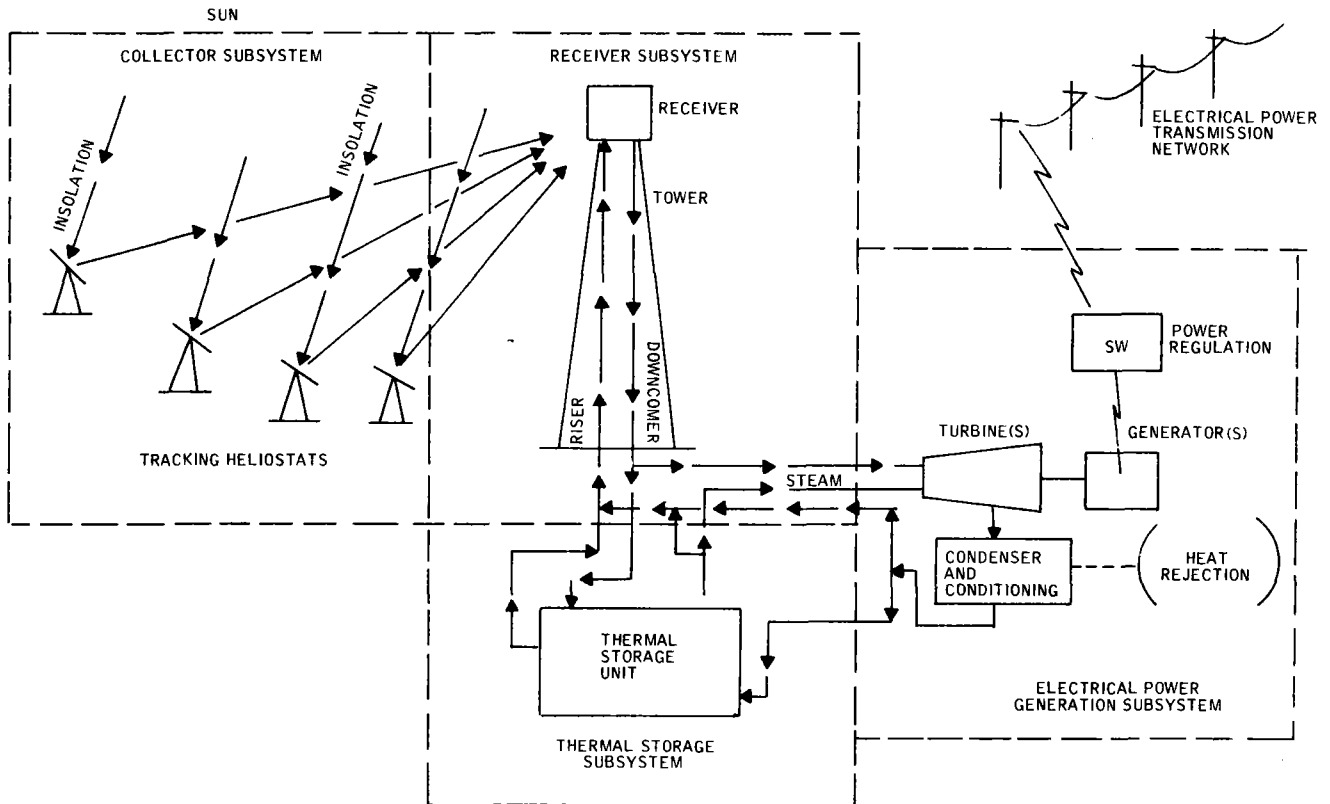


Figure 2-1. Central Receiver Solar Thermal Power Plant Concept

electric power generation system consists of the heat engine which converts the heat-transfer fluid thermal energy to mechanical energy for driving an electrical generator; the electrical generator which supplies electricity for powering the plant auxiliary equipment and for supplying an utility electric grid to meet consumer electric power demands; a heat-ejection system to increase the thermodynamic cycle efficiency; condensate feedwater pumps, feedwater heaters, deaerators, and associated plumbing necessary for accepting heat-transfer fluid from or delivering to the storage and receiver systems; supply for auxiliary, with uninterruptible power to all subsystems, master plant control; and balance-of-plant equipment such as buildings, support equipment, service facilities, power distribution facilities, heat-transfer

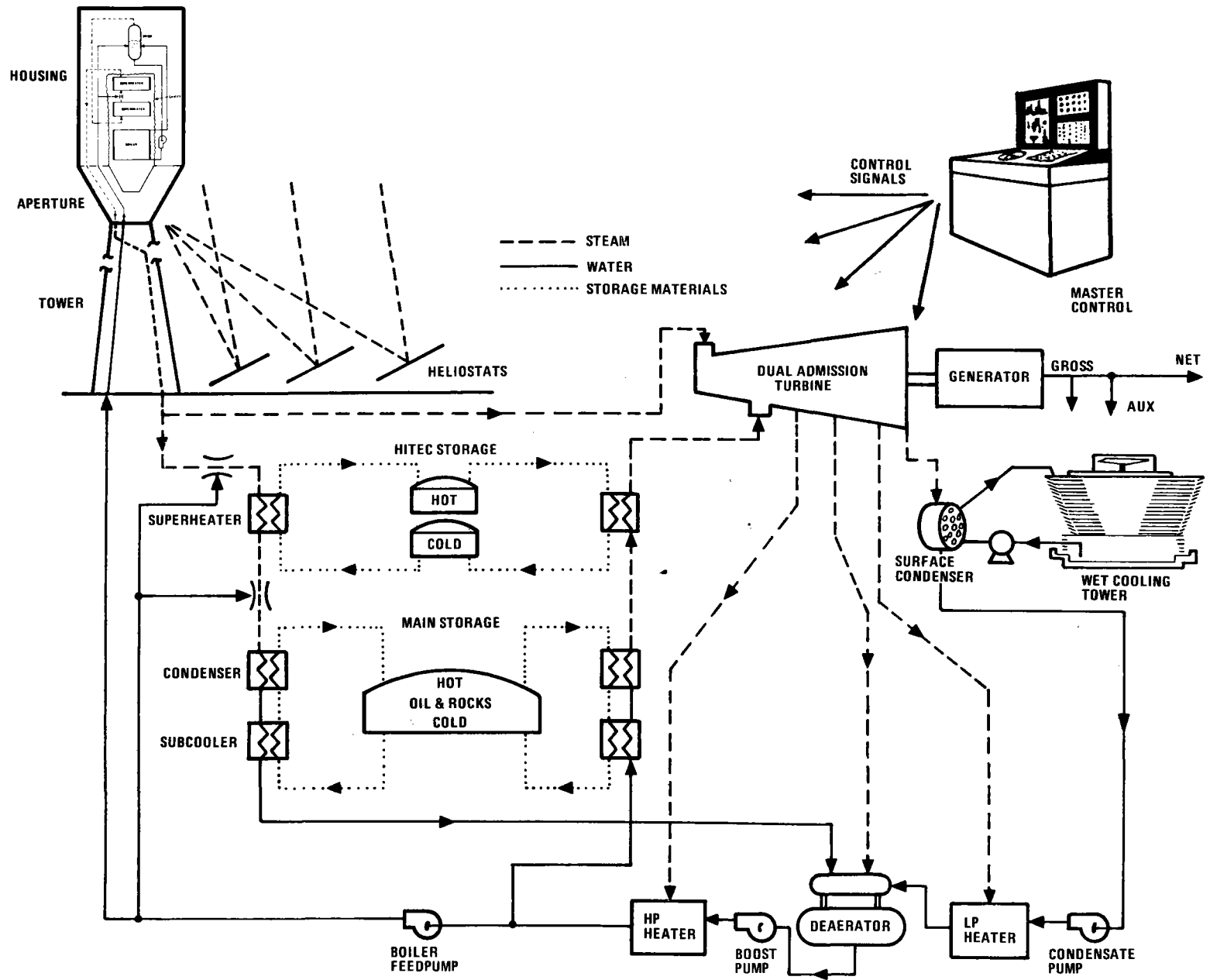
fluid conditioning equipment, etc. The thermal storage subsystem consists of tanks for containing the storage media, heat exchangers, pumps, plumbing and control necessary for accepting the heat-transfer fluid from the receiver to charge the storage media and control necessary to condition the heat transfer fluid for delivery to the heat engine during discharge of the storage media.

PILOT PLANT PRELIMINARY DESIGN

The pilot plant consists of the collector, receiver, storage, and electric power generation subsystems. The electric power generation subsystem contains the balance-of-plant equipments, structures, and plant master control. The preliminary design is shown schematically in Figure 2-2. The physical arrangement of the total plant is shown in Figure 2-3. A major characteristic of the design is the circular collector field with the receiver, storage, and electric power generation subsystems located in a clear area of the collector field one half of the field radius south of the field center. The arrangement of the central plant area is shown in Figure 2-4.

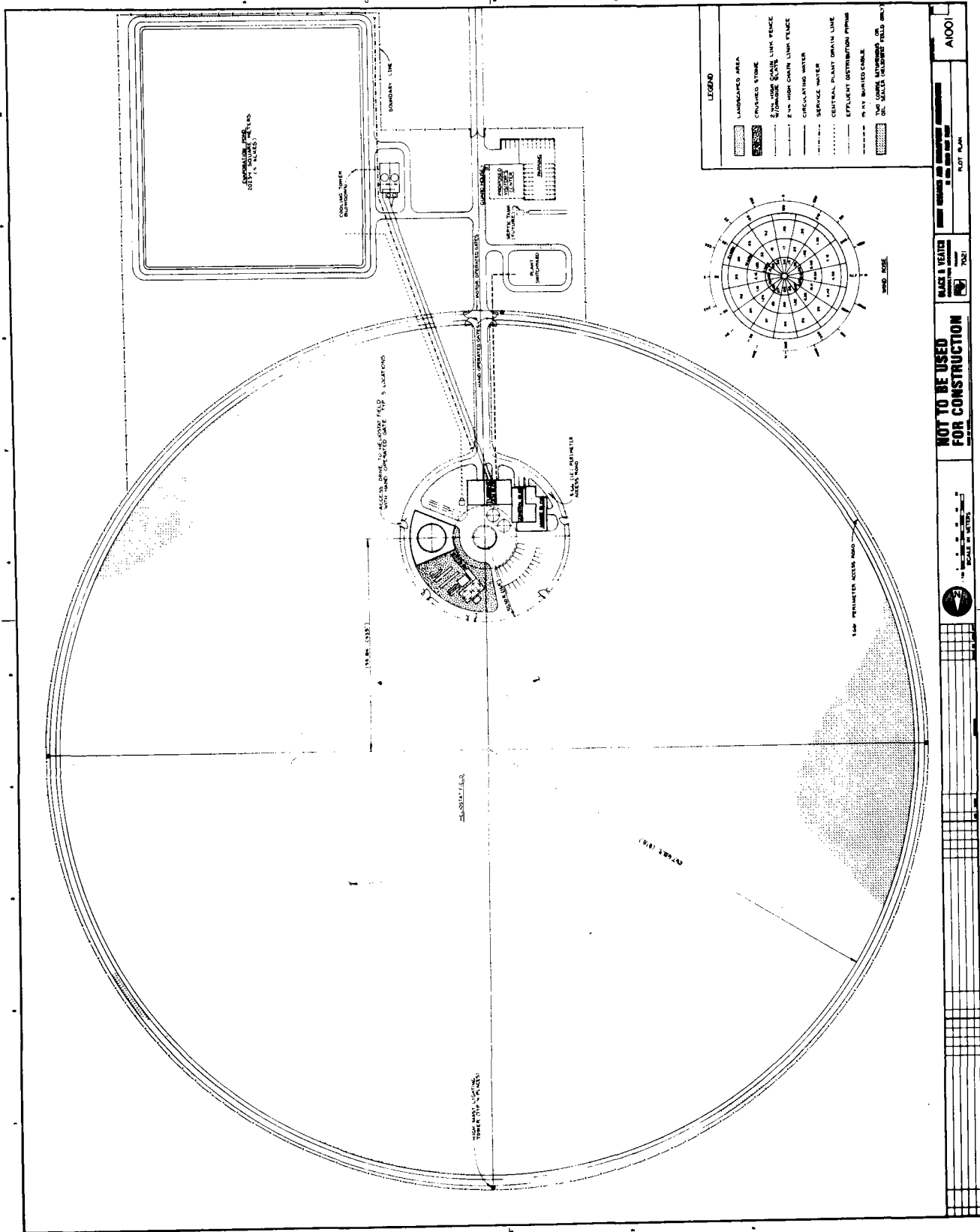
The collector field consists of 1598 heliostats each having four facets or mirrors. The collector field redirects the solar energy into the receiver cavity as shown in Figure 2-5. The four mirrors are spherical-surfaced and focussed at a point equal to the maximum field slant-range from the heliostat to the cavity aperture. The four facets on each heliostat are angularly adjusted to form one image at the aperture. This angular adjustment is made on the heliostat in the field and the amount is dependent on the individual slant range. The redirected solar energy is introduced into the inverted cylindrical, closed-top cavity. The cavity is lined on the cylindrical surfaces with the heat-absorbing surfaces of the steam generator. The cavity top does not contain heat-absorbing surfaces. The top is

40703-II



2-7

Figure 2-2. Pilot Plant Schematic



A1001

NOT TO BE USED FOR CONSTRUCTION

DATE & YEAR

SCALE

NOT TO BE USED FOR CONSTRUCTION

DATE & YEAR

SCALE

NOT TO BE USED FOR CONSTRUCTION

DATE & YEAR

SCALE

NOT TO BE USED FOR CONSTRUCTION

DATE & YEAR

SCALE

NOT TO BE USED FOR CONSTRUCTION

DATE & YEAR

SCALE

NOT TO BE USED FOR CONSTRUCTION

DATE & YEAR

SCALE

NOT TO BE USED FOR CONSTRUCTION

DATE & YEAR

SCALE

Figure 2-3 Pilot Plant

40703-II

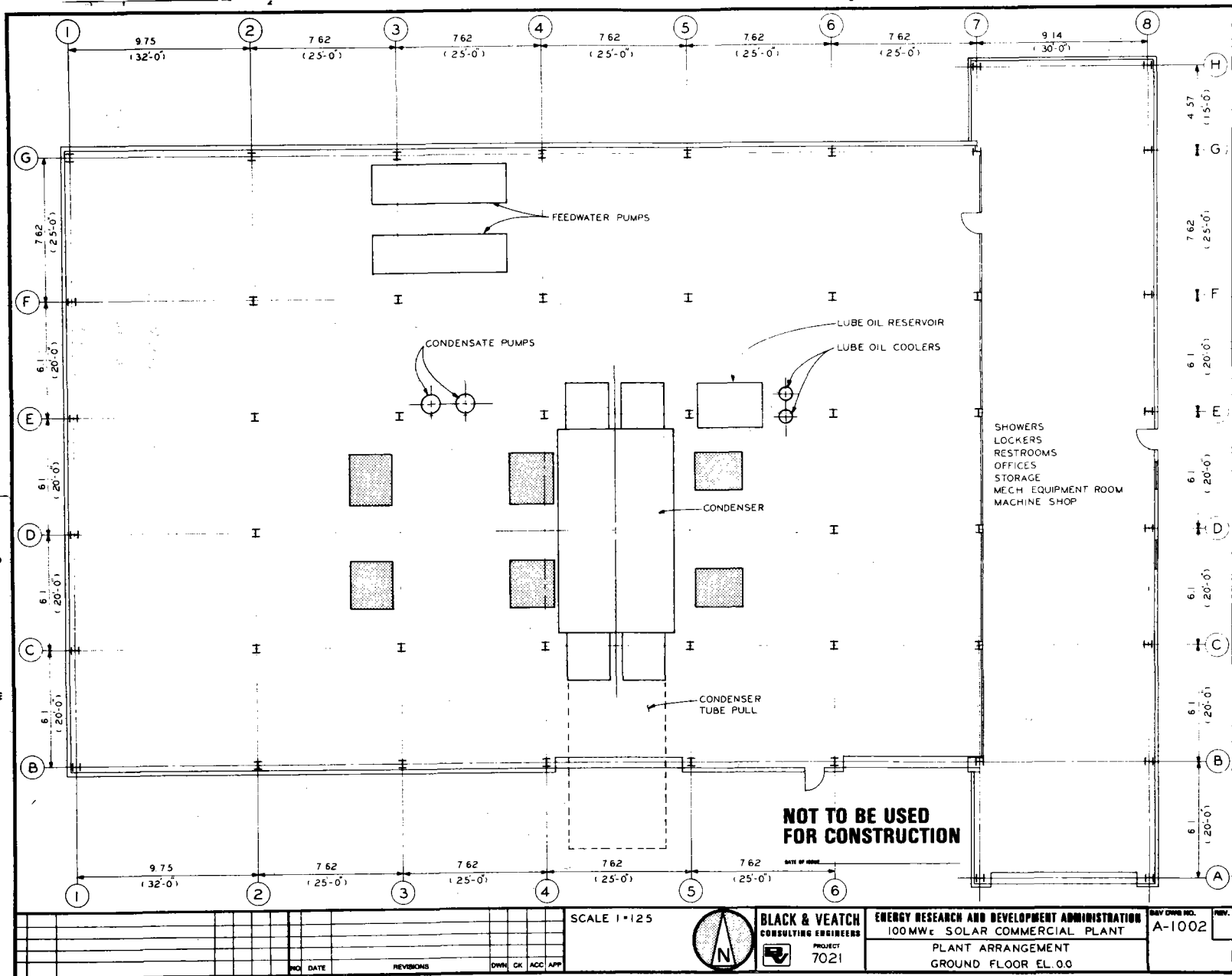


Figure 2-4. Plant Arrangement

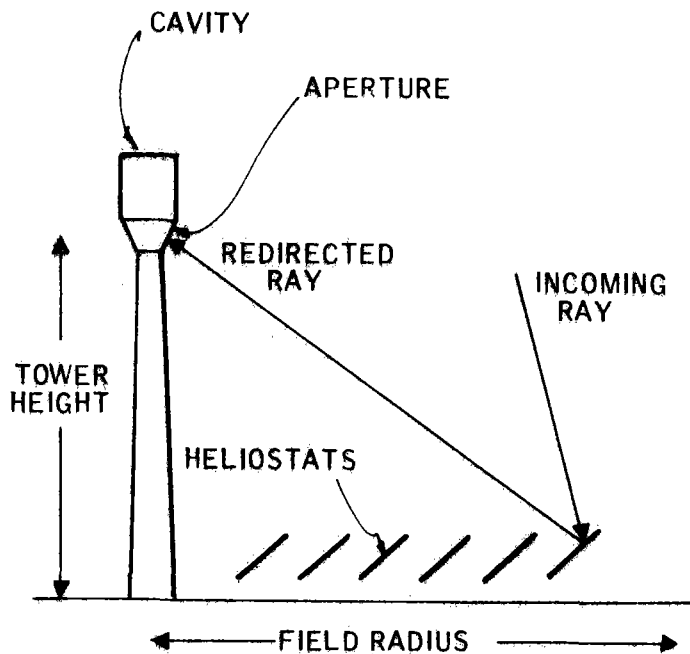


Figure 2-5. Collector/Receiver Interface

movable and is lowered to close the aperture (opening for admitting redirected flux) during periods of no solar insolation – extended cloudy periods or during the night. The aperture is closed to prevent excessive cooldown rates of the steam generator during periods of inoperation, thus permitting rapid startup after down times. The cavity is mounted on the receiver tower supported by three corbels. These corbels maintain the housing and top of tower separation required for the aperture. Steam from the receiver subsystem is used to power the turbine or to supply thermal energy for storage in the thermal storage subsystem.

The thermal storage subsystem stores thermal energy in two stages: a high-temperature stage which is later discharged for supplying superheated steam to the turbine, and a low-temperature stage which is used for preheating and boiling the water prior to admission to the superheater. The thermal energy is stored as sensible heat. Salt material is used in the high-temperature

stage, and an oil and rock material is used in the low-temperature stage. The storage material in both stages is pumped through the heat exchangers for absorbing energy from the receiver steam during charging and for releasing energy to the water during discharging.

The electric power generating system consists of a dual-admission turbine, generator, condenser, regenerative reheaters, and auxiliary plumbing and equipment necessary for supporting the cycle. The turbine is a dual-admission type which accepts steam from the receiver at the throttle and/or steam from the storage subsystem at the secondary admission port.

The operation of the collector, storage, receiver and electric power generation subsystems is controlled by a master controller which commands the individual subsystems to permit proper plant operations to meet the electrical output demands from the electric grid.

COMMERCIAL PLANT PRELIMINARY DESIGN

The commercial plant configuration is shown in Figure 2-6. This plant consists of four independent receiver and collector field subsystems, each supplying one-fourth of the required thermal energy. These four receiver/fields are connected in parallel to furnish absorbed energy to the turbine and storage subsystems located at the centroid of the four towers as shown in Figure 2-7. The four receiver/fields are scaled version of the pilot plant as are the single storage and electric power generating systems.

DESIGN REQUIREMENTS

The Central Receiver Solar Thermal Power Plant requirements are classified into three groups. These are performance requirements, design point

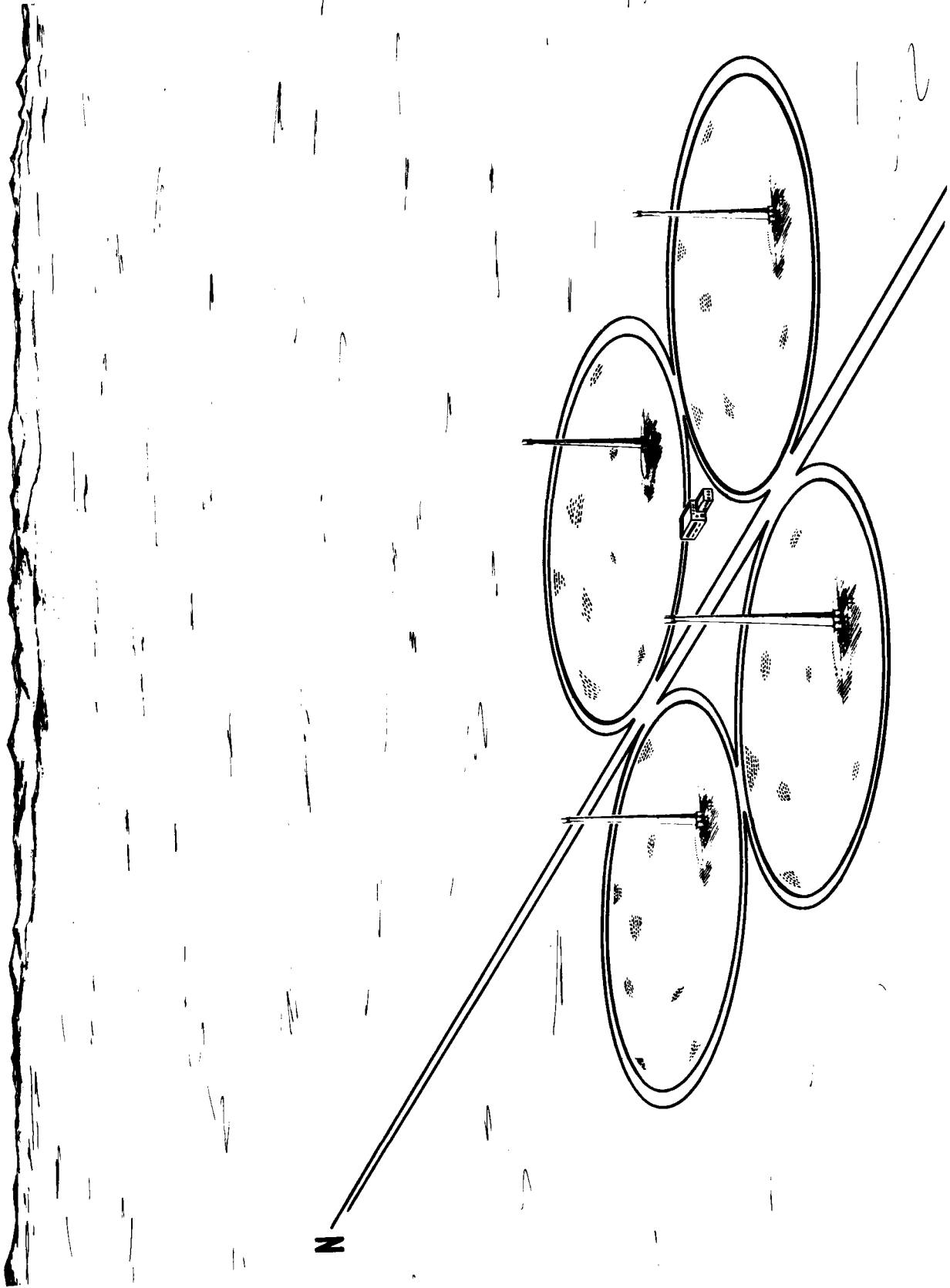
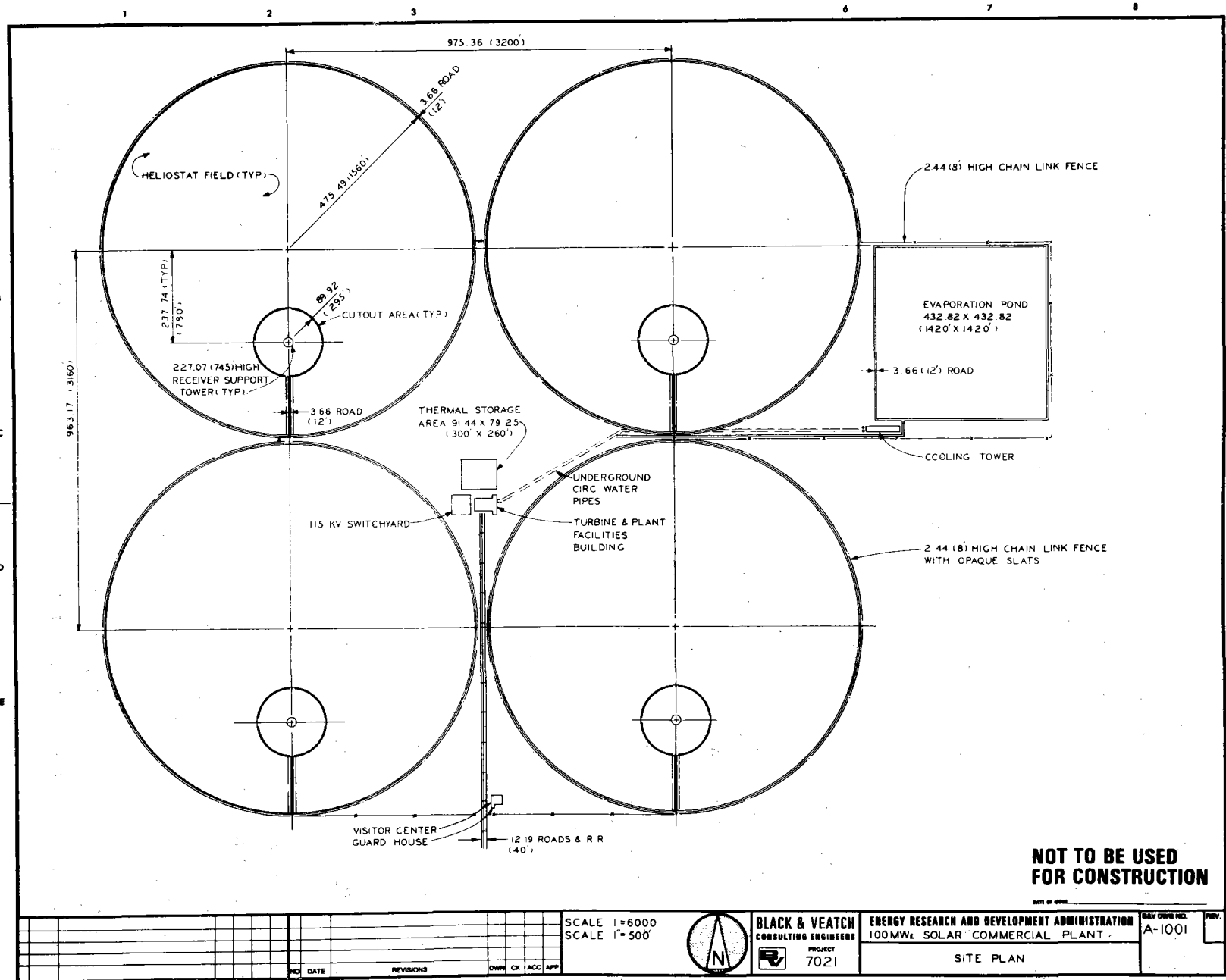


Figure 2-6. Commercial Plant Conceptual Design

40703-II



2-13

Figure 2-7. Site Plan

identification (for specifying a design performance input base), and environmental performance constraints. These requirements are summarized below for both the pilot plant and the commercial scale plant (complete identification of ERDA specifications and requirements is found in Appendix B, along with the plant characteristic affected):

- Design Point Specifications are comprised of specific design time of year and day along with meteorological data. Performance requirements are met under these plant input and weather conditions. The design point is specified in Table 2-1 for the pilot and commercial plants.
- System Performance Requirements are summarized for the pilot and commercial plants in Table 2-2.
- Environmental Constraints include items such as operational wind speeds, temperatures, storm damage criteria, etc. These environmental specifications are listed in Table 2-3 for the pilot and commercial plants.

PILOT PLANT SUBSYSTEM DESCRIPTIONS

Collector Subsystem Description

The heliostat and its control system is called the collector subsystem. The heliostat is a four-faceted, tilt-tilt reflector which redirects the sun light to the receiver. The control system consists of a control computer, calibration array, and miscellaneous equipment.

Heliostat -- The heliostat, shown in Figure 2-8, is the heart of the collector subsystem. The heliostats provide the angular and spatial positioning of the

Table 2-1. Design Point Specifications

Specification	Pilot Plant	Commercial
Design time	12/21, 2 p. m.	3/21, noon*
Dry-bulb temperature	28°C	28°C
Wet-bulb temperature	23°C	23°C
Direct normal insolation	950 W/m ²	950 W/m ²
Wind speed	3.5 m/s at 10 m height	3.5 m/s at 10 m height

* The best sun angle for the collector field

Table 2-2. System Performance Requirements

Performance Characteristic	Pilot Plant	Commercial
Net plant output at design point:		
Receiver steam	10 MW(e)	100 MW(e)
Storage steam	7 MW(e)	70 MW(e)
Solar multiple	- - -	1.7
Storage capacity	131.1 MWh(th)*	961 MWh(th)*
Maximum storage charge rate from receiver	37.7 MW(th)**	247.3 MW(th)***
Storage discharge rate to turbine	To produce: 7 MW(e) net	To produce: 81.5 MW(e) net***
Plant lifetime	30 years	30 years

* Designed to provide storage steam required for 7 MW net electrical output for 3 hours after a 20-hour hold.

** Specification given to be at least 30 MW(th).

*** 50% of the design point thermal power from the receiver at the entrance to the thermal storage.

**** Maximum discharge rate.

Table 2-3. Environmental Design Constraints

Constraint	Pilot and Commercial Plants
Wind speed:	
Operational	13.5 m/s
Survival	40.0 m/s
Temperature (Operational)	-30°C to +50°C
Humidity	Operational without permanent damage
Dust	Operational without permanent damage
Hail	Survival without damage (20 mm dia. at 23 m/s)
Lightning	Survival with repairable damage
Earthquake	UBC Zone 3, NRC Reg. Guide 1.60. 0.25 g horizontal and vertical SSE
Rain	75mm max/24 hr operational with no permanent damage
Snow	250 Pa loading operational with no permanent damage

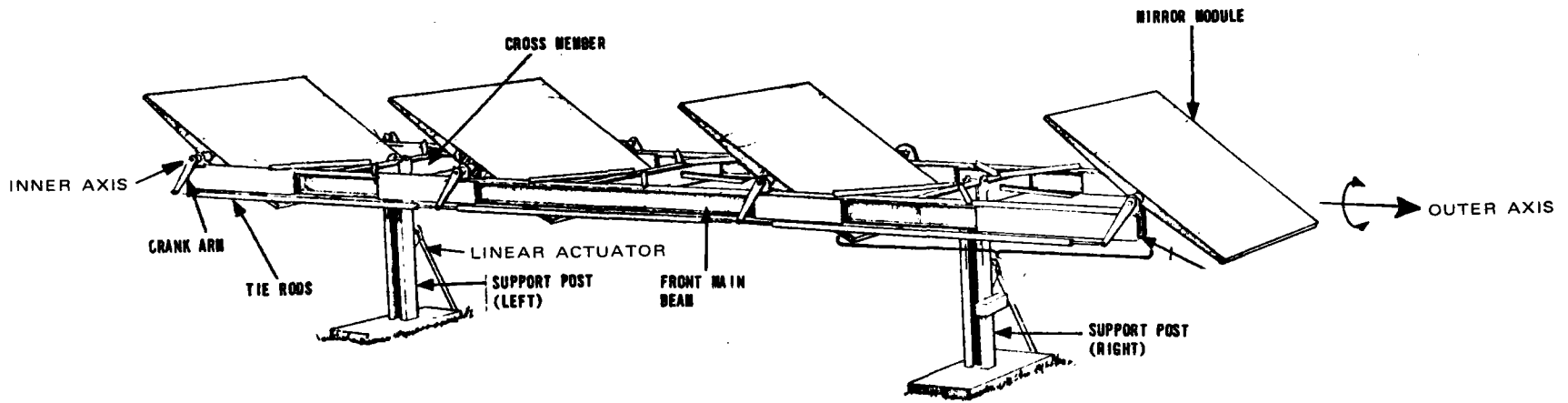


Figure 2-8. Pilot Plant Heliostat

reflected energy onto the receiver. Each heliostat consists of four facets (mirrors), each 10 m^2 with a focal length of 418 m. The facets are composed of an aluminum honeycomb sandwich panel with steel faces and two hubs for the axle (inner rotational axis). The proper contour, for focussing, is achieved by machining an auxiliary surface bonded to the face of the sandwich. A second surface float glass mirror is then attached to each facet.

Each heliostat will be aligned so that each facet is aiming to a preselected point on the receiver aperture. This is done by toeing-in the outer facets slightly more than the inner facets. This alignment will be done for every heliostat in the field.

The heliostats track the motion of the sun to keep the reflected image on the receiver. Tracking is accomplished by rotation of the heliostat frame around the outer axis and the mirror facets about the inner axis. This movement is accomplished by motors operating two ball screw linear actuators for the outer axis and a motor acting on crank arms on each mirror connected to the motor through tie rods. The motors, along with the control electronics on the heliostat, are powered by a d-c battery trickle-charged from the d-c power grid in the field. With this method, power is still available to stow the heliostat in case of a prolonged power failure.

There are 1598 heliostats in a field of 265.7-m radius with a 50-m radius cutout located one-half south of field center. They are nonuniformly packed with an average ground cover (mirror area/field area) of 0.29. That field layout is shown in Figure 2-9.

Control System -- The control system consists of a control computer calibration array and miscellaneous equipment to ensure proper operation of the subsystem.

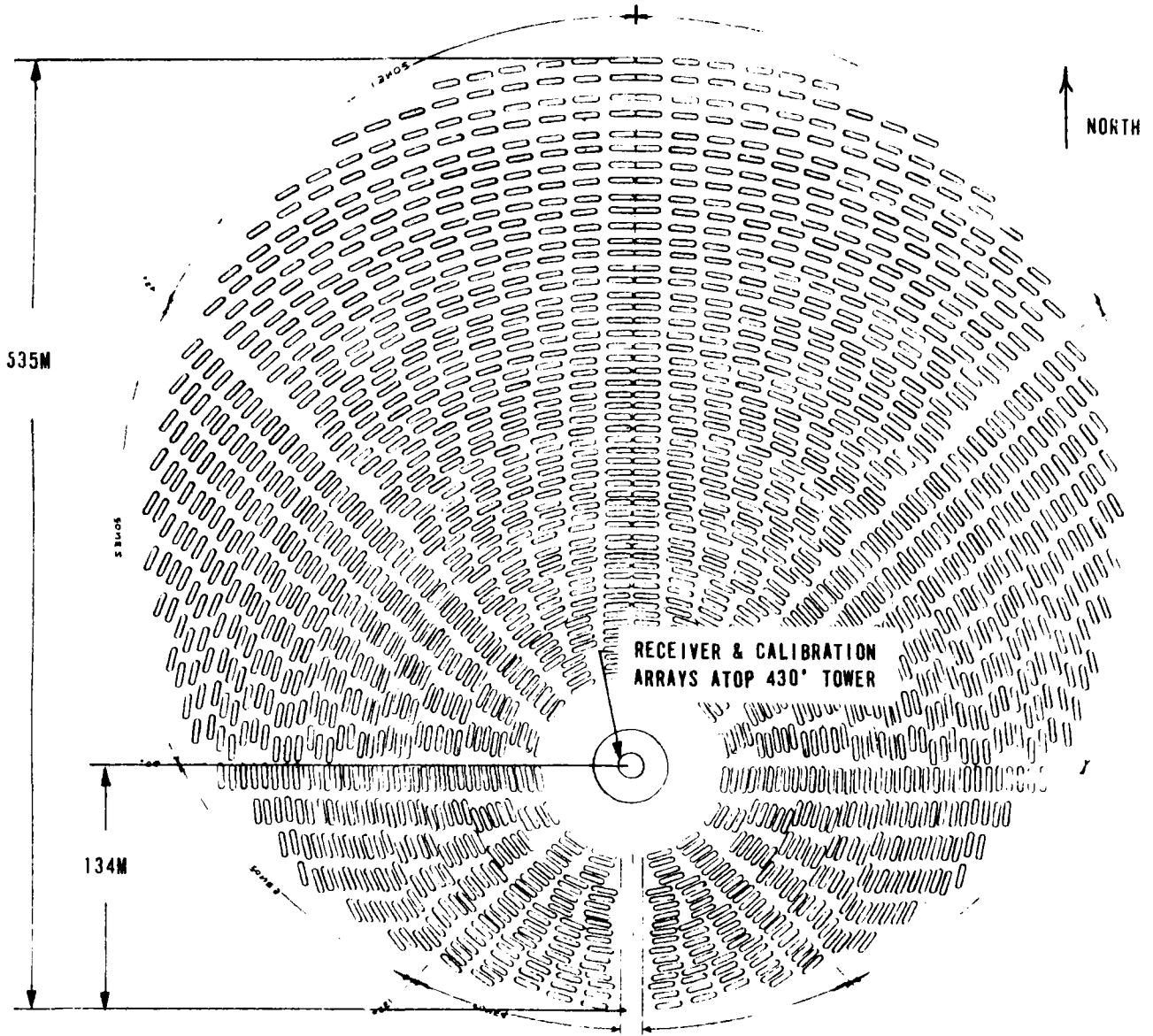


Figure 2-9. Collector Subsystem Tower One-Half South Field Layout

The control computer is the heart of the control system. Using WWV as a timing reference, the computer calculates the time-dependent sun position at 1-second intervals from which gimbals-angle tracking information is computed for all of the field heliostats. As required to maintain track, updates in the form of incremental gimbals-angle step commands, are sent from the computer to the field heliostats. Data are transmitted in serial digital fashion over 18 buried twisted shielded lines.

At the heliostat, the information from the computer is received by the heliostat electronics which decode the data and execute the requested gimbals commands. Gimbals updates can be one-step or 15-step increments. A step is a gimbals drive motor shaft revolution which corresponds to 81 arc-seconds of gimbals travel. One-step commands are used for fine tracking, while 15-step commands are used for controlled speed slewing. All the information for a complete two-axis update is contained in a single eight-bit command word. In the tracking mode, the computer can command the re-directed beam to track the receiver aperture, or any number of secondary targets which can simply be points in space if desired.

In addition to the tracking mode just described, the computer can also command the heliostat to initialize. Initialization provides the means to drive the two heliostat gimbals to known reference positions. It is used to re-establish known gimbals positions (mirrors level glass down) in the computer should they for some reason become lost. All the hardware for the initialization is contained at the heliostat. Initialization is commanded by the setting of a single bit in the command word. The heliostat also contains communications and power line monitors which will automatically initiate a stow (mirrors level, glass down) maneuver should interruptions occur for a sufficiently long time period.

The calibration array is used to make periodic measurements on the re-directed beam. By commanding the re-directed beam to the calibration

array and reading out the array's photodetectors, the computer determines differences between the predicted and measured positions of the beam and makes appropriate corrections. This information is accumulated to help identify possible variations in long-term effects, such as foundation drift, and is used to help predict when washing may be required. Array data are multiplexed to the computer over a twisted shielded pair. Figure 2-10 is a block diagram of the control scheme.

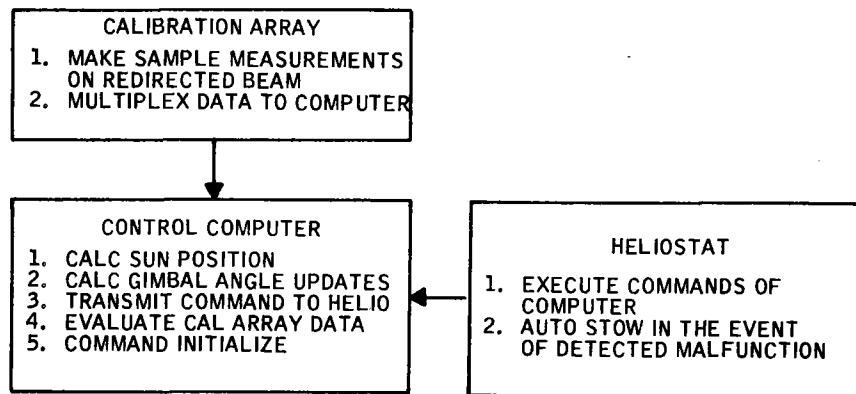


Figure 2-10. Control Scheme

The computer command control scheme which Honeywell has configured for the pilot plant and commercial plant preliminary design consists of a Honeywell Level 6/43 computer providing commands to all heliostats in the given field. These computers have the capability to address more than 25,000 heliostats simultaneously while at the same time performing numerous calculations of sun position and pointing direction as well as compensation for fixed known errors. Part of a system known as distributed processing, the computer design provides a fail-safe design when supplied with uninterruptible power.

Calibration Array -- The calibration array is an array of sensors mounted to a gridwork of a support structure. This array is used to determine the centroid of the "spot" which is defined to be the center of the beam of reflected light. The device was designed and built during the SRE and

has performed well. This calibration array approach has provided capability to accurately measure both beam location and amount of energy in the beam. In the pilot and commercial plant designs, the calibration arrays will be mounted on top of the towers and will be used to correct minor pointing errors as well as to determine when mirrors need washing.

Miscellaneous Equipment -- Operation of the pilot and commercial plants requires some knowledge of the weather and solar radiation. To provide this data, a number of remote weather stations will be provided, located in the collector field. These stations transmit data back to the computer and control room. The data are used to decide when to stow the heliostats as well as to determine effects of insolation passing through the atmosphere (i. e. , refraction, attenuation, and scattering). Cloud data permit control of the plant in the presence of clouds blocking certain sections of the field causing changes in the heliostats to become necessary.

The preliminary design provides an operator's console which permits the operator to control the collector subsystem. The console contains miscellaneous switches and a CRT display which is used to display data and performance information from the computer. The console also provides alarms (e. g. , audible buzzers and flashing lights) to cue operator action.

Subsystem Characteristics -- The overall pilot plant collector subsystem is shown in block diagram form in Figure 2-11, followed by Table 2-4 summarizing the collector subsystem characteristics. The block diagram shows the functional interfaces that are associated with the control and heliostat portions of the collector subsystem.

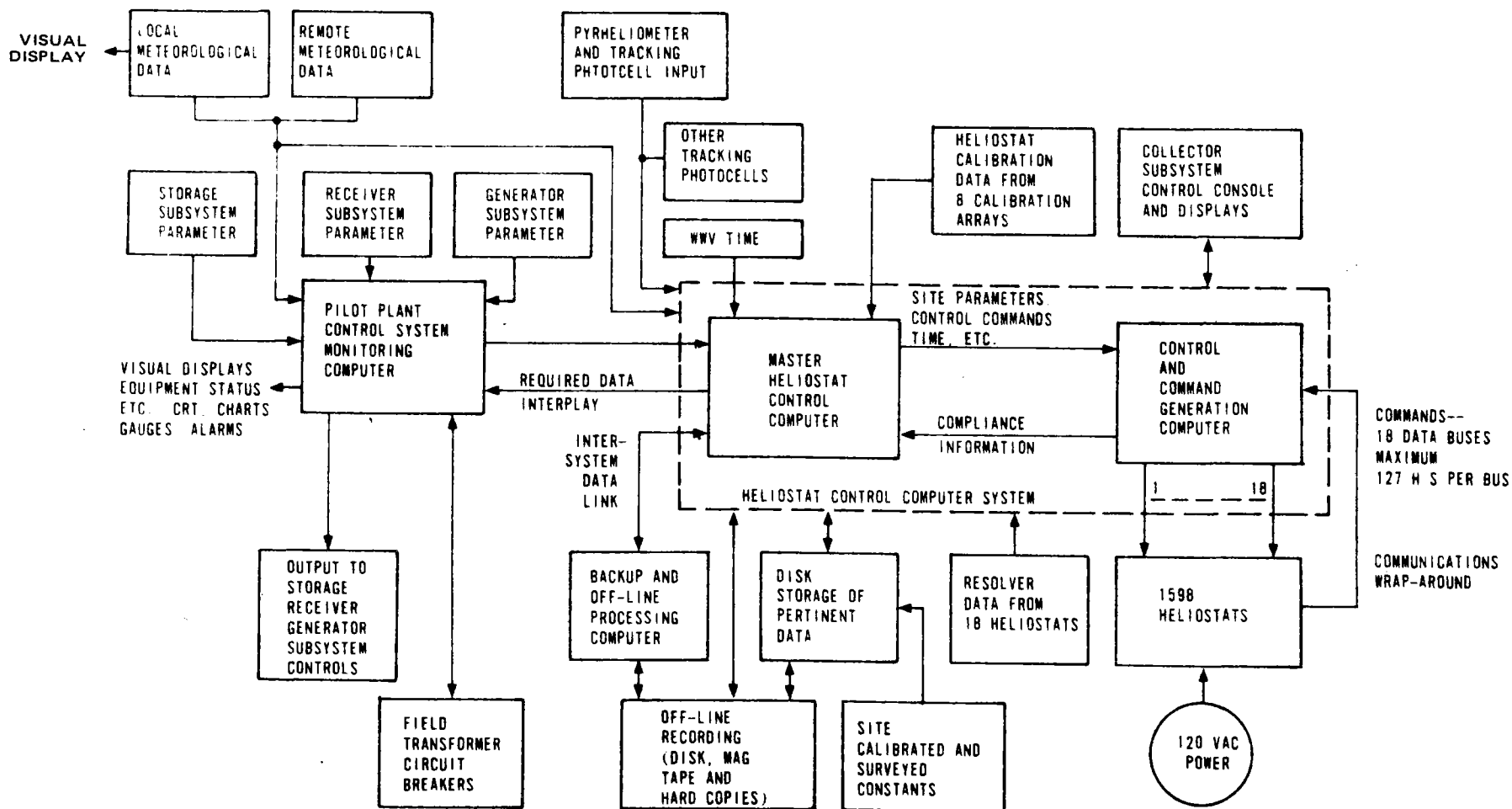


Figure 2-11. Pilot Plant Collector Subsystem Block Diagram

Table 2-4. Pilot Plant Baseline Collector Subsystem Characteristics

Characteristic	Baseline Value
Direct solar radiation (design point)	0.95 kW/m ² , 12/21 1400 hr, 37.50 deg N. lat
Ground cover	Nonuniform, 0.29 mirror/field ratio (avg)
Field layout	Polar, tower 1/2 field radius south of center
Heliostat orientation	Outer axis normal to radial
Facet size	10 m ² , 3.048 m x 3.281 m
Facet spacing	5.08 m
Heliostat weight	6348 kg
Facets per heliostat	4
No. of heliostats	1598
Field outer radius	267.5 m
Field inner radius (plant radius)	50 m
Reflectivity	0.90 clean
Total mirror area	63,920 m ²
Tracking accuracy	1 mr, 1 σ optics 2 mr, 1 σ /axis
Slew rate	23°/hr normal max 1080 deg/hr calibration and emergency
Return to storage time	15 min max

Receiver Subsystem Description

The receiver subsystem consists of the tower, housing, steam generator, and the associated plumbing required to transport feedwater to and steam from the steam generator.

Tower and Receiver Housing -- The tower as illustrated in Figure 2-12 is constructed of concrete and is erected using the "slip form" technique. It is supported on a foundation and has three corbels at the top to support the steam generator and cavity housing. The corbels support the housing above the tower top to form the aperture for admitting the redirected solar energy from the collector field onto the cavity walls which are lined with the heat-absorbing surfaces of the steam generator. Areas around the cavity are covered with heat shields to protect the concrete and metal surfaces from spilled radiation about the aperture.

Details of the housing interior are shown in Figure 2-13. The support for the steam generator is constructed between the vertical corbel extensions, and the outside is covered with an environmental-protective covering. Walkways are provided within the corbels and through the steam generator supporting structure, permitting personnel access to all points. The housing is ventilated by forced air which enters through grills on the housing side. The calibration array (for the heliostats) is mounted near the top of the tower. Characteristics of the tower and housing are shown in Table 2-5.

Steam Generator -- The steam generator consists of a pump-assisted recirculating drum boiler with two superheaters and a spray attenuator for controlling steam temperature (Figure 2-14). Feedwater is piped into the steam generator drum. Slightly subcooled water flows from the drum, through a downcomer, and is pumped through the boiler supply line to the boiler section.

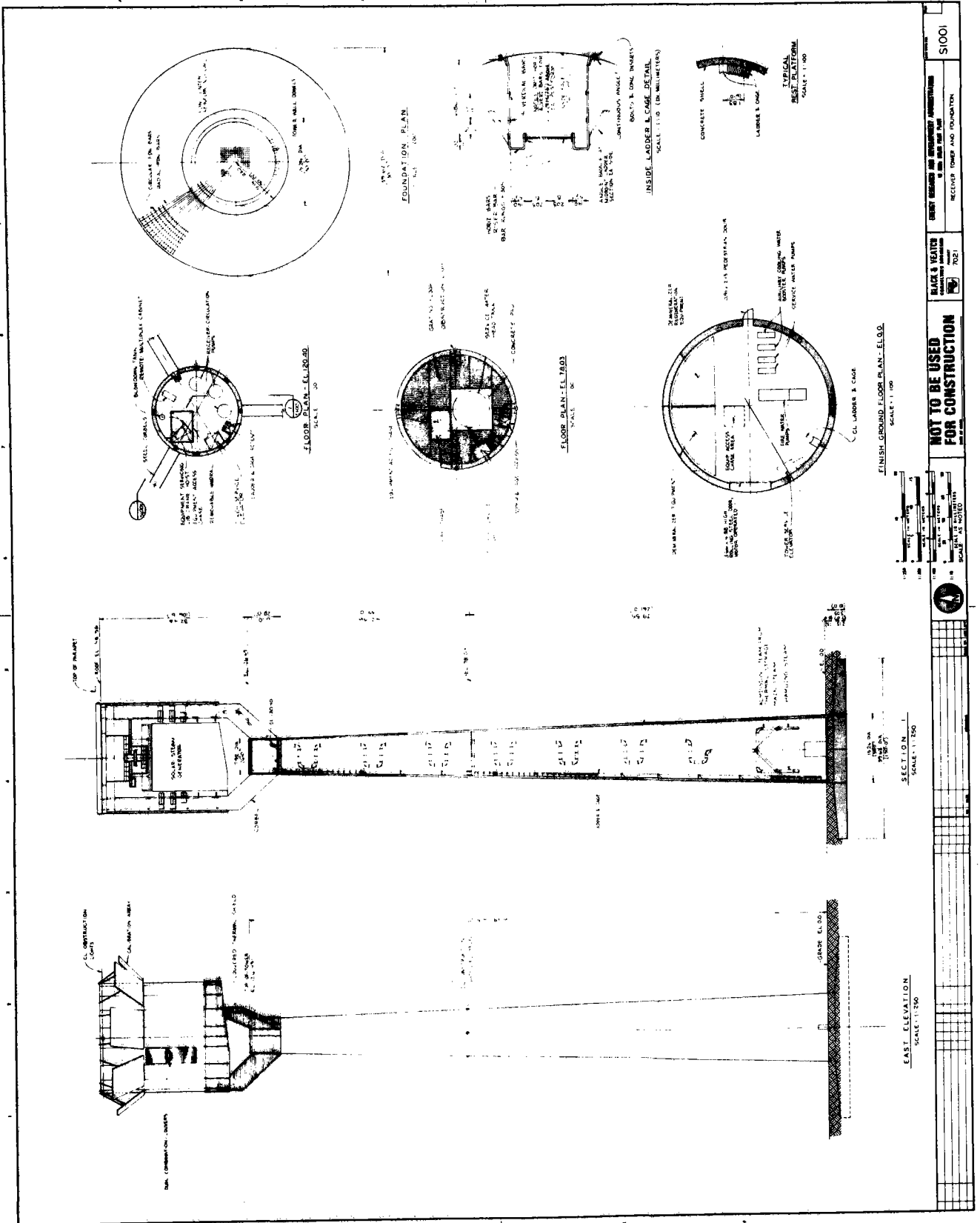
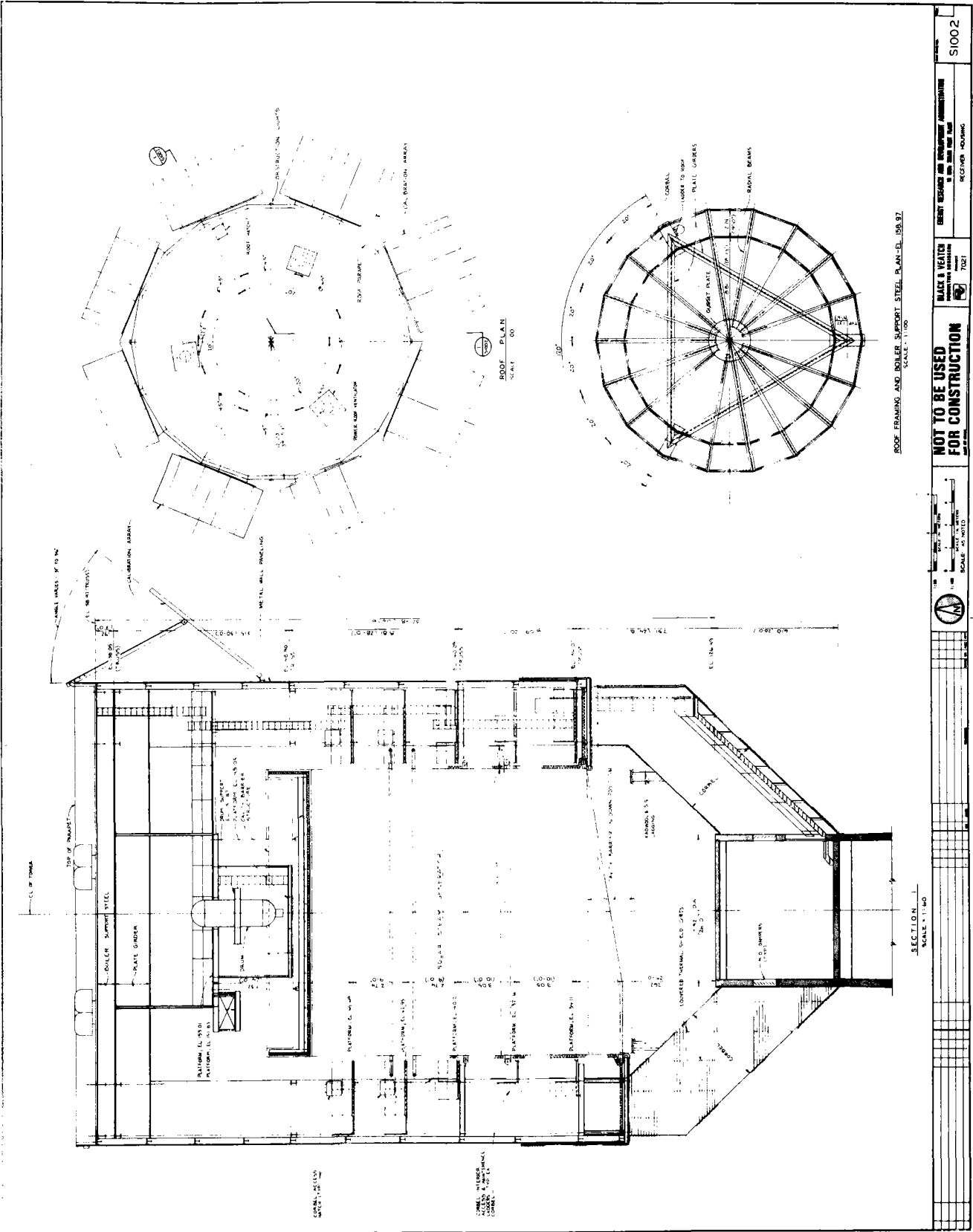


Figure 2-12. Receiver Tower and Foundation



<p>NOT TO BE USED FOR CONSTRUCTION</p>		<p>BLACK & VEATCH ENGINEERS ARCHITECTS 1727</p>	<p>S1002</p>
<p>RECEIVER HOUSING</p>		<p>RECEIVER HOUSING</p>	<p>RECEIVER HOUSING</p>

Figure 2-13. Receiver Housing

Table 2-5. Pilot Plant Receiver Tower Characteristics

Parameter	Value
Tower height	126.5 m
Tower diameter, outside concrete	7.9 m
Corbel width	1.22 m
Corbel spacing	120 deg
Corbel orientation	1 south
Cavity inside diameter	14.94 m
Cavity height, major	16.46 m
Aperture area	218 m ²
Net corbel area	29.0 m ²
Maximum aperture slant height	7.62 m
Aperture lower diameter	7.9 m
Vertical separation (tower to cavity, major)	6.7 m

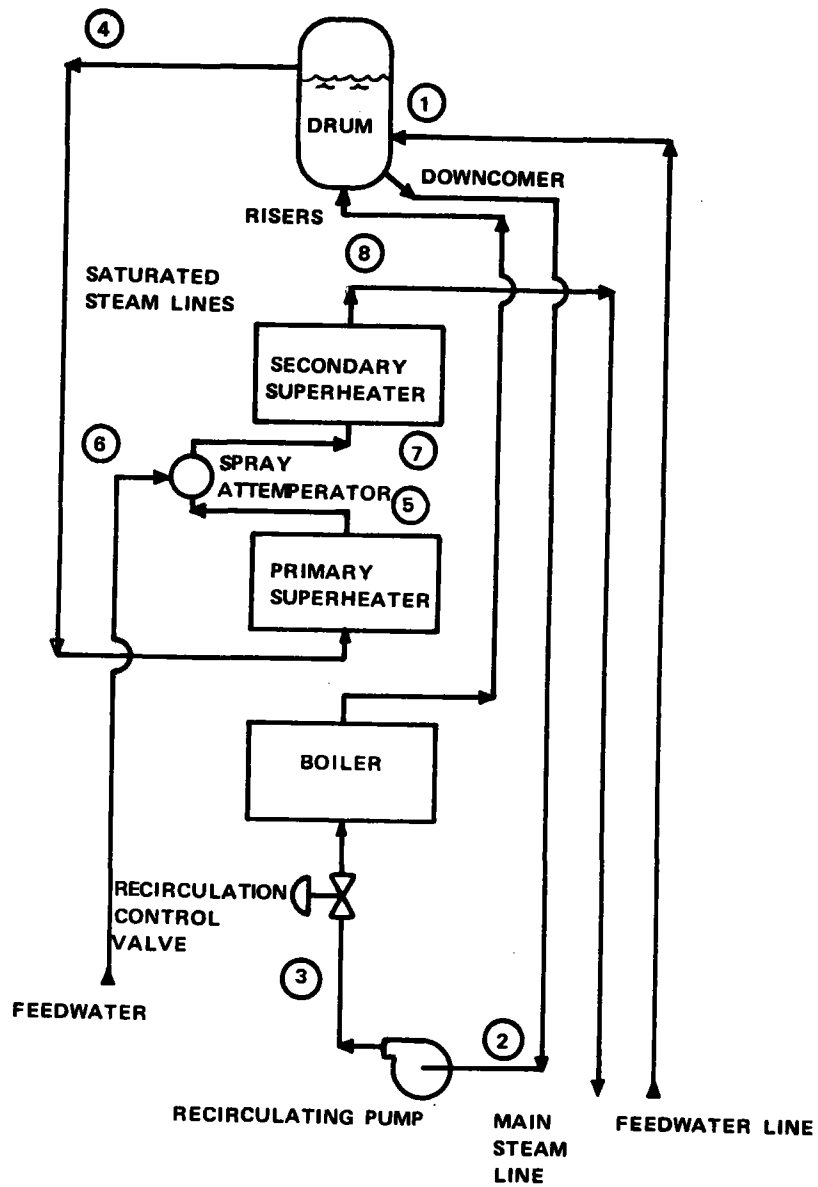


Figure 2-14. Steam Generator Subsystem Flow Circuit

The water is distributed to the boiler section where steam generation takes place. A saturated steam-water mixture at an average quality of 10 percent (at maximum conditions) exits the boiler section and flows through the risers to the steam drum where the water and steam are separated by cyclone separators and scrubbers.

Moisture-free steam from the drum flows through the saturated steam lines to the primary superheater where it is heated to about 475°C (887°F).

The steam exiting the primary superheater passes through the spray attemp-erator where additional feedwater is injected as required to control exit steam temperature.

The attemperated steam enters the secondary superheater at about 375°C (707°F) where it is heated to 515°C (960°F).

The internal diameter and height of the cavity were established as a function of the heliostat field and tower configuration to obtain the required aperture area and cavity efficiency. The steam generator is required to conform to the dimensions shown in Figure 2-15 and summarized as follows:

Diameter, m (ft)	14.93(49)
South side height, m (ft)	16.46(54)
North side height, m (ft)	14.63(48)

The steam generator heat-transfer surface is a polygon having eighteen 20-degree segments that form the interior walls of the receiver cavity. This geometry traps reflected and reradiated energy to increase cavity effective absorptance. The absorptance of the heat-transfer surface is about 0.9 and is achieved by allowing natural oxidation to occur. Reradiation is minimized by locating the cooler heat-transfer surfaces near the bottom of the

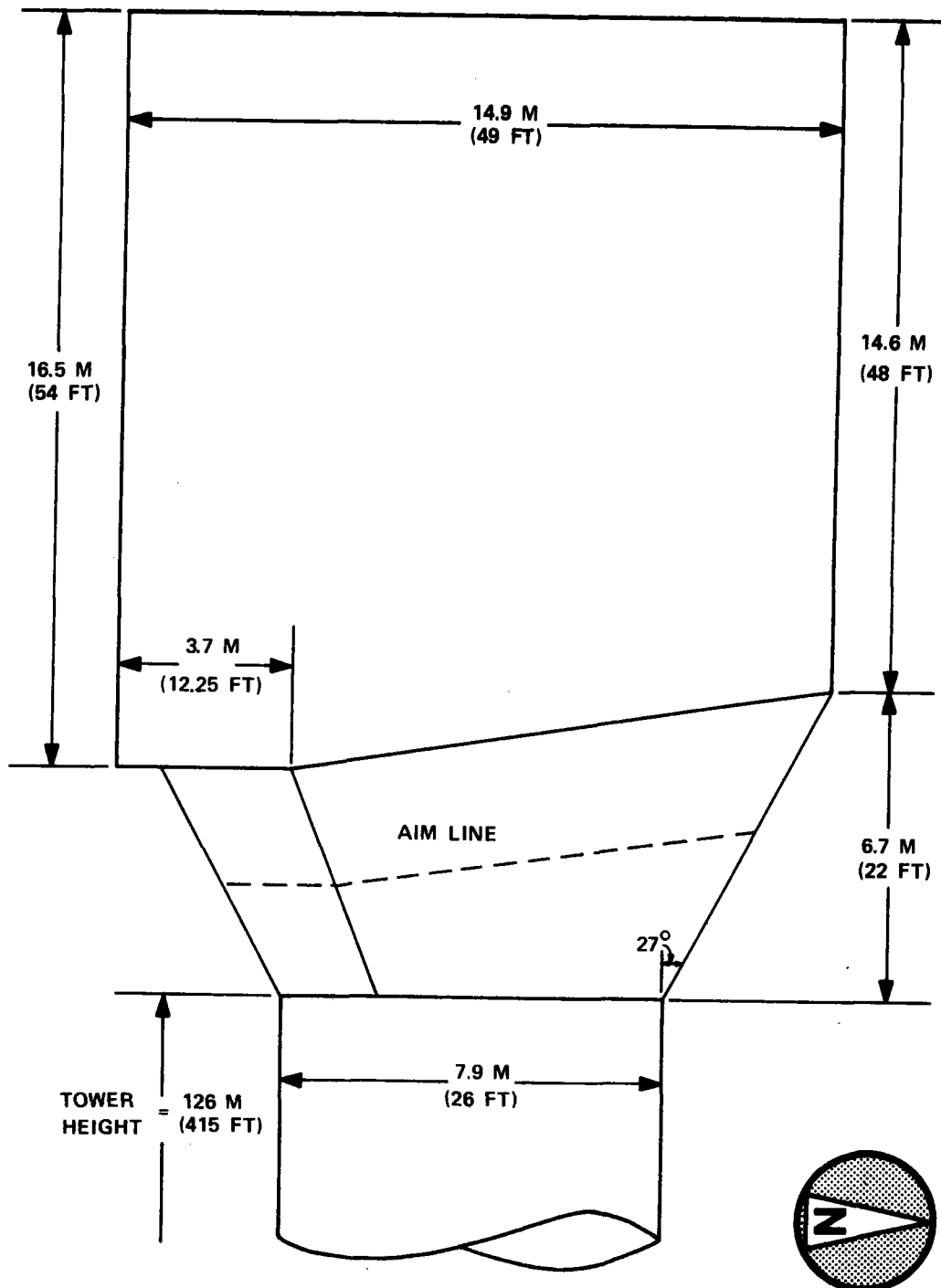


Figure 2-15. Receiver/Cavity Configuration

cavity and the higher-temperature surfaces at the top. The steam generator is thoroughly insulated to minimize conduction losses, and in the absence of wind, the bottom opening cavity does not allow the buoyant hot air to escape, minimizing natural convection losses.

The placement of the boiler and superheaters in the cavity was selected to match the heat flux patterns within the cavity. The flux patterns are determined primarily by the geometry of the heliostat field, tower height, aperture area, and the geometry of the cavity itself. Essentially, energy from the outermost heliostats is incident on the lower part of the cavity, while the innermost heliostats provide the energy for the upper part of the cavity. Since there are more heliostats in the outer portion of the field, incident energy peaks in the lower part of the cavity and tapers off towards the top.

To take advantage of this characteristic, the boiler section, which can be designed to operate at high heat fluxes because it is effectively cooled by a saturated steam water mixture, is located in the lower half of the cavity. The first stage, or primary superheater, which receives saturated steam from the drum, is located in the middle portion of the cavity where heat flux and steam temperatures are moderate. The second stage or secondary superheater, which receives higher-temperature steam from the spray attemperator, is located in the upper portion of the cavity where heat flux is low. As a result of this arrangement of boiler and superheater surfaces, the maximum metal temperatures in the superheater are lowest where thermal stress is high and highest where thermal stress is low.

The boiler and superheater heat-transfer surface areas are determined by the requirements of the steam cycle and by the absorbed heat flux distribution within the cavity. The ratio of the energy required to produce saturated steam from the feedwater to the energy required to superheat the steam is 72 percent at design conditions. Actually, the boiler surface has

been sized to absorb only 65 percent of the total energy. The extra energy absorbed by the superheater is used to vaporize feedwater injected into the superheater circuit at the spray attemperator. At design conditions, the spray attemperator flow is 10 percent of the design steam flow.

The boiler section heat transfer surface is an 18-sided polygon fabricated from membrane panels. It is 8.0 m (26 ft. 3 in.) high on the south side of the cavity and 6.17 m (20 ft. 3 in.) high on the north side. The boiler tubes are 2.223 cm (0.875 in.) outside diameter carbon steel with a minimum wall thickness of 0.376 cm (0.148 in.). Carbon steel membrane bars 0.635 cm (0.25 in.) thick are machine welded between adjacent tubes. The tube spacing for the five panels on the cold north wall is 7.62 cm (3 in.) and 3.81 cm (1.5 in.) for the remaining panels.

The primary and secondary superheaters consist of three horizontal tangent tube modules. Each module has six flat sides and covers 120 degrees of the cavity circumference. The primary superheater is 3.17 m (10 ft. 5 in.) high and the secondary superheater is 4.775 m (15 ft. 8 in.) high. The superheater tubes are Croloy 2-1/4, 2.54 cm (1 in.) outside diameter with a 0.419 cm (0.165 in.) minimum wall thickness.

The steam drum is vertical and contains seven cyclone primary separators and secondary scrubber plates to effectively remove moisture from the saturated steam.

The steam generator structure consists of horizontal and vertical trusses, which transfer the live and dead weight loads from the steam generator pressure parts and the receiver environmental housing to the three receiver corbels. The steam generator structure has been designed to withstand a lateral static equivalent seismic load of 3 g. The steam generator is top-supported from the structure by hanger rods which are free to swing outward to accommodate thermal expansion.

Figure 2-16 is a schematic of the arrangement of steam generator and its relationship to the receiver tower.

The major physical characteristics of the steam generator are listed in Table 2-6.

Thermal Storage Subsystem Description

The thermal storage subsystem consist of two sensible-heat stages, as illustrated in Figures 2-17 and 2-18. The first or main stage contains a rock and oil tank to store thermal energy and is equipped with interconnecting flow loops to transport this energy. The second stage consists of two tanks equipped with interconnecting flow loops to transport energy. Tube-and-shell-type heat exchangers are used to couple the storage fluid loops to the plant steam cycle for the thermal energy transfer.

Charging thermal storage is done by desuperheating receiver-supplied steam for supplying the second stage and condensing and subcooling the steam for main-stage supply. The condensate is returned to the plant deaerator. The system has been designed to accept large variations in receiver steam supply conditions.

Discharging thermal storage is done by preheating and boiling feedwater in the main stage and superheating the steam in the second stage.

During hold periods, the main storage is used to supply steam to the turbine for sealing purposes and to second stage for trace heating of the salt lines and equipment to prevent freezing of the salt. Electric tracing is also provided on valves and selected equipment. Stainless steels are used as material of construction in the second-stage tankage and in the molten salt loops. Low-alloy and carbon-steels are used on the steam charge and discharge

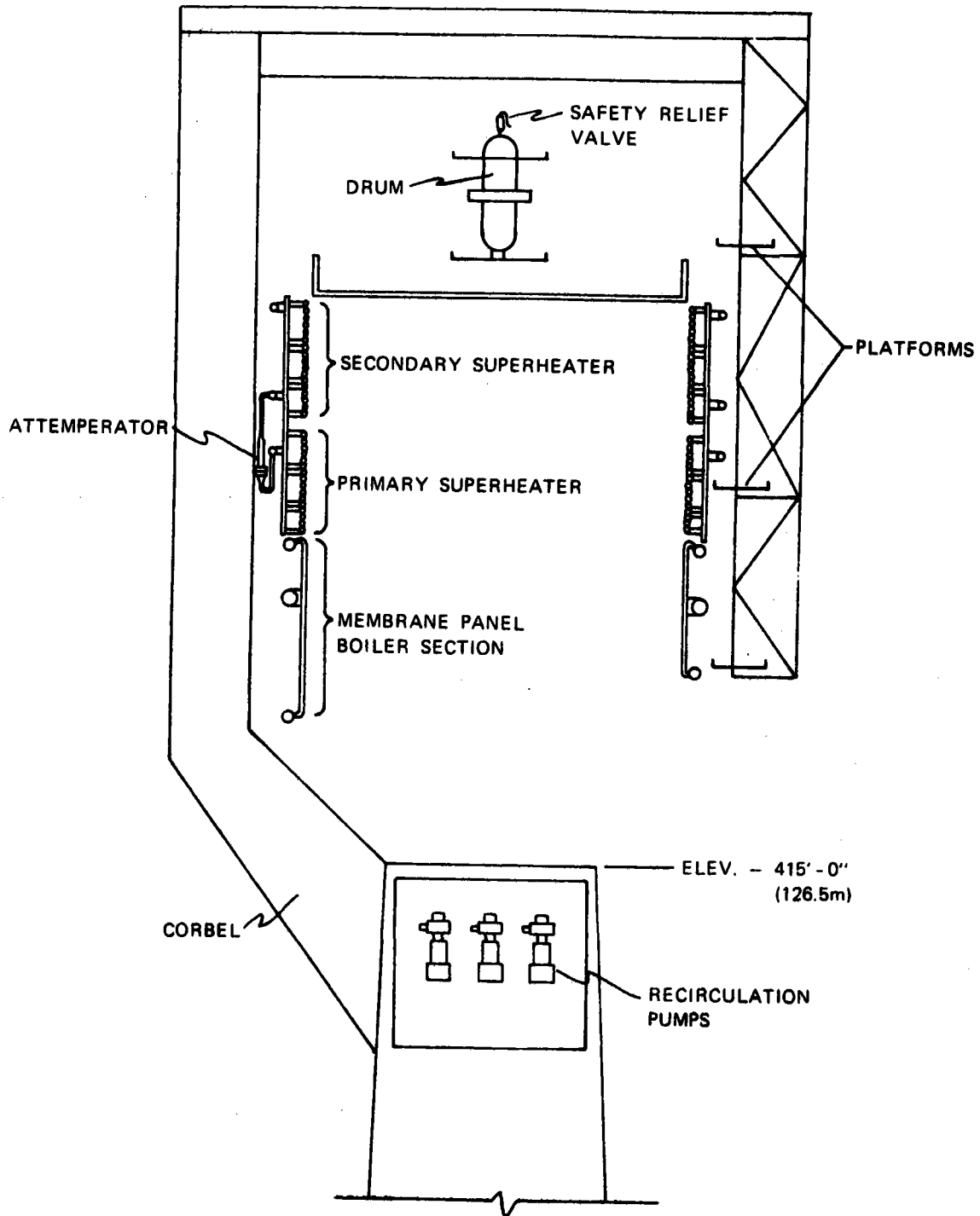


Figure 2-16. Pilot Plant Steam Generator Arrangement

Table 2-6. Steam Generator Physical Characteristics

Parameter	SI Units	English Units
Cavity:		
ID	14.9 m	49 ft
Height	14.6 to 16.5 m	48 to 54 ft
Superheater connecting piping C Diameter	16.9 m	55 ft, 5-5/8 in.
Drum	8.9 cm Thk. x 1.2 m ID x 4.3 m h	3-1/2 in. Thk. x 4 ft ID x 14 ft h
Boiler section height:		
South side	8.0 m	26 ft, 3 in.
North side	6.2 m	20 ft, 3 in.
First-stage superheater height	3.2 m	10 ft, 5 in.
Second-stage superheater height	4.8 m	15 ft, 8 in.
Weight:		
Pressure parts and integral supports	289,198 kg	637,000 lb
Structure	312,806 kg	689,000 lb

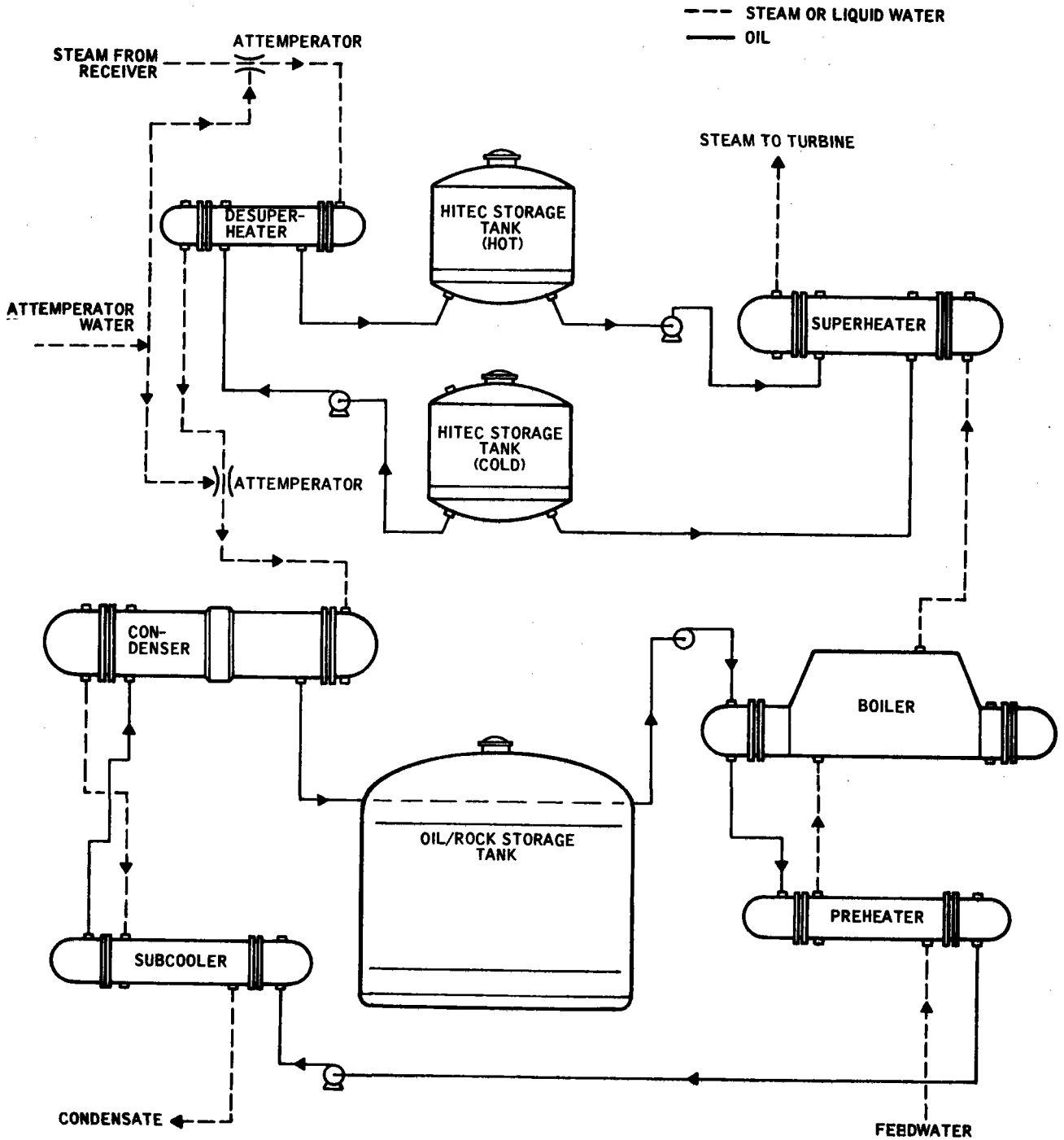


Figure 2-17. Sensible Heat Storage Subsystem

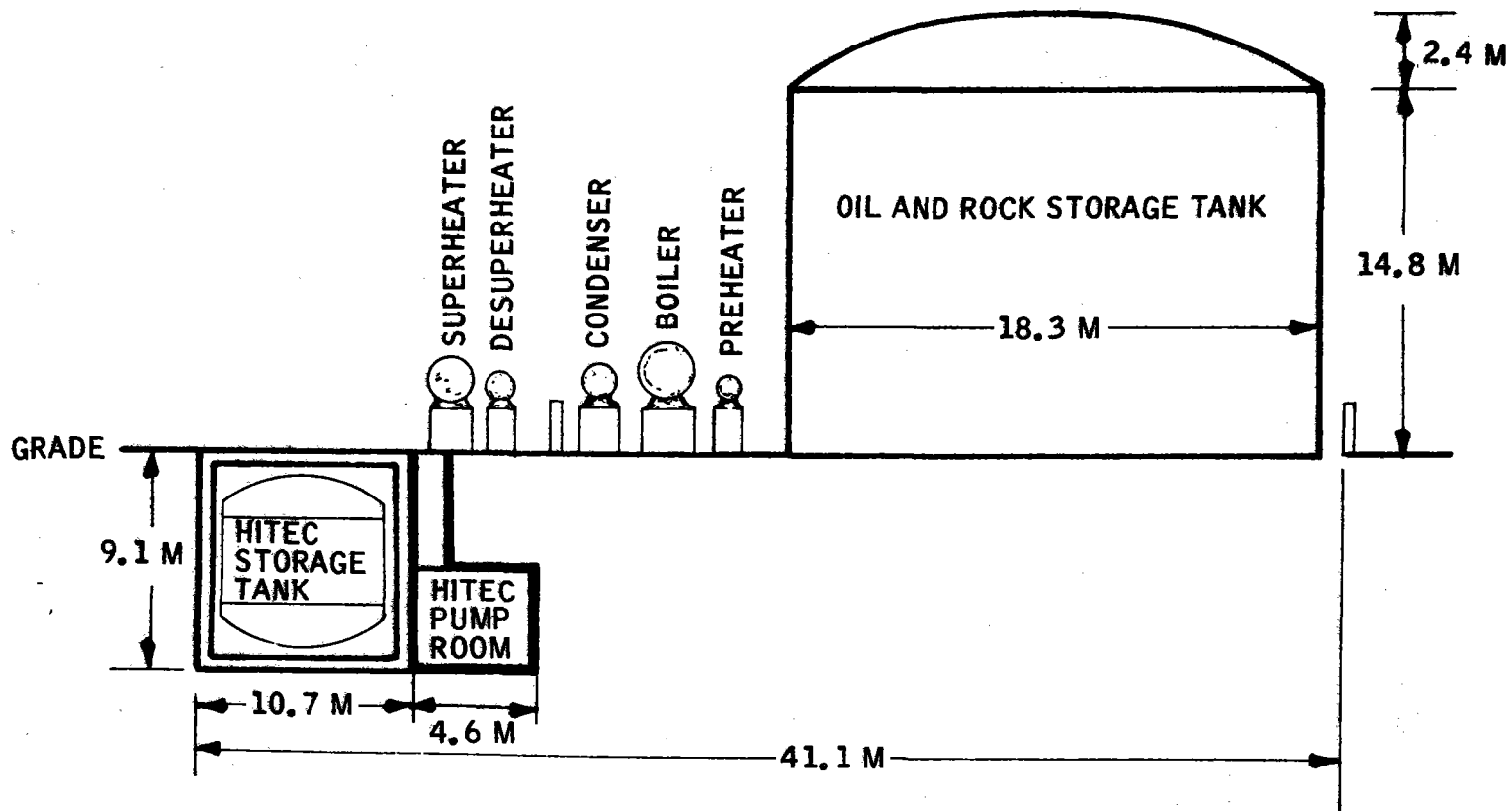


Figure 2-18. Pilot Plant Storage Subsystem Arrangement

side, respectively. Low-alloy steels are used in the main storage tankage and on steam side and carbon steels in the oil flow loops.

The main tank contains a packed bed of nominal 12.7-mm (0.5-in.)-diameter granite pebbles with oil flow manifolds at the top and bottom. Oil fills the voids in the bed and serves as the heat-transfer medium. A single (dual-parallel for commercial) tank is possible because a thermocline is set up and this enables a high degree of temperature stratification to be maintained from the top to the bottom of the 18-m-diameter tank. The bed height is 14.4 m (47 ft). This is sufficient to insure 20 hours of sealing and tracing steam during hold, accommodate the heat losses, and to supply the required steam power through the second stage to the turbine. The main storage tank is charged when the outlet temperature at the lower manifold indicates 290°C (554°F). The tank is discharged when the outlet temperature at the upper manifold indicates 300°C (572°F). The energy utilization factor is 77.4 percent.

Design characteristics are listed in Table 2-7.

ELECTRICAL POWER GENERATION SUBSYSTEM DESCRIPTION

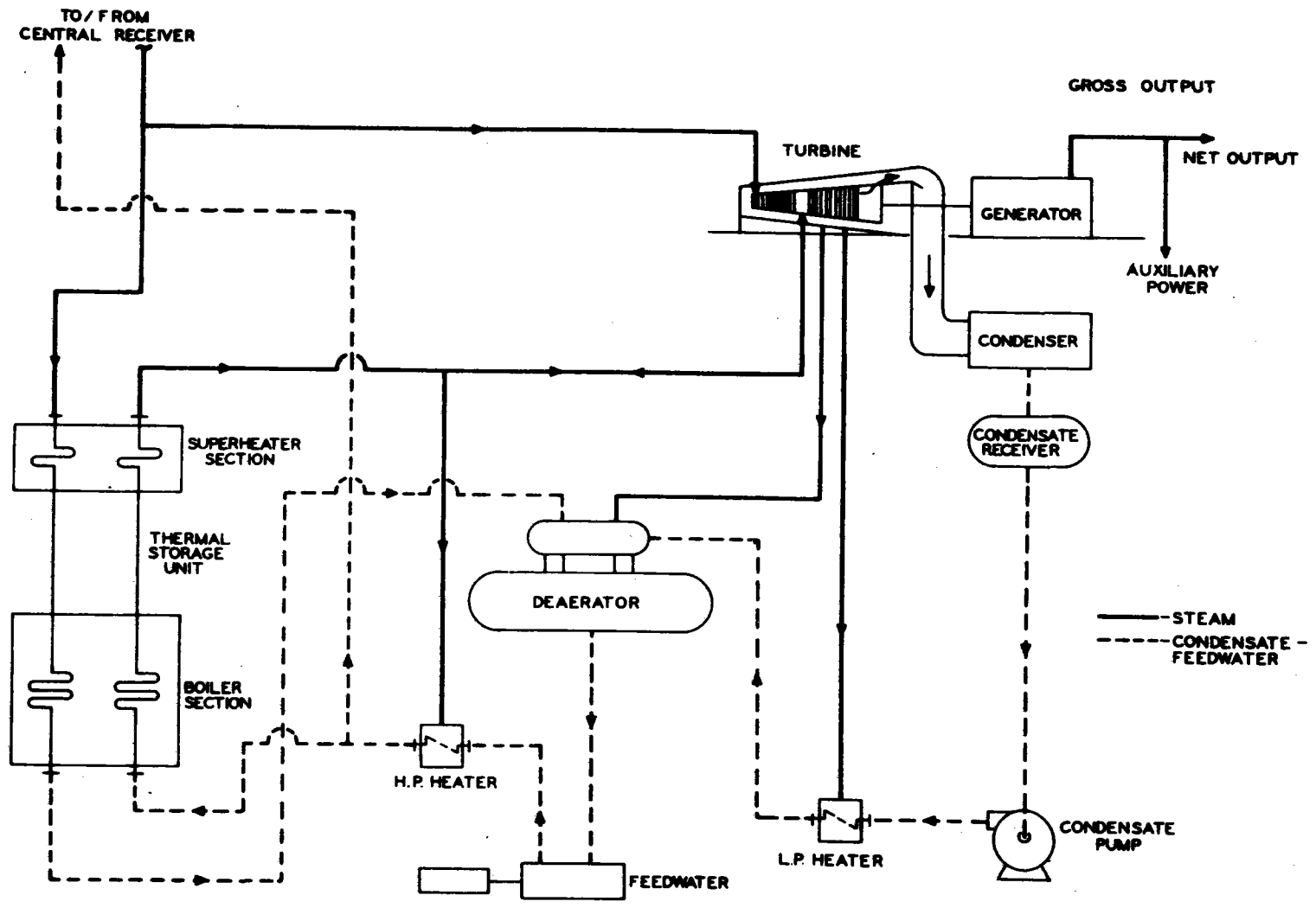
The pilot plant electrical power generation subsystem (EPGS, often referred to as the electrical generation subsystem or ESG) consist of the turbine, generator, condenser, feedwater heaters, and necessary piping, pumps, and auxiliary water-conditioning equipment. Figure 2-19 is a schematic diagram of the system.

The turbine used in the plant is a dual-pressure, automatic-admission, nonreheat, single-shell turbine. High-pressure inlet conditions to the turbine are 10101 kPa (510°C), and low-pressure inlet conditions are 3275 kPa (390°C). The turbine has a nominal rating of 15,000 kW to allow it to

Table 2-7. Pilot Plant Thermal Storage Subsystem Characteristics

Parameter	Value
Total storage capacity	133.1 MWh(th)
Superheater storage:	
No. of tanks	2
Tank capacity	155.1 m ³
Tank size	7 m x 4.3 m
Tank material	SS304
Storage material	Hitec
Material quantity	253,558 kg
Capacity	17.1 MWh(th)
Main storage:	
No. of tanks	1
Tank capacity	3418 m ³
Tank size	18.3 m x 14.6 m
Tank material	Low-alloy steel
Storage material	Granite - 13mm ASTM Grade 6, Oil-Caloria HT-43
Material quantity	Granite - 7161 tons, Oil - 827, 882 liters
Capacity	116 MWh(th)
Superheater Hitec pump:	
Quantity	1
Type	Centrifugal
Flow	12.9 liters/sec
Input power	11 kW
Boiler oil pump:	
Quantity	1
Type	Centrifugal, two-speed
Flow	265 liters/sec
Input power	112 kW
Desuperheater Hitec pump:	
Quantity	1
Type	Centrifugal, constant-speed
Flow	12.9 liters/sec
Input power	11 kW

40703-II



2-41

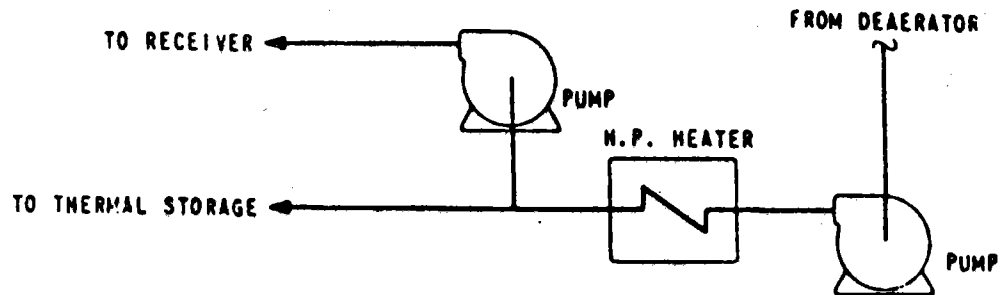
Figure 2-19. Electrical Power Generation Subsystem Schematic Diagram

handle the maximum flow from the receiver. Three extraction ports are used in the turbine, all downstream of the secondary-injection port.

The generator used is of the rotating field synchronous type. It is an air-cooled unit with an output of 18750 kVA.

A water-cooled condenser with a wet cooling tower is the main heat-rejection system for the plant. Design steam load for the condenser is 623 kg/s with a 29°C dry-bulb temperature and a 23°C wet-bulb temperature.

The feedwater pumps are arranged as a series horizontal multistage pump system. A sketch of the concept is shown below. Each of the pumps shown is actually two pumps arranged in parallel.



The three feedwater heaters consist of the low-pressure heater, the deaerator, and the high-pressure heater. Design operating pressures and temperatures are 1888 kPa (209°C) for the high-pressure heater, 547 kPa (155°C) for the deaerator, and 80.6 kPa (94°C) for the low-pressure heater. The deaerator is of the direct contact tray type.

Table 2-8 summarizes EPGS characteristics.

Table 2-8. Electrical Power Generation Subsystem Characteristics

Parameter	Value
High-pressure inlet conditions	10,101 kPa/510°C
Low-pressure inlet conditions	3275 kPa/388°C
Maximum flowrate from receiver	17.3 kg/s
Design flowrate from receiver	13.8 kg/s
Turbine:	
Nameplate capacity	15,000 kW
Type	Dual-pressure admission nonreheat, condensing, bottom exhaust, single-speed
Speed	3600 rpm
No. of extractions	3 plus automatic admission
Generator:	
Type	Rotating field, synchronous, totally enclosed, air-cooled
Capacity	18,750 kVA
Condenser:	
Type	Water-cooled
Design steam load	10.4 kg/s
Deaerator type	Direct contact, tray
Auxiliary cooling unit:	
Type	Air-cooled water chiller
Maximum heat load	1.465 MW(th)
Total pressure drop	13.8 kPa
Maximum cooling water temperature	35°C
Air compressor:	
Number	2
Type	Oil-free reciprocating
Capacity (ea.)	47.2 liters/sec
Discharge pressure	862 kPa

PLANT CONTROL

The solar pilot plant control system incorporates the following basic features:

- Constant-throttle steam pressure
- All available solar energy will be used, either directly by the turbine or subsequently through use of energy storage capabilities of the plant.
- Energy apportionment philosophy:
 - First priority of direct solar-generated steam is to the turbine for megawatt demand satisfaction.
 - Surplus solar-generated steam (steam not required for immediate megawatt demand satisfaction) is used to charge the energy storage subsystem.
 - Where current solar-generated steam is insufficient to meet current megawatt demand, storage-generated steam will be used to supplement the direct solar-generated steam.
- The control system will act to protect major plant equipment from extremes of selected process parameter values and their rates of change.

The simultaneous embodiment of the above features implies a coordinated control system such as the one designed for the solar plant design.

Hierarchy of Control

The following hierarchy describes the control system suggested for the solar pilot plant:

- 1) Coordinated master control, using hardware necessary to recognize overall plant status, energy availability and load demand, and to establish demand signals to each of the major plant subsystem controls as required to implement the overall plant control philosophy.
- 2) Plant subsystem controls, using hardware to receive and respond to demand signals generated by the coordinated master control for each of three major plant subsystems.
 - a) Plant generation control of the turbine and generator for which the major interfacing hardware is the turbine governor. The control is used to regulate turbine speed prior to synchronization, and generator load after synchronization in accordance with the load demand generated in the master coordinated control.
 - b) "Storage-in" control which regulates and apportions surplus solar-generated steam to charge the main and Hitec storage systems in accordance with the requirements of the coordinated master control.
 - c) "Storage-out" control which supervises the generation of steam by the thermal storage subsystem to augment or replace direct solar-generated throttle steam to the turbine as required by the master coordinated control for megawatt demand satisfaction.
- 3) Minor control loops, not specifically mentioned here, but which consist of the numerous tank level, pressure, and temperature control systems having only local involvement with plant

equipment, such as heater and deaerator level controls, auxiliary cooling water temperature control, etc.

The implementation of the first two levels of control is discussed below.

Coordinated Master Control

The coordinated master control represents the highest level in the control hierarchy. Its basic function is to develop coordinated demand signals to the storage-in, storage-out, and turbine governor controls based on the plant megawatt demand and imbalances between current solar steam generation and use rates. The coordinated master control is functionally shown in Figure 2-20.

In operation, the control system senses deviations of generated megawatts from the megawatt demand and commands the turbine governor to increase or decrease load as required. Under conditions where solar steam is generated at rates in excess of the turbine requirements, an increase in turbine load demand preferentially uses solar-generated steam at the expense of the storage-in control demand, thus diverting steam from the storage-charging operation to the turbine. In the event that turbine load demand exceeds the current solar steam generation rates, the system ceases to apply steam to storage and "holds down" the turbine until the resulting megawatt error causes the storage-out control to make up the deficit from storage.

Imbalances between solar steam generation rates and its use for turbine load and storage charging are sensed by throttle pressure variations. Thus, the sum of the throttle steam energy to the turbine and storage is maintained equal to the solar steam generation rate while the apportionment of steam between the turbine and storage is varied according to turbine load demands.

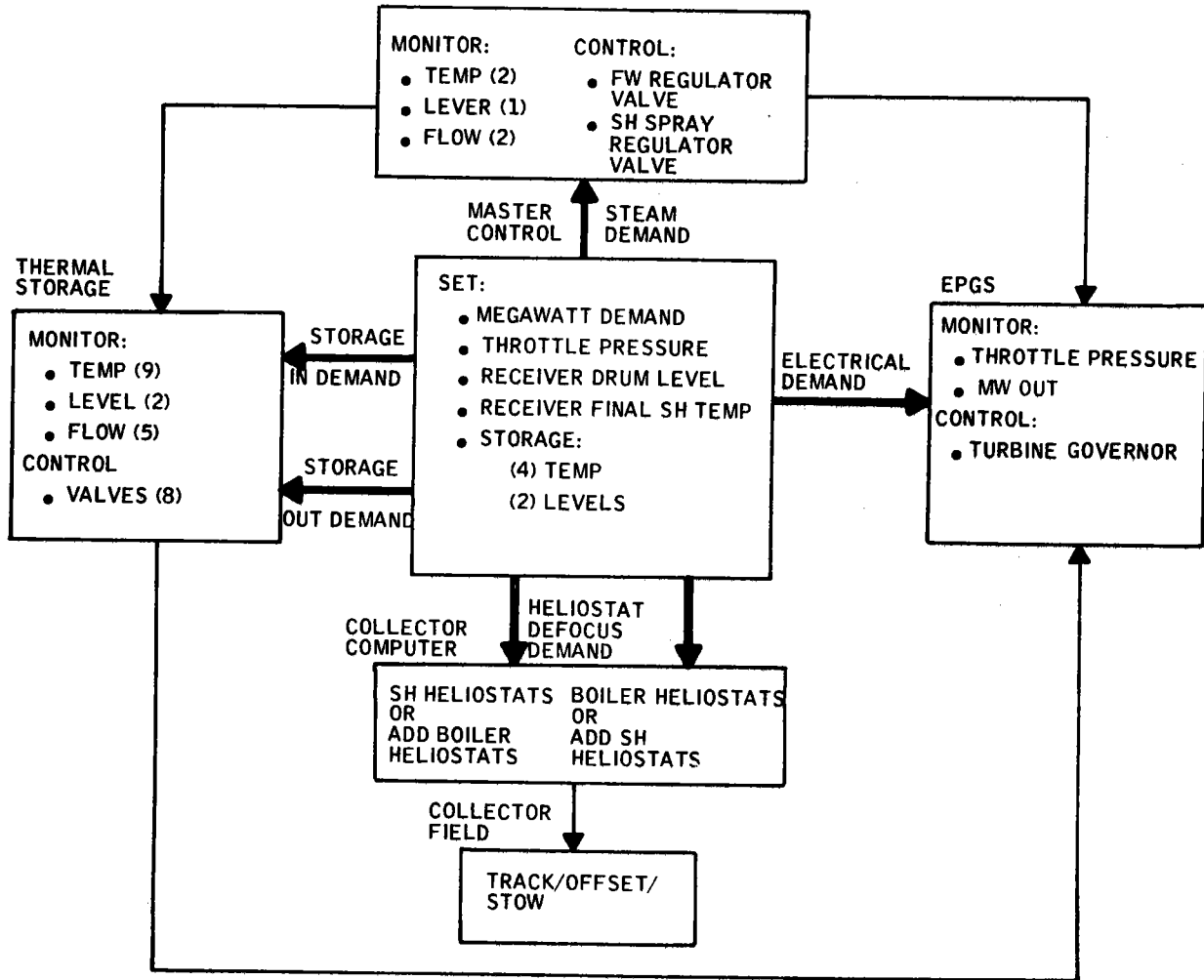


Figure 2-20. Functional Block Diagram of the Master Control

Ultimately, where direct solar-generated steam is insufficient to drive the turbine, even with no flow to charging storage, the enforced megawatt error signal integrates through the -50 percent bias, causing a storage-out demand signal, and initiates steam flow from the storage to the low-pressure turbine inlet. Steam flow from storage is then increased until the demand unit load is maintained under conditions of maximum direct solar steam participation and minimum participation from storage-generated steam.

Feedforward signals from the integrated throttle pressure error and megawatt error signals are used to anticipate changes in the storage-in, storage-out turbine governor demand signals to effect smooth, stable control.

PILOT PLANT PERFORMANCE

Heliostat Field Performance

To describe the pilot plant field performance, we will make use of the familiar tracking efficiency term. Tracking efficiency is defined as the re-directed power divided by the total available power. The total available power is the sun's direct normal intensity multiplied by the total heliostat mirror area. We can modify the tracking efficiency slightly to arrive at an efficiency description of plant performance at any point in the power path. An efficiency can be thought of as the power at any defined place in the optics path divided by the total available power. That is, efficiency can generally be applied to the power after cosine losses, the power after tower shading, mirror and frame shading and blocking, and after power losses at the aperture.

Figure 2-21 shows the efficiency terms as a function of hours from solar noon for an equinox day. In this case, a reflectance of 1.0 has been assumed and no atmospheric attenuation losses are included. The figure

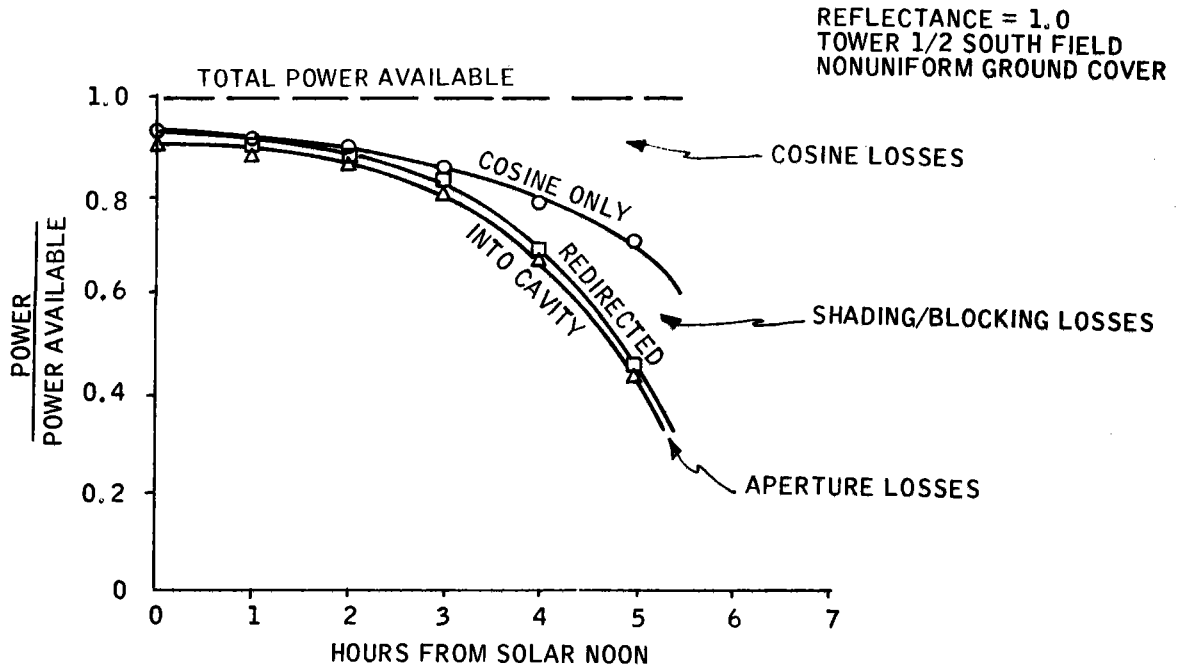


Figure 2-21. Field Efficiency at Equinox Day

shows the total power efficiency simply equal to 1.0. The cosine efficiency is shown to be approximately 0.93 at solar noon. This represents a loss of 7 percent of the total power available. The cosine-only efficiency continually decreases as time gets farther from solar noon. The curve will finally go to zero at sunset, which occurs 6 hours from solar noon.

The next curve in Figure 2-21 is the redirected field efficiency (often called the tracking efficiency). The difference between the cosine-only curve and the redirected-efficiency curve is due to power losses caused by mirror and frame shading and blocking as well as tower shadow loss. It is seen that the shading and blocking losses are increased as we move away from solar noon. This occurs simply because the mirror surfaces must be tilted more vertically to see the sun and the aperture as the sun becomes lower in the sky. Thus, the facets and heliostats will block the view of mirrors behind them. Although the shading and blocking losses become a fairly large

percentage of the available power during early morning and late afternoon hours, the available power itself is relatively low. Thus, the shading and blocking losses are not a significant yearly energy loss term. The final efficiency curve shown in Figure 2-21 is the power into the cavity efficiency. The difference between the redirected power and the power into the cavity represents that power which misses the cavity aperture, power which hits the support structures at the aperture, and power which enters one side of the cavity but exits the other side. The power lost in this way is determined by Monte-Carlo ray trace techniques as described in Section 7 of this volume. The redirected rays are perturbed for solar limb darkening, tracking errors (a 2-rad, 1σ normal distribution is assumed for both areas tracking error budget), and mirror surface slope errors (a 0.9-rad, 1σ normal distribution is assumed). Thus, aperture losses fully account for the beam dispersion due to sun size and mechanical imperfections.

The efficiency data shown in Figure 2-21 can be used to predict power levels for any insolation value. For example, if at 3 p. m. on equinox day a solar direct normal intensity of 900 W/m^2 were available, the total power into the cavity would be found by multiplying the 900 W/m^2 by the power into the cavity efficiency at that time (0.8) and by the total mirror area. The result of this calculation shows a power of 46 MW(th) could enter the cavity. This power must be modified by the mirror reflectance and the atmospheric attenuation loss between the mirror and the aperture.

Field efficiency data have been computed for two other days of the year; winter and summer solstice. Results of all three days are shown in Figures 2-22, 2-23, and 2-24. Figure 2-22 shows the cosine-only field efficiency as a function of hours from solar noon. It is seen that equinox day has the highest cosine efficiency out to approximately 5 hours, 45 minutes from solar noon. At this time the equinox day cosine efficiency crosses the summer solstice curve. Here, the effect of a longer summer day is seen. Note that the summer and winter solstice perform the same

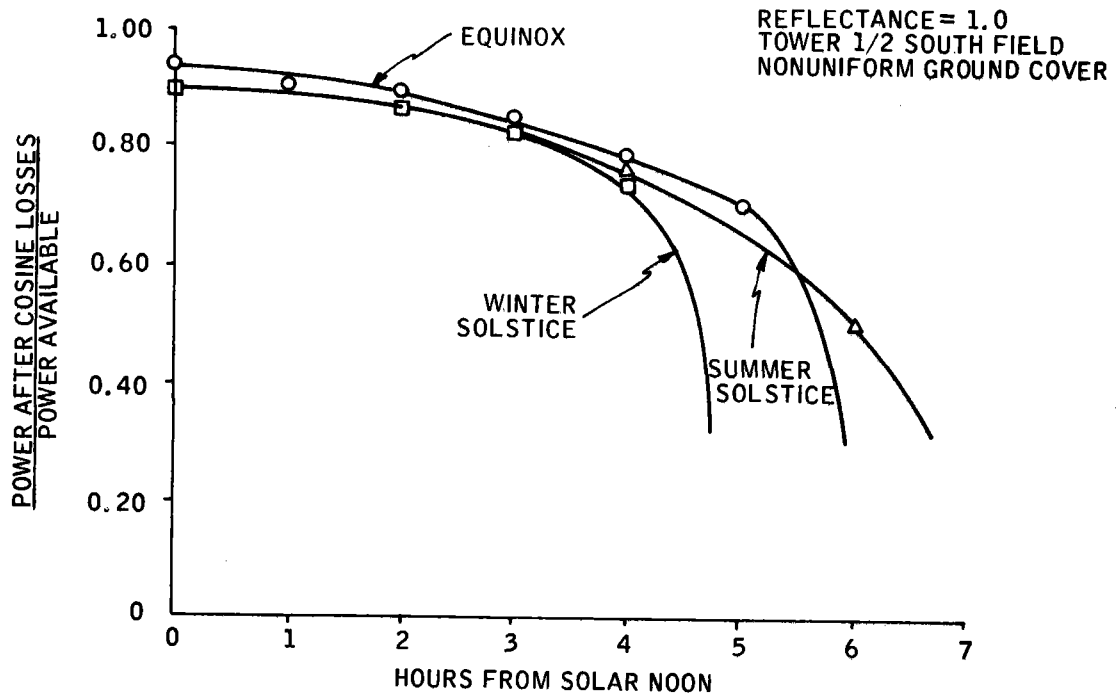


Figure 2-22. Cosine-Only Field Geometry

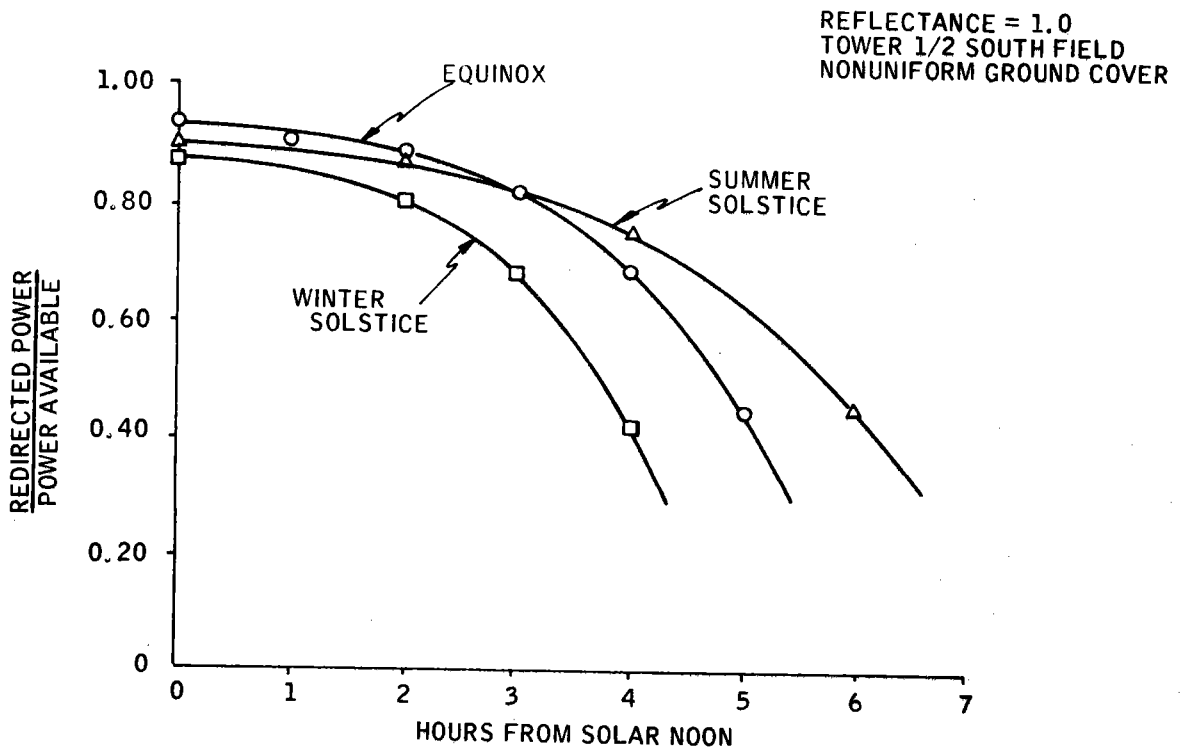


Figure 2-23. Redirected Field Efficiency

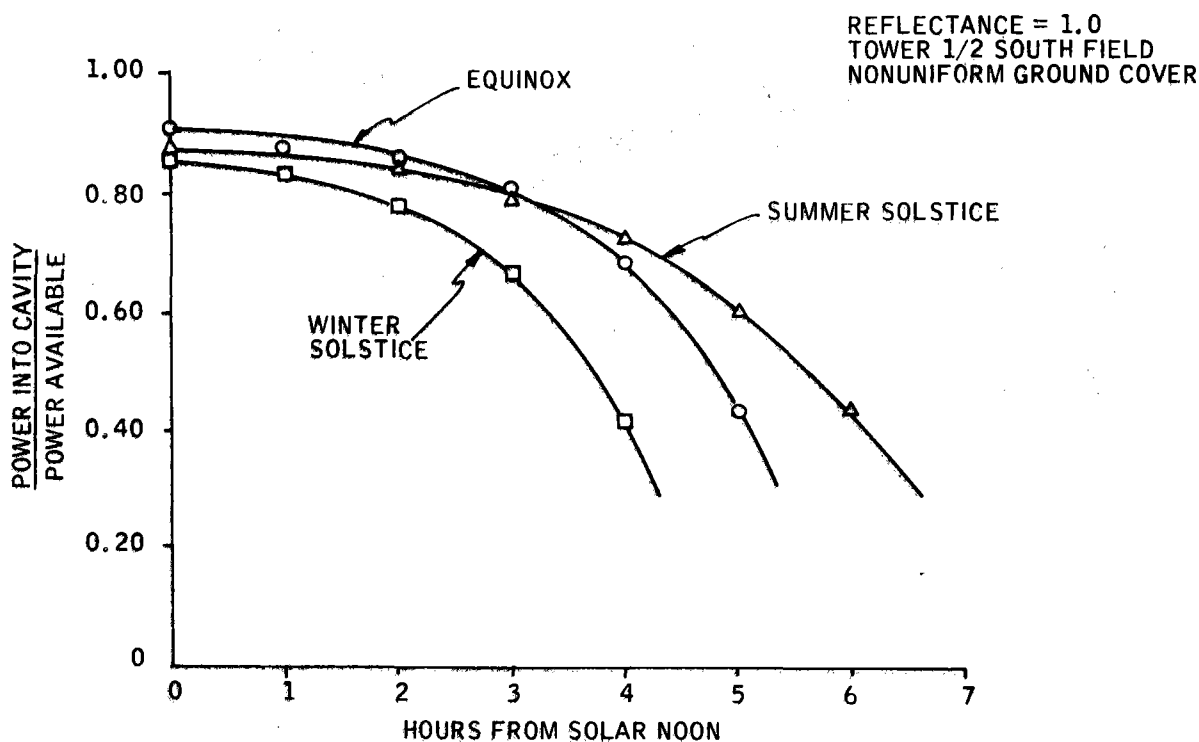


Figure 2-24. Power Into Cavity Field Efficiency

at solar noon with a cosine efficiency of 0.1. Until approximately 3 hours from solar noon, the curves are essentially equal and then the shortened winter day causes the 12/21 efficiency to roll off.

Figure 2-23 shows the redirected field efficiency curves. Again, solar noon, equinox day is when the solar plant is most efficient. For redirected field efficiency, the equinox curve crosses the summer solstice curve at 3 hours from solar noon. The crossover comes earlier than in the cosine efficiency curves because the shading and blocking losses become noticeable earlier for the equinox day. This is caused by a lower sun elevation angle during the equinox day. Also note that the winter solstice day is now the least efficient from solar noon on. This is also explained by the sun elevation position. In the winter, the sun is at its lowest position and hence this is when shading and blocking losses are most noticeable.

Figure 2-24 shows the power into the cavity efficiency values. In this figure, the trend of the curves is identical to that of the previous figure. That is, equinox is best at noon and crosses the summer solstice curve approximately 3 hours from solar noon. Winter solstice still shows the poorest efficiency throughout the day. With the data in Figures 2-21 through 2-24, the cosine-only power, the redirected power, and the power into the cavity may be calculated for any of the three representative days of the year.

Incident Flux Map

Having answered the question of how much redirected power enters the cavity, we are next interested in the way in which the power maps out on the inside of the cavity. As was the case in the field efficiency analysis, the flux distribution question was answered using the ray trace code.

Figure 2-25 is a cavity wall flux map for the equinox day at noon. Isopleths of constant kW/m^2 flux are shown over the cavity interior. The flux shown is an incident, or direct, solar flux striking the cavity walls. The view of the flux map shown has opened the cavity cylinder to look at a planar surface.

The flux map shows two relatively high flux spots on the south wall. South is defined as 180 degrees and north is zero or 360 degrees in the figure. The hot spots occur on the south wall because a majority of the heliostats are in the north field. These heliostats aim at the north aperture opening and the energy strikes the opposite or south wall. At the bottom of the south wall we see that the flux isopleths run off the cavity. The slight loss of flux is approximately one percent of the redirected power. This loss could be avoided if the receiver had been designed with a larger upper aperture tilt angle. The baseline aperture tilt was selected to optimize the net annual energy and some loss through the aperture is acceptable. The pilot

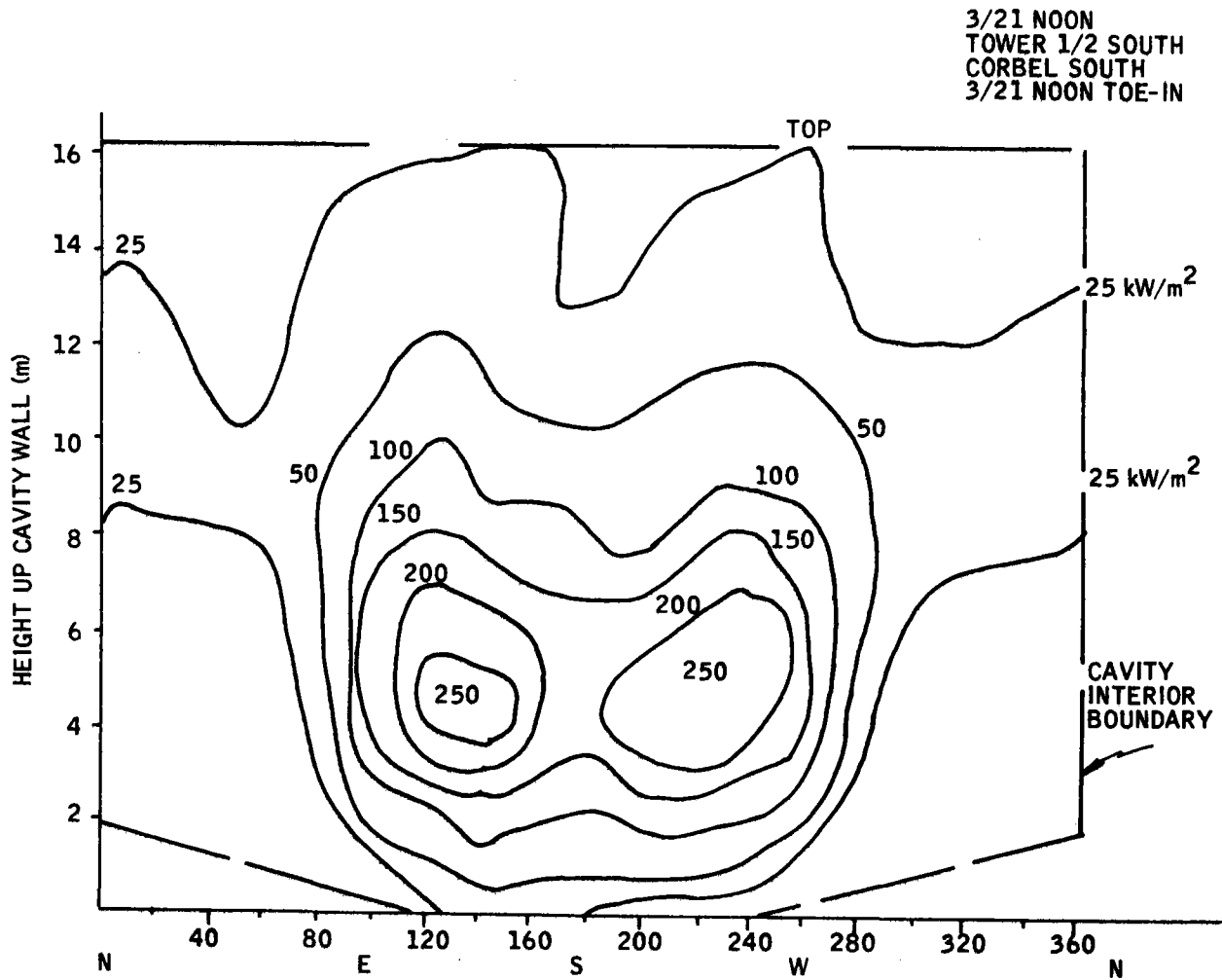


Figure 2-25. Cavity Wall Incident Flux Map for Noon on Equinox Day

plant preliminary design receiver upper aperture tilt is shown in the flux map figure by the cavity interior boundary.

It is important to point out that the high flux regions are located at the bottom half of the cavity wall where the boiler surface is present. The boiler surfaces can accept a local flux peak of 400 kW/m^2 , while the superheater surfaces should not exceed 150 kW/m^2 absorbed flux. The differences in allowable peaks is primarily due to the poorer heat transfer in the superheater tubes. Poor heat transfer can cause overtemperature and stress problems. In the upper, or superheater regions, a slightly more uniform circumferential flux distribution is shown, with the flux peak near 100 kW/m^2 .

Cavity/Steam Generator Performance

Cavity performance characterization involves the estimation of three types of losses: reradiation losses out of the aperture, convection losses out of the aperture, and conduction losses through the cavity walls. The reradiation and conduction losses are calculated with the rerad rubber model and the convection losses are calculated from an equation based on a paper written by J. Fox, "Heat Transfer and Air Flow in a Transverse Rectangular Notch," International Journal of Heat and Mass Transfer, Volume 8, pp. 269-279, 1965.

Figure 2-26 shows the results of the analysis of cavity efficiency as a function of power into the cavity at various windspeeds. The 3.5-m/s wind speed (at 10 m off the ground) curve was used for design purposes. The 10 m height is a reference height. Velocity at the receiver is found by using the relationship $V_h = V_{10m} (h/10m)^{0.15}$. The entire family of curves was used in the annual energy calculations.

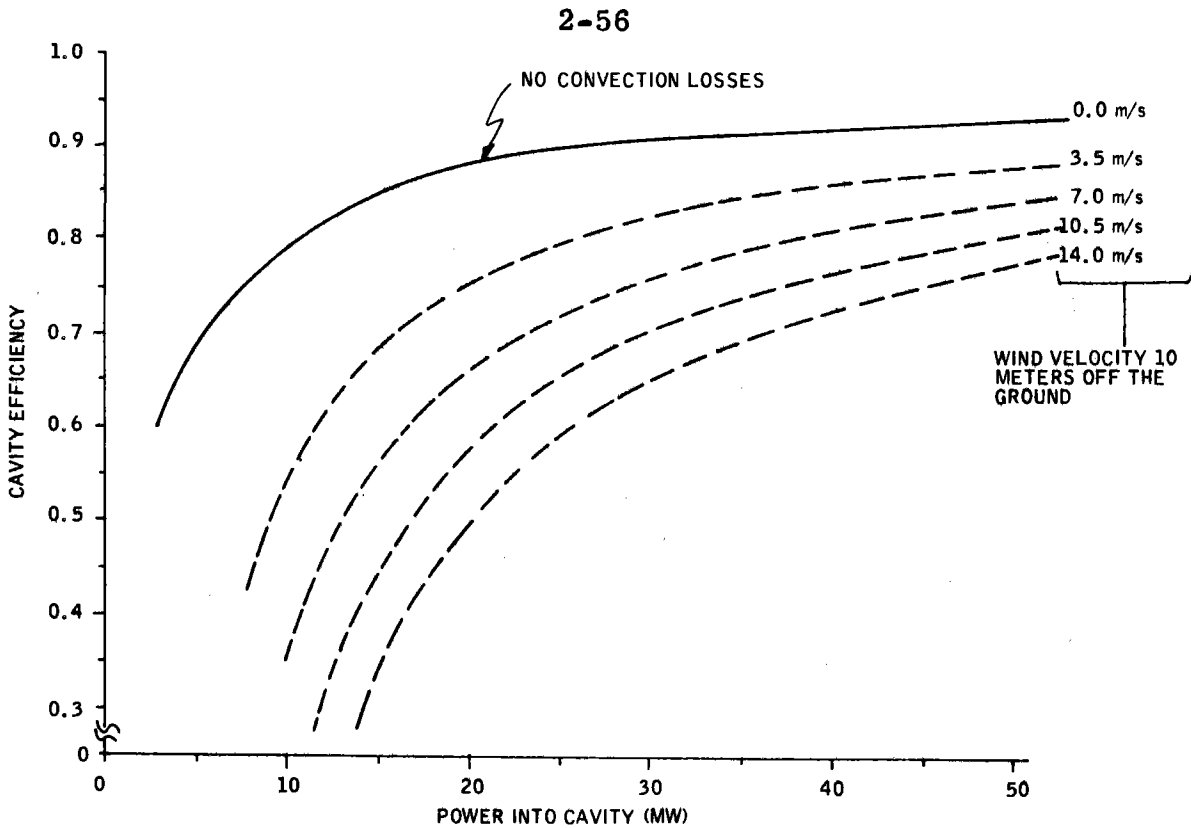


Figure 2-26. Cavity Efficiency versus Power Into Cavity at Various Windspeeds

The no convection loss case can be divided into three losses: solar incident power reflected back out of the aperture, IR radiation from the hot metal surfaces out of the aperture, and conduction losses through the cavity walls. The reflected solar power is proportional to the incident solar power for similar incident flux distributions. The IR and conduction losses can be further subdivided into losses from inactive surfaces (ceiling, tower top, uncooled areas) and active surfaces (boiler and superheater surfaces). The active surfaces are maintained at nearly constant temperature by the boiling water and the atemperator control. The temperatures of the inactive surfaces vary as a function of the incident power. The combination of all of these losses leads to an equation for losses with two terms: a constant term independent of incident power, and a loss term which is a function of incident power.

The constant-loss term accounts for the rolloff of cavity efficiency at low input power levels. At low power levels, this term becomes a larger proportion of the incident power – in other words, a larger fraction of the incident power is expended in just keeping the heat-transfer surfaces at the required temperatures to generate rated steam.

Convection losses are nearly independent of power into the receiver. This additional constant-loss factor gives a rolloff starting at higher input power levels as the wind speed increases.

Figures 2-27 and 2-28 show the values of the ratio of the absorbed power to the incident power on the active surfaces as a function of position on the cavity wall. The discontinuity in the graph between the two superheaters is due to the temperature discontinuity generated by the atemperapor.

The values of the ratio of absorbed-to-incident power are almost all above 1 in the high incident power (3/21 noon) case. The highest values are seen on the hottest active surfaces near the outlet of the second superheater. This is due to the fact that there is significant power incident on the ceiling. Farther down in the cavity, the cooler boiler shows a lower value of power absorbed/power incident due to the higher view factor out the aperture for these surfaces. The power ratio does not trail off near the bottom of the boiler because of the mediating effect of the hot (780°F) surface at the bottom of the aperture.

The power ratio graph looks considerably different for the low incident power (3/21 7 a. m.) case. In this case, the lowest power ratios are seen at the outlet of superheater 2. In both the 7 a. m. and noon cases, the percent of total power incident on the ceiling is about the same (10 percent). The ceiling sees nearly the same temperature environment in both cases, since metal temperatures are controlled by the steam and water. The ceiling temperature is a function of absolute power in and not the relative

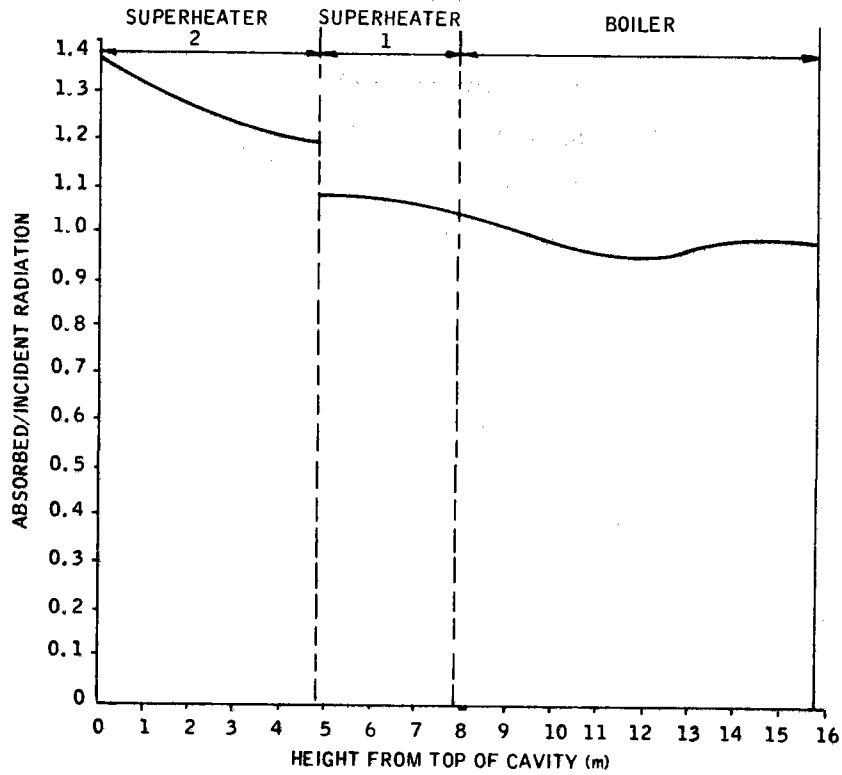


Figure 2-27. Absorbed/Incident Radiation versus Cavity Position for 3/21 Noon (No Convection Losses)

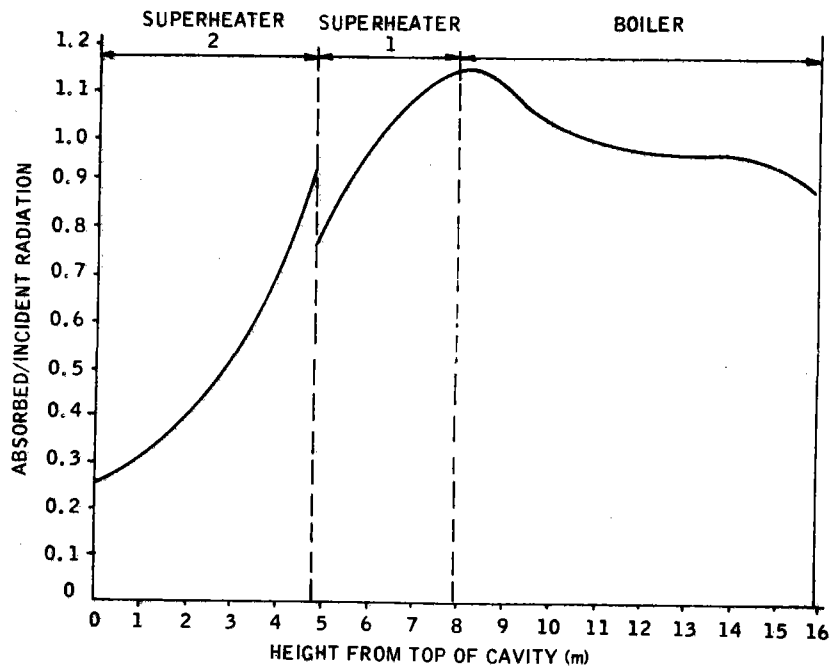


Figure 2-28. Absorbed/Incident Radiation versus Cavity Position for 3/21 7 a. m. (No Convection Losses)

power input levels. Therefore, lower incident power levels generate cooler ceilings and lower power ratios for the upper superheaters.

The decrease in power ratio on the upper superheater with a decrease in incident power directly affects the controllable steady-state range of our design. There is a certain power level below which we cannot maintain a steady-state rated steam temperature without defocussing boiler heliostats. At present, in the absence of convection losses, that power level is about 13 MW. When the collected power is below this level, the steam could be used for the charging of thermal storage. The morning time period when the power is below 13 MW is likely to be exceeded by the time required for startup. During startup periods, the steam temperature is below rated output temperature and the steam generator is well within its control limits.

Convection losses affect cavity performance in two ways. The first is by reducing net cavity efficiency. The dotted lines on Figure 2-26 show the effect of convection losses on cavity efficiency at various windspeeds.

The other way in which convection losses can impact our design is by their effect on the boiler/superheater interface. The convection loss equation calculates a net rate of heat loss from the entire cavity. To determine the effects of convection losses on the boiler/superheater interface, a temperature flow rates, and steam outlet temperature, it is necessary to know the rate of heat loss from any given surface within the cavity.

Table 2-9 presents the results of a series of runs made with the rerad software under the assumption of different distributions of a constant total convection loss (2.54 MW). The constant flux model is that where the convection heat flux from the inside of the cavity is a constant independent of the position in the cavity. The linearly varying flux model assumes the convective flux loss varies linearly from zero on the ceiling as a function

**Table 2-9. Attemperator Flows and Outlet Steam Temperatures for
Different Convection Loss Models**

Time of Year	Power In (MW)	Constant Flux Convection Loss Model (Loss=2.54 MW)		Linearly Varying Flux Convection Loss Model (Loss=2.54 MW)		No Convection Losses	
		% Attemp Flow*	Steam T Out**	% Attemp Flow*	Steam T Out**	% Attemp Flow*	Steam T Out**
3/21 7 a. m.	13.71	0	882	2.15	960	2.32	960
3/21	49.30	7.08	960	9.68	960	8.81	960

*% Attemp Flow = (Attemperator flow/boiler feedwater flow) * 100.

**Steam T Out = Steam temperature out of second superheater.

40703-II

2-60

of distance down the cavity wall from the top. The different convective loss distributions are shown in Figure 2-29.

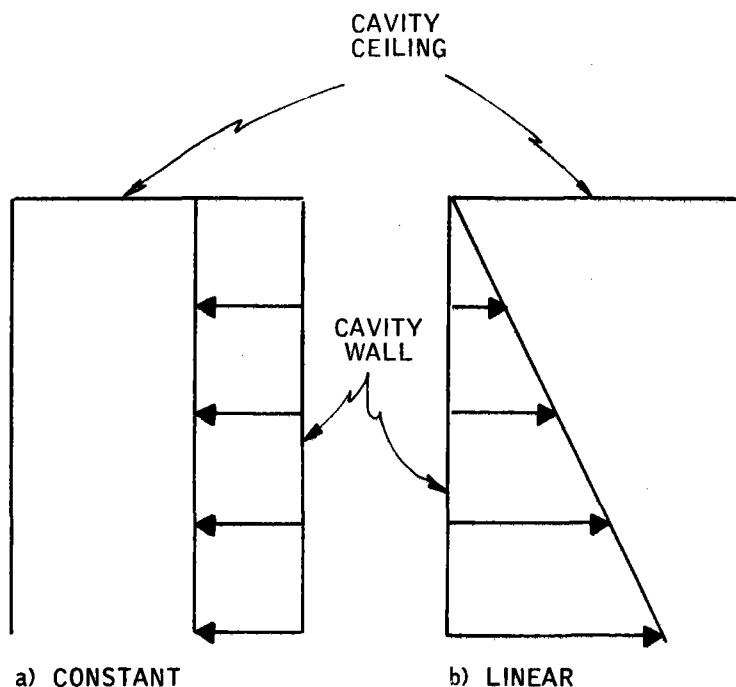


Figure 2-29. Convection Heat Loss Vertical Distribution

The results show a wide variation in the effect of convection losses on steam outlet temperature and atemperator flow rates. In the case where the convective lost flux is a constant, we are unable to make rated steam at 13.7 MW. The linearly varying flux model does not strongly affect the relative amount of superheat energy absorbed into the steam, as shown by the small changes in percent atemperator flow from the base case (no convection losses).

There is a lack of work reported in the literature on convective losses from cavities. The additional problem of determining the heat loss as a function of cavity position (or the air mass temperature and velocity inside the cavity as a function of position) has received no work. Further work in the determination of heat losses and heat loss distribution from a cavity is needed.

Thermal Storage Subsystem Performance

The pilot plant thermal storage subsystem will produce 7 MW(e) net for 3 hours after a 20-hour hold period. During the 20-hour hold period, there are losses both from thermal conduction and from sealing and tracing steam requirements. Tracing steam requirements are for 600 kg/hr of steam at 239 kPa and 121°C. Table 2-10 summarizes the heat loss rates from thermal storage.

The maximum output rate from storage is set to give 7 MW(e) output after supplying all auxiliary power necessary to operate the plant from the storage subsystem. The resulting discharge rate for storage is 31.6 MW(th). The storage charge rate was sized to match the storage discharge rate. Because charging of thermal storage is only 83.8 percent efficient, the design requires a gross charge input rate from the receiver of 37.7 MW(th). The 83.8 percent efficiency represents a minimum plant installed and operating cost. Both the charge and discharge systems can operate at any flow rate from zero up to the maximum. The discharge system can maintain the outlet steam at rated conditions throughout the range of flow rates.

The thermocline main storage system is charged with oil at 303°C and has cold oil returned to it at 249°C. The system has a use factor (fraction of total volume from which energy can be extracted through one cycle) of 0.774 after a 20-hour hold period, during which time the system has been supplying sealing and tracing steam. The use factor is based on charging thermal storage until the oil outlet temperature from the bottom of the thermocline rises to 290°C and discharging thermal storage until the oil outlet temperature from the top of the thermocline drops to 300°C. Total time required to charge the system is 4 hours.

The estimated maximum time for storage to switch from hot standby to rated power output is less than 1 minute. A return to standby can be achieved in approximately the same period of time.

Table 2-11 summarizes the major performance characteristics of the solar plant. More detail is available in the storage subsystem volume (Volume V).

EPGS/Balance-of-Plant Performance

The electrical power generation subsystem (EPGS) and the balance of plant (BOP) discussed here will include turbine operation, cooling tower performance, and auxiliary power requirements for the pilot plant. Detailed discussion of the EPGS/BOP, including seismic considerations, master control mechanisms, and building design and layout, is presented in Volume VI.

Table 2-12 lists the base EPGS turbine parameters for the pilot plant design. The turbine has been selected as a dual-port, automatic-admission turbine manufactured by GE. Turbine nominal rating and respective high- and low-pressure port steam inlet considerations are as given in the table. The EPGS includes a wet cooling tower and three stages of feedwater heating. Figure 2-30 is a schematic of the heat balance for the design throttle steam flow condition. This figure shows steam conditions at various locations in the EPGS cycle, including the condenser and feedwater heaters.

The EPGS gross turbine efficiency is defined as the gross electrical output of this generator divided by the thermal power input to the turbine. Figure 2-31 shows the gross turbine efficiency for the pilot plant system. The figure shows a curve of efficiency for operation from throttle steam (receiver) only, and operation from admission steam (storage) only. Curves for simultaneous throttle and admission steam operation will lie roughly proportionately between the two curves. The gross turbine efficiency curves are based on a turbine backpressure of 6.8 kPa at all steam flows.

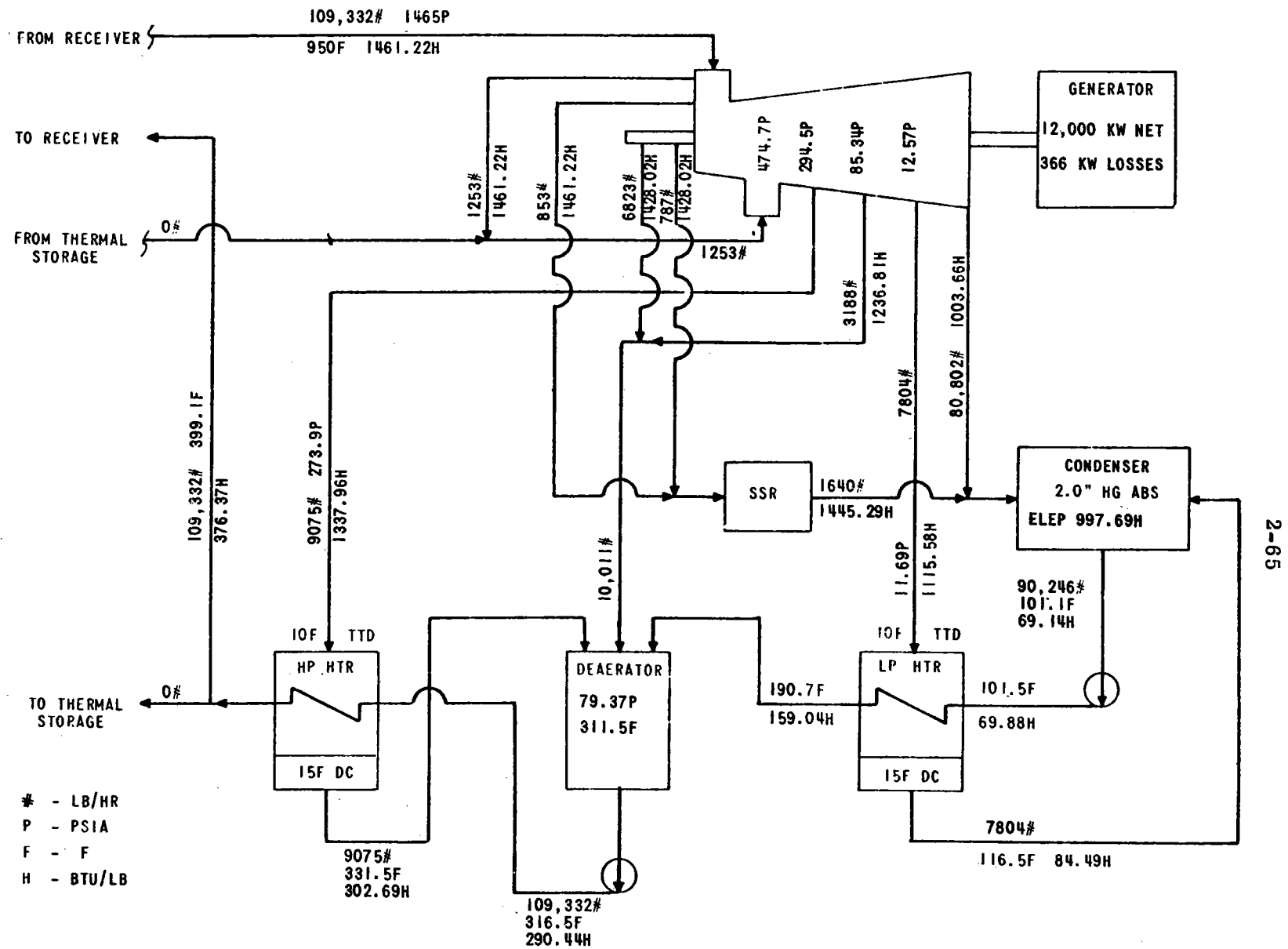
Table 2-10. Thermal Storage Subsystem Heat Losses
(100-Hour basis)

Item	Percentage of		
	Main Storage Capacity	Superheater Storage Capacity	Total Capacity
Tankage	11.6	16.9	12.3
Piping	3.2	6.4	3.6
Heat exchangers	2.5	2.7	2.5
Steam lines	1.4	9.6	2.4
Total	18.7	35.6	20.8

Table 2-11. Thermal Storage Subsystem Baseline Characteristics Performance

Parameter	Value
Net electric output	7.0 MW(e)
Output duration	3.0 hr
Charge steam pressure/temperature	10,101 kPa/510°C
Discharge steam pressure/temperature	3620 kPa/390°C
Hot Hitec temperature	454°C
Cold Hitec temperature	299°C
Hot oil/rock temperature	303°C
Cold oil/rock temperature	249°C
Gross thermal efficiency	0.285
Maximum charge rate	31.6 MW(th)
Maximum discharge rate	31.6 MW(th)
Charge efficiency	0.838
Thermocline utilization efficiency	0.774

40703-II



$$\text{GROSS TURBINE HEAT RATE} = \frac{109,332 (1461.22 - 376.37) \frac{\text{BTU}}{\text{HR}}}{12,000 \text{ KW}} = 9,884 \frac{\text{BTU}}{\text{KW-HR}}$$

Figure 2-30. Pilot Plant Design Heat Balance Schematic

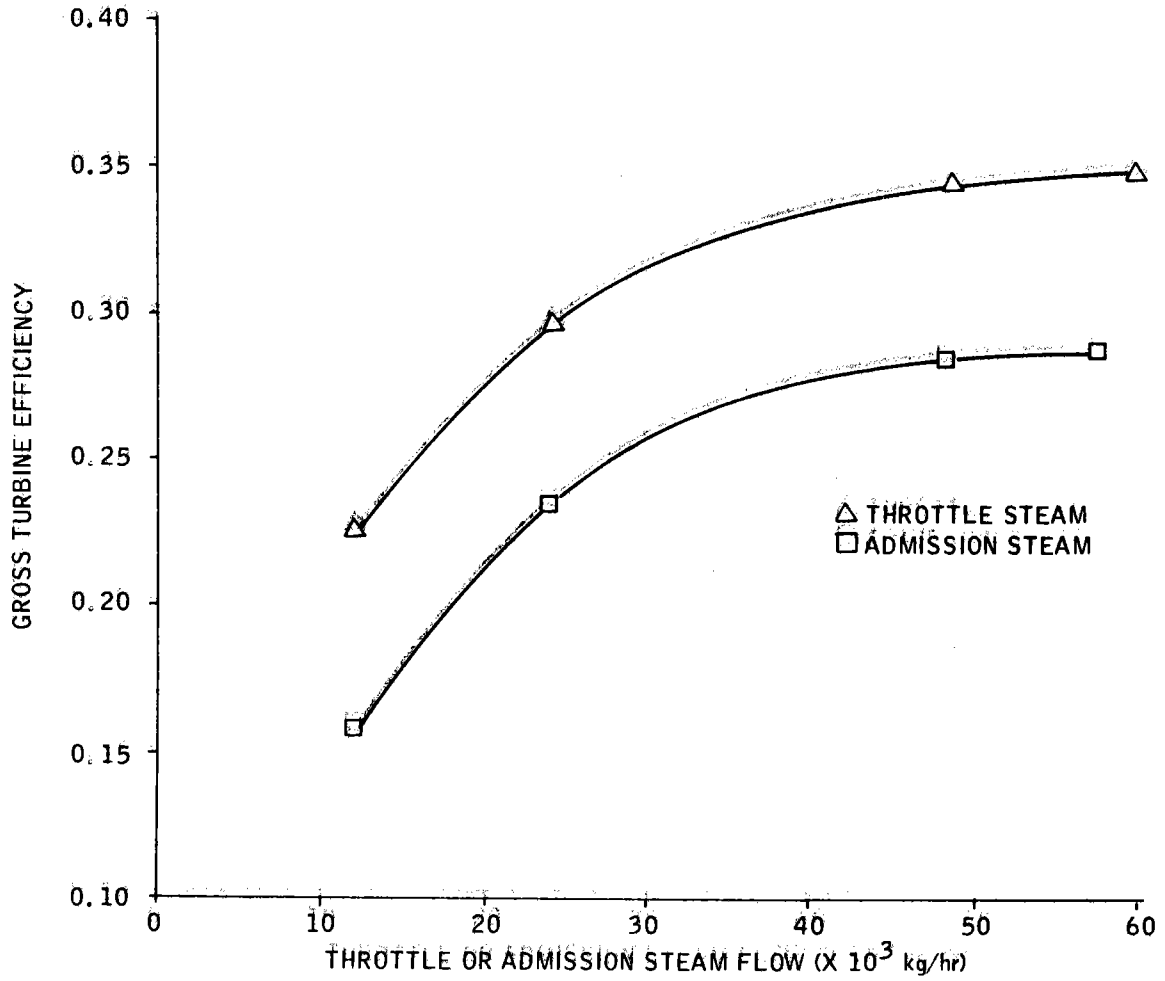


Figure 2-31. Pilot Plant Gross Efficiency

Table 2-12. Electrical Power Generation Subsystem Parameters

Parameter	Pilot Plant
Turbine type	Dual-port, automatic-admission
Turbine nominal rating	15 MW(e)
Throttle pressure	1010 kPa
Throttle temperature	510°C
Admission pressure	3275 kPa
Admission temperature	378°C
Number of feedwater heaters	3
Heat rejection type	Wet cooling tower

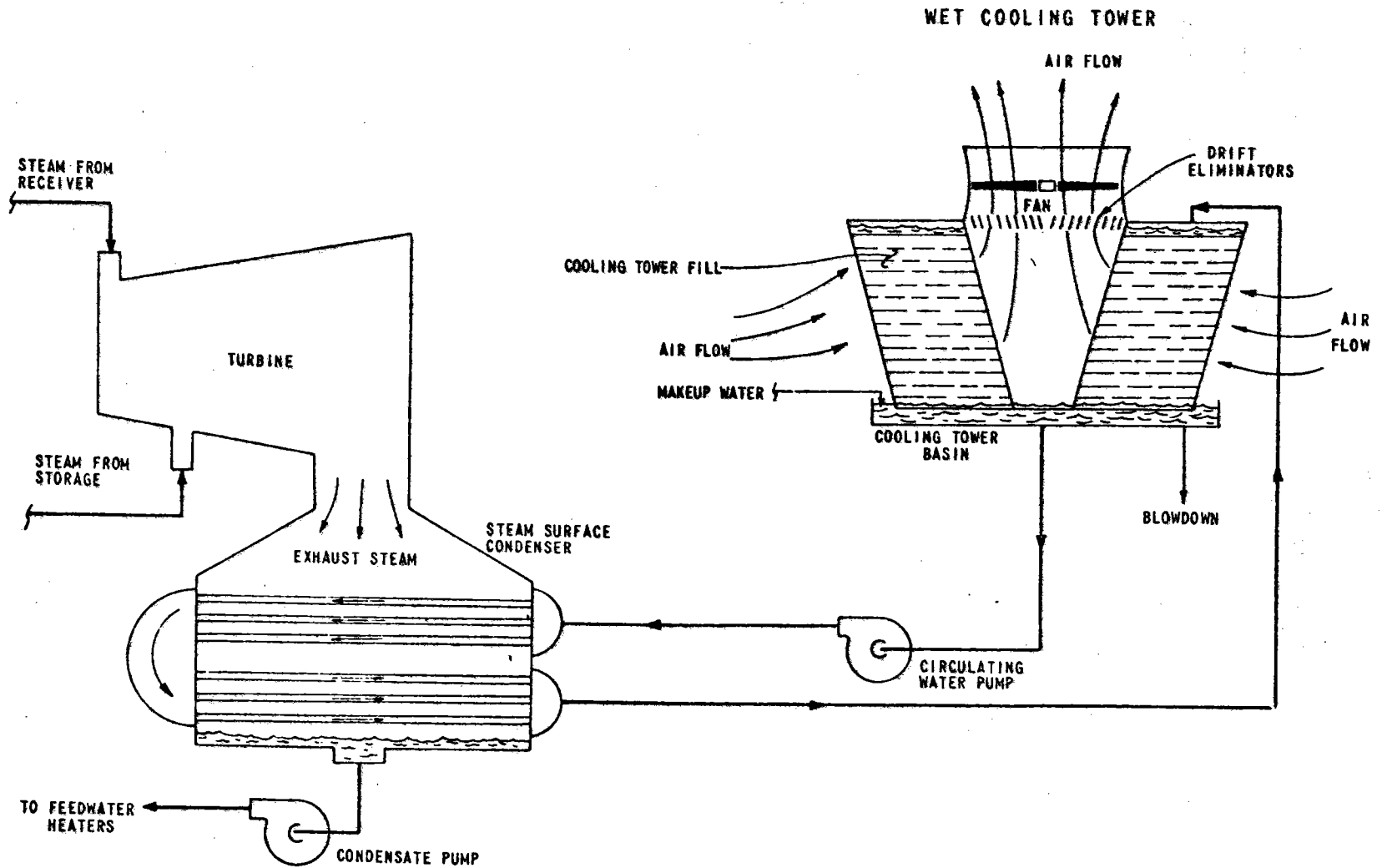
The pilot plant uses a wet cooling tower for heat rejection. Figure 2-32 is a drawing of the condenser and cooling tower.

The condenser pressure, which is also the turbine backpressure, is a function of the ambient wet-bulb temperature and mass flow rate.

Figure 2-33 shows the relation of condenser pressure to mass flow rate and wet-bulb temperature.

The gross cycle efficiencies are given based on a turbine back pressure (condenser pressure) of 6.8 kPa. Figure 2-33 shows that condenser pressure is a function of mass flow rate and ambient wet-bulb temperature. Figure 2-34 shows a correction of the gross electrical output at various condenser pressures other than 6.8 kPa.

40703-II



2-68

Figure 2-32. Wet Cooling Tower with Steam Surface Condenser

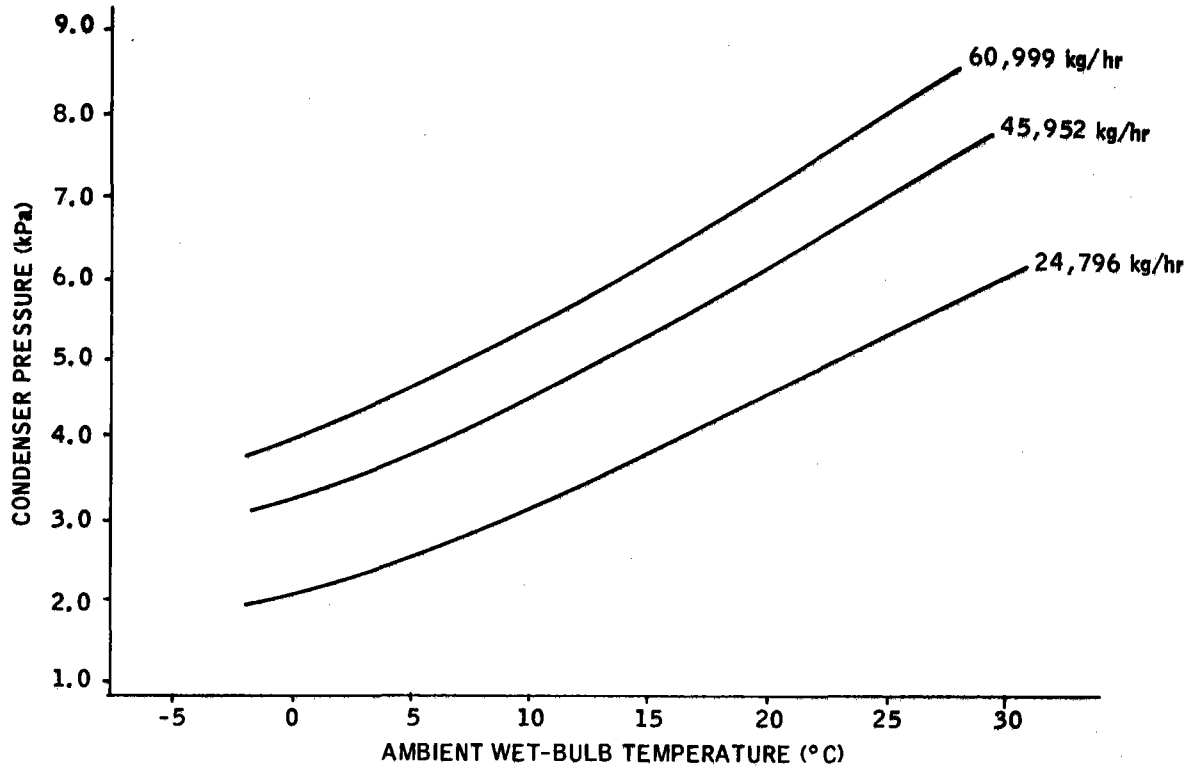


Figure 2-33. Condenser Pressure versus Wet-Bulb Temperature at Various Throttle Steam Flows

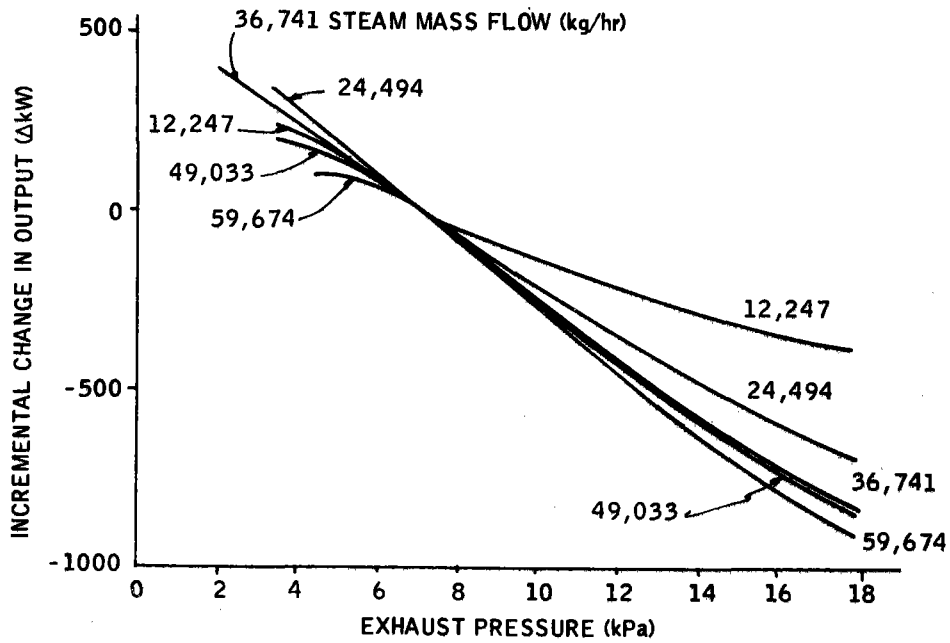


Figure 2-34. Correction Curve for Various Condenser Pressures

Pilot plant auxiliary power requirements include power required for collector operation, receiver recirculation pumps, storage recirculation pumps, condenser fans, condensate pumps, BOP heating, lighting, air condition, etc. Auxiliary power is a function of ambient wet- and dry-bulb temperature and feedwater mass flow rate, as well as mode of operation. Table 2-13 lists pilot plant auxiliary power requirements for each subsystem and operation mode. Operation mode refers to the combination of turbine steam source and storage condition. The values given in Table 2-13 are for fixed-design ambient conditions and mass flow rate.

Pilot Plant Design Point Performance

The pilot plant design point has been established as winter solstice at 2 p. m. solar time. The 2 p. m. time is a design point specification. Winter solstice was chosen to meet the requirement that the design day be the day of the year for which the plant produces the least power at 2 p. m. Other design time specifications are:

- Sun's direct normal intensity -- 0.95 kW/m^2
- Wind speed -- 3.5 m/s at reference height of 10 m
- Wet-bulb temperature -- 23°C
- Dry-bulb temperature -- 28°C
- 10 MW(e) net electric output

Using the performance predictions already presented, the requirements listed were combined to establish a pilot plant heliostat field. It was found that 1598 heliostats, arrayed in nonuniform polar packing field, can fulfill design time specifications. A stair step of the design time field and plant performance is shown in Figure 2-35.

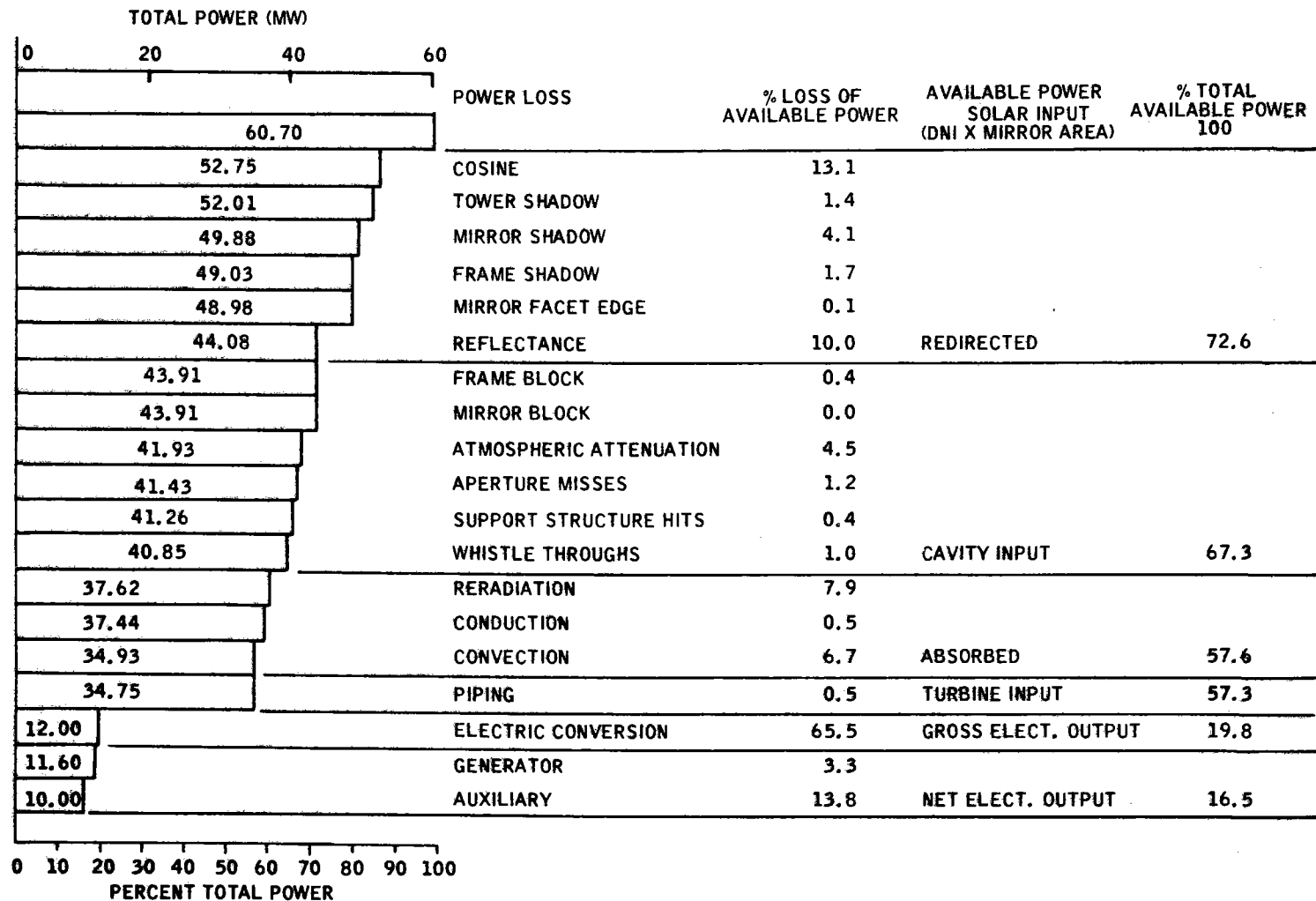
Table 2-13. Pilot Plant Auxiliary Power Requirements

Mode		Subsystem Power Requirements (kW)				Total Mode Auxiliary Power (kW)
Turbing Steam Source	Thermal Storage Condition	Collector	Receiver	Storage	EPGS and Balance of Plant	
Receiver steam	Hold	78	124	44	1741	1987
Receiver steam	Charge	78	124	337	1741	2280
Receiver and storage steam	Charge and discharge	78	124	401	1495	2062
Receiver and storage steam	Discharge	78	124	207	1495	1868
Storage steam	Charge and discharge	78	124	401	1271	1874
Storage steam	Discharge	0	0	207	1271	1478
Sealing steam	Discharge	0	0	98	854	952

40703-II

2-71

40703-II



2-72

Figure 2-35. Pilot Plant Design Point Power Stair
Step - 12/21 2 p. m.

Starting at the top of the stair step, it is shown that the total available power is 60.7 MW(e). The first loss shown is due to the cosine effect. Cosine losses represent a loss of 13.1 percent of the total available power. Proceeding down the stair step, the next losses include the tower shadow (1.4 percent, mirror shadow (4.1 percent, frame shadows (1.7 percent, and mirror facet edge loss (0.1 percent). The mirror facet edge losses account for the fact that the mirror modules are made from nine mirror pieces of sub-facets. The subfacets have a small spacing between them and a small amount of power is lost at these edges. At this point, in the stair step, there is 48.98 MW(th) available. A mirror reflectance of 0.9 was used for the design point performance estimates. This assumes that each mirror in the heliostat field is clean and thus represents an idealized performance. The redirected power is 44.08 MW(th), which corresponds to a tracking efficiency, including reflectance, of 72.6 percent.

Losses between the mirrors and the aperture are due to frame and mirror blocks and atmospheric attenuation losses. Atmospheric attenuation losses were predicted by using the loss model described in Section 7. We used typical winter afternoon conditions of relative humidity at 7 to 12 percent and a temperature of 10°C to 16°C as determined by averaging 1963 Inyokern data for several clear days near winter solstice. For these conditions, the atmospheric attenuation losses are estimated at 4.5 percent. Attenuation losses are due to both absorption and scattering of the redirected power.

At the receiver aperture, the redirected power can miss the aperture high, wide, or low, it can hit one of the support structures, or it can whistle through. These losses account for a 2.5 percent loss of the power which reaches the receiver. Of the total power available, Figure 2-35 shows that 40.85 MW(th) reaches the receiver.

Of the power which enters the cavity, some is scattered directly back out the aperture opening and some is absorbed by the metal surfaces to be either transferred to the steam or lost due to reradiation, conduction through the aperture walls, or convection from the metal surfaces. The total design-time power absorbed by the steam is 34.93 MW(th). After piping losses, the power input to the turbine is 34.75 MW(th).

The turbine thermal cycle efficiency and the generator losses combine to give a gross electric output of 11.6 MW(e). Plant auxiliary power requirements (used to operate the boiler feed pump, the recirculating pump, the condensate pump, the heliostat motor, computer systems, lighting, etc.) are approximately 1.6 MW(e), so that the net electrical output is 10 MW(e). This represents a net conversion efficiency, from total available thermal power to net electric power, of 16.5 percent.

Net Annual Energy Performance

The net annual energy calculations are made for two cases: pilot plant using receiver steam only to drive the turbine, and pilot plant using diurnal charge and discharge of storage. The net annual energy calculation model uses weather data taken from the Inyokern tape to perform a quasi-steady-state analysis of pilot plant performance over a period of a year. The net annual energy calculation model is described in Section 7 of this volume.

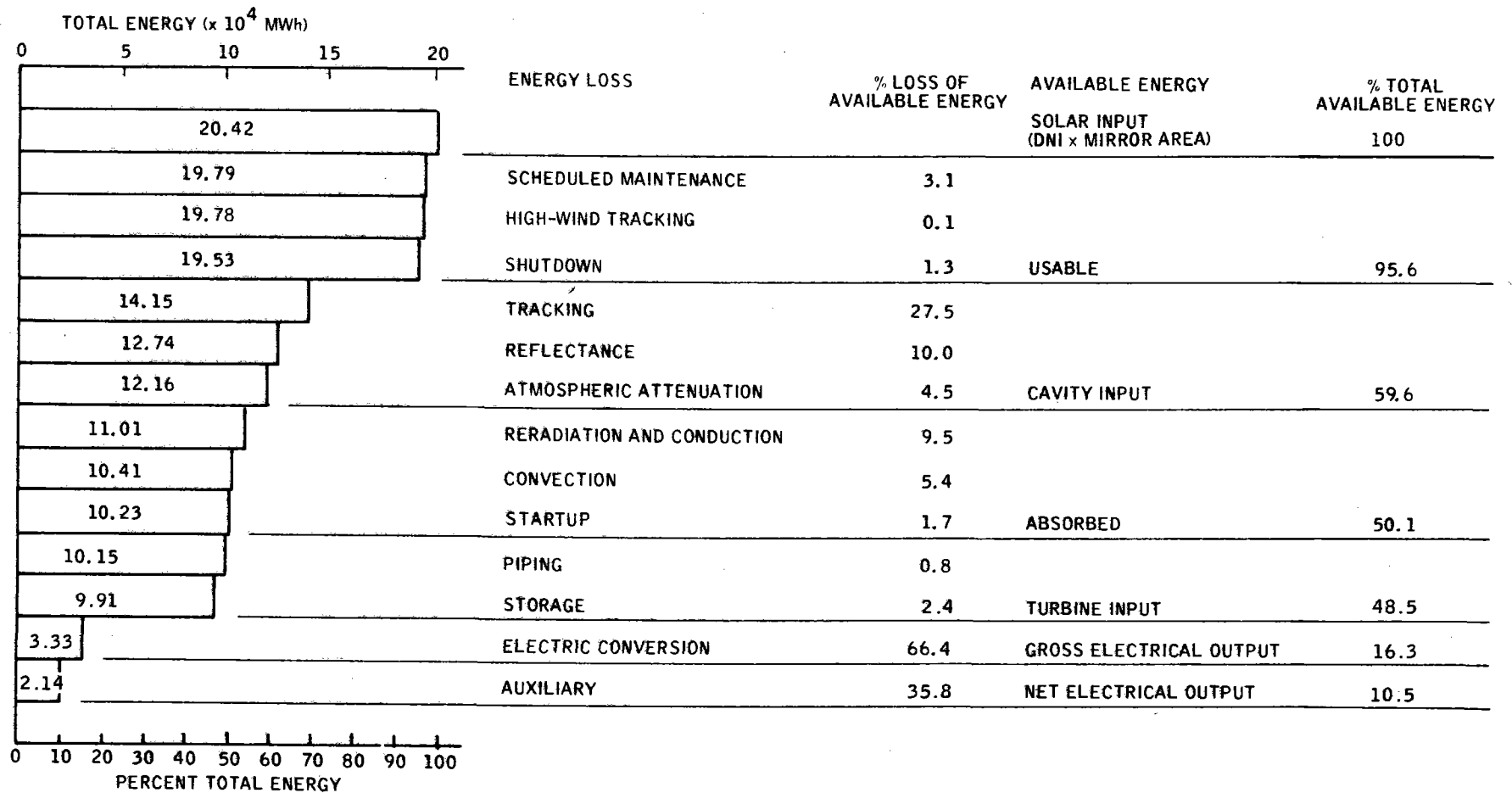
Operational Strategies -- The first strategy is to operate the turbine from receiver steam only and is referred to as the receiver-only strategy. Excess energy that cannot be accepted by the turbine at maximum conditions will be bypassed into storage. The energy in storage will only be used for sealing steam protection. Energy from the receiver is selectively passed to storage to guarantee 48 hours of sealing steam protection at sunset of each day that has sufficient insolation to meet this criterion.

The second strategy, referred to as the diurnal charge and discharge of storage strategy, is a representation of an actual operational strategy that might be used in the pilot plant. For this strategy, turbine output will be limited to 10 MW(e) net output. Any energy collected by the receiver above the amount required to produce this output will be used to charge storage. Storage will be discharged each day at a turbine net output of 7 MW(e) to prolong the length of time that electrical energy can be produced. Sealing steam will be provided by storage, with minimum requirements of 20 hours of protection. This amount differs from the 48 hours used in the first case because the storage subsystem can in fact supply sealing steam for several weeks beyond the 20-hour requirement by suffering thermal degradation below the normal storage operating temperature limits. If degradation should occur, the storage must be recharged to appropriate operating temperatures before storage can be used to supply admission steam to the turbine.

Figures 2-36 and 2-37 show stair step pilot plant net annual energy calculation results for the two operational strategies of receiver-only operation and diurnal charge and discharge of storage. Tabular values of the net annual energy results are given in Table 2-14. Each step in the stair step figures represent a loss of available energy and is described as follows:

- DNI x Mirror Area - The direct normal intensity (DNI) mirror area product yields the maximum total possible energy that is available to the pilot plant. DNI is given on the Inyokern weather tape in kW/m² integrated in 1-hour intervals. The mirror area is based on 1598 heliostats at 40 m² each for a total mirror area of 63920 m².

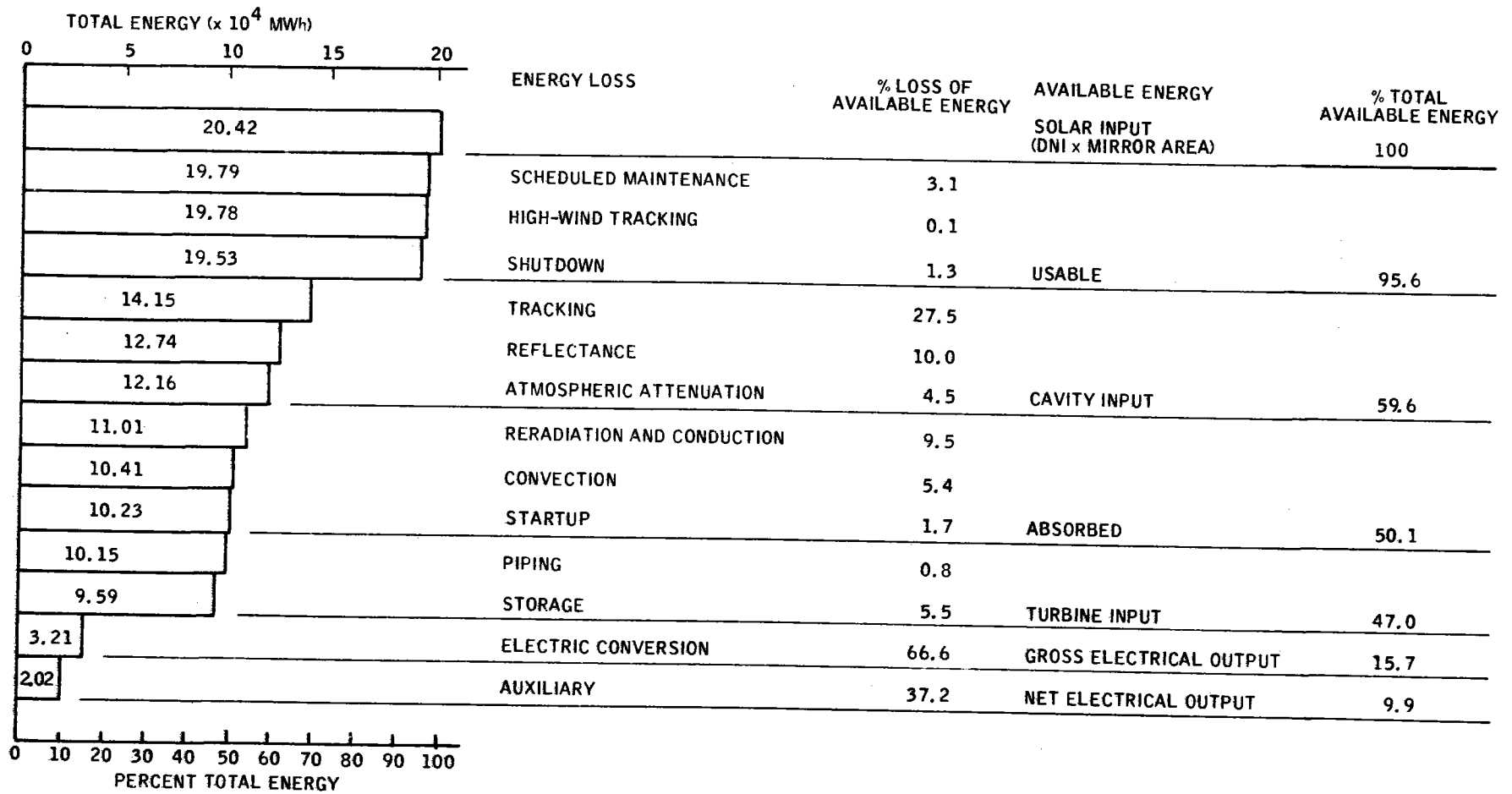
40703-II



2-76

Figure 2-36. Pilot Plant Net Annual Energy Stair Step (Receiver-Only Operation)

40703-II



2-77

Figure 2-37. Pilot Plant Net Annual Energy Stair Step (Diurnal Charge and Discharge at Storage Operation)

Table 2-14. Pilot Plant Net Annual Energy Results

Parameter	Receiver Only	Diurnal Charge and Discharge of Store
DNI x Mirror Area	2.042 x 10 ⁵ MWh(t) 3.195 MWh(t) / m ²	2.042 x 10 ⁵ MWh(t) 3.195 MWh(t) / m ²
Gross Output	3.328 x 10 ⁴ MWh(e) 0.521 MWh(e) / m ²	3.209 x 10 ⁴ MWh(e) 0.502 MWh(e) / m ²
Net Output	2.135 x 10 ⁴ MWh(e) 0.334 MWh(e) / m ²	2.017 x 10 ⁴ MWh(e) 0.316 MWh(e) / m ²

Average Collection Efficiency

$$\left[\frac{\text{Energy into Cavity}}{\text{Usable Energy}} \right] \quad 62.3\% \quad 62.3\%$$

Average Cavity Efficiency

$$\left[\frac{\text{Absorbed Energy}}{\text{Energy into Cavity}} \right] \quad 84.1\% \quad 84.1\%$$

Average Net Cycle Efficiency

$$\left[\frac{\text{Net Output}}{\text{Energy into Turbine}} \right] \quad 21.6\% \quad 21.1\%$$

- Maintenance Loss - The pilot plant is assumed to undergo 2 weeks of scheduled maintenance each year. The maintenance period is chosen to occur at the end of the year. Energy loss from unscheduled maintenance is ignored in the annual energy model. Maintenance periods represent a direct loss of available energy from the heliostat field.
- High-Wind Tracking Loss - The heliostats are designed so that at wind speeds below 13.5 m/s, sufficient tracking resolution can be maintained. At wind speeds above 13.5 m/s, tracking errors substantially increase. Interrogation of the Inyokern weather tape shows that for only 6 hours out of a yearly possible of 8760 hours does the wind speed exceed 13.5 m/s. Although energy can be collected when the wind speed exceeds 13.5 m/s, the assumption is made for the annual energy calculations that the heliostat field is stowed at wind speeds above 13.5 m/s. High-wind tracking loss represents a loss of available energy incident on the heliostat field.
- Shutdown Loss - As the insolation value decreases in the evening, the receiver steam mass flow rate and net electrical output decrease. At rated temperature and pressure, the minimum steam mass flow necessary to produce net electrical output is approximately 6800 kg/hr. The absorbed power required to maintain this flow is approximately 3 MW(th), which corresponds to approximately 7 MW(th) incident on the heliostats at sunset on the equinox. When power levels incident on the heliostats fall below the 7 MW(th) threshold, net electrical output cannot be produced and the heliostats are defocussed and the receiver closed up. Available insolation which could have been collected after heliostat shutdown is designated shutdown loss.

- Tracking Loss - Tracking losses occur from cosine losses, blocking, shading, aperture misses, and whistle throughs. The net annual energy model uses the steady-state overall field tracking efficiency versus the sun's azimuth and elevation angles as the basis for tracking losses.
- Reflectance Loss - The mirrors are assumed to be clean with reflectance of 0.9.
- Atmospheric Attenuation - Transmittance losses between the mirror and the receiver are based on the results of studies presented in Section 7 of this volume. The net annual energy model uses an average value of 4.5 percent loss of power from the mirrors to the receiver.
- Reradiation and Conduction Loss - Energy lost by reradiation and conduction is given by the cavity efficiency, which is defined as the power absorbed after reradiation and conduction loss divided by the power into the receiver. The net annual energy model uses steady-state cavity efficiency as a function of power into the cavity.
- Convection Loss - Convection losses for the net annual energy calculations are given as a function of ambient temperatures and wind speed:

$$\dot{Q} = 1.0036 (10^{-5}) (h + d/4) \left[Vd (H/10)^{0.15} \right]^{0.8} (\Delta T)$$

where

\dot{Q} = Convection heat loss (MW)

h = Cavity height (m)

d = Cavity diameter (m)

V = Wind velocity at 10 m height (m/s)

H = Tower height (m)

ΔT = T cavity avg. - T ambient ($^{\circ}\text{C}$)

T cavity avg = $(T_{\text{boiler}} + T_{\text{superheater}}) / 2$

- Startup Loss - Startup loss is defined as the energy absorbed during startup that produces no net electrical output. This energy is used to warm metal surfaces and begin pressure and temperature ramps. Results from the dynamic simulation model discussed in Section 7 indicate that an average value of absorbed energy needed to start up and produce net electrical output is approximately 5 MW(th). Due to lack of other theoretical or experimental data, the net annual energy calculation model will assume that the first 5 MW(th) absorbed each day will be startup loss and will produce no net electrical output.
- Piping Thermal Loss - Piping thermal losses are assumed to be fixed at the design condition for all losses. Design piping thermal losses are based upon 5.6 $^{\circ}\text{C}$ temperature drop in the downcomers, with the loss rate equal to 192 kW.
- Storage Losses - Storage losses include storage thermal losses, sealing and tracing steam requirements, and the storage charging efficiency loss. Fixed values based on design conditions for storage losses are used as shown in Table 2-15.

Table 2-15. Pilot Plant Storage Losses

Parameter	Receiver Only	Diurnal Change and Discharge of Store
Thermal loss	68 kW	300 kW
Seal and tracing steam	340 kW	450 kW
Charging efficiency	0.86	0.86

In addition to storage losses, the storage initial condition is chosen such that the storage condition at the end of the year is the same as at the start of the year.

- Excess Energy - Excess energy can be absorbed when the turbine cannot use all of the available energy and storage is completely full. At such time, steam can be vented off or heliostats can be selectively defocussed. Results of the annual energy calculations indicate that for the strategies chosen there is no excess energy absorbed.
- Gross Electric Conversion Loss - The gross cycle efficiency versus thermal power available at the turbine is given from GE turbine data. Gross cycle output is also adjusted for varying turbine back pressures as a function of the ambient wet-bulb temperature as described previously.
- Auxiliary Energy Loss - Auxiliary energy requirements used for the pilot plant annual energy calculations are the design values for each operating mode. The auxiliary energy includes overnight balance of plant use. Although auxiliary energy is a

function of ambient conditions and steam mass flow rate as well as mode of operation, deviations from the fixed values given are expected to be small and the net annual energy calculation model will assume that such deviations are small.

COMMERCIAL PLANT DESCRIPTION

The commercial plant is a four-tower, four-field design with a single central electric power generation facility. A dual-injection turbine is used with front port inlet conditions of 1.00×10^4 kPa/510°C and second port inlet conditions of 3.28×10^3 kPa/390°C. The plant uses the oil/rock main storage and Hitec superheat storage as an energy storage system.

Field Plant Layout

The commercial plant consists of four circular fields with the tower in each field located one-half radius south of center. There is a small circular cutout area with no heliostats inside of it around the base of each tower.

The heliostats used in the commercial plant are of the same design as those used in the pilot plant. The heliostats are radially spaced with a decreasing ground cover ratio as the distance from the fields tower is increased. Table 2-16 summarizes the commercial plant field and heliostat parameters. Figure 2-38 shows the layout of the four fields.

The plant site is arranged with priority given to facilities which are the most difficult to manipulate. The heliostat fields are located as close to each other as possible and still leave adequate space for intermediate access. The plant and thermal storage facilities are located to equalize piping to the receiver towers and to minimize the total piping required. The cooling

Table 2-16. Field Layout Parameters

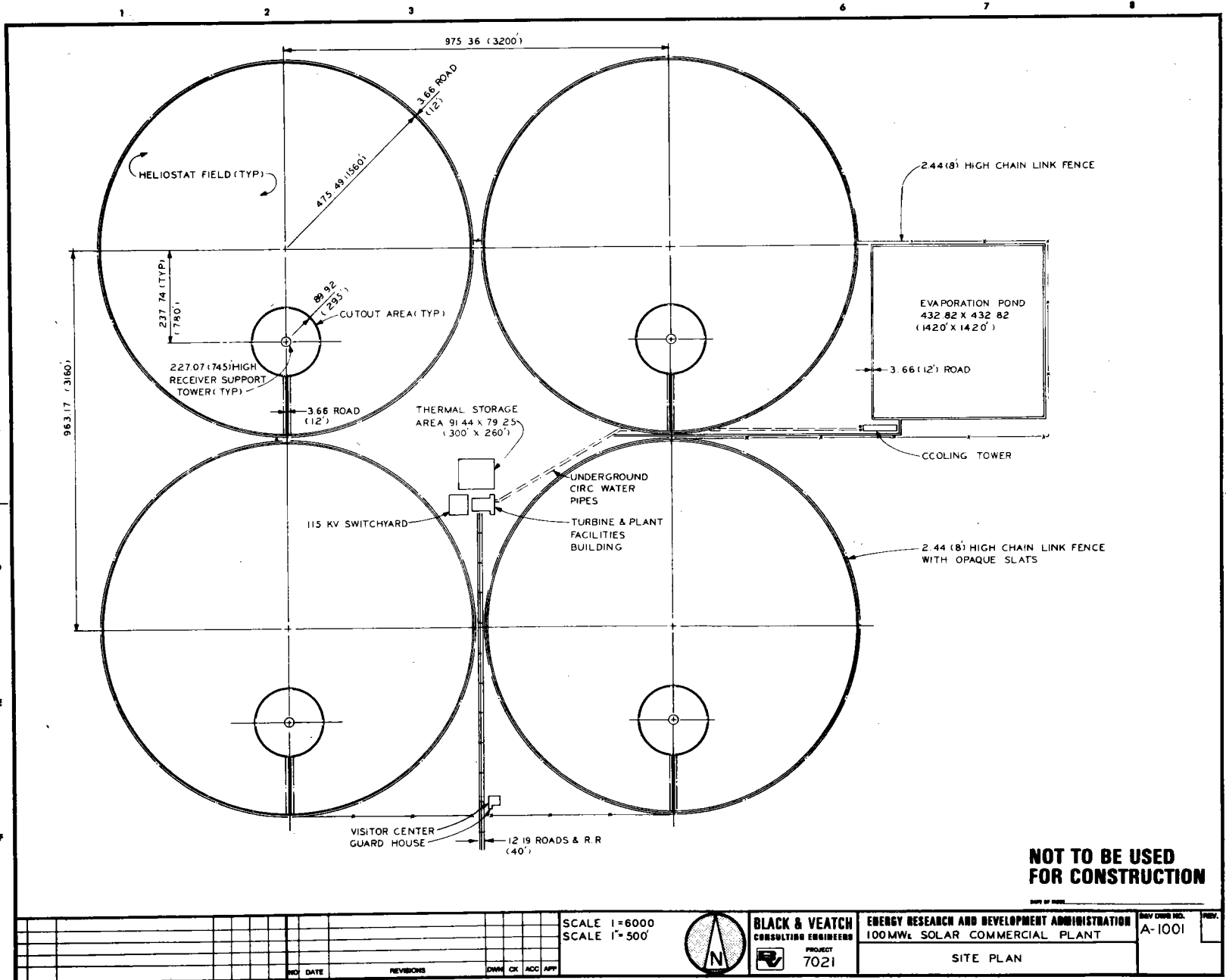
Parameter	Value
Heliostat type	Tilt-tilt, 4-facet
Heliostat mirror area	40 m ²
Number of fields	4
Number of heliostats/field	5055
Average ground cover ratio	0.29
Field outer radius	681 m
Cutout radius	90 m
Tower location	340.5 m south of field center

tower and evaporation pond location is dictated by prevailing winds, which are assumed to be the same as for the pilot plant. Table 2-16 summarizes the layout.

The steam piping layout for the commercial four-module design is shown in Figure 2-39. Horizontal piping from each receiver tower to the header point is below ground in covered trenches. Due to the high pressure and temperature design requirements for the main steam pipe, chrome-moly ASTM Specification A335 Grade P12 pipe is used. Twelve-inch Schedule 160 pipe is used from each receiver tower to keep the pressure drop in each branch line below 1034 kPa. Piping loops are provided in the vertical and horizontal runs of piping to account for thermal expansion.

The feedwater piping is to follow the same routing as the main steam piping except the number of loops will be reduced. Hence, a layout for the feedwater piping is not shown. The feedwater piping is carbon steel ASTM Specification A106 Grade B. Eight-inch Schedule 140 pipe is used for each receiver branch to keep the pressure drop in each branch below approximately 276 kPa.

40703-II



2-85

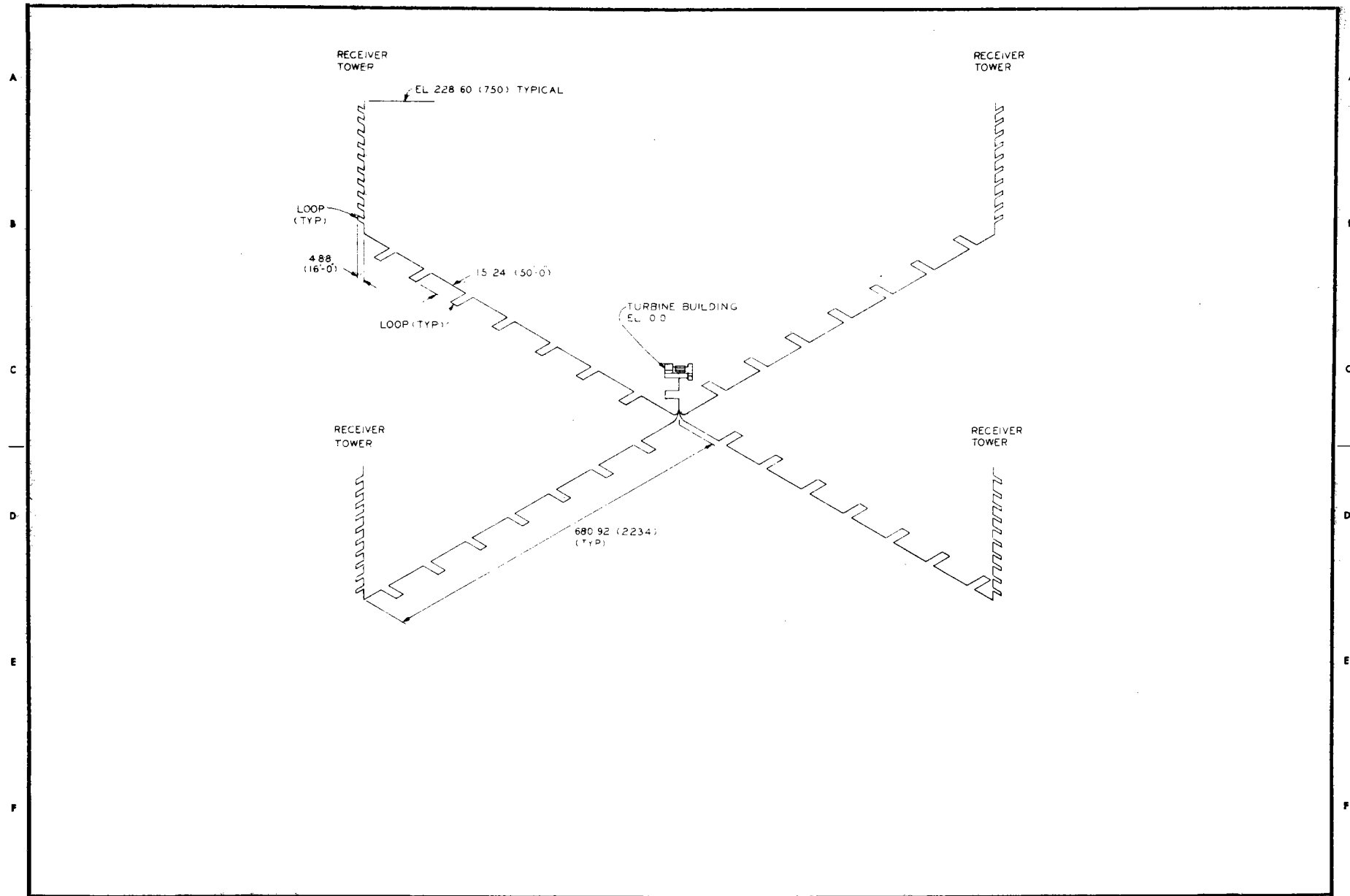
NOT TO BE USED FOR CONSTRUCTION

<table border="1"> <tr> <td>NO.</td> <td>DATE</td> <td>REVISIONS</td> <td>DRAWN</td> <td>CHK</td> <td>ACC</td> <td>APP</td> </tr> <tr> <td> </td> <td> </td> <td> </td> <td> </td> <td> </td> <td> </td> <td> </td> </tr> </table>										NO.	DATE	REVISIONS	DRAWN	CHK	ACC	APP								SCALE 1"=6000 SCALE 1"=500'		BLACK & VEATCH CONSULTING ENGINEERS PROJECT 7021	ENERGY RESEARCH AND DEVELOPMENT ADMINISTRATION 100 MW _e SOLAR COMMERCIAL PLANT	SHEET NO. A-1001
NO.	DATE	REVISIONS	DRAWN	CHK	ACC	APP																						

Figure 2-38. Field - Plant Layout

40703-II

2-86



										NOT TO BE USED FOR CONSTRUCTION		BLACK & VEATCH CONSULTING ENGINEERS		ENERGY RESEARCH AND DEVELOPMENT ADMINISTRATION 100 MW _e SOLAR COMMERCIAL PLANT		DRAWING NO. M-1001		REV.
												PROJECT 7021		MAIN STEAM PIPING LAYOUT				
NO.	DATE	REVISIONS			DWY	CR	ACC	APP	DATE OF ISSUE									

Figure 2-39. Steam Line Piping Layout

For sizing the piping to the thermal storage subsystem, 50 percent of the total steam flow generated from the four receivers is used. Table 2-17 summarizes the main steam and feedwater piping lines in the plant.

Tower Receiver Design

The tower concept is patterned after the 10 MW(e) pilot plant tower structure. The tower height and top diameter are fixed by the field design, and the bottom diameter is scaled to provide adequate structural support and correct tower proportioning in accordance with current design practice. Tower construction is to be by the slip form or jump form method. Table 2-18 summarizes the tower dimensions.

Interior levels are at those locations necessary to provide maintenance and equipment support. Access platforms are provided at the strobe light levels, and an equipment room floor is provided at the top of the tower. Consistent with the pilot plant tower, access to all levels is provided by an elevator, a fixed ladder, and an equipment hoist. Figure 2-40 shows the tower design.

The solar receiver support system and housing are essentially a direct scale-up from the 10 MW(e) pilot plant receiver. Access is provided into the housing from the receiver tower through one corbel. The radiation shielding extends above and below the aperture opening a distance equal to one-half the aperture height. The cavity barrier is operated by hoists mounted in the upper portion of the housing. Figure 2-41 is a schematic of the housing and support system. Figure 2-42 shows the exterior housing and interior steam generator dimensions.

From a structural standpoint, the receiver housing and support system represent the largest departure from conventional power plant structures that will be encountered in the commercial-size plant. All structural

Table 2-17. Feedwater and Steam Pipe Sizes and Materials

Description	Design Conditions [press (kPa)/temp(°C)]	Material	Nominal Size (m)	Schedule
Feedwater booster pump discharge	$4.65 \times 10^3 / 232$	A106 GrB	0.304	Std wt
Feedwater to thermal storage	$4.65 \times 10^3 / 232$	A106 GrB	0.203	Std wt
Feedwater pump discharge	$1.69 \times 10^4 / 232$	A106 GrB	0.304	140
Feedwater to each receiver	$1.69 \times 10^4 / 232$	A106 GrB	0.203	140
Condensate return from storage	$1.03 \times 10^4 / 260$	A106 GrB	0.203	80
Mainsteam from each receiver	$1.14 \times 10^4 / 524$	A335 GrP12	0.304	160
Mainsteam common header	$1.14 \times 10^4 / 524$	A335 GrP12	0.508	160
Mainsteam to turbine	$1.14 \times 10^4 / 524$	A335 GrP12	0.406	160
Charging steam to storage	$1.14 \times 10^4 / 524$	A335 GrP12	0.406	160
Admission steam from storage	$3.79 \times 10^3 / 399$	A106 GrB	0.508	30

Table 2-18. Tower Dimensions

Parameter	Value
Tower height	227 m
Tower top diameter	14.08 m
Tower bottom diameter	23.47 m
Tower wall thickness at top	0.69 m
Tower wall thickness at bottom	0.91 m
Tower base diameter	73.2 m
Tower base maximum thickness	6.1 m

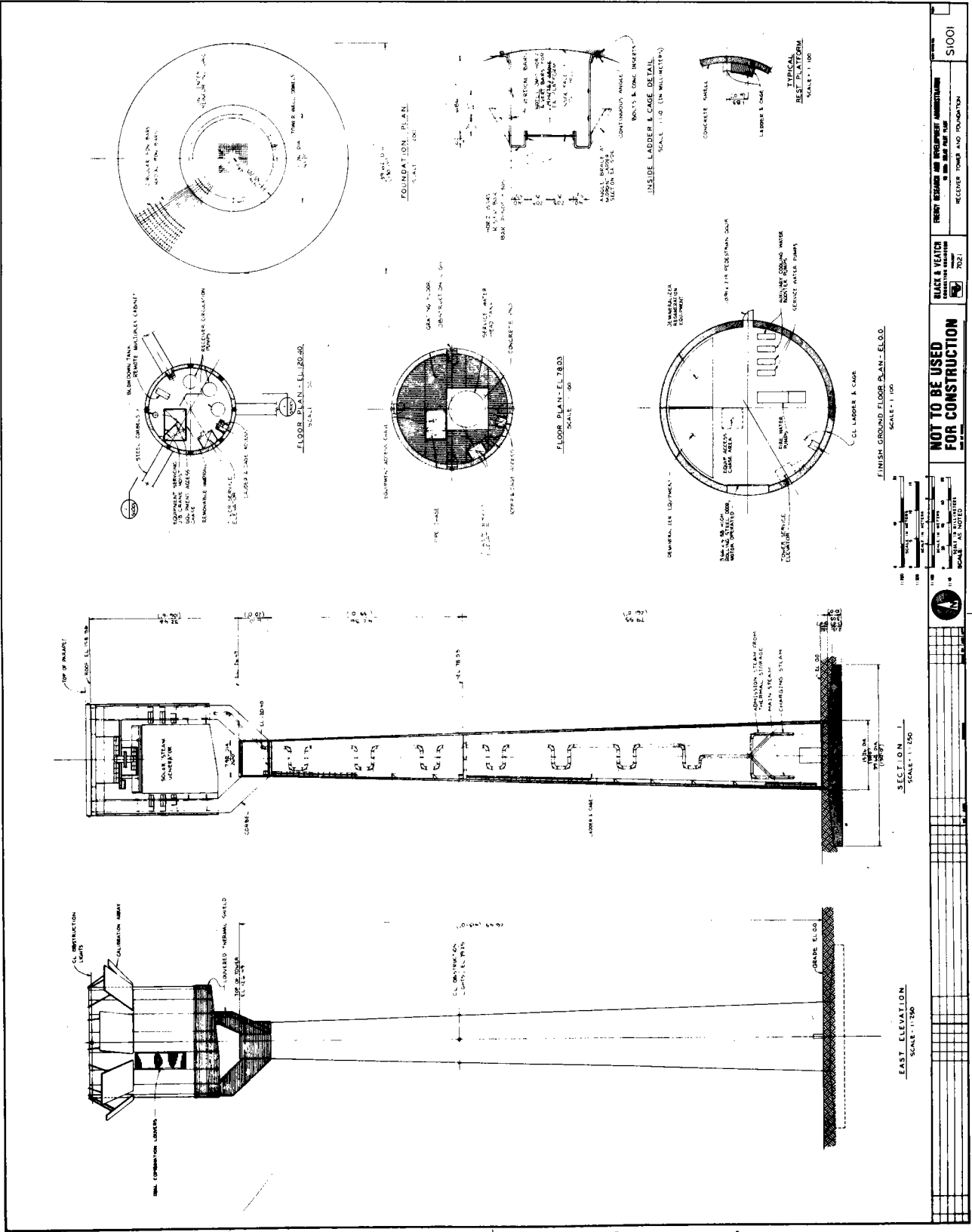


Figure 2-40. Tower Design

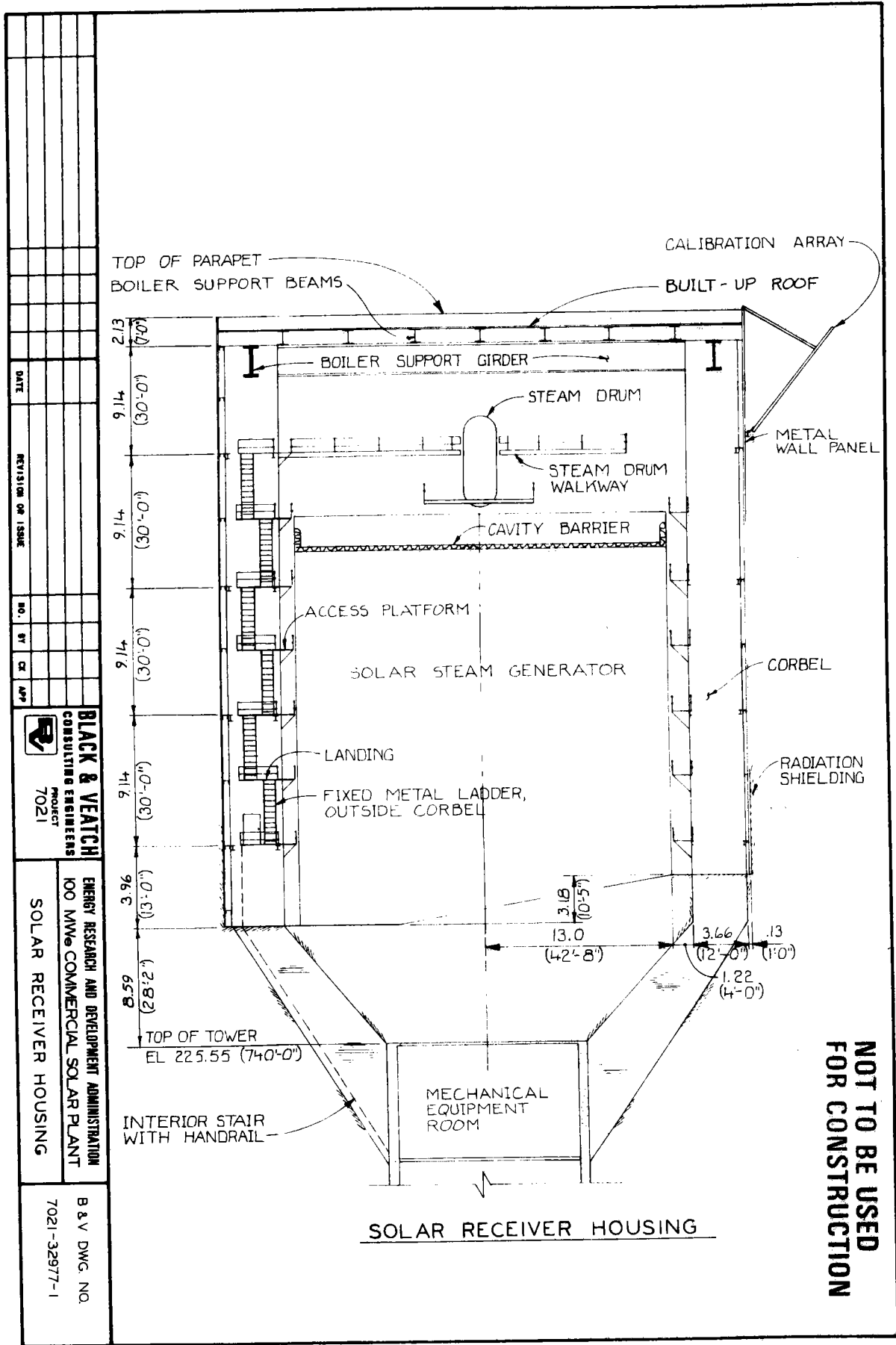


Figure 2-41. Receiver and Supports

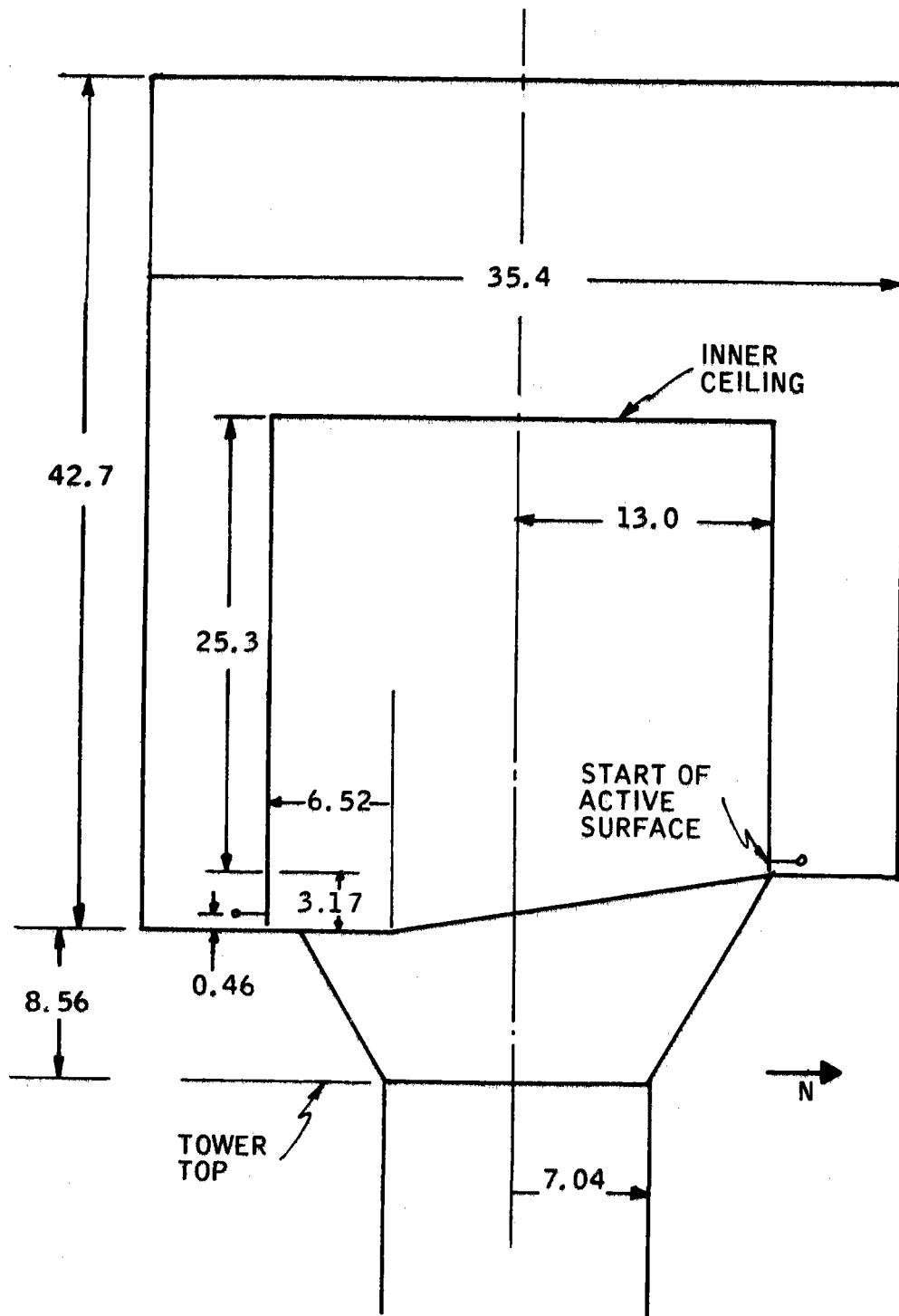


Figure 2-42. Commercial Plant Receiver Configuration
(Dimensions are in meters)

aspects of the receiver can presently be designed with current engineering technology. However, the box girder-type corbels are a major structural design item due to their inherent physical complexity and multidirectional loading requirements under design conditions.

Storage System

The storage system is a scaled-up version of the pilot plant. It consists of a Hitec superheat storage system and an oil/rock thermocline main storage system. Preheat storage will be a part of the main storage system. Inlet charge and outlet discharge steam conditions are identical to those used in the pilot plant system.

Figure 2-43 shows a system schematic for the commercial plant storage system. The number shown in parentheses in each of the boxes is the number of subunits of the given type in the commercial plant. All of the subunits of a given type are connected in parallel.

Table 2-19 is a listing of the major design parameters for the commercial thermal storage system. More detail is available in the thermal storage volume.

Balance of Plant

The commercial balance-of-plant design consists of the turbine generator, condenser, feedwater heaters, cooling tower, and turbine buildings. The sizing of the equipment for the commercial-size solar plant is based on conventional GE nonreheat turbine generator units in the size range from 80 to 120 MW(e). Figure 2-44 is a schematic of the EPGS.

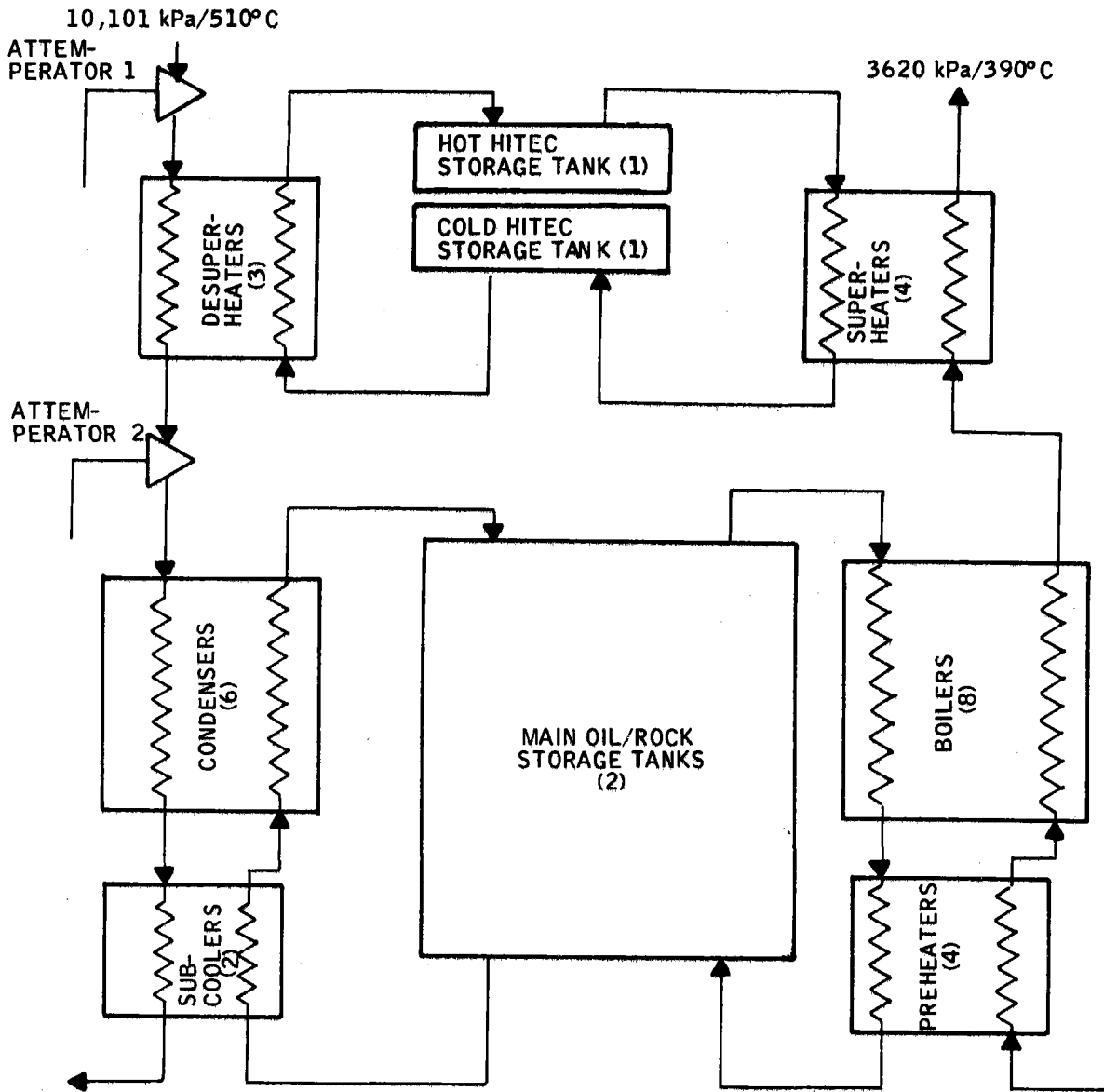


Figure 2-43. Storage System Schematic

Table 2-19. Thermal Storage Design Parameters

Parameter	Value
Main storage media	Caloria oil/rocks
Superheat storage media	Hitec salt
Thermal storage temperature:	
Main storage	303°C ↔ 249°C
Superheat storage	465°C ↔ 299°C
Main storage capacity	831 MWh(th)
Superheat storage capacity	130 MWh(th)
Gross turbine efficiency	0.318
Maximum discharge rate	284.5 MW(th)
Maximum charge rate	247.3 MW(th)
Sealing and tracing steam	2154 kg/hr

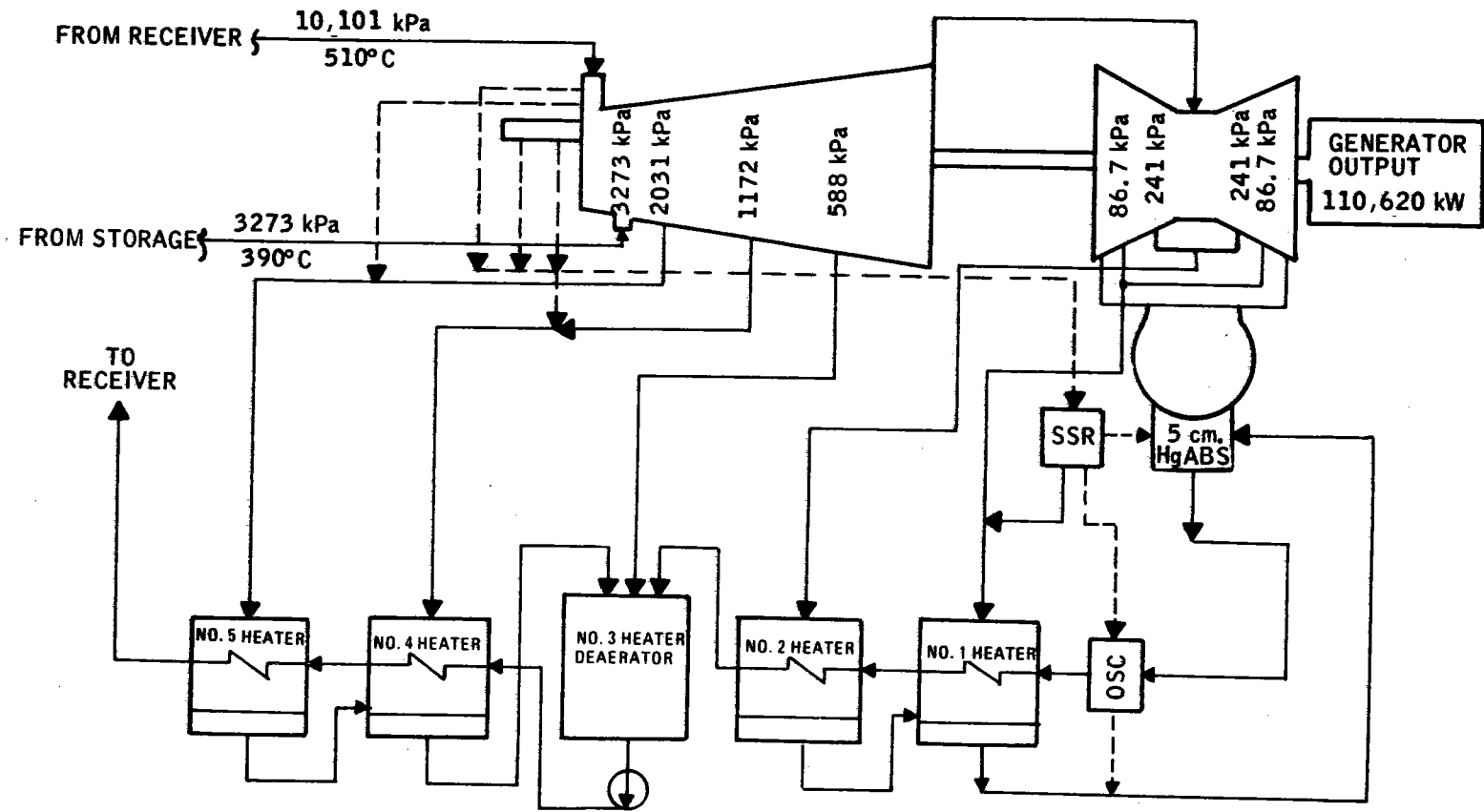


Figure 2-44. Schematic of the 100-MW(e) Electrical Power Generation Subsystem

Tubular feedwater heaters were sized and designed for the following heat transfer rates:

<u>Service</u>	<u>Transfer Rate (W/m²°C)</u>
Desuperheating	510
Condensing	3690
Subcooling	2554

Tube side velocities for the feedwater heaters were limited to a maximum of 2.74 m/s for maximum steam flow to the electric power generation subsystem and thermal storage, and a minimum of 1.37 m/s for maximum flow to the electric power generation subsystem, with zero flow to thermal storage.

The deaerating heater size was established by the Chicago Heater Company for the maximum mass flow and a guaranteed maximum oxygen content of 0.005 cc/liter. The deaerator storage tank was sized for a minimum storage capacity of 10 minutes.

Table 2-20 summarizes the design data for the feedwater heaters. The numbers in this table refer to Figure 2-44. Figure 2-45 is a schematic of the deaerator.

The condenser is designed for the maximum steam and condensate flow conditions using 29.5°C cooling water at a maximum flow rate of 7570 liters/sec, and maintaining an operating pressure of 5 cm Hg absolute. The condenser is designed to have a heat-transfer coefficient of 3234 W/m²-°C and a total heat-transfer surface area of 10,233 m².

Table 2-20. Heater Design Data

Item	Heater Number			
	1	2	4	5
1. Heat Transfer Duties, W/m^2 :				
a) Desuperheating	None	2.69×10^5	1.04×10^6	3.07×10^6
b) Condensing	2.02×10^7	1.25×10^7	9.46×10^6	1.85×10^7
c) Subcooling	3.05×10^6	6.60×10^5	9.12×10^5	1.00×10^6
d) Total	2.33×10^7	1.34×10^7	1.14×10^7	2.25×10^7
2. Heat-Exchange Surface, m^2 :				
a) Desuperheating zone	None	48.0	71.5	128.0
b) Condensing zone	253.0	236.0	211.0	290.0
c) Subcooling zone	61.2	17.5	47.0	28.4
d) Total	31.4	301.0	329.0	447.0
3. Design				
a) Tube side:				
Pressure, kPa	1034	1034	4755	4755
Temperature, °C	149	149	232	232
b) Shell side:				
Pressure, kPa	517	517	1308	2170
Temperature, °C	149	149	260	343
4. Tubes:				
a) Material	304 SS	304 SS	304 SS	304 SS
b) Size-O. D., m	1.59×10^2	1.59×10^2	1.59×10^2	1.59×10^2
c) BWG	22	22	22	22
d) No. of U-Elements	316	316	486	486
e) Average tube length, m (1/2 of U-Element)	9.97	9.57	6.78	
5. No. of Passes, Tube Side	2	2	2	2
6. Approximate Dimensions:				
a) O. D., m	0.711	0.711	0.864	0.864
b) Overall length, m	11.05	10.7	7.93	10.4
7. Pressure Drop Tube Side, kPa	127.6	123	138(max)	172(max)

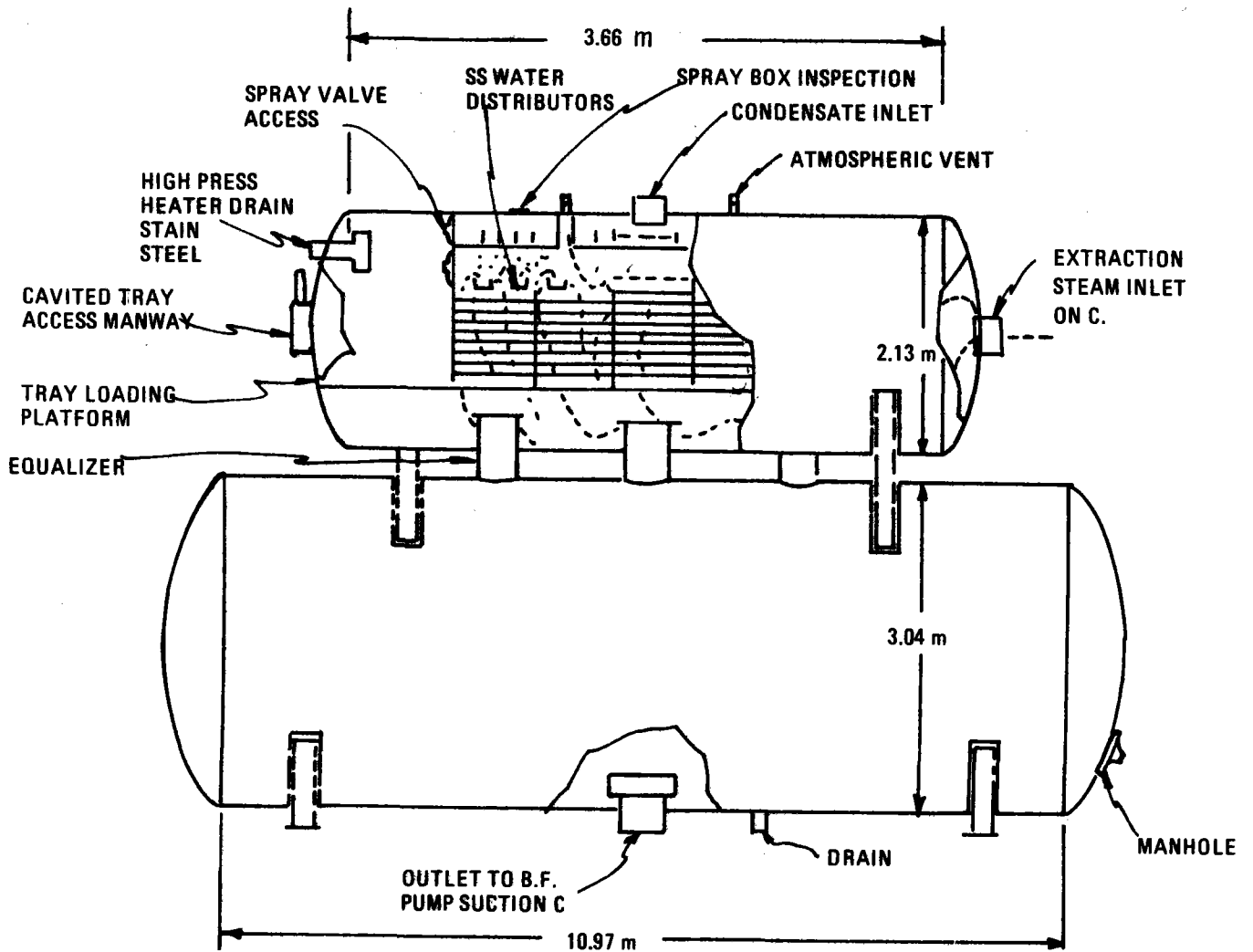


Figure 2-45. Utility Cycle Tray Deaerating Heater for 100-MW(e) Commercial Pilot Plant

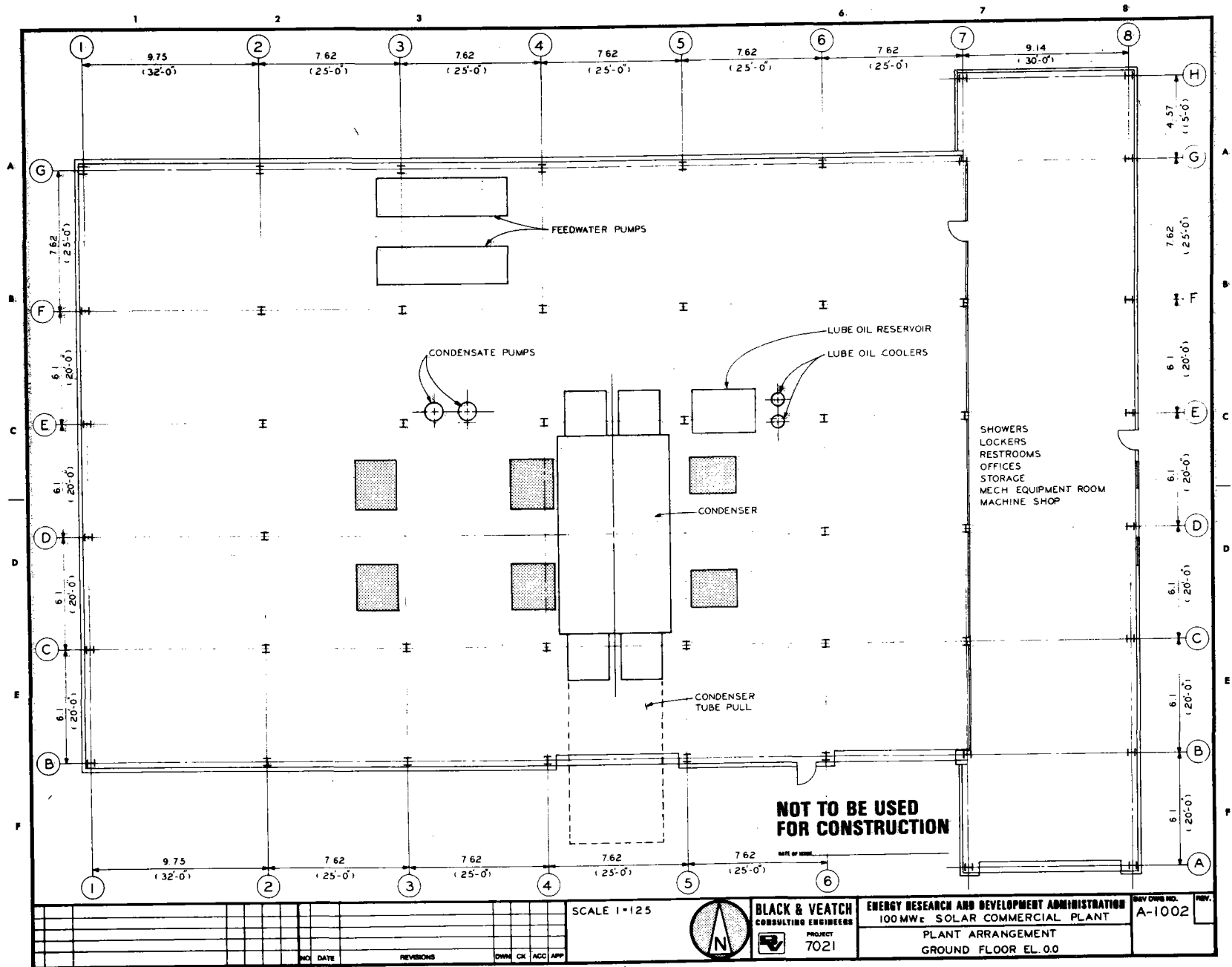
The cooling tower was sized by Marley Company for a duty of 209.2 MW(th) when providing 8831 liters/sec of cooling water at 29.5°C with a wet-bulb temperature of 23.0°C. Table 2-21 summarizes the cooling tower design. Of the 8831 liters/sec, 7570 liters/sec are for the turbine condensing duty and 1261 liters/sec are for the auxiliary cooling requirements.

The turbine building foundation requirements are similar to those of a conventional fossil-fueled plant of comparable size. Soil characteristics at the commercial plant site are assumed to be similar to those at the 10 MW(e) pilot plant site. All foundations within the turbine building area are reinforced concrete spread footings with pedestals to grade, sized for a maximum soil-bearing pressure of 24000 kg/m². The footings are founded a minimum of 1.5 m below grade. A grade slab is to be poured for the ground floor finish slab. The turbine generator foundation will require 875 m³ of reinforced concrete, and the column support footings for the turbine building will require 191 m³ of concrete.

The size and type of foundations required for the turbine building are sensitive to soil conditions at the final site. Final design should incorporate differential settlement calculations. Total settlement of 13 mm (0.5 in.) and differential settlement of 6 mm (0.25 in.) are not unusual and are acceptable with spread footing foundation systems.

Figures 2-46 through 2-49 are schematics of the turbine building design for the commercial plant. A modular design concept is used in the development of the plant arrangement. The main turbine generator building includes an enclosed ground floor and mezzanine floor and an open operating floor and deaerator platform. The control room and computer room are at the same level as the turbine generator and are enclosed. All electrical equipment is located on the mezzanine and ground floors under the control and computer rooms.

40703-II



2-100

Figure 2-46. Turbine Building Ground Floor Plan

SCALE 1=125

BLACK & VEATCH
CONSULTING ENGINEERS

PROJECT 7021

ENERGY RESEARCH AND DEVELOPMENT ADMINISTRATION
100 MWE SOLAR COMMERCIAL PLANT

PLANT ARRANGEMENT
GROUND FLOOR EL. 0.0

DATE OF ISSUE

REV. A-1002

40703-II

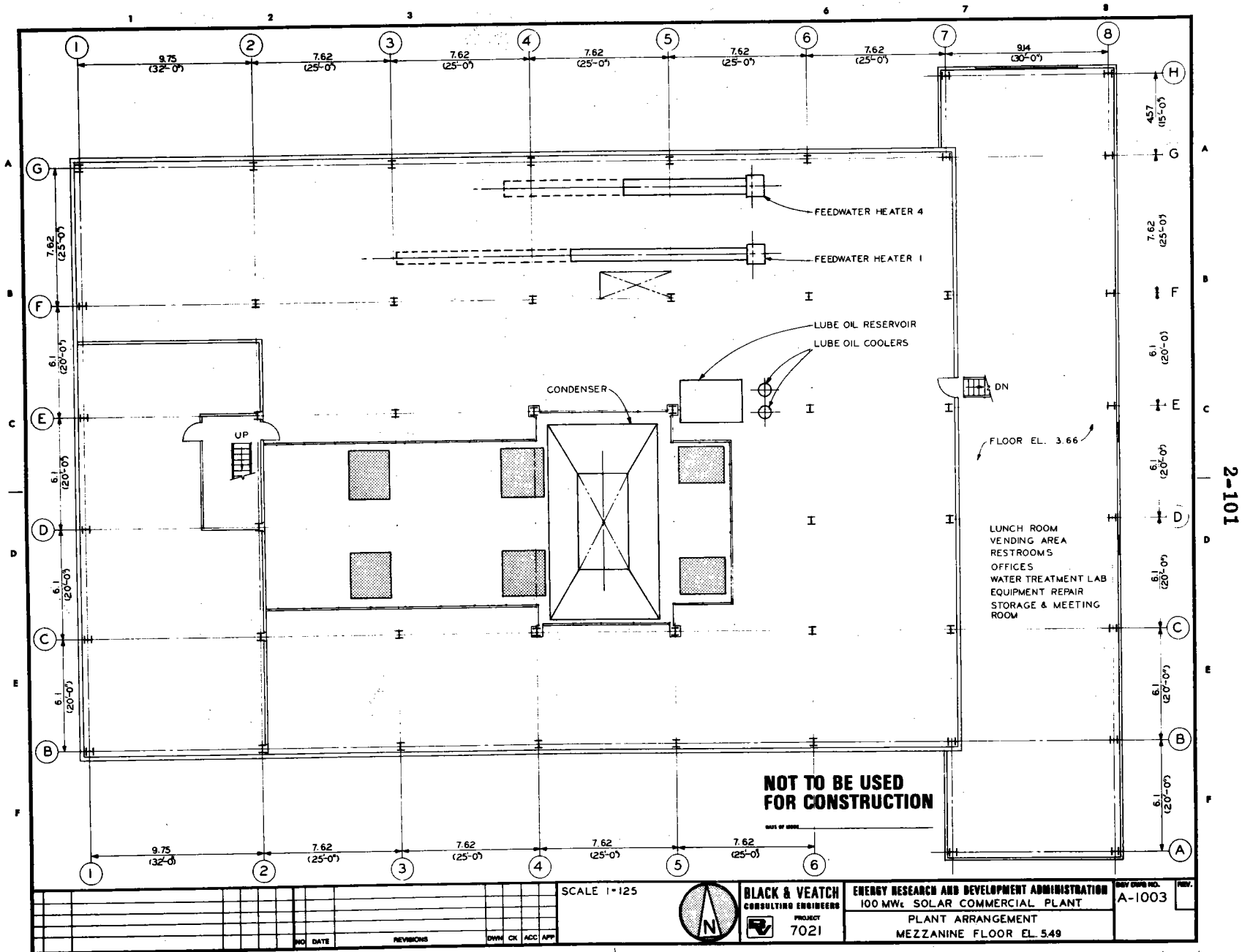
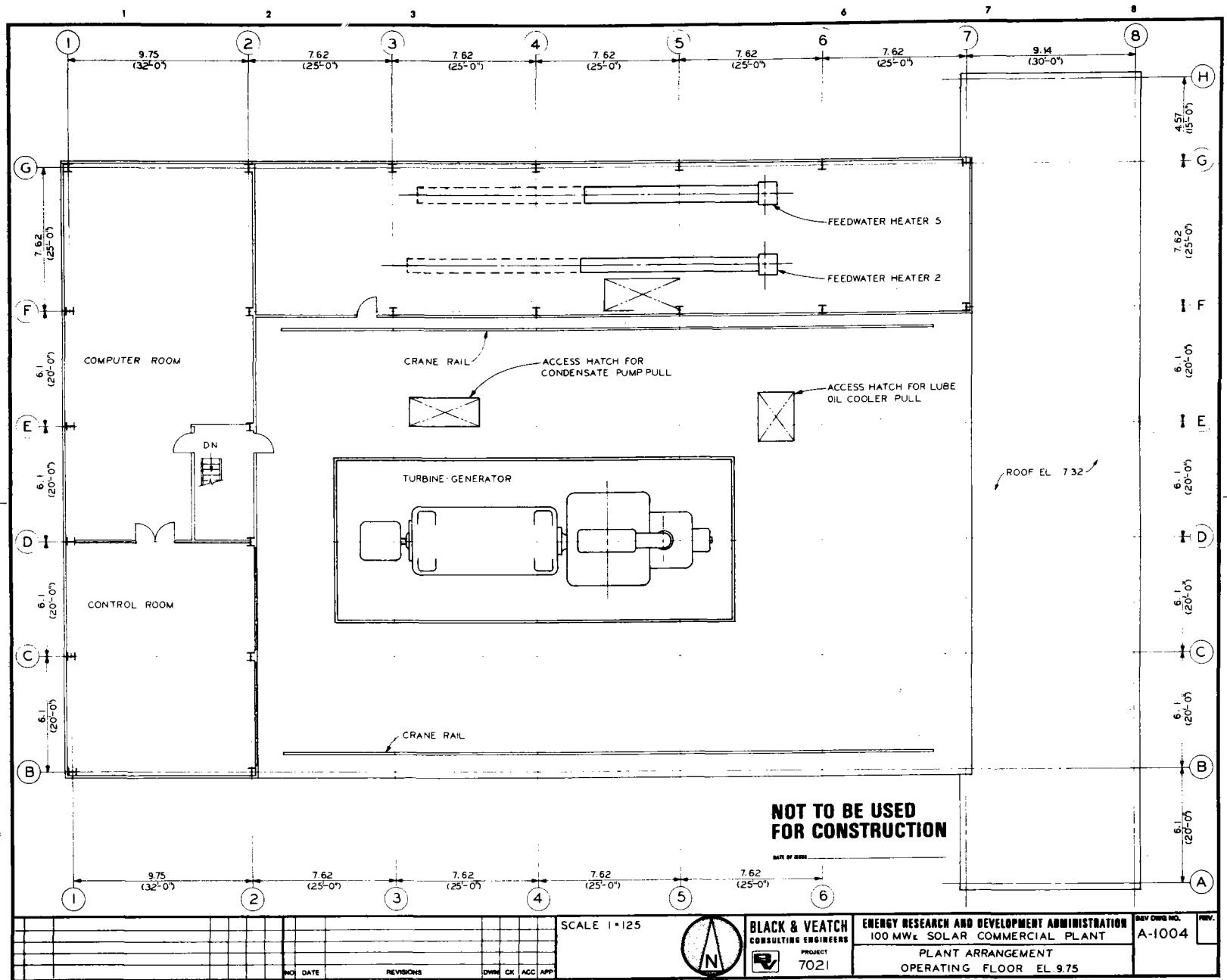


Figure 2-47. Turbine Building Mezzanine Floor Plan

40703-II



2-102

NOT TO BE USED FOR CONSTRUCTION

DATE BY 0000

NO.	DATE	REVISIONS	DWN	CK	ACC	APP

SCALE 1"=125'



BLACK & VEATCH
CONSULTING ENGINEERS
PROJECT 7021

ENERGY RESEARCH AND DEVELOPMENT ADMINISTRATION
100 MW_e SOLAR COMMERCIAL PLANT
PLANT ARRANGEMENT
OPERATING FLOOR EL. 9.75

DEV. DWG. NO. A-1004
REV.

Figure 2-48. Turbine Building Operating Floor Plan

Table 2-21. 100 MW(e) Cooling Tower Design Data
(Marley Company)

Parameter	Value
Water outlet rate	8831 liters/sec
Water temperature	29.5°C
Wet-bulb temperature	23.0°C
Heat load	209.2 MW(th)
Tower Model No.	6516-4-07
Number of fans	7
Power required per fan	130 kW
Cooling tower basin size	15.54 m x 85.65 m
Pumping head required	10.97 m

All plant facilities are located on two floors, with the first floor at ground level. The first floor includes the machine shop, mechanical equipment room, storage area, showers, lockers, restrooms, and offices. The second floor includes an equipment repair and storage area, the water treatment lab, a lunchroom and vending area, restrooms, a meeting room, and additional offices.

Space requirements are estimated from data available on other 100 MW(e) units and preliminary equipment sizing computations. All floor layouts are arranged to provide adequate space for inspection, maintenance, and safe operation of turbine auxiliary equipment, pumps and piping.

COMMERCIAL PLANT PERFORMANCE

A commercial plant design consisting of four towers and heliostat fields with a central electrical generating system and storage has been selected as the baseline configuration. Each heliostat field and tower is assumed to be a scale-up of the pilot plant geometry.

Collector System Performance

The ray trace code was used, assuming the commercial plant geometry is a scale-up of pilot plant geometry, to estimate commercial plant heliostat field performance. Thus, previous field performance data given for the pilot plant can be used in estimating the commercial plant performance. Pilot plant field geometric factors which remain the same for the commercial plant are:

- Ground cover = 0.29 average (nonuniform)
- Field area/(tower height)² = 13.6

Figure 2-50 shows heliostat field tracking efficiency for the various effects of cosine losses, blocking, and shading. Tracking efficiency is defined as the power available after the specific loss or losses divided by the DNI mirror area product. The heliostat mirror reflectance is 0.9. Estimated commercial plant losses at the design point are given in Table 2-22.

Receiver Optical and Thermal Losses

Optical losses at the receiver are accounted for in the following manner:

(1) the power which misses the aperture completely; (2) that which strikes the receiver supports; (3) that which enters one side of the aperture but

40703-II

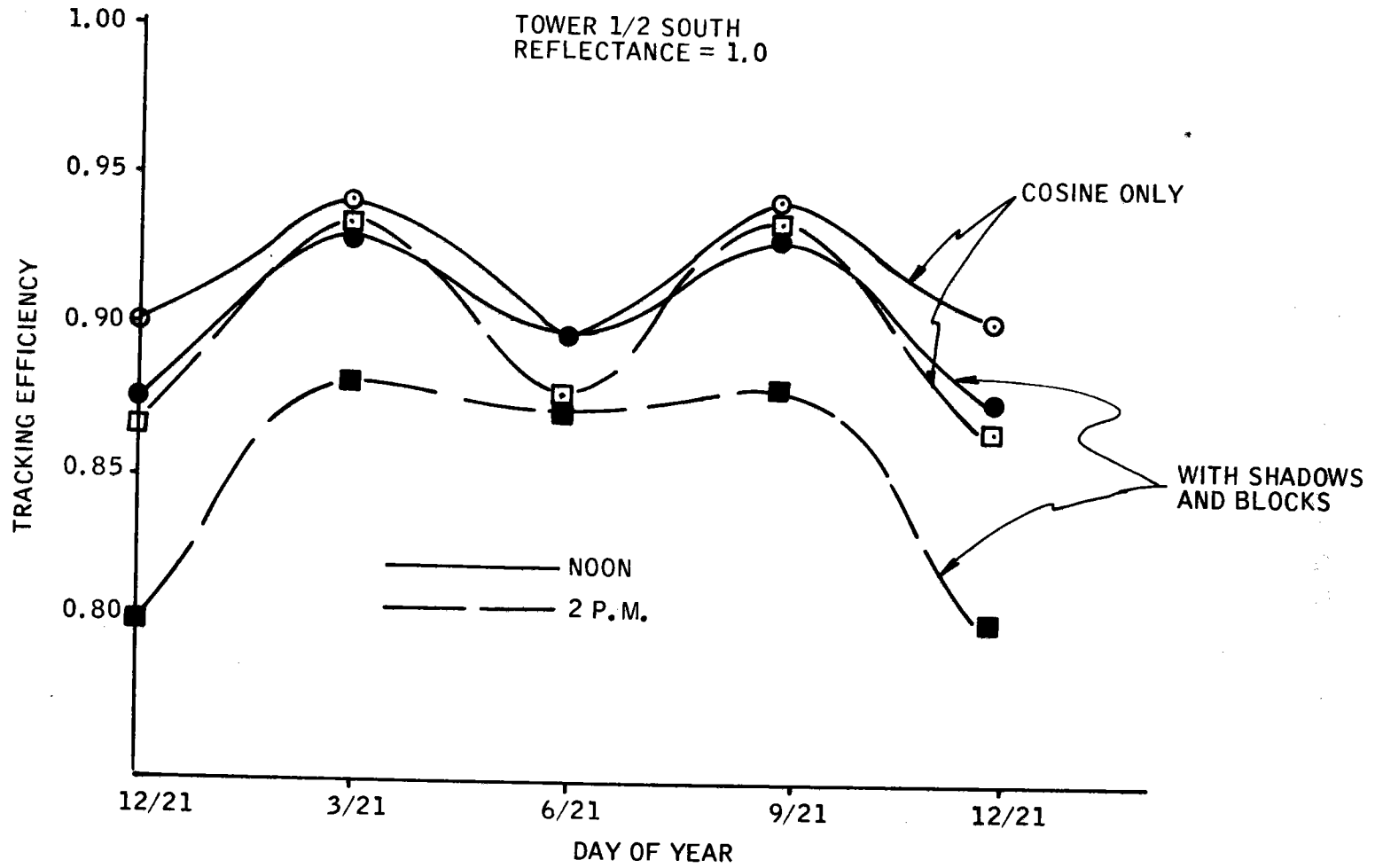


Figure 2-50. Collector System Efficiencies for Various Times of the Year

2-106

Table 2-22. Collector System Performance

Type of Loss	Percent Loss of Available Power
Cosine	6.5
Tower shadow	0.4
Mirror shadows	0.0
Frame shadows	0.1
Mirror facet edges	0.1
Reflectance	10.1
Frame blocks	0.1
Mirror blocks	0.0

misses the receiver (known as whistle through); and (4) atmospheric attenuation between heliostat and receiver. The first three are output from the optical ray trace model. Volume IIA discusses these losses in detail, so no further discussion will be done here. Atmospheric attenuation is discussed in the analysis/model section of the volume and likewise will not be discussed here. Table 2-23 lists the commercial plant receiver optical losses as a percent loss of power redirected from the heliostat field.

Thermal losses considered include convection, conduction, and reradiation. The convection loss is expressed as follows:

$$\begin{aligned}
 h &= 3.195 U^{0.8} / D^{0.2} \\
 A &= \pi D (H + D/4) \\
 T_{\text{cavity}} &= (T_{\text{SH}} + T_{\text{SAT}}) / 2 \\
 \Delta T &= T_{\text{cavity}} - T_{\text{amb}} \\
 \dot{Q} &= hA \Delta T
 \end{aligned}$$

Table 2-23. Receiver Optical Losses

Optical Loss	Percent Loss of Available Power
Aperture misses	1.2
Receiver support hit	0.3
Whistle throughs	1.0
Atmospheric attenuation*	6.9

Atmospheric attenuation condition: 10% relative humidity
 30-km visibility
 3/21 noon
 82.6°F (29°C)

where

- \dot{Q} = Convection loss (W)
- h = Cavity heat transfer coefficient ($W/m^2 \cdot ^\circ C$)
- A = Cavity inside surface area (m^2)
- D = Cavity inside diameter (m)
- H = Cavity average height (m)
- T_{cavity} = Average temperature of cavity ($^\circ C$)
- T_{amb} = Ambient temperature ($^\circ C$)
- ΔT = Temperature difference ($^\circ C$)
- T_{SH} = Superheater exit temperature ($^\circ C$)
- T_{SAT} = Saturation temperature at drum pressure ($^\circ C$)
- U = Wind velocity at cavity aperture (m/s)

The reradiation and conduction losses are assumed to be of the following form:

$$P_o = f(P_I, A_p/A_c, L/D)$$

where

- P_o = Power out of receiver cavity (MW)
 P_I = Power into receiver cavity (MW)
 A_p = Aperture area (m)
 A_c = Internal receiver surface area (m)
 L = Receiver height (m)
 D = Receiver diameter (m)

Reradiation is separated into two terms: (1) solar reflection--that energy which is reflected from the cavity interior back out the aperture; and (2) infrared radiation due to the cavity surface to ambient temperature difference of the form $w = \sigma^4$. The equations are respectively:

$$P_o = \left[0.01705 \left(\frac{D}{L} \right) + 0.01763 \left(A_p/A_c \right) \right] P_I$$

and

$$P_o = P_I \left[0.01966 \left(\frac{D}{L} \right)^3 + 0.03579 \left(A_p/A_c \right) \right] + A_p \left[8.786 \times 10^{-3} - 1.1222 \times 10^{-2} \left(\frac{L}{D} \right) \left(A_p/A_c \right) \right]$$

for $0.85 < L/D < 1.50$

$0.18 < A_p/A_c < 0.45$

The constants are parametrically determined by the reradiation "rubber" model described in the analysis/model section of the volume.

The conduction losses are assumed to be of the same form. The equation is:

$$P_o = 4.720 \times 10^{-4} P_I + 2.199 \times 10^{-4} A_c$$

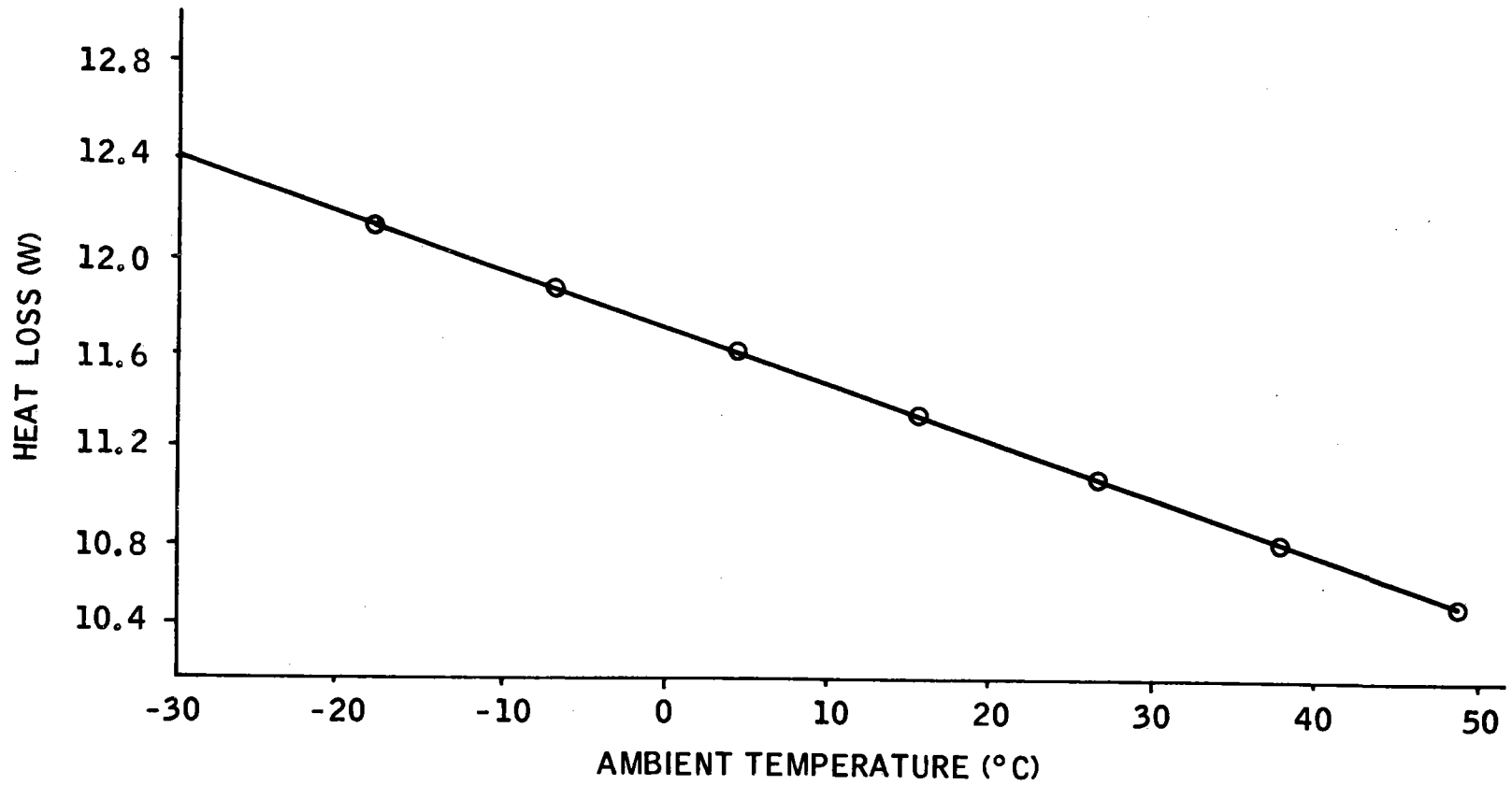
The previous three equations were used to determine the receiver thermal losses. The results were tabulated and are presented in Table 2-24.

Table 2-24. Receiver Thermal Losses

<u>Loss Type</u>	<u>Percent Loss of Available Power</u>
Reradiation	7.1
Conduction	0.4
Convection	5.4

Figure 2-51 is a plot of piping loss versus ambient temperature for the four-tower design with a common receiver header and the EPGS located equidistant from the four-tower centers. Design point commercial plant piping losses are estimated at 3.0 percent loss of available power.

40703-II



2-111

Figure 2-51. Commercial Plant Estimate of Receiver Steam Total Piping Heat Loss from Receiver to Turbine Building (Assuming Four Receivers and a Common Header)

Gross Cycle Efficiency

The gross cycle efficiency for the commercial plant turbine with a back-pressure of 6.8 kPa is:

0.385 = Gross turbine efficiency when operating from receiver steam only (includes generator losses), and

0.318 = Gross turbine efficiency when operating from storage steam only (includes generator losses).

Because of the 1.7 solar multiple, 58.8 percent of the power available at the turbine building goes to the turbine. The balance of the power is used to charge storage for later use.

Auxiliary Power Losses

The auxiliary power requirement can be thought of as system electric losses, since this power must be generated in excess but is never available for useful work. This power is distributed among the following subsystems:

- Balance-of-plant equipment
- Collector field
- Steam generator subsystem
- Electric power generation subsystem
- Charging storage

Since the commercial plant must deliver the excess steam generated to the storage charging system, the power required to operate the storage charging loop is included in the auxiliary power requirements.

The EPGS and BOP auxiliary power requirements are estimated as follows:

[8.34 tower height (m) + 7000]kW(e) for receiver-only operation

The only significant auxiliary power requirement in the steam generator subsystem is the required brake power from the recirculation pumps. The following equation is used to estimate that power:

$$W_r = C_R W_{sm}$$

$$P_B = \frac{W_r h g}{n}$$

where

C_R = Recirculation ratio

P_B = Brake power (W)

W_r = Recirculation flow rate (kg/s)

W_{sm} = Maximum steam flow (kg/s)

h = Head (m)

n = Pump efficiency

g = Acceleration due to gravity, (m/s²)

The following data were used for the commercial plant:

C_R = 10

n = 0.82

The power required by the collector field is used almost totally by the electric motors for tracking. It was assumed that 600 kW(e) would be consumed at the design time.

The storage auxiliary power requirement is a function of storage input/output rate. Storage pumps are single-speed pumps. The power required by each pump is independent of the mass flow. This type of pump was chosen over variable speed pumps because of lower capital cost.

The summary auxiliary power requirements are shown in Table 2-25.

Table 2-25. Auxiliary Power Requirements

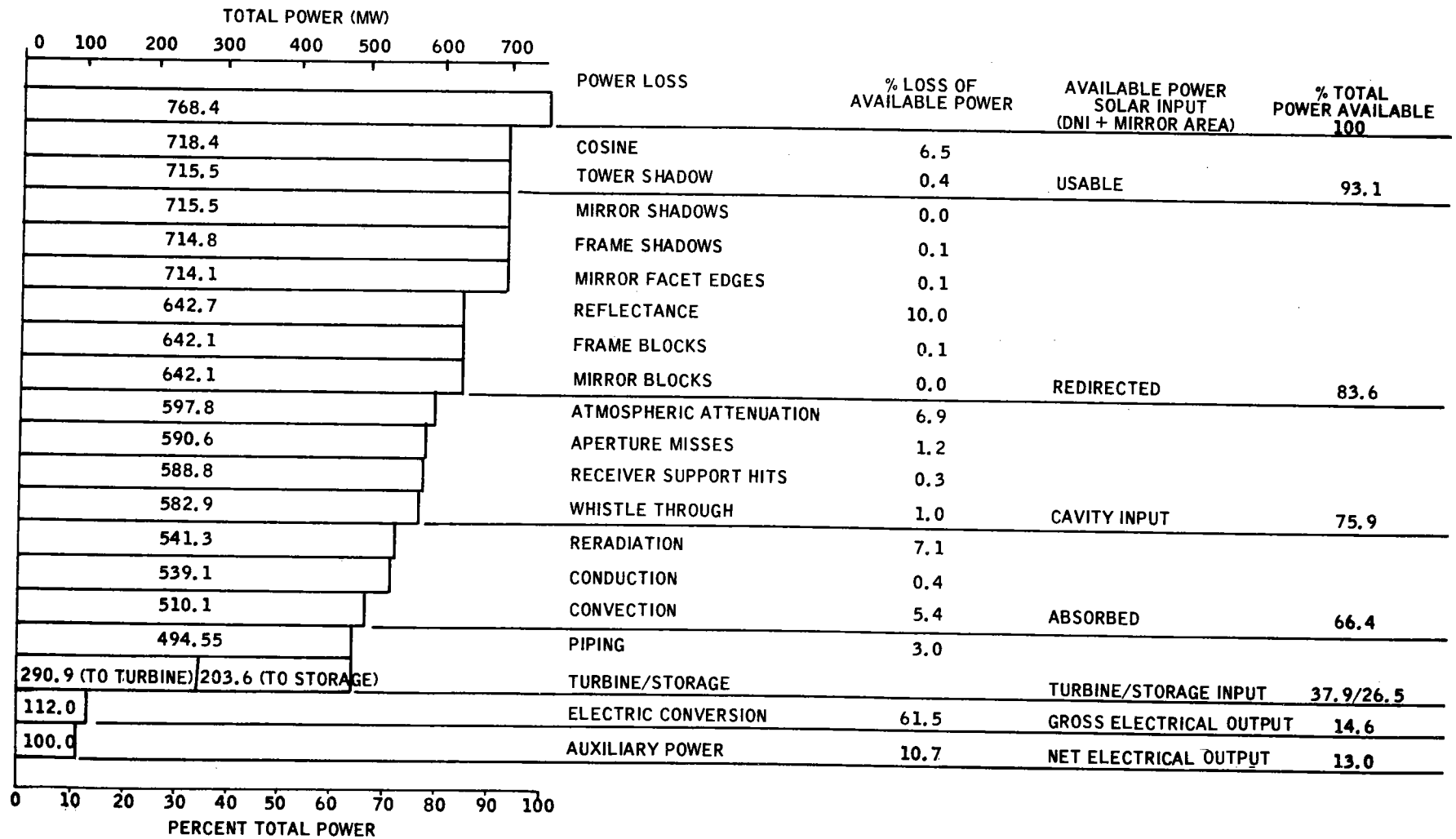
<u>Auxiliary Power Required</u>	<u>kW(e)</u>
EPGS + BOP	8880
SGS	1000
Heliostat field	600
Storage	1520
TOTAL	12,000

The above auxiliary power requirements are the estimates that were used for commercial plant design.

Performance Results

The commercial plant performance is shown in Figure 2-52 which is the design point stair step. Each step in the stair step figure represents a loss of available power as described above.

40703-II



2-115

Figure 2-52. Commercial Plant Design Point Performance

SECTION 3

DESIGN TRADEOFF ANALYSIS

APPROACH

Honeywell's approach to the performance analysis and tradeoff studies was to base the design decisions on a combination of cost and performance data. At each design decision point, the best available cost and performance data were combined to select an optimal design. In all cases, the costs used reflected our estimates of commercial-scale costs. That is, each element of the total plant was assumed to be commercially available equipment instead of new subsystem elements with high costs associated with tooling and design. For example, both the heliostat and storage subsystems were costed based on large-quantity component purchase price and low design costs. These costs were used in arriving at design decisions for both the pilot and commercial plant. In fact, since the pilot plant is simply a scaled-down replica of the commercial plant, the performance is much the same and design decisions made on the basis of the pilot plant performance can be applied equally as well to the commercial plant. Since the project was aimed at the preliminary design of the pilot plant, the performance data we developed naturally pertained mainly to the pilot plant, but the primary concern in each design decision was to obtain a pilot plant which represents an optimal scaled-down version of the commercial plant.

To facilitate the performance analysis, the basic ray trace software (optical model, described in Section 7) was continually modified, improved, and exercised to evaluate the plant power and annual energy. The ray trace code can evaluate the plant power and annual energy. The ray trace code can evaluate instantaneous power levels at selected time points as well as perform an annual integrated energy determined by Monte-Carlo integration technique.

The code was used in studying the tower location, tower height, field layout, heliostat packing density, aperture size and shape, and the internal receiver geometry. It is the single most powerful analytical tool available for analyzing the optical performance of solar power plants.

For any solar power plant, the optimization of field layout, heliostat packing density, tower height, aperture size, etc., are all closely coupled. The selection of a particular heliostat packing density strongly influences the tower height and aperture size selection. For example, given a field layout (fixed heliostat size and shape, packing density, and tower location), a short tower will be relatively inexpensive but will degrade the overall plant performance. Short towers have the disadvantages of creating a poor cosine and high probability of shadowing and blocking in the field. Tall towers, on the other hand, will cost more but will allow higher cosine performance and less shadowing and blocking. Clearly, the shadows cast from a heliostat are a function of the sun position and the heliostat position. The tradeoff issues and performance details will be discussed in depth later in this section. It is our purpose here to point out the close dependence of the various design decisions on one another. It can be said that performance differences between different design options are strongly dependent on the time of year for which the designs are compared. Because of desire to effectively tradeoff all of the interdependent design issues at once, and because of the obvious differences in performance over time, we were led to the position of performing all optimizations on the basis of annual energy.

The annual energy value for the tradeoff studies was based on a clear-air model of the available solar energy. The clear-air model solar intensity and plant annual performance were evaluated at a 33-degree north latitude for the tradeoff studies. This latitude was chosen as typical for acceptable solar power plant sites within the continental United States.

The clear-air model is based on surface observations of the available solar energy and is thus an average value. Actual solar intensity may well be considerably above or below the predicted value. Since the 1963 Inyokern weather tape was to be used for the final plant annual performance values, we compared the tape data and the predicted clear-air model data.

The first comparison we made was simply to evaluate the difference in total annual direct normal energy available. This available energy is the sum of the direct normal intensity and the result is shown below:

<u>Clear Air</u> <u>33°N. Lat</u>	<u>1963 Inyokern</u> <u>Weather Tape</u>
3206 kWh/m ²	3203 kWh/m ²

The difference in the model estimates is negligible and in itself should cause no change in plant performance predictions.

A second comparison was made by replacing the clear-air model insolation data with the weather tape data in the ray trace computer code. Annual performance was evaluated by a Monte-Carlo draw over a year's time for a possible pilot plant design.

The time draw was from sunrise to sunset for the Inyokern latitude. The Monte-Carlo results showed a decrease in total direct normal energy to 3156 kWh/m². This decrease is attributed to the weather tape data format.

Since the data are an hourly average, some of the insolation falls before or after sunrise or sunset (i. e., when sunrise occurs at 6:30, the insolation from 6:30 to 7:00 will be averaged over the time frame of 6:00 to 7:00 and placed in the 7:00 insolation record, effectively placing some insolation in the 6:00 to 6:30 time frame). This insolation will be lost in the computer code calculations.

To correct for the lost insolation, annual plant performance comparisons were made using data multiplied by the ratio of 3202/3156. Table 3-1 compares the annual performance of a pilot plant design using the clear-air model and the weather tape data. The pilot plant design is for a circular heliostat field with 1682 tilt-tilt heliostats each with 40 m^2 in mirror area. The tower is located one-half of a field radius south of the field center. The total absorbed energy per meter squared of mirror is approximately 100 kWh/m^2 , lower for the weather tape data than for the clear-air data. The difference is mainly due to increased losses in cosine effect, tower shadow, and mirror shadows. These differences can be explained by comparing the distribution of incident energy as modeled by the two insolation sources.

Two typical clear winter days are shown in Figure 3-1. The important disparity between the clear-air model and the Inyokern weather tape is that the weather tape has a flatter distribution of incident power. Of the total energy incident each day, the weather tape data have a larger percentage available in the early morning or late afternoon hours than the clear-air model. During early morning or late afternoon, the sun's elevation angle is small and cosine and shadow losses are large. It is obvious, then, that a larger percentage of available energy during low sun-angle times will result in a decreased redirected energy over the day. Since this trend holds true over the entire year's insolation data, the decrease in total annual absorbed energy for the Inyokern weather tape case is due almost entirely to the flatter distribution.

We feel the clear-air model is a better representative of the distribution of normal incident insolation expected in desert sites. It has the advantage of being a smooth, continuous function which is better suited to the design analysis and tradeoff studies for the plant. We note that both the clear-air model and the weather tape insolation data are estimated based on empirical data and curve fits. A preference based on the correctness of the absolute

Table 3-1. Annual Performance Sensitivity to Insolation Model
(Tower One-Half South Pilot Plant)

	Performance Sensitivity	
	Clear Air 33° N. Lat.	Weather Tape* 35.68° N. Lat.
Total Annual Normal Incident Energy	3206 kWh/m ²	3203 kWh/m ²
Losses:		
Cosine effect	16.5%	17.8%
Tower shadow	0.3%	0.6%
Mirror shadow	4.9%	7.4%
Reflectance	10.0%	10.0%
Blockage	0.0%	0.0%
Misses	1.1%	1.3%
Corbel hits	0.9%	1.1%
Whistle through	0.0%	0.0%
Rerad	10.0%	10.0%
Total Annual Absorbed Energy	2012 kWh/m ²	1915 kWh/m ²

* Monte-Carlo Values Corrected for Time Draw.

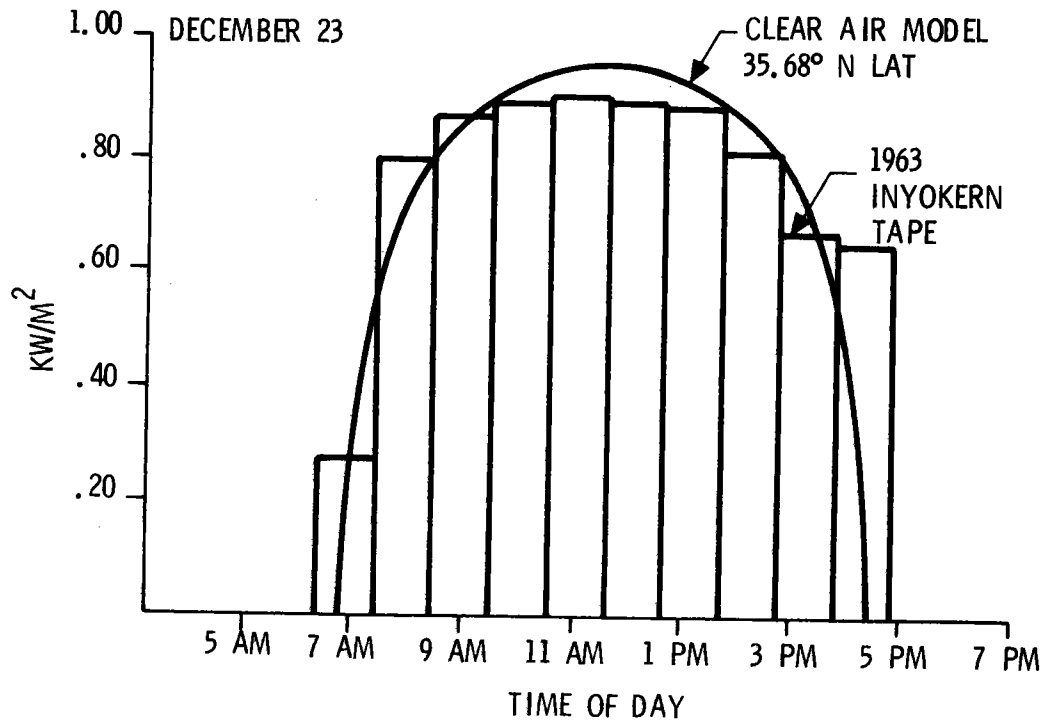
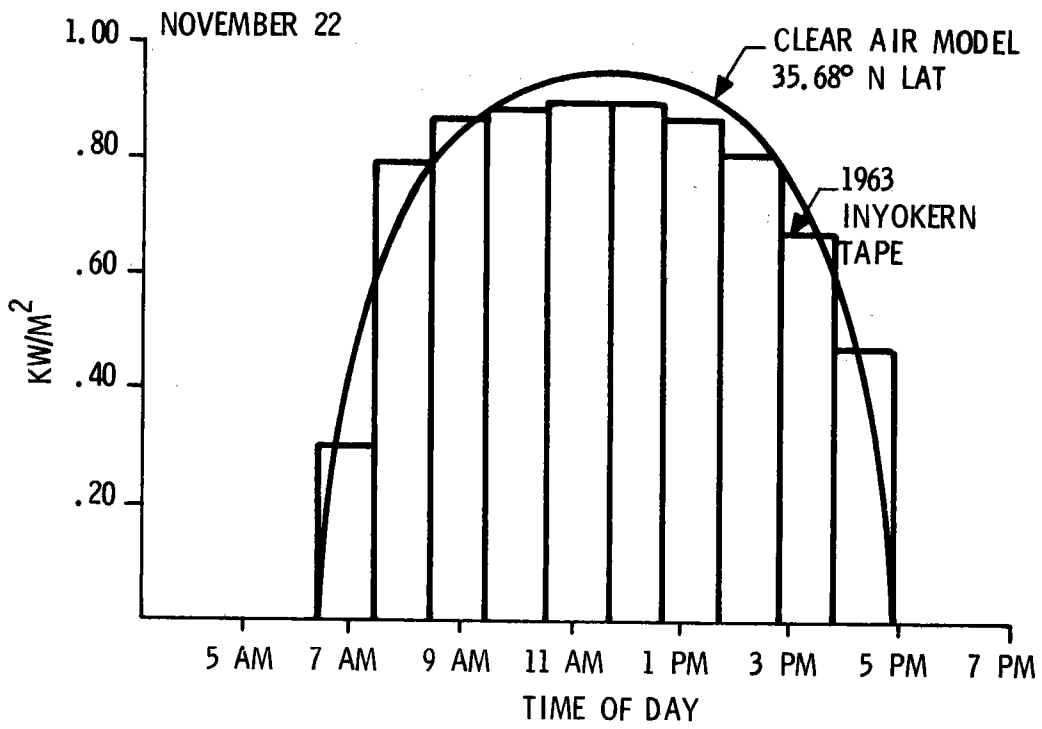


Figure 3-1. Weather Data Model Differences

value of either model would be arbitrary. For the tradeoff studies, the more generalized clear-air model data were used throughout the analysis.

Before going into the system and subsystem analysis, it should be pointed out that throughout the design decision process our intent has been to maintain the basic plant configuration described in our original proposal. To review, the proposed pilot plant design and the final preliminary design reported have the following features:

- Heliostat Subsystem:
 - Focused mirrors
 - Multifacet low-profile design
 - Central computer control
 - 360-degree field

- Receiver Subsystem:
 - Cylindrical cavity
 - Drum boiler

- Electrical Generation Subsystem:
 - Turbine sized for maximum power
 - 510°C (950°F) throttle temperature
 - 5861 kPa (850 psig) throttle pressure (proposed design)
 - 9997 kPa (1450 psig) throttle pressure (preliminary design)

- Storage Subsystem:
 - Latent heat (proposed design)
 - Sensible heat (preliminary design)

The change from latent to sensible heat in the storage subsystem was dictated by program redirection. The latent heat storage proposed has many potential advantages over the sensible heat system; however, it was felt that the sensible-heat technology was further developed and hence represents a lower risk. Since the basic rationale for a pilot plant is to prove the solar subsystem technology, the uncertainties in a latent-heat storage device may be unjustified in the preliminary design. Test data of experimental latent-heat storage devices could upset this rationale. Unfortunately, we were unable to proceed with planned tests to prove or disprove the latent-heat storage viability. Without sufficient data on the latent-heat storage design, the storage subsystem was changed to a sensible-heat design which can be justified by available data. Because both competing Pilot Plant Preliminary Design teams were funded to design, build, and test sensible-heat subsystem research experiments (SREs), we have designed a sensible-heat storage device which can be justified by their test data. Accordingly, the sensible-heat storage subsystem configuration appears quite similar to these designs.

In the electrical generation subsystem, the major change from the proposed system was the cycle modification. The pressure changed from 5861 kPa (850 psig) to 9997 kPa (1450 psig) at the turbine throttle valve. In addition, the turbine concept was changed early in the design effort from a single-admission to a dual-admission turbine. Both of these changes are consistent with available turbo-machinery for both the pilot and commercial-scale plants. The rationale for the changes are documented later in this section.

No major changes to the basic proposed configuration have been made in the unique solar plant subsystems: the heliostat and receiver subsystems. All design changes and optimizations have proceeded with this as a guideline.

HELIOSTAT SUBSYSTEM TRADEOFFS

Early conceptual design studies clearly showed that the heliostats are the prime cost element in the economics of central receiver power plants. It is imperative, therefore, that a majority of the performance analysis and trade-off studies be concerned with the heliostat subsystem optimization. We have analyzed the heliostat configuration and field layout issues to design a practical and effective solar power plant. Design choices made as a result of our tradeoff studies include:

- Heliostat Configuration:
 - Number of facets
 - Size of facets
 - Facet spacing
 - Facet planform
 - Optical quality
 - Tracking error
 - Gimbal orientation

- Field Layout:
 - Heliostat packing density
 - Heliostat orientation
 - Tower height
 - Tower location

Each design decision and the decision criteria will be discussed in this report. Much of the heliostat evaluation process is described in Volume III, and only a summary is given in this section. Those features of the heliostat subsystem which affect overall system performance will be addressed here.

Heliostat Configuration Tradeoff

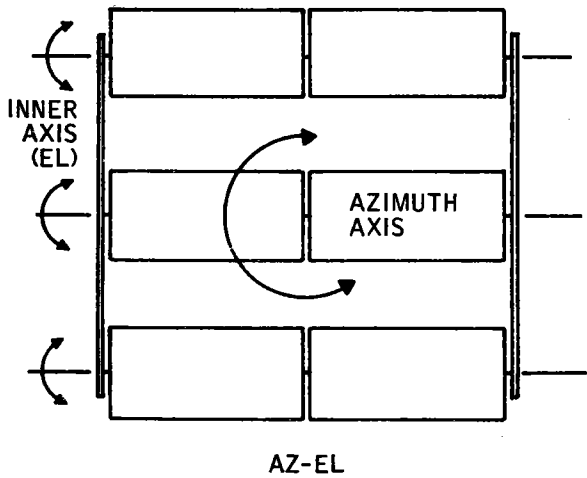
The basic cost and performance evaluation process used in the heliostat evaluation was to compare different heliostat concepts on an "optimal-to-optimal" basis. That is, each concept must be designed at or near its optimal configuration and only then compared. The search for the optimal configuration can be thought of as two separate studies. The two basic areas are optical performance and structural optimization. In the area of optical performance, each configuration was adjusted to achieve a maximum net annual energy within the constraints of various heliostat and field geometries.

The structural optimization basically involved a search for the minimum weight, and hence cost, heliostat structure which met the desired accuracy and survival specifications. In each case, all configurations met all specifications at both operational and maximum survival wind speeds. The measure number which results from the structural optimization is the installed cost per unit mirror area deployed ($\$/\text{m}^2$).

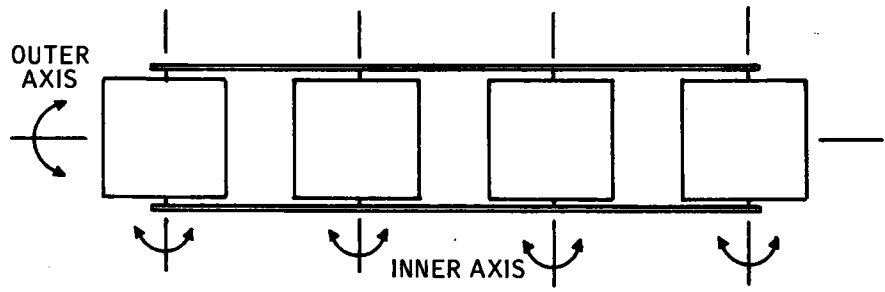
The optical performance measure and the structural performance measure are combined to yield the relative energy cost. Energy cost is an objective cost and performance measure against which the configurations can be compared. The evaluation methodology used in the heliostat configuration study was the same for all configurations, which helps ensure a fair comparison between configurations.

The primary objective of the heliostat evaluation study was to compare the proposed Az-El heliostat configuration with a tilt-tilt heliostat configuration. Both configurations are multifacet heliostats and are shown in Figure 3-2. The basic difference between the two candidate configurations is the tracking-axis (gimbal) orientation. The Az-El configuration uses one axis of rotation which is vertical so that the entire frame structure rotates in a horizontal plane. This axis is called the outer-axis drive, and the inner axis refers to

40703-II



AZ-EL



TILT-TILT

Figure 3-2. Az-El and Tilt-Tilt Heliostat Configurations

3-11

the facet rotation axis. The tilt-tilt configuration has a similar inner-axis drive but the outer rotation axis lies in a horizontal plane and tilts the entire frame structure.

A brief review of the analysis work prior to and during the heliostat configuration evaluation is included here. The tradeoffs were concerned with accurately comparing the performance of possible heliostat configurations rather than creating a final pilot and commercial plant baseline field layout or aperture. As such, the tower location was set at the field center, the heliostat packing density was assumed uniform, and the ratio of the field area to the tower height was fixed. Tower location, tower height and uniform packing density will not change the comparison between heliostat configurations. The impact of these parameters on system design was therefore left to be investigated after the heliostat configuration was determined.

Receiver Effects

To choose one heliostat configuration over another, each heliostat must be evaluated at its optimal aperture. An optimal aperture is one which allows a maximum net annual energy to be collected. The first step in the evaluation of the correct aperture size was to run the ray trace code with proposed Az-El heliostat configuration at 45 percent ground cover to compute the net annual energy per unit mirror area.

The results of these Monte-Carlo calculations are shown in Figure 3-3. The ordinate is net annual energy per unit heliostat area (incident annual flux minus reradiated flux), and the abscissa is aperture area. Each curve represents a constant separation distance (Sep) between the lower aperture boundary and its upper boundary. The aperture is an inverted cone frustum. Each different area is a larger- or smaller-diameter cone. The cone angle was fixed, as its optimal value as determined by other computer runs.

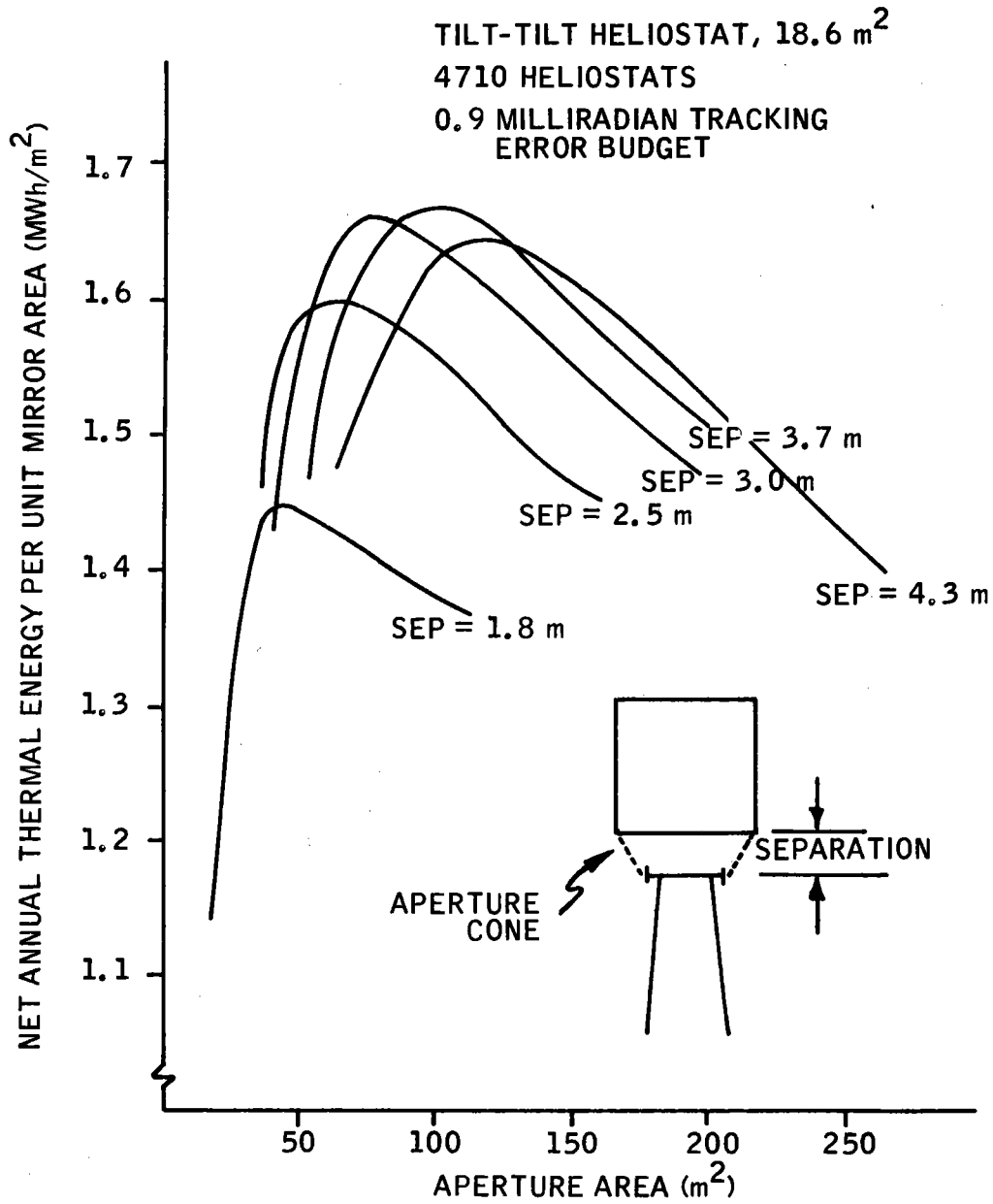


Figure 3-3. Net MWh(th) versus Aperture Area for 45 Percent Ground Cover

Notice that for each separation (cone frustum height) there is a different optimal area (diameter). At low diameters, many rays miss the cone on either side. At large areas (diameters), almost all rays are captured, but the unnecessarily large area reradiates more energy and hence the curves roll off. The optimal aperture on this plot is clearly 100 square meters area with a 3.7 m (12-ft) cone height (Sep = 12).

This optimization required an excessive amount of computer time when considering that each possible heliostat configuration needed to be composed with its own optimal aperture. To speed up the optimization, the ray trace software was modified to automatically find the upper and lower aperture location (relative to the aim circle) which yields the maximum net annual energy. Figure 3-4 shows the aperture and aperture nomenclature.

All heliostats are aimed at a circle which is on the cone frustum that is the cavity aperture. The aimpoint for each heliostat is essentially along its

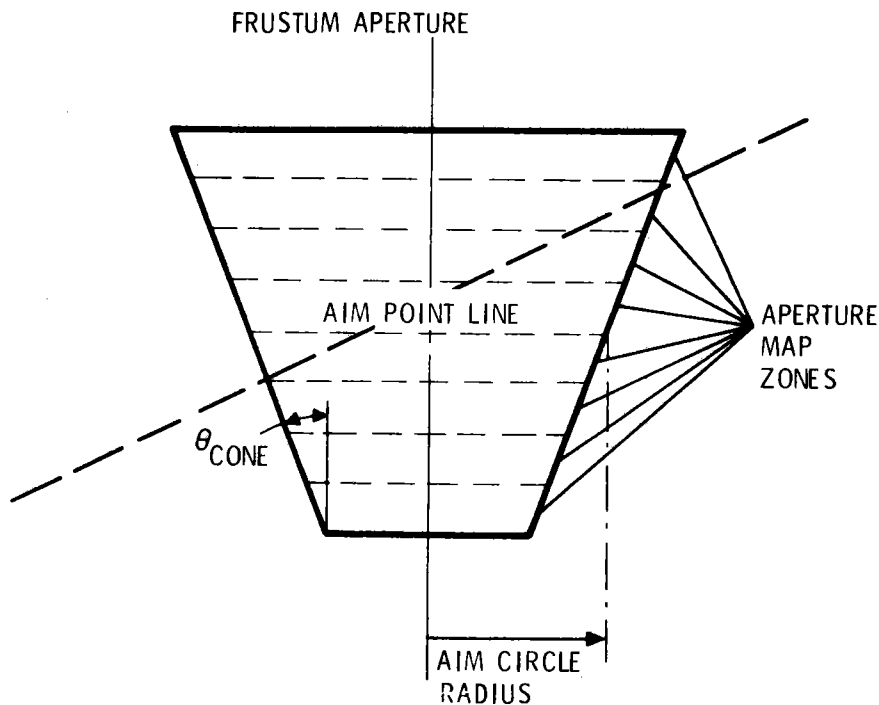


Figure 3-4. Aperture Upper and Lower Boundary Determination Methodology

radial position line on the aim circle. Each heliostat aimpoint is shifted as needed to miss the support structures which interrupt the aperture.

The user of the software specifies the radius of the aim circle, the cone angle of the aperture cone frustum, and the cone height ranges to be considered. The cone frustum is divided into many discrete zones. All possible connected assemblies of zones which could form an aperture are evaluated with one set of ray traces. The best aperture of the set is chosen by the software. The user must perform a parametric sweep over radius to find its optimal value, but he is spared the task of sweeping over the upper and lower aperture boundaries for each aim circle radius. All ray trace results shown herein were calculated at or near the optimal aperture configuration.

Heliostat Size Effects

The impact of heliostat size on the aperture design can be discussed in terms of ray trace data available for both the Az-El and tilt-tilt configurations. Figure 3-5 shows net annual energy collected (energy into cavity minus reradiation losses) versus the aperture aim circle radius for three different Az-El heliostat sizes. The aim circle radius is a measure of the aperture mean radius. Because of off-axis aberration effects, the optimal aperture size must be larger for the larger heliostats. The larger aperture has more reradiation losses, and hence less net annual energy per unit mirror area is available as heliostat size is increased. These results are for the Az-El heliostat with tracking and optics errors of 0.9 miliradian (1σ). The heliostat shape was held square for all sizes. Since larger heliostats require larger apertures and hence yield less net annual energy, the cost of the larger heliostats must pay for this decrease. The cost analysis of the Az-El and tilt-tilt heliostats showed that cost versus area is much more sensitive than the performance versus area. For example, an increase in heliostat size from 18.6 m² to 37.2 m² reduces heliostat cost by more than 25 percent

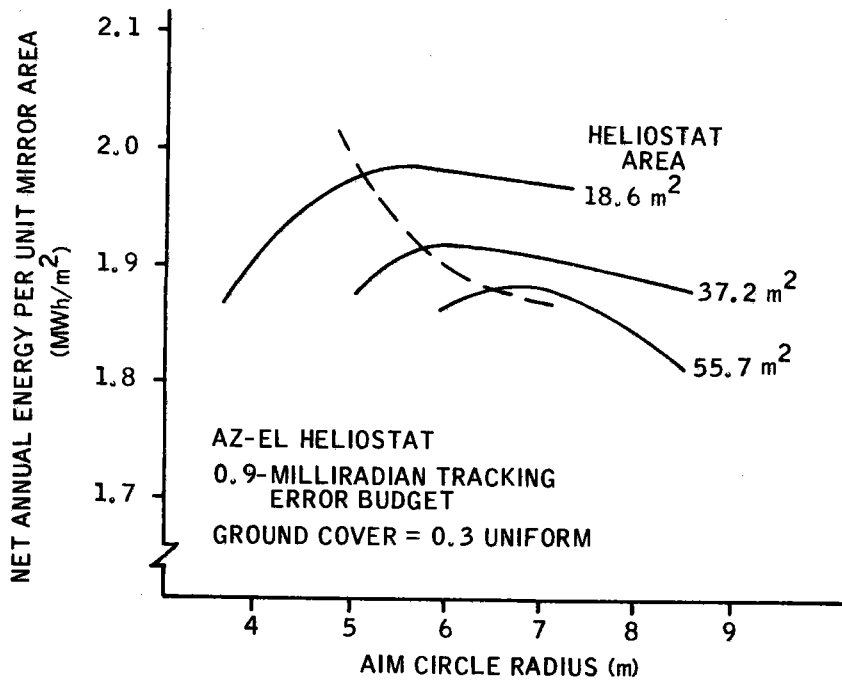


Figure 3-5. Heliostat Size versus Performance for the Az-El Configuration

for both the Az-El and tilt-tilt configurations. However, from Figure 3-5, it is seen that the reduction in net annual energy is less than 5 percent. The larger heliostats will clearly pay for this loss in performance. The optimization of the heliostat size showed that a 40-m² tilt-tilt heliostat is near optimal for the pilot and commercial plants.

Tracking Error Effects

To investigate the effect of tracking accuracy on annual energy performance, an Az-El heliostat of 18.6 m² mirror area was analyzed at three different tracking accuracy specifications with no other design change. Shown in Figure 3-6 is the net annual energy per unit mirror area for 0.005, 0.10, and 0.15-degree rms tracking error (i. e., one standard deviation equal to 0.05, 0.10, and 0.15 degree). The mirror slope uncertainty ("waviness")

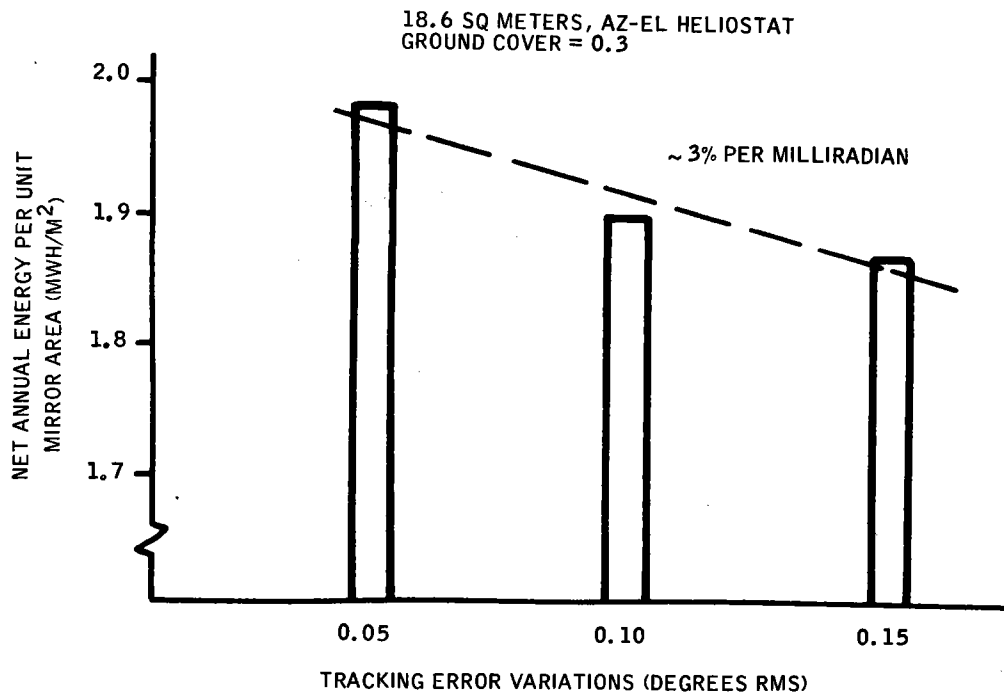


Figure 3-6. Tracking Error Variations (Degrees RMS)

was left fixed at 0.05 degree. For each tracking accuracy, the optimal aperture was found. The larger tracking error budget designs required a larger aperture and were less efficient. Over the range of errors considered, the energy loss is approximately 3 percent loss for each milliradian of additional tracking uncertainty.

Additional ray trace computer runs were made at different heliostat areas. Figure 3-7 shows the net annual energy per unit mirror area versus heliostat mirror area for 0.05 and 0.115 degree tracking error runs (0.9 and 2 milliradians). Since the heliostats are the same shape and have the same optics error budget (same mirror surface slope error = 0.05 degree), the image size is equal at equal heliostat area along both curves in Figure 3-7. Because of off-axis aberrations, the image size increases with increasing heliostat area. The 2-milliradian curve is lower in net annual energy because the image position is more apt to be misplaced from the aimpoint, and a larger

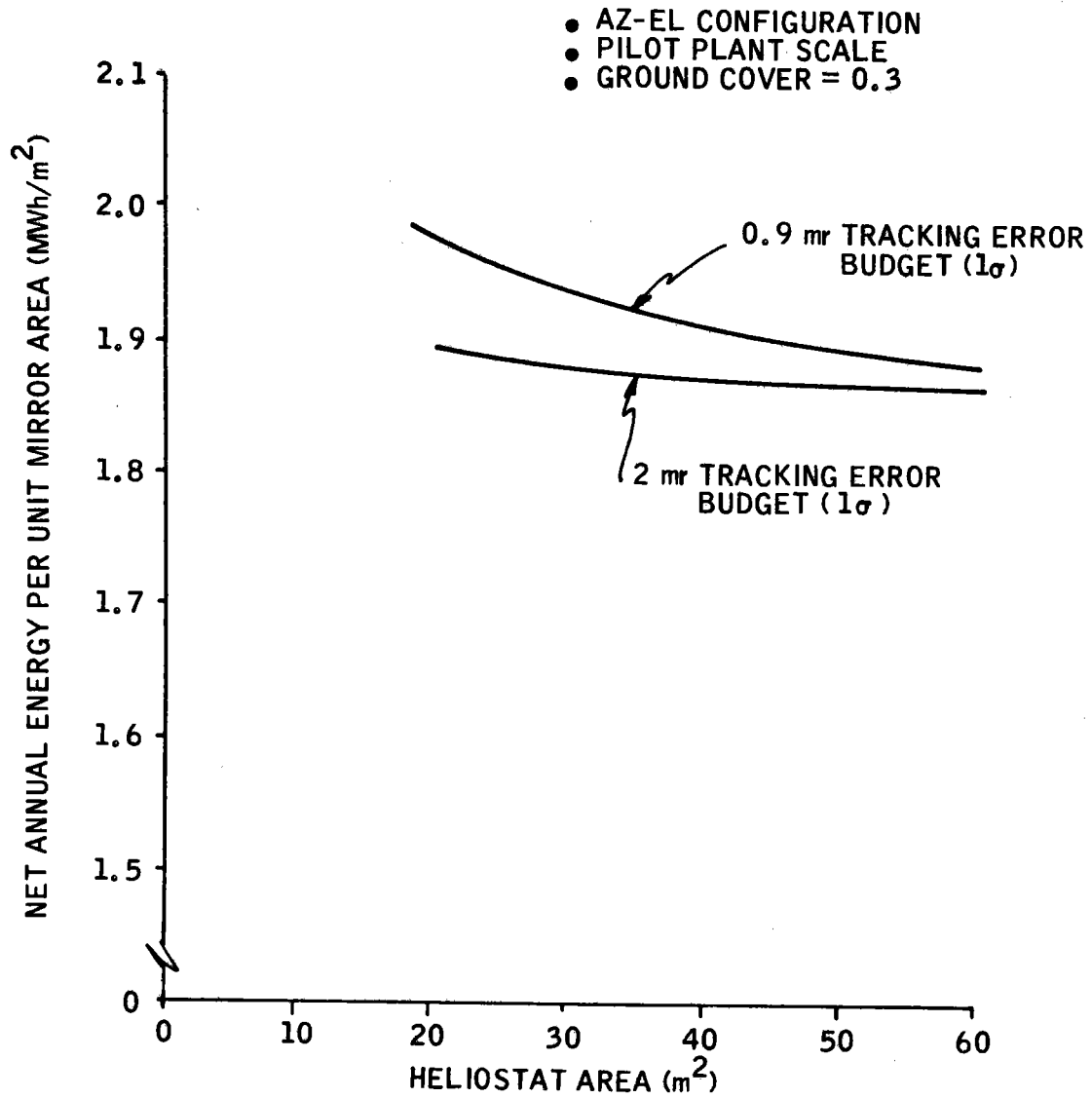


Figure 3.7. HelioStat Performance versus Size

aperture is required to collect the energy. As the heliostat area gets large, the two curves tend to approach a single value of net annual energy. This is because the tracking error becomes less important than the image size in determining the aperture required. The tracking error misdirects images so that the increase in aperture area required is nearly constant independent of the heliostat size. Thus, as the heliostats get larger and the aperture gets larger due to larger image size, the required increase in aperture size due to the tracking errors becomes a smaller and smaller percentage of the total aperture area. At very large heliostat areas (greater than 100 m²), the difference in aperture area due to a 1-milliradian increase in tracking error budget would not be noticeable.

The data presented in Figures 3-6 and 3-7 can be combined with cost data to specify the most cost-effective tracking accuracy. For a 40-m² tilt-tilt heliostat, an increase in tracking error budget from 0.9 to 2 milliradians reduces heliostat cost by approximately 7 percent, while annual performance is degraded only 2 percent. Further increase in allowable tracking error does not significantly reduce cost, and the parametric analysis showed that a 2-milliradian tracking error budget (1σ error value) is near optimal. The reader is again reminded that Volume III provides the details of the cost analysis and heliostat configuration tradeoffs.

Field Heliostat Packing Effects

In order to decide between the various heliostat configurations, the best field layouts for each configuration must be found. We have considered the four types of field layouts shown in Figure 3-8. The upper left-hand array is simple north and south rectangular rows and columns of heliostats. The upper right-hand array represents what we call polar packing. With polar packing, all heliostats are arranged on concentric circles centered on the tower base. Two types of hexagonal close packing are shown on the lower

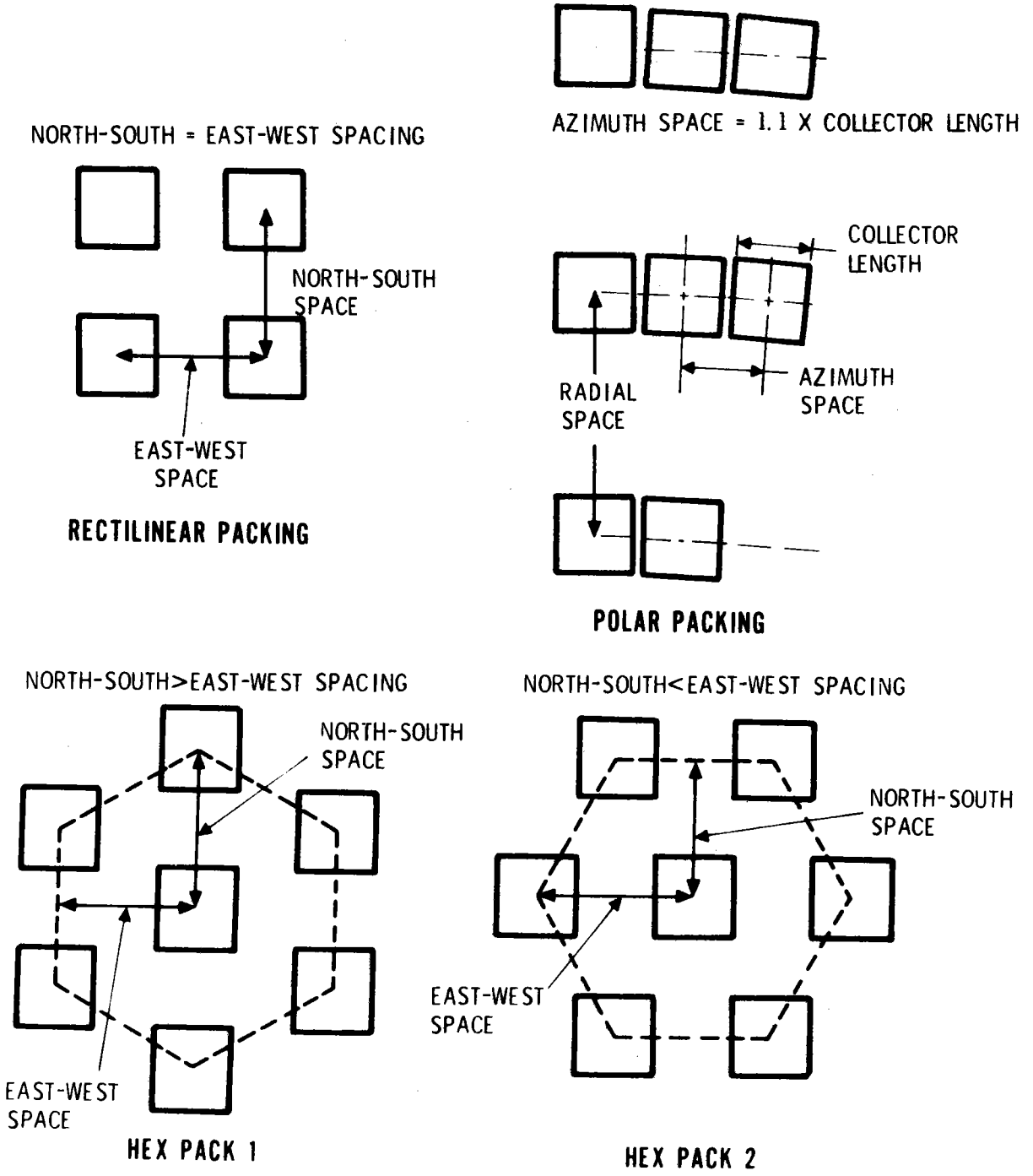


Figure 3-8. Field Packing Geometries

right and left. The two layouts differ in that the basic repeating hexagonal "unit cell" of heliostats is rotated 60 degrees, one relative to the other. This affects the shading and blockage throughout the day and year. The layouts selected as best for each heliostat are shown in Table 3-2.

Table 3-2. Selected Field Layouts

Heliostat Configuration	Rectilinear Packing	Polar Parking	Hexagonal 1	Hexagonal 2
Az - El	Choice	N/A	Acceptable	Acceptable
Tilt-Tilt	N/A	Choice	N/A	N/A

The layers selected were used when comparing the Az-El and tilt-tilt heliostat configurations.

The packing density (ground cover) for each heliostat configuration was also varied for the analysis study. For the heliostat configuration tradeoff studies, the ground cover was assumed to be uniform everywhere in the field. After selecting a heliostat configuration, we investigated nonuniform field packing density. For each uniform ground cover, the aperture was sized to be near or at the optimal. We found that the ground coverage has significant system-wide impact. At low ground cover, the field must get very large to accommodate the required number of heliostats. This forces the tower higher. At high ground coverage, the heliostats get into each other's way (shading and blockage). As ground cover is reduced, a threshold ground cover is reached so that all the reduction in shading and blockage which can be achieved has been achieved. Further ground cover reduction yields little or no additional energy. Figure 3-9 is a plot of net annual energy per unit mirror area versus ground cover. The figure shows the threshold ground cover to be 0.30 for each configuration. The rolloff in performance for the Az-El design at lower ground cover fractions is probably not necessary. If the facet

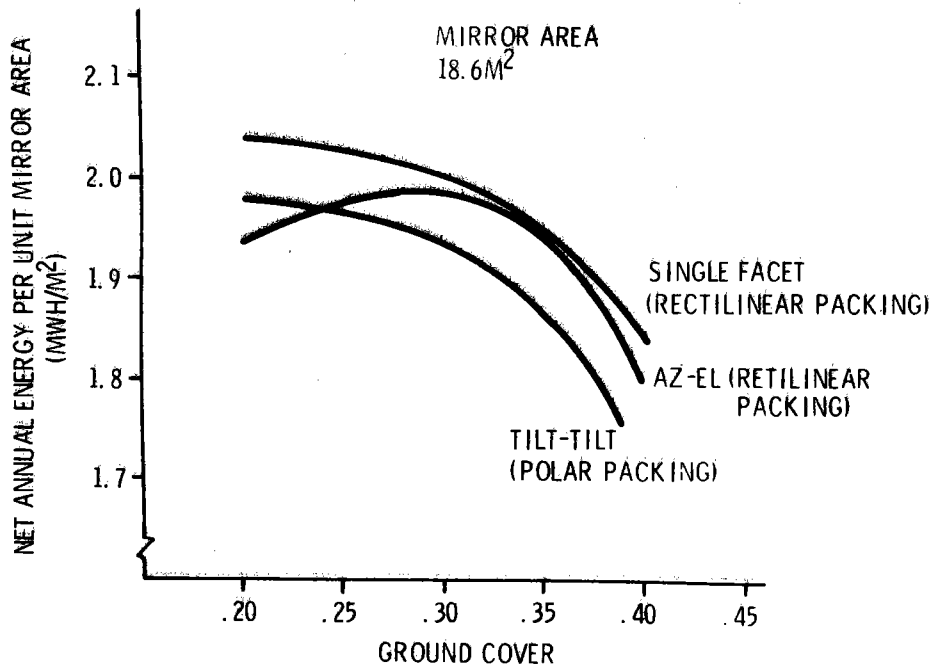
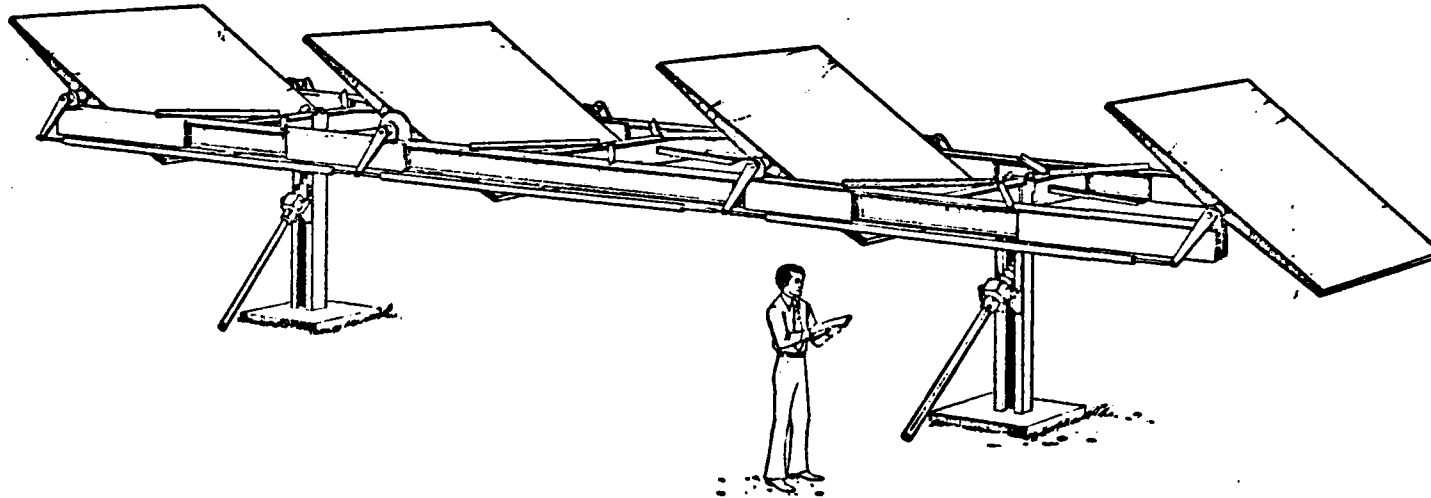


Figure 3-9. Ground Coverage Determination

spacing were varied for the low ground cover Az-El design, the Az-El curve would probably follow the asymptotic trend of the other two configurations. This additional work was not, however, performed. It should be pointed out that all three configurations are within 3 percent of each other on annual energy performance. Clearly, the choice between configurations must be made on cost estimates.

Heliostat Configuration Selection

The end result of the cost tradeoff between the Az-El and the tilt-tilt heliostat was to select a tilt-tilt configuration. The rationale for the selection of 40-m² mirror area and a 2-milliradian tracking error has already been described. The overall dimensions and geometry of the baseline tilt-tilt heliostat are given in Figure 3-10.



TOTAL MIRROR AREA	-	40 m ²
ORIENTATION	-	OUTER-AXIS NORMAL TO TARGET LOS
TRACKING RATE	-	23 DEG/HR MAXIMUM NORMAL 1080 DEG/HR EMERGENCY
TRACKING ERROR BUDGET	-	2 mr (1 σ) EACH AXIS
OPTICAL ERROR BUDGET	-	1 mr (1 σ)
FACET RADIUS OF CURVATURE	-	840 m

Figure 3-10. Selected Heliostat Configuration

The selection of the basic heliostat shape was also a result of the configuration evaluation study. For the tilt-tilt heliostat, the overall heliostat planform can affect the aperture choice. Some results of an effort to determine differences in performance due to planform is shown in Figure 3-11. Three possible tilt-tilt configurations are shown, each with a total of 18.58 m^2 (200 square feet) of mirror area. Notice that for the polar packing field arrangement, the first heliostat performed best and was the most nearly square planform. As the planform was changed to be longer than it was wide, the overall performance was degraded. The long, six-facet heliostat obviously seemed a poor design, since the end facets were very far off the optical axis (center of the heliostat). These facets would not focus as well as facets closer to the heliostat optical center; thus, a larger aperture was required. The performance differences between a variety of other possible planforms is very small and cannot be considered significant. The final choice of the planform was determined by the cost analysis.

Field Analysis

After selecting a baseline heliostat configuration, we began an effort to create a more detailed heliostat field design. The heliostat field analysis work was intended to improve upon the proposed baseline heliostat field performance. A first step in this direction was taken during the investigation of the candidate heliostat configurations. During this early study, we found that a lower ground cover (low packing density) than proposed could reduce shading and blocking losses without significantly reducing the receiver efficiency. The scope of the detailed field design effort included studies of the effects of:

- Cosine-only field losses
- Shading and blocking losses
- Nonuniform packing density
- Tower location
- Tower height

NET ANNUAL ENERGY PER UNIT MIRROR AREA
(MWH/M²)
GROUND COVER = 0.3

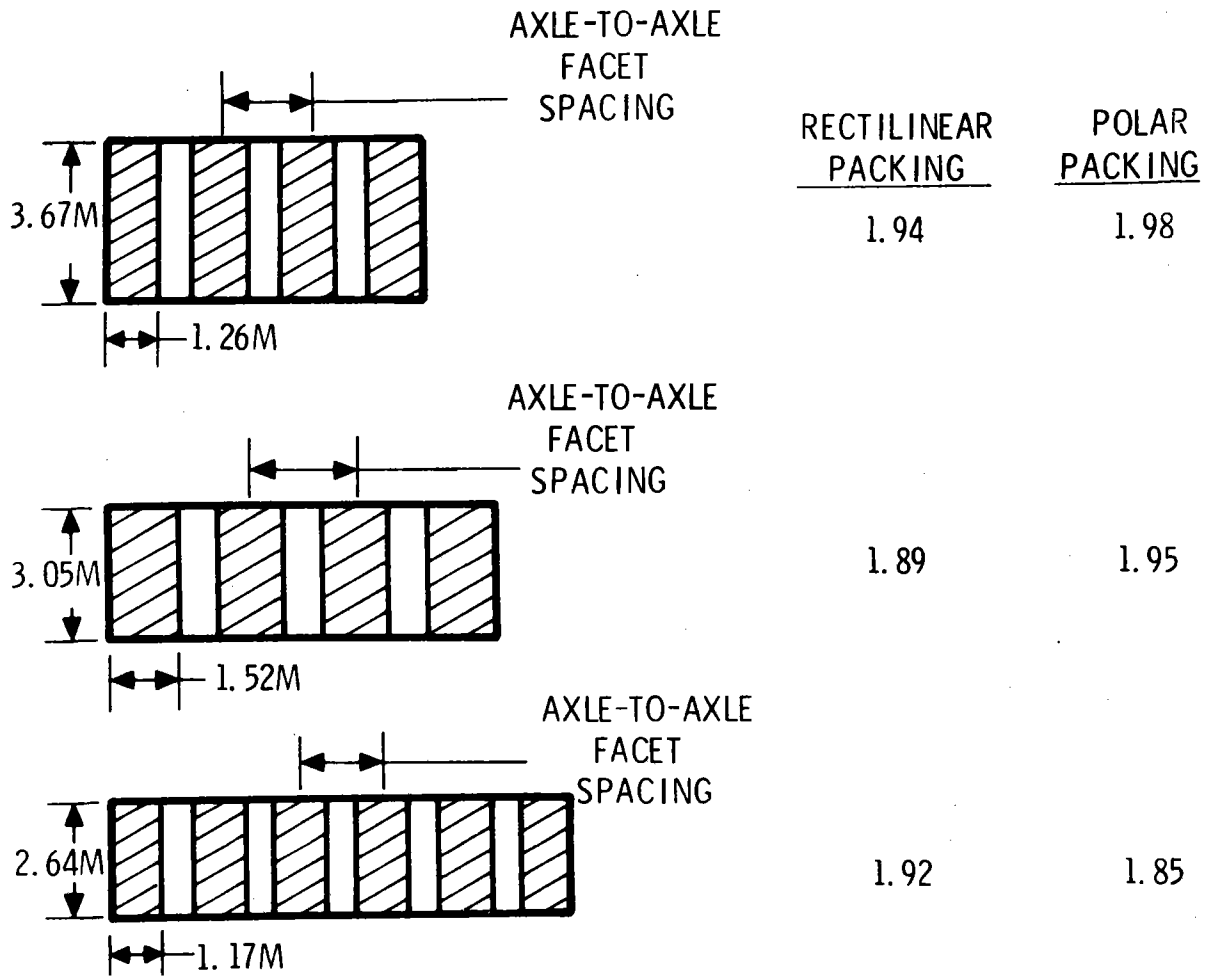


Figure 3-11. Tilt-Tilt Summary

Throughout the field design analysis, we evaluated the field performance on the basis of an efficiency value. One popular efficiency criterion is called the field tracking efficiency. Tracking efficiency is commonly defined as the redirected power per square meter of mirror surface area divided by the direct normal intensity per square meter. Offshoots of this definition include replacing redirected power by power incident on the mirrors or power absorbed by the receiver. In other words, the power anywhere along the optics path can be used in the numerator of an efficiency calculation.

The path of energy is shown in Figure 3-12. The figure establishes the nomenclature used throughout the heliostat field analysis work.

Cosine Effect -- The cosine of the angle described by the position of the sun and the mirror normal position determines the fraction of direct normal intensity which can be redirected by the mirror. This fraction varies over a heliostat field because the mirror normals vary to position each mirror so that the redirected energy is aimed at the receiver. The cosine for any single mirror (singly defined field position) is calculated simply by the dot product of the unit mirror normal vector and the unit sun vector (see Figure 3-13).

This cosine defines the mirror surface area as seen by the sun (mirror surface projected onto a plane normal to the sun vector). The cosine would be 1.0 for mirrors which redirect energy directly back at the sun. These mirrors would be in the receiver shadow and they represent a maximum possible redirected power per meter squared of mirror. The redirected power possible for all other mirrors is a fraction of this maximum, where the fraction is defined by the cosine of the angle between the sun vector and the mirror normal vector.

A computer program (FIELD) was written to calculate the cosine for various heliostat field positions and any selected sun position. The program also calculates the annual tracking efficiency of discrete field positions. The annual

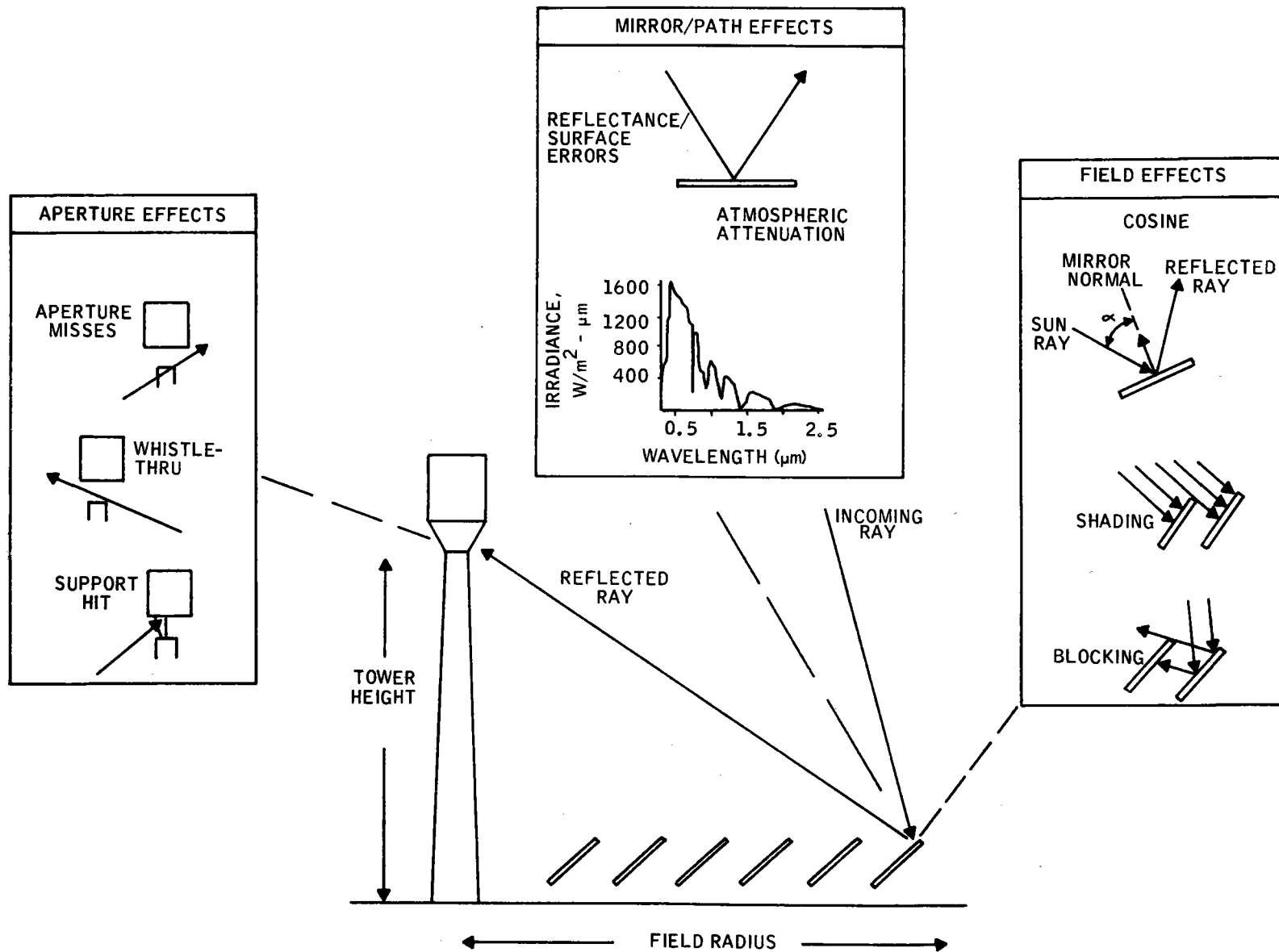


Figure 3-12. Ray Trace Energy Path

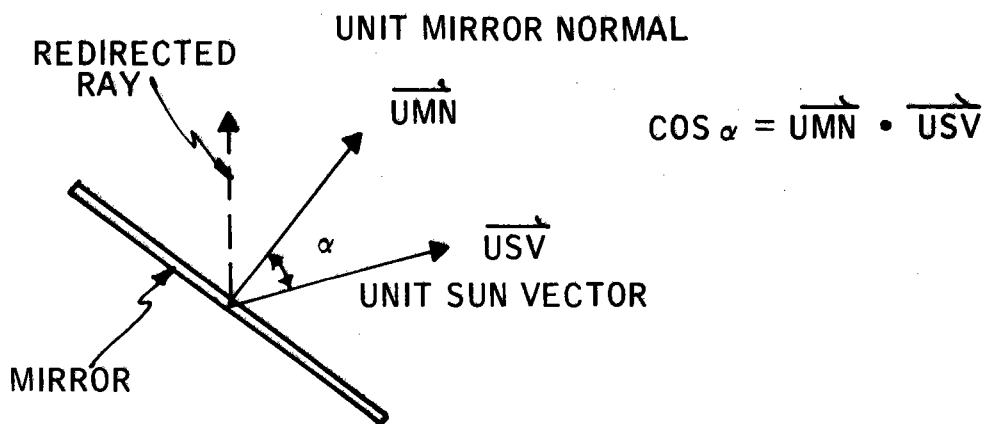


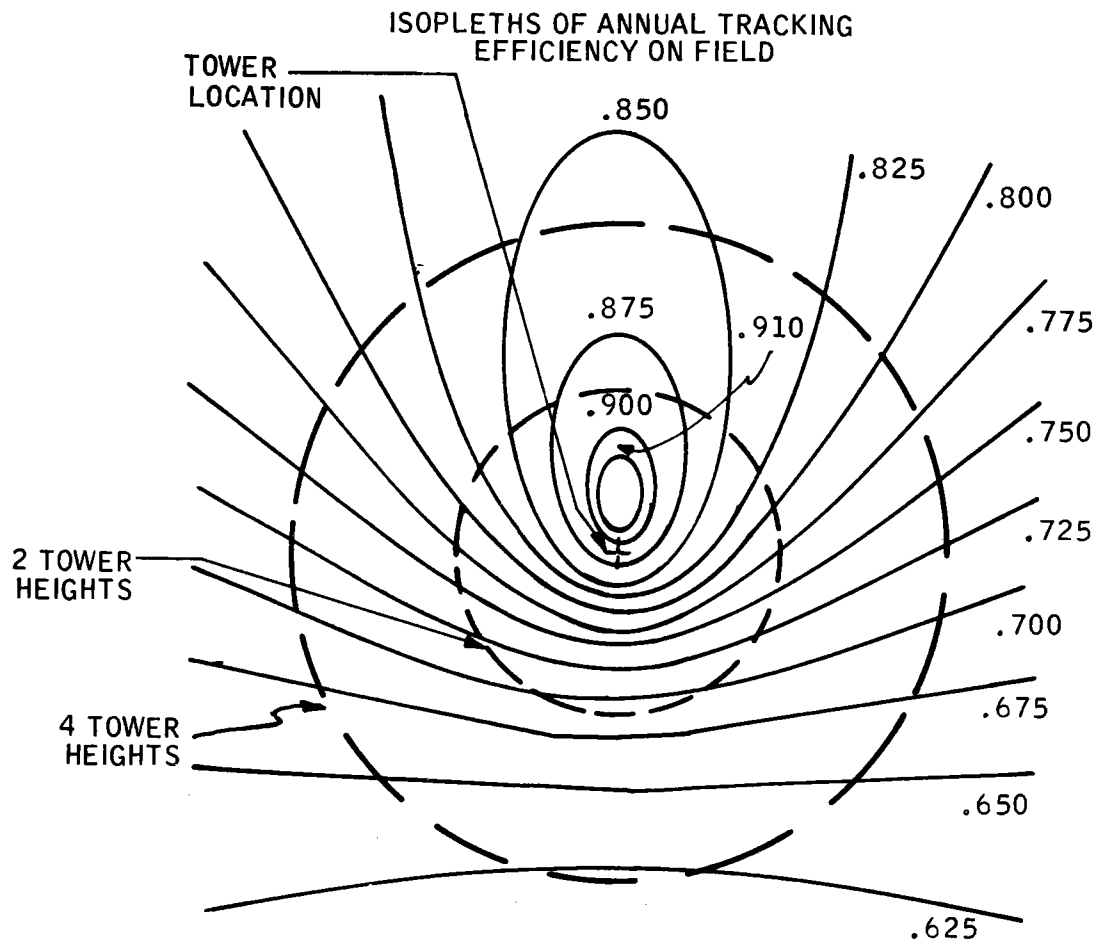
Figure 3-13. Cosine Definition

tracking efficiency is defined by the integrated redirected flux (yearly sum of cosine times direct normal intensity) divided by the total incident normal energy. Figure 3-14 shows isopleths of annual tracking efficiency out to four or more tower heights from the tower location.

The dashed circles in Figure 3-14 are at distances of two and four tower heights from the tower location in the field. The annual tracking efficiency shown is a maximum in the sense that no shadows are cast and a mirror reflectance of 1.0 is assumed. The isopleths of highest intensity (0.91, 0.90, etc.) lie generally north of the tower location simply because the plant was assumed to be at a 33 degree north latitude. Since the sun is always south of this latitude, mirrors north of the tower will be positioned more nearly normal to the sun vectors than mirrors in the south. It is apparent from Figure 3-15 that the north field proponents have an edge when comparing fields on the basis of the cosine effect.

To quantify the differences between a north field and a tower-centered or off-set field, the average annual tracking efficiency over various field sizes and shapes was calculated. Figure 3-15 shows the results for three different

40703-II



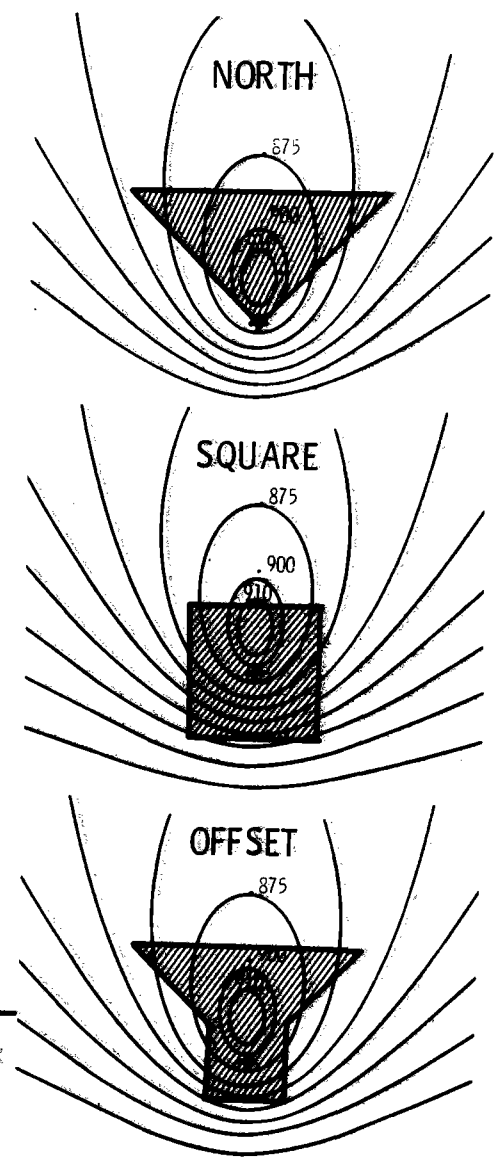
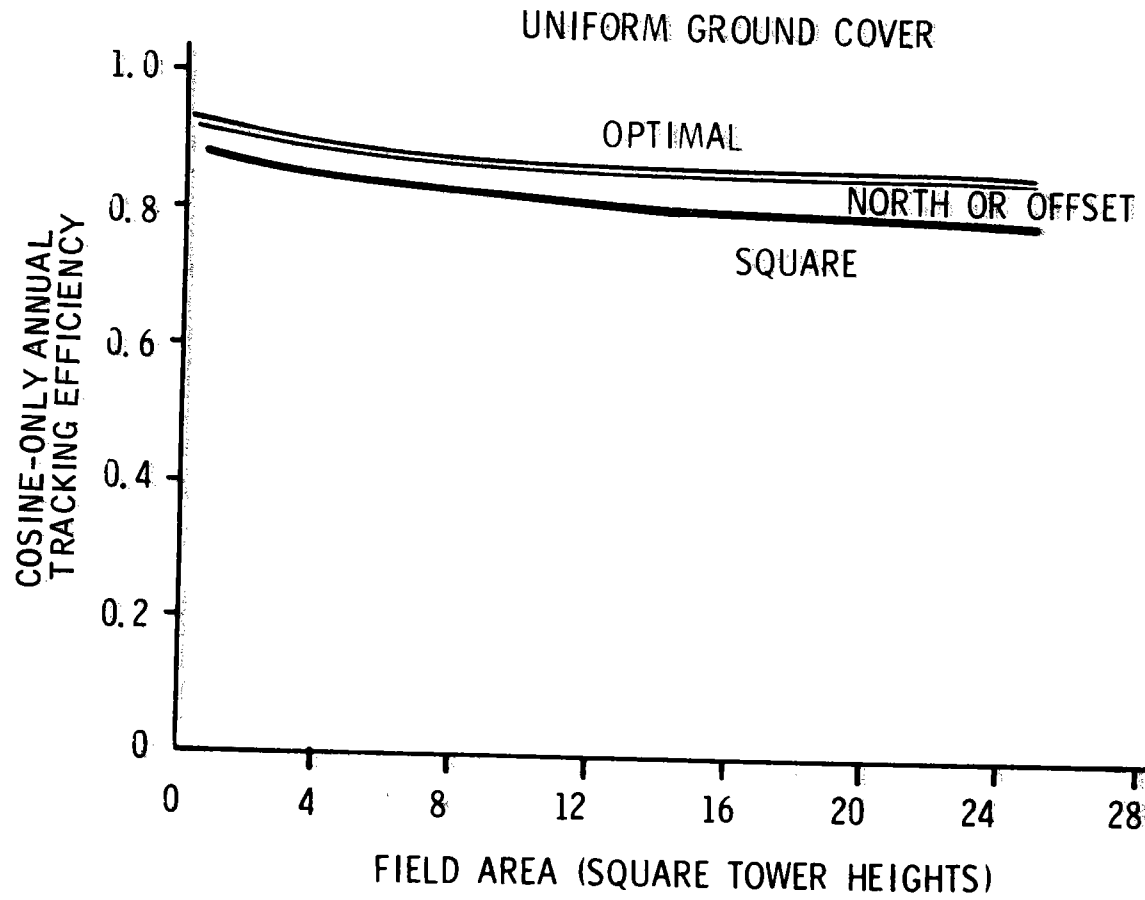
ISOPLETHS OF ANNUAL TRACKING EFFICIENCY ON FIELD

- 33° NORTH LATITUDE
- CLEAR-AIR MODEL
- NO SHADING OR BLOCKING BETWEEN MIRRORS
- NO TOWER SHADOW
- NO REFLECTANCE LOSS

3-29

Figure 3-14. Cosine-Only, Annual Tracking Efficiency

40703-II



3-30

Figure 3-15. Cosine Performance for Various Fields

field shapes. The three field shapes are defined by the drawing on the right side of Figure 3-15. The shaded areas shown are roughly four square tower heights in field area. Several isopleths from Figure 3-14 are shown with each field shape to give an idea of how well each field makes use of high tracking efficiency isopleths. The curves in Figure 3-15 show the average annual tracking efficiency, assuming each position in the field contributes an equal portion of mirror area to the average efficiency (uniform ground cover). The efficiency is plotted versus the field size in square tower heights. For example, a square field of 16 square tower heights would be four tower heights long on a side. This would be slightly more area than a circular field of two tower heights as shown by the inner dashed circle of Figure 3-14.

Field area nondimensionalized by the square of the tower height makes the data applicable to any scale solar power plant. For example, a plant with a field area of four square tower heights may have a tower 100 m tall; in which case, the field area is simply 40,000 m², or 200 m tall, in which case the field area is 160,000 m². In either case the cosine-only annual tracking efficiency is the same.

As shown in Figure 3-15, as the field area is increased, the extremities of the field get further from the tower location and encompass zones of lower tracking efficiency so that the average annual tracking efficiency is decreased. As expected, the north or offset field is better than the square field. For a tower-centered circular field baseline shown in the figure, the tracking efficiency is 0.855 for the north field as compared with 0.805 for the square field. The line labeled "optimal" corresponds to fields which are bounded by the isopleths shown in Figure 3-14. For example, the area within the 0.875 isopleth corresponds to a field area of approximately four square tower heights. Very little increase in tracking efficiency over the north or offset field is gained by considering isopleth field boundaries.

Note also that for any field (any tower location) the curves in Figure 3-15 show that the tracking efficiency decreases as the nondimensional field area is increased. An increasing nondimensional field area implies that the tower height is getting smaller relative to the field size. That is, for a given field of any number of heliostats within a fixed boundary, a tall tower implies high-cosine-only tracking efficiency, and, as the tower height decreases, the mirrors must aim lower and consequently the cosine efficiency drops off on an annual basis. To give one example, assume a field exists with no tower shadow, no mirror shading or blocking, and perfect mirror reflectance. Say an offset field mirror area is $100,000 \text{ m}^2$, roughly a pilot plant-scale field. For a tower 158 m tall, the nondimensional field area is four square tower heights and the tracking efficiency, from Figure 3-14, is 0.884. A tower 63 m tall would give a nondimensional field area of 25 square tower heights and a tracking efficiency of 0.842. Thus, on an annual basis, the 158-m tower will yield 5 percent more redirected power than the 63-m tower. Ignoring receiver losses, the extra 95 m of tower height are worthwhile only if the total annual average plant cost is increased by less than 5 percent to pay for the tower.

Clearly, from the cosine-effect-only studies, the north field selection would be popular. It is important to note that the north field far boundary will necessarily be further from the tower location than the square or circular field far boundary. The image from these far mirrors will be larger than produced by the square field, and consequently the receiver may have to have a larger aperture. If a nonuniform field is used, the north field far mirrors will probably be less tightly packed than in a square field; however, the total number of mirrors may be less due to increased tracking efficiency in the north.

The tradeoffs associated with the tower height, nonuniform field density, and distance from the tower issues have been addressed by first analyzing the shading and blocking of adjacent heliostats.

Shading and Blocking Effects -- The ray trace code was modified to do field-only analysis and to study the effects of ground cover and tower height on heliostat shading and blocking. A tower-centered circular field at 33 degrees north latitude was modeled (see Figure 3-16). This field was zoned into 10 radial zones and eight azimuth zones. The field was defined so as to have a radius equal to four tower heights.

Tilt-tilt, four-square facet heliostats with a total mirror area of 40 square meters were modeled. The heliostats were laid out in a polar packing arrangement.

Tower height was 122 m; field radius 607 m; cutout radius 30 m.

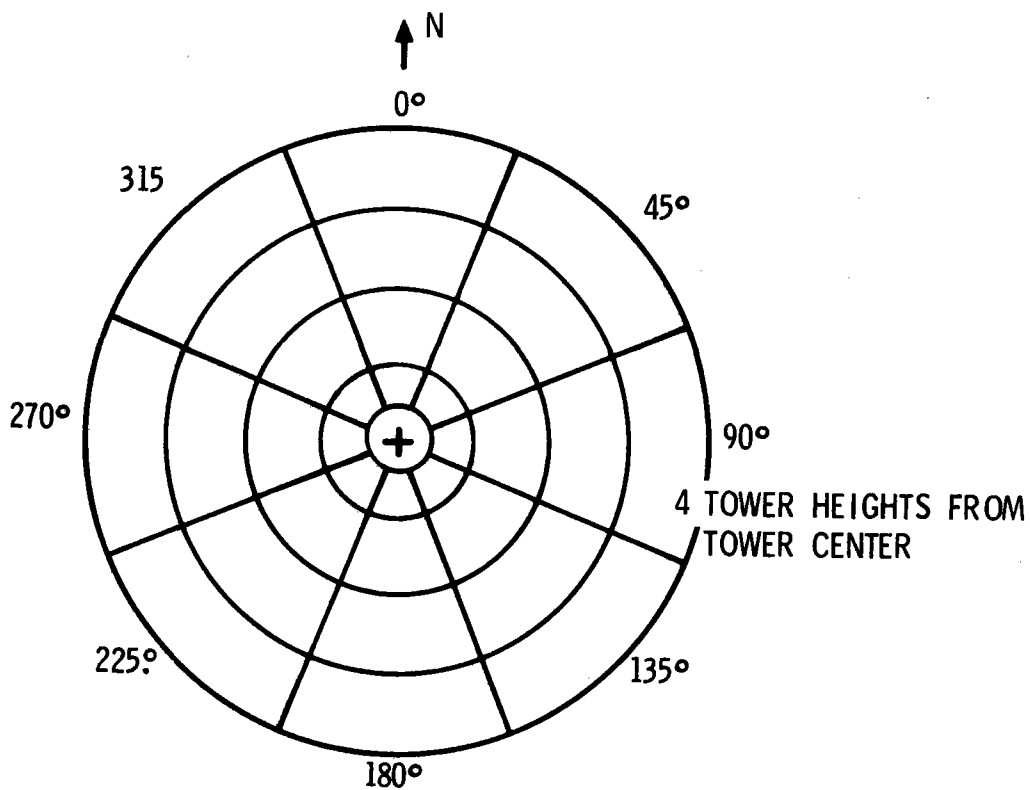
Output parameters were total energy on the field, energy lost to facet shading, energy lost to blockage, and total energy lost.

Figure 3-17 is a graph of percent of annual energy lost versus radial distance from tower center for a ground cover of 0.3. Because of east-west symmetry, curves for azimuth zones 225, 270 and 325 degrees are not shown as they would lie on top of the 135-, 90-, and 45-degree curves, respectively.

Note that for radial distances of less than 1.5 tower heights, the curves are flat. These losses are due entirely to shading along the outer gimbal axis (facet-to-facet shading), and remain relatively constant throughout the field. At radial distances greater than 1.5 tower heights, blockage becomes a factor, and accounts for a significant increase in flux lost in distant radial zones.

In those radial zones greater than 1.5 tower heights, Figure 3-17 shows that blockage losses are smallest in southern zones and highest in the zero-degree azimuth or north zone.

FIELD ZONING - 8 AZIMUTH ZONES



TILT-TILT (4 FACET) HELIOSTAT

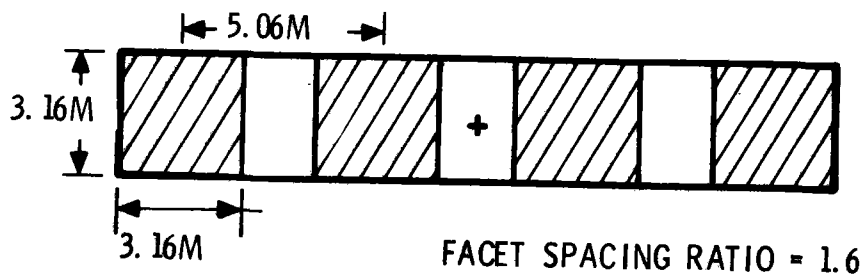


Figure 3-16. Shading and Blocking Simulation Parameters

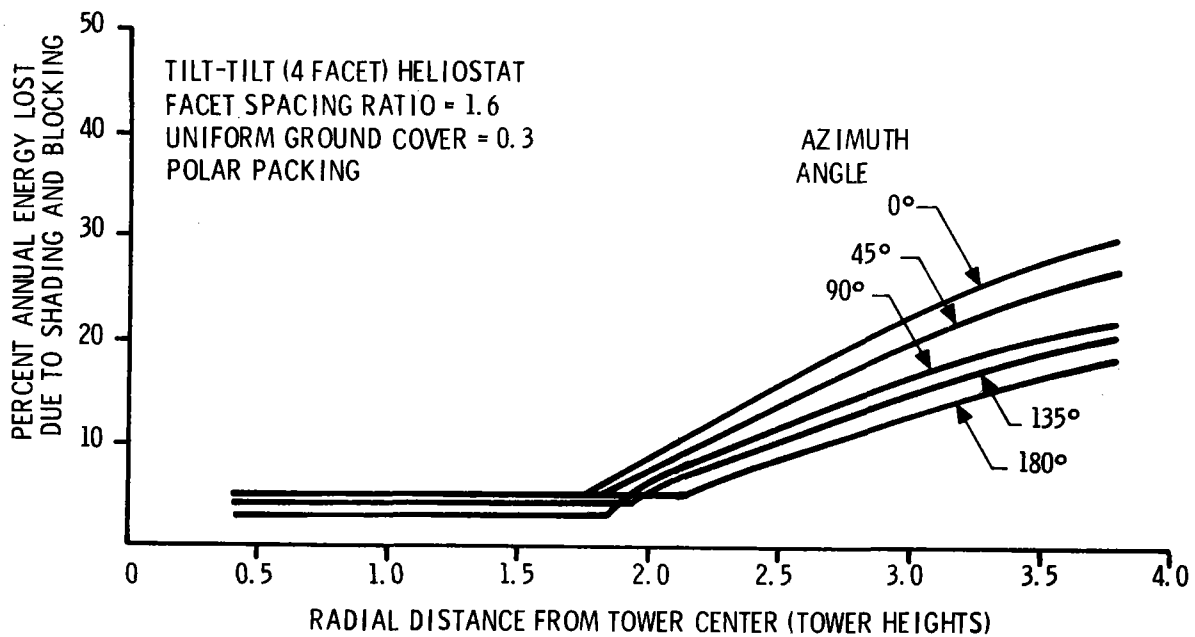


Figure 3-17. Annual Shading and Blocking Energy Losses versus Field Position

The increase in losses in distant radial zones comes about because heliostats in these zones are tilted up more, in order to redirect the sun's rays. Because of the generally southerly position of the sun at 33 degrees north latitude, mirrors in the north field must be tilted up more than mirrors in the south field, thus accounting for the larger blockage losses in the north field.

Figure 3-18 is also a plot of percent of annual energy lost versus radial position. In this graph, we are looking at only the zero degrees (northern) azimuth zone with a range of ground covers. Facet spacing is held constant at 1.6, as was designed for the baseline heliostat.

As expected, losses become significantly higher for higher ground covers. At a ground cover ratio of 0.1, there is no blockage out to the four-tower height distance evaluated. For a ground cover of 0.3, the percentage losses are at a minimum out to approximately 1.6 tower heights from the tower

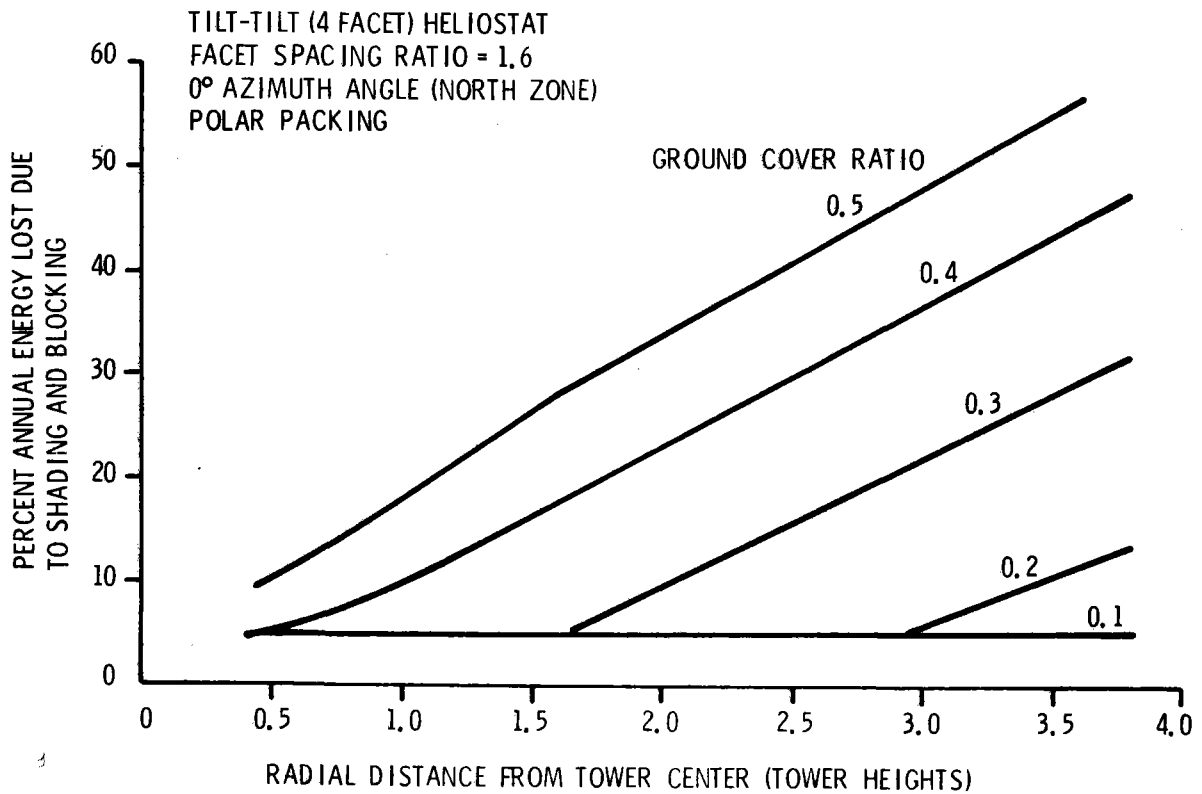


Figure 3-18. Annual Shading and Blocking Energy Losses versus Radial Distance from the North Field

location. Beyond this distance, blocking between adjacent rows of heliostats begins and losses increase nearly linearly.

The data presented in Figure 3-18 can be helpful in the selection of a desired field packing density. It is clear that higher packing densities close in to the tower location will not lose as much energy due to shading and blocking as the same density further out in the field. Thus, in terms of shading and blocking losses it would be beneficial to use a high ground cover close in to the tower and a low density further out. This type of layout can also increase the field cosine efficiency by placing the majority of the heliostats close in to the tower where the isopleths of cosine tracking efficiency were shown to be highest.

Thus, the two objectives of a field layout selection will be to use the highest possible ground cover to take advantage of cosine effects and to choose a ground cover consistent with the goal of minimizing shading and blocking losses.

Nonuniform Ground Cover -- Referring to Figure 3-18, if we define the points at which the curves begin to break upward as being an acceptable level of loss for a particular ground cover, we can plot maximum ground cover versus radial position for each azimuth zone. This is shown in Figure 3-19. The maximum ground cover, then, is that ground cover which is as high as possible without incurring any blockage losses. The losses (approximately 5%) which remain are due almost entirely to facet-to-facet shading for the baseline tilt-tilt heliostat.

Naturally, a tradeoff exists between the choice of ground cover and the tower and aperture size. We could select a ground cover higher than those indicated as a minimum loss level in Figure 3-19. A small added loss in

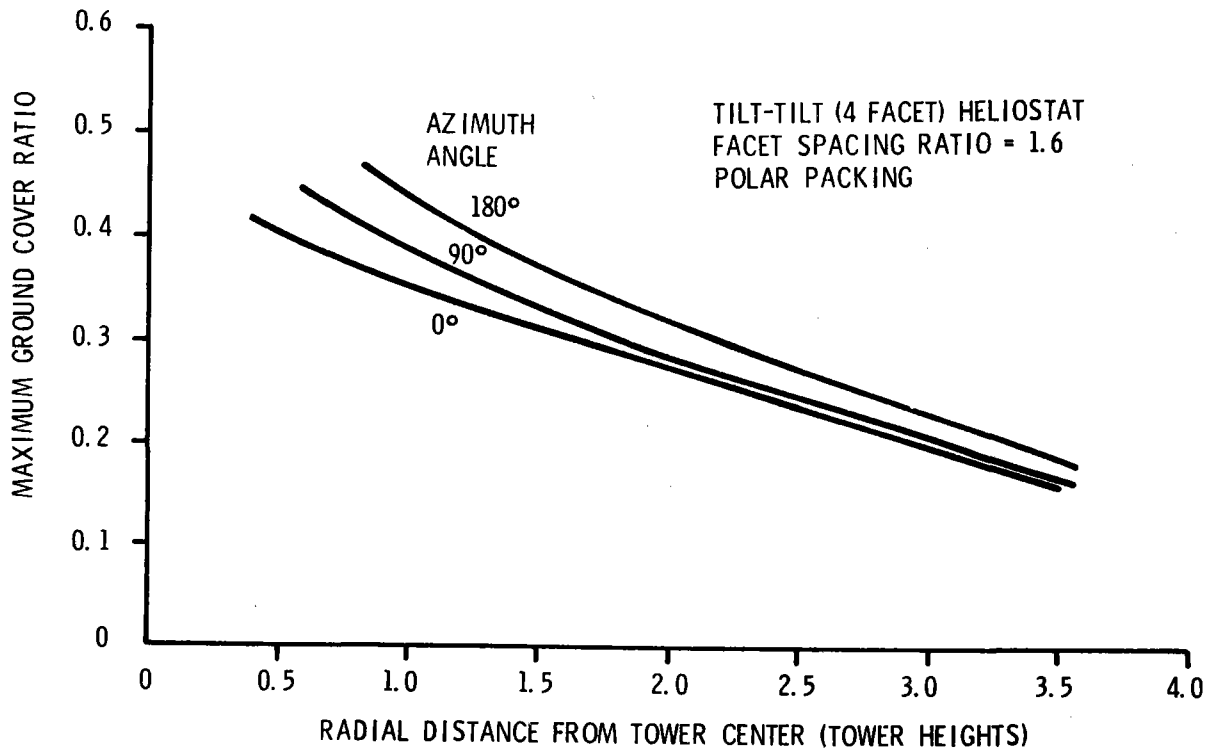


Figure 3-19. Maximum Ground Cover Ratio versus Field Position

annual field shading and blocking losses will result, but the field area required for a fixed annual energy will be smaller and, if tower height is held constant, then cosine efficiency is increased. For small changes in ground cover choice, very small gains and losses in net annual energy result. A review of the variables involved in this tradeoff can show why this is true.

To discuss the selection of the ground cover and tower height, we will use the case of a tower located one-half the way south from the field center to the southern field boundary. This is our baseline tower location for the pilot and commercial plant design. Those performance parameters which are dependent on the choice of ground cover and tower height are:

- Cosine-only tracking efficiency
- Shading and blocking losses
- Tower shadow
- Aperture spillage
- Whistle-through losses
- Reradiation losses
- Convection losses

Each parameter variation as a function of ground cover and tower height selection will be discussed.

The cosine-only tracking efficiency has already been, in part, addressed for a tower half-south configuration. The cosine-only tracking efficiency for this configuration is much like that of what we previously called an off-set field. Figure 3-20 shows the cosine-only tracking efficiency versus nondimensional field area for a tower half-south field. Here, the tracking efficiency has been modified slightly to account for a nonuniform ground

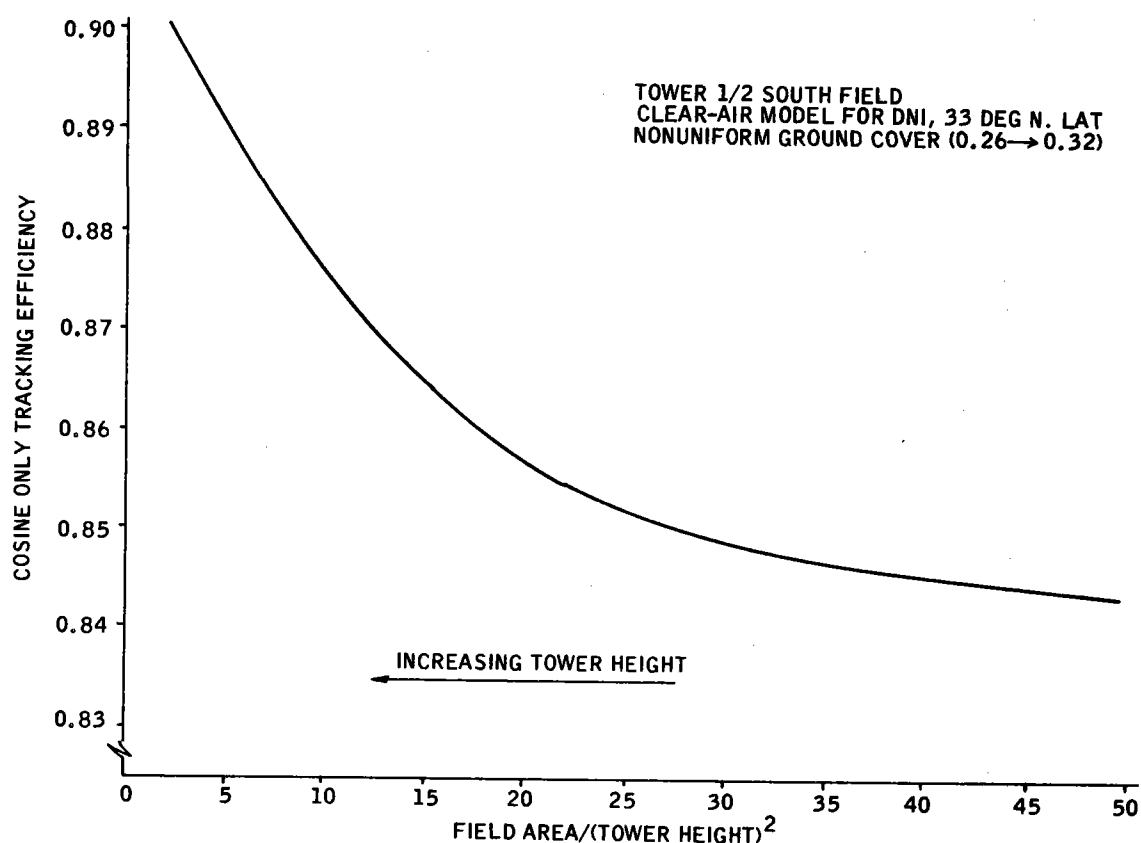


Figure 3-20. Cosine Only, Annual Average Tracking Efficiency

cover. Any nonuniform ground cover will attempt to pack heliostats more densely in zones of low shading and blocking losses. These zones are generally closer in to the tower and correspond to zones of high annual average cosine-only tracking efficiency (see Figure 3-14). We evaluated the impact of the nonuniform density and found that the cosine-only tracking efficiency can be increased by approximately 1 percent over that achievable by a uniform ground cover field. More will be said about this later. The curve of Figure 3-20 can be used for any selected nonuniform ground cover that follows the slope of decreasing ground cover versus distance from the tower as shown in Figure 3-19.

To more conveniently discuss the tradeoff issues involved in the selection of tower height and ground cover, we will analyze the case of a fixed number of heliostats. A given number of heliostats may be spaced nonuniformly at various average ground covers. For each possible ground cover, the field area becomes fixed and variations in performance can be established. For the purpose of quantifying performance differences, we arbitrarily use 1575 tilt-tilt heliostats each with a mirror area of 40 m^2 . An average ground cover of 26, 29, or 32 percent will be considered. Tower height is varied from 88 m to 165 m. Given these parameters, the cosine-only tracking efficiency of the alternative plants can be found and used to obtain cosine-only loss percentage as shown in Figure 3-21. The data in Figure 3-21 are simply determined by establishing the nondimensional field area in square tower heights for each of our plant alternatives. For example, at a tower height of 120 m and an average ground cover of 29 percent, the field area over tower height squared is:

$$\frac{\text{Field Area}}{(\text{Tower Height})^2} = \frac{(1575 \times 40 \text{ m}^2)/0.29}{(120 \text{ m})^2} = 15.09$$

Using a nondimensional field area of 15.09 square tower heights, the cosine-only tracking efficiency is 0.864, as previously shown in Figure 3-20. Thus, the cosine loss percentage is 13.6 percent. For each possible combination of ground cover and tower height, the nondimensional field area is found, the efficiency is taken from Figure 3-20, and the data are replotted in the format of Figure 3-21. It can be seen that the cosine losses are least for higher ground covers and for taller towers.

Shading and blocking losses as a function of ground cover and tower height can also be estimated from previous data. Figure 3-22 shows our estimates of losses as a function of ground cover for various tower heights. Each ground cover is an average over a field, where the heliostat packing density

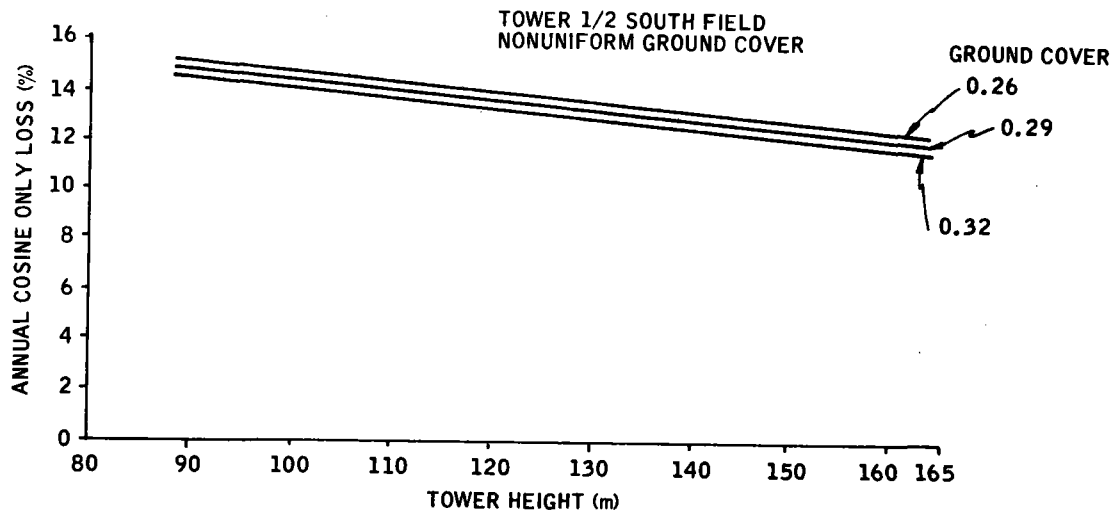


Figure 3-21. Cosine-Only, Percentage Loss versus Tower Angle

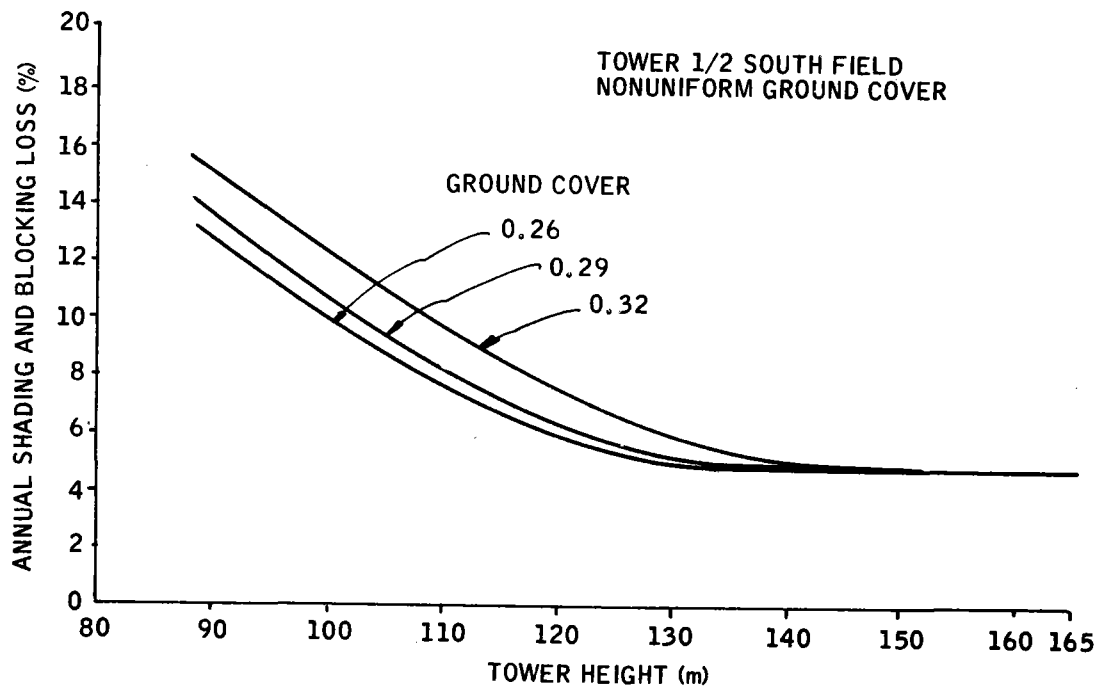


Figure 3-22. Shading and Blocking Loss versus Tower Height

is nonuniform. In each case, heliostat density is highest close in to the tower and lowest further out. Taller towers are most effective at eliminating shading and blocking losses because the heliostats point more nearly vertically than when aiming at the top of shorter towers. Obviously, as ground cover is increased, the losses are higher for any given tower height because the heliostats are packed more closely together.

Tower shading of the heliostats is a small contribution to the overall loss. Figure 3-23 shows the tower shading losses versus tower height for the three ground covers under investigation. In all cases, losses are less than 1/2 of 1 percent.

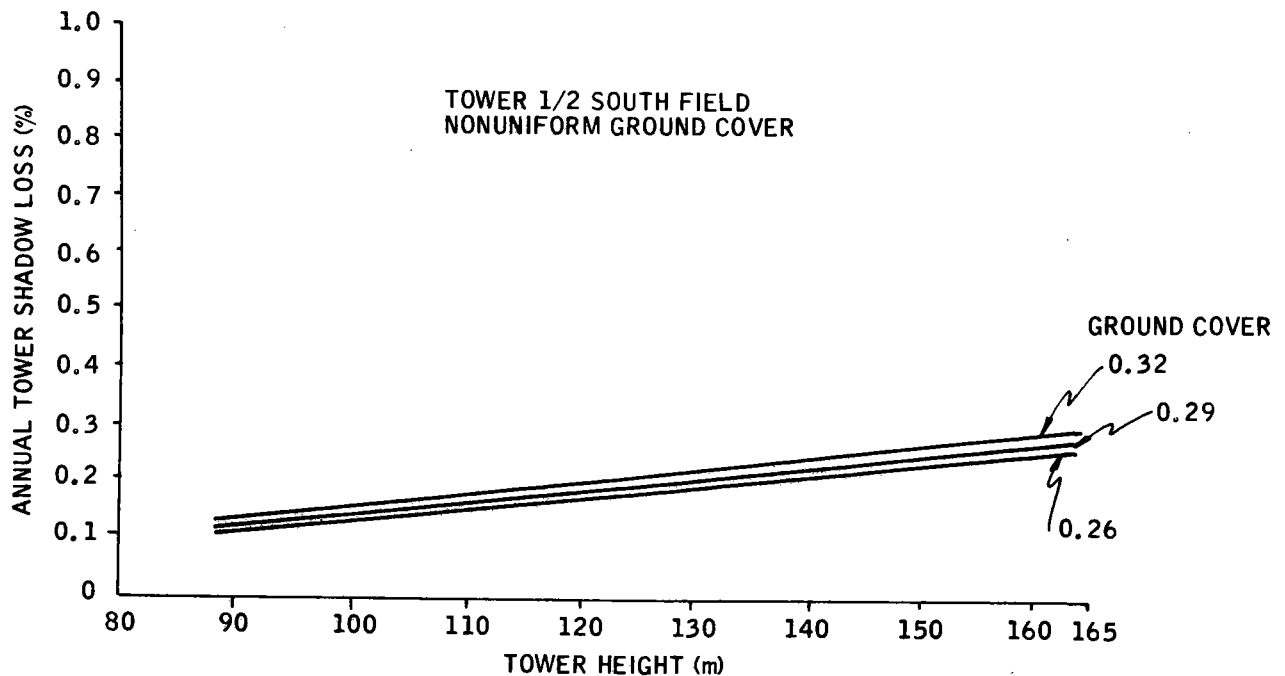


Figure 3-23. Tower Shadow Loss versus Tower Height

Losses at the aperture are shown in Figure 3-24 and include spillage and heat losses. Given a total redirected energy which reaches the receiver, there exists a tradeoff between increasing the aperture size to catch all incoming energy and decreasing the aperture size to prevent reradiation and convection heat losses. Our approach has been to open the aperture to

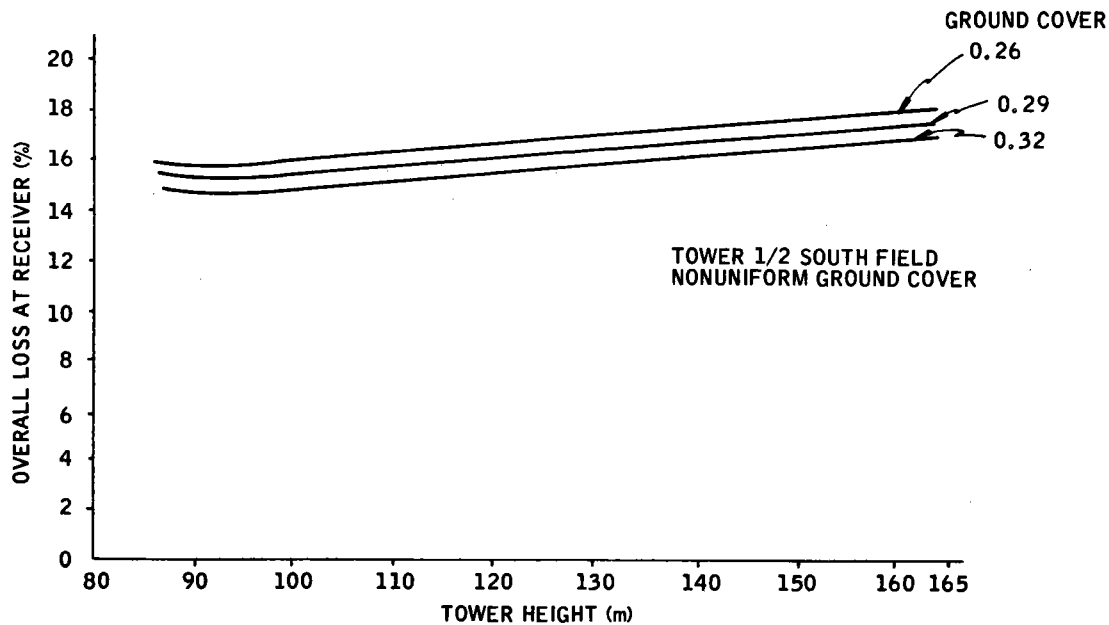


Figure 3-24. Overall Receiver Loss versus Tower Height

a size which maximizes the net (absorbed) annual energy. That is, as the aperture gets larger, more energy enters the cavity, but it is also true that more energy can escape via reradiation and convection. There exists a point at which the energy in minus the energy out is at a maximum. The data in Figure 3-24 reflect an optimized aperture size for each point. As towers get taller, the average optical path length, and hence average image size at the aperture, will increase. The optimal aperture size selected will be slightly larger than for shorter towers but not large enough to avoid spillage. This will cause a slight increase in both the amount of energy which misses the aperture opening and in the amount loss due to reradiation and convection. The amount of energy which whistles through (enters one side of the aperture opening and exits the other) counteracts the increased losses by decreasing as the tower gets taller. Overall, our estimates show that taller towers will have slightly more losses than shorter towers up to a point where energy which whistles through will preclude

shorter towers. The loss estimates also show that higher ground covers can more efficiently gather the redirected energy. A further discussion of the issues related to the choice of an aperture design is presented later. For a parametric study of tower height and ground cover, the data of Figures 3-21 through 3-24 contain our best information as to the performance of all optimal design points.

With the information on losses between the sun and energy absorbed into the steam complete, the overall plant tracking efficiency can now be determined.

Each combination of tower height and ground cover is assumed to have perfect mirrors (reflectance = 1.0), and efficiency is defined by the thermal energy absorbed divided by the available direct solar energy. The overall annual tracking efficiency versus tower height is shown in Figure 3-25. This efficiency is a measure of the relative annual energy performance of each possible plant. As shown in Figure 3-25, all plants, independent of average ground cover, perform better the higher the tower up to a point where taller towers no longer gain shading and blocking efficiency and the receiver losses become larger than cosine gains. The figure also shows that the highest ground cover, 0.32, is best for towers taller than 131 m. Below 131 m, the 0.29 ground cover is best until approximately 114 m, where the 0.26 and 0.29 ground cover plants perform equally for all shorter towers. This suggests that for each tower height there exists an optimal ground cover. In fact, we expect that this must be true down to a point where no decrease in tower height can decrease shading and blocking losses or aid in aperture efficiency. For each tower height higher than this minimum an optimal ground cover exists simply because as ground cover increases, the plant performance is degraded by increased shading and blocking losses, but is improved by a more efficient field cosine and aperture.

To select a tower height and ground cover combination, we need to add cost data to the performance data. Cost information to select a best tower height

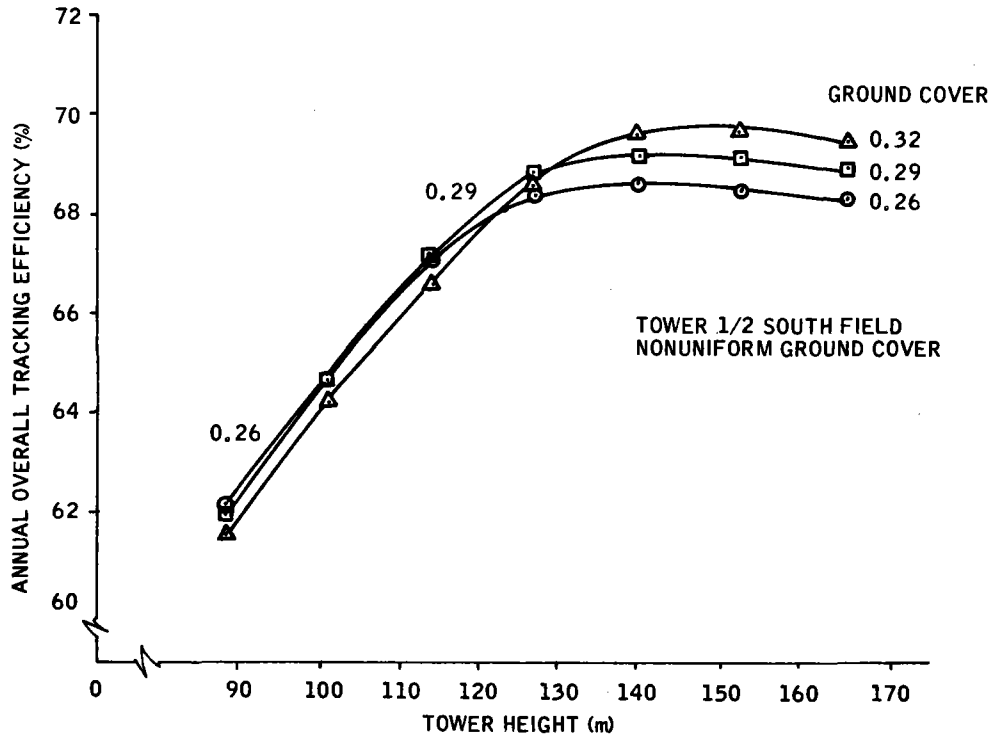


Figure 3-25. Annual Tracking Efficiency versus Tower Height

has been a problem. Our early costing activities indicated that the tower and receiver together would contribute approximately 6 percent of the total plant cost. This 6 percent estimate included the piping and steam generator equipment. For the tower alone, some parametric cost data showed that the tower cost would vary as the square of the tower height. For our trade-off analysis, the heliostat count is fixed and the peak plant power output for all possible combinations of tower height and ground cover will be a constant. Thus, the only plant cost which will change as a function of tower height will be the tower and receiver. We assume that this cost would vary as the square of the tower height so that the relative plant cost can be written as:

$$\text{Relative Plant Cost} = 94 + 6 \frac{\text{TH}}{\text{TH}_{\text{base}}}^2$$

where TH is the plant tower height and TH_{base} is the tower height of the base plant costed at 6 percent for the tower, receiver, and piping. The base case was costed for a commercial plant, but the tower height can be scaled to a 126-m tower for our analysis case. The relative plant cost can be thought of as a percentage cost of the base plant. The cost per unit annual energy is the value which we wish to minimize. This value can be obtained by simply dividing the relative plant cost by the annual energy as indicated by the tracking efficiency. The result is shown in Figure 3-26. The minimum cost

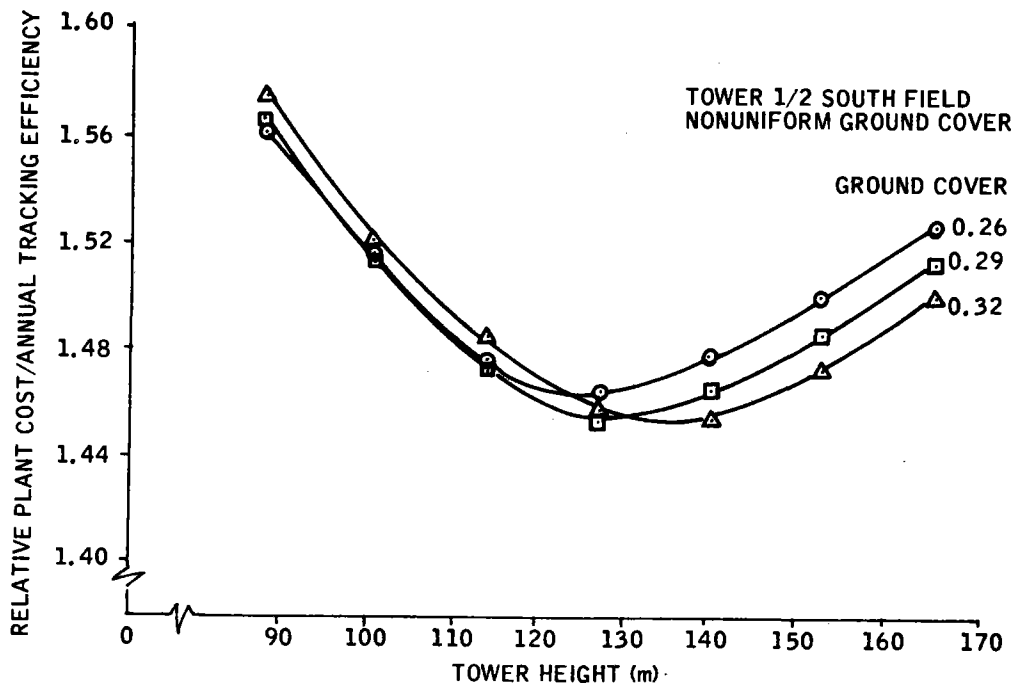


Figure 3-26. Cost Per Unit Energy versus Tower Height

point is different for each ground cover. Had we investigated all possible ground covers, a curve of cost per unit energy versus tower height would be one curve for the optimal ground cover at each tower height. If it were possible to very accurately define the cost of all tower height-related issues, we would design at the optimal, which appears to be a tower between 122 m and 146 m high and a ground cover between 0.29 and 0.32. Since the cost model is not sufficiently detailed, and because the optimization is relatively weak, we chose a tower height and ground cover of 126 m and 0.29 respectively. For the cost data base, this choice seems conservative. We recognize that the optimization is sensitive to the tower and receiver parametric cost assumptions. To determine how sensitive, we changed the cost model to assume the tower height-related costs represent 16 percent of the plant cost and again vary as the square of the tower height. The result was that the best configuration had a tower height between 107 and 122 m with a ground cover of approximately 0.29 or 0.30. Although this design was different, the change in cost per unit energy is less than 1 percent. Thus, we see no strong cost pressure to change the chosen baseline tower height or ground cover. The nonuniform ground cover as determined in Figure 3-19 was used for the remainder of the pilot and commercial plant performance analysis.

The actual means by which the maximum ground cover ratio result was implemented in the ray trace code was to specify the radial spacing per unit collector width as a function of field position. The radial spacing is set so that the ground cover ratio decreases linearly with radial distance from the tower center. The radial spacing versus radial distance is shown in Figure 3-27. Using these curves, the ground cover ratio maximum shown in Figure 3-19 is not met at distances less than one tower height, and beyond one tower height the calculated ground cover maximum lays nearly on top of the curve shown in Figure 3-19.

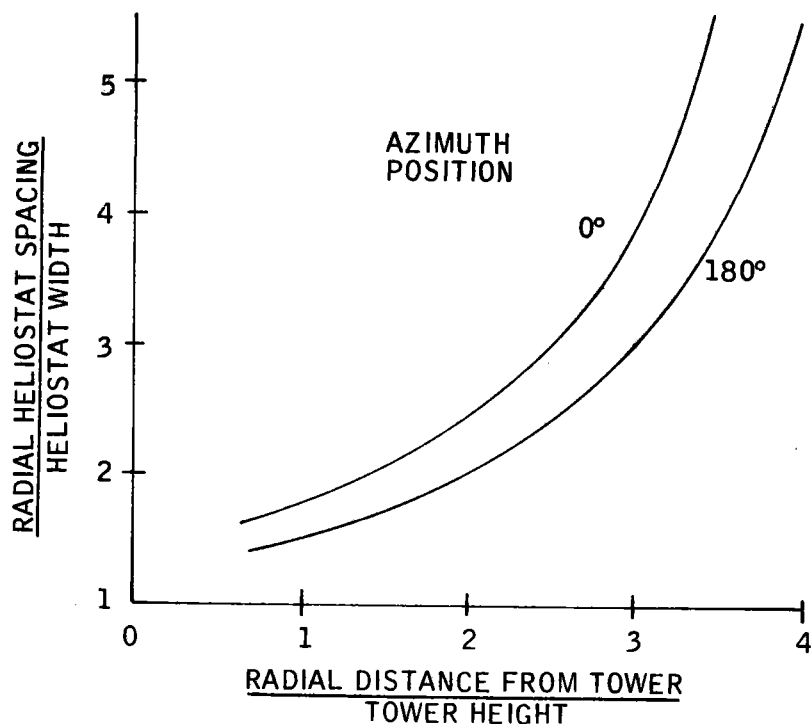


Figure 3-27. Radial Spacing versus Distance from Tower

The field layout in the ray trace code consists of eight azimuth zones, with the radial spacing specified separately for each zone (see Figure 3-28). For example, for each azimuth zone, the maximum allowable ground cover ratio decreases linearly according to the curve for a zero-degree azimuth position as shown in Figure 3-19. The actual ground cover ratio for a particular portion of the field may be less than the maximum allowable because of integer rounding of heliostats in a zone. Integer rounding effectively increases the edge-to-edge or circumferential spacing of the heliostats. The maximum allowable ground cover assumes that circumferential spacing is done so that the spacing between heliostats equals the spacing between facets on a single heliostat. When the nonuniform field layout is accomplished, each row of each of the eight zones must have an integer collector count. For zones close to the tower with large heliostats, the number of heliostats would be small; in fact, 1.6 heliostats would fit per-

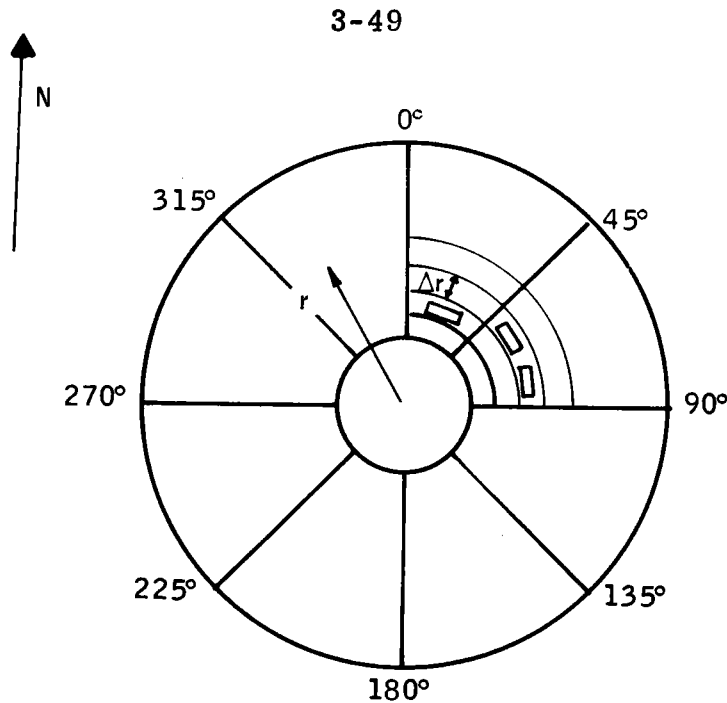


Figure 3-28. Nonuniform Heliostat Packing Density Field Zones

fectly in some cases. To avoid heliostats overlapping into another zone, the heliostat count in this case would be reduced to 1.0 and the circumferential spacing is allowed to increase without changing the radial spacing. This strategy is used for simplicity in the ray trace code and is not meant to define actual plant heliostat location. The heliostat field layout in the plant would use the radial spacing rules only.

Tower Location -- To examine the effects of tower location on plant performance, the ray trace code was modified to accept a tower located at any point north or south of the field center. Quite a number of field perimeters may be considered for study. A practical and workable selection of general field perimeter geometry, which allows a variety of field characteristics to be investigated, is to simply keep the outer field perimeter circular.

A series of computer runs were made to find the annual tracking efficiency for pilot plant-scale fields. Table 3-3 presents some of the pertinent data for these runs. Table 3-3 shows the new nonuniform field data, as well as

the 12/21, 2 p. m. power and annual energy data for a 0.3 uniform ground cover, tower-centered power plant.

The tower-centered, nonuniform ground cover data show an increase in annual tracking efficiency over the uniform ground cover case (0.752 to 0.763). Part of this increase, approximately 80 percent, is due to the greater density of mirrors closer to the tower, where the isopleths of tracking efficiency have been shown to have higher values. A second reason for the increase is the elimination of the far north field blocking losses which occurred with a uniform (0.3) ground cover ratio.

A plot of the annual tracking efficiency versus tower location is shown in Figure 3-29. As expected, the efficiency, with or without shading and blocking losses included, increases as the tower is located further south of the field center.

Returning to Table 3-3, it can be noted that each nonuniform field run was done with a constant field radius equal to 274.3 m (900 ft). The collector count decreases as the tower is moved south because the average ground cover maximum must be decreased for the north field. The north field far boundary becomes farther and farther from the tower location so that a ground cover of 0.12 is used at the north edge of a north-only heliostat field. Although this field has a higher tracking efficiency than tower-centered fields, it would produce less energy over 1 year's time. To produce more energy, more heliostats would have to be added and the tower height would increase to maintain the same field area in square tower heights. Assuming that the proper field area in square tower heights is chosen, the added expense of a taller tower could be weighed against the reduced heliostat cost gained by higher tracking efficiency as the tower location is moved south.

Table 3-3. Effect of Tower Location on Performance

Parameter	Annual Energy Data						12/21, 2 p. m.	
	Center	Center	1/4 South	1/2 South	3/4 South	South	Center	1/2 South
Field radius, m	2920	274.3	274.3	274.3	274.3	274.3	292.0	274.3
Tower height, m	137.2	129.5	129.5	129.5	129.5	129.5	137.2	129.5
Tower location	Center	Center	1/4 South	1/2 South	3/4 South	South	Center	1/2 South
Heliostat count	1938	1872	1816	1682	1472	1308	1938	1682
Unshadowed, unblocked tracking efficiency	0.799	0.809	0.840	0.835	0.850	0.863	0.773	0.862
Tracking efficiency	0.752	0.763	0.795	0.790	0.804	0.821	0.734	0.821
Average ground cover ratio	0.300*	0.328	0.318	0.295	0.258	0.230	0.300*	0.295
							Redirected Power	51 MW(th)
								49.6 MW(th)

* Uniform ground cover.

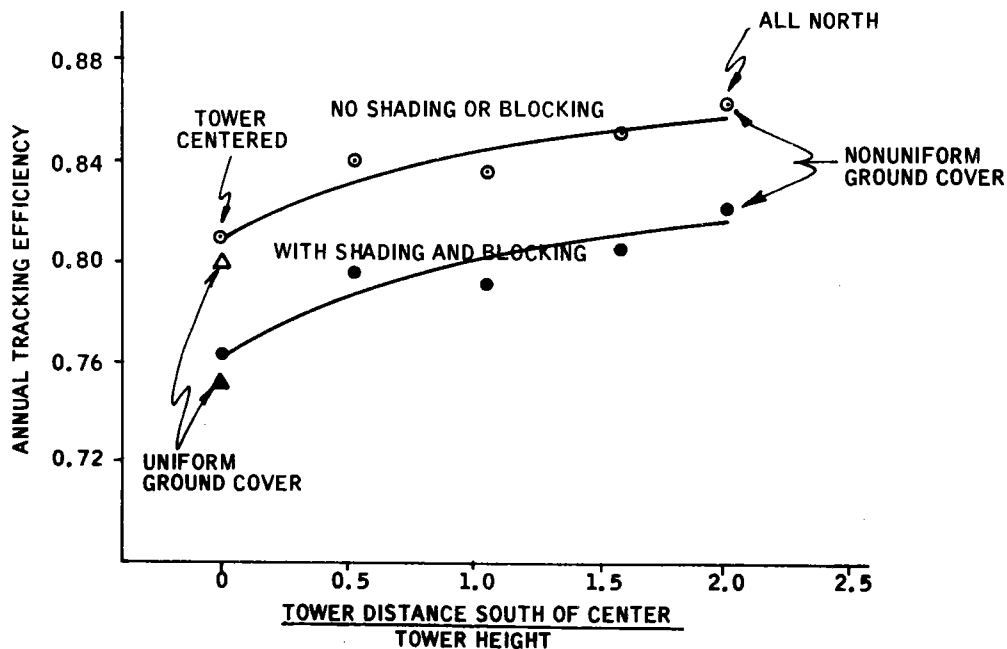


Figure 3-29. Annual Tracking Efficiency versus Tower Location

The added tower cost assumes that the ratio of field area to tower height is the same for each plant type. Actually, this ratio must be optimized for each plant. If receiver characteristics are ignored, the ratio of field area to square tower heights would be optimal at relatively small towers. When receiver characteristics are considered, the tower may have to be higher to avoid missing available energy via whistle-throughs.

The optimal tower height for each possible tower location is also affected by the aperture size. As the tower height is decreased, the average ground cover ratio will probably need to be decreased to avoid shading and blocking losses. The reduced ground cover ratio, as well as reduced tracking efficiency, forces the field boundary to expand, which in turn means that the image from the far heliostats is larger at the receiver aperture. The larger image requires that a larger aperture be used and, consequently, the reradiation losses are expected to be larger. The effects of all field and aperture issues are different for different tower locations. Because of the large numbers of variables in a detailed tower height and ground cover optimization, an accurate cost comparison between various possible tower locations is beyond the scope of the present work. Any cost comparisons which can be made are open to criticism, and we can only give our subjective judgment on the merits of the final design choice.

We believe that because of advantages in tracking efficiency, it is desirable to design a tower-south-of-center field layout. The distance the tower is moved south is restricted by the requirement that the receiver baseline configuration remains essentially unchanged in appearance and operation. This implies that the aperture will need to be an annular opening so that incident flux is directed to all active surfaces of a circular steam generator and superheater. It is assumed that minor modifications to the boiler/superheater interface configuration are allowable.

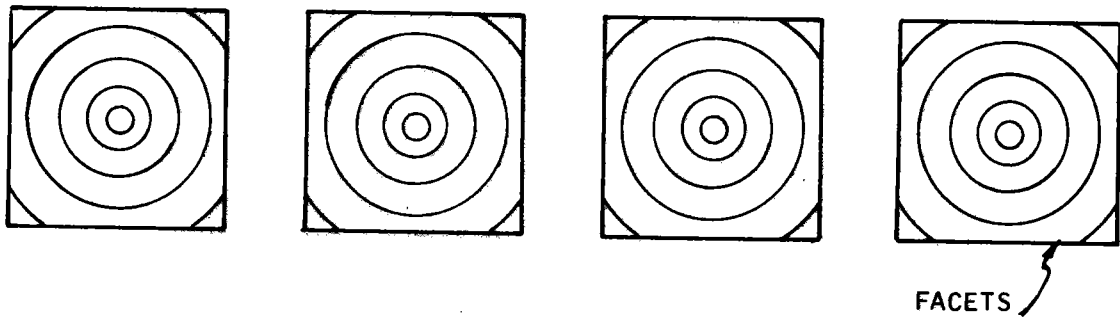
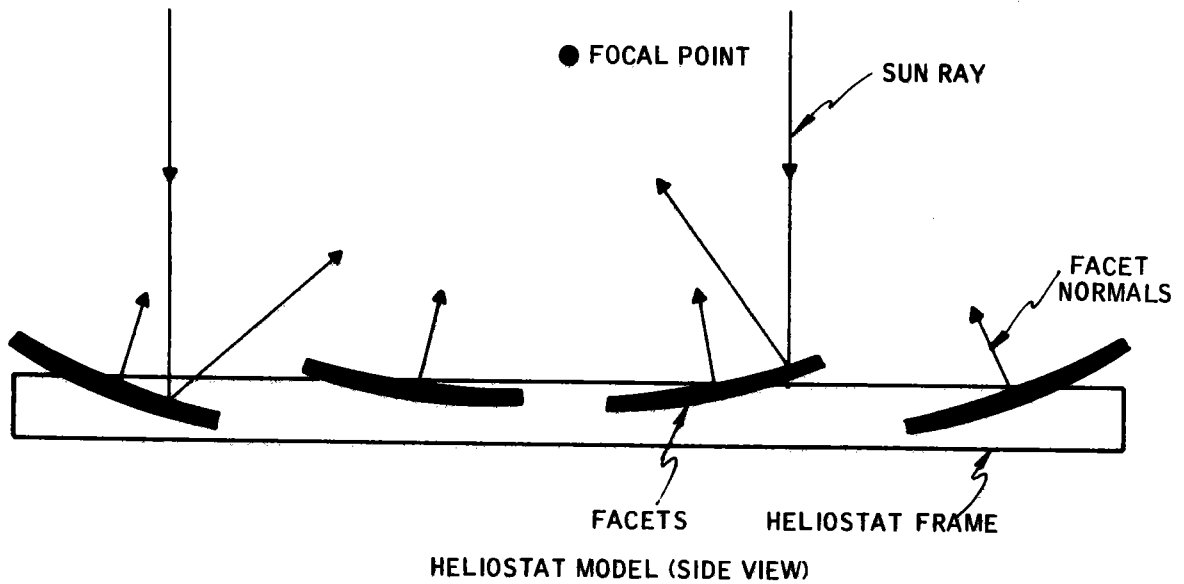
A practical limit to the distance the tower is moved south can be set at approximately one-half the distance from field center to the far south boundary. Moving the tower farther south than half-way would be inconsistent with an annular aperture. The south side of the aperture would have to be large enough to accept the image size of a relatively few south heliostats but a very low flux concentration would pass through this opening. For fields where the tower is located very far south, the south aperture opening could reradiate more energy than was admitted. If the tower were to be moved more than half-way to the south, it would most likely be best to move it fully south so that a north-only field and aperture could be used. This was not considered an allowable option. Thus, we located the tower one-half way south for the pilot and commercial plant baseline configuration.

Facet Focusing and Toe-In

The baseline tilt-tilt heliostat configuration has four mirror modules or facets. A design decision on the facet focal length and the facet toe-in was made by analyzing the performance issues associated with the decision. Figure 3-30 shows how the baseline heliostat was modeled.

Each facet may be toed-in, or canted slightly toward the heliostat center, to improve the total heliostat image characteristics. This toe-in is simply a fixed rotation about the inner axis of the heliostat. The toe-in angle is specified in terms of a reference time or sun position for which the mirror facets are aligned to redirect incoming rays as nearly as possible to a single focal point. At times other than the reference time, the facets may not be aligned to create a single focal point.

The baseline heliostat facets are modeled as a portion of a spherical surface. Each facet on a single heliostat has the same radius of curvature. The focusing issues are concerned with the question of radius of curvature as a function of field position.



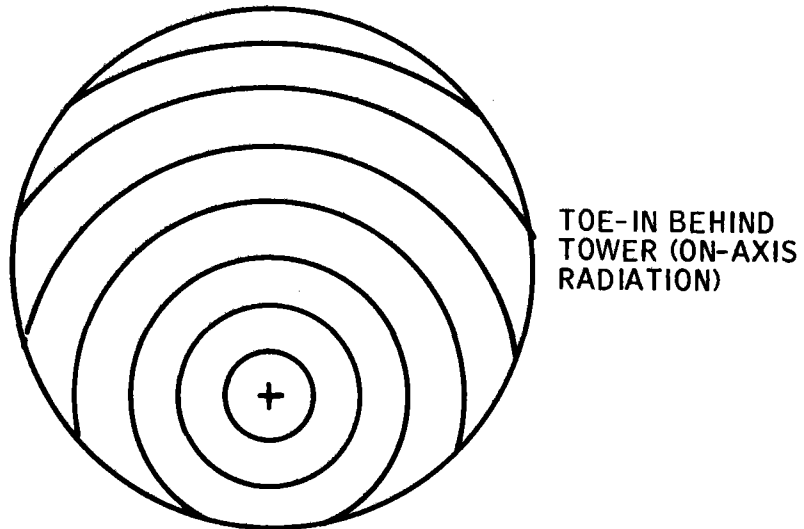
FACET SPHERICAL REPRESENTATION (TOP VIEW)

Figure 3-30. Heliostat Optical Modeling

The ray trace code was used to establish the sensitivity of the plant annual performance to the choice of toe-in and focusing strategy. The ray trace code used in this study can divide the field in a number of zones (1 to 10) for which the heliostat facet focal length and toe-in angles are constant. If one zone is chosen, then all heliostats in the field have a constant facet radius of curvature and constant toe-in angles. Similarly, 10 zones would create 10 different facet radii of curvature and 10 sets of toe-in angles. The code can also use a focusing and toe-in strategy which is tailored for each heliostat in the field. That is, each heliostat would have a separate facet radius of curvature set equal to twice the slant range to the aperture opening and the toe-in angles would also be selected individually based on a reference sun position and the heliostat position relative to the tower. The toe-in of each facet, for example, can be set so that the facets form a single image, at the focal length, for on-axis radiation. This toe-in strategy would mean that each heliostat is perfectly toed-in only when the sun, the target (the tower top), and the heliostat all fall in one straight line. This situation occurs at a different reference time of year for each heliostat in the field. Another possible toe-in strategy would be to align the facets of all heliostats to form a single image for a single reference time.

To establish preliminary sensitivity, we used the strategy of toe-in for on-axis radiation either for each heliostat individually or by zones. When one or more zone was used, the toe-in and radius of curvature were set by a mid-zone position and applied to all heliostats in the zone.

Figure 3-31 shows typical field zones and the results of initial Monte-Carlo ray trace simulations. Four simulations were made at the 12/21 2 p.m. design time and two simulations for annual performance. The aperture was set at one size and shape for all runs so that the reported power and energy values indicate how performance is degraded by increased image spread due to various focusing and toe-in strategies. To examine the effect of focal length, the toe-in was individually set for each heliostat and the radius of



SIMULATION TYPE	TOE-IN STRATEGY	FOCUS STRATEGY	POWER/ENERGY (kW/MWh)
12/21 2 P. M.	EACH INDIVIDUALLY	EACH INDIVIDUALLY	42.3
12/21 2 P. M.	EACH INDIVIDUALLY	1 ZONE	42.3
12/21 2 P. M.	1 ZONE	EACH INDIVIDUALLY	39.6
12/21 2 P. M.	EACH INDIVIDUALLY	5 ZONES	42.3
ANNUAL	EACH INDIVIDUALLY	EACH INDIVIDUALLY	14,800
ANNUAL	EACH INDIVIDUALLY	5 ZONES	14,800

Figure 3-31. Sensitivity to Toe-In and Focus Strategies

of curvature of the facets was set either individually, one radius of curvature for all facets, or five zones of constant radius of curvature.

The results of Figure 3-31 show that the performance is equal in all three design time runs and both annual energy runs where toe-in is done individually. The only performance decrease shown occurs when the toe-in was set at a constant angle for all facets. It was concluded that the performance can be quite sensitive to toe-in strategies but relatively insensitive to facet focal length.

Hence, we elected to set the radius of curvature to one value for all facets on all heliostats. The selected radius of curvature for both the pilot and commercial plants is approximately equal to twice the slant range of the heliostats in the far north field.

A constant mirror module radius of curvature has obvious manufacturing advantages. Each mirror module is identical and may be located anywhere in the field. On the other hand, the toe-in angle may be different for each heliostat in the field. This should not create a cost disadvantage because each heliostat will be constructed in the field. That is, the frame and mirror module subassemblies will be shipped separately. When the complete heliostat is assembled in the field, the toe-in angle of each mirror module can be set according to field location. The proper toe-in of each heliostat was examined next in the analysis.

For the toe-in analysis, we made use of a single heliostat ray trace code. The code models the baseline tilt-tilt heliostat, redirecting the sun's ray onto a test target of any orientation. The program was written to be used to simulate the SRE heliostat test setup and thereby aid in verifying the heliostat optical model. A simple drawing of the setup modeled is shown in Figure 3-32. The model is described in Section 7. To determine toe-in image spread, we simply used the code to find the facet center target hit-point. Tracking errors were ignored.

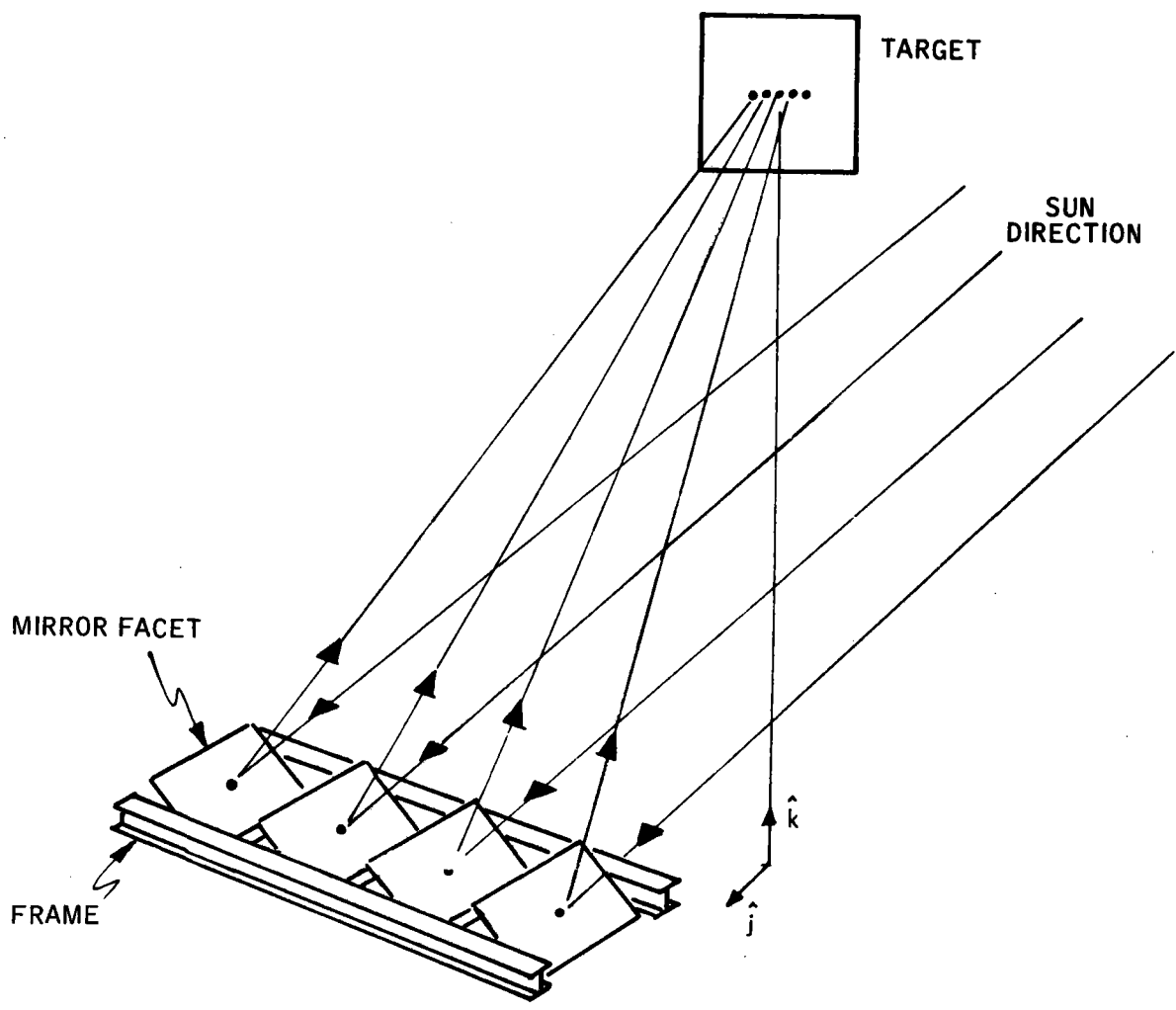


Figure 3-32. Single-Heliostat Ray Trace Model

The heliostat tracking drives are always positioned based on the heliostat optical center, which lies at the geometric center. Facets are rotated together, or gang-driven, to a calculated position so that an imaginary mirror facet at the heliostat center redirects energy from the sun's center to the target aimpoint. Since the facet centers do not coincide with the heliostat optical center, the facet centers will redirect energy to a point slightly off the aimpoint for all but the reference sun position. For example, assume that a heliostat is toed-in so that perfect on-axis energy is all directed to the center of a target. When the sun is positioned off-axis, the off optical-axis facets will redirect energy off the target center. These situations are shown in Figure 3-33.

To compare the differences in image spread caused by various toe-in angles, the rms value of the facet center hitpoint error is used. Referring to Figure 3-33, a facet center hitpoint error is the distance from the heliostat aimpoint to the facet hitpoint. Some rms heliostat facet center errors are shown in Figure 3-34 for an east field heliostat. The rms error is plotted for three days of the year and for three toe-in times. The toe-in times specify the sun angle for which the facet centers all redirect energy as closely as possible to a single aimpoint. Thus, when the toe-in is adjusted for 3/21 2 p.m., we see a minimal rms error at this time point. The error is not precisely zero because the toe-in is accomplished only on the inner axis. A small error remains due to outer-axis misalignment of off-optical center facets. From the data in Figure 3-34, it is obvious that east field heliostats will perform the poorest during early morning hours. This fact is expected, since the sun is in the east in the morning and the heliostat sees the largest off-axis angles at this time. It can also be seen that a 3/21 10 a.m. toe-in reference time would be a poor choice for the east field heliostate. It is unknown as to whether the 3/21 noon or 3/21 2 p.m. toe-in time is preferable.

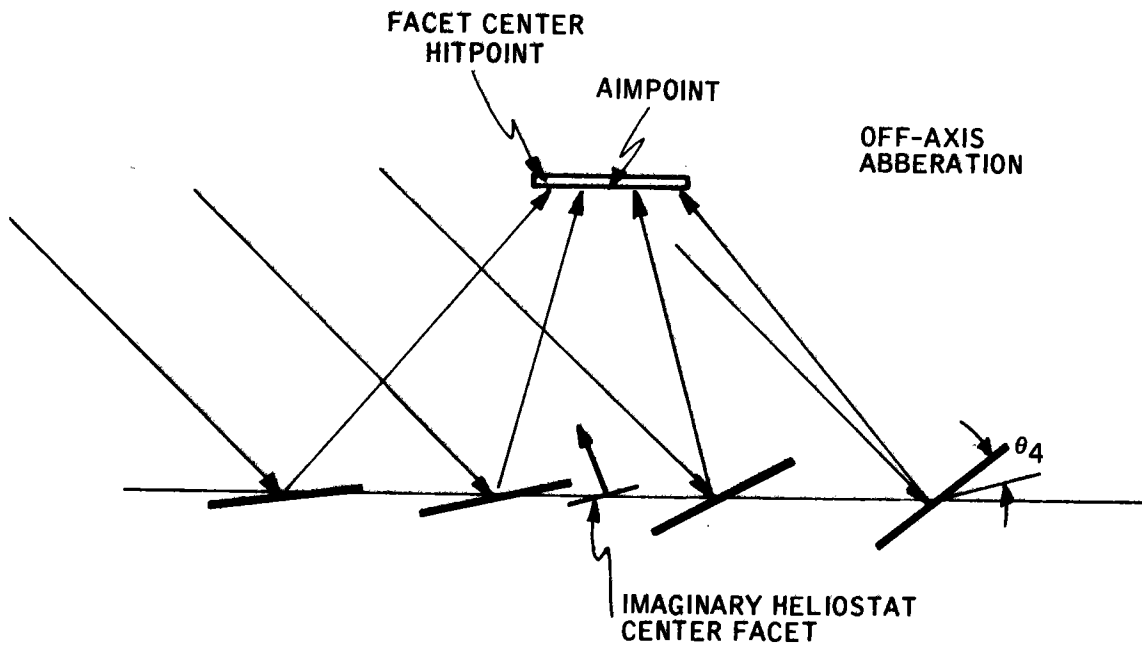
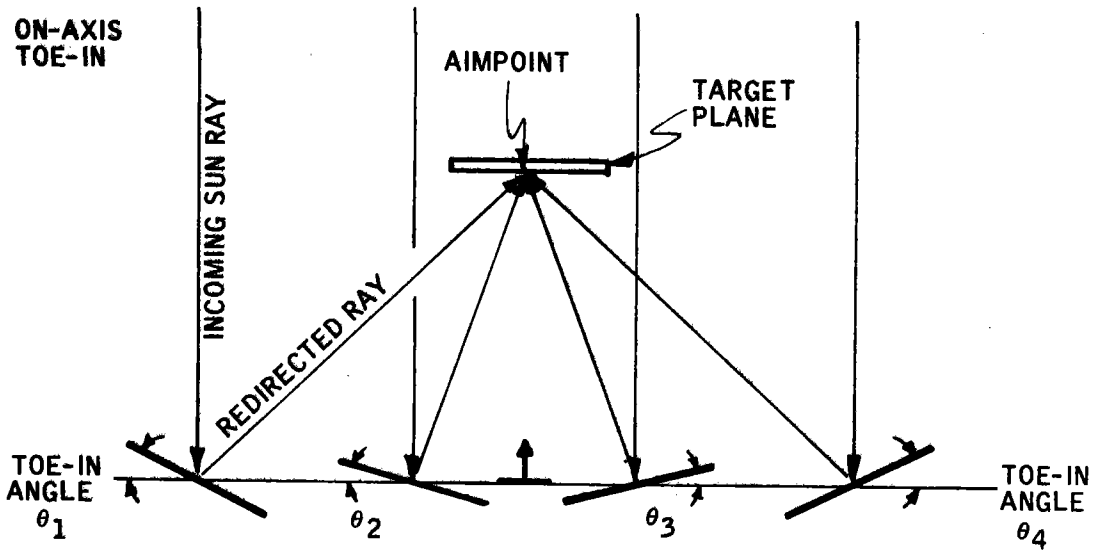
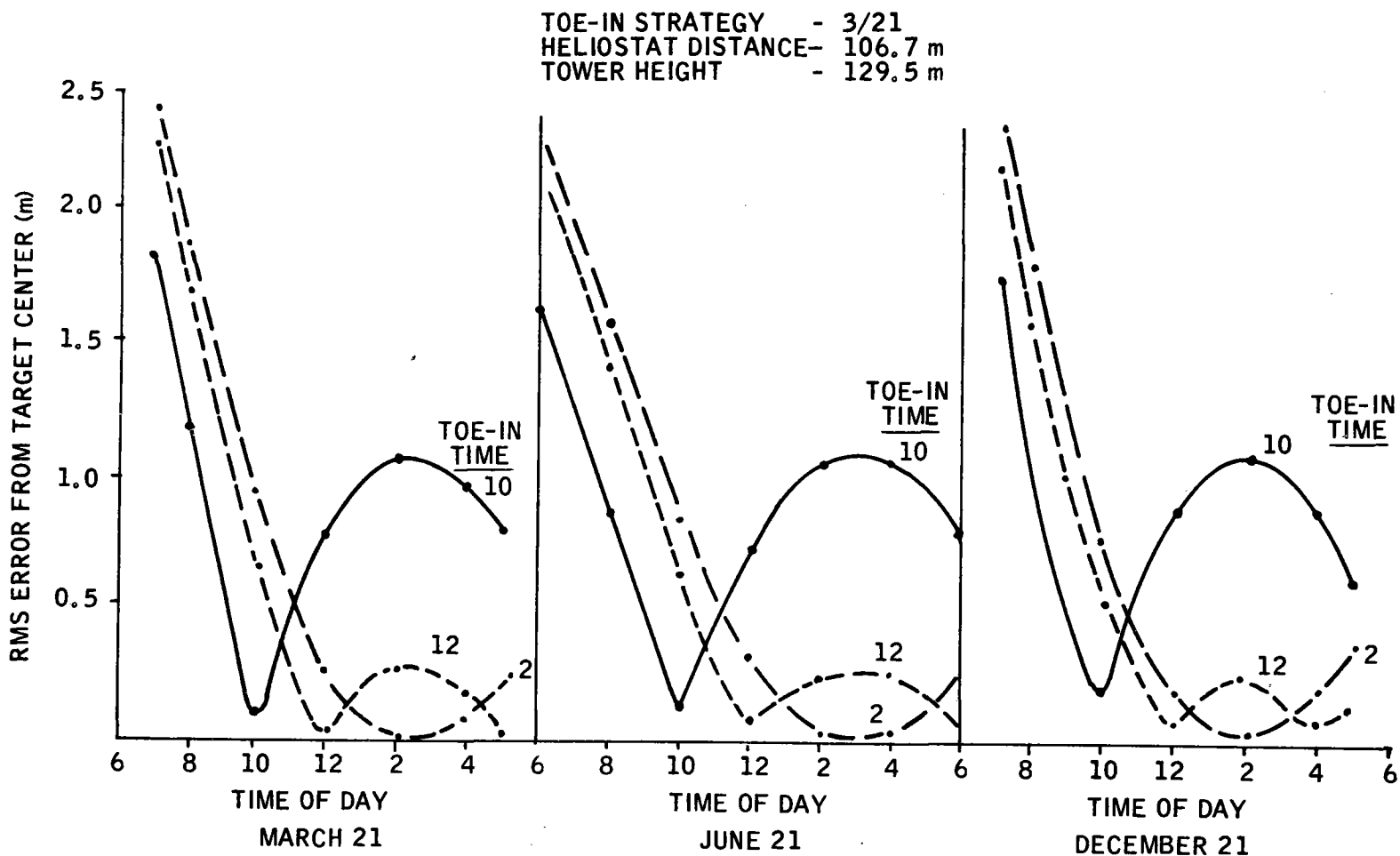


Figure 3-33. Heliostat Toe-In

40703-II



3-61

Figure 3-34. Aiming Accuracy for a Heliostat Directly East of Tower

For the same east field heliostat, we ran several more possible toe-in times. The results of rms error versus time of day for three days of the year is shown in Figure 3-35.

Examining all data and all possible toe-in times, we are unable to determine a best toe-in time. It appears that any toe-in day with a toe-in time of noon or 2 p.m. is acceptable for this particular heliostat location. The optimal toe-in time should be decided on the basis of maximum net annual energy. This is influenced by aperture design. Because of the many heliostat locations, and because of time and budget constraints, we have not performed this optimization for all heliostats. We have, however, run the single-heliostat code at typical south and north heliostat locations and plotted the rms error versus time of day for various toe-in times. The results are shown in Figures 3-36 and 3-37. From these results, we can see that a 3/21 noon toe-in, for all heliostat locations studied, should perform nominally as well or better than the other toe-in times investigated. Without further analysis, we choose to use the 3/21 noon toe-in time for calculating the reference sun position and toe-in angles.

RECEIVER SUBSYSTEM TRADEOFF

Because of the strong interaction between the heliostat field and the receiver, much of the field analysis section included a discussion of the receiver subsystems tradeoffs. As such, this subsection begins with a continued discussion of the aperture analysis.

EAST FIELD
HELIOSTAT DISTANCE = 107 m
TOWER HEIGHT = 130 m

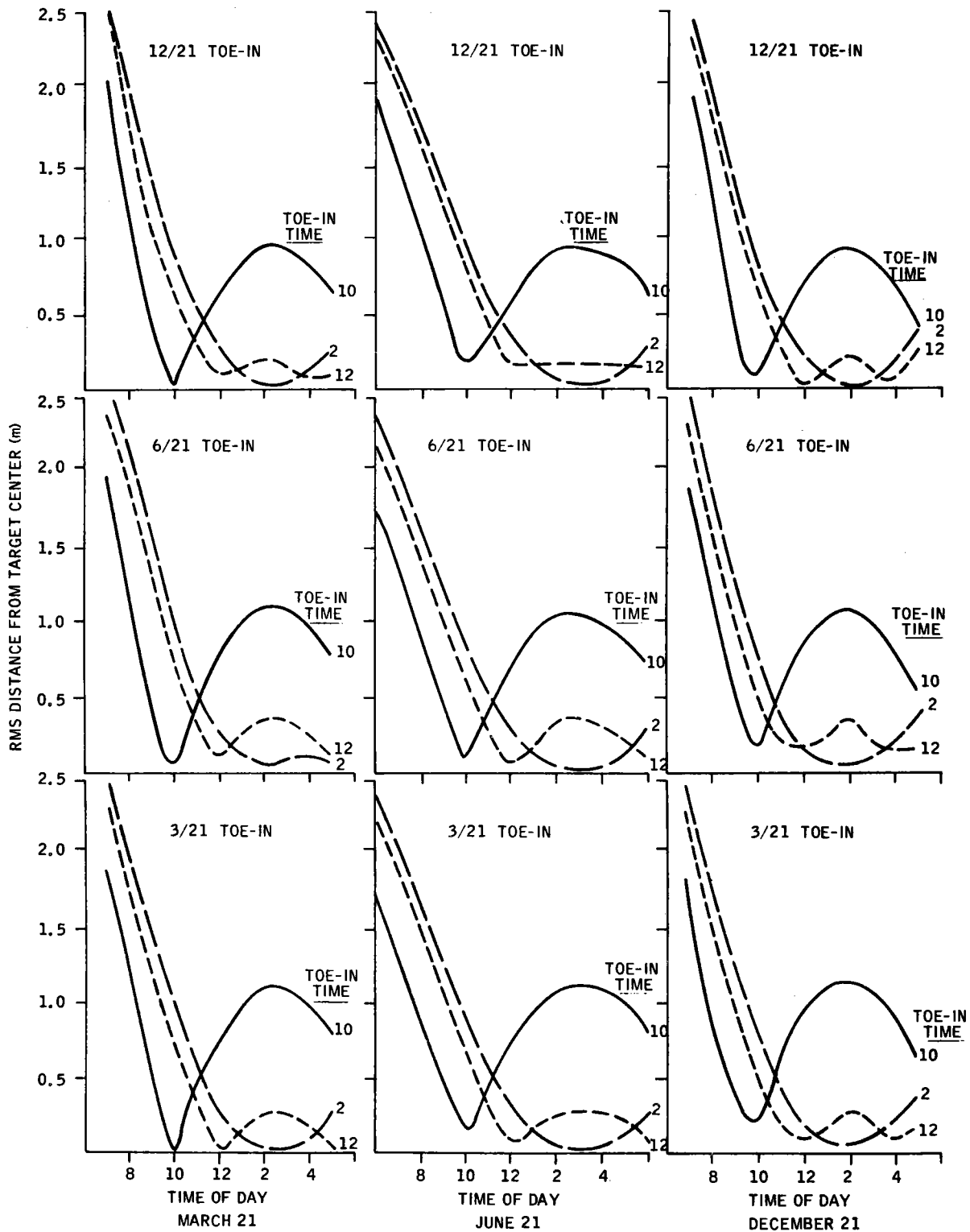


Figure 3-35. RMS Dispersion Over the Day for Various Toe-In Times - East Field
40703-II

3-64

SOUTH FIELD

HELIOSTAT DISTANCE = 107 m

TOWER HEIGHT = 130 m

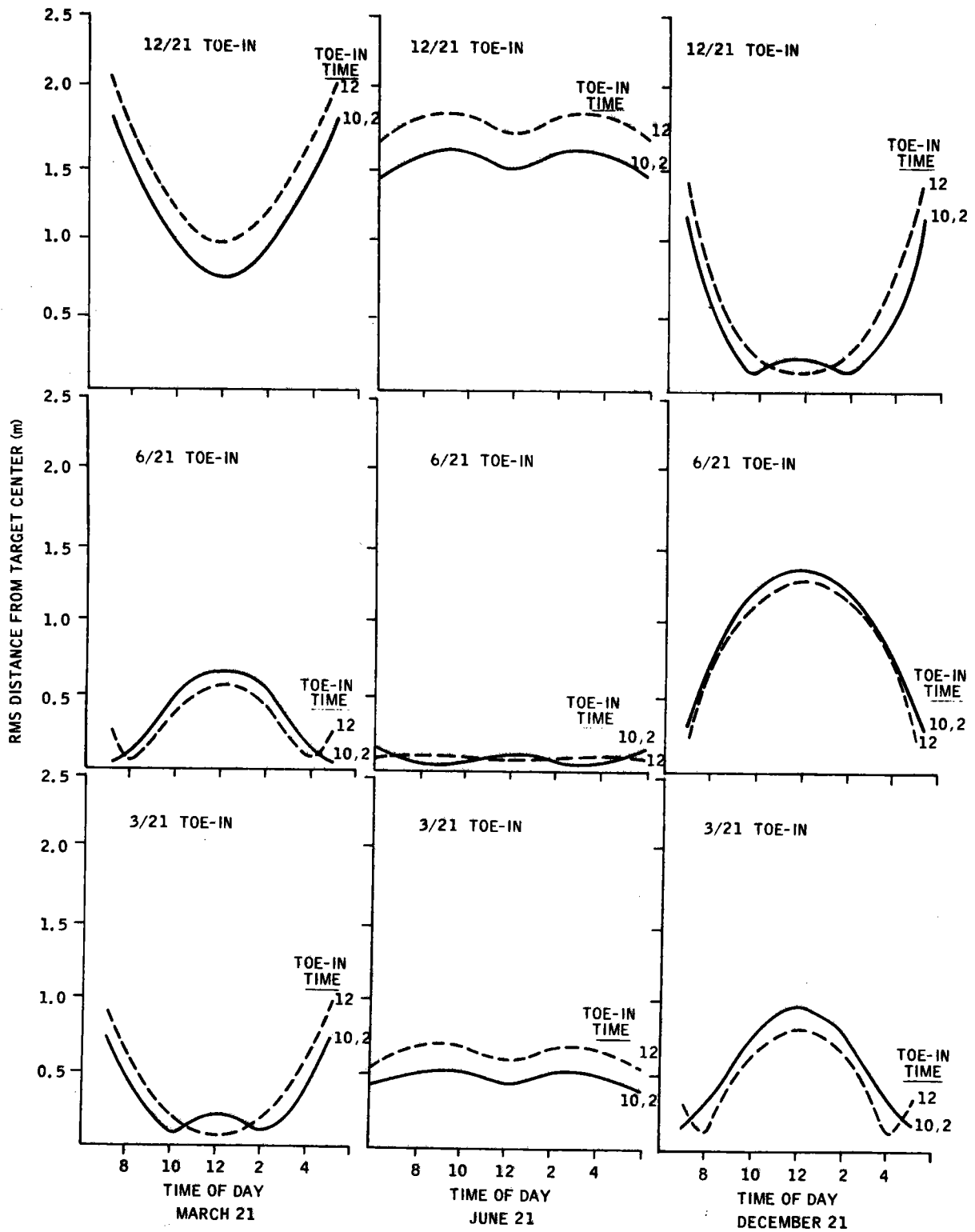


Figure 3-36. RMS Dispersion Over the Day for Various Toe-In Times - South Field

40703-II

NORTH FIELD
HELIOSTAT DISTANCE = 305 m
TOWER HEIGHT = 130 m

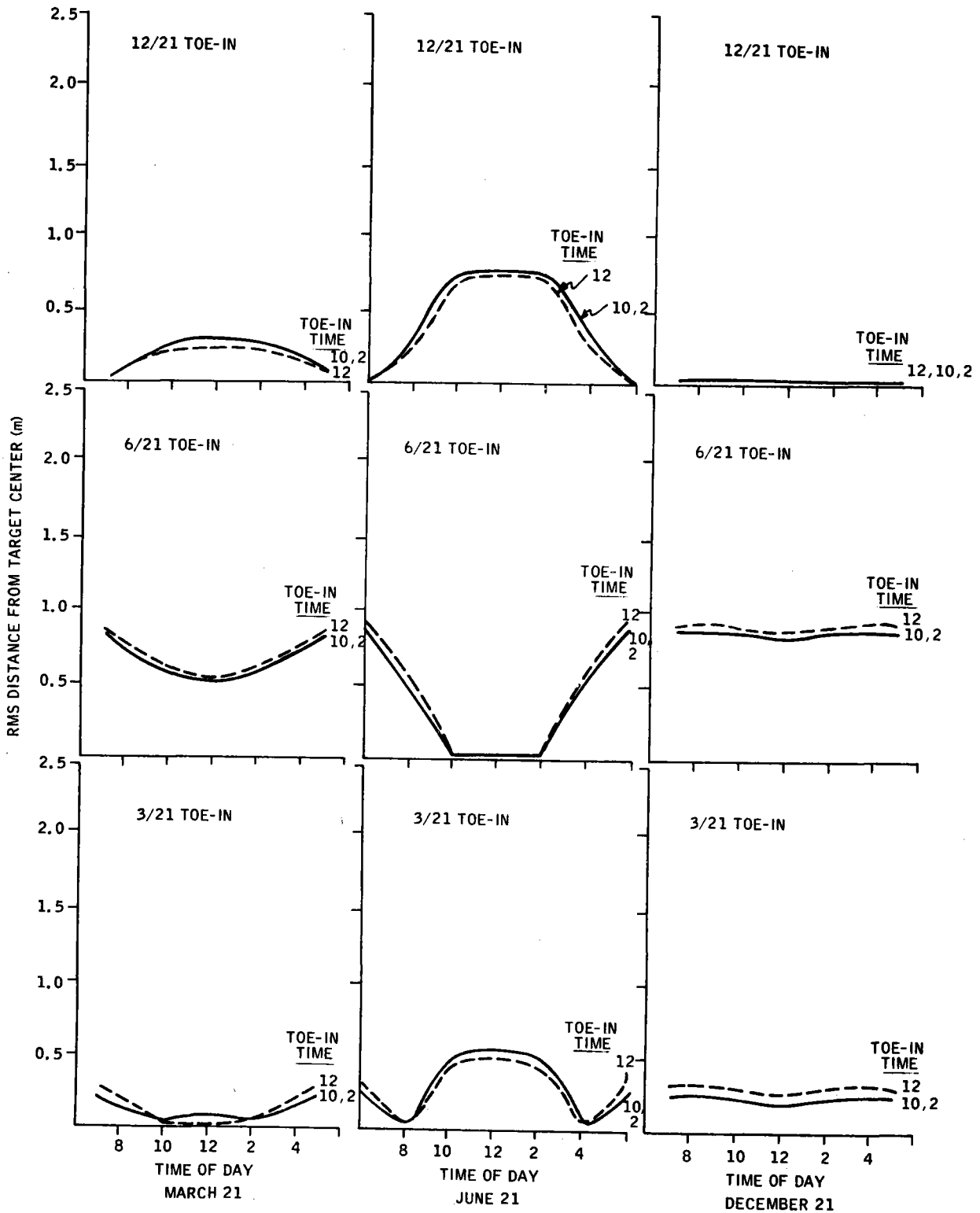


Figure 3-37. RMS Dispersion Over the Day for Various Toe-In Times - North Field

Aperture Analysis

Given that the tower is moved to a position part-way south of the heliostat field center, the question of the best annular aperture and receiver configuration is raised. A desirable aperture geometry would be one which was large enough in size, as seen from all locations in the field, to admit nearly all incoming flux without suffering large losses in scattered and reradiated flux. Furthermore, the aperture should minimize whistle-throughs (whistle-throughs refers to flux which enters one side of the aperture and passes out the other side instead of entering the cavity).

The first step in the tower half-south aperture analysis was to select a possible aperture configuration and modify available software to simulate aperture performance. To keep the ray trace code modifications simple and yet flexible enough to design an efficient aperture, a general aperture shape of a section of a cone, tilted with respect to local normal, was initially selected. The cone angle (θ_{cone}) and angle of cone tilt with respect to local vertical (θ_{tilt}) are selected so that the normal to the aperture opening points directly at the field mid-area location in the north and south field. Figure 3-38 shows the arrangement. The desired cone angle is determined by the distance from the tower center to the north and south field mid-area location and by the tower height. The angle from local vertical to the north aperture edge ($\theta_{\text{ape N}}$) is simply the inverse tangent of the tower height divided by the distance to the mid-area point:

$$\theta_{\text{ape N}} = \tan^{-1} \left(\frac{TH}{X_N} \right)$$

Similarly, the south aperture angle is:

$$\theta_{\text{ape S}} = \tan^{-1} \left(\frac{TH}{X_S} \right)$$

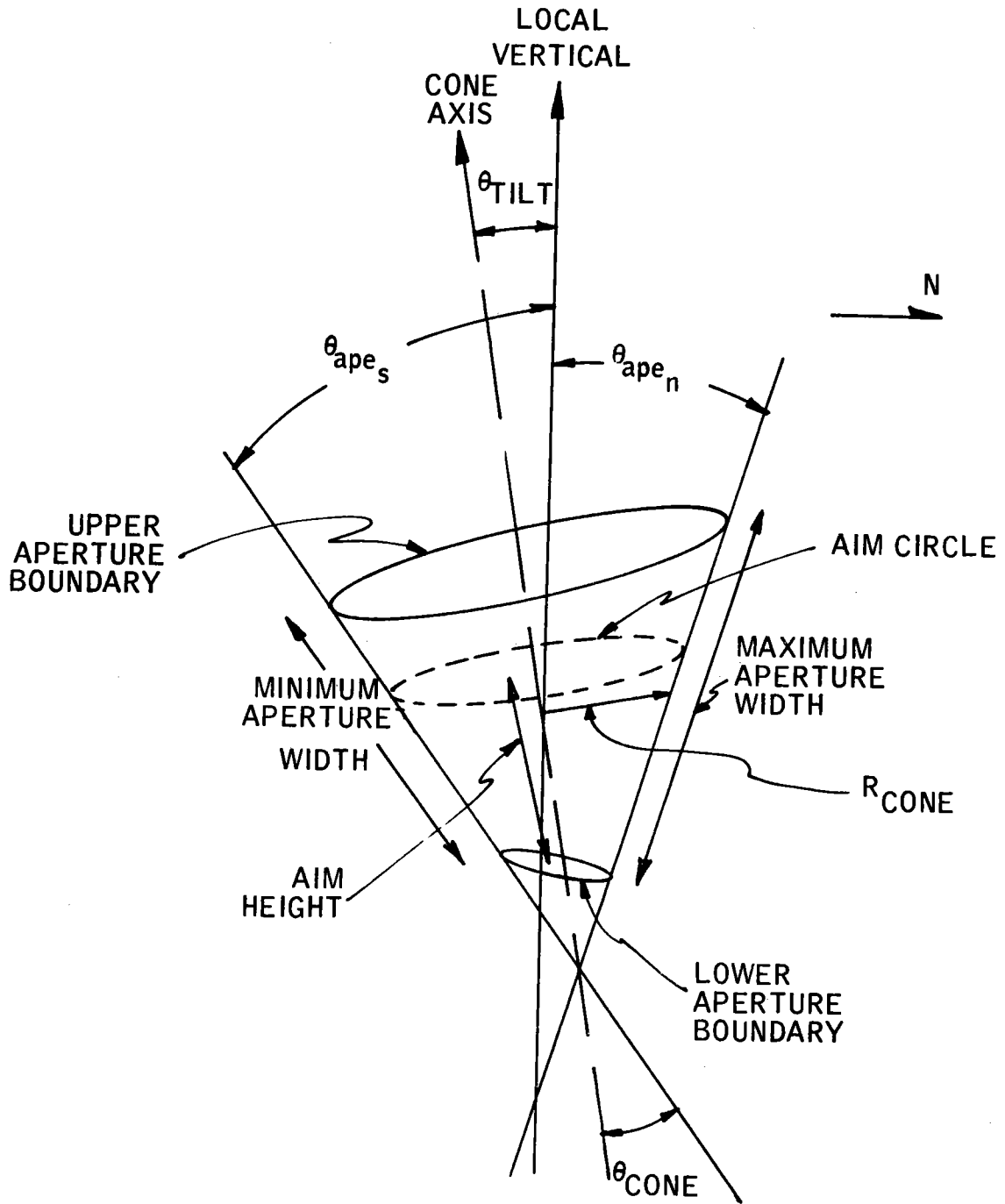


Figure 3-38. Tilted-Cone Aperture

Where TH is tower height and X_N and X_S are ground distances from the tower center to the mid-north and mid-south field positions, respectively.

To enable a cone to aim at both the north and south aperture angles, a cone angle and tilt angle are defined by:

$$\theta_{\text{cone}} = (\theta_{\text{ape N}} + \theta_{\text{ape S}}) / 2$$

$$\theta_{\text{tilt}} = \theta_{\text{ape S}} - \theta_{\text{cone}}$$

Ideally, the annular opening would be selected so that the aperture normal points at the field mid-area point for all field azimuth angles. The cone is a fairly good choice for this desired condition. For example, a due-east aperture angle of 37 degrees would be ideal for a pilot plant-scale field with the tower one-half way south. The depression angle actually presented by using a tilted cone aperture is 37.6 degrees. This small difference will not noticeably affect the performance of the power plant.

The upper and lower aperture boundaries on the cone section are determined by inputting desired maximum and minimum aperture slant heights assumed to be located due north and south, respectively. Aperture width is varied linearly between the two extremes. The aperture width is defined at the middle of the slant height and is an input to the ray trace program. The aim strategy allows the heliostats to be aimed above, at, or below the middle of the aperture. All heliostats are aimed off the corbels. Three corbels are assumed to be equally spaced around the aperture.

To establish approximate aperture width and slant height for this aperture design, the ray trace code was exercised using the cone-mapping option. With this option, no receiver flux maps are obtained and the cone aperture is intentionally oversized vertically. Flux incident on the cone aperture is

mapped so that optimal aperture height is established as the aperture height which maximizes the net annual energy (incoming flux minus losses). A simple algorithm for the losses as a function of incoming energy and aperture area was based on previous reradiation work. The results of the cone-mapping computer runs are shown in Table 3-4 and Figures 3-39 and 3-40. All runs are for a 274-m outer radius heliostat field with 1682 heliostats. The heliostats are four-facet tilt-tilt heliostats as selected for the pilot plant baseline. The tower is located 137 m south of the field center and is 130 m high.

Table 3-4 shows the computer-selected aperture height and annulus area for each of the aim circle radii which were run. At the smallest aim circle radius (3.66 m), the aperture selected allows 1.43×10^5 MWh of redirected energy to enter the cavity and 1.34×10^5 is absorbed. The total redirected energy is approximately 1.56×10^5 MWh. A portion of the redirected energy which does not enter the cavity was lost by whistle-through (1.2 percent of the redirected energy), misses wide (2.8 percent, or by energy hitting the support structure (1.3 percent). As the aim circle radius is increased, the fraction of redirected energy lost by these mechanisms is reduced. The remainder of the energy lost is due to rays which hit the cone above or below the computer-selected aperture height zones. For the 3.66-m aim circle radius, this is 3.3 percent of the redirected energy. The fraction of energy which misses high or low decreases until the aim circle radius gets beyond 5.5-m, where an increase in misses high and low is due to the computer selection of a smaller aperture height. The smaller height is selected because at large radii the reradiation losses are larger for each accepted increase in height than they are at smaller radii. The actual difference in selecting one height over the other is inconsequential in this case; less 0.5 percent of net annual energy is gained or lost by an increase or decrease of 0.6-m in aperture height.

Table 3-4. Computer Results for Cone Mapping Runs

Aim Circle Radius (m)	Computer-Selected Aperture Height (m)	Computer-Selected Aperture Area (m ²)	Energy (MWh)	Net Energy (MWh)	Fraction of Redirected Energy Which Whistled-Through	Fraction of Redirected Energy Which Missed Wide	Fraction of Redirected Energy Which Hit Supports	Fraction of Redirected Energy Which Missed High or Low
3.66	4.57	145	1.43×10^5	1.34×10^5	0.012	0.028	0.013	0.033
4.27	5.49	186	1.49	1.38	0.007	0.017	0.006	0.015
4.88	5.49	212	1.52	1.39	0.003	0.007	0.004	0.013
5.49	5.49	239	1.54	1.40	0.001	0.003	0.003	0.010
6.10	4.57	208	1.51	1.39	0.000	0.000	0.001	0.029
6.71	4.57	230	1.50	1.36	0.000	0.000	0.002	0.035

40703-II

3-70

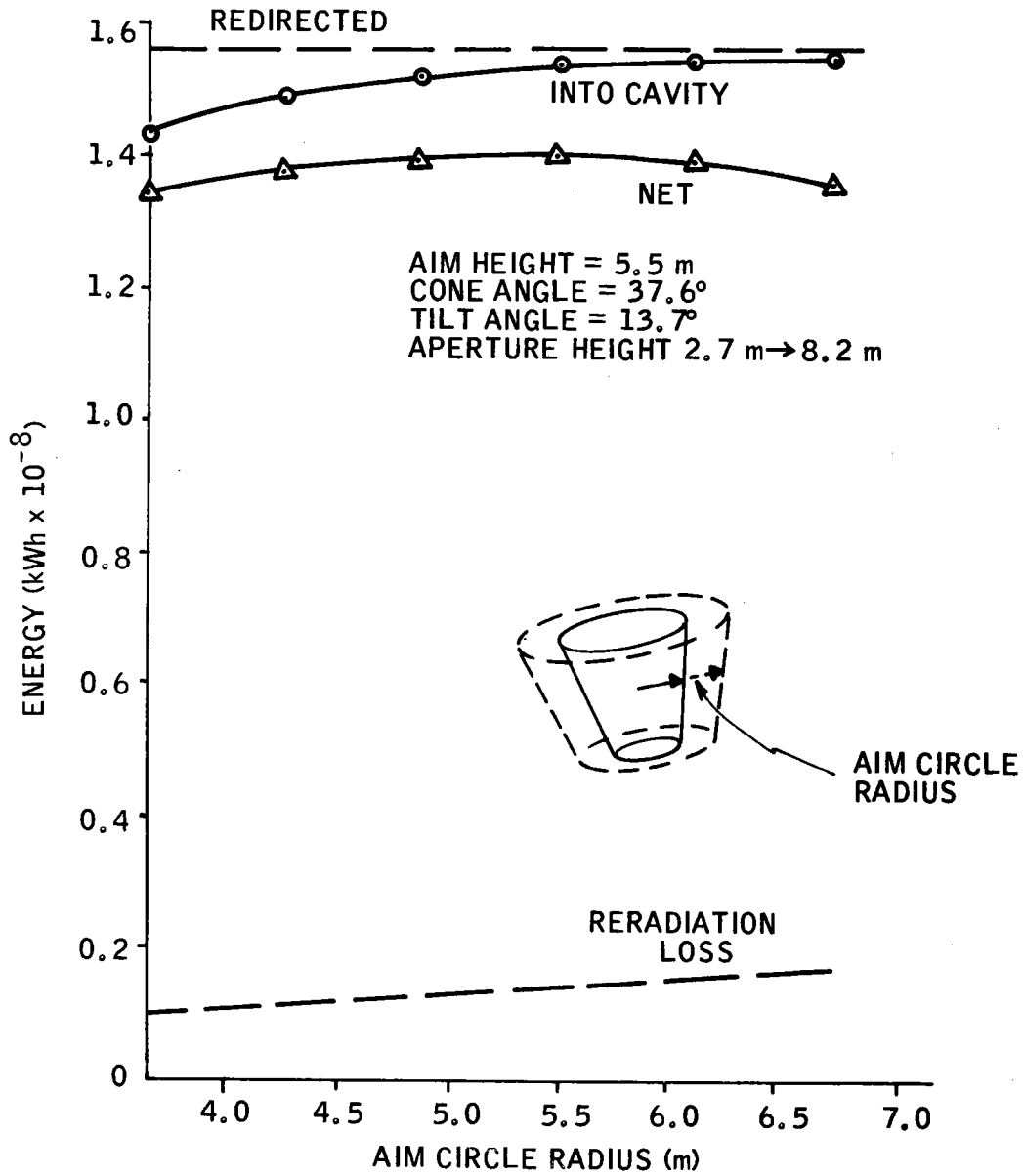


Figure 3-39. Energy versus Aim Circle Radius

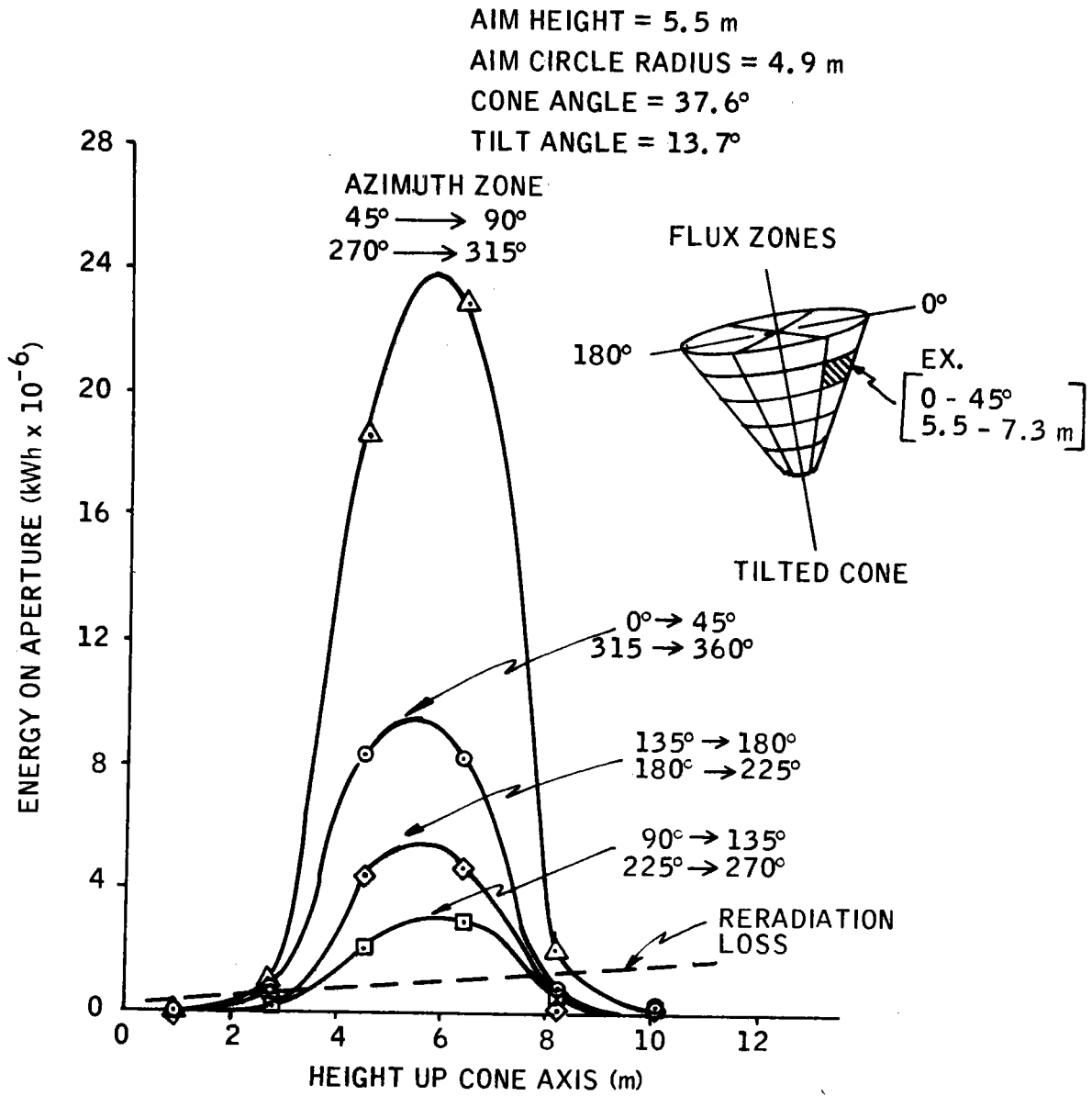


Figure 3-40. Flux into Aperture in Polar Zones

Figure 3-39 shows energy versus aim circle radius with the aperture height held constant. This is a common method of comparing one aperture size with another. The energy into the cavity increases with aim circle radius until a maximum of 1.55×10^5 MWh is reached. The maximum is not quite all the redirected energy because of the energy which goes above or below the specified aperture height. The net energy is simply the energy in minus the losses. Reradiation losses are shown as a dashed line in Figure 3-39. The net annual energy appears to be fairly flat across the aim circle radii investigated.

However, a best choice of aperture radius does appear to exist at approximately 5.2 m. The selection of aperture height is based on an aperture flux map as shown in Figure 3-40.

The flux map in Figure 3-40 shows the energy on the cone aperture as a function of height and azimuth angle. The small drawing on the right side of the figure shows how the cone aperture was zoned. A total of six height zones was used. The energy versus height shows that the energy increases as height up the cone is increased until a maximum is reached at the aim height (5.5 m). The curves then fall to zero as height is increased. The maximum flux enters through the 45- to 90-degree zone, not the zero-degree zone because a corbel is zero degrees. Similarly, the minimum energy peak is in the zone of the other corbels: 90 to 135 degrees and 225 to 270 degrees.

The maximum and minimum aperture slant heights are determined by the intersection of the flux curves and the reradiation loss line in Figure 3-40. The height up the cone should be chosen so that the energy entering the cavity always exceeds the reradiation loss. A first approximation of this condition would set the maximum aperture height bounds at 2.4 and 8.5 m and a minimum height at 3.4 and 7.6 m. For a 37.6-degree cone angle, these height boundaries translate to a maximum and minimum slant height of 7.3 and 5.5 m, respectively.

Using the above conceptions and dimensions, a promising aperture design was configured as shown in Figure 3-41. Flux maps were obtained using the ray trace code. A sample flux map is shown in Figure 3-42. The receiver inner diameter is 14.4 m, and a peak incident flux of approximately 350 kW/m^2 occurs on the south wall. Note that the peak incident flux for any azimuth location occurs at varying heights up the cavity. The farther the azimuth position from due south, the higher up the cavity wall the peak flux occurs. This is due to the increasingly higher angle of incoming flux for field positions farther and farther from due north. The flux peak on the south wall is relatively low on the cavity, since a large number of heliostats in the north are relatively far away and enter the cavity at low angles to the horizontal.

The angle is much higher for the flux redirected from heliostats in the south field, and thus most of the energy gets farther up the cavity before striking the cavity wall.

The next logical task in the performance analysis was to determine the cavity operating characteristics. The work was initiated using the reradiation computer code called the RERAD rubber model.

Because of the tilted aperture opening, the RERAD model was modified to simulate a cavity with one non-axisymmetric boiler node. A flat-bottom geometry and the tilted-bottom geometry are shown in Figure 3-43. The tilted-aperture geometry was modeled as a notch or cutout from the flat-bottom geometry. The notch is referred to as a shield which captures energy which would whistle through the aperture had there been no shield. Referring to the flat-bottom geometry, when the aperture is opened far enough to accept a majority of the energy from the north, we found that a significant percentage went straight through the aperture. Thus, the tilted geometry and consequent modification of the RERAD code. During the RERAD runs, it became apparent that the new tilted aperture had a drawback. The large

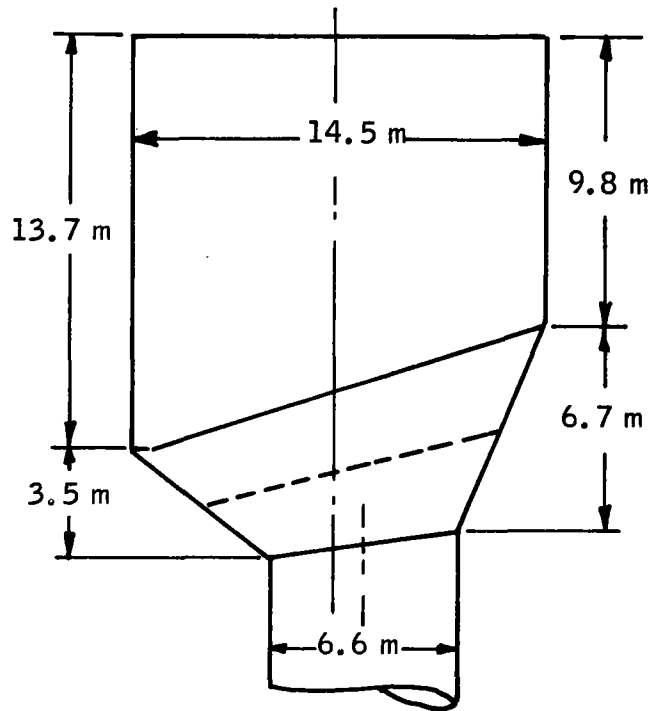


Figure 3-41. Tilted-Cone Aperture and Receiver Geometry

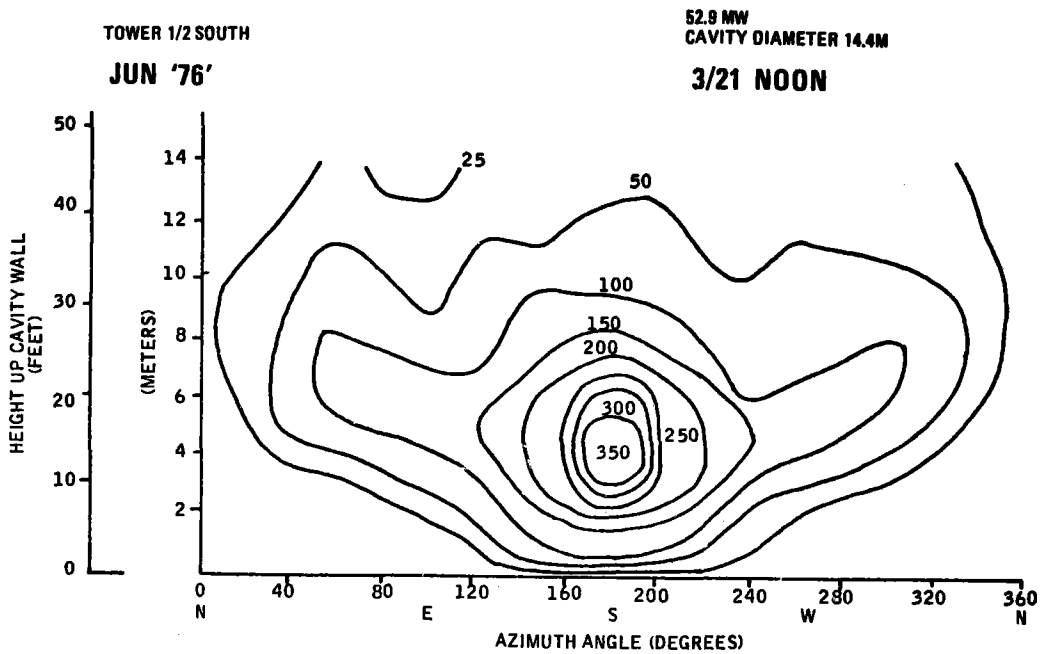


Figure 3-42. Cavity Wall Incident Flux Map

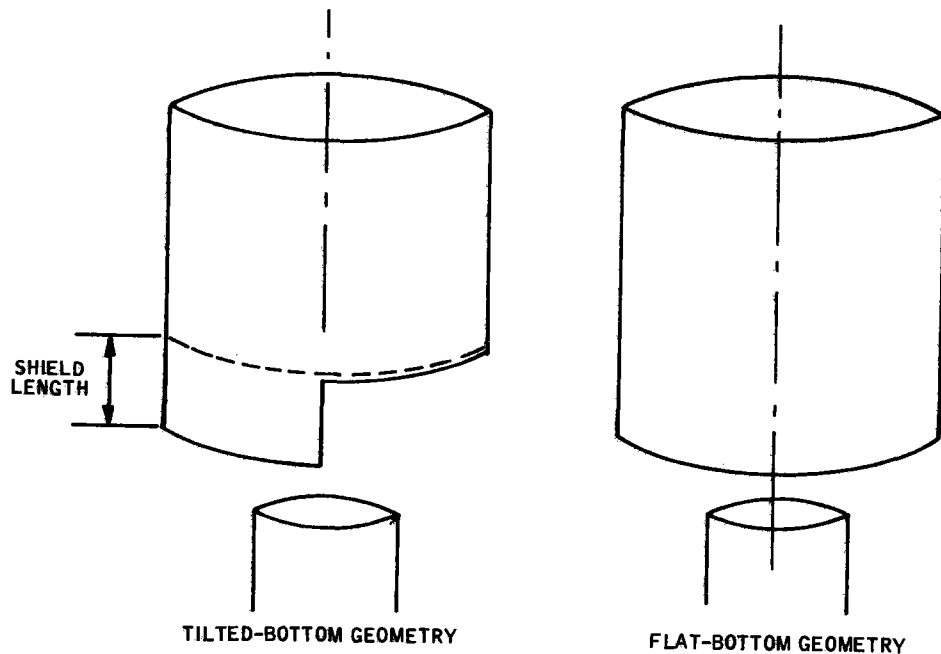


Figure 3-43. Rerad Cavity / Aperture Models

tilt of the aperture, which is effective for avoiding whistle-through losses, creates a large area of boiler surface which has a large view factor to the aperture opening. The power from the far north field strikes this surface and, because of the large view factor, the cavity efficiency is less than would be available with the flat-bottom geometry. It is obvious that a tradeoff between the losses due to reradiation and those due to whistle-through energy can be performed. We examined a sample case which is representative of the cavity performance throughout the year. The shield length was varied and the power losses were computed. Results are shown in Figure 3-44. It can be seen that the whistle-through losses are 4.2 percent for a flat-bottom geometry large enough to admit most of the redirected power. As shield length is increased, the power lost via whistle-throughs is reduced and finally reaches zero loss at a shield length of approximately 3.3 m. This corresponds to the tilted aperture design described previously. The reradiation and conduction losses are 8.1 percent with no shield and 10.1 percent with a shield of 3.3 m where the shield has boiler surface. Without

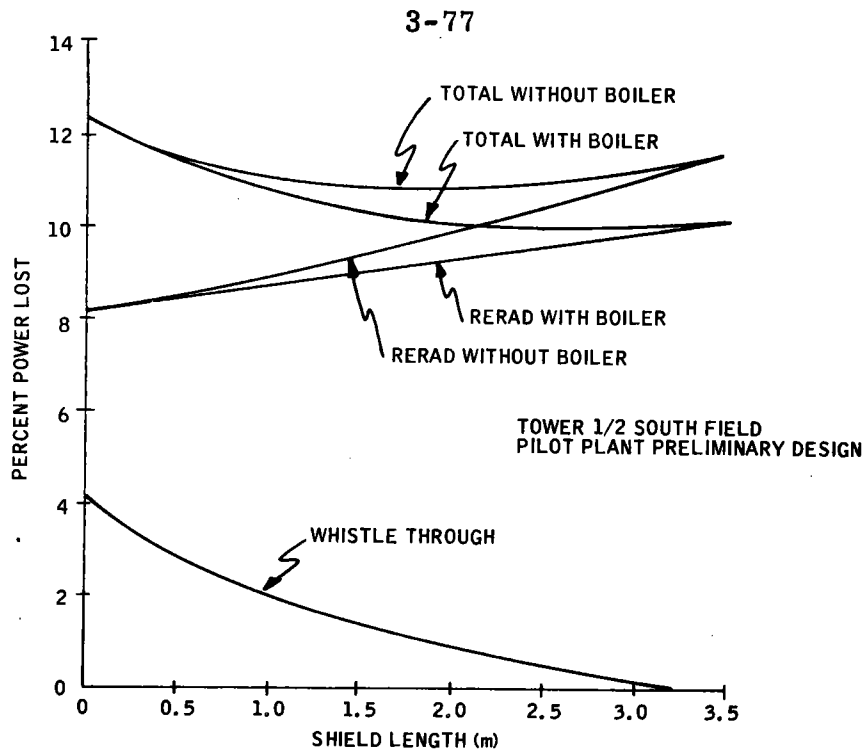


Figure 3-44. Power Loss versus Shield Length

an active surface, a shield of 3.3 m would lose 11.4 percent of the incoming power. We elected to maintain an active surface on the shield. The sum of the losses is also shown in Figure 3-44. There is little difference in performance between shield lengths of 1.8 m and 3.3 m so that the performance alone indicates the tilted aperture geometry is acceptable.

From the standpoint of structural design, the tilted aperture causes some difficulty. The configuration centers the receiver over the upper aperture, which is not centered over the lower aperture boundary. Figure 3-41 shows an offset between the cavity axis and the apparent tower axis. We could design around this problem. However, because performance differences are negligible, we chose to center the cavity over the lower aperture axis. To enable such a design, we shortened the shield length to 1.8 m and rearranged the aperture design to that shown in Figure 3-45. This is our baseline aperture configuration for both the pilot and commercial plant designs.

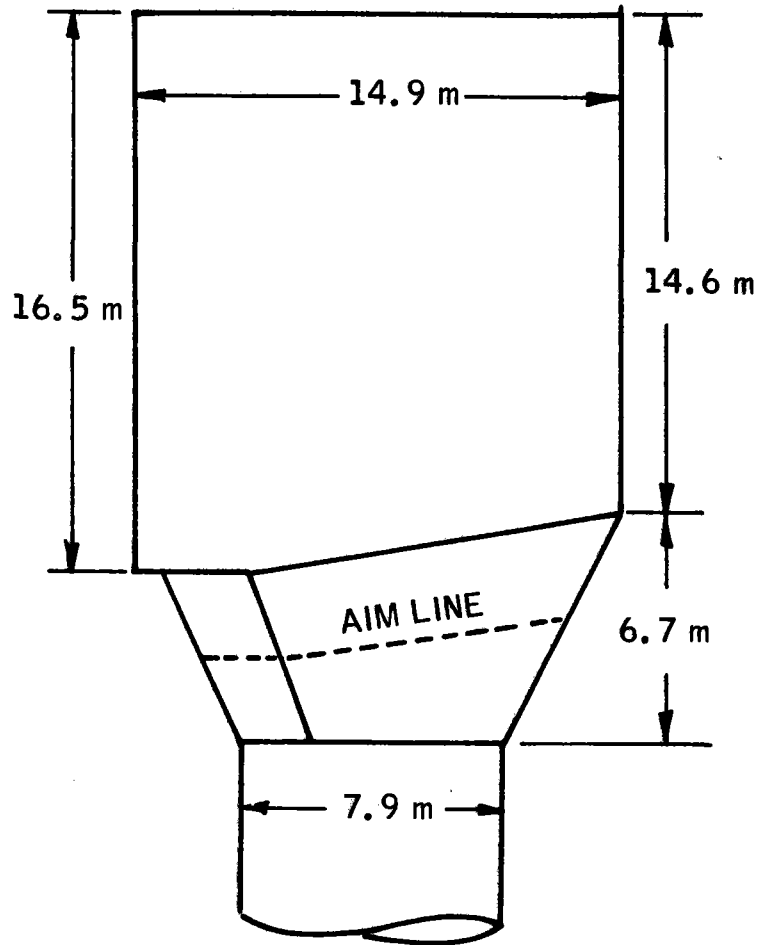


Figure 3-45. Baseline Aperture Configuration

Note that the corbel location has been shifted to one corbel south instead of north. This design change simply allows the far north field to view the largest aperture opening.

Steam Generator Configuration

The general steam generator arrangement selected for the preliminary baseline design is shown in Figure 3-46. The boiler, first-stage superheater, and second-stage superheater heat transfer surfaces are arranged to cover the surface area of the right circular cylinder of the cavity. The boiler section, which has the relatively cool heat transfer surface, is on the bottom portion of the cavity; there the reradiation losses through the cavity aperture are reduced. The first and second stages of the superheater are arranged on the remaining portion of the cavity so that the second-stage superheater has to be in the lowest heat input zone for metal temperature protection.

The rationale behind the baseline configuration selection was to minimize risk, yet maintain operational flexibility. One choice in the design was the recirculating drum versus the once-through boiler. The recirculating drum boiler was chosen to meet the difficult control requirements associated with rapid startup. The recirculating drum can effectively be controlled to follow the sun. Another design consideration involved the selection of the pump-assisted circulation as opposed to natural circulation. The pump-assisted drum boiler allows the use of smaller-diameter tubes, resulting in a lighter structure and reduced thermal stress.

These design selections are typical of the rationale used throughout the steam generator development. The basic design process which best minimizes risk is one which uses known fossil boiler technology within the constraints of the operational peculiarities of a solar plant. In many of the design decisions, a fossil boiler peaking unit is inherently similar to the solar boiler and past

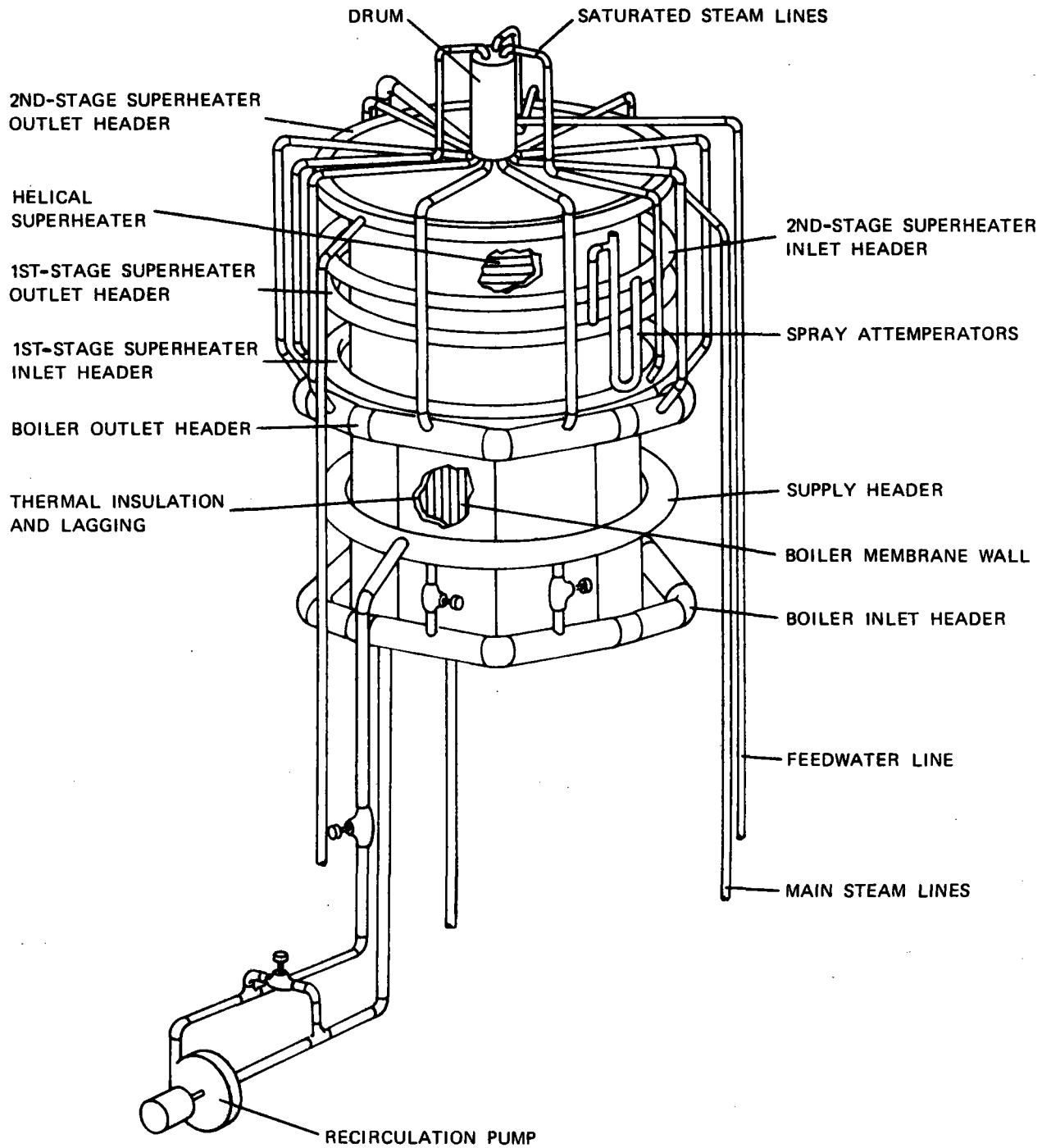


Figure 3-46. Steam Generator Configuration

experience has been applied. Volume 4 of this report details much of this design rationale and the key design features.

ELECTRICAL GENERATION SUBSYSTEM TRADEOFFS

The electrical generation subsystem has important interfaces with the receiver and thermal storage subsystems; in fact, the selection of a basic turbine cycle directly impacts the design of the storage and steam generator. There are basically three parameters which we evaluated in the system tradeoffs analysis. These are the turbine throttle valve pressure and temperature as delivered by the receiver subsystem, the type of turbine (single-port or secondary-admission), and the turbine operating pressure/temperature from storage.

The tradeoffs on these three variables are primarily economic. Design optimization of the cycle choice parameters was performed using the plant sizing software. The program physically sizes the plant based on performance parameters such as mirror efficiencies, heat transfer coefficients, receiver efficiencies, and parasitic power losses. It then costs the elements of the plant based on the physical size of the equipment which it calculated and the input cost data.

The program can simultaneously optimize two variables. Optimization is performed by checking a series of fixed-point designs. The value of one of the design variables to be optimized is chosen and the value of the second design variable to be optimized is scanned incrementally; a full plant design is performed for each set of values of the variables to be optimized. The value of the first variable is then incremented and the process is repeated. The optimum design is the point design which gives the minimum mills/kWh annual electric energy. The procedure used to investigate turbine cycle parameters was to optimize cycle pressure and storage pressure in a plant with the two different types of turbines.

The throttle valve pressure/temperature choice quite obviously sets the boiler and superheater pressure/temperature. This in turn determines materials choices, wall thicknesses and warmup/cool-down times for the steam generator. We know of no unmanageable system limits caused by the impact of the final throttle valve design pressure/temperature. However, the allowable rate of change of metal temperature is affected by wall thickness and material choice. This is an important control and safety consideration for both the steam generator and turbine.

During the turbine cycle selection, we adhered to the ground rule that the choice be made on the basis of what is best at commercial scale. Quite early in the study, we reexamined our proposed single-admission 5861 kPa/510°C turbine selection. Based on turbine manufacturer recommendations, a higher-pressure cycle with dual admission was selected.

Figure 3-47 shows the annual energy cost as a function of cycle pressure for a plant with a dual-admission turbine and two different storage systems. These results do not include any increased cost associated with the high-pressure cycles such as increased piping costs, turbine costs, and equipment costs. These factors, combined with the fact that there are at present commercially available secondary injection turbines for the 1450 cycle, led us to a "Knee of the curve" choice of the 1450 cycle. It was felt that the unknown costs and problems associated with the higher-pressure cycles outweighed the small cost advantage shown on Figure 3-47.

So far as the issue of dual-versus single-admission turbines is concerned, the economic choice is a dual-admission turbine. Figure 3-48 shows the relative plant cost for the two turbine types versus pressure ratio (the pressure in the storage boiler divided by the pressure in the receiver steam drum) at a receiver steam drum pressure of 9997 kPa. The results at other steam drum pressures are similar.

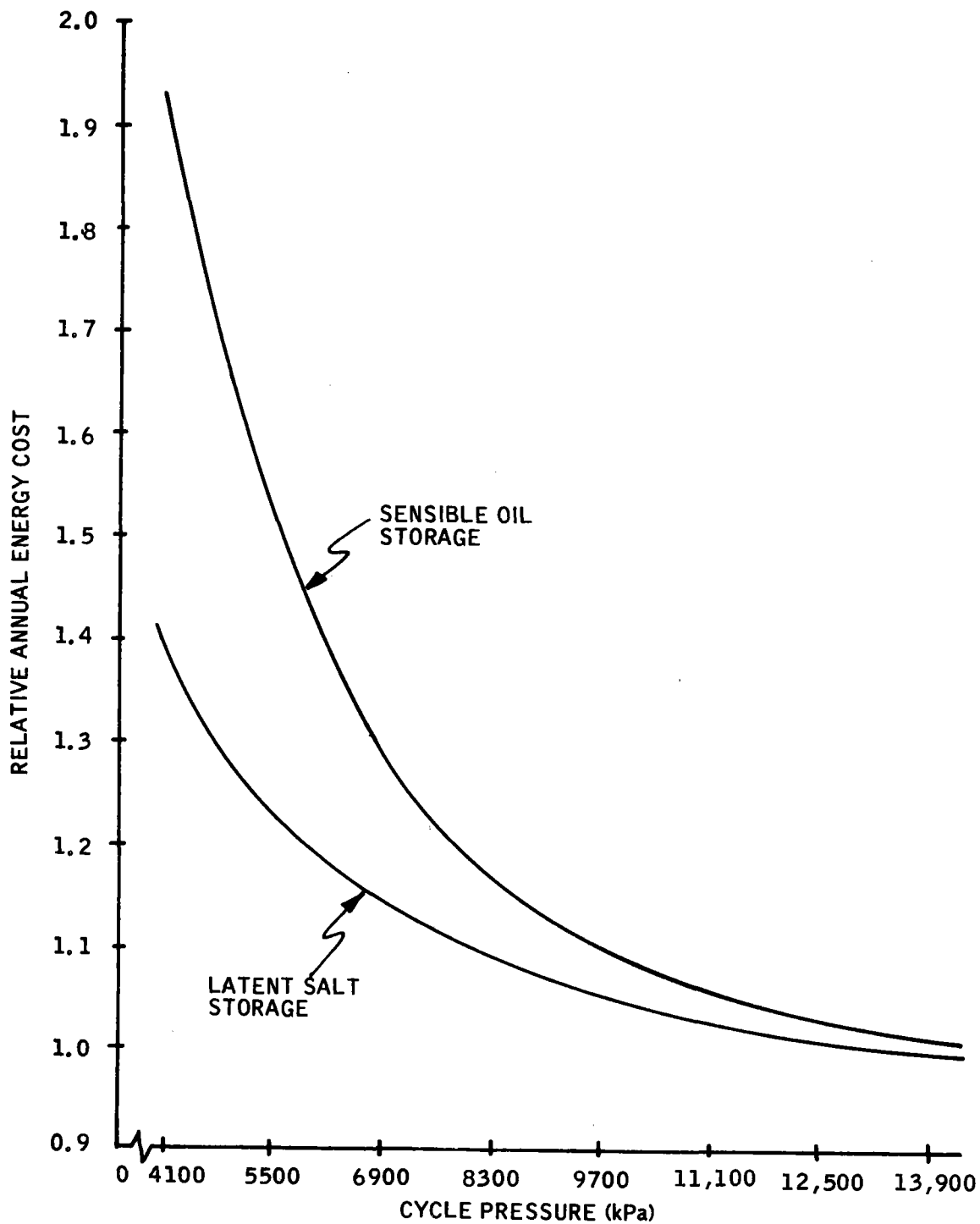


Figure 3-47. Comparison of Oil and Salt Storage Annual Energy Cost versus Cycle Pressure

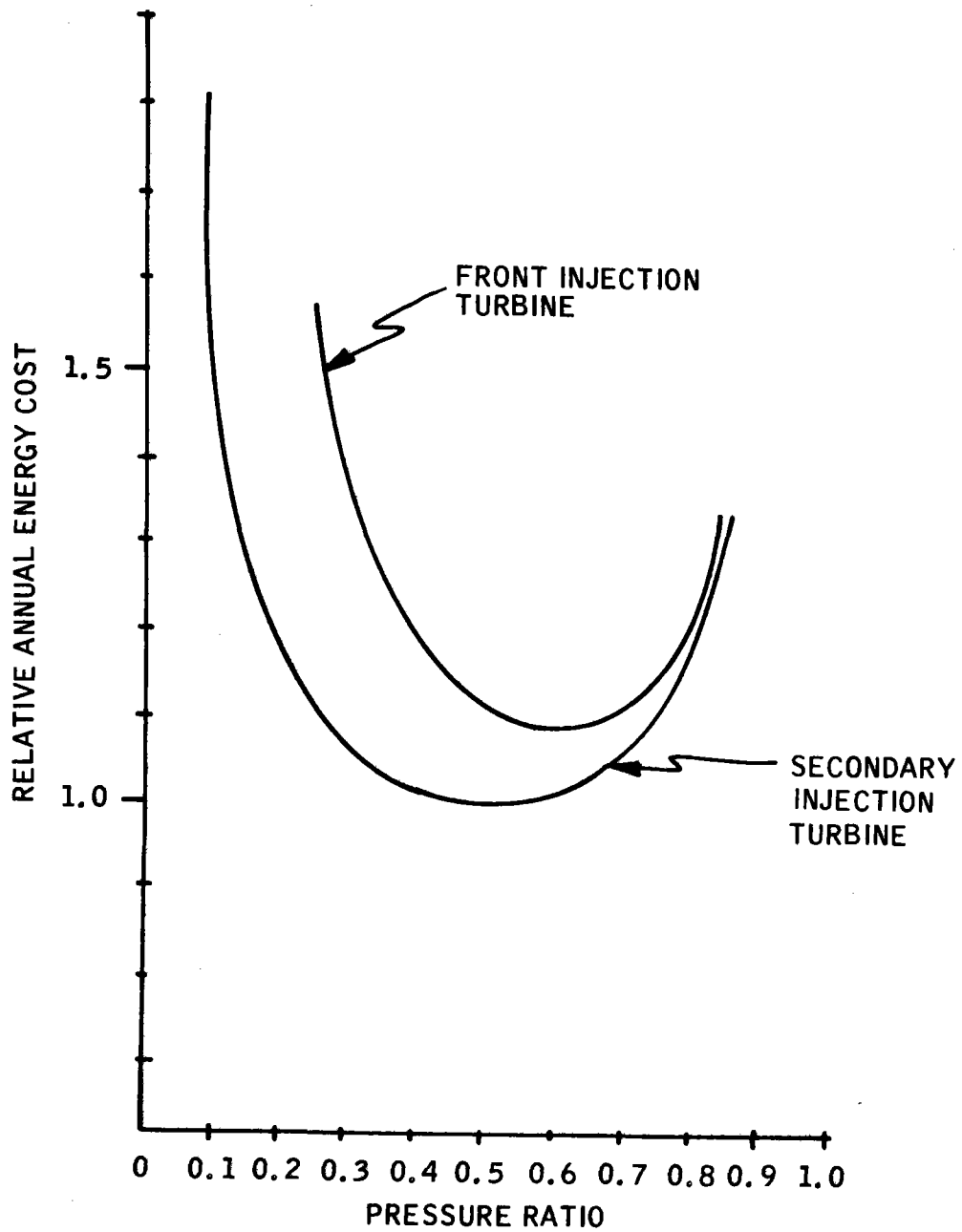


Figure 3-48. Relative Energy Cost versus Pressure Ratio for the Two Turbine Types a 9997 kPa Receiver Pressure with Latent Heat Storage

The secondary-injection turbine was found to be the more cost effective in all cases. This result is due to the fact that front-port-injection turbines require considerable oversizing of their front stages in order to pass the required mass flow of the lower-pressure, low-density storage steam. Secondary-injection turbines do not require oversizing, since steam is injected into the larger downstream stages.

Both types of turbines show an optimal pressure ratio. At high pressure ratios, reduced heat transfer ΔT across the storage system increases the cost of the storage subsystem. At very low pressure ratios, reduced thermal efficiency from storage steam increases both the capital cost of the storage system (by increasing the required thermal capacity of storage for a given electric output) and the amount of degradation of the receiver thermal energy cycled through the storage system. The front-port-injection turbine shows a higher optimal pressure ratio than the secondary-injection turbine because of the increase in mass flows due to lower thermal efficiency and resulting greater oversizing of the turbine at lower pressure ratios for the front-port turbine.

The final cycle parameters to be chosen are the pressure and temperature when operating from the storage subsystem. The tradeoffs associated with these parameter choices are governed by the storage subsystem economics. A discussion of the issues is left for the storage subsystem tradeoffs in the next section.

STORAGE SUBSYSTEM TRADEOFFS

Honeywell originally proposed a latent-heat storage subsystem and had developed a conceptual design for the pilot plant. In addition, a Subsystem Research Experiment (SRE) was designed, fabricated, and assembled.

Honeywell was directed to cease work on the latent-heat concept and to proceed with a preliminary design based on a near-term sensible-heat storage. It was determined that such a system must contain materials and equipment demonstrated by contractor SRE's. Consequently, a candidate system must contain oil, rock and oil, and/or Hitec salt as the storage and heat-transfer material. The evolution of the design choices is discussed here.

Early tradeoff studies dealt with both latent-heat and sensible-heat storage systems. An obvious system design decision to be made was the pressure when operating the turbine from storage. The pressure can conveniently be discussed in terms of a pressure ratio defined as the pressure from storage divided by the throttle valve pressure. Figure 3-49 gives the results of a sweep of pressure ratio for the two different types of storage system; latent-heat salt and sensible-heat oil. At higher pressure ratios, delta T across the storage system decreases and storage system costs increase. At lower pressure ratios, both storage capital cost and energy degradation of thermal energy cycled through the storage system increase.

Sensible-heat storage systems show a lower optimal pressure ratio than latent-heat systems. The delta T across storage for sensible-heat systems influences both the heat-exchanger size and the amount of storage media, whereas the latent-heat systems, the delta T across storage only influences the heat-exchanger sizes. The effect of decreasing storage media costs at higher storage delta T's (lower pressure ratios) in sensible-heat systems forces these systems to lower optimal pressure ratios than latent-heat systems. The results indicate optimal pressure ratios of 0.3 to 0.4 for a sensible-heat system and 0.5 to 0.55 for a latent-heat salt system.

Later tradeoff studies updated the above analysis for the sensible-heat storage system. For the updated analysis, the storage discharge conditions were selected so that the steam state matches the turbine expansion line. Turbine manufacturer information indicated that a transfer of steam sources,

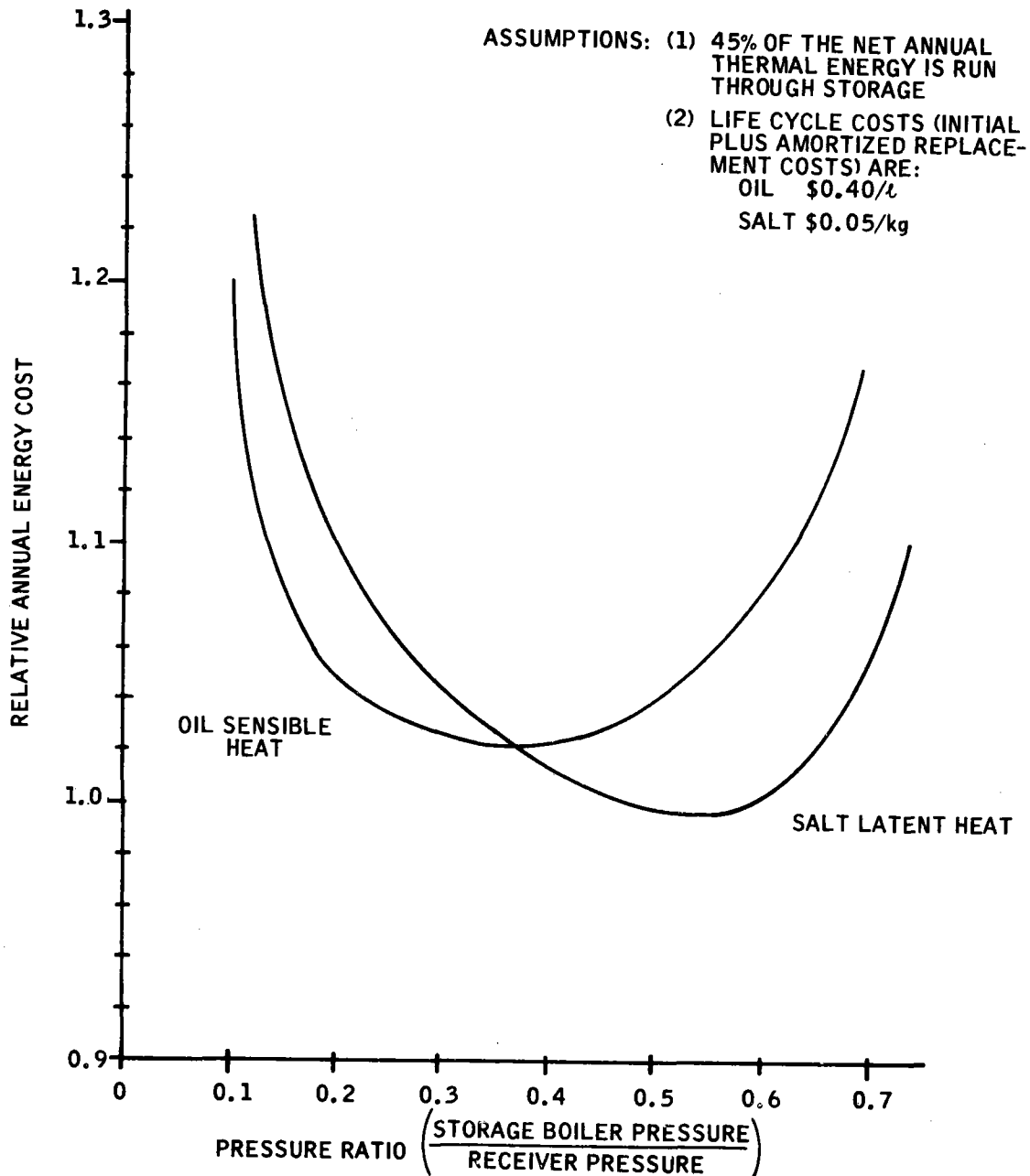


Figure 3-49. Comparison of Annual Energy Cost for Sensible Oil and Latent Salt Storage Systems

either from receiver to storage or storage to receiver steam, can be made nearly instantaneously if the secondary-admission port steam conditions are at the turbine expansion line pressure and within approximately 55.6°C of the temperature. To assure maximum flexibility when switching steam sources and to promote long turbine and component life, the storage steam discharge state was set to match the assumed expansion line. For the 9997 kPa turbine cycle, the assumed expansion line is shown in Figure 3-50. Choosing a storage or admission port pressure of 3275 kPa, we see that the turbine full-flow expansion line temperature is 387.8°C . At turbine flows less than 100 percent, the expansion line will shift (the turbine becomes slightly less efficient). For example, at 50 percent flow, the steam is expanded so that at 3275 kPa the steam temperature is approximately 415.6°C . The storage discharge steam is maintained at the design outlet temperature of 387.8°C , and a 27.8°C temperature mismatch results. This is within the 55.6°C mismatch limit for which instantaneous steam source transfer is allowable. In fact, we will be within the 55.6°C limit down to approximately 20 percent flow.

Using the expansion line matching criteria, the effects of the storage discharge pressure choice were analyzed next. The most important impacts of the choice of storage discharge pressure are the ΔT available to charge the storage and the turbine efficiency when operating from storage. As the discharge pressure is decreased, the temperature drop across the main storage (boiler storage) is larger and thus requires less sensible-heat material to store energy.

Figure 3-51 shows a temperature/enthalpy diagram for a possible discharge pressure of 4137 kPa. The storage charge and discharge steam conditions are shown. The selection of a storage discharge pressure sets the discharge temperatures in order to match the assumed turbine expansion line. In this case, 4137 kPa requires a discharge temperature of 407.2°C . The steam available to charge storage is set at the conditions available from the receiver.

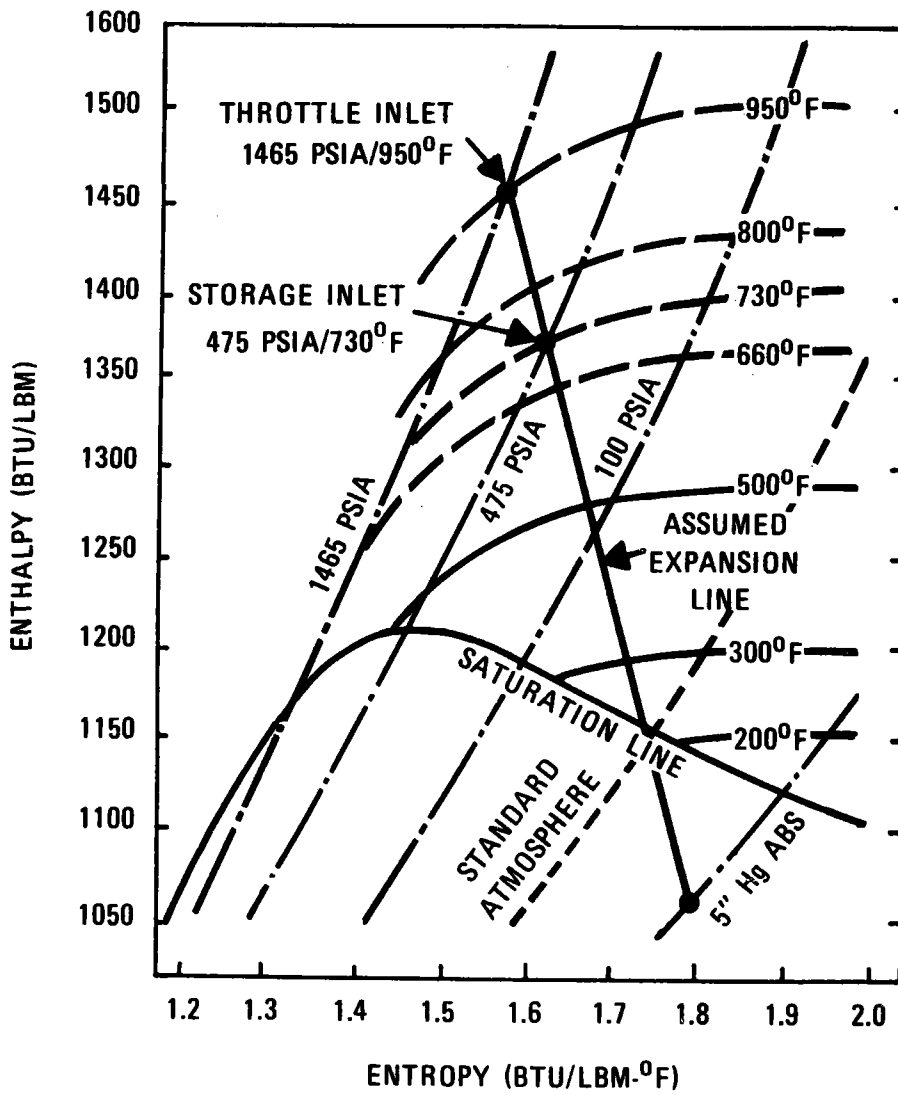


Figure 3-50. Expansion Line Matching (Shown in English Units for Convenience)

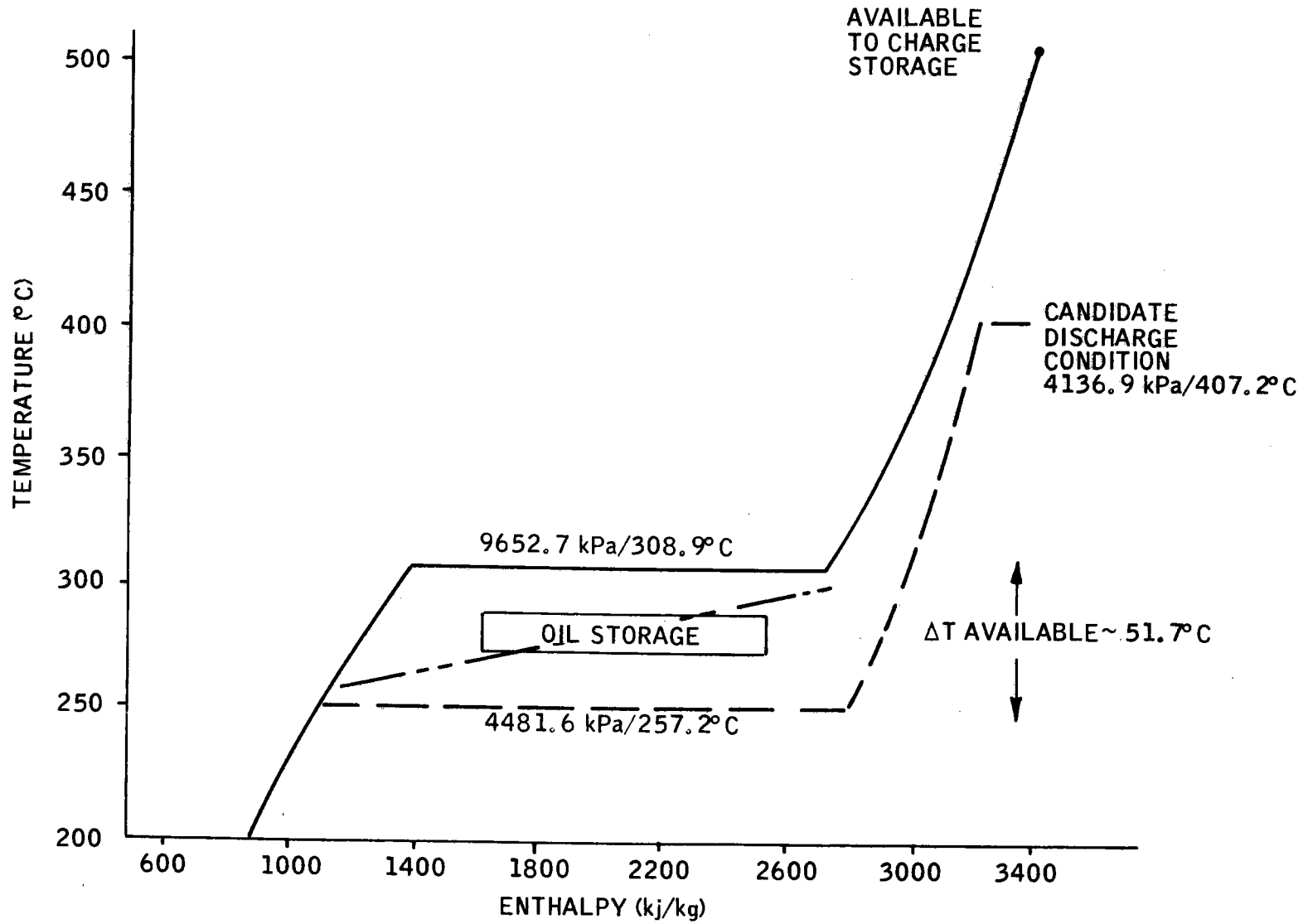


Figure 3-51. Temperature/Enthalpy Diagram for Storage

Most of the energy in the charge steam from the receiver must be extracted by condensing the steam. Similarly, the discharge steam is generated using primarily the process of boiling. The charge and discharge steam conditions shown in Figure 3-51 define the upper and lower temperature bounds for the storage media.

It can be seen that much of the energy storage must take place between the condensing (charge) steam saturation temperature of 308.9°C and the boiling (discharge) steam saturation temperature of 257.2°C. Therefore, the sensible-heat storage must store a large portion of the energy with a temperature differential of not more than 51.7°C. The storage stage which performs this function is referred to as the main or boiler storage. The function to superheat above saturation must also exist. A diagram of the sensible-heat storage configuration is shown in Figure 3-52. The rationale for the selection of the number of heat exchangers and the consequent subcooling and preheating capabilities are discussed in Volume 5.

For each candidate storage discharge pressure, the delta T available to charge storage and the temperature out of the storage superheater is shown in Figure 3-53. As the pressure is increased, the available temperature difference is decreased and the outlet temperature is increased. For all cases a pressure drop of 448 kPa on the charge side and 345 kPa on the discharge side was assumed to arrive at the saturation temperatures. The effect of decreasing the available delta T on the storage system design is to increase the quantity of main storage sensible-heat material required to store a given thermal energy. Counteracting this, the higher admission-port pressure associated with small delta T's will increase the turbine efficiency. An increase in turbine efficiency simply means that stored thermal energy can more effectively be used. Thus, to generate a specified electric energy, less thermal energy need be stored as pressure is increased.

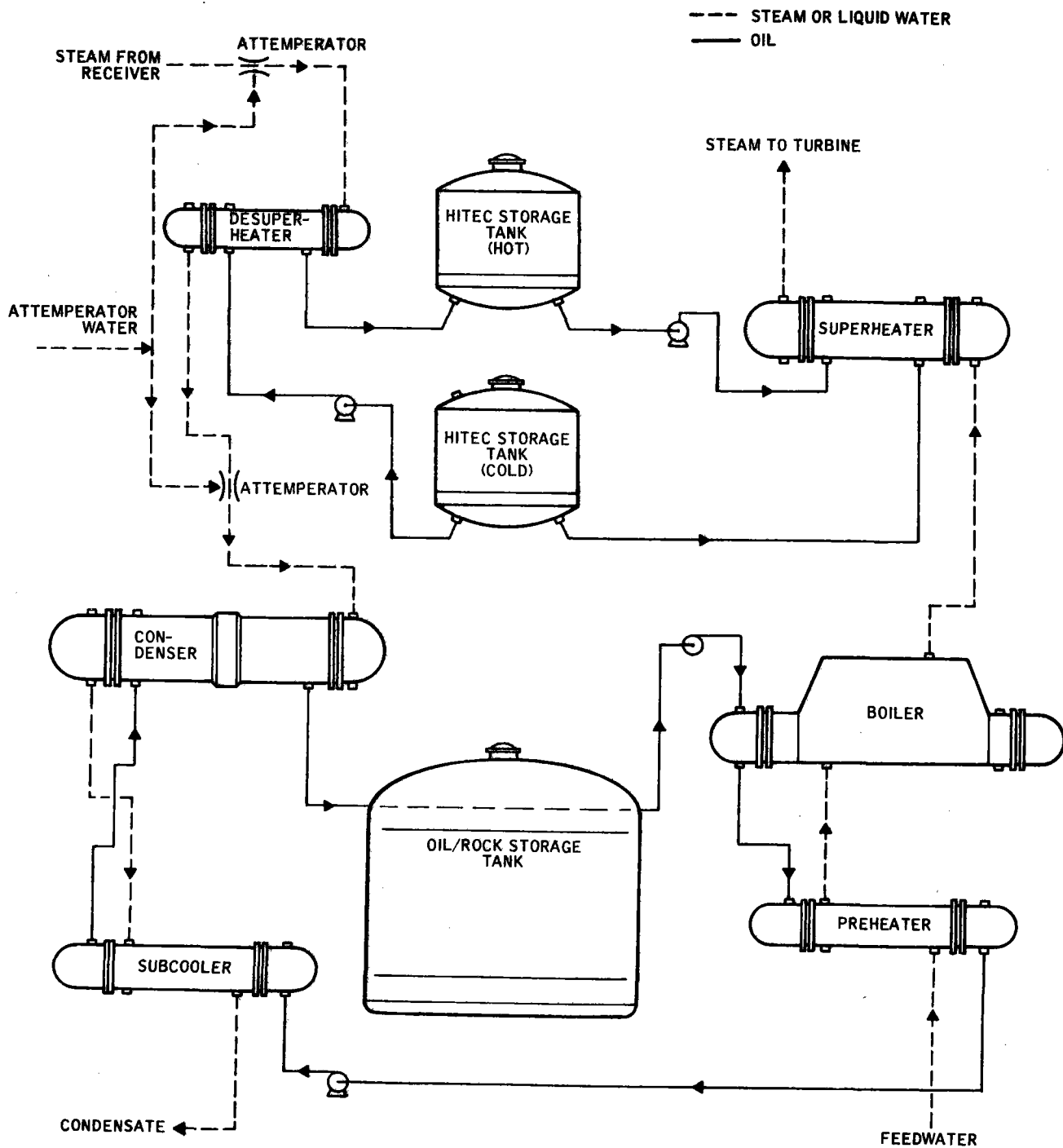


Figure 3-52. Sensible Heat Storage Subsystem

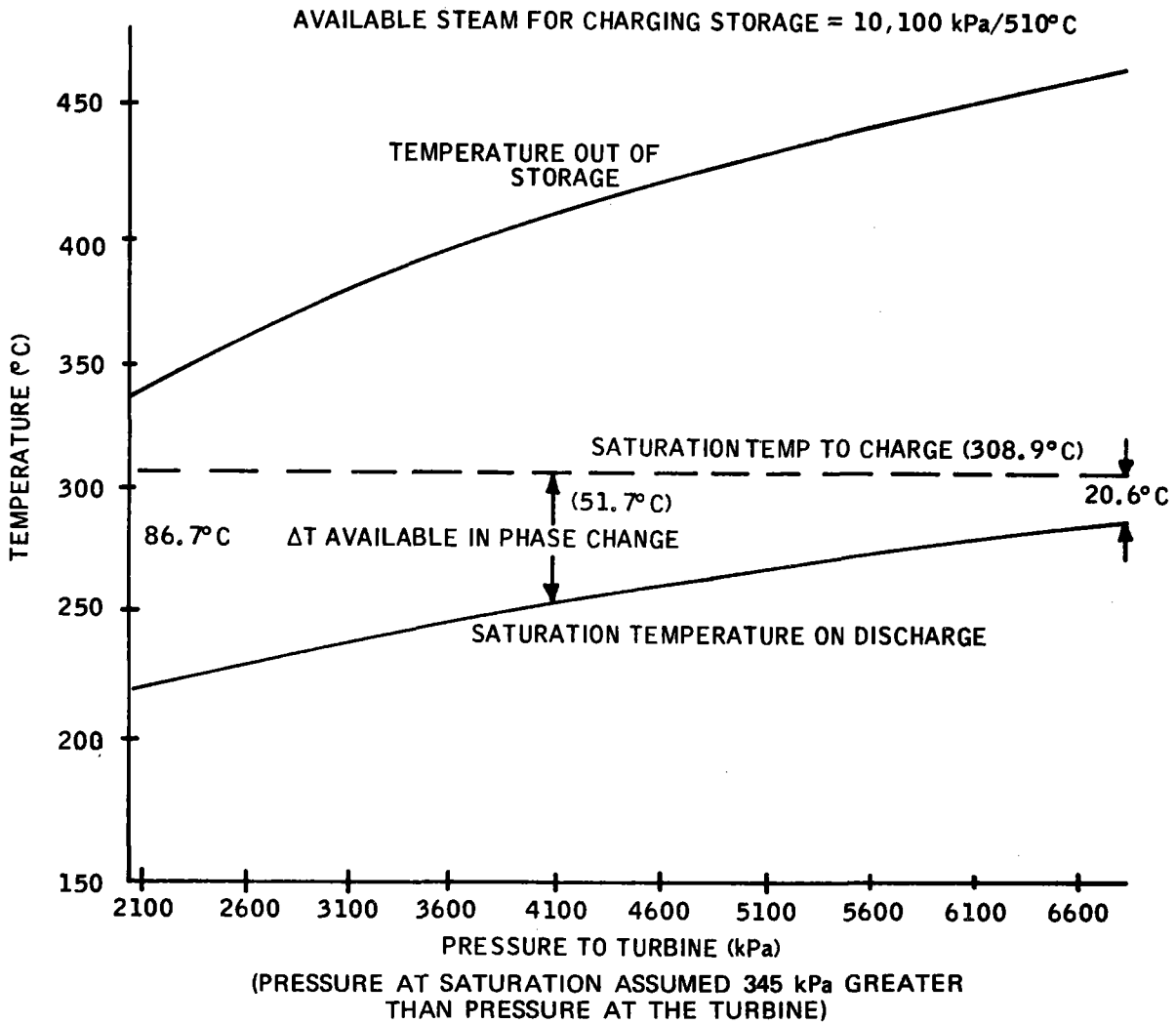


Figure 3-53. Storage Temperatures versus Turbine Admission Pressure

Turbine efficiency and required thermal storage capacity to produce 7 MW(e) for 6 hours are shown in Figure 3-54. The sensible-heat storage material quantity required for any admission-port pressure can be calculated dividing the required thermal energy capacity by the material specific heat and the temperature change the material undergoes in storing energy. This temperature change for main storage was assumed equal to the delta T available shown in Figure 3-53 minus 5.6°C for heat-exchanger pinch-points on each side of storage.

The oil quantity required is shown versus admission pressure in Figure 3-55. It is apparent that the available delta T is driving the result to show continually increasing storage media quantity required as pressure is increased. This figure is for a system of oil only in the main storage tank. For this system we costed the required oil, the storage tanks and insulation, the heat exchangers, and the superheater section material. The superheat material was assumed to be Hitec. For pressure greater than 300 psia, all costs tend to increase as storage discharge pressure is increased. At the lower discharge pressures, the capital costs tend to level out. In fact, the capital cost will begin to rise below 300 psia because the efficiency out of storage becomes more important than the gain in available delta T. The selection of the proper discharge pressure depends on the assumed storage usage. If the storage is used very little, then the lowest possible discharge pressure will be best simply because this will minimize the capital cost. However, if storage is used frequently, then a higher discharge pressure, and hence higher turbine cycle efficiency, may be the best economic choice. The best economic choice is that discharge pressure which minimizes the overall plant annual energy cost. If the storage system receives 45 percent of the annual energy output from the receiver, the oil/Hitec system discharge pressure should be approximately 2758 kPa to minimize annual energy cost. This corresponds to a pressure ratio of 0.27.

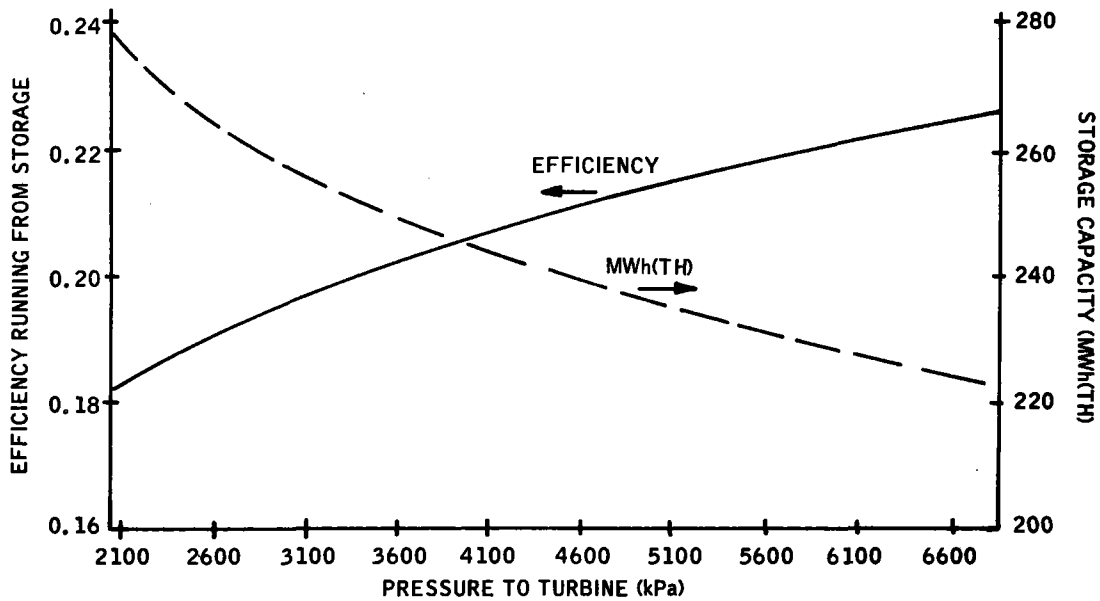


Figure 3-54. Turbine Efficiency and Thermal Storage Capacity versus Turbine Admission Pressure

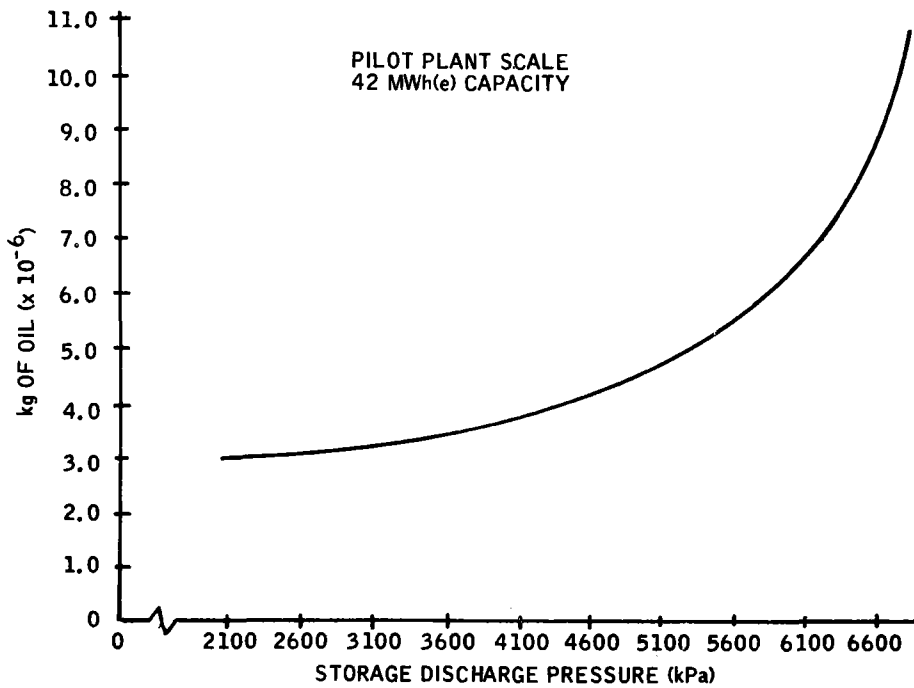


Figure 3-55. Oil Quantity versus Storage Discharge Pressure

The optimal pressure ratio for the oil/Hitec system and an oil/rock and Hitec system is shown in Figure 3-56. The oil/rock and Hitec system was chosen for the sensible-heat baseline because of an economic advantage as shown in Figure 3-56. The optimal pressure ratio is approximately 0.32, which corresponds to admission-port conditions of 3275 kPa/387.8°C. The curves in Figure 3-56 are for 45 percent of the annual energy going through the storage system.

The choice of the oil/rock main storage depends on the maintenance of a thermocline in the tank.

Honeywell is reasonably satisfied that the thermocline principle has been adequately demonstrated and that the rock does not adversely influence the long-term stability of the oil at temperatures less than 304.4°C. Consequently, a system consisting of rock and oil in the main stage was selected.

The candidate materials for the heat transfer into and out of the superheater storage section include hydrocarbon oils, synthetic oils, and inorganic salt mixtures.

Hydrocarbon oils, although less expensive than synthetics, are limited to 315.6°C maximum, due to thermal and catalytic cracking. Synthetics can be used but are extremely expensive. On the other hand, the high-temperature sensible-heat capability of inorganic salts at temperatures to 482.2°C is free from thermal decompositions and will provide lower costs for electrical power than either synthetic or hydrocarbon oils.

Consequently, a superheater system consisting of Hitec was designed to provide matching steam temperatures at the turbine was selected.

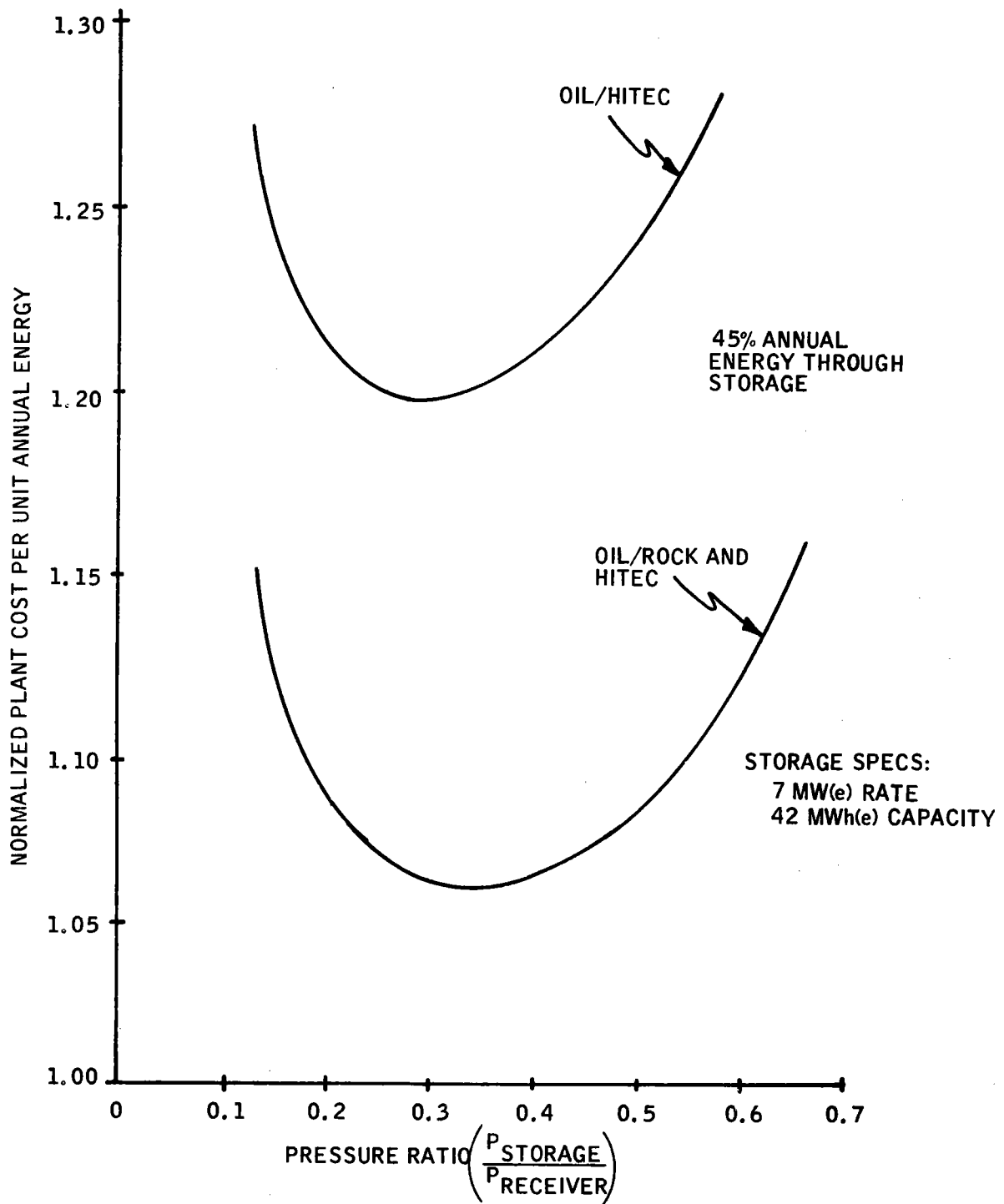


Figure 3-56. Cost Optimization of Storage Discharge Pressure

COMMERCIAL PLANT DESIGN TRADEOFFS

Throughout the pilot plant design effort, the philosophy adopted was that the pilot plant is a scaled version of the commercial plant. Both plants use the same receiver/field physical design - the tower one-half south of center field layout, sensible-heat storage, and tilt-tilt heliostats.

Design Guidelines

The design point for which the commercial plant analysis was made was defined by Sandia Corporation and is repeated below:

- Site: Inyokern, California
- Direct normal insolation: 950 W/m^2
- Sun angle: That which occurs at the time of the year when the peak thermal power from the receiver at the turbine generator building is at a maximum, assuming the insolation specified above (i. e. , the best sun angle)
- Wind Speed: 3.5 m/s (8 mph) at a height of 10 m
- Wet-bulb temperature: 23°C (74°F)
- Dry-bulb temperature: 28°C (82.6°F)

The commercial plant was designed using Sandia guidelines which assume a 100-MW(e) peak net output while operating on receiver steam. In addition, the plant was sized with a solar multiple of 1.7 to deliver the excess steam generated to the storage charging system. Solar multiple is defined by the following ratio:

$$SM = \frac{P_t}{P_n}$$

Where

P_t = Thermal power from receivers after accounting for downcomer and piping losses measured at the design point

P_n = Thermal power required to operate the turbine generator at the design point to produce the peak net electrical output when operating from receiver steam only, and accounting for auxiliary losses.

The basic commercial plant design and sizing requirements used are shown below:

- The storage discharge rate is sized to allow net electrical power production at a minimum of 70 MW(e),
- The storage charge rate is sized to accept 50 percent of the design-point thermal power from the receiver at the entrance to the thermal storage units.
- The commercial plant is equipped with a wet cooling type of heat rejection.
- The design is based on the same site data -- soil, seismic, etc. -- as used on the pilot plant design.

The steam conditions for which the commercial plant was assumed to operate are:

- Receiver steam at the turbine throttle valve = 10100 kPa/510°C (1465 psia/950°F)
- Storage steam at the turbine admission port = 3275 kPa/388°C (475 psia/730°F).

Design Alternatives

Initially the commercial plant concept was considered to consist of one tower. However, an analysis of the commercial plant design, not limited to a one-tower/receiver configuration, was analyzed. Included in the analysis were one-tower, four-tower, and 12-tower configurations. The 12-tower configuration is approximately 12 pilot plant fields. The one- and four-tower configurations are scale-ups of the pilot plant geometry. Figure 3-57 represents a commercial plant module, be it one-tower, four-tower, or 12-tower design. Following is a description of each part of the module: design time, collector system performance, optical losses, thermal losses, cycle efficiency, and auxiliary power requirements. The commercial plant analysis and selection was based on the following tower heights: one-tower design = 439 m; four-tower design = 219 m; 12-tower design = 126 m. Seismic considerations and atmospheric attenuation losses are treated separately.

The time of year for which the peak thermal power from the receiver at the turbine generator building is at a maximum is defined to be the "best" sun angle. This angle is found by determining the time of year for which tracking efficiency is at a maximum.

The maximum tracking efficiency occurs at noon on the vernal (3/21) and autumnal (9/21) equinoxes. This is the "best" sun time and is used as the design time for the commercial plant.

The collector system performance study was made to estimate commercial plant field performance and receiver aperture size. The ray trace code was used, assuming any commercial plant geometry is a scale-up of pilot plant geometry, i. e.:

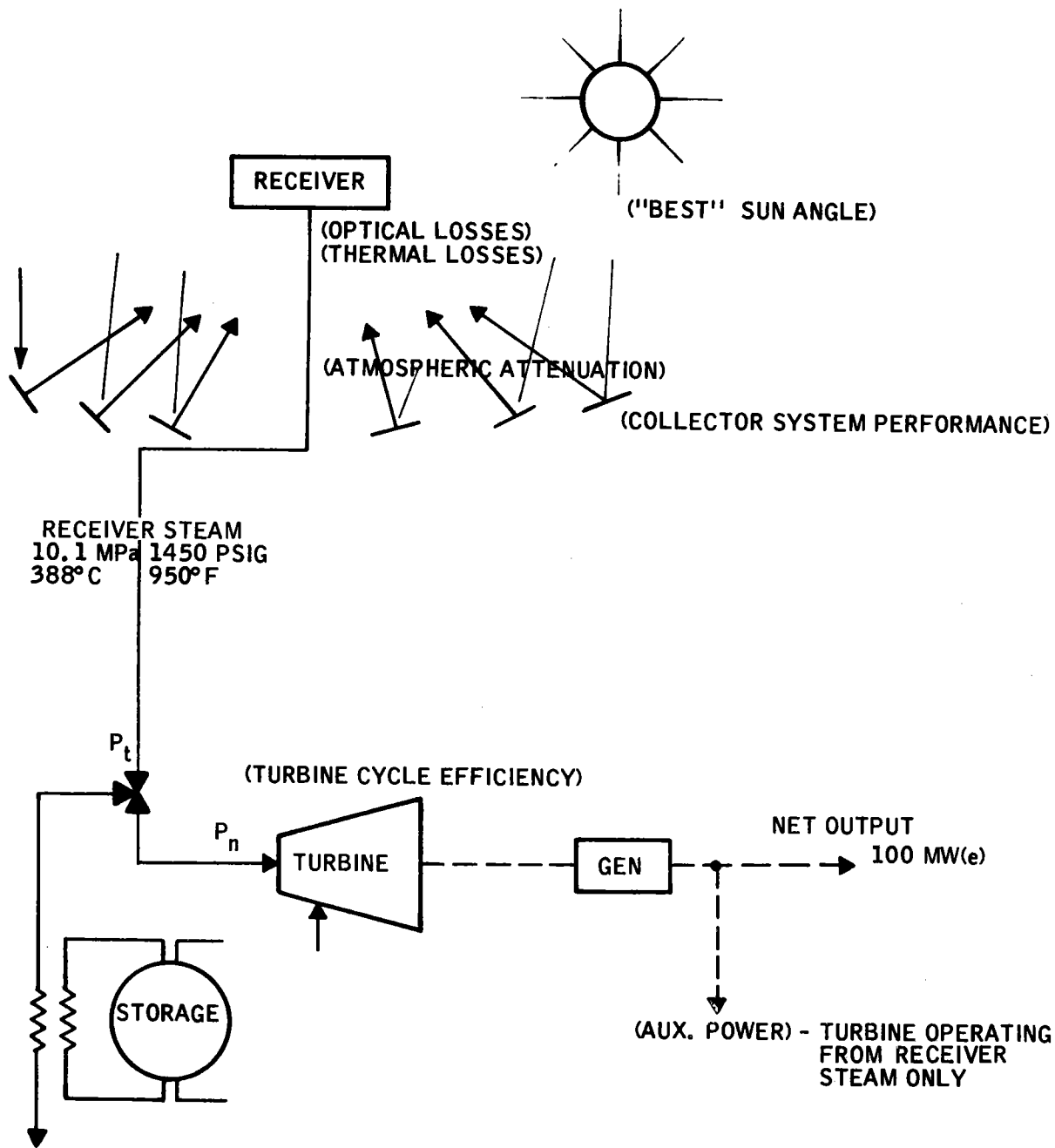


Figure 3-57. Commercial Plant Module

- Ground cover = 0.29 average (nonuniform)
- Field area/(tower height)² = 13.6
- Design time = 3/21 or 9/21 noon

The following results were obtained (3/21 noon design time):

- Cosine losses = 6.5 percent
- Shading and blocking losses = 0.6 percent

Figures 3-58 and 3-59 show the absorbed power versus aperture area for the four-tower and one-tower configurations, respectively. The 12-tower configuration is the same as the pilot plant.

Optical losses at the receiver are accounted for in the following manner:

1) the power which misses the aperture completely; 2) that which strikes the receiver supports; 3) that which enters one side of the aperture but misses the receiver (known as whistle-through); and 4) atmospheric attenuation between heliostat and receiver. The first three are output from the optical ray trace model (Book 2 of this volume discusses the derivation of these losses in detail). Atmospheric attenuation, however, is not part of the ray trace model and is discussed in the analysis model section of this document. Included here is only the magnitude of the attenuation for each of the designs considered.

The following results were obtained:

- Optical losses = 2.5 percent (all designs)
- Atmospheric attenuation losses
(see top of page 3-105):

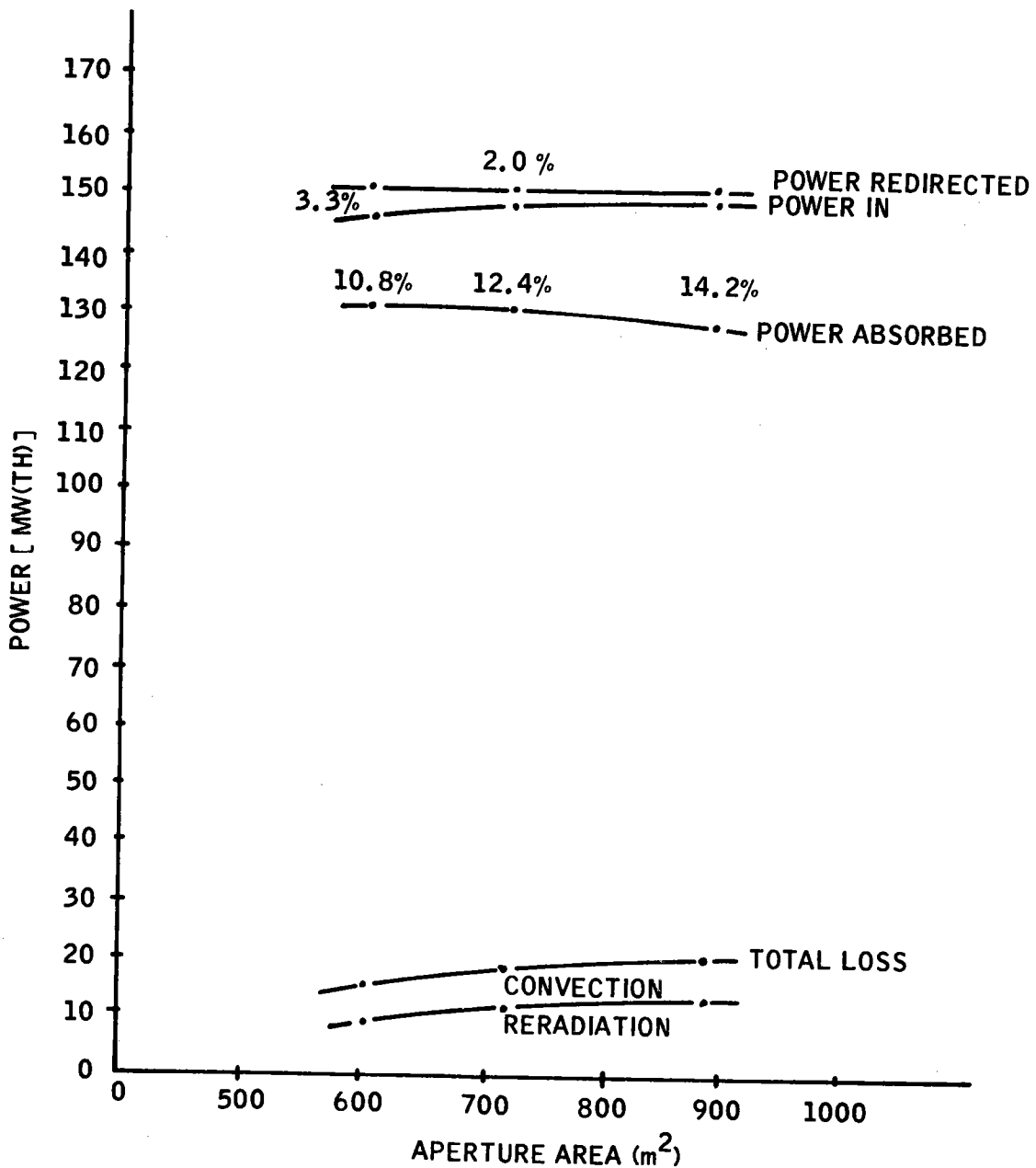


Figure 3-58. Commercial Plant Design Computer Results--Power versus Aperture Area for Four-Tower Concept. Tower Height = 720 ft. (219.5 m)

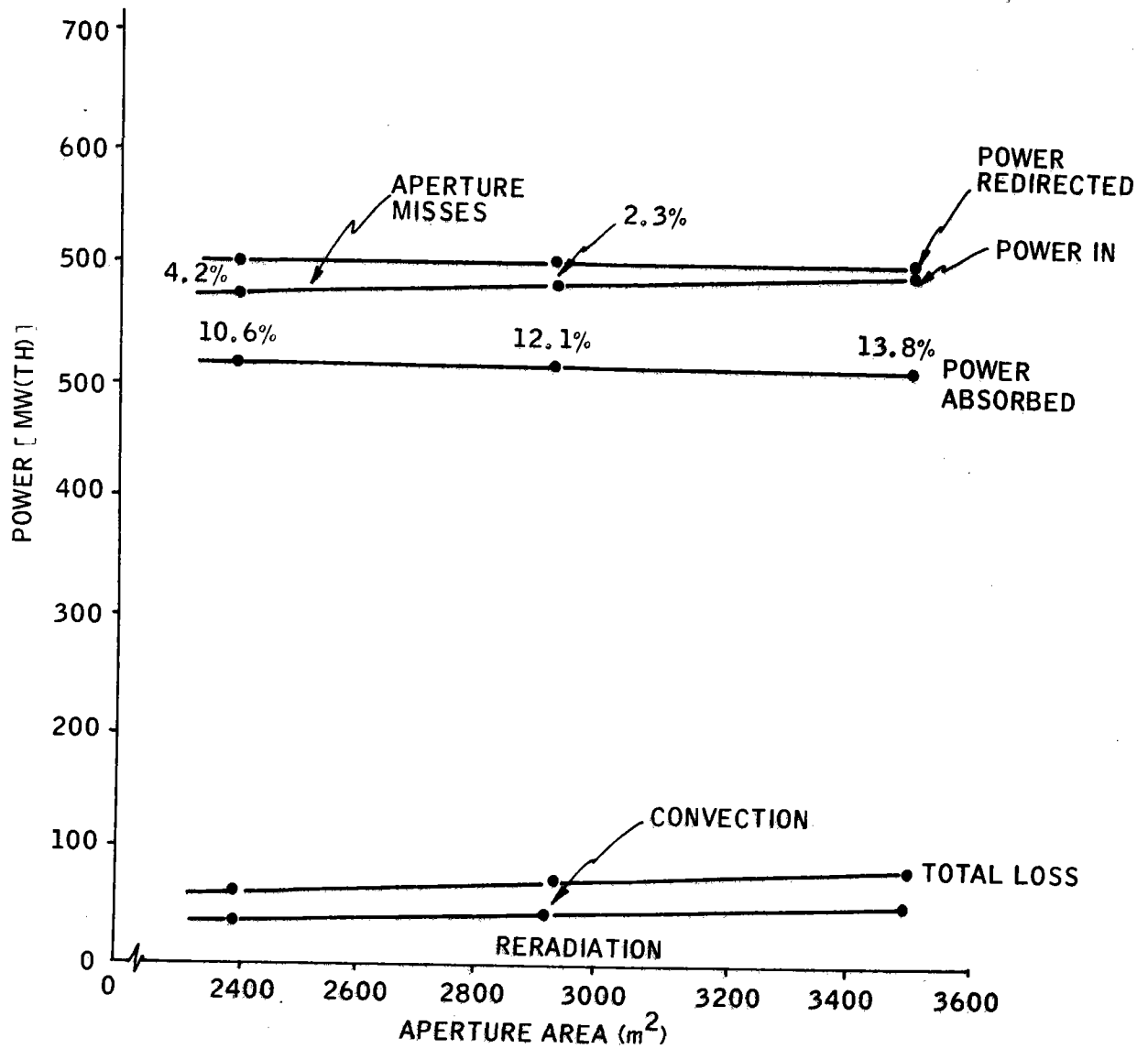


Figure 3-59. Commercial Plant Design--Power versus Aperture Area for Single-Tower Concept, Tower Height = 1440 ft. (439 m)

<u>Configuration</u>	<u>Atmospheric Losses</u>
12-tower	6.3%
4-tower	8.8%
1-tower	13.5%

Thermal losses considered were convection, conduction, and reradiation.

The convection loss is expressed as follows:

$$h = 3.195U^{0.8} / D^{0.2} \quad (3-1)$$

$$A = \pi D (H + D/4) \quad (3-2)$$

$$T_{\text{cavity}} = \left(T_{\text{SH}} + T_{\text{SAT}} \right) / 2 \quad (3-3)$$

$$\Delta T = T_{\text{cavity}} - T_{\text{amb}} \quad (3-4)$$

$$\dot{Q} = hA \Delta T \quad (3-5)$$

where

\dot{Q} = Convection loss, W/hr

h = Cavity heat transfer coefficient, $W/m^2 \cdot ^\circ C$

A = Cavity inside surface area, m^2

D = Cavity inside diameter, m

H = Cavity average height, m

T_{cavity} = Average temperature of cavity, $^\circ C$

T_{amb} = Ambient temperature, $^\circ C$

T = Temperature difference, $^\circ C$

T_{SH} = Superheater exit temperature, $^\circ C$

- T_{SAT} = Saturation temperature at drum operating pressure, °C
- U = Wind velocity at cavity aperture, m/s

This expression is taken from a paper by J. Fox, "Heat Transfer and Air Flow in a Transverse Rectangular Notch," International Journal of Heat and Mass Transfer, Volume 8, pp. 269-279, 1965.

The data from this paper were obtained from tests on a 5.08-cm-wide cavity in a flat plate. Extrapolating these data to a cavity approximately 1000 times larger in diameter and located on a tower rather than a flat plate is obviously uncertain. Additional research beyond the scope of Phase 1 will be required to verify convection losses.

The reradiation and conduction losses are assumed to be of the following form:

$$P_o = f(P_I, A_p/A_c, L/D) \quad (3-6)$$

where

- P_o = Power out of receiver cavity
- P_I = Power into receiver cavity
- A_p = Aperture area
- A_c = Internal receiver surface area
- L = Receiver height
- D = Receiver diameter

Reradiation is separated into two terms: 1) solar loss, i. e., that energy which is reflected from the cavity interior back out the aperture, and 2) IR losses due to surface temperature, i. e., of the form $W = \sigma T^4$. The equations are, respectively:

$$P_o = \left[0.01705 \left(\frac{D}{L} \right) + 0.01763 \left(\frac{AP}{AC} \right) \right] P_I \quad (3-7)$$

and

$$P_o = P_I \left[0.01966 \left(\frac{D}{L} \right)^3 + 0.03579 \left(\frac{AP}{AC} \right) \right] + A_p \left[8.786 \times 10^{-3} - 1.122 \times 10^{-2} \left(\frac{L}{D} \right) \left(\frac{A_p}{A_c} \right) \right]$$

for $0.85 < L/D < 1.50$

$0.18 < A_p/A_c < 0.45$

The constants are parametrically determined by the reradiation "rubber" model described in Section 7.

The conduction losses are assumed to be of the same form as reradiation and conduction losses. The equation is as follows:

$$P_o = A_c \left(4.720 \times 10^{-4} P_I + 2.199 \times 10^{-4} \right)$$

The previous three equations were used to determine the receiver thermal losses. Results are tabulated in Tables 3-5, 3-6, and 3-7.

Table 3-5. Four-Tower Design (TH = 219 m)

Aperture Area (m ²)	Power In (MW)	Reradiation Conduction Losses (MW)	Convection Losses (MW)	Net Power Absorbed (MW)	Cavity Efficiency at 150 MW
605	146.25	9.65	6.18	130.4	.8935
738	148.37	11.57	6.80	130.0	.8771
883	148.25	13.57	7.41	127.3	.8595

Table 3-6. One-Tower Design (TH = 439 m)

Aperture Area (m ²)	Power In (MW)	Reradiation Conduction Losses (MW)	Convection Losses (MW)	Net Power Absorbed (MW)	Cavity Efficiency at 600 MW
2399	578.1	37.99	23.20	516.9	.8966
2926	586.3	45.46	25.53	515.3	.8806
3507	592.5	53.78	27.88	510.8	.8632

Table 3-7. 12-Tower Design (Pilot Plant) (TH = 126 m)

Aperture Area (m ²)	Power In (MW)	Reradiation Conduction Losses (MW)	Convection Losses (MW)	Net Power Absorbed (MW)	Cavity Efficiency at 61 MW
261	40.85	3.45	2.50	34.92	.855

Table 3-8 shows the estimated pipe length and estimated percentage of power lost for the designs considered. These losses for the 12-tower and one-tower designs were scaled from the four-tower design calculated piping loss.

Table 3-8. Thermal Loss Due to Piping Lengths

	12-tower	4-tower	1-tower
Pipe length, m	5901	3591	457
% Power Lost	2.6	1.2	0.2

Electrical Power Generation Subsystem Requirements

For purposes of choosing a commercial plant design, the gross turbine efficiency was assumed a constant. This is reasonable, since all plants have approximately the same mass flow at entrance to the turbine. The values used for this analysis at an assumed back pressure of 2 inches of mercury are:

0.385 = Gross turbine efficiency when operating from receiver steam only (includes generator losses)

0.318 = Gross turbine efficiency when operating from storage steam only (includes generator losses).

The auxiliary power requirement can be thought of as system electric losses, since this power must be generated in excess of that available at the busbar.

This power is distributed among the following requirements:

- Balance-of-plant equipment (BOP)
- Collector field
- Steam generator subsystem
- Electric power generation subsystem
- Charging storage

Since the commercial plant must deliver the excess steam generated to the storage charging system, the power required to operate the storage charging loop is included in the auxiliary power requirements.

A summary of auxiliary power requirements for the three configurations is presented in Table 3-9.

Table 3-9. Auxiliary Power Requirements

Location	Auxiliary Power Required [kW(e)]		
	12-Tower Design [kW(e)]	4-Tower Design [kW(e)]	1-Tower Design [kW(e)]
Electrical generation subsystem and balance of plant	7070	7110	7230
Steam generator subsystem	500	800	1500
Heliostat field	600	600	600
Storage	1020	1020	1020
TOTAL	9190	9530	10350

Cost Tradeoffs

Cost estimates for the different designs are based on estimates generated by the plant sizing software. The major costs that changed with tower number were the tower costs, steam generator/receiver costs, and piping costs from each field to the central electric generating complex. Since the plant has only one central generating complex, one turbine generator, and one storage system, these costs are invariant with tower number. The costs which vary with tower number are the elements of the plant whose cost estimates are the weakest.

Table 3-10 shows the commercial plant design cost estimates for each of the concepts.

Table 3-10. Commercial Plant Design Cost

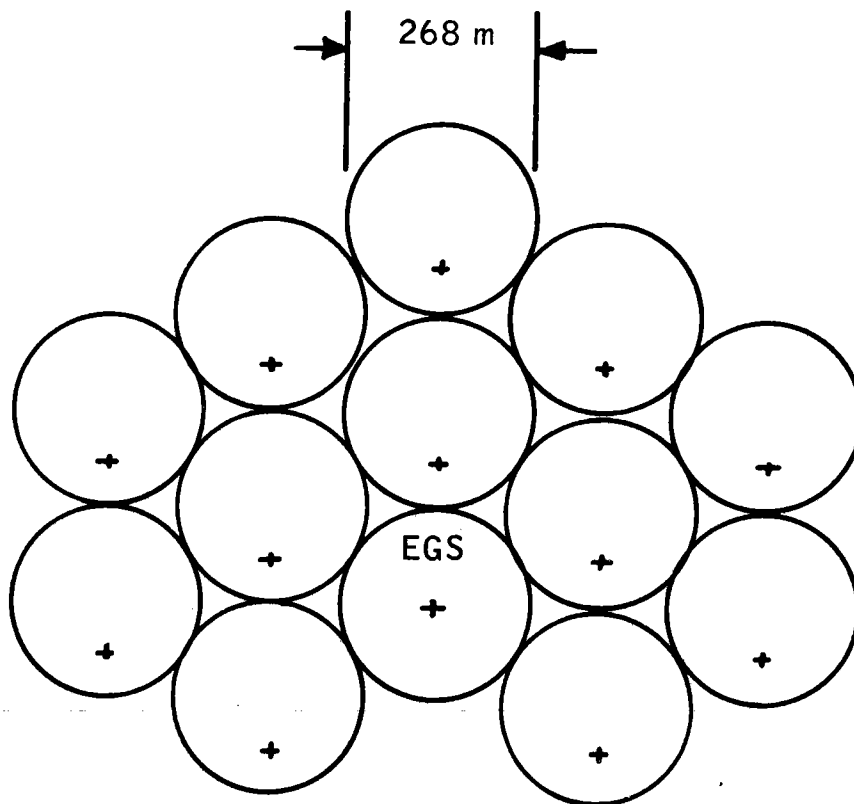
Hardware	<u>Cost Factor (\$/kW)</u>		
	<u>Number of Towers</u>		
	1	4	12
Heliostats (\$100/m ²)	797	805	825
Turbine generator	110	110	110
Balance of plant	190	190	190
Storage	287	287	287
Tower	267	341	421
Steam generator	367	597	681
Piping	37	110	83
Subtotal	2055	2440	2598
Indirects, Cont (21%)	431	512	546
Total	2486	2952	3144

Heliostat cost estimates are based on a cost of \$100/m² heliostat surface area. Turbine generator costs are based on data taken from the GE price-book. Balance-of-plant receiver, and storage cost estimates are based on a scale-up of the pilot plant cost estimates. Tower cost has two components: the cement structure which is estimated to vary as 9.8 times the tower height (in meters) squared, and the generator housing, support structures, and miscellaneous tower hardware which is scaled up from the pilot plant costs.

Design Selection

The data in the previous section compare the performance and cost of three commercial plant configurations. The selection of one is not easy to make. Many questions about the construction and operation of solar plants still remain unanswered. Cost estimates on very tall towers with a heavy receiver at the top are, at best, educated guesses, especially with concrete structures. Furthermore, since 100 MW(e) may not be the optimum-size commercial plant with respect to performance and cost, all discussions here apply only to the one size.

The figures following show how the various concepts considered could look. Figure 3-60 shows the 12-tower concept (tower height = 126 m). The electrical generation subsystem is located out of the plant perimeter to permit easy access by plant personnel and railroad delivery. Figure 3-61 shows the four-tower concept (tower height = 219 m). The electrical power generation subsystem is located as near as possible to the centroid-of-tower center to minimize piping length. The distance between the fields permit easy access as with the previous concept. Figure 3-62 shows the one-tower design (tower height = 450 m). This concept is a scaled version of pilot plant.



PIPE LENGTH ON GROUND = 4383 m

TOWER HEIGHT = 126 m

TOTAL PIPE LENGTH = 5900 m

Figure 3-60. Commercial Plant Modular Field Layout (12 Powers)

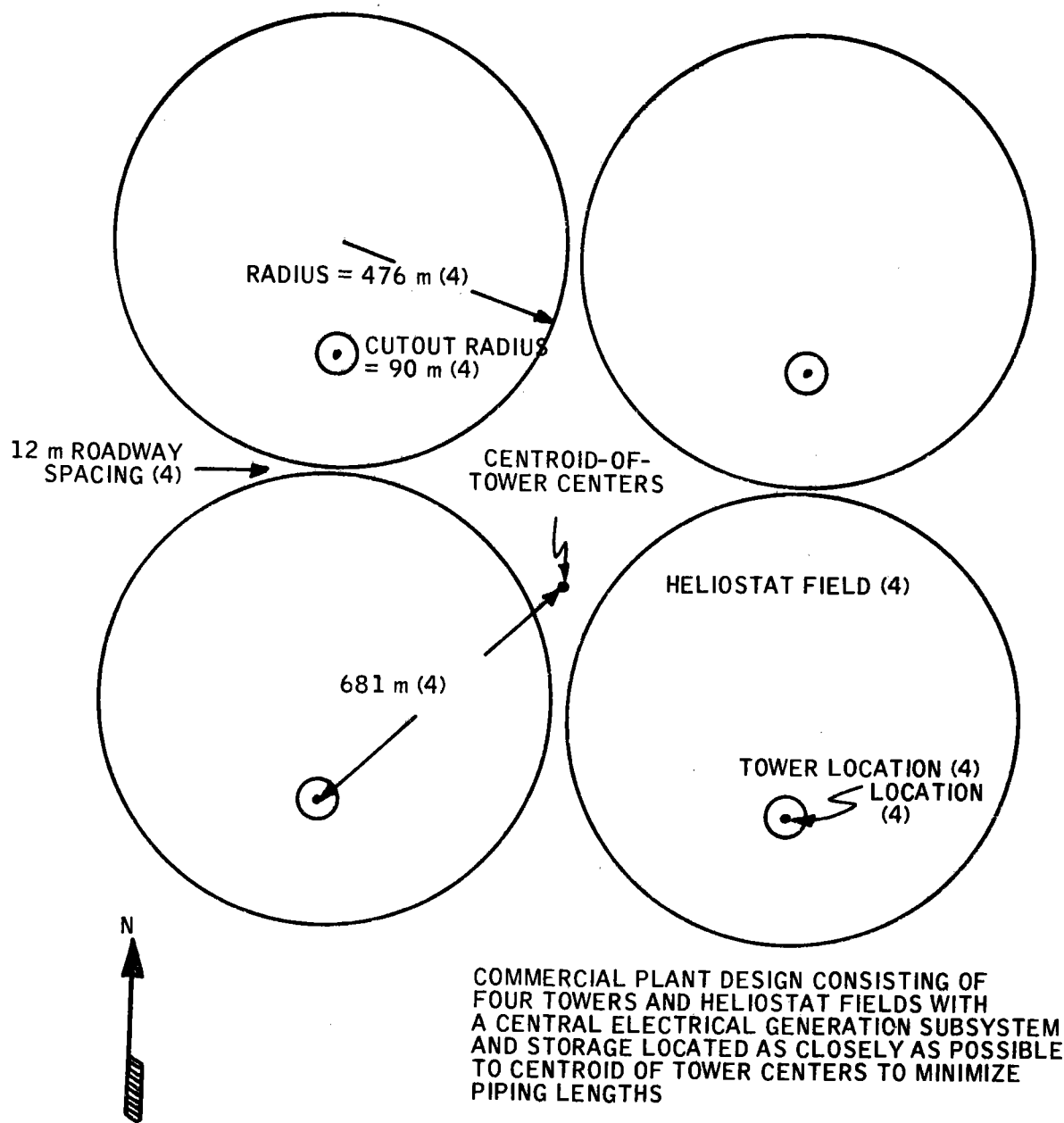
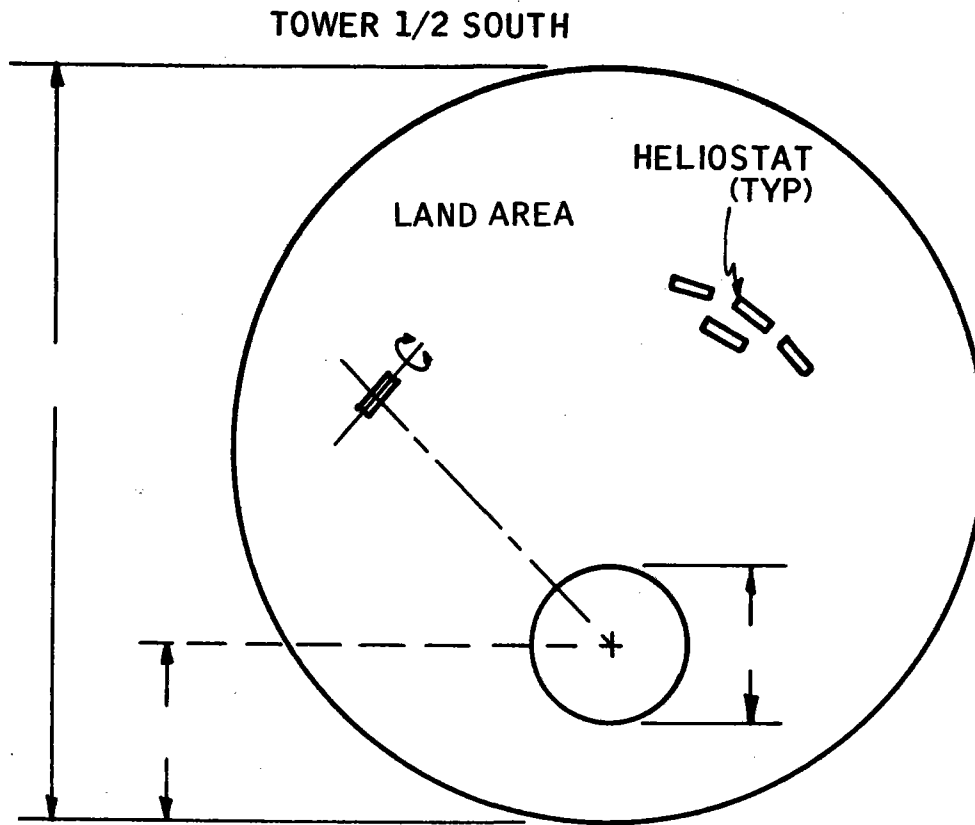


Figure 3-61. Commercial Plant Modular Field Layout (Four Towers)

40703-II



- TOTAL MIRROR AREA
- NUMBER OF HELIOSTATS
- TOWER HEIGHT = 429 m
- NONUNIFORM POLAR PACKING, AVERAGE GROUND COVER 0.29

3-115

Figure 3-62. Single-Tower Design

Table 3-11 compares performance characteristics and cost for the three design concepts. Based on performance alone, no significant difference in these design options could be identified.

Based on cost comparison, one would lean toward selecting the single-tower design. However, the quoted cost does not include the extra cost to build the tower to withstand the seismic disturbances predicted to occur in many proposed plant locations. Furthermore, very tall towers, over 305 m (1000 ft), are judged to be aesthetically displeasing.

Thus the four-tower concept was chosen, on the basis of cost, as the commercial plant design. One further iteration has been made on the four-tower configuration to fine tune the performance characteristics. A discussion of that configuration is contained in Section II of this volume.

It is felt that the four-tower concept which has been selected is the best of those concepts considered. However, commercial plants of the future are expected to be similar to present day power plants in that the size is dependent upon the particular location and need. No one commercial plant can be optimal in a location if a need for it does not exist.

Table 3-11. Comparison of Performance Characteristics and Cost

	Performance Characteristic		
	1-Tower*	4-Tower*	12-Tower*
Number of heliostats	18,519	18,568	18,960
Tower Height, m	431	215	126
Field radius, m	912	456	266
Plant radius, m	171	86	50
Total field area, m ²	2.52 x 10 ⁶	2.52 x 10 ⁶	2.57 x 10 ⁶
Power away from field, MW (th)	704	706	720
Atmospheric attenuation, %	13.5	8.8	6.3
Receiver optical losses, %	2.5	2.5	2.5
Receiver thermal losses, %	12.1	12.4	14.5
Piping losses, %	0.2	1.2	2.6
Auxiliary power, MW (th)	10.35	9.53	9.19
Plant cost, \$/kW	2486	2952	3144

*These configurations were used for the commercial plant tradeoff analysis. An update of the design parameters was performed for the selected four-tower configuration.

SECTION 4

PILOT PLANT OPERATION

This section of the report summarizes:

- Modes of pilot plant operation
- Operator sequences for startup and shutdown
- Analysis of pilot plant transient performance

MODES OF PILOT PLANT OPERATION

Compared with conventional power plants, the pilot plant will be required to operate under conditions which are more variable (and less controllable) for the plant operator. For example, diurnal startup and shutdown will be mandated by total loss of solar power. In addition, the plant will occasionally be subjected to partial or total disruption of the incident solar power (e. g., clouds), thereby requiring switchover to an alternate source of steam power (i. e., thermal storage).

This greater variability in the operating environment requires a plant design which affords operating mode flexibility in order to efficiently use the plant. The plant is capital intensive, with relatively low variable operating cost, and as such, it must be used to its maximum capacity on a daily basis to prove the plant is economically feasible. Consequently, the plant must respond to a variety of constantly changing heat supply situations, as well as expected normal power plant changes in load demand.

Throughout a typical day, normal plant operational functions will include:

- Plant Startup -- Returning the plant to nominally rated steam conditions after overnight shutdown.
- Charging Thermal Storage -- Replacing thermal energy extracted during prior evenings power generation operations, energy consumed for overnight plant maintenance requirements, or energy extracted for supplementary electrical power generation (as for cloud transients).
- Discharging Thermal Storage -- Extracting thermal energy for supplementary electrical power generation needs, or for plant maintenance needs.
- Plant Shutdown -- Preparing the plant for overnight, or possibly extended period, plant shutdown.

Generally, the plant shutdown function is similar to that of a conventional power plant. The other three functions -- startup, charging, and discharging thermal storage -- are generally unique to the pilot plant and are therefore the main topic of discussions in this section.

The preliminary design of the pilot plant incorporates six operating modes as identified in Table 4-1. These modes permit the plant to perform any of the four functions described above under either total or partial automatic control.

Figure 4-1 illustrates the basic working fluid flow diagram for the electrical power generation subsystem (EPGS), generally referred to as the electrical generation subsystem (EGS). All operating modes identified in Table 4-1

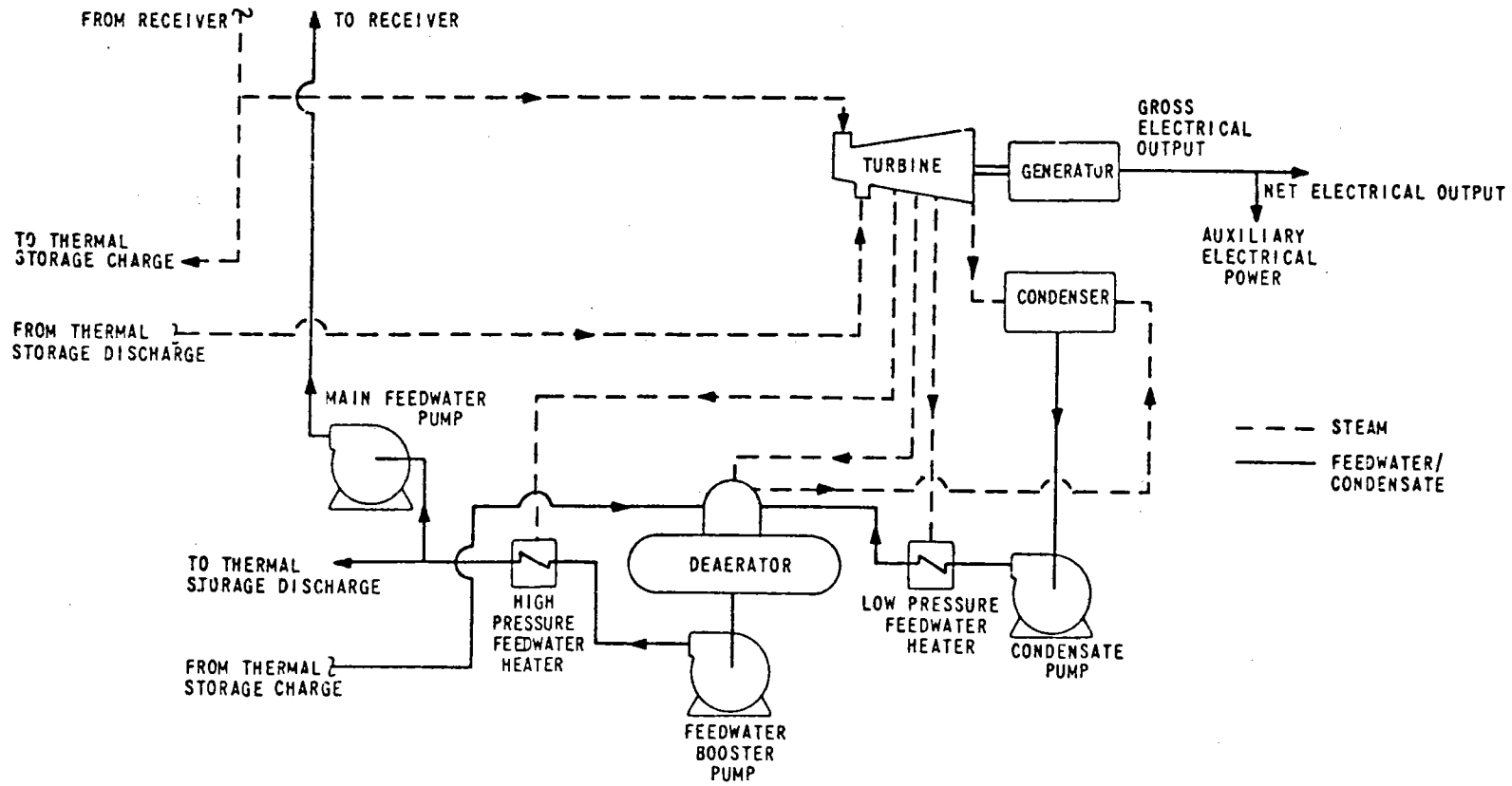


Figure 4-1. Basic Electrical Generation Subsystem Working Fluid Flow Diagram

Table 4-1. Pilot Plant Operating Modes

Mode	Receiver Generating Steam	EPGS Turbine Steam Source		Thermal Storage		
		From Receiver	From Storage	Charging	Discharging	Holding
A	X	X				X
B			X		X	
C	X	X	X		X	
D	X			X		
E	X	X		X		
F	X	X	X	X		

are variations in flow paths of this flow chart. Figures 4-2 through 4-7 illustrate EGS working fluid flow diagrams for each of the six individual operating modes.

As described in Section 2, the master controller acts as the centralized coordinator for determining the plant operating mode at any instant of time. During normal operation, for example, the master controller orchestrates the various plant subsystems through continuous reselection of operating modes. Consequently, the plant can be operating in Mode 2 (see table 4-1), switch to Mode 5 when a cloud shades the heliostat field, and then switch back to Mode 2 after the cloud passes.

The overall design of the plant master controller, which has available a variety of operating mode options, permits wide flexibility in selection of operating strategy. The plant is completely responsive to different settings of load demand and will permit the plant operator a spectrum of setting choices as how to best use the plant. For example, the operator may choose to use a 7-MW(e) setting for the entire day, permitting storage charging for times of excess steam generator power generation. Alternately, the operator may choose a type of sun-following mode, converting all available steam generator power into electrical power. For any demand setting chosen, the master controller will respond to deliver the desired electrical power while protecting plant subsystems from excessive overstressing due to overtemperatures, etc.

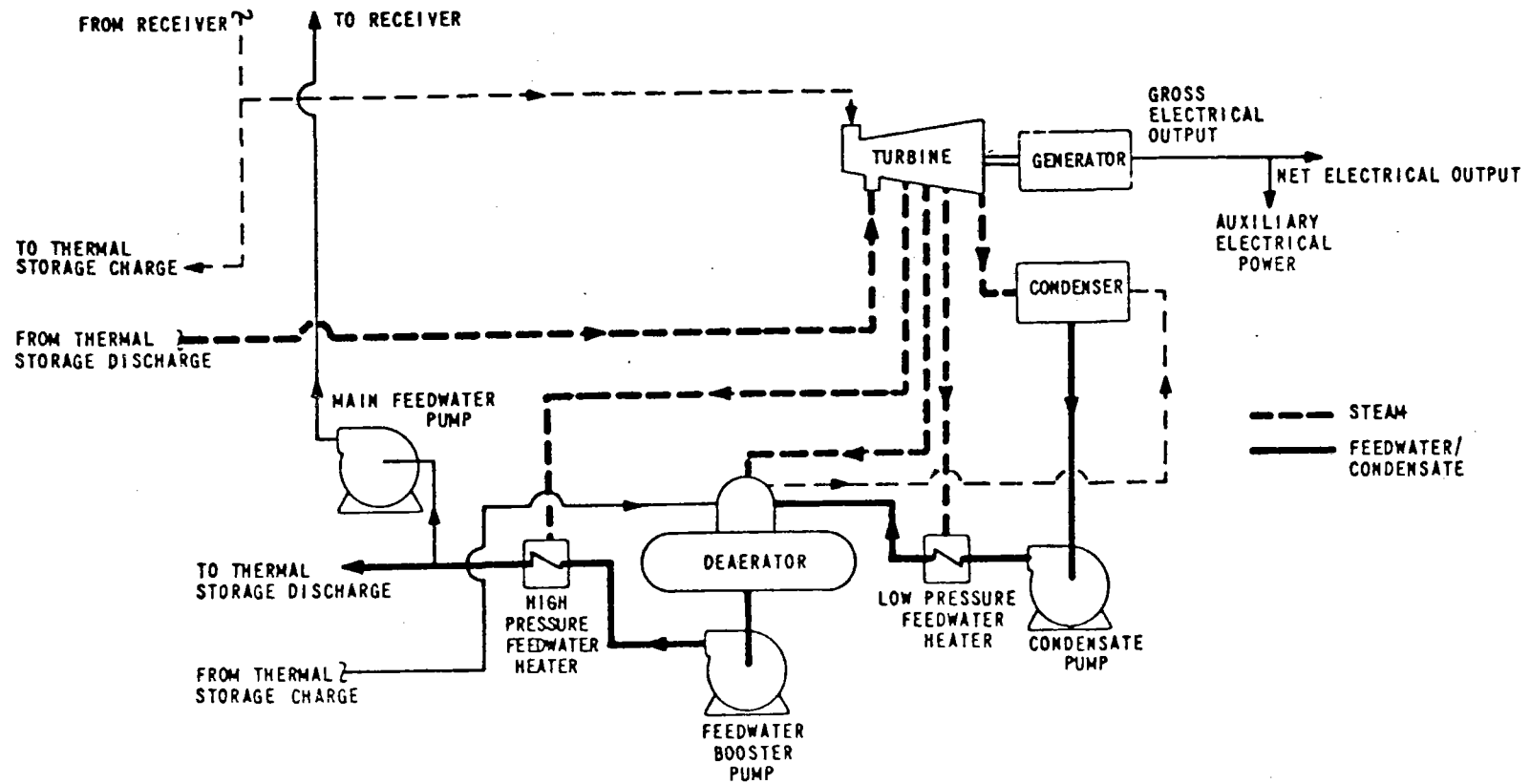
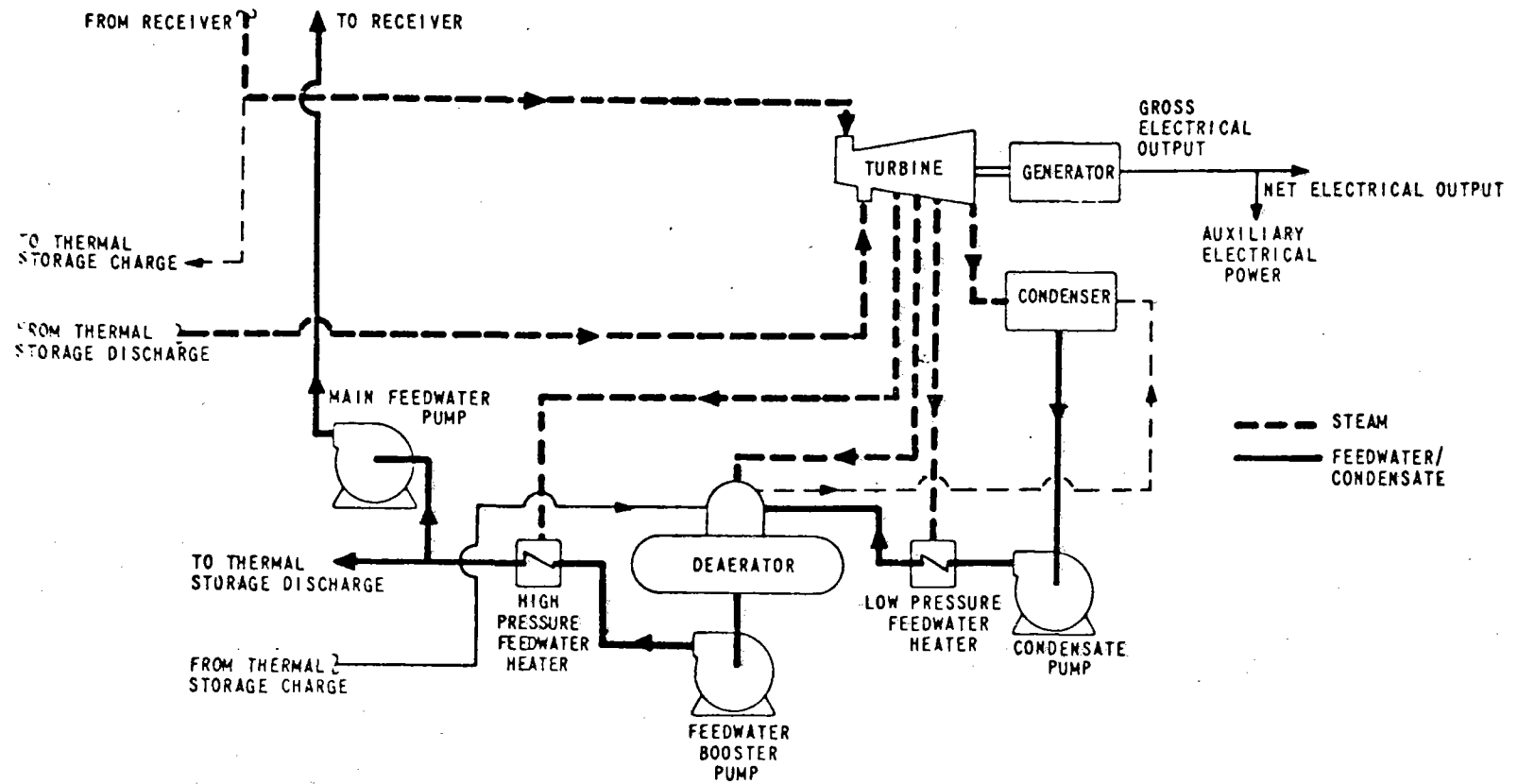


Figure 4-3. Electrical Generation Subsystem Working Fluid Flow Diagram for Operating Mode B (Receiver Off, Storage Driving Turbine)

40703-II



4-8

Figure 4-4. Electrical Generation Subsystem Working Fluid Flow Diagram for Operating Mode C (Receiver and Storage Driving Turbine)

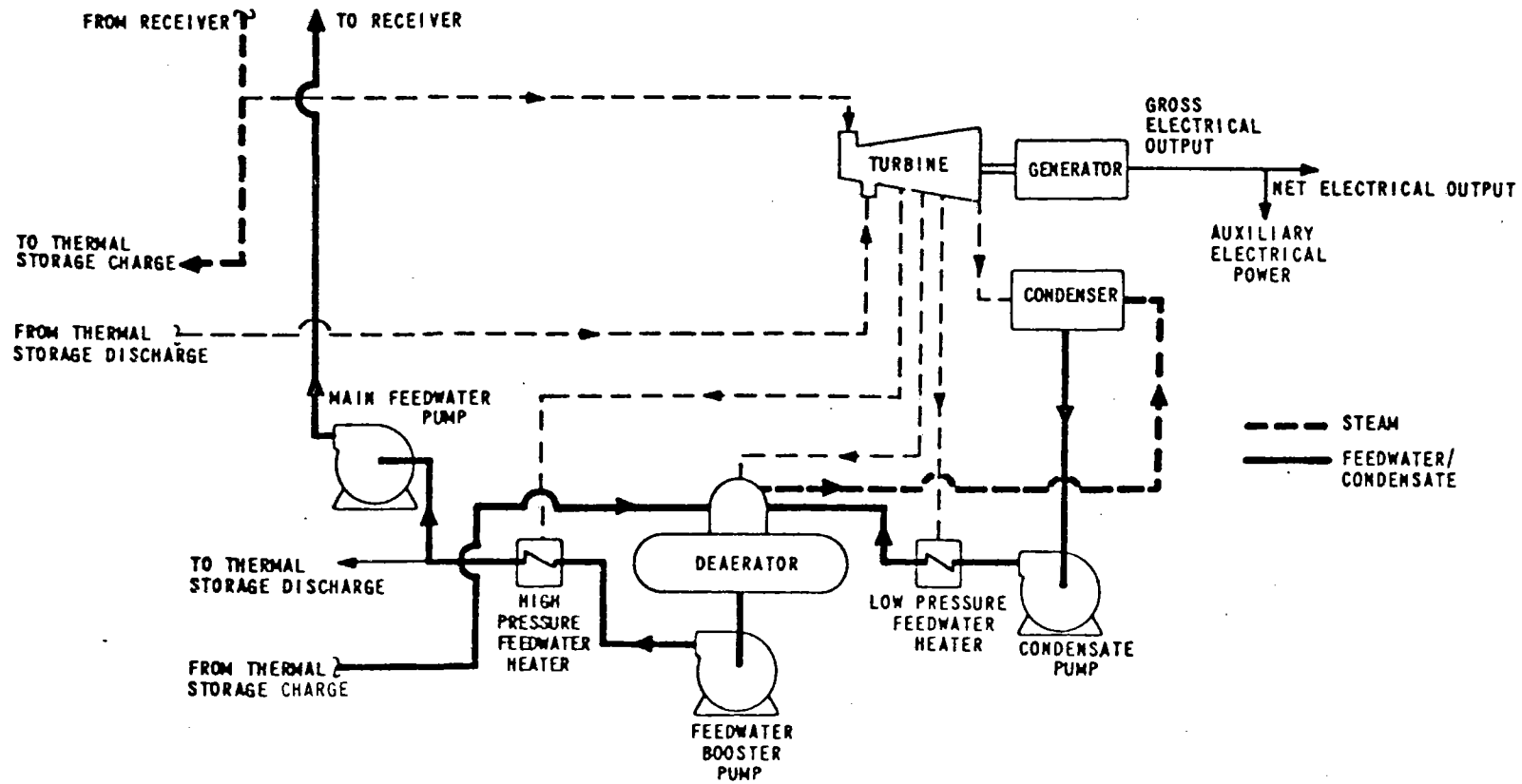


Figure 4-5. Electrical Generation Subsystem Working Fluid Flow Diagram for Operating Mode D (Receiver Charging Storage, Turbine Off)

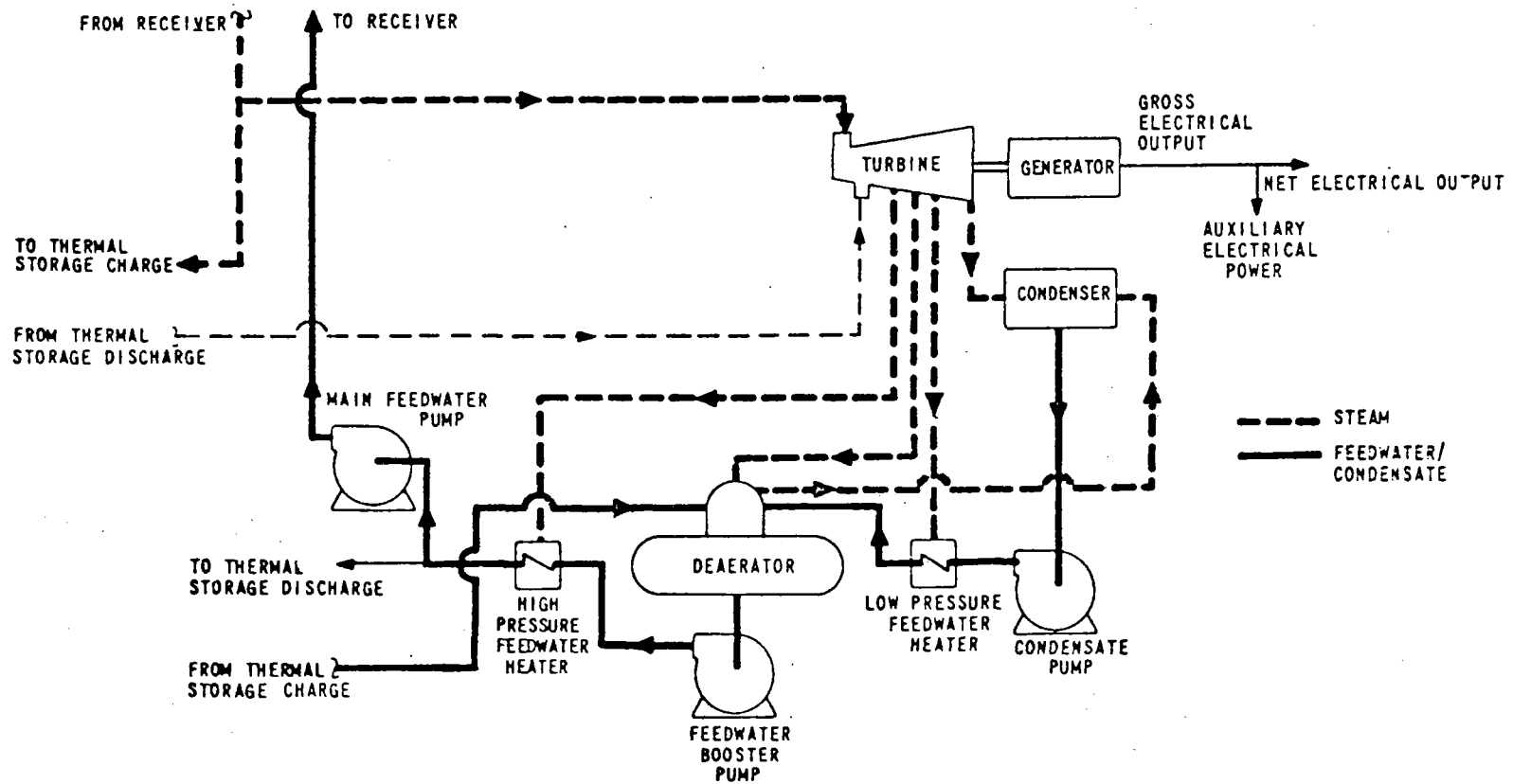


Figure 4-6. Electrical Generation Subsystem Working Fluid Flow Diagram for Operating Mode E (Receiver Driving Turbine and Charging Storage)

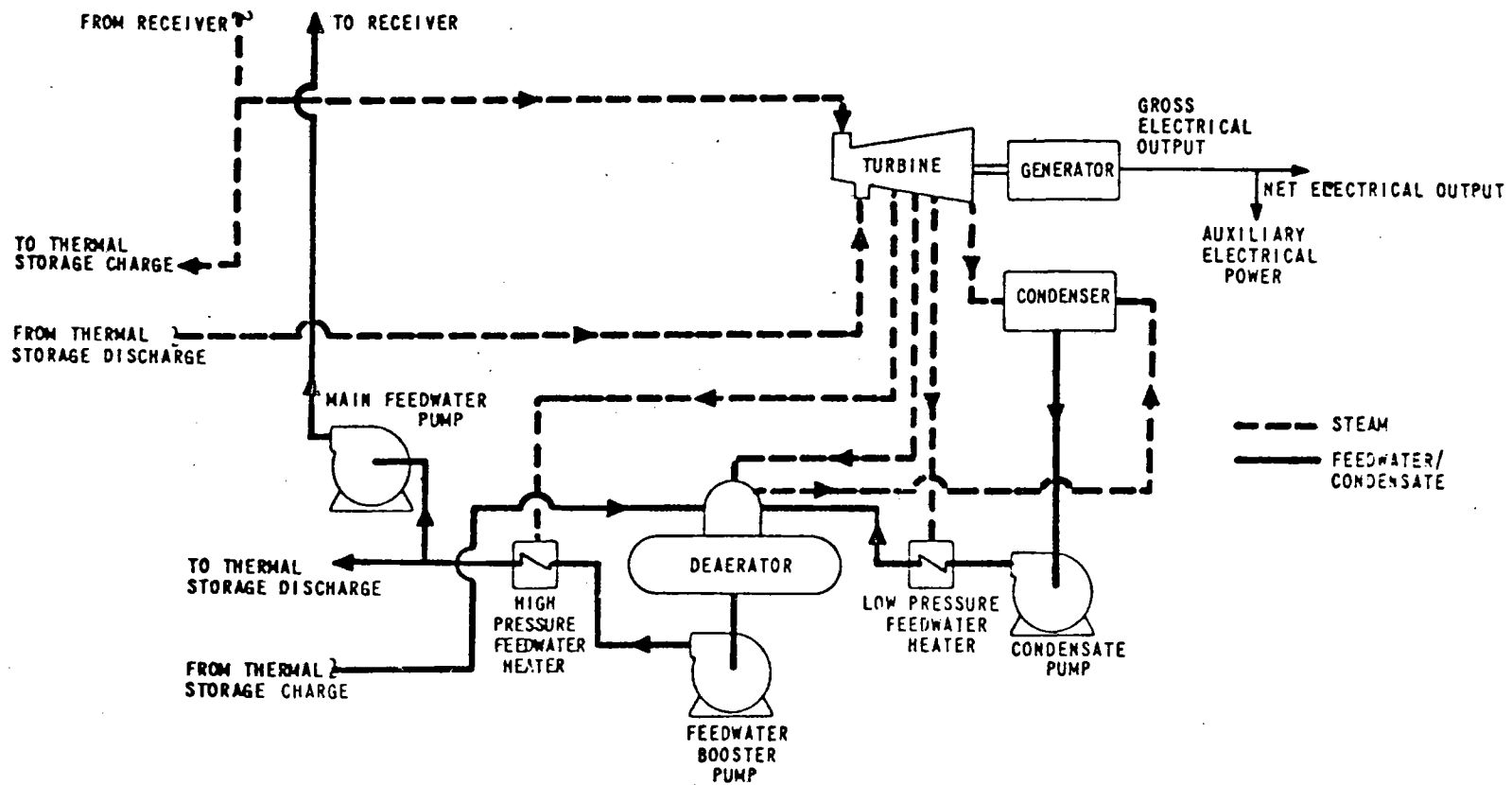


Figure 4-7. Electrical Generation Subsystem Working Fluid Flow Diagram for Operating Mode F (Receiver and Storage Driving Turbine, Storage Charging)

OPERATOR SEQUENCES FOR STARTUP AND SHUTDOWN

Pilot plant startup or shutdown operating sequences have been identified for the preliminary design. These sequences are summarized in Tables 4-2 through 4-6. These sequences are indicative of the plant operator steps required for initial plant, storage charge, or storage discharge startup, or for preparing for plant shutdown (either diurnal, extended, or emergency).

ANALYSIS OF PILOT PLANT TRANSIENT PERFORMANCE

Once in operation, the solar pilot plant will normally perform, at best, in a quasi-steady-state manner. Daily diurnal startups and shutdowns, for example, will cause expected time-dependent variations in the generated electrical output. Weather-dependent incident solar insolation will require a flexible operating strategy, and will impose a requirement for rapid responsiveness of the solar pilot plant to changing conditions. In addition, emergency conditions, such as equipment malfunctions, may require a change in plant operational modes to maintain the solar pilot plant on-line with productive output. Consequently, the ability to predict the transient behavior of the solar pilot plant is of extreme importance in establishing the feasibility of the preliminary plant design.

This section of the report summarizes expected transient solar pilot plant performance based on a computer simulation of the pilot plant dynamics. Detailed mathematical models for each of the principal solar pilot plant subsystems has been derived using available preliminary design data. These models, summarized in Section 8 (Analytical Models) , and described in

Table 4-2. Pilot Plant Cold Startup Sequence
(Following 2 to 3 Days Shutdown)

Conditions

- Steam generator at ambient temperature
- Turbine steam seals "off"
- Condenser vacuum broken
- Storage depleted

Startup Sequence

- Energize auxiliary electrical system using reserve auxiliary power transformer.
- Begin steam line warming using electric heaters about 15 hours before sunrise.
- Start circulating water, auxiliary cooling water, and compressed air systems.
- Start receiver boiler feed pumps, establish boiler drum level.
- Start receiver boiler recirculating pump.
- Uncover receiver boiler heating surface.
- Begin heating boiler, using heliostats selectively.
- Open steam line and turbine stop, drain valves as steam generation begins.
- Start steam supply to deaerator when steam pressure reaches 345 kPa (50 psia)
- Start one main recirculating pump.
- Start steam supply to turbine seals
- Start condenser vacuum pump.
- Start superheating steam.
- Roll turbine when pressure reaches 1379kPa (200 psia) and synchronize generator.
- Ramp pressure to rated condition.
- Place system under master control direction when rated conditions are reached.

Table 4-3. Pilot Plant Diurnal (or Warm) Startup Sequence

Conditions

- Steam generator cooled to about 1379 kPa/193° C (200psia/380° F)
- Turbine on sealing steam.
- Following subsystems have operated overnight:

-Auxiliary electric	-Condensate*
-Auxiliary cooling water	-Condenser vacuum
-Control air	-Storage discharge*
-Service air	-Circulating water*
-Steam line electric heat	

Startup Sequence

- Start one circulating water pump, one cooling tower fan.
- Start one condensate and one storage boiler pump.
- Start storage discharge oil and HITEC pumps.
- Operate receiver boiler feed pump to establish drum level.
- Start receiver boiler circulating pump.
- Uncover receiver heating surfaces.
- Place heliostats in "track" mode at sunrise.
- Transfer to receiver from storage discharge steam.
- Place all EGS auxiliaries in full operation for load and pressure ramp.
- Raise steam pressure/load as permitted by available energy.
- Place plant under master controller direction when rated conditions achieved.

* operated at reduced capacities overnight using small pumps, reduced speed on normal pumps, etc.

Table 4-4. Pilot Plant Storage Charge Startup Sequence

Conditions

- Storage in "hold" mode.
- Plant has been shutdown (either diurnal or extended period)

Storage Startup Sequence

- Energize plant auxiliary electrical system
- Start warming steam lines by electric heat (about 15 hours before sunrise).
- Start circulating water, auxiliary cooling water, compressed air.
- Start boiler feed pump to establish receiver boiler drum level.
- Start receiver boiler circulating pump.
- Uncover receiver heating surfaces.
- Start heating boiler, through selective heliostat useage at sunrise.
- Open steam line drain valves when steam generation begins.
- Open steam block valves to storage charge system.
- Start HITEC and oil pumps when rated pressure reached.
- Begin superheating steam.
- Place plant under master controller direction.

Table 4-5. Pilot Plant Storage Discharge Startup Sequence

Conditions

- Turbine on turning gear.
- Condenser vacuum broken
- Steam seals off.
- No solar energy available.
- All plant auxiliaries available for service.

Storage Discharge Startup Sequence

- Start one circulating water pump and one cooling tower fan.
- Start one condensate and one storage boiler feed pump.
- Start discharge oil and HITEC pumps.
- Start condenser vacuum pumps.
- Place turbine steam seals in operation.
- Roll turbine off turning gear (about 10 minutes after starting vacuum pump)
- Synchronize generator to line (about 20 minutes after roll off from turning gear)
- Raise generator to desired level.
- Place plant under master controller direction.

Table 4-6. Pilot Plant Shutdown Sequence

Diurnal Shutdown

- Reduce turbine load during final 30 minutes of operation
- Trip turbine and generator.
- Supply steam to turbine seal using storage discharge steam.
- Shutdown receiver boiler feed pump and recirculating pump.
- Close receiver aperture door.
- Place turbine on turning gear after deceleration (about 30 minutes after trip).
- Operate storage discharge, condensate, circulating water subsystems at reduced capacity.
- Continue turbine seal system.

Extended Shutdown

Same as above except:

- Remove turbine sealing steam.
- Deactivate auxiliary subsystems.
- Place turbine on turning gear if startup anticipated in 2-3 days.

Emergency Shutdown

- Engage automatically or use emergency trip push button.

detail in Book 3 of the volume, have been subsequently translated into a computer simulation program (the solar pilot plant dynamic simulation) to provide a working tool for investigation of solar pilot plant expected performance.

Using this computer program, preliminary analysis of the solar pilot plant transient performance characteristics has been completed. These performance results are summarized and analyzed in the remainder of this section. Book 3 of this volume contains supplementary computer run results of plant performance investigations, including statistical summary and Calcomp (computer-generated) plots.

Transient Analysis Study Results

A series of 16 computer simulation cases were made to produce performance results indicative of the trend of pilot plant performance. Table 4-7 is a summary of the run conditions. As shown, the 16 cases consist of;

- 1 - Plant startup
- 11 - Cloud transients
- 1 - Load demand change
- 3 - Failure effects

Because of the preliminary nature of the design process, it is cautioned that these results should not necessarily be construed as the exact performance expected from a pilot plant which has been subjected to a detailed design process. For example, greater deviations in busbar power occur in these results than might be expected to occur after the detailed design is completed. The primary reason for this situation is the design of the control system, for which no optimization of gain and other parameter values has been performed. Rather, the control system design parameters were

Table 4-7. Run Schedule for Solar Pilot Plant Dynamic Simulation
Computer Results

Run No.	Run Type	Run Time (min.)	Run Description	Cloud Data				Data Tape Hour (hr.)	
				Speed km/hr. (mph)	Length km (mi)	Approach Direction	Field Coverage		
300	Plant startup	200	Variable-pressure startup from 1379 kPa (200 psia/193°C(380°F))			N/A			
302	Cloud transient	18	Cloud from west, entering field at t = 3 minutes	11.4 (7.1)	1.8 (1.12)	W	All	25.2	
303		18	(Varying cloud speeds, lengths, field coverage)	11.4 (7.1)	1.8 (1.12)	W	N-1/2	24.2	
304		18		11.4 (7.1)	1.8 (1.12)	W	S-1/2	26.2	
305		18		21.9 (13.6)	1.8 (1.12)	W	N-1/2	31.2	
306		12		21.9 (13.6)	1.8 (1.12)	W	S-1/2	33.2	
307		12		32.9 (20.4)	1.8 (1.12)	W	All	39.2	
308		18		11.4 (7.1)	0.6 (0.42)	W	All	4.2	
309		14		32.9 (20.4)	0.6 (0.42)	W	All	18.2	
311		18		Cloud from north, entering field at t = 3 minutes	11.4 (7.1)	1.8 (1.12)	N	All	22.2
312		18		Cloud from south, entering field at t = 3 minutes	11.4 (7.1)	1.8 (1.12)	S	All	28.2
313	Load demand change	35		Starting at t = 2 minutes, ramp demand up at 4%/minute from 7 to 12 MW(e); Ramp back down starting at t = 18 minutes.	← N/A →				
314	Failure effects	7	Recirculating pump flow rate in steam generator subsystem reduced 50% at t = 2 minutes.	← N/A →					
315		7	HP heater failure; feedwater temperature goes to 149°C(300°F) at t = 2 minutes.	← N/A →					
316		7	Collector field failure - solar incident power on boiler only reduced by 20% at t = 2 minutes.	← N/A →					
317	Cloud transient	138	Plant operation for cloud corrupted day starting at hour 4643.3 on Sandia data tape.	← N/A →					

40703-II

4-19

based primarily on selection of values which first provided stability, and second provided reasonable responsiveness.

The results are, however, believed to be useful in judging relative feasibility of the pilot plant design. They may be used in judging the limiting factors in the design, if any, and the effects of these limiting factors on total plant performance.

Morning plant startup sequence -- Two relevant startup issues were identified as the focal point for investigating morning plant "hot" startup performance following overnight shutdown:

- Issue No. 1 -- How long does it take to reach the desired midday load demand?
 - Early after daybreak, direct normal solar intensity is available to the heliostats. However, the relatively poor tracking efficiencies (high cosine losses plus heliostat shading and blocking) will not permit the plant to operate at a particularly high efficiency level during these early daylight moments.
 - In addition, the various receiver metals and working fluid will have cooled overnight. Drum pressures of about 1379 kPa (200 psia) and saturation temperatures of 193°C (380°F) are anticipated when the aperture doors are first opened in the morning. Before commencing rated electrical power generation, the metal and working fluid require additional energy, necessitating time for the incident solar power to change the plant's overall energy level. The basic performance question

relates to this length of time required to achieve related steam outlet conditions.

- Issue No. 2 -- How much net busbar energy can be generated during the plant startup procedure?
 - Beginning at the time the plant startup process begins, the plant begins drawing power (approximately 2 MW(e)) from the grid to run the plant auxiliaries. The generator won't begin generating any gross power for some time later, however, as the overall energy level of the metals, and fluid must be increased to raise the superheat temperature of the outlet steam.
 - Generally, this time of first steam admission to the turbine can occur when both the steam temperature and the turbine shell temperature match. Expected startup temperature of the turbine shell is expected to be about 371°C (700°F).
 - The time integral of power needed to run plant auxiliaries, less the integral of gross generator power, determines the net busbar energy that the plant can deliver. Obviously, since the plant initially draws grid power, it operates as a relatively large energy consumer. Only after some later time will the plant be able to replace this energy and begin generating net positive busbar energy. The primary question relates to the timing of this energy consumption and replacement, and the amount of useful energy supplied during startup.

In addressing these issues, a simulated morning plant startup computer run was made (Run No. 300). The starting conditions for this run were as follows:

- Solar Intensity: 0 kW/m²
- Heliostats: Stowed
- Steam Generator:
 - Pressure - 1379 kPa (200 psia)
 - Temperature (metal and fluid) - 193°C (380°F)
 - Drum level At setpoint
- Receiver-to-Turbine Pipe Temperature: 371°C (700°F)
- Turbine:
 - Shell temperature - 371°C (700°F)
 - On turning gear/
storage steam -

The objective of the startup run was to satisfy the load demand setting (7 MW(e)) as quickly as possible.

Prior to presenting the plant startup simulation results, a review of significant events and event timing is useful to better understand the assumed variable pressure startup sequence of activities employed. A startup time line is shown in Figure 4-8. Significant event times are described for this figure as follows:

- t = 0 (Sunrise):
 - Aperture doors are opened, permitting heliostat redirected power to enter the cavity.

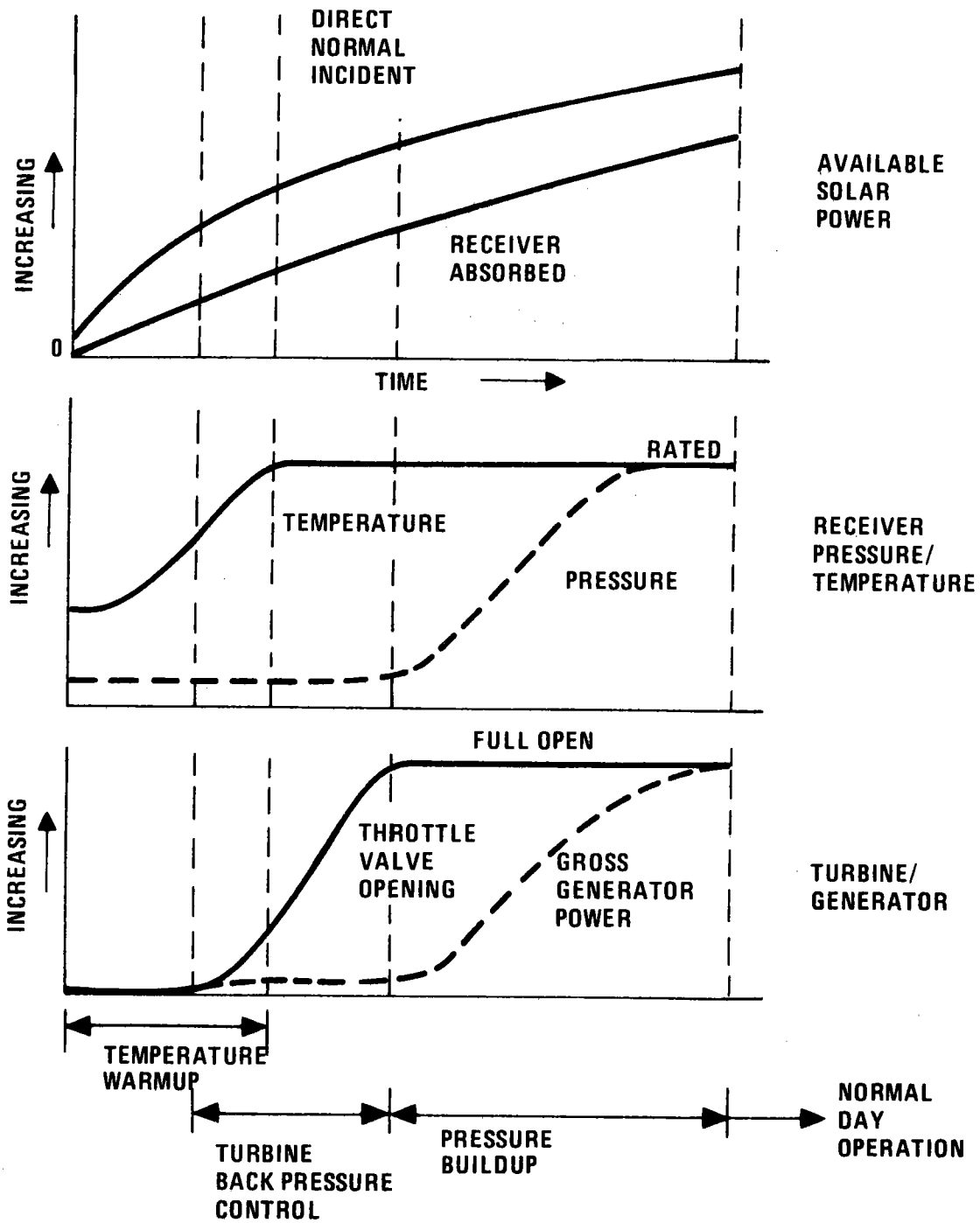


Figure 4-8. Plant Startup Time Line for Transient Analysis Studies

- Plant auxiliaries are put into operation (pumps, motors, etc.).
 - Heliostats are commanded to a "track" mode.
 - Steam valve is opened, permitting steam to flow from the receiver to condenser (i. e., bypass turbine). Pressure will be controlled to 1379 kPa (200 psia) by adjusting the bypass valve opening.
- $t = t_1$ (Steam Temperature = 371^oC (700^oF)):
 - Direct normal and receiver absorbed power levels have increased with time, causing an increase in the energy level of the steam generator metal and the working fluid.
 - As the steam temperature has now reached a point of matching the turbine shell, the throttle valve will be opened.
 - Since turbine synchronization is expected to take approximately 34 minutes, it is assumed for simulation purposes that storage admission steam has been used for this function. This expedites the plant startup procedure.
 - Pressure will remain controlled to 1379 kPa (200 psia) by using the throttle valve to control backpressure. Megawatt control is deactivated.
- $t = t_2$ (Steam Temperature at Rated Condition = 573^oC (955^oF)):
 - Temperature is at rated condition; attemperator spray will now be used to control temperature at this condition.
 - Throttle valve continues to open as the increasing energy

state of steam generator requires increased steam flow out to maintain 1379 kPa (200 psia).

- $t = t_3$ (Throttle Valve Full Open = 1.0 pu):
 - In response to controlling backpressure, the throttle valve is now fully opened.
 - At this time, the throttle valve is "pegged" at the full open position (1.0 pu) and throttle pressure is allowed to increase in response to incoming absorbed power.
- $t = t_4$ (Rated Throttle Pressure = 10.1 MPa (1465 psia)):
 - Rated pressure is reached, wherein the megawatt control function is engaged to control busbar power to the desired load demand level.
 - The plant is now ready for normal daytime operation.

A 200-minute simulated plant startup run was made using the solar pilot plant dynamic simulation. Figure 4-9 through 4-14 illustrate summarizing results of this computer run. Additional results are contained in Book 3 of this volume. In all the run results, time $t = 0$ represents the time of first available solar intensity (i. e., sunrise). The run was terminated at an arbitrary time of 200 minutes.

The assumed variation with time of direct normal intensity is shown in Figure 4-9 for this startup run. The intensity data are taken from Sandia data (Ref. 1)* beginning at $t = 3846.0$ hours, and obviously represents a cloudless morning condition. Time corresponds to a June 10 morning.

* Letter from Sandia Corporation, "Transient Operation of Central Receiver Plants," dated February 25, 1977.

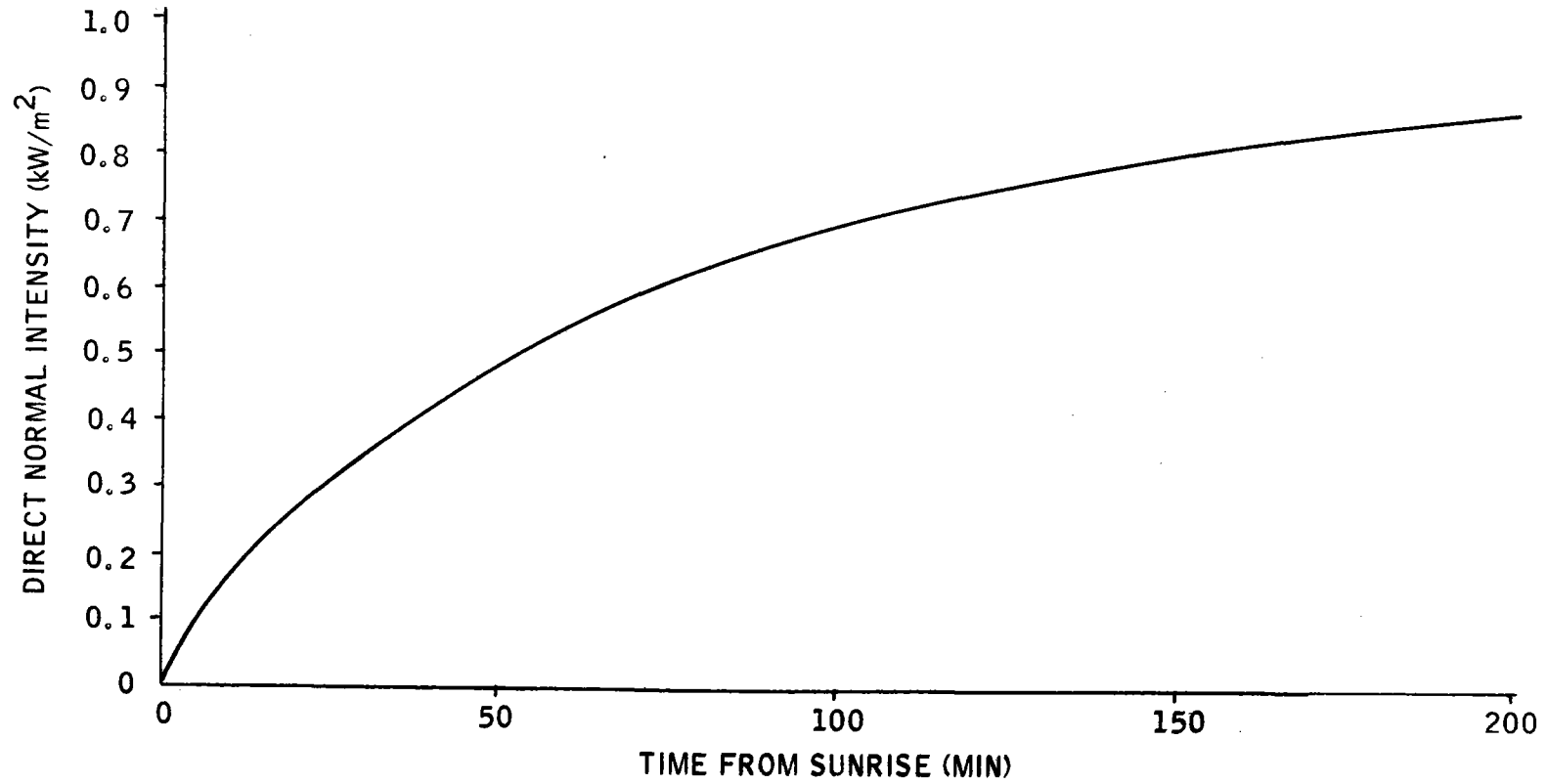


Figure 4-9. Direct Normal Intensity versus Time for Run No. 300
(Variable-Pressure Plant Startup)

Plots of parameters similar to those of the startup time line discussed previously (Figure 4-8) are plotted in Figure 4-10. Using this figure, the significant time events occurring throughout the run can be identified:

- t = 32 Minutes -- Steam temperature has risen to 371° (700° F). The throttle valve is now commanded to be opened, and will be used to control steam generator backpressure. Flow to the condenser is about 6954 kg/hr (15,331 lb/hr), or about 11.4% of maximum rated flow. At this time, about 1.1 MW(e) hours of electrical energy has been consumed by plant auxiliaries to initiate startup.
- t = 33.3 Minutes -- The throttle valve has opened to full open position (1.0 pu); at this time, it is pegged to this position. Throttle pressure is at 1.6 MPa (231 psia).
- t = 46 Minutes -- Outlet steam temperature is at rated condition of 513° C (955° F). Attemperator spray flow will now be used for steam temperature control. Throttle pressure is a 1.55 MPa (224 psia). Steam flow is 9272 kg/hr (20,441 lb/hr), or 15.2% of full rated flow. A net 1.3 MW(e) hours of electrical energy has been consumed by the plant. The generator is putting out 1.29 MW(e) gross power.
- t = 96 Minutes -- The plant has reached a zero energy balance state relative to the grid system -- it has now generated sufficient energy to just replace that consumed during startup.

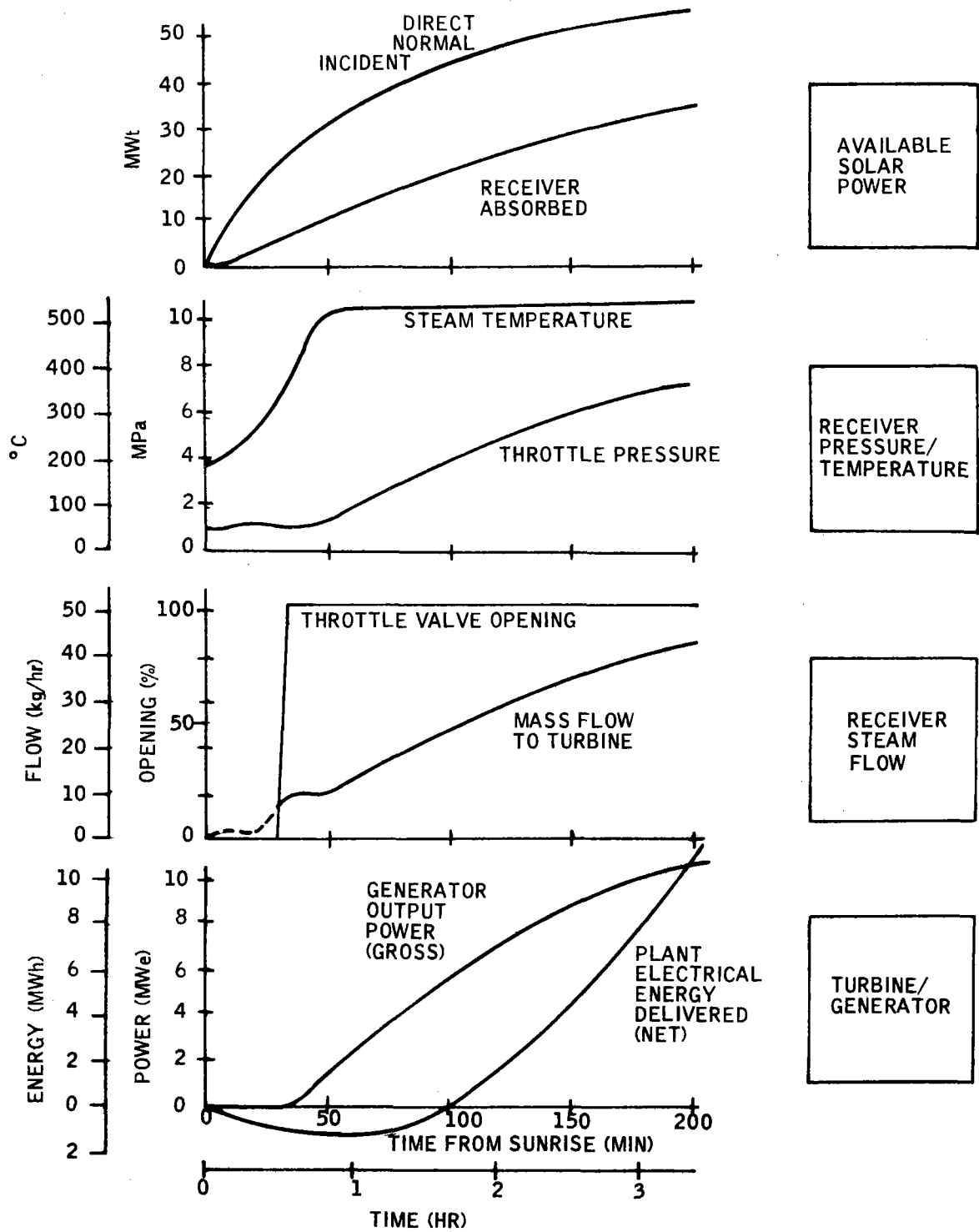


Figure 4-10. Plant Startup Results for Transient Analysis Studies

- t = 156 Minutes -- Net busbar power generated is 7.0 MW(e).
- t = 200 Minutes -- End of run. Gross power generation is 10.45 MW(e). The plant has generated 11.2 MW(e) hours net busbar energy. Throttle pressure is at 7.07 MPa (1026 psia). Steam flow is at 41,358 kg/hr (91,177 lb/hr), or 67.8 percent of maximum rated flow.

Table 4-8 lists some of the more significant power and energy statistical results from this plant startup run.

Table 4-8. Plant Startup Summary Results for Transient Analysis Studies

Source	Power Type	Avg	Max
Solar	Direct normal intensity (kW/m ²)	0.6167	0.858
	Incident available [MW(th)]	39.419	54.861
	Heliostat redirected power [MW(th)]	22.8534	39.207
	Receiver absorbed power [MW(th)]	22.4390	38.405
	Redirected to incident power	0.523	0.715
	Absorbed-to-incident ratio	0.513	0.700
Steam Generator	Net thermodynamic power out [MW(th)]	17.92	31.97
Turbine/Generator	Gross generator power [MW(e)]	5.37	10.47
Source	Energy	MWh	
	Available solar direct incident	131.1	
	Redirected solar	76.0	
	Net steam generator delivered	58.0	
	Gross turbine/generator out	17.9	
	Net plant [2 MW(e) aux. power]	11.2	

At the top of the table, various solar power terms are summarized. Maximums reflect the largest values computed during the 200-minute run time. The average value represents a time average.

An average of 0.6167 kW/m^2 direct normal intensity was available during startup, corresponding to the plotted direct normal intensity data of Figure 4-9. Incident available power, defined as the direct normal intensity times total heliostat mirror area ($63,920 \text{ m}^2 = 1598 \text{ heliostats} \times 40 \text{ m}^2/\text{heliostat}$), is indicative of total available power for perfect reflectance mirrors without tracking losses. As indicated in Table 4-8, this amounted to an average power of 39.419 MW(th). This value corresponds to the topmost curve in Figure 4-11.

Figure 4-11 also illustrates the variation with time of redirected solar power into the cavity (after heliostat tracking losses). As indicated in Table 4-7, this amounts to an average of 22.85 MW(th). On the average then, only 52.3 percent of the total available incident power is redirected into the cavity. The reason for this relatively low tracking efficiency is shown in the plot of "redirected solar power to cavity - percent of available" in Figure 4-12. At sunrise, when the sun is still very low in the horizon, the heliostat tracking efficiencies are relatively low, due primarily to heliostat blocking and shading and to cosine effects. The minimum value of this redirected to incident power ratio is 0.16 at sunrise. However, as the sun rises in the sky, this ratio increases to a maximum value of 0.715 as tracking efficiencies improve.

These results beg the question of whether it is worthwhile beginning plant operation early in the morning when the sun is just rising, since tracking

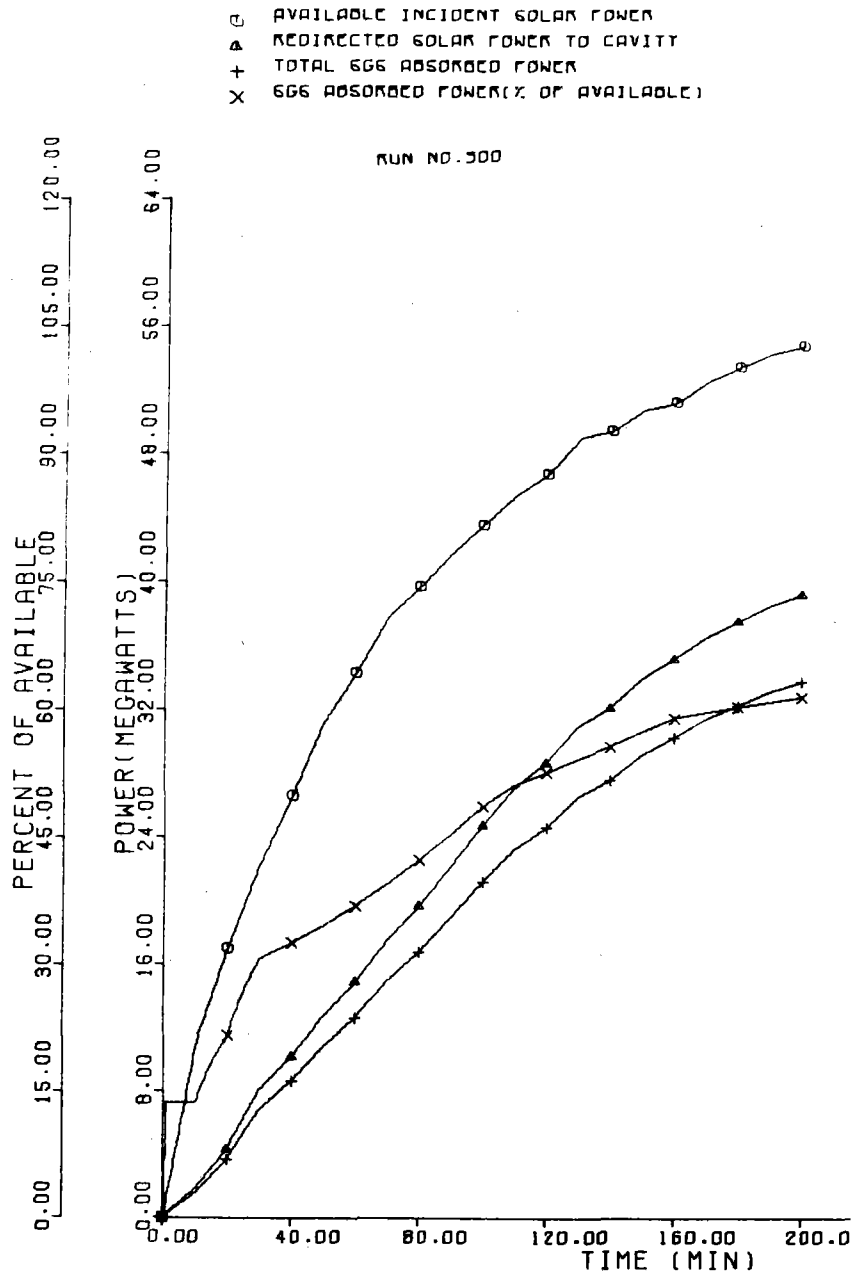


Figure 4-11. Various Solar Power Parameter Variations with Time for Variable-Pressure Startup (Run No. 300)

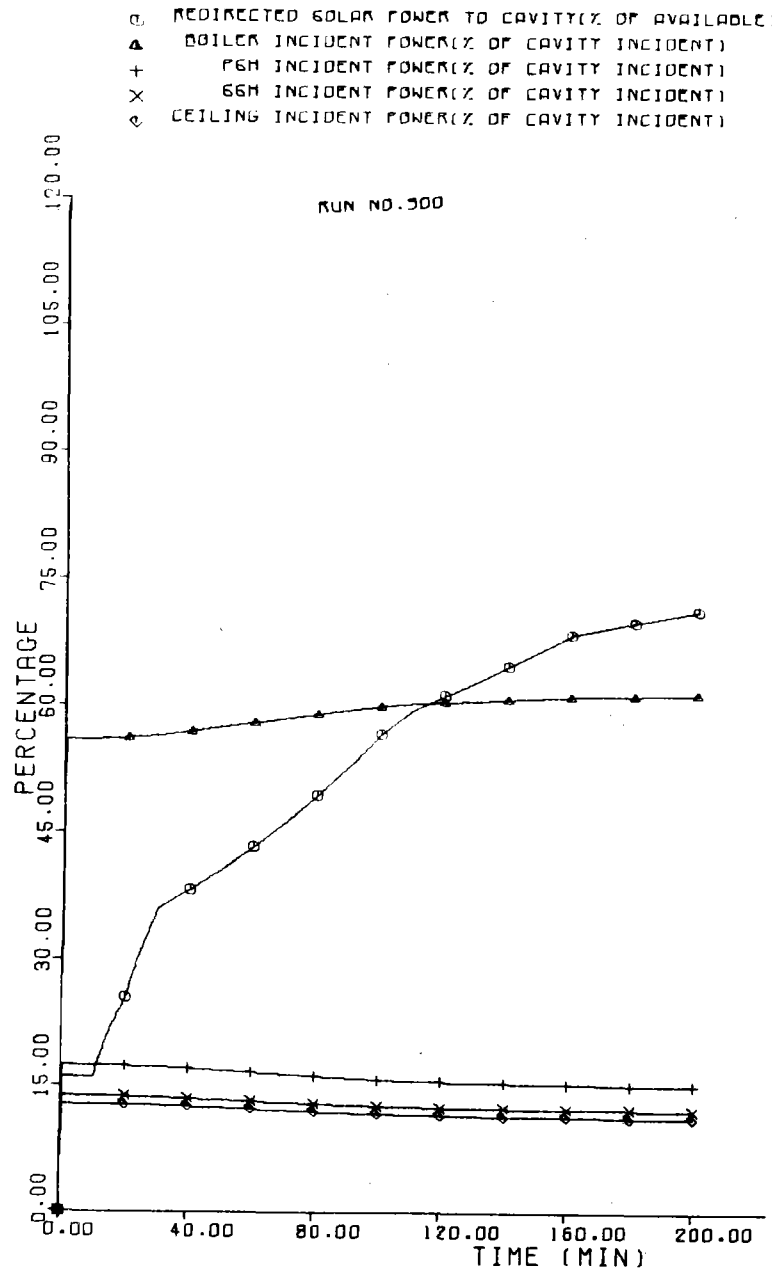


Figure 4-12. Redirected and Incident Solar Power Variations for Variable-Pressure Startup (Run No. 300)

efficiencies are so low. By waiting until 30 minutes after sunrise, for example, the redirected-to-incident power ratio curve in Figure 4-12 would almost double the tracking efficiency -- to about 0.35 -- as compared with the sunrise time. The answer to this startup time question could best be answered by a tradeoff of net plant energy gains and losses due to auxiliary power versus generated power analyses. At this time, such a tradeoff has not been performed.

Figure 4-12 shows the distribution of redirected power into the cavity among the four cavity surfaces: ceiling, primary and secondary superheaters, and boiler. As shown, the distribution balance is generally constant over time, with a slight tendency for the boiler incident power to increase in proportion to the other three cavity surfaces. On the average, over the 200-minute run, the boiler has received 60.2 percent of the redirected power. Other cavity surface values were: primary superheater (15.7 percent); secondary superheater (12.6 percent); ceiling (11.58 percent).

Figure 4-11 illustrates the variation of total absorbed power by the steam generator versus time. As indicated in Table 4-8, this amounts to an average power of 22.39 MW(th). The absorbed-to-direct normal incident power ratio is also plotted in Figure 4-11. This varies from a minimum of 15.7 percent at sunrise, when tracking efficiencies are low, to a maximum of 70 percent at time $t = 200$ minutes, when tracking efficiency has improved. The time average is 51.3 percent.

Table 4-8 indicates that the steam generator is able to produce an average of 17.92 MW(th) net output steam power. Because a portion of this energy is bypassed around the turbine to the condenser for the first 32 minutes, it

will be used primarily to heat feedwater in the system. On the average, we note that the generator gross output is 5.37 MW(e), reaching a maximum of 10.47 MW(e) at 200 minutes.

In terms of energy exchanges, Table 4-8 indicates the energy distributions among available incident, redirected, steam generator-delivered, turbine-generator output, and net plant output. As shown, the plant produces 11.2 MW(e) hours of electrical energy over 200 minutes, while the available direct normal incident energy was 131.1 MW(th) hours. Thus, the "plant efficiency" in terms of energy delivery was $11.2/131.1 = 0.085$. In terms of plant output to redirected energies, this efficiency ratio improves somewhat to $11.2/76.0 = 0.147$.

Figures 4-13 and 4-14 illustrate steam generator metal temperature rates, and metal and steam temperatures versus time. In Figure 4-13, it is noted that after 46 minutes, the outlet steam (secondary superheater, or SSH) temperature has risen to 513°C (955°F) the rated condition. At this event time, attemperator spray flow capability is initiated to maintain steam temperature at the setpoint value. The secondary superheater metal temperature also follows this nearly constant temperature trend due to the ability of the attemperated steam flow to remove heat from metal at the same rate that it is being absorbed.

As shown in Figure 4-13, the primary superheater metal and outlet steam temperatures continue to rise after the secondary superheaters stabilize. At about $t = 70$ minutes, these temperatures peak and begin to decrease for the remainder of the run, as indicated by the primary superheater metal temperature rate of change curve in Figure 4-14. The reason for this

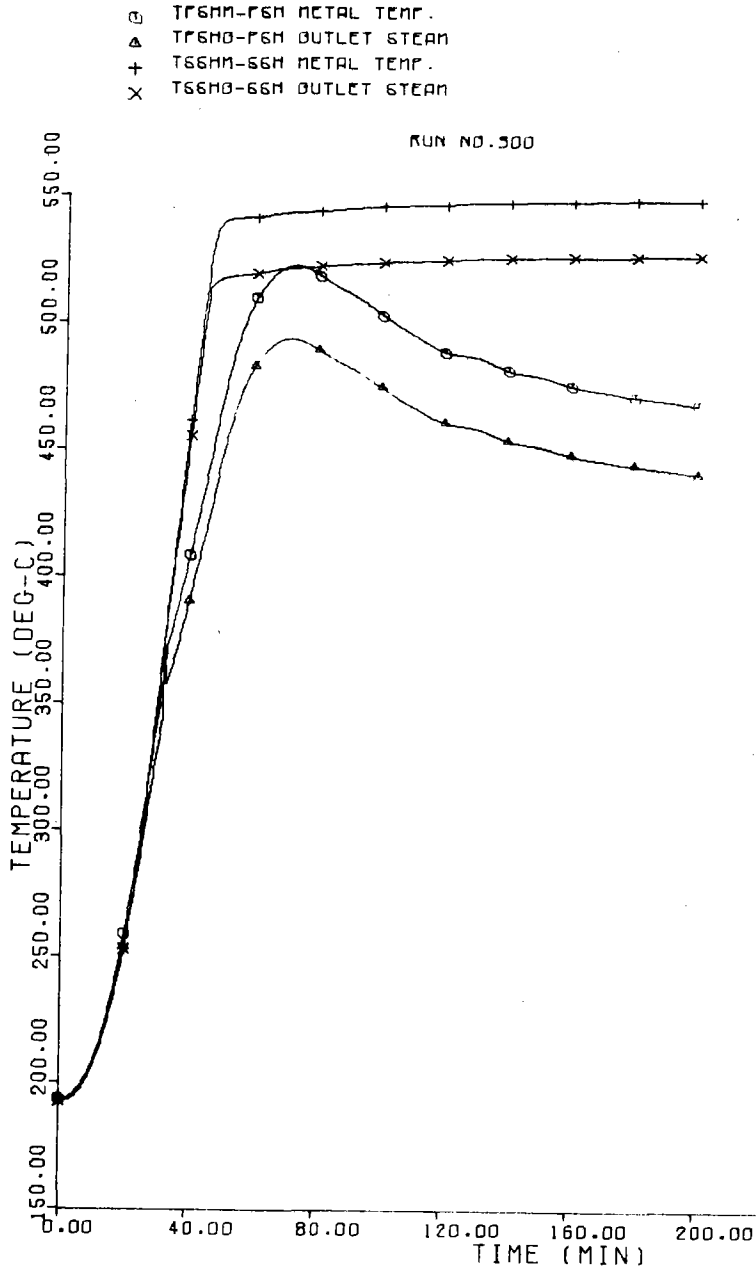


Figure 4-13. Steam Generator Metal and Steam Temperatures for Variable-Pressure Startup (Run No. 300)

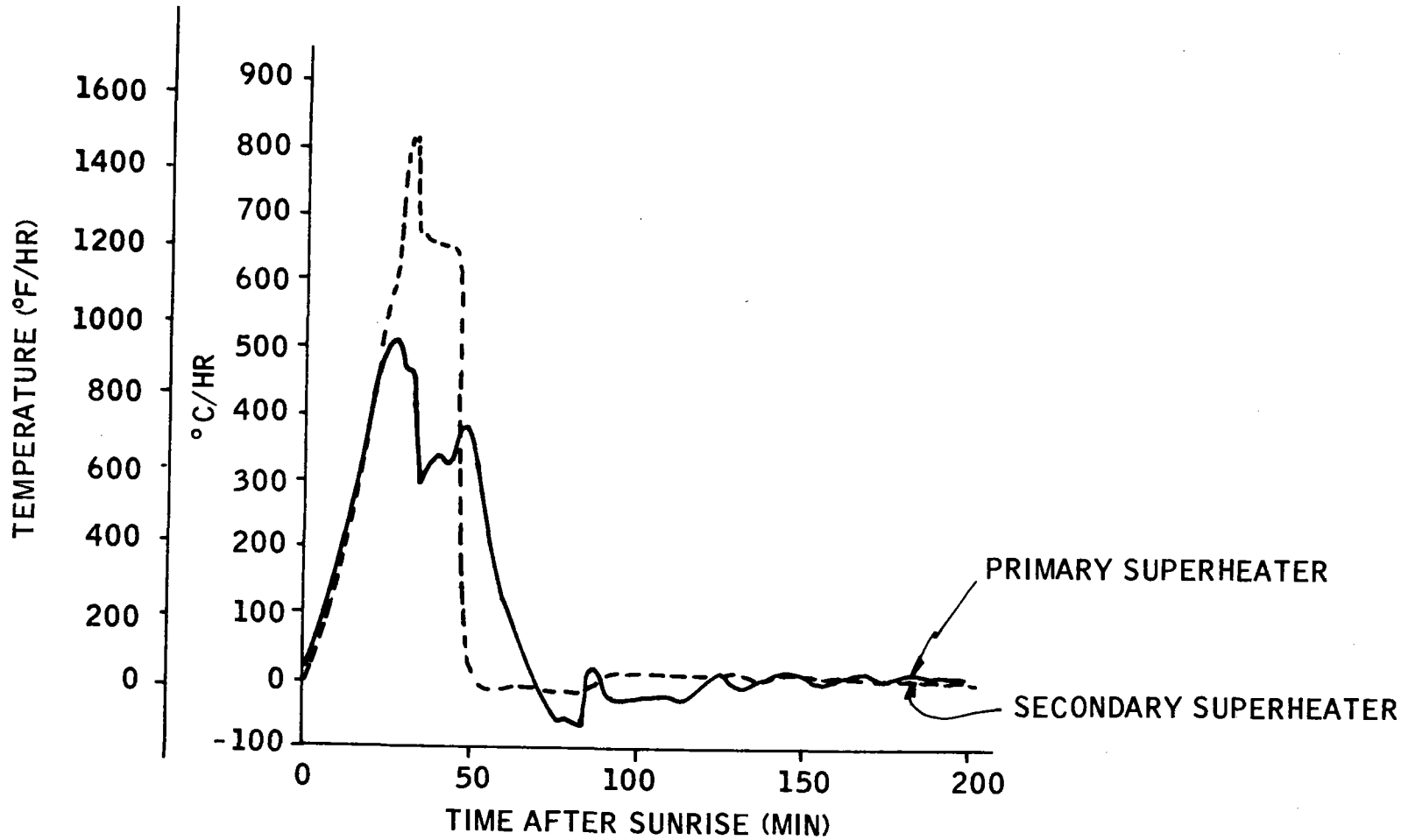


Figure 4-14. Steam Generator Metal Temperature Rates for Variable-Pressure Startup (Run No. 300)

reversal in temperature rate is that now sufficient steam flow is passing through the primary superheater to begin withdrawing heat energy at a rate faster than it is being added by the absorbed power due to solar redirected energy.

Although the plant never reaches rated throttle pressure (see Figure 4-10) after 200 minutes of time, the operating procedure could have been altered to produce this result. One method would be to ramp the throttle pressure setpoint up at some fixed ramp rate until it reaches the nominal rated setpoint. In this case, the throttle valve would have been at less than full open, thereby effectively retaining more energy within the steam generator (for pressure buildup) at the expense of less net generated busbar energy. This may be the more desirable strategy to follow for pilot plant operation, since it would permit the turbine/generator to operate closer to rated pressure/temperature conditions earlier in the day, which will improve the mechanical power conversion efficiency of the turbine.

In conclusion of the plant startup sequence results, the following observations are appropriate:

- 1) Variable-pressure startup is feasible. It permits relatively rapid use of steam flow, once the superheat temperature has reached a level matching the turbine shell. A time of about 32 minutes was required to add 100°C (320°F) superheat to match the turbine shell temperature. This time could be reduced by waiting longer after sunrise for heliostat tracking efficiency to improve. Consideration of the effect of higher metal temperature rates of change in the steam generator must be addressed, however, if the startup time is delayed.

- 2) From a net energy viewpoint, delay of plant startup until after sunrise may also be warranted. The plant requires about 1.1 MW(e) hours of electrical energy to run the plant auxiliaries until the first generator power is produced. Approximately 52 minutes were required for the plant to begin putting out any net busbar power (i. e. , when gross generator output equals plant auxiliary power). Again, a key consideration of the proper startup time is dependent on the amount of steam generator, steam piping, and turbine shell metal temperature rates of change that can be withstood without overdue stressing.
- 3) The startup procedure to reach rated pressure could have been somewhat accelerated by pegging the throttle valve at some smaller value when rated outlet steam temperature was reached, instead of pegging it at the full-open, 100 percent position. This procedure would have preserved more energy within the steam generator, instead of using it for immediate electrical power generation.
- 4) The plant was controllable and responsive throughout the startup procedure. Heliostats were not defocussed during the startup, indicating compatibility between the normal balance of absorbed power on the various superheater sections, the total amount of absorbed power, and attemperator spray control authority.

Cloud transients --

Background -- Partial or full occluding of the heliostat field will, understandably, ultimately prevent normal steam generation by the receiver. In these situations, the thermal storage system must act as the net difference supplier of steam power to the turbine for continued satisfaction of load demand.

Cloud occlusion of the field will occur unequally over the heliostat field, shading heliostats sequentially from one perimeter location, as the cloud enters the field, to another perimeter location as the cloud exits.

Figure 4-15 illustrates a downward-looking view of the circular heliostat field, with a corresponding side view of the tower and representative ground-level heliostat locations.

As shown, the far north heliostats, because they are relatively farther away from the receiver tower base, redirect solar power only onto the boiler (bottom-most) segment of the steam generator. As heliostats close in to the tower base are considered, the redirected power is incident on the segments of the steam generator higher into the cavity, namely the superheaters.

Consequently, a cloud approaching the heliostat field from the north will shade the boiler-only heliostats first, proceeding with time to shade the primary, and finally the secondary superheaters. Of course, the situation is compounded somewhat by the fact that as the cloud enters from the north in our example, only the south side of the boiler heliostats will be shaded initially. Progressively with time, the shadowing effect will proceed azimuthly as well as upwardly on the various steam generator segments.

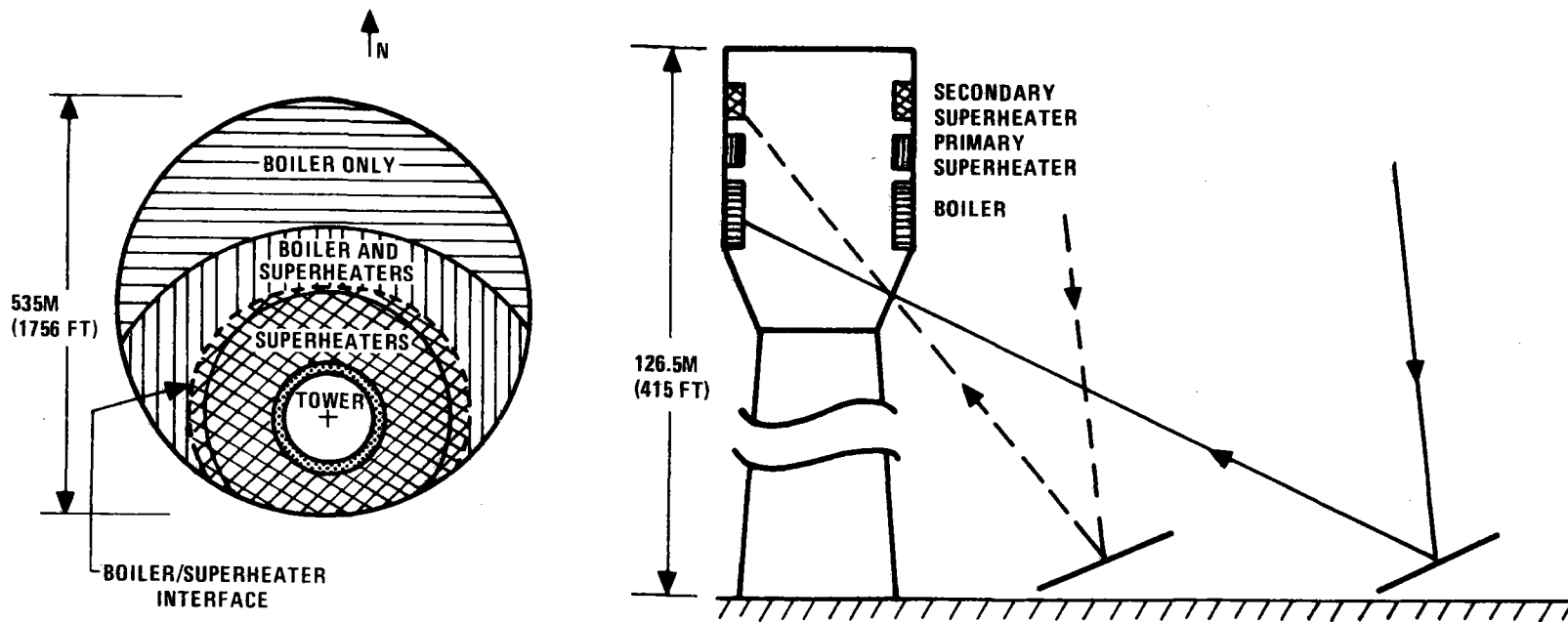


Figure 4-15. Heliostat Field Location Effects on Steam Generator for Transient Analysis Studies

Since the heliostat field is relatively large (535-m (0.33-mi) diameter), cloud shading of various heliostats can occur over a fairly long time interval. For example, a cloud 1.61-km (1-mi) long traveling 16.1 km/hr (10 mph) can require up to 0.133 hour, or 8 minutes to entirely pass through the field. Depending on the location of the heliostats in the field, time-varying shading patterns of incident, and therefore, redirected power on various portions of the steam generator, will occur. This fluctuation of power incident on the steam generator is therefore a subject of special analysis to determine the overall effects on: 1) the steam generator itself, and 2) the ability of the plant to continue smooth power generation.

One alternative, of course, is to protect the steam generator from excessive temperature stressing by redirecting heliostats in accordance with a strategy which minimizes flux distribution imbalances on the steam generator metal. At the same time, turbine/generator electrical power could be allowed to fluctuate in response to the changing ability of the steam generator to supply steam power. This would result in an electrical load supply which varied somewhat randomly with time, without a guarantee to the load dispatcher to supply energy other than "to give it what the pilot plant can deliver." Practically, this solution is undesirable, since the load dispatcher would be unable to count on the pilot plant (or later, commercial-scale plants) delivering continuous power in response to relatively fixed-load demand levels.

Thermal storage theoretically provides the means necessary to smooth this load supply in the presence of clouds occluding the field. The primary thrust of examining cloud transient phenomena is then to investigate the timely ability of the plant to coordinate the alternating supplies

of steam power from either the receiver or thermal storage.

Cloud transient issues -- Fundamentally, the primary issues for cloud transient studies for the pilot plant are twofold:

- Issue No. 1 -- Does time varying cloud occluding of the heliostat field create energy imbalance problems for the steam generator?
 - Unless cloud approach instrumentation is provided, clouds will approach the pilot plant on a random basis (speed, length, amount of heliostat field coverage), from generally random directions, occluding the heliostat field in a time-varying manner.
 - The changing conditions of heliostat shadowing will be manifested as changes in absorbed flux distributions on the steam generator sections. This will precipitate differential changes in metal temperatures at varying time rates of change, dependent on the location of the steam generator segment of interest. These resultant temperature changes, in combination with associated temperature rates of change, can shorten the expected life of the steam generator through accelerated metal fatigue effects.
 - The magnitude of the steam generator metal stress problem, for the situation where heliostats are not defocussed in response to cloud occlusion, must first be examined. Then,

if the problem warrants, means to incorporate heliostat defocussing based on sensing field or steam generator parameters can be incorporated.

- Issue No. 2 -- Can a constant load demand be continuously satisfied in the presence of clouds?
 - Reduction of absorbed power on the steam generator will necessitate reduction of outlet steam flow, and possible variations in outlet steam pressure and temperature. These factors all affect the turbine/generator's ability to continue smooth delivery of electrical power using receiver steam power.
 - Thermal storage must be capable of responding in a timely manner to offset this reduction in receiver steam power flow. The master controller must sense the appropriate system parameters indicative of the steam generators's inability to continue delivering the required steam power, and command thermal storage to deliver the makeup steam power difference to meet load demand.
 - The switchover process from receiver to storage steam involves repositioning a number of valves in the system, including repositioning steam valves for throttle and admission steam control, closing the storage charge-side steam valve, and opening oil and Hitec valves on the storage system. The ability to coordinate these various valve movements in a timely manner, and the resultant responses of various fluid flows

(steam, feedwater, oil, Hitec), will dictate the pilot plant's ability to continue continuous electrical power generation in response to load demand.

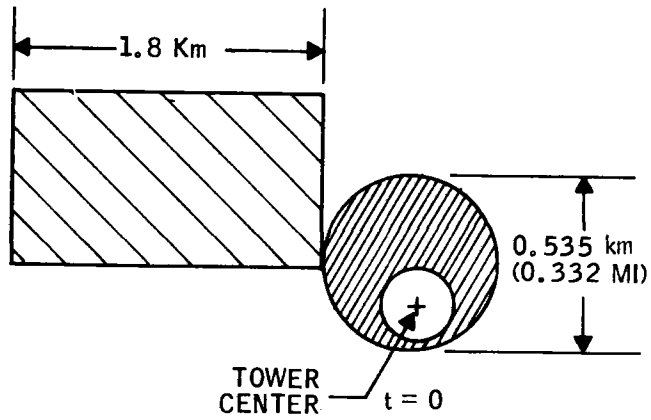
Cloud Transient Simulation Results -- A total of 11 computer simulation runs were made to investigate the effects of cloud transients. Ten of these runs were relatively short in time span (12 to 18 minutes) directed toward investigating the effects of varying cloud speeds, lengths, directions of approach, and field coverage. One run was made over a relatively long time period (2.3 hours, or 138 minutes) to investigate plant performance in response to typical Southwestern U.S. insolation characteristics as per data provided by Sandia in the referenced letter.

The approach in reviewing these results will be:

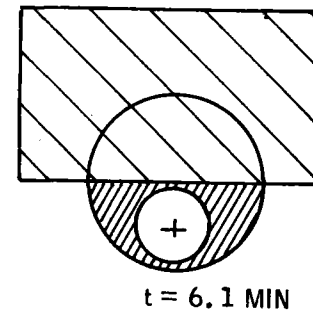
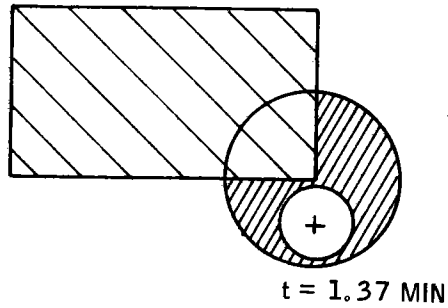
- 1) To examine a typical short-run time case of a cloud passing over the field (Run No. 303).
- 2) To review other short-run time cases in light of this previous case.
- 3) To examine results of the relatively long-run time case.

None of simulation results incorporate heliostat defocus control capability in response to measurement of direct normal intensity or steam generator metal temperature parameters.

Consider initially, a typical cloud situation as shown in Figure 4-16. In this figure, a cloud is approaching from the west at 11.4 km/hr (7.1 mph). Cloud length is 1.8 km (1.12 mi). These conditions represent



CLOUD
 DIRECTION : W → E
 SPEED : 11.4 km/HR (7.1 MPH)
 LENGTH : 1.8 km (1.12 MI)
 COVERAGE : NORTH 1/2



40703-II

4-45

Figure 4-16. Cloud Scenario for Transient Analysis Studies

the most probable scenarios for Southwestern U.S., according to the referenced Sandia letter.

As shown, the cloud will approach the field, eventually covering all the north-half heliostats. The total time between nonoccluded field coverage will be 12.2 minutes.

In this situation, the cloud will initially begin shading boiler-only heliostats as the leading edge of the cloud begins entering the western-most portion of the field. After 1.37 minutes, Figure 4-16 shows the cloud's leading edge having traversed a distance of one field radius. At this time, nearly half of the boiler-only heliostats and a significant portion of the superheater heliostats will be occluded. As the leading edge reaches the far east field perimeter ($t = 2.74$ minutes), the maximum amount of field shading will occur.

Figures 4-17 and 4-18 are CALCOMP plots of this cloud scenario. A direct normal intensity steady-state value of 0.9807 kW/m^2 is assumed in these runs, typical of midday. Figure 4-17 illustrates the reduction due to cloud occluding in average absorbed power levels, expressed as a function of maximum total design level. Initially, in steady state, the total absorbed power level (top curve) is 93.45 percent of the maximum design value.

The cloud initially begins entering the field at the west edge at $t = 3.1$ minutes; at about $t = 5.84$ minutes the cloud's leading edge has reached the field's farthest east perimeter. At this time, the maximum heliostat shading effect has occurred. The total absorbed power level has dropped from 93.5 to 45.3 percent, for a total decrease of 48.2 percent (Figure 4-17).

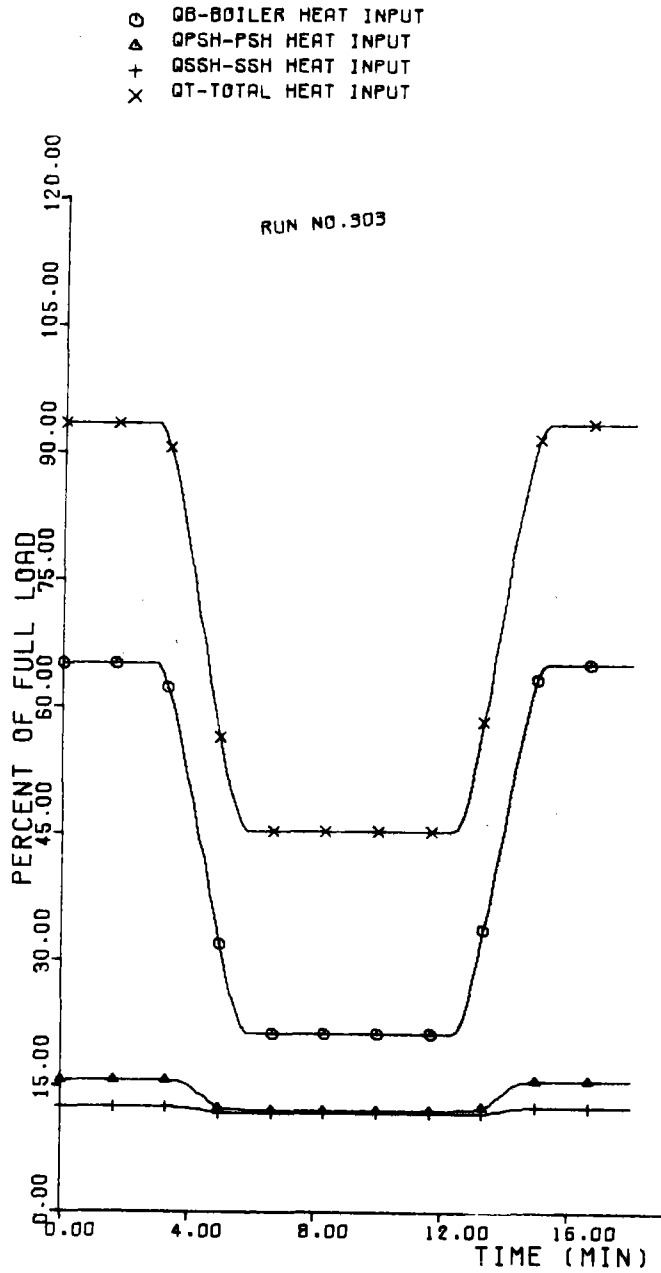


Figure 4-17. Effect of Cloud Traveling to East, Covering North Field Half on Steam Generator Subsystem Absorbed Power Levels

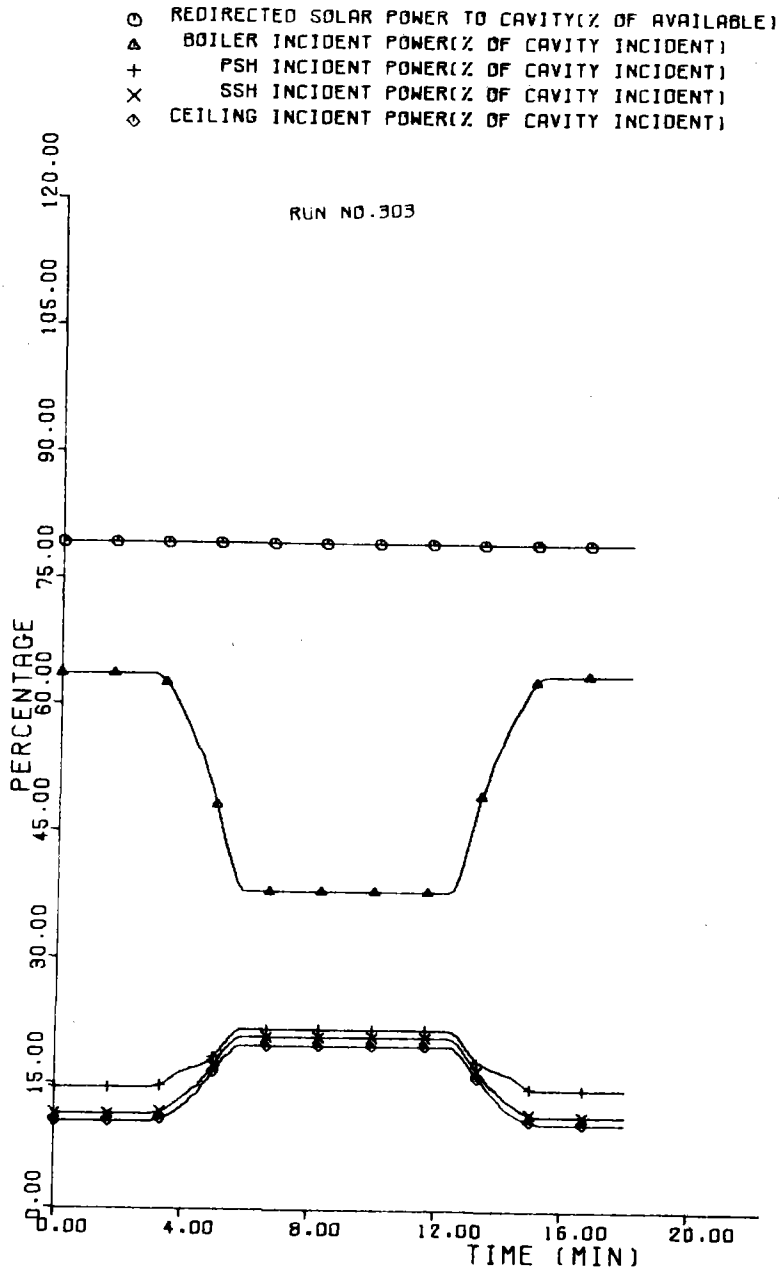


Figure 4-18. Effect of Cloud Traveling to East, Covering North Field Half on Steam Generator Sub-system Absorbed Power Ratios

As was expected, however, the effect of this total absorbed power level drop is spread disproportionately among the various steam generator segments, as Figure 4-17 indicates. The boiler power has dropped the most, for example, from 65.1 to 21.3 percent (a 43.8 percent change) while the secondary superheater power has decreased only very slightly (12.6 to 11.8 percent, or a -0.8 percent change). The primary superheater power level has dropped similarly (from 15.7 to 12.2 percent, or a -3.5 percent change). Consequently, the effect of a cloud covering only the north half has blocked the boiler heliostats to a far greater extent than either of the superheaters due to the relative field locations of the heliostats.

Figure 4-18 reiterates this effect with a plot of percentage changes in proportions of redirected solar power incident on the various cavity surfaces. The boiler experiences a net reduction in the portion of redirected power it receives, from 63.5 to 38.0 percent (-25.5 percent change); the primary superheater has a net gain in the portion of power it receives (14.5 percent, increasing to 21.6 percent - a change of + 7.1 percent); and the secondary superheater increases from 11.4 to 20.7, a +9.3 percent gain.

The time rates of change of the various absorbed power levels can be determined by taking the change in absorbed power, expressed as a percentage of maximum design level, divided by time. For the cloud entering the field results shown in Figure 4-17, these rates of change values are:

- Boiler: - 28.65 percent/minute
- Primary superheater: -4.33 percent/minute

- Secondary superheater: -0.98 percent/minute
- Total: -33.96 percent/minute

Thus, as we might expect, since absorbed power level changes occur over roughly the same time interval, the boiler experiences the largest rate of change, as well as the most absolute level of change; the secondary superheater experiences the least absolute change and also rate of change.

Figure 4-19 illustrates additional solar parameters plotted versus time:

- Available incident solar power (direct normal intensity times heliostat mirror area), in MW(th)
- Redirected solar power into cavity, after tracking efficiency corrections, in MW(th)
- Total steam generator absorbed power, in MW(e)
- Steam generator absorbed power as a percentage of available incident power

Effects of absorbed power changes upon various steam generator parameters are shown in Figures 4-20 and 4-21. Figure 4-20 shows the resultant primary and secondary superheater time rates of change and drum level change (from setpoint). Figure 4-21 shows the outlet steam and average metal temperatures for the two superheaters. Average, maximum, and minimum values of the temperature parameters noted during the entire 18-minute computer run time are noted in Table 4-9.

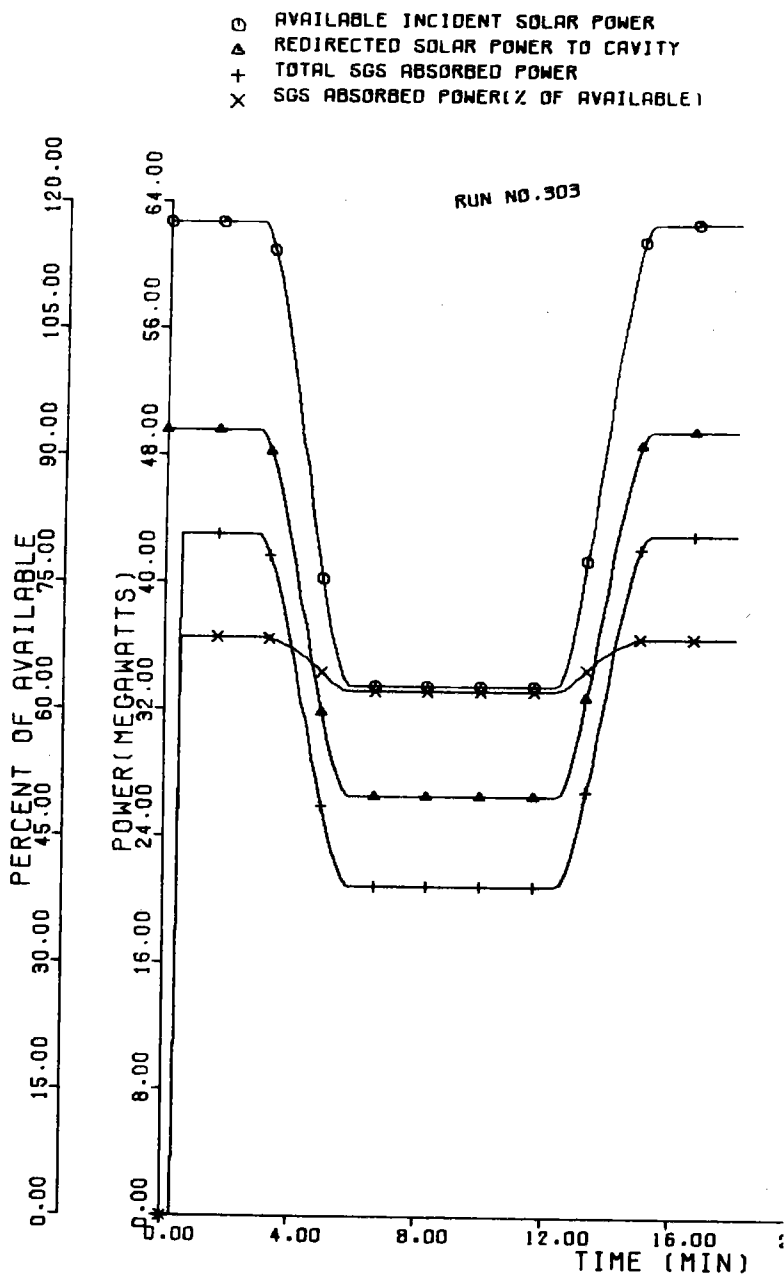


Figure 4-19. Effect of Cloud Traveling to East, Covering North Field Half on Various Solar Power Parameters

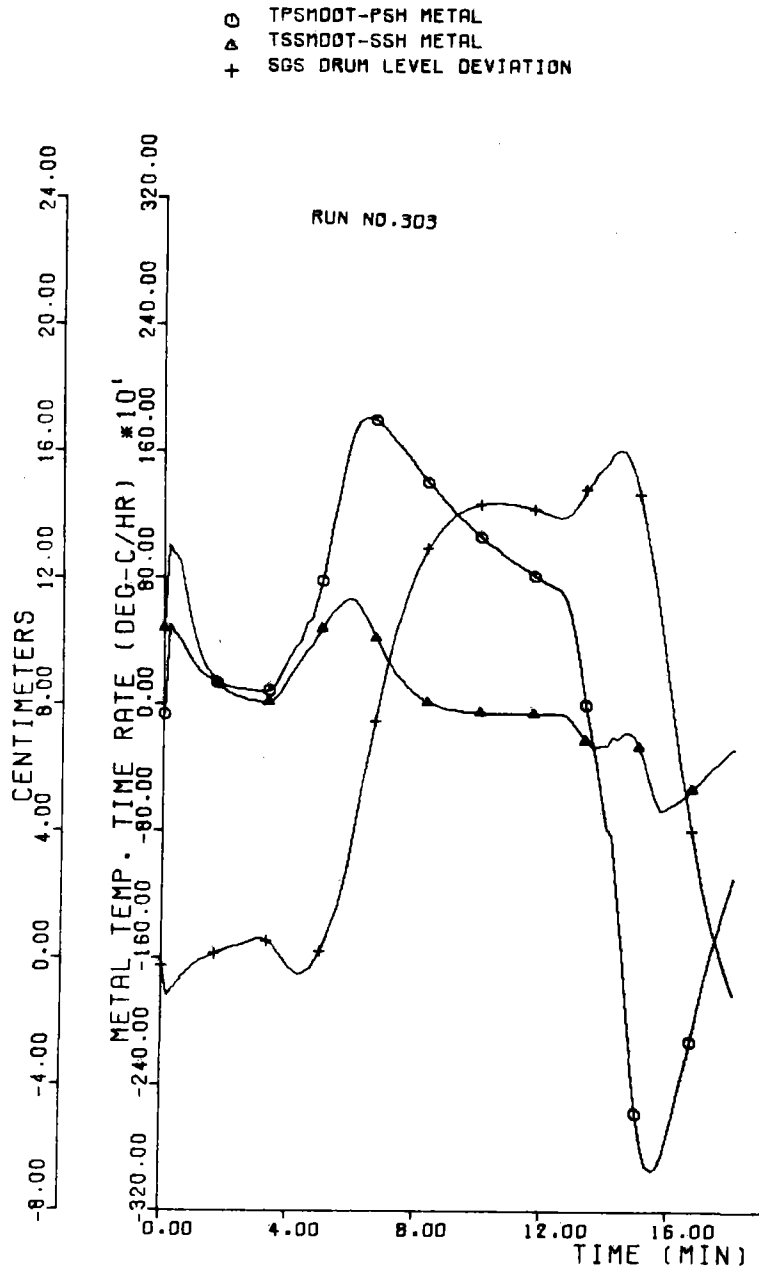


Figure 4-20. Effect of Cloud Traveling to East, Covering North Field Half on Steam Generator Subsystem Metal Temperature Rates and Drum Level

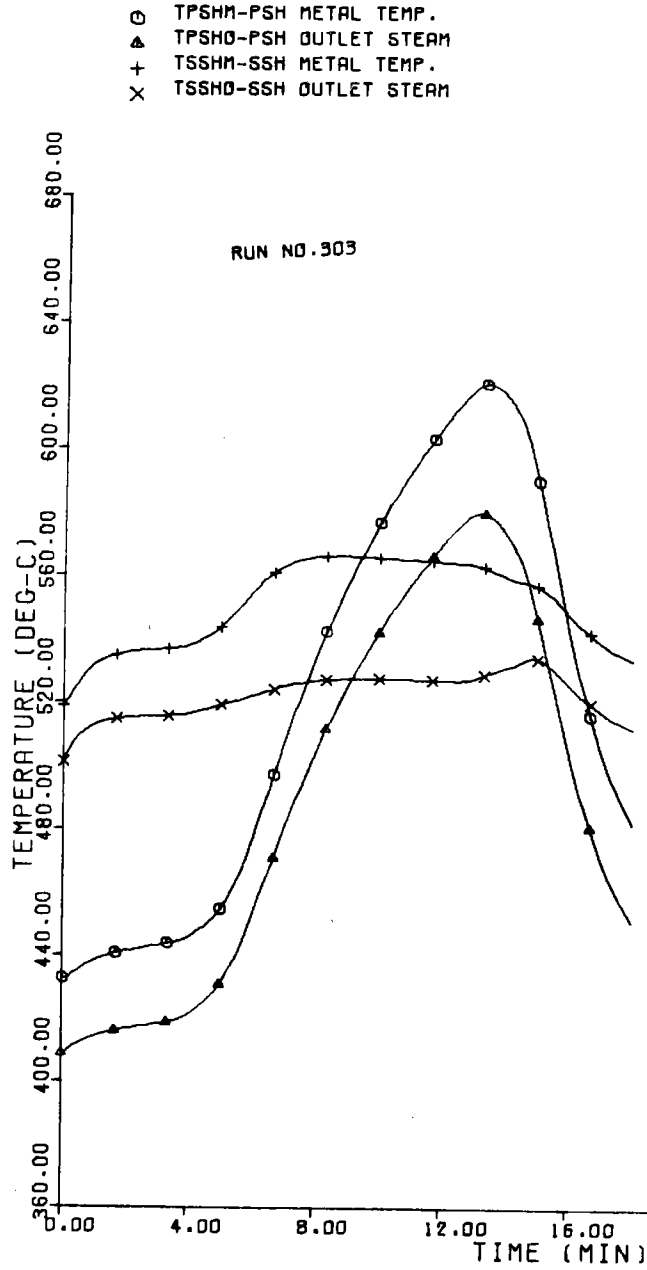


Figure 4-21. Effect of Cloud Traveling to East, Covering North Field Half on Steam Generator Subsystem Steam and Metal Temperatures

Table 4-9. Various Statistics for Metal and Steam Temperatures for Cloud Transient Run No. 303

Parameter	Average	Maximum	Minimum
Primary Superheater: <ul style="list-style-type: none"> ● Metal: <ul style="list-style-type: none"> - Temperature rate of change °C/hr 141.3 1817.4 -2944.0 (°F/hr) (286.4) (3303.3) (-5267.3) - Temperature °C 525.4 620.8 435.7 (°F) (977.7) (1149.4) (816.2) ● Steam Temperature: <ul style="list-style-type: none"> °C 493.3 580.0 411.8 (°F) (919.9) (1076.0) (773.3) 			
Secondary Superheater: <ul style="list-style-type: none"> ● Metal: <ul style="list-style-type: none"> - Temperature rate of change °C/hr 7.11 700 -665.4 (°F/hr) (44.8) (1292.0) (-1165.8) - Temperature °C 552.2 566.2 526.3 (°F) (1026.0) (1051.2) (979.4) ● Steam Temperature: <ul style="list-style-type: none"> °C 523.1 534.3 509.6 (°F) (973.6) (993.8) (949.2) 			

Referring to Figure 4-21, as the cloud first enters the field, metal and steam temperatures begin to rise as they receive a disproportionately greater amount of incident (and absorbed) power. In addition, as shown later in the results, cooling steam flow will be reduced to preserve pressure energy within the steam generator. Primarily, it is this latter affect that is manifested as an increase in the superheater metal temperatures.

The summarizing results of Table 4-9 indicate comparatively large metal temperature changes and rates of change, especially for the primary superheater. The primary superheater change in metal temperature is shown in Figure 4-21 to be about 180°C (356°F) as the cloud is leaving the field ($t = 14$ minutes). A minimum rate of change value of $-2944.0^{\circ}\text{C/hr}$ ($-5267.3^{\circ}\text{F/hr}$) is noted as the cloud leaves the field at about $t = 15.5$ minutes.

This rate of change value is greater for the primary than the secondary superheater primarily because the secondary superheater has additional cooling steam flowing through it due to the added attemperator (located between the two superheaters) steam flow effect. This attemperator flow, shown in Figure 4-22, amounts to about 8000 kg/hr ($17,637\text{ lb/hr}$) as the cloud is exiting the field, adding almost 50 percent more total flow through the secondary superheater. (Flow through the primary superheater, in Figure 4-22, is equivalent to the drum outlet steam flow).

The secondary superheater temperature, which has an advantage of the attemperator spray flow cooling effect, is shown in Figure 4-21 to have a more moderate rise in metal temperature -- approximately 30°C (86°F). Corresponding metal temperature rates are also less -- peaking at 700°C/hr (1292°F/hr) -- as the cloud enters the field.

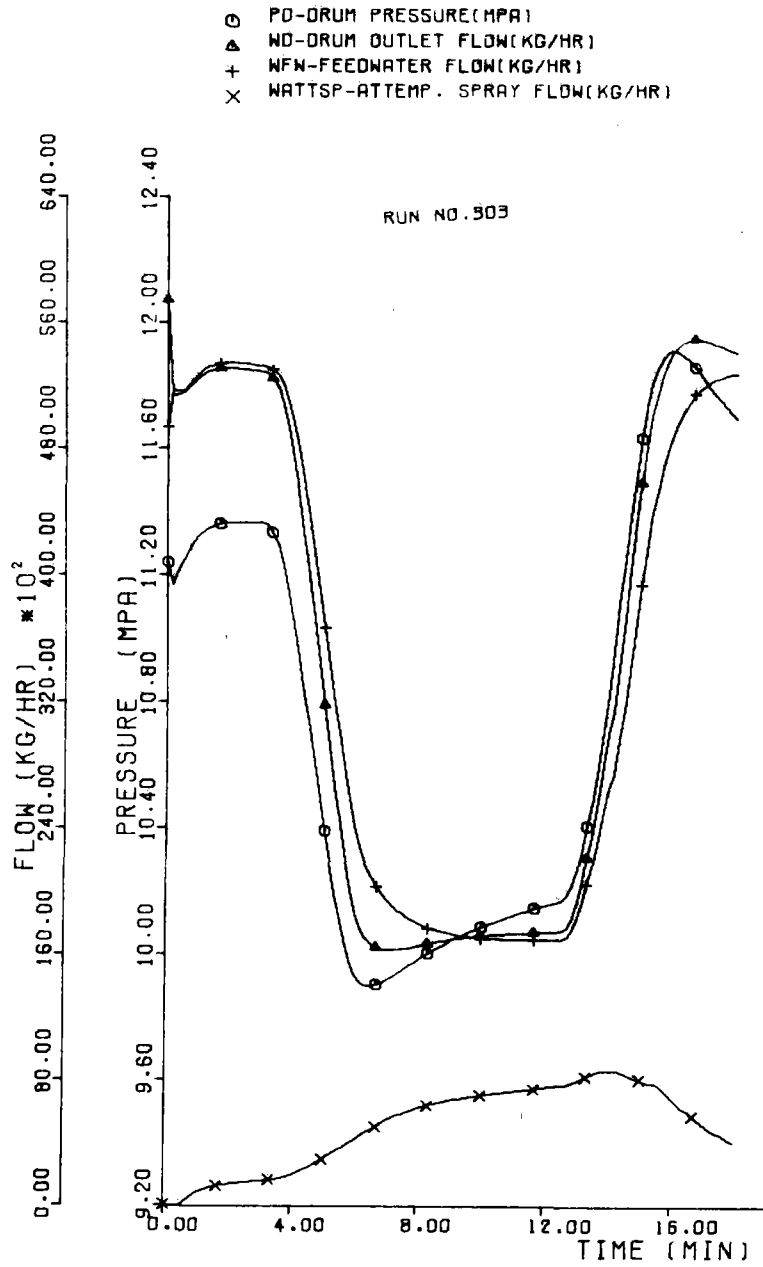


Figure 4-22. Effect of Cloud Traveling to East, Covering North Field Half on Various Steam Generator Subsystem Flow and Pressure Parameters

The exact impact of the metal temperature variations on steam generator life has not been determined at this time. Further details on the frequency and characteristics of cloud cover would be required. In addition, the effect of treating the superheaters as single nodes would need to be factored into such an analysis. From a preliminary design viewpoint, however, it would appear that the observed metal temperatures changes and metal temperature rates of changes are probably greater than desired, so that some type of heliostat defocus feedback control scheme will be required.

Now turning from the steam generator to the remainder of the plant operation for cloud transient Run No. 303, the primary variables of interest are plotted in Figure 4-23. The topmost plot again shows total steam generator absorbed power versus time. Generated busbar power is also shown, along with various steam mass flow parameters, in the other curves.

As Figure 4-23 indicates, there is a tendency for the busbar power to dip by about 0.7 MW(e) or 10 percent, shortly after the cloud enters the field. Similarly, a rise of about half this amount is manifested as the cloud again leaves the field. These fluctuations are due primarily to nonoptimized gain parameters in the master controller, since there were no interent subsystem limitations (i. e., valve rate limits, etc.) noted in analyzing the run. In summary, it is believed that with additional design efforts on the master controller, the busbar power could have been maintained nearly constant at 7 MW(e) throughout the run.

The interplay between various steam flows in the system required to provide continuous busbar power during cloud transients is illustrated in

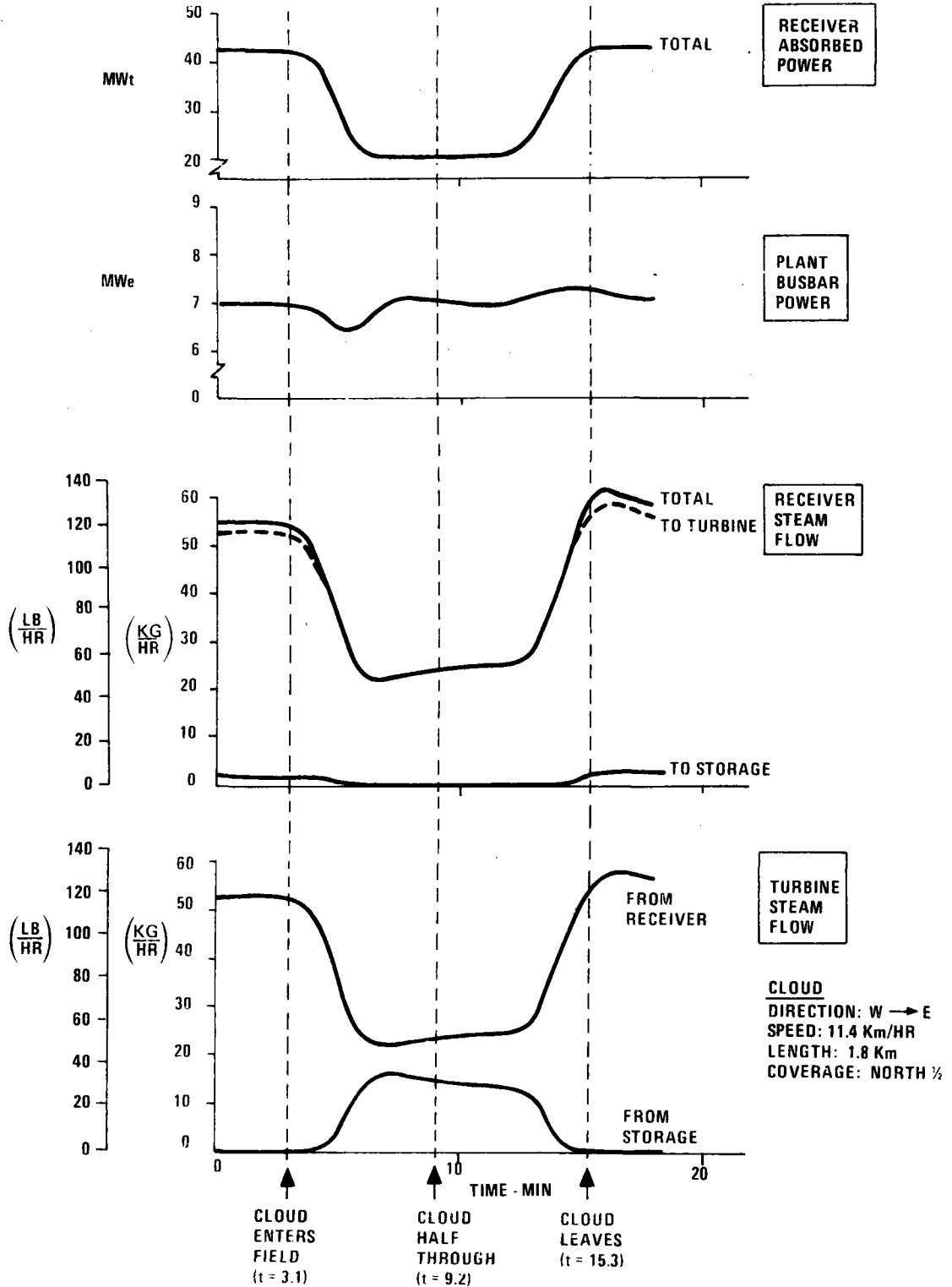


Figure 4-23. Cloud Transient Effects on Plant for Transient Analysis Studies

the two bottom curves of Figure 4-23. As shown, total receiver steam flow is reduced by more than 50 percent when the cloud is midway through the field. This was necessary to conserve pressure energy within the steam generator as determined by the master controller.

As a first priority, the master controller reduced flow to charge storage. Then, as the steam generator was still not capable of supplying sufficient steam power to the turbine to meet demand, discharge steam flow from storage was requested. This is shown most vividly in the bottom plot of Figure 4-23, where storage discharge steam flow is increasing in near-time synchronization with the decrease in receiver steam.

Additional illustrations of the switchover process from receiver to storage steam to the turbine are shown in Figure 4-24. High-pressure (receiver) steam flow, along with the governor valve opening area, are shown in the two topmost curves. Corresponding variables for the admission port are shown in the remaining two curves. As expected, the admission valve is initially closed, opens to the 25 to 30 percent level during maximum cloud occlusion, and returns to a shutoff position after the cloud passes from the field.

Figure 4-25 illustrates the throttle pressure variation with time for this cloud transient run. The average throttle pressure is 9.96 MPa (1444 psia), with maximum variations of +4.1/-2.9 percent from this average. Steam generator pressure, prior to piping pressure drops to the turbine, is also shown. These relatively small pressure deviations are considered indicative of an overall well-balanced design.

Various parameters associated with the master controller are shown in Figure 4-26. The two primary control error signals -- integrated pressure

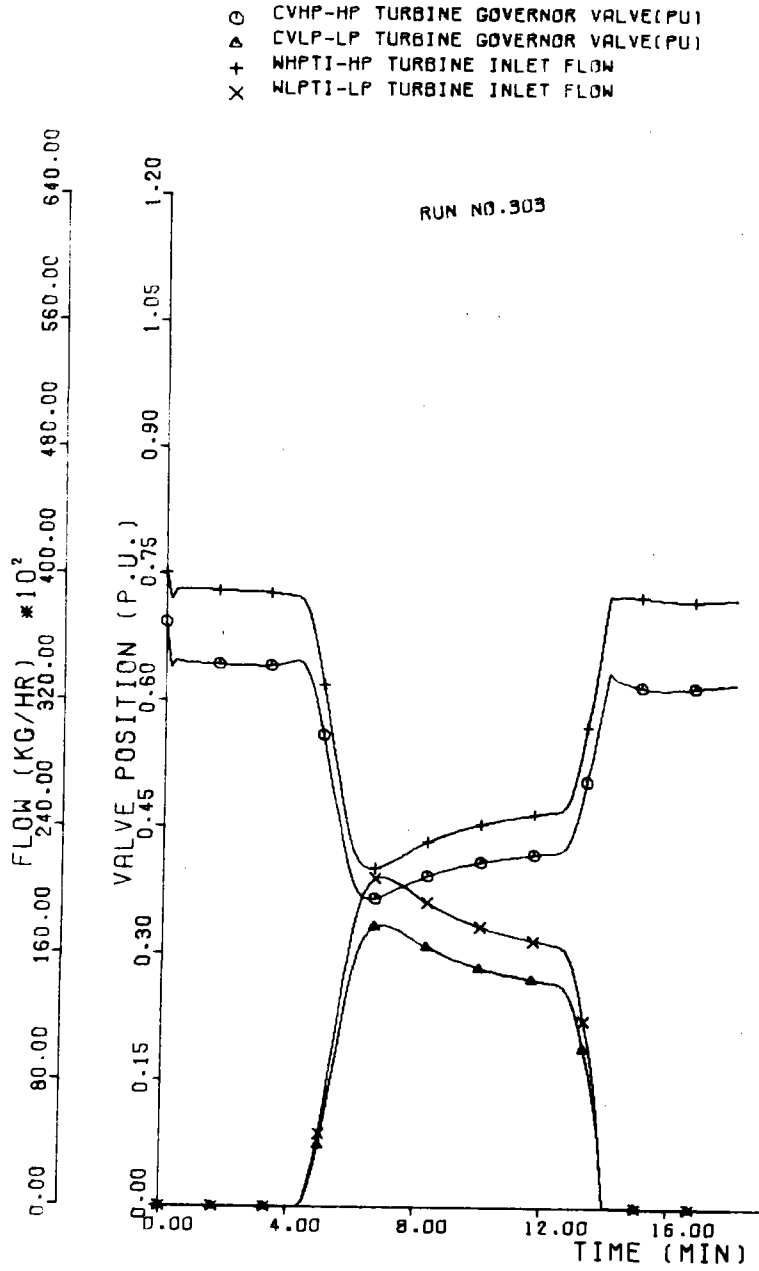


Figure 4-24. Turbine Valve and Inlet Flow Parameters for Cloud Transient Run No. 303

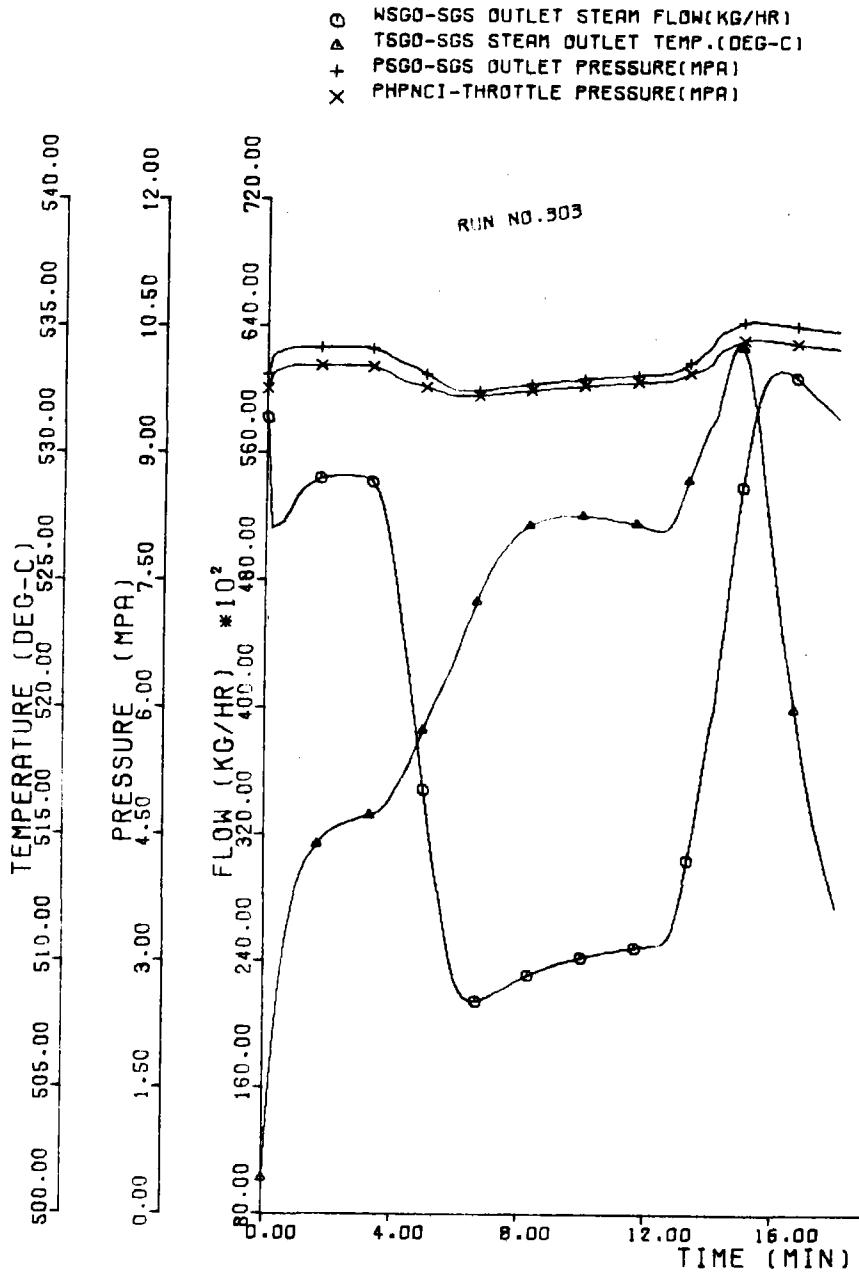


Figure 4-25. Pressure, Temperature, Steam Flow Parameters for Cloud Transient Run No. 303

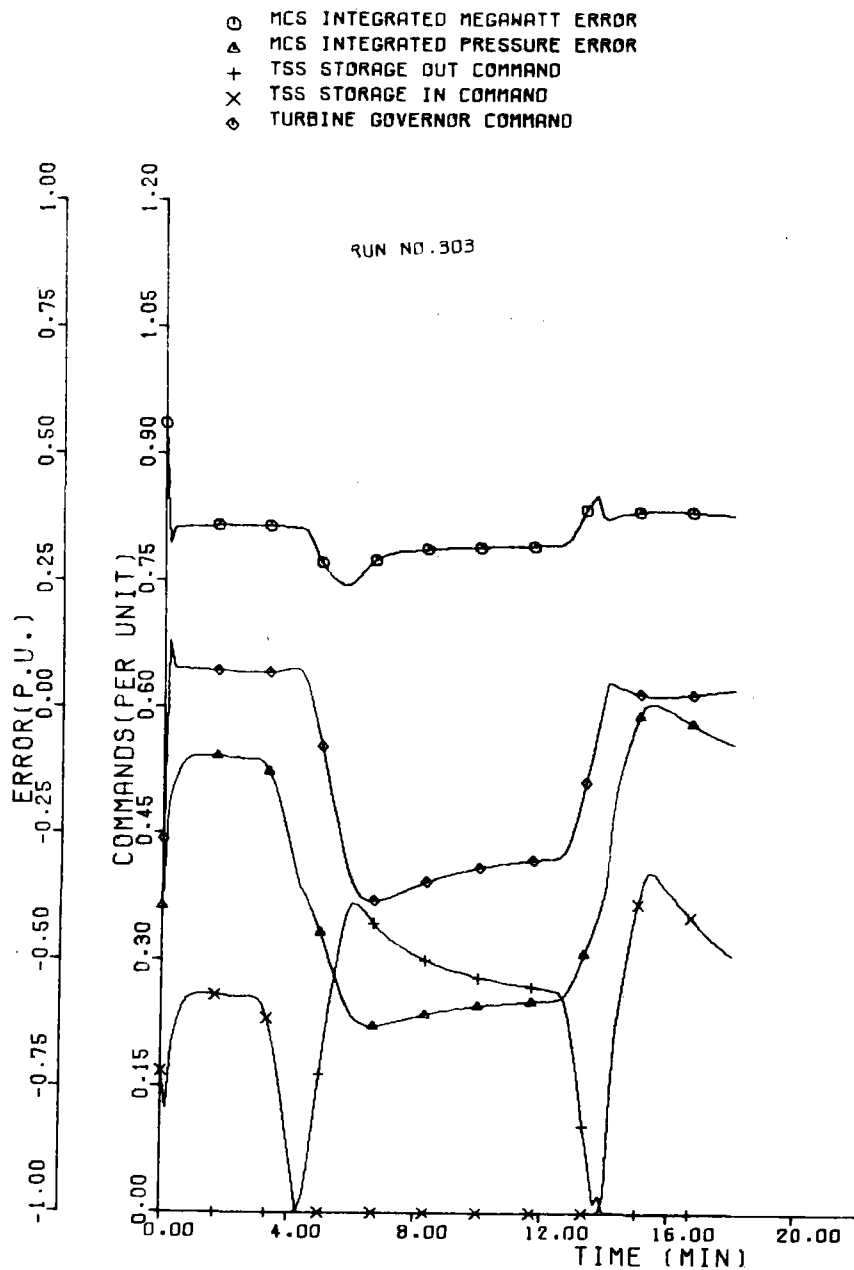


Figure 4-26. Master Controller Operation During Cloud Transient Run No. 303

and megawatt errors -- are the control signals required to effect the three command signals emanating from this subsystem: storage-in, storage-out, and turbine governor. As shown, the storage-in command, initially at about 0.25 pu, drops to zero (i. e., command to stop charging storage) as the maximum cloud shading effect occurs. The storage-out command increases to the 0.25 to 0.35 pu region during the cloud shading period, which then commands the turbine admission valve to admit storage discharge steam. As expected, the turbine governor command is reduced by about 30 percent (from 0.65 to 0.45 pu) as the cloud shades the field.

Figure 4-27 shows steam generator net power and energy delivered during the cloud transient run. After the initial run startup transient period, about 38 MW(th) are being delivered. This dips by about 47 percent (to about 20 MW(th)) during the cloud coverage, prior to building up again as the cloud passes. The integral of this power delivery -- net energy -- is also plotted. A total of 8.53 MW(th) hours was delivered over 18 minutes. Megawatt demand (gross level) was 0.615 pu.

Finally, several power and energy terms are shown plotted in Figure 4-28. Particularly, we note that thermal storage energy change with time is shown in the bottommost plot. As storage is initially being charged, the energy level is increasing. At about $t = 4$ minutes, energy begins to be removed, and the energy curve begins turning downward. At $t = 14$ minutes, charging steam is beginning to flow once again to storage, and discharge steam flow is shut off, causing a rising trend in the energy level once again.

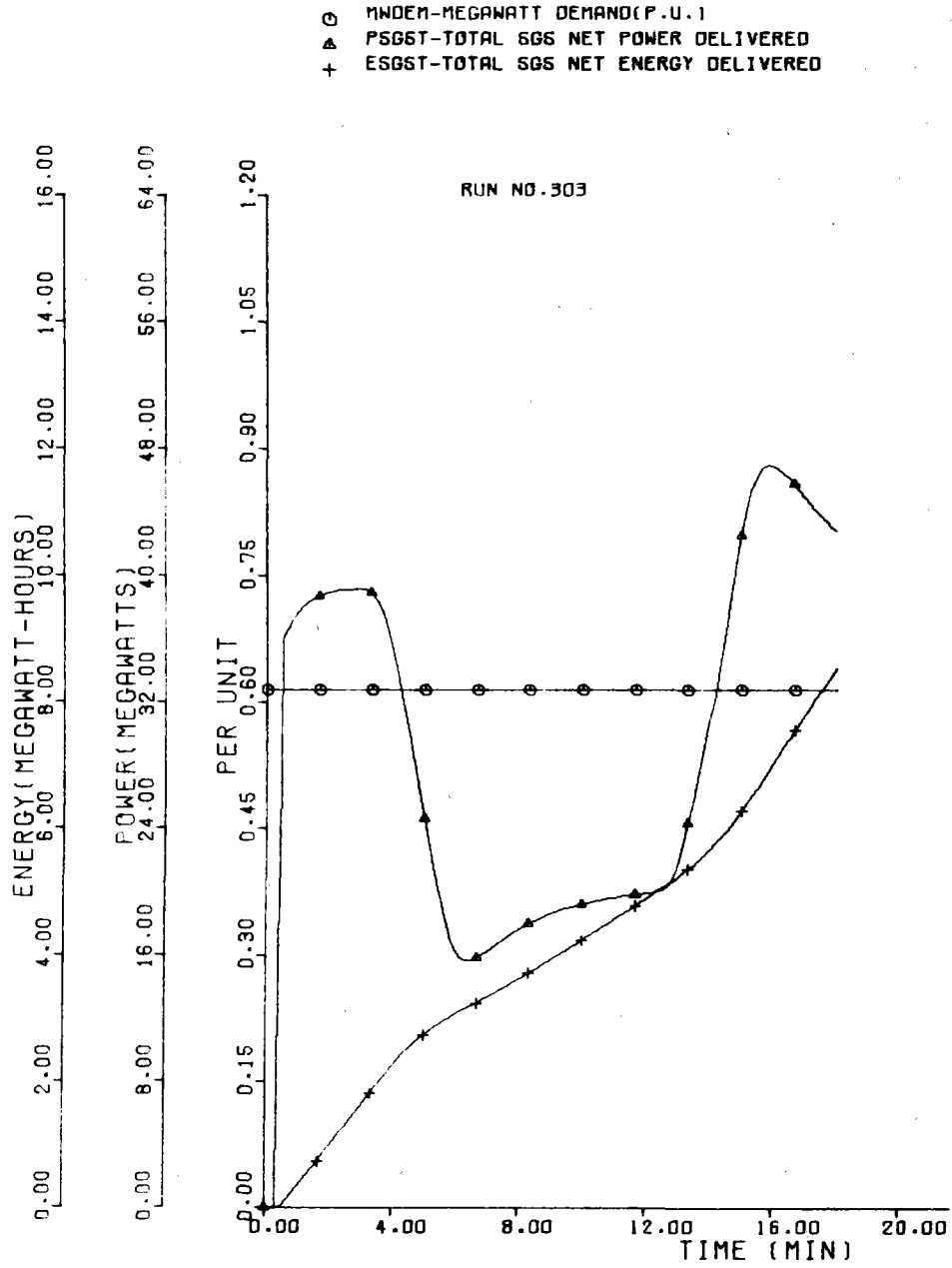


Figure 4-27. Megawatt Demand and Steam Generator Subsystem Power, Energy-Delivered Variations for Cloud Transient Run No. 303

- QR-SGS RADIANT INPUT/5(MWT)
- ▲ MNE-GENERATED BUSBAR POWER(MWE)
- + EGEN-GENERATED BUSBAR ENERGY(MWE-HRS)
- × ETSS-CHANGE TSS ENERGY LEVEL(MWT-HRS)

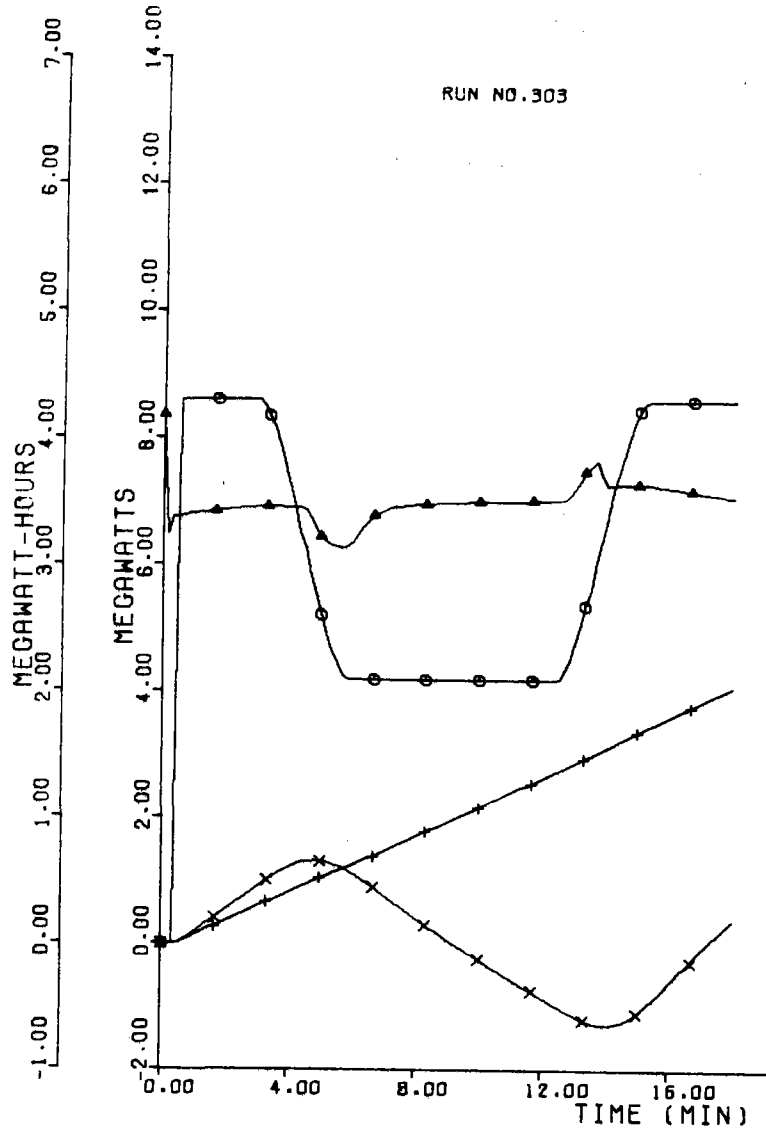


Figure 4-28. Various Energy and Power Parameters for Cloud Transient Run No. 303

In conclusion, the cloud transient run has demonstrated that the pilot plant can tolerate cloud interference of the heliostat field. Relatively smooth busbar power continues to be supplied in response to a fixed load demand, due to the ability of thermal storage to offset the reduced capacity of the steam generator to continue delivering the necessary turbine steam power. Relatively high average metal temperature rates of change and temperature changes -- particularly in the primary superheater -- were noted. Improvements in control system design -- integrated heliostat feedback control for example -- could reduce this level of severity. Optimization of other master controller parameters could ultimately improve the plant's ability to maintain near-constant busbar power.

Other Cloud Transient Simulation Results -- As Table 4-7 indicates, nine other short runtime (12 to 18 minutes) cloud transient effects were examined during the course of the transient analysis study. These are identified as Runs No. 302, and 304 through 312. Most of the cases used clouds approaching from the west, stated to be the predominant direction of travel for the Barstow, California, pilot plant site. Variations in speed, cloud length, and heliostat field coverage were made for most of these runs. In addition, single cases of clouds approaching from the north and south were investigated.

Table 4-10 summarizes a number of statistical parameter data for these various cloud transient runs. Figures 4-29 through 4-31 illustrate summarizing plots of some of the Table 4-10 data.

Figure 4-29 is indicative of changes in steam generator temperature rates of change, temperature change (from average), and absorbed power rates of change for various approach directions and field coverages.

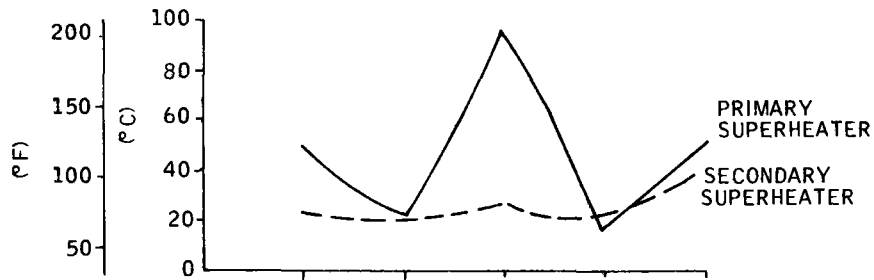
Table 4-10. Summary of Cloud Transient Run Results - Statistical Parameters

Run No.	Approach Direction/Coverage	Cloud Speed (km/hr) Length (km)	Primary Superheater (PSH) Metal						Secondary Superheater (SSH) Metal						Throttle Pressure			SGS Outlet Steam Temperature		
			Temperature °C (°F)			Temperature Rate °C/hr (°F/hr)			Temperature °C (°F)			Temperature Rate °C/hr (°F/hr)			MPa (psia)			°C (°F)		
			Avg	Max	Min	Avg	Max	Min	Avg	Max	Min	Avg	Max	Min	Avg	Max	Min	Avg	Max	Min
302	W/all	11.4/1.8	430 (806.1)	451.8 (845.3)	414.7 (776.5)	34.3 (61.8)	1672.8 (3011.0)	-1268.8 (-2283.9)	524.8 (976.6)	543.2 (1009.7)	510.3 (950.5)	42.6 (76.7)	1884.8 (3392.6)	-1102.4 (-1984.3)	9.85 (1428.6)	10.48 (1520.4)	9.38 (1360.7)	511.3 (952.4)	521.2 (970.2)	497.6 (927.6)
303	W/N-1/2	11.4/1.8	525.4 (977.7)	620.8 (1149.4)	435.7 (816.2)	159.1 (286.4)	1835.2 (3303.3)	-2926.3 (-5267.3)	55.2 (1026.0)	566.2 (1051.2)	526.3 (979.4)	24.9 (44.8)	923.2 (1661.8)	-647.7 (-1165.8)	9.96 (1444.3)	10.36 (1503.0)	9.67 (1402.4)	523.1 (973.6)	543.3 (993.8)	509.6 (949.2)
304	W/S-1/2	11.4/1.8	390.8 (735.5)	440.8 (825.5)	342.6 (648.6)	1.6 (2.8)	2187.9 (3938.3)	-1926.2 (-3467.2)	451.6 (844.8)	535.7 (996.3)	363.1 (685.6)	13.1 (23.6)	2786.8 (5016.3)	-2195.6 (-3952.0)	10.00 (1450.0)	10.22 (1482.1)	9.83 (1426.0)	439.6 (823.3)	515.1 (959.1)	358.2 (676.8)
305	W/N-1/2	21.9/1.8	480.4 (896.8)	562.8 (1045.1)	435.7 (816.2)	43.9 (79.1)	1971.1 (3548.0)	-2286.5 (-4115.7)	543.4 (1010.2)	566.9 (1052.4)	526.3 (979.4)	18.7 (33.7)	962.3 (1732.1)	-622.2 (-1119.9)	10.02 (1453.9)	10.29 (1492.6)	9.63 (1397.1)	518.2 (964.8)	533.9 (993.0)	509.6 (949.2)
306	W/S-1/2	21.9/1.8	404.2 (759.5)	440.1 (824.1)	357.7 (675.9)	8.9 (16.1)	2407.8 (4334.0)	-2318.4 (-4173.2)	479.7 (895.4)	534.7 (994.4)	411.0 (771.8)	29.9 (53.9)	2295.8 (4132.5)	-2378.7 (-4281.7)	9.98 (1448.0)	10.13 (1469.9)	9.81 (1423.4)	465.5 (869.9)	514.4 (958.0)	401.1 (754.0)
307	W/all	32.9/1.8	435.3 (815.5)	449.5 (841.1)	411.3 (772.3)	53.4 (97.9)	2592.7 (4666.8)	-2460.8 (-4429.5)	530.4 (988.7)	541.4 (1006.5)	512.9 (955.2)	58.3 (105.0)	2387.5 (4297.5)	-1974.3 (-3553.7)	9.93 (1440.5)	10.28 (1490.7)	9.28 (1346.2)	513.3 (955.9)	519.5 (967.1)	502.6 (936.7)
308	W/all	11.4/0.67	440.4 (824.7)	454.2 (849.5)	415.3 (779.6)	40.2 (72.3)	1726.4 (3107.6)	-1248.2 (-2246.7)	532.8 (991.0)	543.6 (1010.5)	512.0 (953.6)	35.8 (64.5)	1789.7 (3221.5)	-1102.9 (-1985.3)	10.01 (1451.3)	10.27 (1490.1)	9.37 (1359.6)	514 (957.2)	521 (970.0)	499.4 (931.0)
309	W/all	32.9/0.67	443.2 (829.9)	450.4 (842.7)	412.3 (774.1)	53.1 (95.6)	2565.8 (4618.4)	-2460.7 (-4429.3)	534.8 (994.7)	541.0 (1005.8)	513.3 (955.9)	45.2 (81.4)	2397.3 (4315.2)	-1974.3 (-3553.7)	10.03 (1454.2)	10.15 (1471.8)	9.39 (1362.1)	514.7 (958.5)	518.9 (966.1)	501.8 (935.3)
311	N/all	11.4/1.8	450.8 (843.4)	462.4 (864.4)	434.3 (813.7)	28.4 (51.1)	1023.6 (1842.4)	-1415.1 (-2547.1)	535.1 (995.1)	544.6 (1012.2)	514.1 (957.4)	40.1 (72.2)	1089.6 (1961.3)	-989.1 (-1780.3)	9.88 (1433.1)	10.43 (1513.3)	9.38 (1360.9)	512.1 (953.7)	518.6 (965.4)	500.1 (932.2)
312	S/all	11.4/1.8	411.2 (772.1)	461.4 (862.6)	378.4 (713.1)	35.7 (64.2)	3038.9 (5470.1)	-2349.4 (-4229.0)	505.9 (942.7)	547.1 (1016.8)	476.2 (889.1)	39.8 (71.7)	2862.2 (5151.9)	-2329.6 (-4193.2)	9.87 (1431.7)	10.5 (1523.8)	9.35 (1356.5)	492.8 (919.1)	524.1 (975.3)	466.7 (872.0)

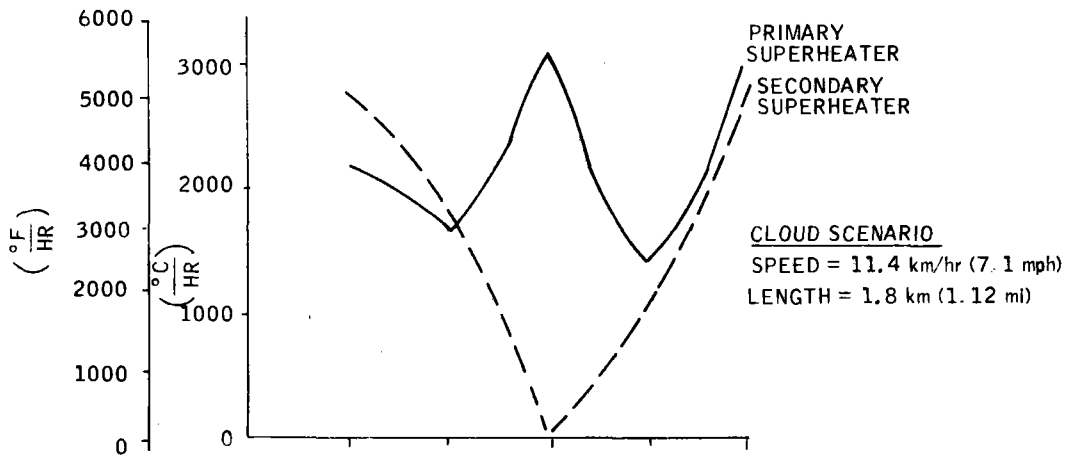
40703-II

4-67

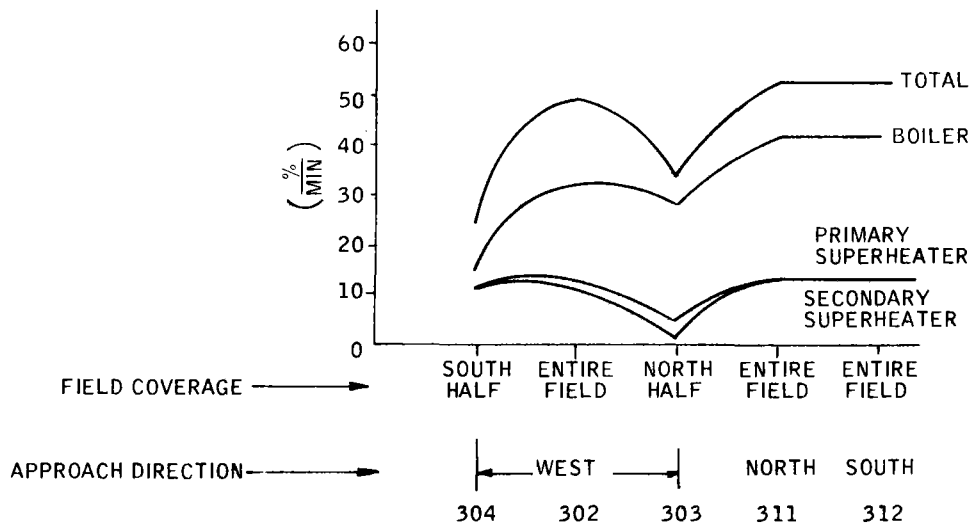
Run No.	Incident Available Power [MW(th)]			Steam Generator Subsystem (SGS) Absorbed Power Levels (% of design maximum)												SGS Absorbed Power Level Maximum Rates of Change (%/min)				Net Busbar Power [MW(e)]	
				Boiler			PSH			SSH			Total			Boiler	PSH	SSH	Total		
	Avg	Max	Min	Avg	Max	Min	Avg	Max	Min	Avg	Max	Min	Avg	Max	Min						
302	28.9494	62.6863	0	30.0746	65.1230	0	7.2729	15.7487	0	5.8107	12.5823	0	43.158	93.454	0	31.515	12.187	11.633	49.626	6.90	5.38
303	46.9867	62.6863	33.5150	41.5344	65.1230	21.2933	13.8503	15.7487	12.2213	12.1676	12.5823	11.8118	67.552	93.454	45.326	28.630	4.324	0.974	33.929	6.97	6.27
304	44.6490	62.6863	29.1713	53.6632	65.1230	43.8297	9.1713	15.7487	3.5273	6.2253	12.5823	0.7705	69.060	93.454	48.127	14.984	11.176	11.385	25.729	6.76	6.44
305	54.5226	62.6863	33.5150	52.8570	65.1230	21.2933	14.7615	15.7487	12.2213	12.3667	12.5823	11.8118	79.985	93.454	45.326	55.054	8.316	1.874	65.244	6.97	5.85
306	48.4205	62.6863	29.1713	56.0593	65.1230	43.8297	10.5466	15.7487	3.5273	7.5545	12.5823	0.7705	74.160	93.454	48.127	28.819	21.495	21.896	49.486	6.77	6.54
307	44.8978	62.6863	0	46.4630	65.1230	0	11.2796	15.7487	0	9.0118	12.5823	0	66.934	93.454	0	90.903	35.153	33.574	143.268	6.86	4.44
308	50.0979	62.6863	0	52.0543	65.1230	0	12.5861	15.7487	0	10.0556	12.5823	0	74.687	93.454	0	31.495	12.180	11.625	49.637	6.96	5.36
309	57.0309	62.6863	0	59.2479	65.1230	0	14.3279	15.7487	0	11.4471	12.5823	0	85.023	93.454	0	90.825	35.123	33.526	143.145	6.92	4.45
311	28.9494	62.6863	0	30.0747	65.1230	0	7.2730	15.7487	0	5.8107	12.5823	0	43.158	93.454	0	41.743	12.832	12.842	52.699	6.93	5.47
312	28.9493	62.6863	0	30.0746	65.1230	0	7.2729	15.7487	0	5.8107	12.5823	0	43.158	93.454	0	41.743	12.832	12.842	52.700	6.80	5.11



a) PEAK METAL TEMPERATURE CHANGES (FROM AVG.)



b) PEAK METAL TEMPERATURE RATES OF CHANGE



c) ABSORBED POWER RATES OF CHANGE

Figure 4-29. Peak Steam Generator Subsystem Metal Temperature Changes and Rates of Change, Absorbed Power Rates of Change for Various Cloud Conditions

Primary superheater metal temperature changes are greatest for the case previous described (Run No. 303), whereby the cloud is traveling west to east and covering only the north half of the field. Primary superheater metal temperature rates are also highest for this situation, although a south-approaching cloud also induces similarly high rates. Clouds approaching from the north appear to disrupt the primary superheater the least.

In most cases, the secondary superheater is not affected as greatly as the primary superheater in terms of temperature rates and changes. This is due largely to the compensating effect of the attemperator cooling steam flow which only affects the secondary superheater. For a cloud traveling east and covering the south half of the field, Figure 4-29(b) shows the secondary superheater rates are higher than those of the primary. This is due to the attemperator flow being cut off as the cloud passes through the field, since the outlet steam temperature is dropping below the setpoint.

Absorbed power rates of change (Figure 4-29(c)), are generally largest for clouds covering the entire field. This is due to the clouds shading a larger portion of the heliostats in the same relative time interval, thereby increasing the rate of change values.

Figure 4-30 is a scatter plot of metal temperature change (from average) versus corresponding metal temperature rates. As shown for the primary superheater (top curve), the following trends are seen in the results:

- Clouds traveling east covering only half the field (Runs 303, 304) cause the largest temperature changes, and induce temperature rates among the largest values observed.

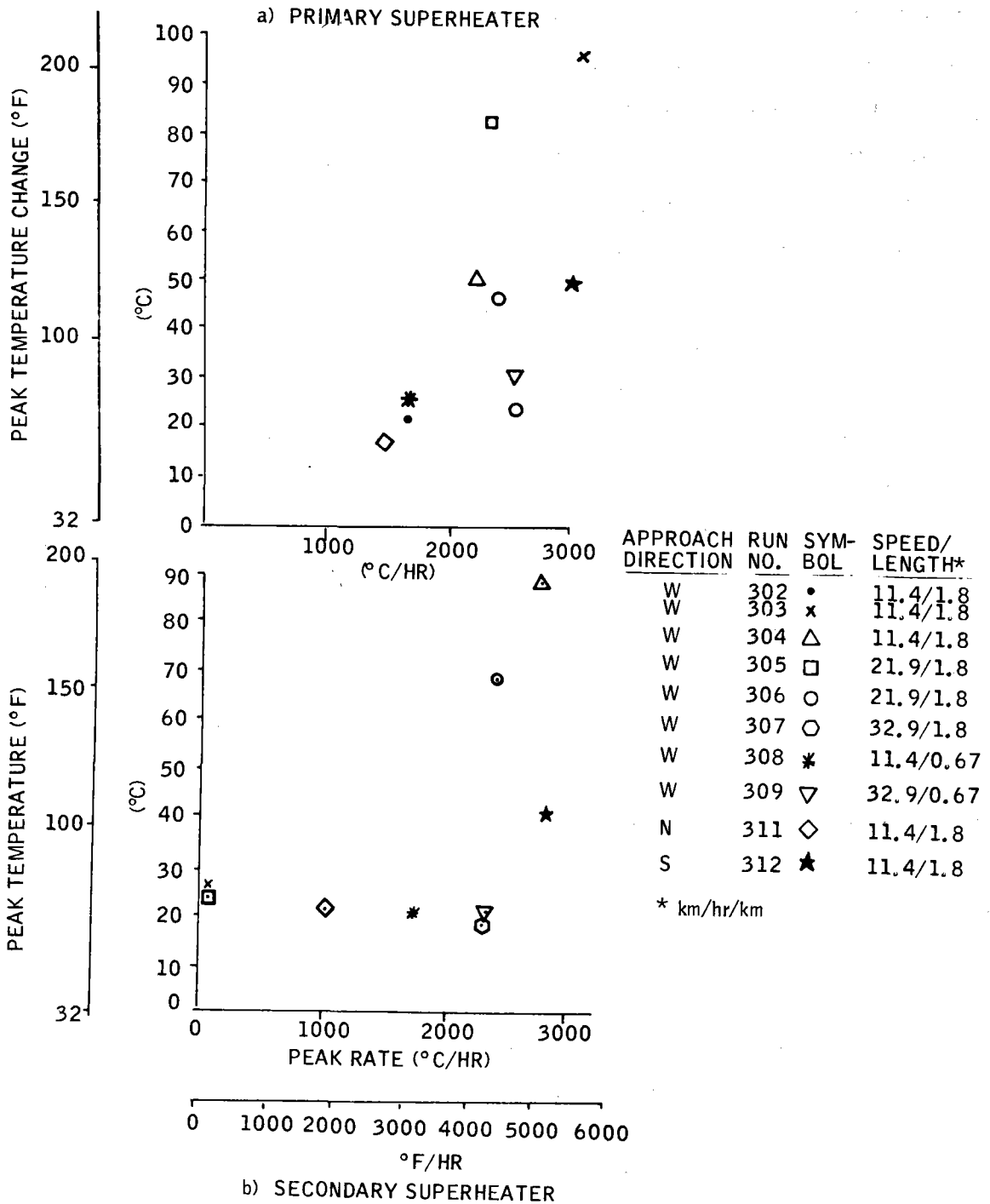


Figure 4-30. Peak Steam Generator Subsystem Metal Temperature Change (From Average) versus Rate of Change for Various Cloud Conditions

- Clouds traveling east covering the entire field at 11.4 km/hr (7.1 mph) shown little fluctuation in the temperature parameter changes for short (0.67-km) or long (1.8-km) (0.42- and 1.12-mi, respectively) clouds, as signified by Runs 302 and 308. For these conditions, then, cloud length is not a sensitive parameter relative to temperature parameters.
- For clouds covering the entire field traveling at 11.4 km/hr (7.1 mph) and 1.8-km (1.12-mi) long, clouds approaching from the south cause the largest temperature rates and temperature changes as compared with clouds approaching from the west and north (Run 302, 311, 312).

For the secondary superheater, the scatter plots of Figure 4-30 indicate the following trends:

- Most situations seem to cause temperature changes on the order of 20°C (68°F). Faster clouds increase temperature rates, with length not a particularly sensitive factor (for example, Runs 309 and 307 are variations of length only).
- As seen previously, clouds covering the south half field only (Runs 304, 306) cause the largest temperature rates and temperature changes.
- Clouds approaching from the south also induce some of the largest temperature rates (e. g., Run 312).

Figure 4-31 illustrates the cloud speed variational case for a westerly approaching cloud condition. Again, the increasing trend in temperature change and temperature rate of change with speed is evident.

For all of these runs, Table 4-10 shows the largest net electrical busbar power dips occurring for the fastest-approaching clouds (32.9 km/hr, or 20.4 mph). In these cases (Runs 307, 309) power output drops from a nominal 7 MW(e) to about 4.45 MW(e) (-36 percent drop). Apparently, the master controller does not have enough "anticipation" information to take preventative control measures to switch to storage steam quicker, thereby reducing the magnitude of the power dip.

To conclude the discussion of cloud transient results, a single simulation run (No. 318) was made over a relatively long time period (138 minutes, or 2.3 hours). Insolation data used were taken from the Ref. 1, beginning with hour 4643.3. Figure 4-32 illustrates this segment of the day, which is frequently subjected to total or near-total cloud shading. Figures 4-33 through 4-37 illustrate principal plotted results from this run.

Figure 4-33 shows the solar incident, redirected, and absorbed power variations with time. As shown, the direct normal intensity is a short "spike" type drop in insolation at about $t = 20$ minutes, followed by total shading of the field beginning at $t = 70$ minutes, extending for nearly an hour. This cloud occluding is assumed to occur instantaneously over the entire field.

Variations of steam generator metal and steam temperatures are plotted in Figure 4-34. A maximum secondary metal temperature of 543°C

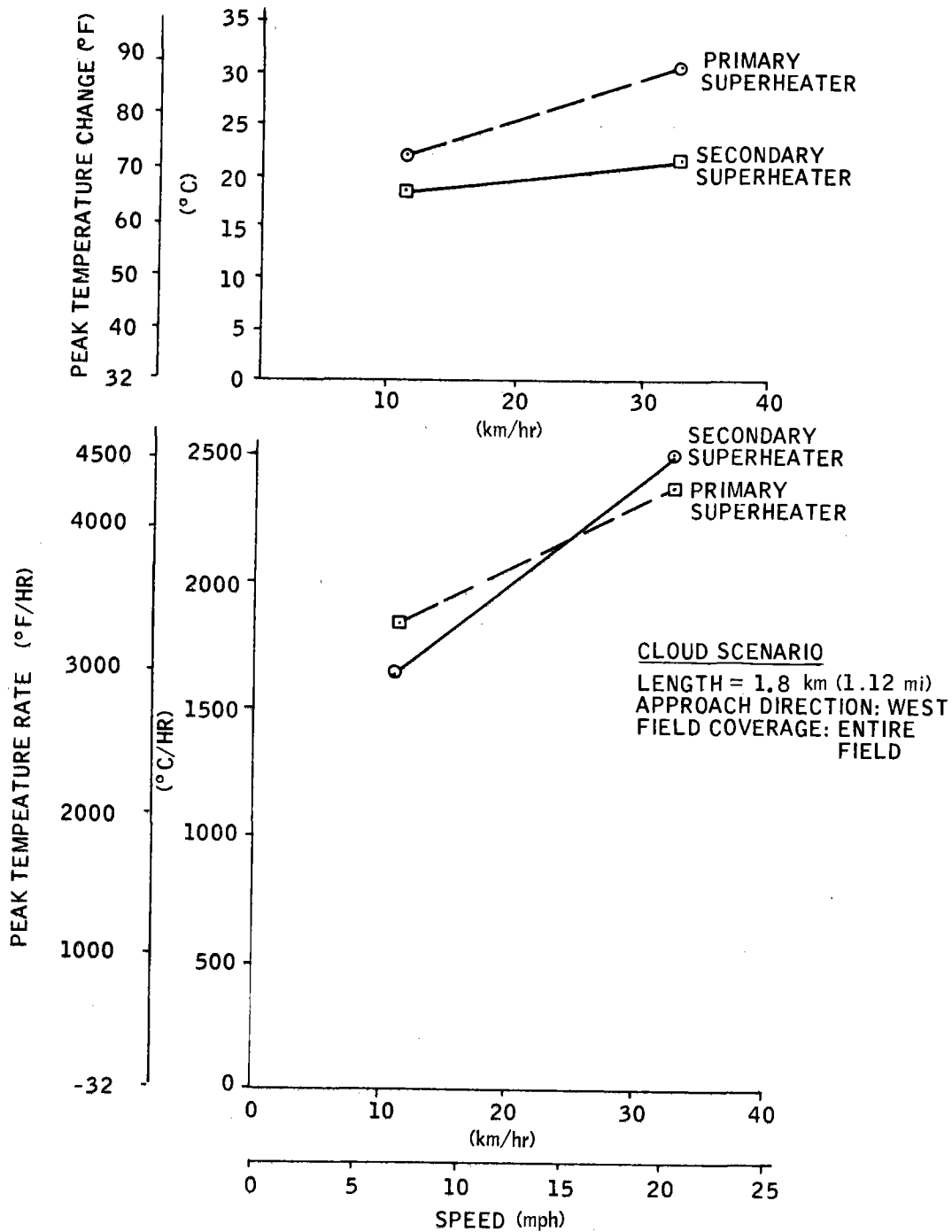


Figure 4-31. Peak Steam Generator Subsystem Metal Temperature Rates of Change and Temperature Change versus Cloud Cover

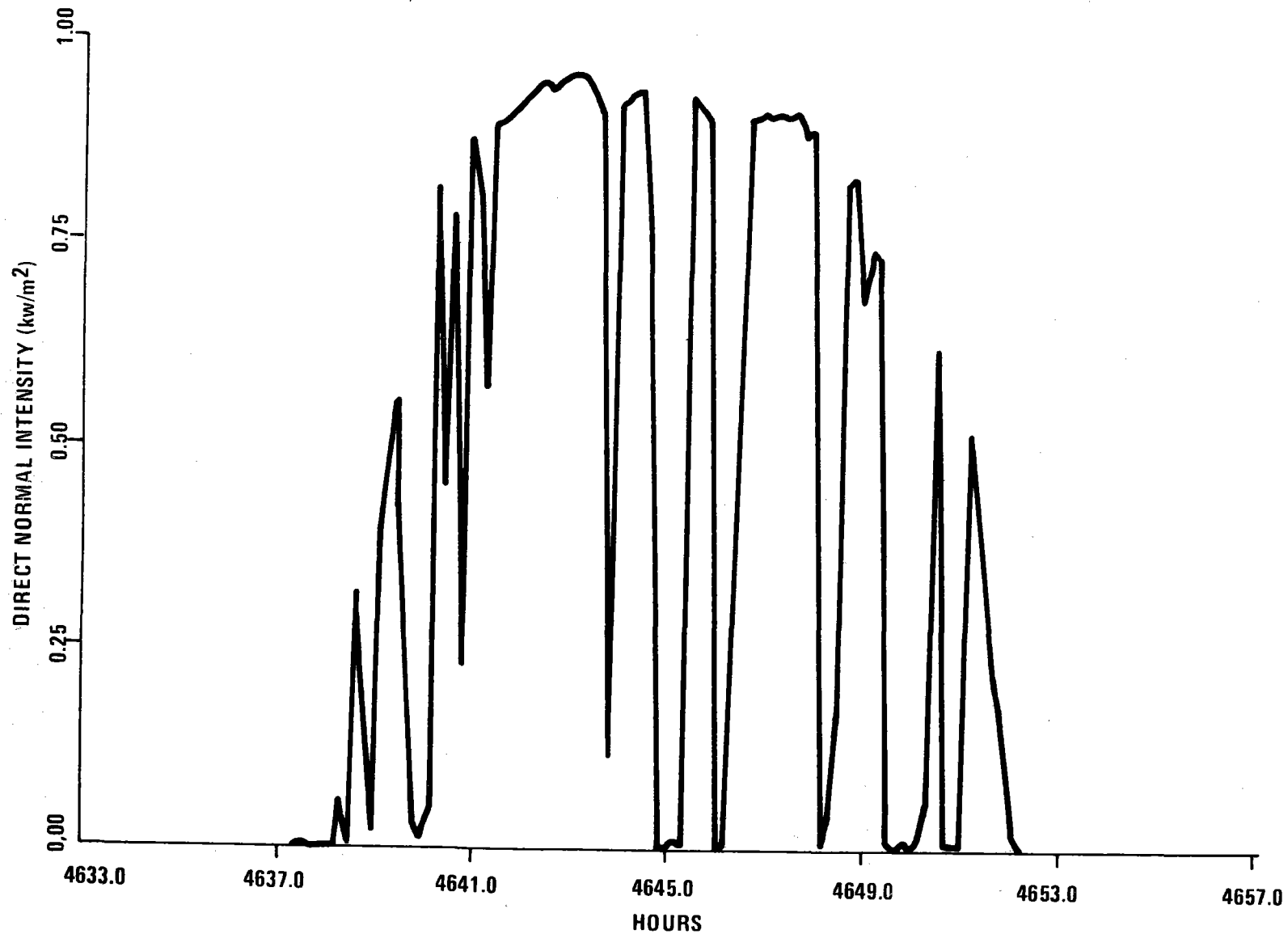


Figure 4-32. Insolation Data Segment Used for Simulation Run No. 317

- AVAILABLE INCIDENT SOLAR POWER
- ▲ REDIRECTED SOLAR POWER TO CAVITY
- + TOTAL SGS ABSORBED POWER
- x SGS ABSORBED POWER (% OF AVAILABLE)

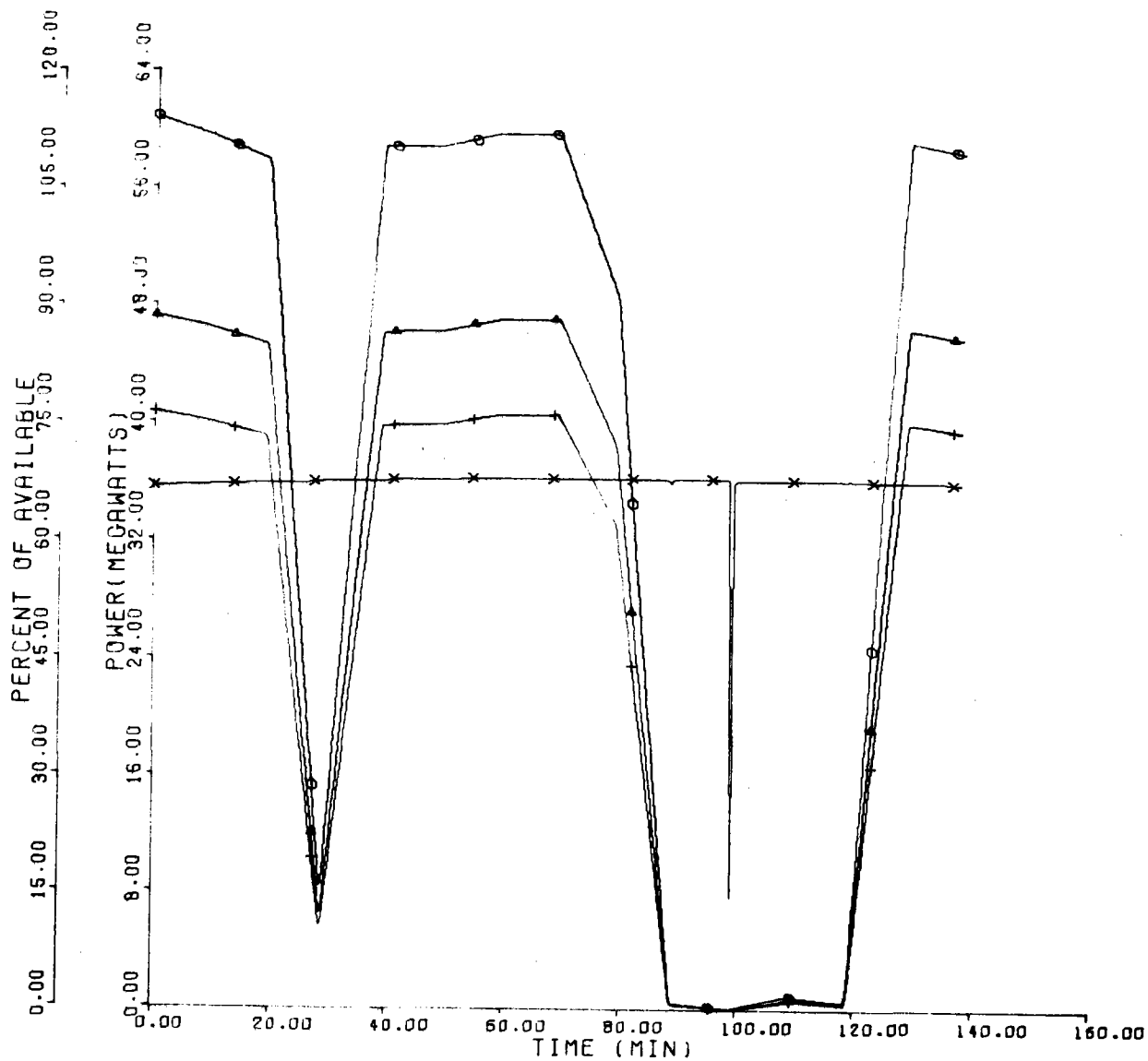


Figure 4-33. Solar Power Parameters versus Time for Cloud Transient Run No. 317

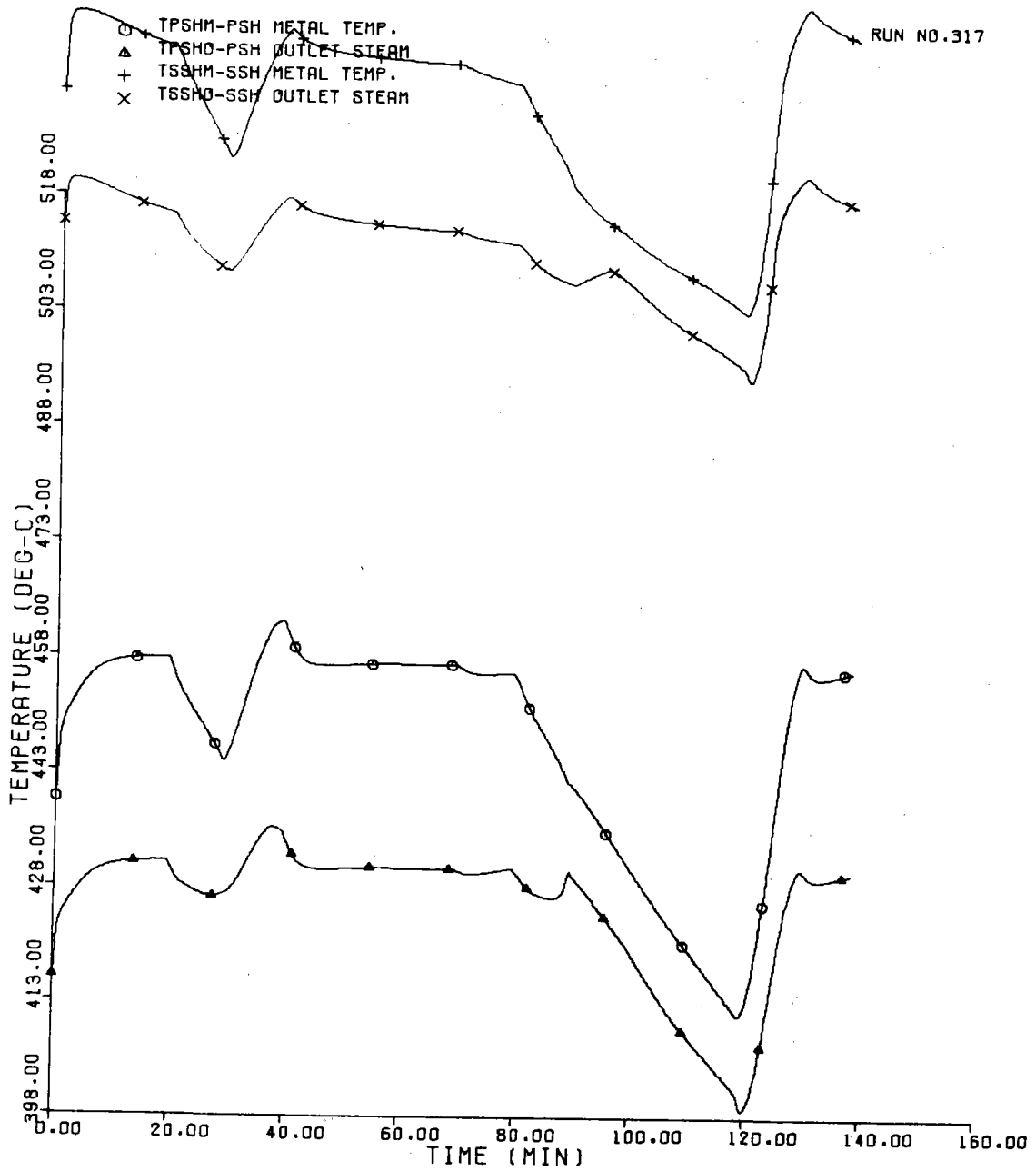


Figure 4-34. Steam Generator Subsystem Steam and Metal Temperature Variations for Cloud Transient Run No. 317

(1009°F) was noted. Outlet steam temperature averaged 511.3°C (952.4°F), with occasional changes of, at most, 4 percent. Generally, maximum metal temperature rates of change were less than 150°C/hr (302°F/hr). These temperature changes and rates of change are considered quite acceptable.

Figure 4-35 illustrates outlet steam flow, pressure, and temperature variations with time. Throttle pressure is also shown. Pressure was held very nearly constant in spite of extended periods of cloud interruption, averaging 10.08 MPa (1462 psia) throttle pressure. Deviations from this average were less than -4.3 percent.

Turbine inlet valve positions and flows are shown in Figure 4-36. Valve positions are the results of commands from the master controller. Steam mass flow from the receiver (high pressure) and/or storage (low pressure) act to smooth the generator power generation characteristics.

Figure 4-37 illustrates various power and energy characteristics of the plant. Net change of thermal storage energy is indicated to be increasing during the first 80 minutes of the run, when cloud shading has been relatively minor. As the extended cloud coverage period begins at about $t = 70$ minutes, the net storage energy decreases, indicating the need to supply continued steam power to the turbine.

From this relatively long duration run with significant cloud disturbance, we can conclude that:

- 1) The plant responds by effectively using thermal storage to:
 - a) supplement steam power demands when a cloud significantly obscures the field, and
 - b) act as an energy sink during

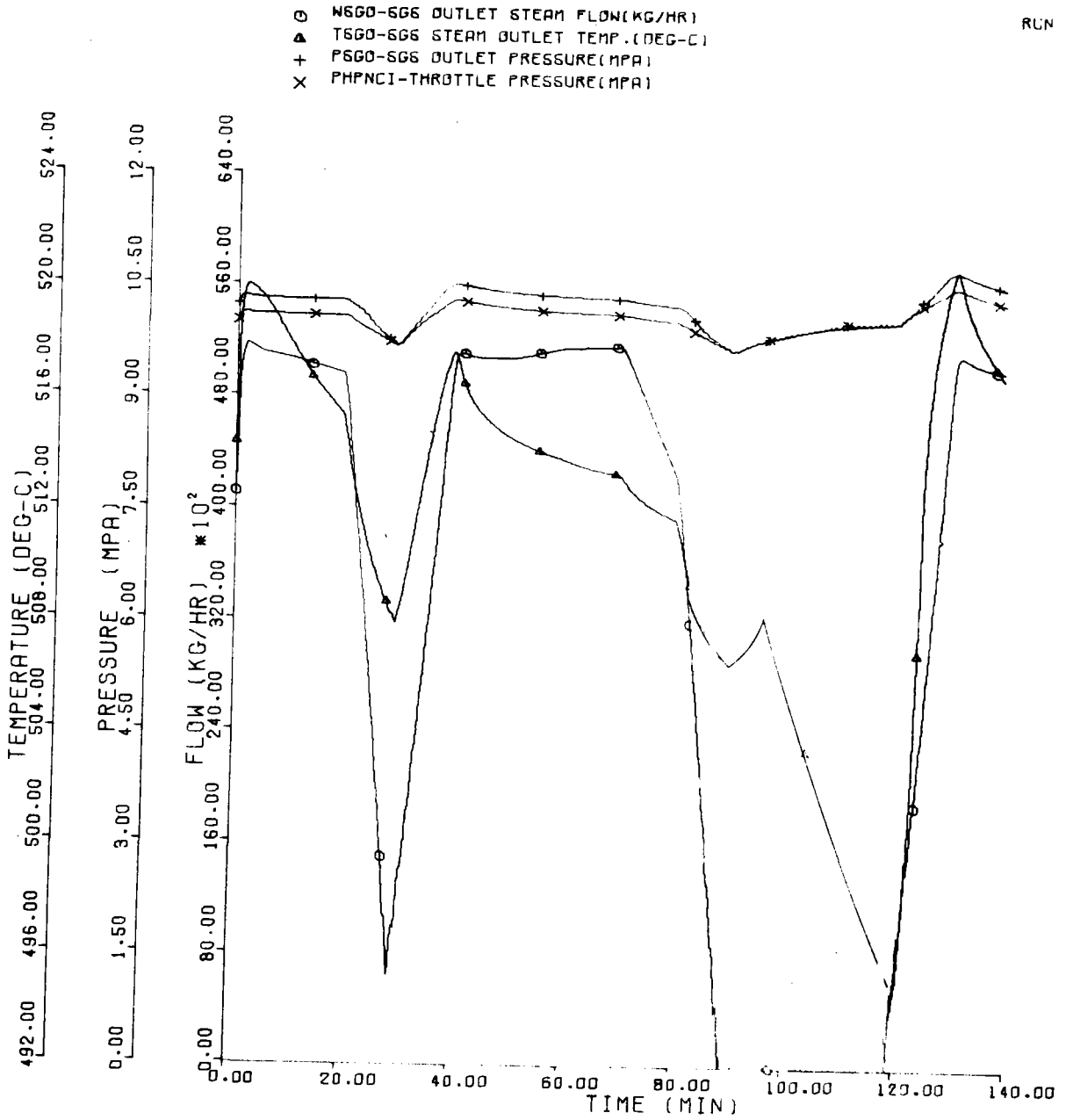


Figure 4-35. Steam Generator Subsystem Outlet Conditions for Cloud Transient Run No. 317

- ⊖ CVHP-HP TURBINE GOVERNOR VALVE(PU)
- ▲ CVLP-LP TURBINE GOVERNOR VALVE(PU)
- + WHPTI-HP TURBINE INLET FLOW
- X WLPTI-LP TURBINE INLET FLOW

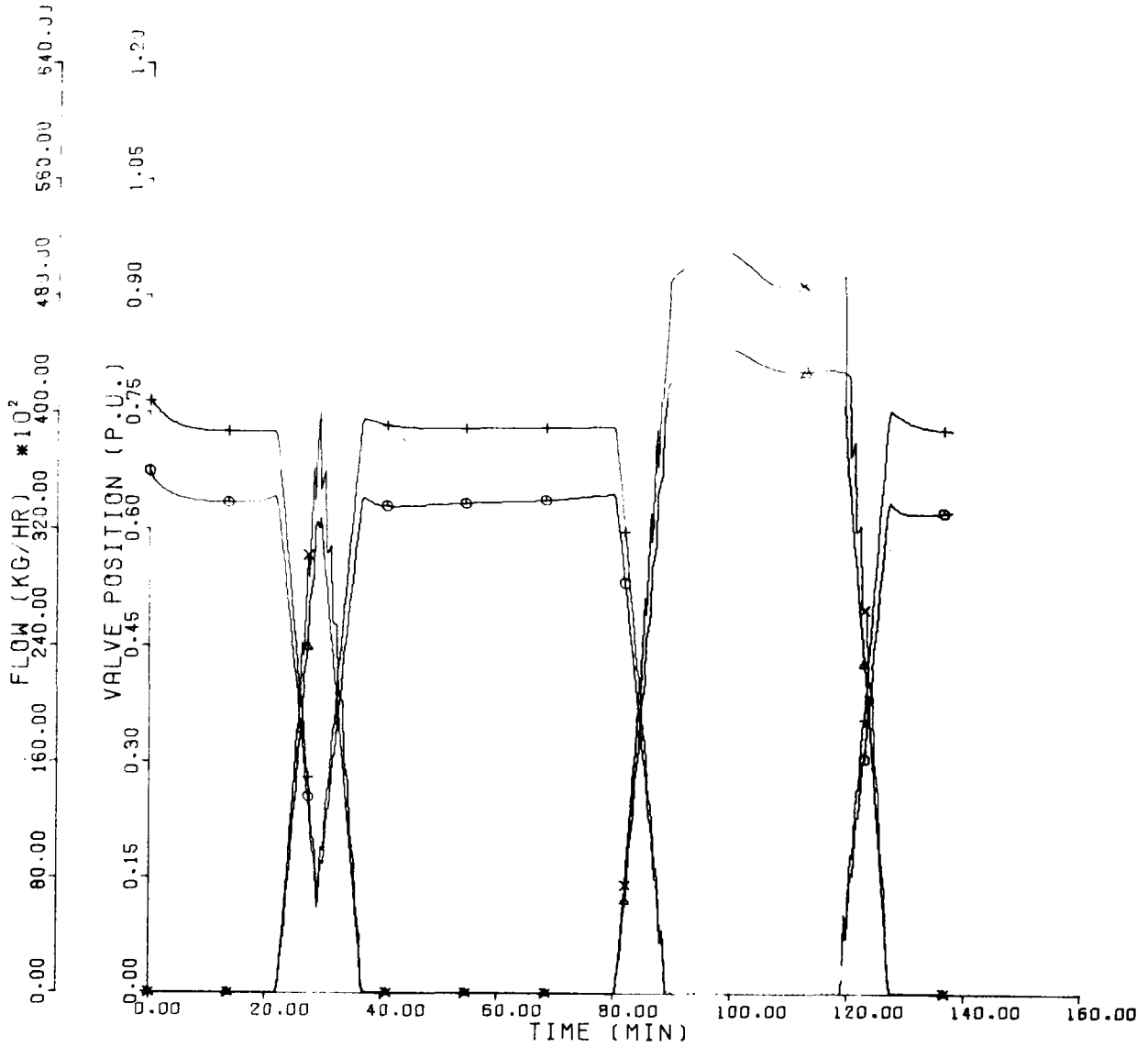


Figure 4-36. Turbine Inlet Valve for Flow Parameters for Cloud Transient Run No. 317

O QR-SGS RADIANT INPUT(S(MWT))
 ▲ MNE-GENERATED BUSBAR POWER(MWE)
 + EGEN-GENERATED BUSBAR ENERGY(MWF-HRS)
 X ETSS-CHANGE TSS ENERGY LEVEL(MWT-HRS)

RUN NO. 317

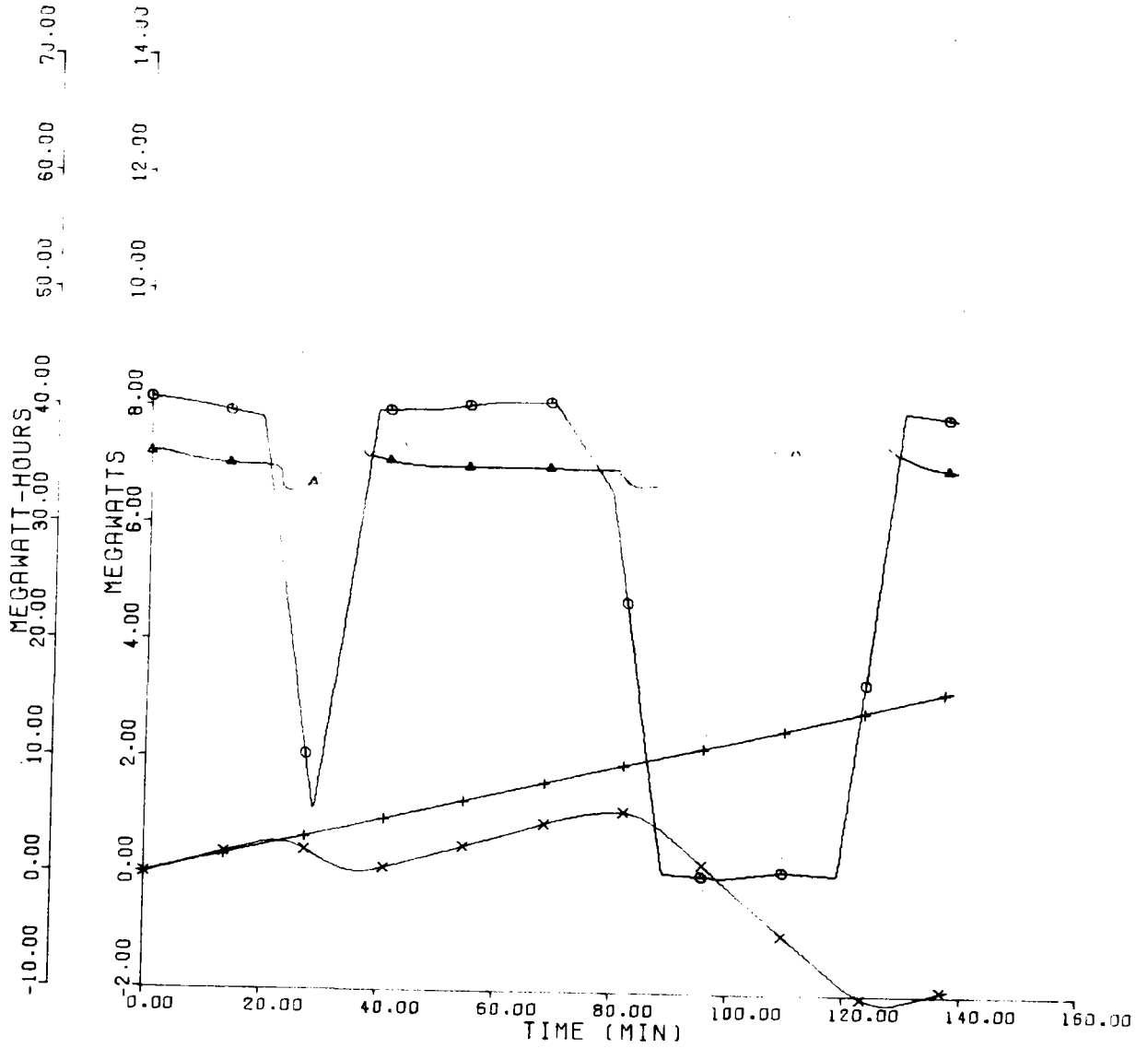


Figure 4-37. Various Power and Energy Parameters for Cloud Transient Run No. 317

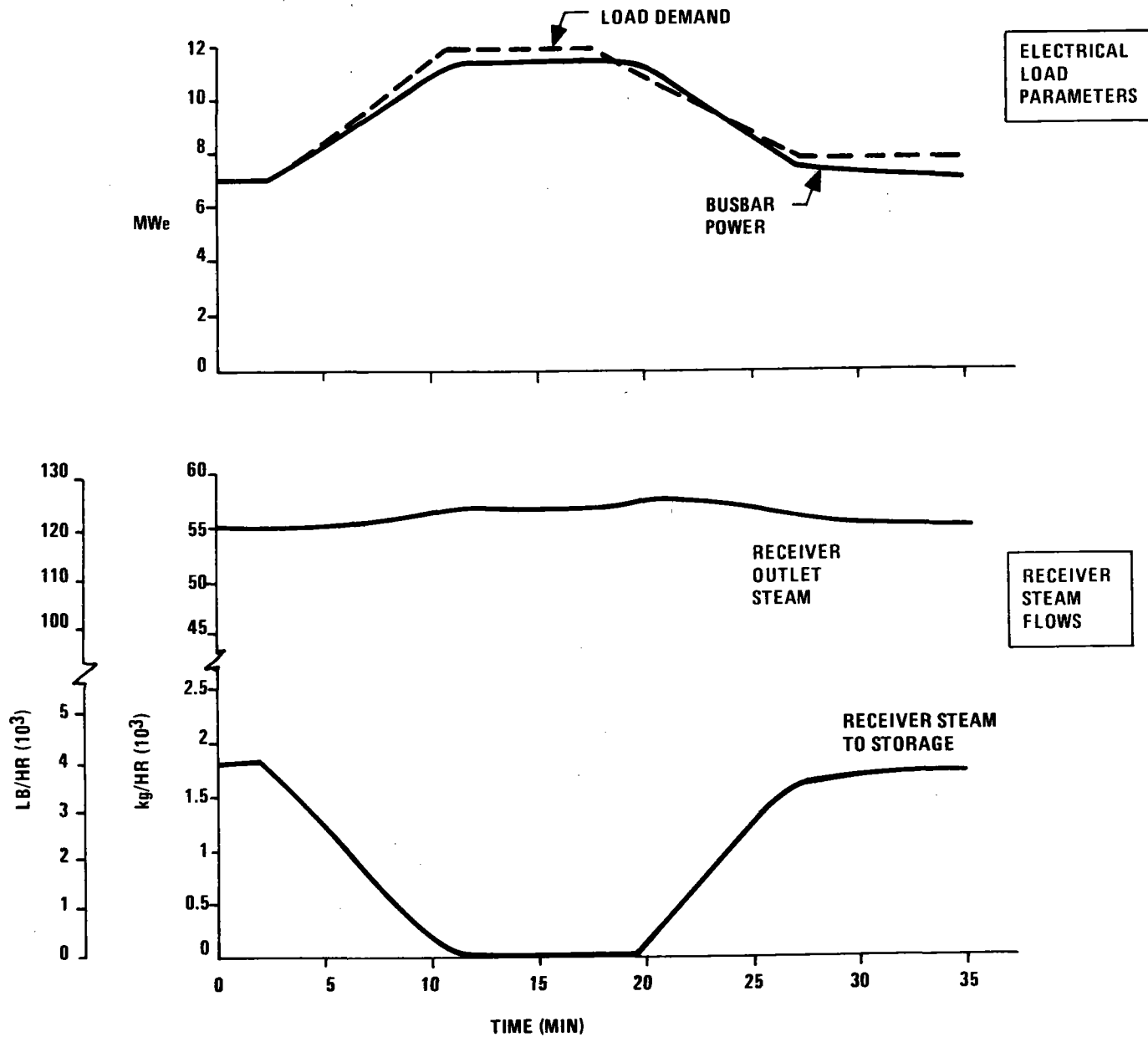
times of excess steam generator production capability.

- 2) Electrical power generation is maintained relatively constant in the presence of extended cloud coverage.
- 3) Steam generator temperatures are maintained reasonably close to design values, and metal temperature rates are relatively moderate.

Response to Load Demand Changes - Run Results -- A single simulation run (No. 313) was made to investigate plant response to load demand changes. For this run, a load demand increase (from 7 to 12 MW(e) (net busbar power) is first induced). After sufficient time for stabilization, a load demand decrease back to 7 MW(e) is commanded. Load increases and decreases are commanded using "ramp" functions with rates of change limited to ± 4 percent/minute. Throughout the 35-minute run, solar insolation is held constant at 0.9807 kW/m^2 .

Figure 4-38 shows the principal results from this run. At the top of the figure, load demand and delivered load are plotted. The plant was not quite capable of satisfying the 12-MW(e) load demand because: a) the solar intensity was not sufficient to develop steam power at a rate compatible with MW(e) electric power generation, and b) the master controller was simulated by not allowing any thermal storage steam flow to be commanded for load demands in excess of storage's rated output (i. e., 7MW(e) net busbar). Consequently, for load demands greater than 7MW(e), the steam generator was required to generate all steam power to the turbine.

40703-II



4-82

Figure 4-38. Plant Response to Load Demand Changes for Transient Analysis Studies

The "hangoff" between demand and generated power during the last portion of the run is due principally to a buildup in integrated megawatt error in the previous part of the run. If the load demand had been set to somewhat less than 12 MW(e) midway in the run (e.g., 11 MW(e)), this megawatt error signal would not have built up over time, and could have been removed more quickly near the end of the run. This would have produced a result of closer matching between generated and demanded load.

The remainder of Figure 4-38 shows steam flows from the receiver in terms of total and storage charge flow. As per the master controller design, flow to storage was reduced to zero whenever the maximum amount the steam generator could deliver was required by the turbine to meet load demand.

Failure Effects Simulation Results -- Three simulated failure cases were run to obtain plant response data. These simulated failures were:

- Recirculating pump failure in steam generator (Run 314)
- High-pressure heater failure in electrical generation subsystem (Run 315)
- Partial collector field failure (Run 316)

Constant solar insolation of 0.9807 kW/m^2 was used. Load demand was constant at 7 MW(e).

A recirculating pump failure was simulated by reducing flow through the boiler by 50 percent at $t = 2$ minutes into the run. The most noticeable effect of this run was a reduction in drum level of about -3.2 cm (-1.26 in) as shown in Figure 4-39. Generated power continued at a near-constant level.

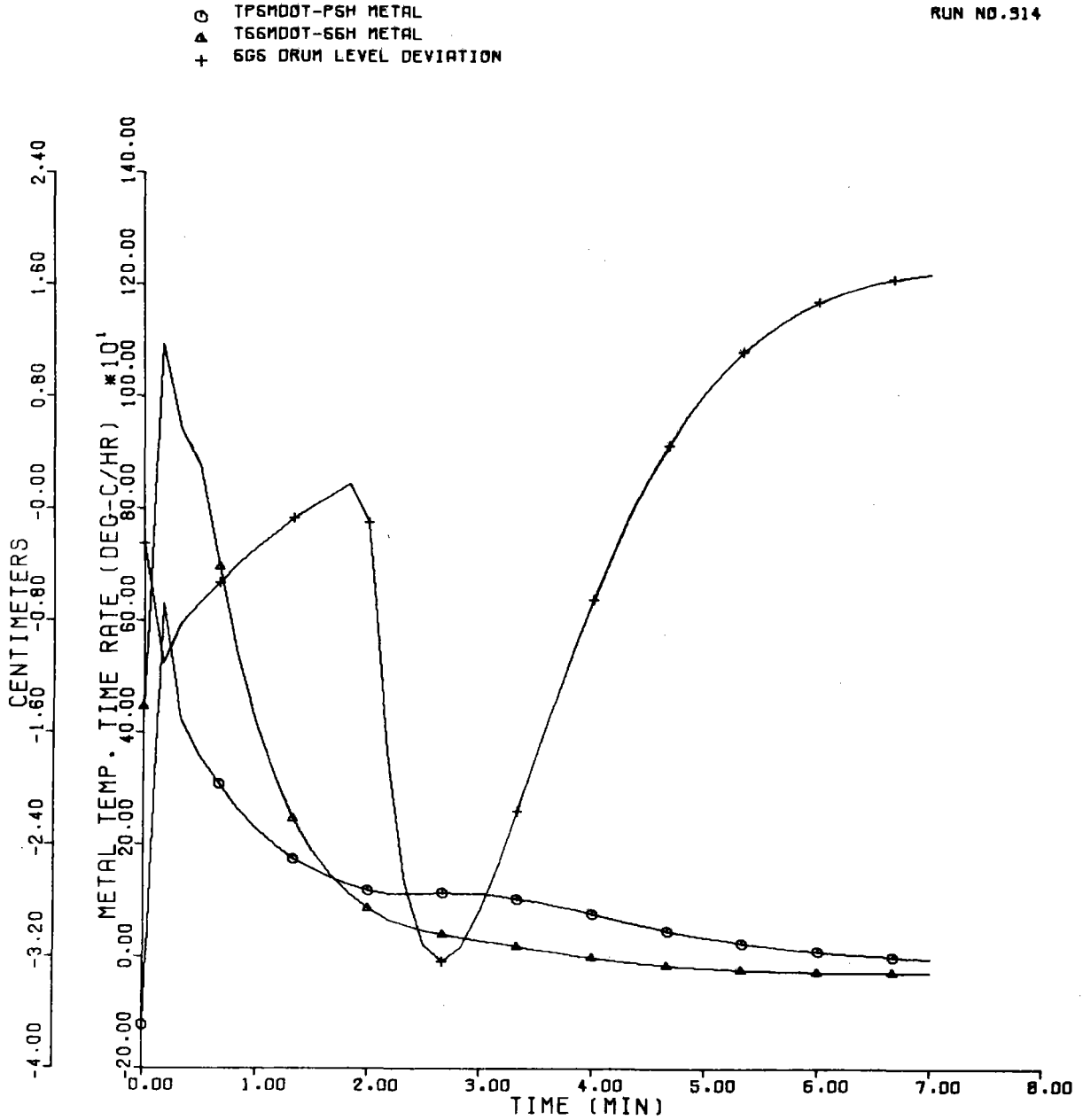


Figure 4-39. Steam Generator Subsystem Metal Temperature Rates and Drum Level Change Due to Simulated Recirculating Pump Failure

Figure 4-40 illustrates the effects on drum pressure of a simulated HP heater failure at $t = 2$ minutes. In this case, the outlet temperature of the heater is instantaneously decreased to 149°C (300°F) from about 192°C (377.6°F). Drum pressure drops by about 0.26 MPa (37 psia) in response to this sudden colder inflow of feedwater.

Figure 4-41 shows steam generator metal and steam temperatures variations over time for the simulated HP heater failure. Primary superheater temperature parameters show a tendency to increase with time. This temperature rise is due to the approximate 11 percent reduction in cooling steam flow through the primary superheater, as indicated by the drum outlet flow parameter in Figure 4-40.

This flow reduction is due to the master controller reducing steam flow demand from the steam generator to preserve pressure energy, as shown in Figure 4-42. In this figure, steam pressures (both steam generator outlet and throttle) remain very stable, while outlet flow is reduced about 7.4 percent from about $54,000$ to $50,000$ kg/hr ($119,048$ to $110,229$ lb/hr) -- beginning at the time of failure ($t = 2$ minutes). An outlet steam temperature rise of about 4°C (7.2°F) also accompanies these changes, before the attenuator controller can stabilize steam temperature to the setpoint.

For the HP heater failure, other plant functions continued to operate close to normal.

The final simulated failure run involves a 20 percent reduction in redirected power on to the boiler only. This failure mode would result from a large segment of boiler-only heliostats being instantaneously aimed away from the

O PD-DRUM PRESSURE(MPA)
 ▲ WD-DRUM OUTLET FLOW(KG/HR)
 + NFW-FEEDWATER FLOW(KG/HR)
 X WATTSP-ATTEMP. SPRAY FLOW(KG/HR)

RUN NO. 315

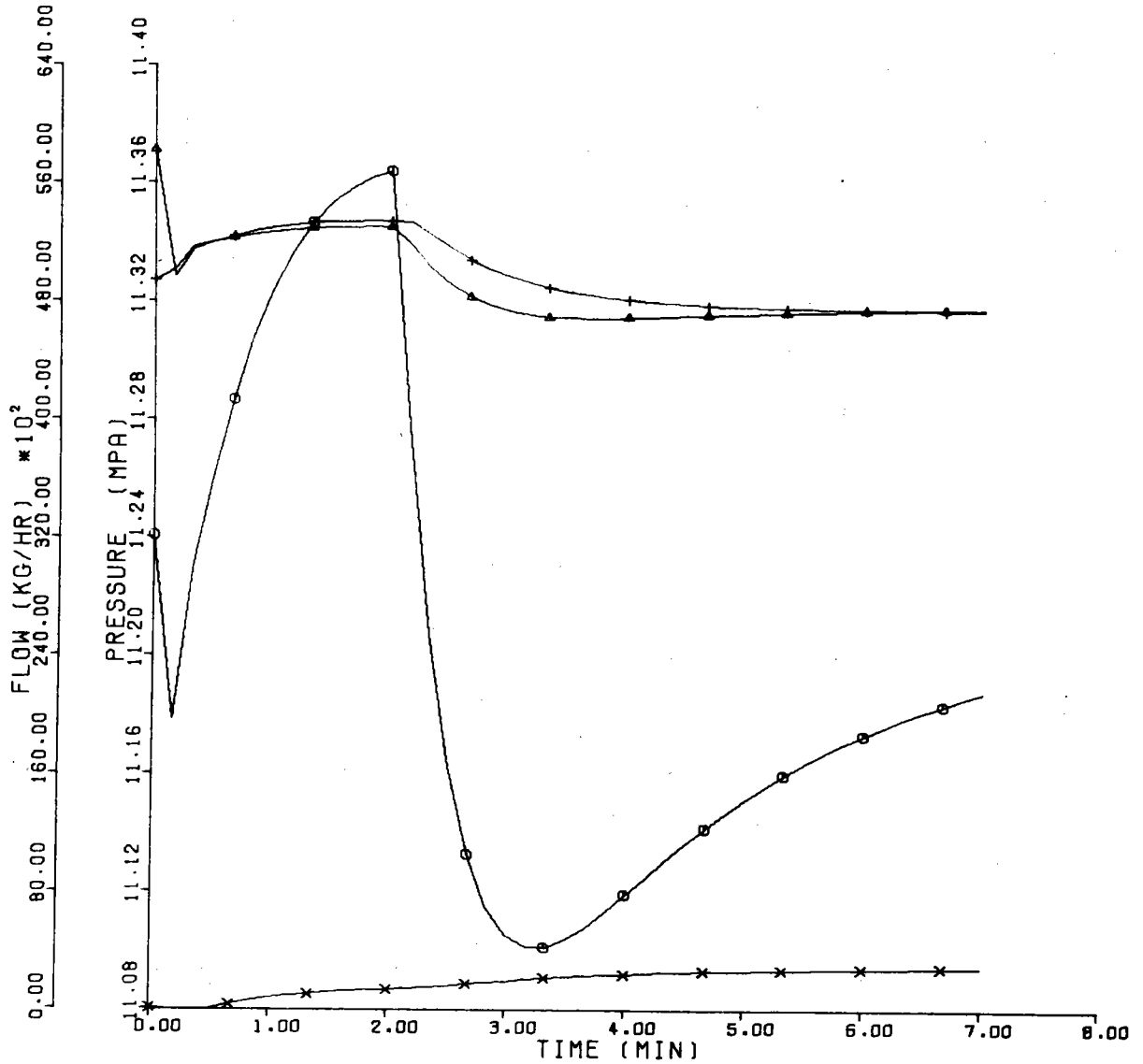


Figure 4-40. Steam Generator Drum Pressure and Various Flows for Simulated HP Heater Failure (Run No. 315)

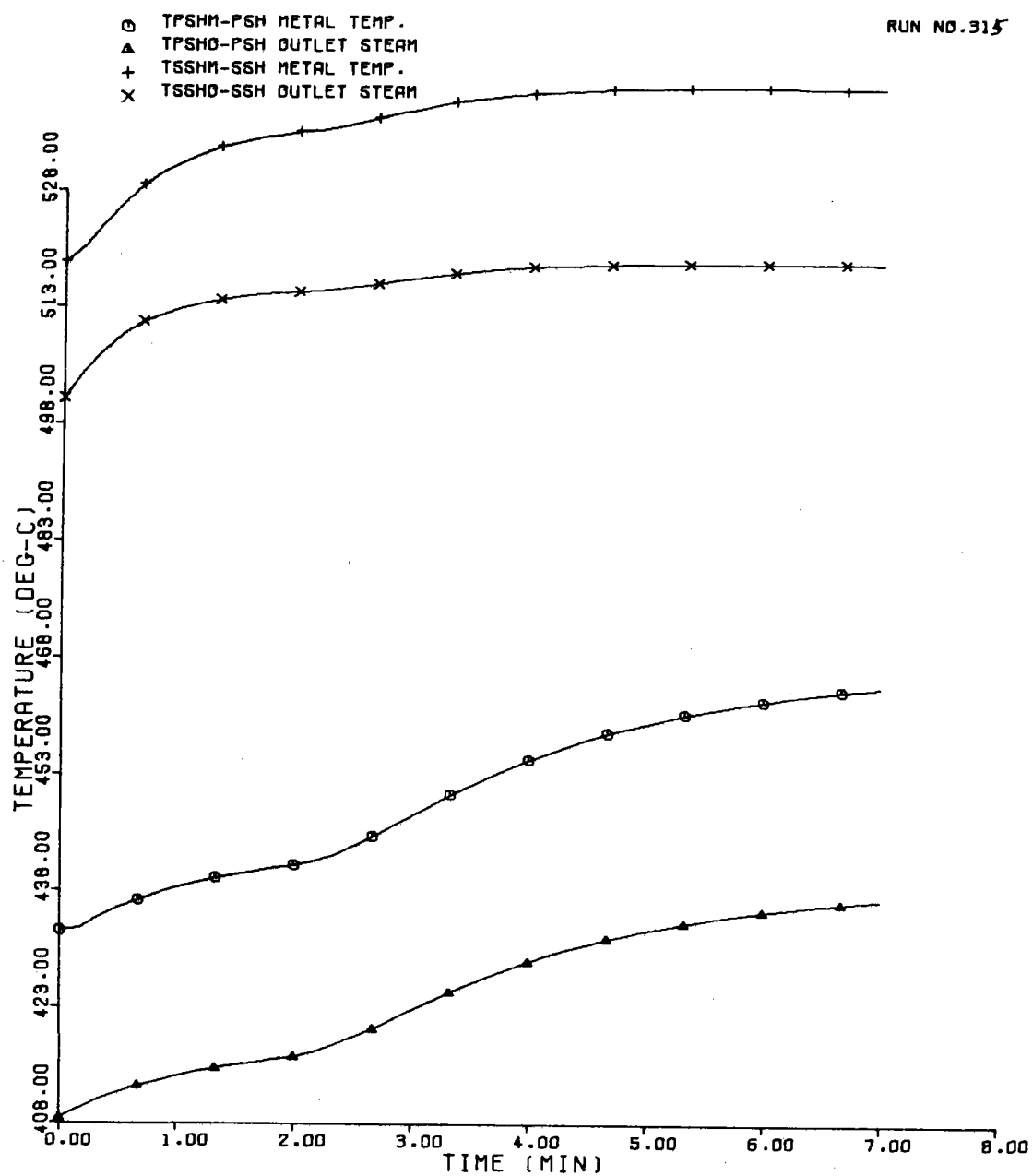


Figure 4-41. Steam Generator Metal and Steam Temperature Changes Due to Simulated HP Heater Failure (Run No. 315)

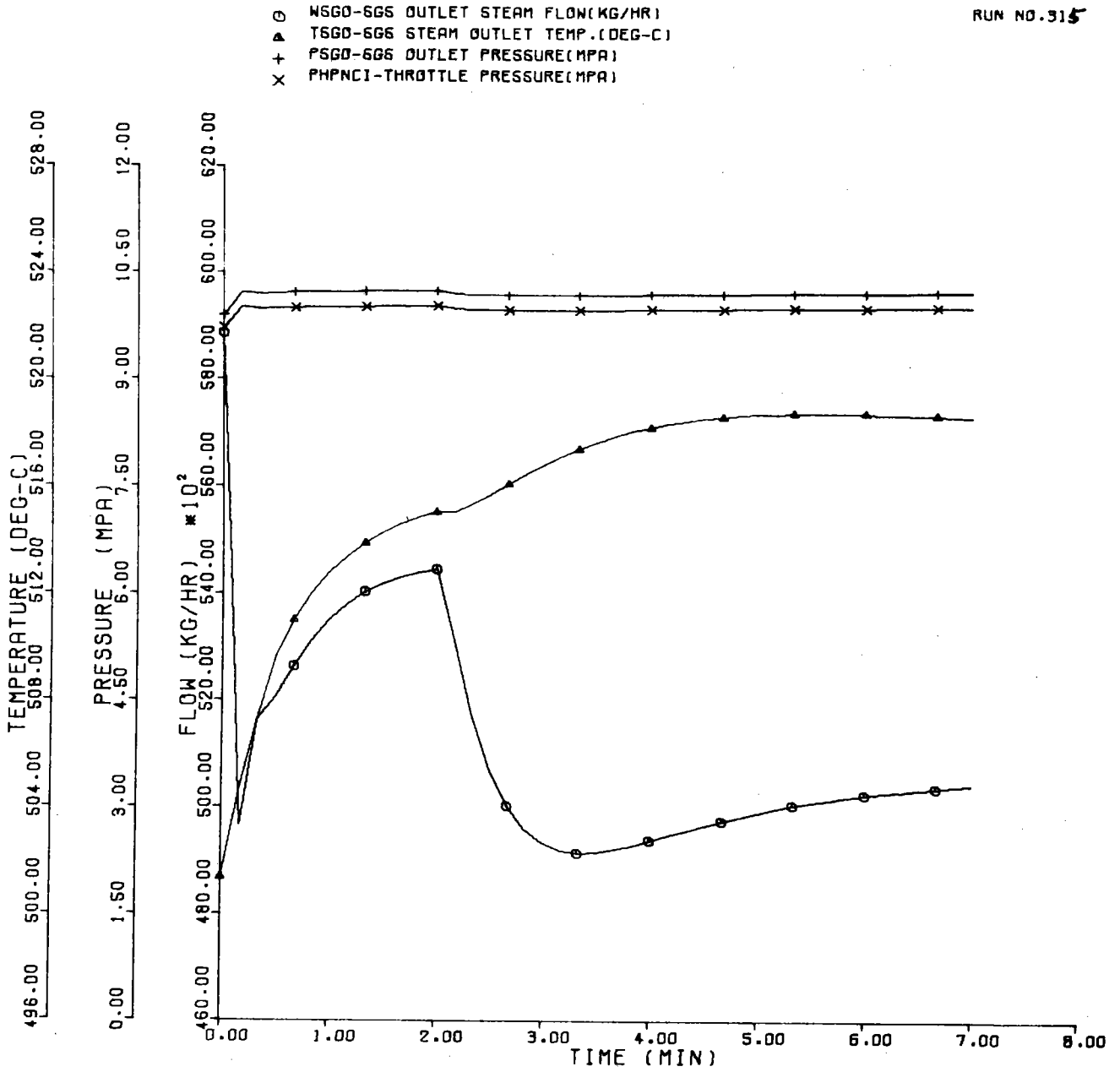


Figure 4-42. Steam Generator Outlet Flow, Pressure, and Temperature for Simulated HP Heater Failure (Run No. 315)

aperture. It is noted that this is an almost impossible failure mode due to the hardware design layout of heliostat computers, communications lines, power distribution, etc. However, the simulated failure was induced anyway to determine the degree of plant responsiveness to this type of occurrence.

Figure 4-43 shows steam generator drum pressure variations after the failure introduction of $t = 2$ minutes. A maximum drop of 0.45 MPa (65.3 psia), or about 4 percent occurs in drum pressure within about 1.5 minutes after the failure. Peak metal temperature rates of change of 404.4°C/hr (760°F/hr) for the primary superheater, and 164.4°C/hr (328°F/hr) for the secondary superheater were noted after this failure. Figure 4-44 illustrates the tendency for metal and steam temperatures within the steam generator to increase with time as a result of the failure.

Megawatt power generation continued nearly constant, due to the ability of the master controller to react quickly to this failure situation.

CONCLUSIONS OF TRANSIENT ANALYSIS STUDY

Based upon this preliminary design phase investigation of the pilot plant transient operation, the following conclusions are made:

- Overall --
 - The plant is responsive, stable, and controllable in the environment of a number of uncontrollable stimuli (e.g., solar intensity variations with time, cloud obscuring) and controllable stimuli (e.g., plant startup sequence, load demand changes).

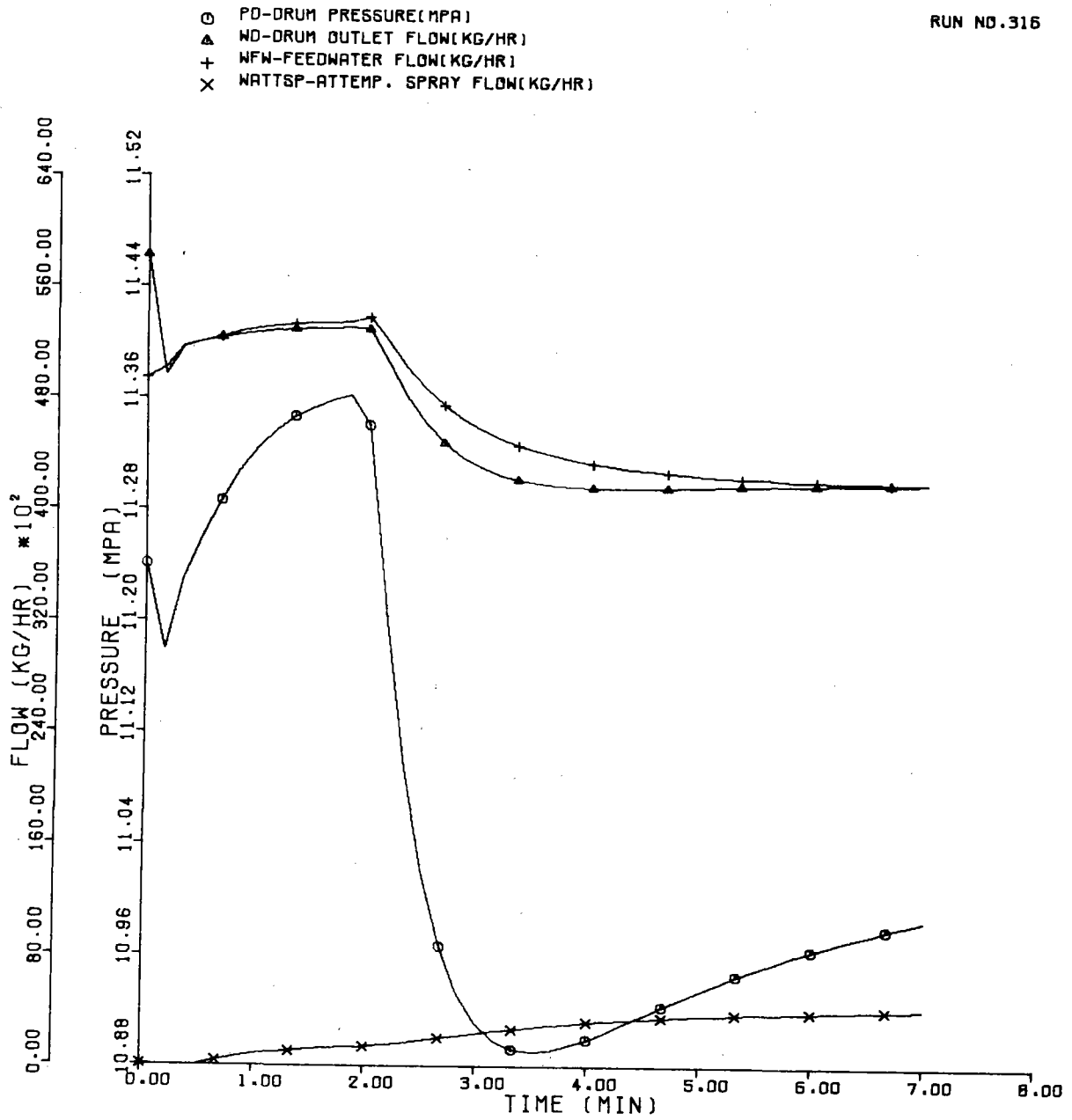


Figure 4-43. Steam Generator Drum Pressure and Steam/Water Flows for Simulated Collector Field Failure (Run No. 316)

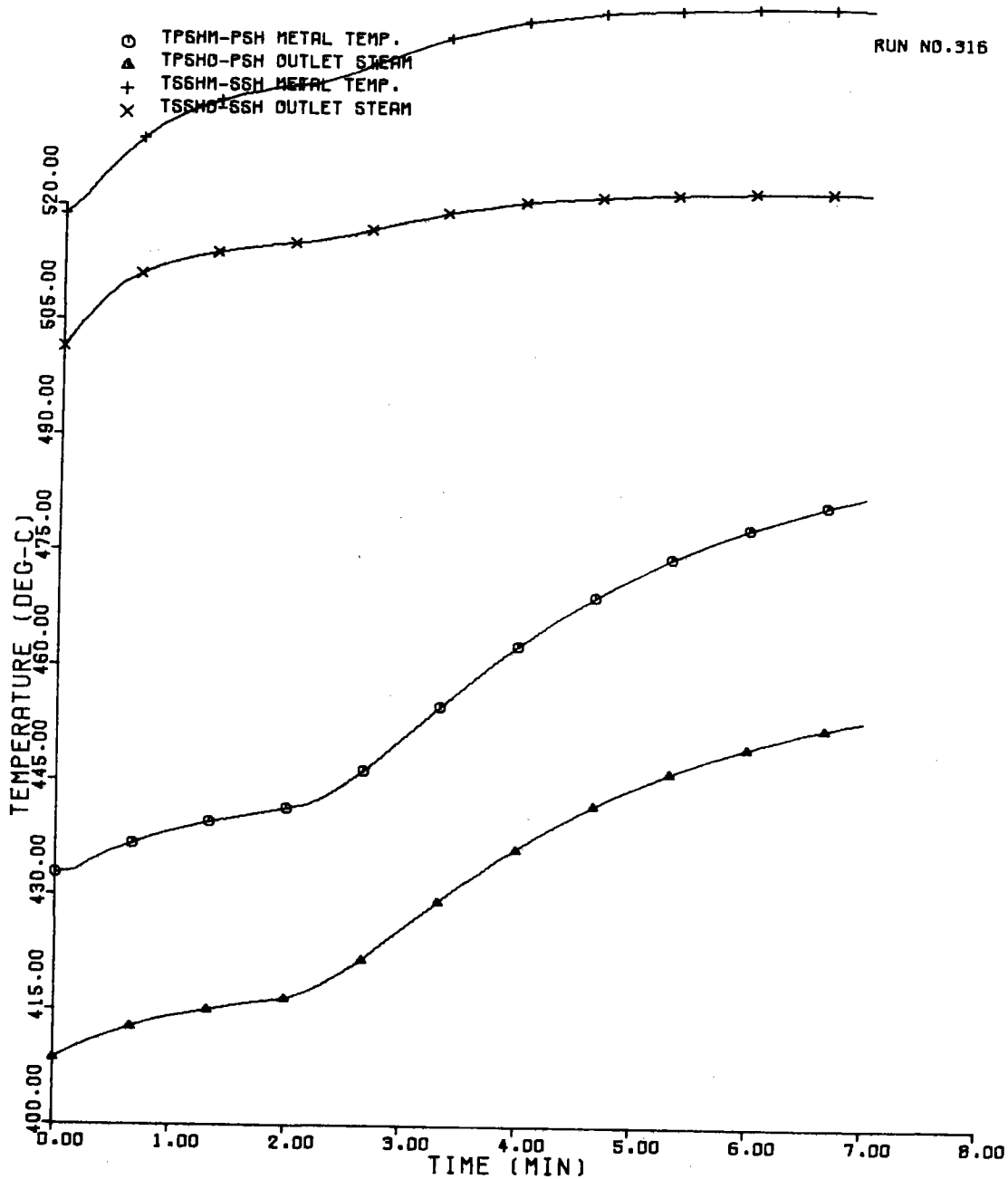


Figure 4-44. Steam Generator Metal and Temperature Variations After Simulated Partial Collector Field Failure (Run No. 316)

- The master controller design serves an integral plant coordinating function for all plant subsystems. The basic design is compatible with a variety of plant operating strategies. It provides good overall plant power generation characteristics in response to load demands even while sensing only two plant feedback variables (throttle pressure and megawatts generated).
- Thermal storage is responsive to demands from the master controller whenever excessive steam (beyond the needs of the turbine) power generation capability is available from the steam generator, or whenever a deficit steam generator power generation situation arises.
- The steam generator itself is sufficiently responsive to changing demands (e. g., steam flow) placed upon it, yet can mitigate the effects of relatively severe off-design disturbance effects (e. g., absorbed power flux imbalances).

- Plant Startup Response --

- A variable-pressure plant startup sequence is feasible, permitting relatively rapid introduction of steam flow at temperatures compatible with those of the turbine shell.
- Initial plant startup can be initiated at sunrise. A number of plant parameters should be traded off in future studies, however, to select the optimum timing and startup sequence as indicated by the results herein. These tradeoff parameters should include auxiliary power requirements, low-flow

turbine efficiencies, various temperature rates of change, turbine generator synchronization time, and desired load demand functions. The tradeoffs should be viewed with careful attention to plant equipment constraints such as temperature rates of change, possible heliostat limitations at low sun angles, various temperature matching requirements, etc. Use of thermal storage for startup functions beyond nighttime sealing steam supply should be considered. For example, turbine synchronization using storage steam may improve overall plant efficiency.

- Cloud Transients --

- As expected, cloud occluding of the heliostat field degrades the ability of the steam generator to maintain adequate steam power flow to the turbine supply. However, near-constant electrical power generation can be continued through timely switchover to thermal storage steam power.
- Steam generator metal and metal temperature rates of change values were relatively high for certain conditions of cloud shading onset. Heliostat defocussing control is speculated to be a means to reduce the degree of this severity. Limitations on the scope of the current study did not permit evaluation of this technique however.
- The speed of cloud shading onset of the heliostat field is a particularly sensitive parameter relative to steam generator metal temperature rates of change and total change. Faster

traveling clouds induce greater excursions in these parameters.

- The direction of cloud approach to the field also affects these steam generator temperature parameters, due to the assymetry of the heliostat layout about the tower and its relatively large size compared with cloud velocities. The direction of cloud approach determines which sections of the steam generator will be most significantly affected in terms of temperature effects.
- Continued investigation of cloud transient effects upon pilot plant performance, using representative pilot plant site cloud data, appears warranted. Clouds are the single most-sensitive parameter of all uncontrollable environmental variables likely to affect plant performance, and these effects should be appropriately addressed in a detailed analytical study.
- Load Demand Changes --
 - The plant is responsive to the desired load demand changes. Thermal storage acts integrally as an energy storage buffer for the steam generator during these changing demand periods, thereby not requiring heliostat refocusing maneuvers.
- Failure Effects --
 - For the limited number of simulated failure cases investigated no serious plant imbalance effects were observed. Normal power plant failure mode protection techniques appear adequate.

SECTION 5
SUPPORTING DATA

Pilot plant safety, availability, support equipment, and test and evaluation are discussed in this section.

PILOT PLANT SAFETY CONSIDERATIONS

Safety criteria for the design and operation of the Pilot Plant have been established and are briefly reviewed in this section. Criteria and regulations contained in OSHA, ASME, ANSI, NFPA, NEC, State and Local Codes as they apply are not discussed. These applicable codes and standards were considered and reflected in the preliminary design. The safety aspects of the redirected flux from the heliostat field is discussed in some detail however. This particular issue is peculiar to the Central Receiver Concept and will require special consideration during detail design, fabrication, and operation of the Pilot Plant. Coordination with governmental and citizen groups will be mandatory to permit uninterrupted use of the facility. No genuine safety hazard exists although proper education and information exchange will be necessary for the operating personnel and the adjacent community.

Inherent Hazards

A solar thermal power plant contains hazards that are unique to solar applications as well as the typical or common industrial hazards. These solar thermal power plant hazards are as follows:

- a) The most significant pilot plant hazard is the concentrated solar beam with its attendant potential to damage unprotected structures and cause serious injury to personnel. An individual heliostat presents no major structural hazards but if personnel are at or near the focal point it can be a human tissue hazard. If more than one heliostat reflects beam concentrations to a specific location then serious hazards may exist dependent upon beam intensity, slew time, source distance and source angle. Concentration of an intense heat source on a surface results in potential damage to the structure and potential personnel hazards from reradiated energy as well as direct thermal damage to the retina of the eye and exposed skin tissue. Hazard exposures of the general public to these beams in the vicinity of the power plant, on the ground and in the airspace above, are a basic safety hazard that must be avoided.
- b) During operation the receiver system has the basic hazards of high pressures and temperatures during the generation of superheated steam from the concentration of solar flux on the receiver surfaces. Illumination of the receiver surfaces causes a strong reradiated light source and is a potential local personnel hazard. These hazards are normal operational characteristics of the solar receiver and can be controlled by personnel exclusion areas, access interlocks, eye protection equipment, and personnel training. However, the associated hazards with high pressures and temperatures and the potential for component/system failure can result in explosions, fragmentation, component/line whipping, and parts falling from the receiver/tower. Personnel working in the receiver/tower may also be subjected to access/egress to or from limited work locations as well as the potential of falling from dangerous heights.

- c) The Thermal Storage System presents no unique solar hazards but the application of this system to a solar plant does present inherent hazards. These hazards are high temperatures and pressures of the storage tanks, high temperatures of the heat storage fluid, and the use of superheated steam in the heat transfer process. The exposure of personnel to heat and pressures of the storage system are the primary concern but the storage media may also have corrosive or toxic properties. Oil systems also have a fire potential if improper insulation materials are used in areas subject to system leaks. Area insulation and proper work station selection should reduce these hazard potentials to acceptable levels consistent with commercial operations.
- d) The electrical power generation system possess the common utility hazards of exposures to high voltage, superheated steam, equipment generated high noise levels as well as high pressures and temperatures. The selection of specific system controls for the protection of the turbine and grid interface equipment will be based upon the turbine selected and the requirements of the utility user. Personnel protection requirements are also based upon the utility and state in which the system is used.
- e) The general inherent hazards located throughout the pilot plant include the potentials for electrical shock/electrocution, falls from elevated work platforms/areas, handling of chemicals or cleaning liquids as well as the specific system related hazards identified in the previous paragraphs.

There is a damage potential from solar radiation to personnel and structures from energy reflected from the collector field. During normal operation, when the heliostats are directing flux into the aperture, heat shielding has been provided to protect the receiver housing from aperture flux spillage. Also the standby aimpoint is selected to be far enough from the housing so that the heat shields will continue to protect the receiver structure. The

heliostat control system is programmed to prevent coincident aiming of multiple heliostat reflected beams during start-up or storage. Reflected beam control will be accomplished by keeping the mirror side away from the sun until the mirrors are nearly horizontal. The mirror normal will remain less than 90 degrees from the vector from the sun while operating between storage and standby. Sequential operation of the field by zones further reduces the probability of many coincident aims at a particular time.

Structural protection during abnormal operation is provided by control provisions to prevent coincident aiming outside of standby, or operation, and fail-safe return to stowage upon command failure.

The protection for personnel requires a consideration for the reflected beam intensity levels as a function of the distance from the heliostat.

There exists some limit to the physical dimensions within which the "beam" can usually be considered hazardous. This paragraph attempts to define that zone for the pilot plant and the commercial plant.

Figure 5-1 shows a single facet curved for focus and illuminated by an area source (the sun). From the figure it should be clear that the beam angle γ is the sun angle (α) plus twice the focal half angle (here defined as β). Thus an approximation of "beam" diameter is γ (in radians) times the slant range (in meters). Since the maximum energy is the insolation (incident on the mirror) times the mirror area this number will be used. Thus the following calculations:

$$\text{Insolation} = 1000 \text{ W/m}^2$$

$$\text{Mirror} = 10 \text{ m}^2$$

$$\text{Total power} = 10 \times 1000 = 10 \text{ kW}$$

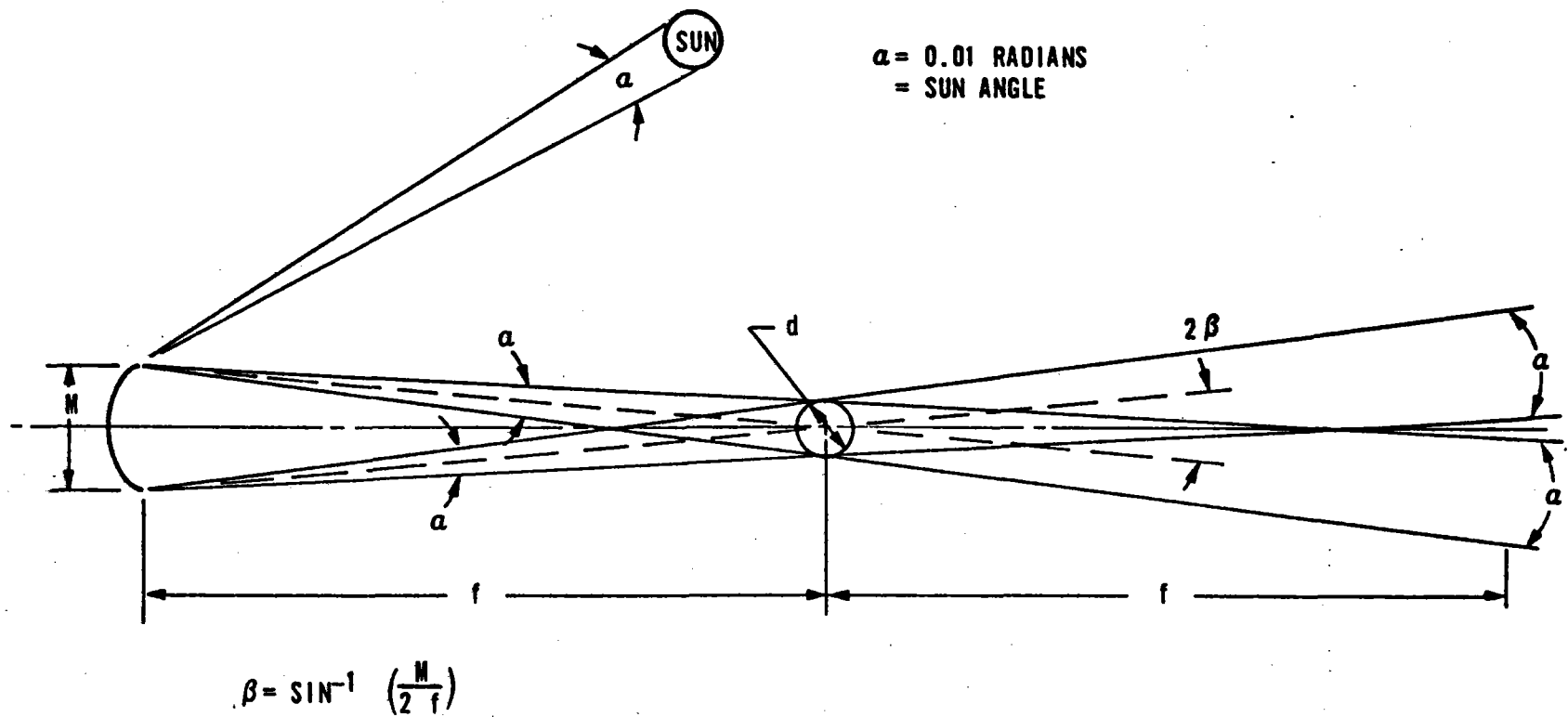


Figure 5-1. Single-Facet Curved Mirror

At slant range of 345m beam diameter is

$$\text{Dia} = \gamma \text{ SR} = 0.01947 \times 345 = 6.72\text{m}$$

$$\text{Area} = \frac{\pi c/2}{4} = 35.4 \text{ m}^2$$

$$\text{Flux} = \frac{10 \text{ kW}}{35.4 \text{ m}^2} = 282 \text{ W/m}^2 \text{ compared}$$

to incident sunlight of 1000 W/m^2 . Using this number and the calculations of Table 5-1, we conclude the zone of concern to be two focal lengths (or less) away from four heliostat mirrors.

Consider now Figure 5-2 which shows the four-facet geometry. Note since the facets are spaced on $1.6 \times$ facet size dimensions that there appears to be a larger spread angle beyond the focal area. Again consult Table 5-1 for γ and at the distance f_0 past the focal area the spot or beam diameter is

$$\text{Dia}_4 = \gamma_4 \times \text{SR} = 0.03308 \times 408 = 13.5$$

$$\text{Area} = \frac{\pi(\text{Dia})^2}{4} = 143 \text{ m}^2$$

Using four facets at 10m^2 each and insolation of 1 kW/m^2 yields:

$$\text{Flux} = 40 \text{ kW} \div 143\text{m}^2 = 279 \text{ W/m}^2$$

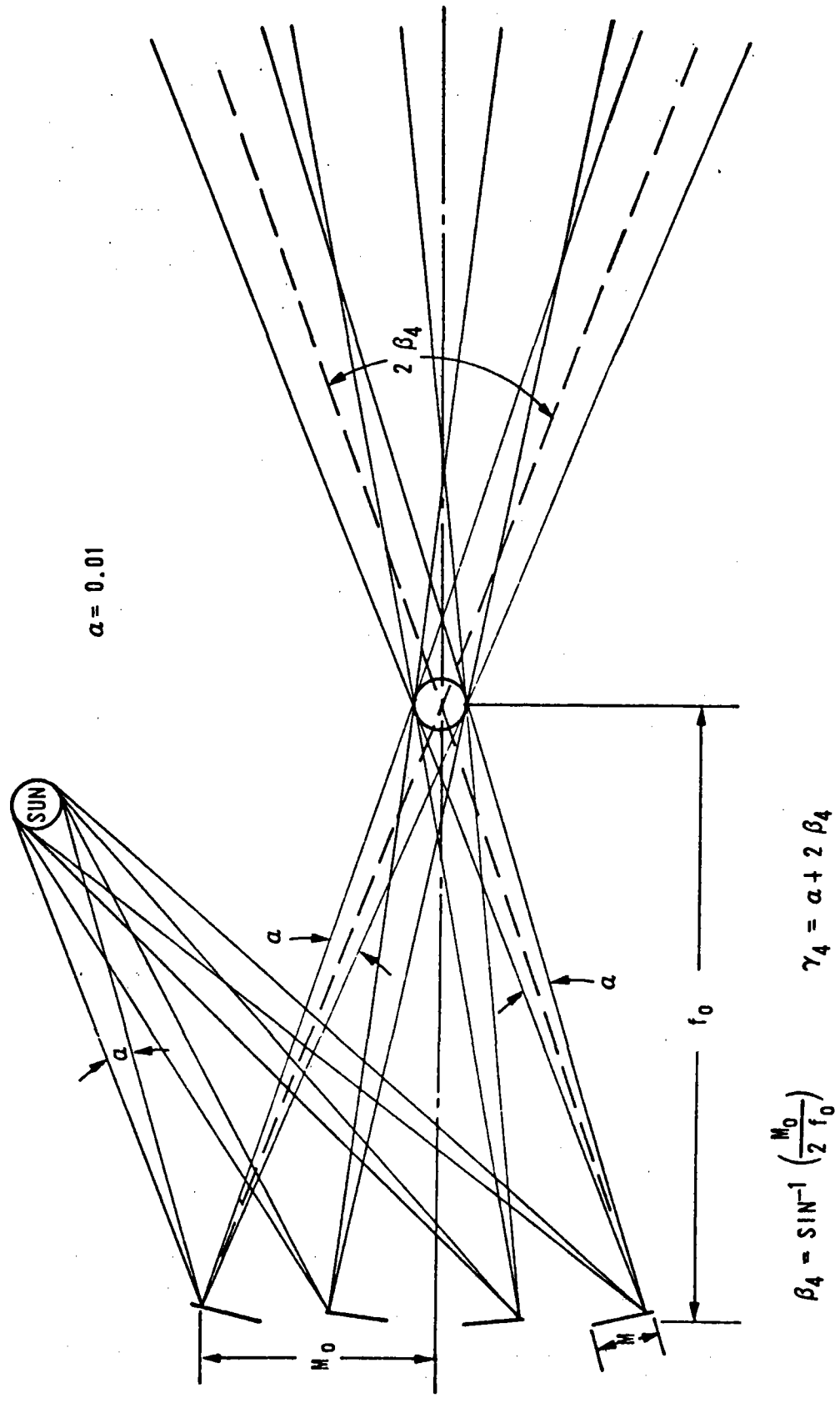
again a relatively safe level compared to the basic 1 kW/m^2 available from the sun.

The zone of concern will not be more than two focal lengths from the heliostat. as is shown in Figures 5-3 and 5-4, and Table 5-2. Light barriers are used to protect personnel and inner field structures from reflected flux as shown in Figure 5-5.

Table 5-1. Single- and Four-Facet Mirror Characteristics

<u>Characteristic*</u>	<u>Units</u>	<u>Figure 5-1 Dimensions</u>	<u>Figure 5-2 Dimensions</u>
M*	Meters	3.16 x 3.16	3.16 x 3.16
f	Meters	345	408
β	Radians	0.00947	N/A
α	Radians	0.01	0.01
	Radians	0.01947	N/A
M _o	Meters	N/A	9.4
f _o	Meters	N/A	408
β_4	Radians	N/A	0.01153
4	Radians	N/A	0.03308

*Reference Figures 5-1 and 5-2.



$$\beta_4 = \sin^{-1} \left(\frac{M_0}{2 f_0} \right)$$

$$\gamma_4 = \alpha + 2 \beta_4$$

Figure 5-2. Four-Facet Mirror

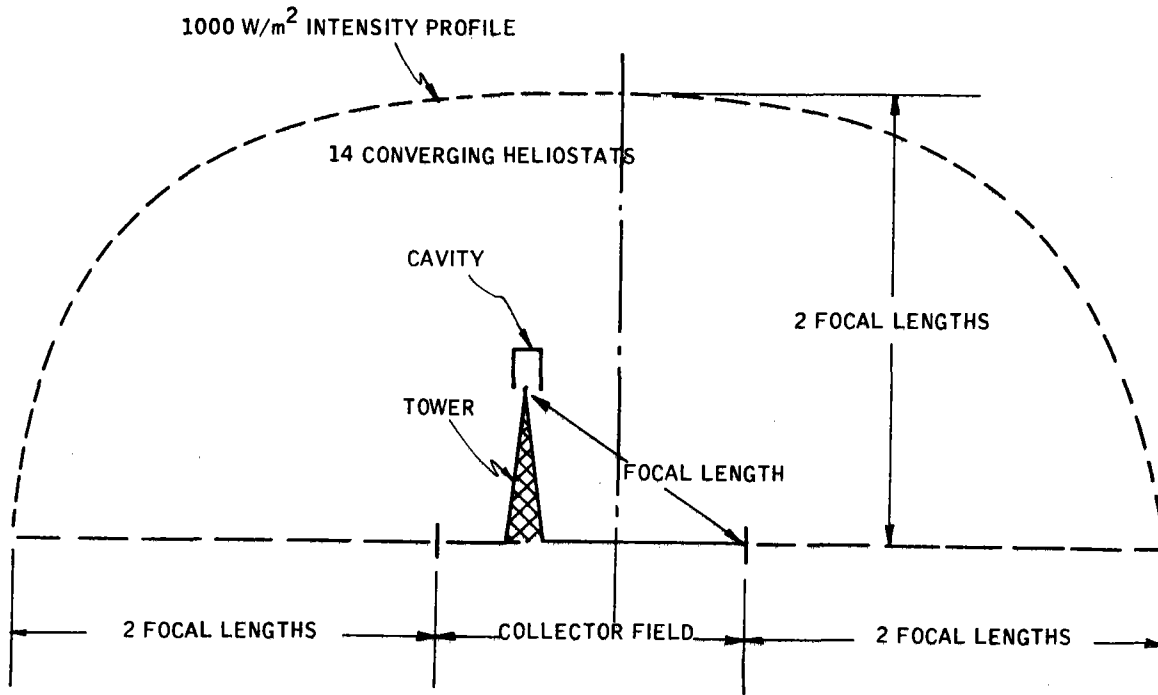


Figure 5-3. One-Sum Intensity Limit

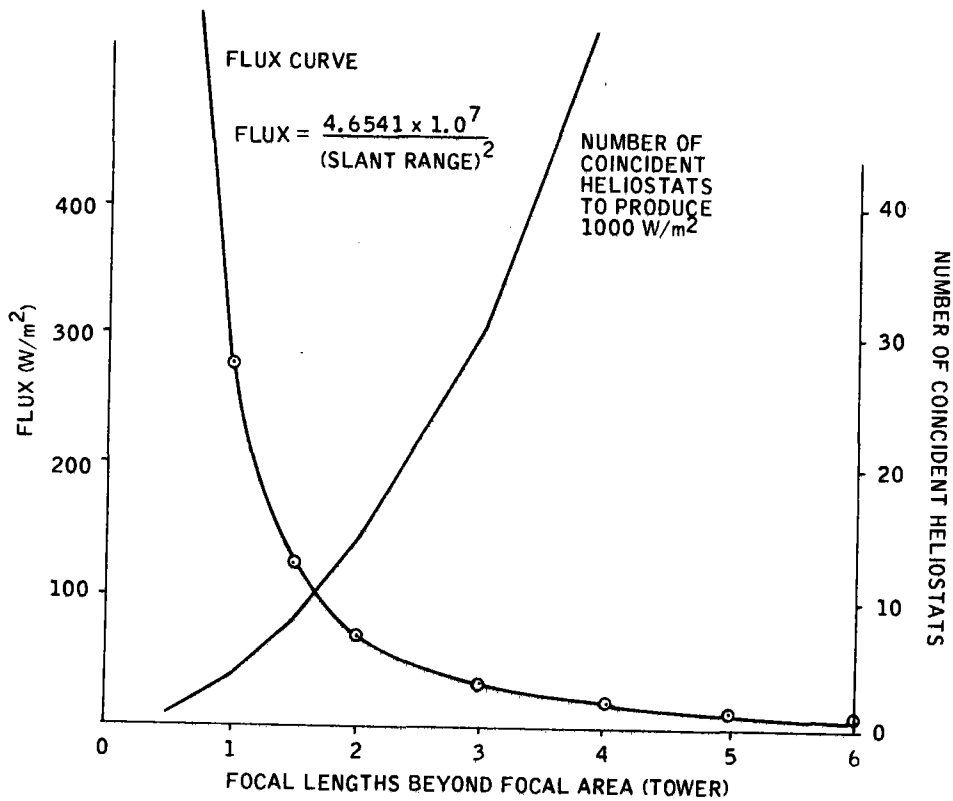


Figure 5-4. Flux versus Distance

Table 5-2. Flux versus Slant Range for Four Facets

<u>Focal Length</u>	<u>Slant Range</u>	<u>Flux</u>	<u>No. of H/S to Produce 1000 W/m</u>
1/2	204	1118.35	0.9
1	408	279.59	3.5
1 1/2	612	124.26	8.1
2	816	69.90	14.3
3	1224	31.07	32.3
4	1632	17.47	57.2
5	2040	11.18	89.5
6	2448	7.77	128.7

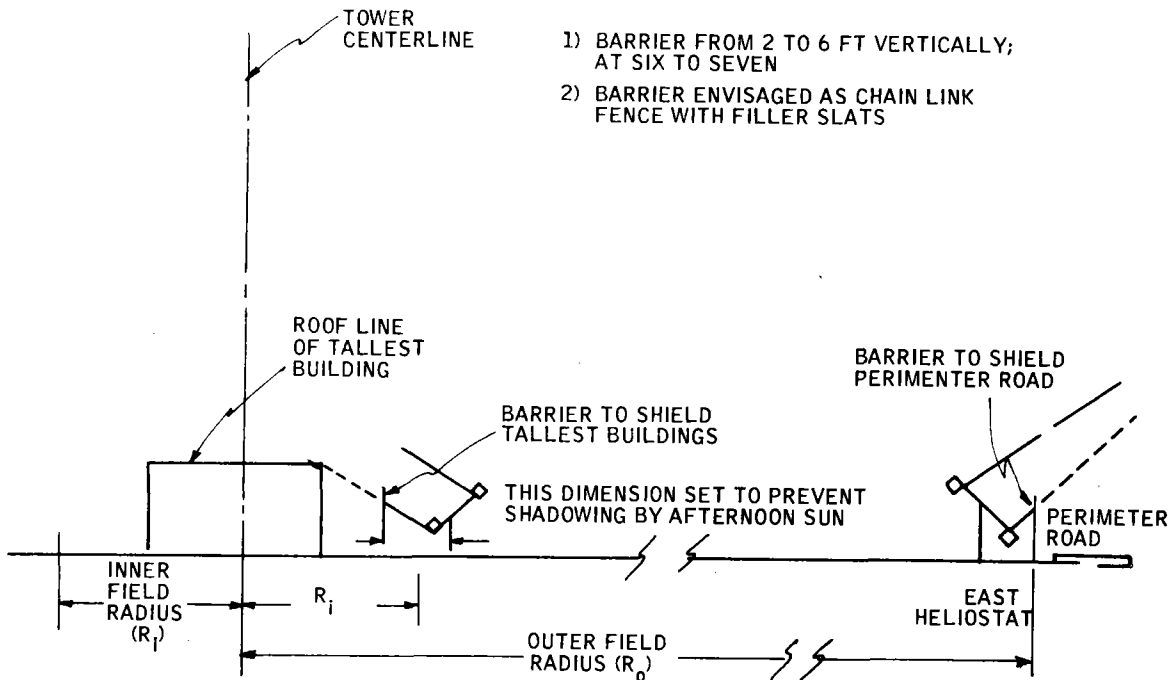


Figure 5-5. Barrier Concept

The barrier will be opaque to sunlight but shall also not cause substantial structural loads from wind environments. To meet these goals a chain link fence with filler slats is employed. The inside barrier will protect buildings and grounds near the base of the tower. The outside barrier shall protect external facilities as well as the perimeter road.

Low-flying planes of a fixed-wing variety present little or no problems, even for the multiple focal convergence of several heliostats, as pilots and passengers would be protected by their rapid passage through the high-flux pattern.

Of special concern are helicopters and lighter-than-air aircraft with their hovering capability. Because of this, the FAA will be petitioned to make an area of up to 5km from the center of the collector field as a hazardous area for slow-moving aircraft (see Figure 5-6).

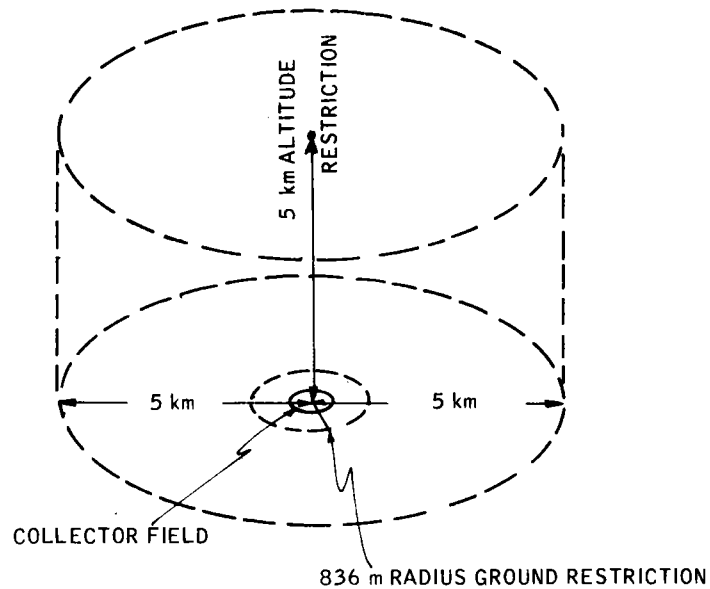


Figure 5-6. Aircraft Restricted Zone

Collector Subsystem Criteria

1. Casual personnel and aircraft protection has been discussed in the preceding section.
2. A heliostat beam control method/procedure has been developed and incorporated as a function of the heliostat control system design which will safely control beam positions during standby and stow/acquisition maneuvers. The control method/procedure:
 - a) Excludes movements of beams through normally occupied facility areas;
 - b) Avoids movement of beams through normally occupied facility structures not specifically protected to withstand concentrated solar flux.

3. The heliostat control system incorporates a fail-safe design such that any failure of primary electrical power will not result in an unsafe beam condition insofar as collector/collector field orientation is concerned.
4. Loss of primary electrical power to the heliostat control system results in all heliostats being placed to a safe standby position and then to a stow position. A secondary (standby/emergency) power source is available for safe shutdown of the system upon loss of primary power.
5. Loss of primary electrical power or control response of any heliostat(s) that could result in a safety hazard results in the initiation of a fail-safe action by the collector control system.
6. The collector field will not be left in an up-stow position during insolation hours with multiple heliostats having convergent optical axis. Only parallel or divergent heliostat optical axis stow positions, with respect to individual heliostats, are used during insolation hours.
7. Heliostats have "safe" stow positions which will be used during periods of maintenance, high winds, at night, in stormy weather, or in case of other emergencies.
8. The ability exists to detect out-of-limit or malfunctioning heliostats and provide a method to position the heliostat to a safe standby or stow position.
9. The heliostat design includes the capability of local (manual or electronic) control at the individual heliostat location for maintenance and setup, all other modes of control are locked out when the heliostat is in the local control mode.

10. The heliostat is designed so that accessibility to potential maintenance/ adjustment points such as electronic units, motors, drives, mirrors, etc., presents no inherent personnel hazard.
11. The ability to safe a heliostat(s) exists if a single failure mode is possible that would fail a heliostat(s) in a hazardous orientation.
12. The heliostat control system possesses the capability to identify/ recognize the existence of a hazardous condition, initiate safe corrective action, and verify that corrective action has occurred.

Receiver Subsystem Criteria

1. The receiver provides the necessary sensors and control equipment to monitor and control the pressure and temperature of the working fluid and to detect a malfunction and initiate a fail-safe shutdown or corrective action.
2. Venting of pressure vessels and their safety valves will be in accordance with the ASME Boiler and Pressure Vessel Code and will be located and/or guarded so that escaping gases or liquids present no personnel hazards.
3. The receiver incorporates a redundant fail-safe shutdown or corrective action control system. Location of the redundant paths of the control system is so that an event which damages one path is not likely to damage the second.

4. Safety interlocks/access controls are provided in the receiver tower to prevent personnel from entering the tower space in the vicinity of the receiver anytime one or more heliostats are directed on the receiver tower. The tower is of enclosed construction; the access limit will be established at the one-half (1/2) tower height.
5. The external surfaces of the receiver tower that will be subjected to solar flux radiation will be protected in such a manner as to preclude structural damage to the tower that would create a hazardous condition for operating personnel from falling objects inside or outside of the tower structure.
6. Equipment located within the tower structure will be grounded and suitable precautions taken to protect the tower and equipment against lightning. The lightning arrestors and grounding wires are installed inside of the tower structure and they will be enclosed and will be located well away from personnel passageways.

Thermal Storage Subsystem Criteria

1. Earth berms and/or retaining walls will be provided around thermal storage tanks containing flammable or combustible liquids. The design shall be in accordance with Title 29-Labor (Ref. CFR Parts 1910.106 and 1926.152).
2. A protective barrier will be provided between non-compatible substances to prevent mixing.
3. The thermal storage subsystem will accept and execute control commands, detect a malfunction, and initiate fail-safe shutdown or alternate operating procedures through a control system.

4. The ability exists to detect hazardous leaks in the thermal storage system and provide a method to isolate this leak from the rest of the system.
5. Adequate monitoring capability is provided to detect potentially hazardous conditions (e. g., fluid mix and steam mix; in the various closed loop systems of water, steam oil, salt, etc), and provide adequate capability to perform corrective action as required.
6. Safety showers and eye wash fountains are provided for in the vicinity of tanks containing toxic materials in accordance with Title 29-Labor requirements (Ref. 1910. 151.)
7. Closed cell insulation is installed for all areas where an oil leak may occur. The principle candidate areas for closed cell insulation is at all system penetrations or non-welded connections, such as, instrument connections, valve packing glands, flanges, etc.
8. The design includes provisions to monitor heat transfer media temperatures throughout heat-up operations to ensure that localized temperatures do not exceed system design values.
9. The inert gas blanket system(s) for the TSS will have a safety relief device to protect against pressure buildup which may exceed design levels.

Electric Power Generating System Criteria

1. The electrical power generation system provides the necessary sensors and control equipment to monitor/control critical turbine parameters in accordance with the requirements of Southern California Edison Company and the recommendations of the selected turbine supplier.

2. The design includes provisions to monitor steam inlet temperatures and turbine temperatures to detect lead temperatures and ramp rates in excess of turbine design values.
3. The system has the capability to detect or eliminate by design the occurrence of a steam leak at the closed trip-throttle valve to minimize condensation on the internal surfaces of the turbine which may produce erosion-corrosion problems.
4. The design provides for monitors to detect the occurrence of excessive vibration during operation and control excessive temperature bow during shutdown periods.
5. The design ensures that cold steam headers are drained before admitting steam, and the drains remain open until the line is sufficiently warmed.
6. All turbine and electrical safety trip controls which require periodic functional verifications will be identified during design/procurement and their frequency of performance established.
7. Parts or components with elevated temperatures will be insulated against contact with, or exposure to, personnel.
8. Any moving elements will be shielded to avoid entanglement and safety override controls will be provided for servicing.

Existing Applicable Codes and Standards

As the site of the solar-thermal power plant has been selected to be in California (near Barstow), the sections of Title B, California Administrative Code (CAL/OSHA) as supplemented by the California administrative register

shall be the highest order of code in effect at the site. Also in effect is the Federal Occupational Safety and Health Administration (OSHA) Standards (CRF 29) parts 1910 and 1961, and the local building codes of the county of San Bernadeno, California. Any disagreement between these codes shall result in the most restrictive definition being enforced. These codes will be enforced during the operational life of the facility.

By direction of these codes, also included (but not limited to) are the applicable sections of the following:

- National Fire Protection Association (NFPA) including the National Electrical Code
- American National Standards Institute (ANSI) Boiler and Pressure Vessel Code Sections 1, 2, 5, 8, and 9.

SOLAR PILOT PLANT AVAILABILITY ANALYSIS

Summary

This cursory analysis includes the definitions/groundrules, operational strategy, and model which have been established for use in the solar pilot plant availability analysis. The analysis addresses the RFP, Annex 1, System Requirements Specification,"3.2.5 Availability. Ninety percent of the time based on reliability and maintainability exclusive of insolation conditions." Since ERDA has provided no guidance in this area, the definitions, groundrules, and operational strategy set forth herein have been used. From the results of the analysis, the availability of the solar pilot plant is predicted to be greater than 93 percent.

Inclusion of features to maximize solar pilot plant availability is inherent in the design process. A few examples of how availability improvement has been considered are:

- Components meeting the requirements of ASME codes are used where available to maximize component reliability and life.
- Automatic control valves are isolated and are paralleled with manual valves to permit repair or replacement without degradation of plant performance.
- Transmitters and indicators are appropriately placed and monitored so that the loss of any one item will be accommodated by making deductions from the information from the rest of the items during repair or replacement of the failed item.
- Valves with readily removable trim are widely used to permit replacement of trim rather than replacement of the whole valve in case of failure.
- Redundancy features will be incorporated in the control portions of the solar pilot plant to permit much "on-line" repair or to permit delay of the repair to free-time maintenance without performance degradation.
- Battery packs will provide backup power for the heliostats in case of electrical failure.
- Receiver circulating pumps are redundant in that only two of three are required under full load.
- Several major components are dual and the loss of one would not degrade performance during the time required to make the repair. They include:

- Main feedwater pumps
- Booster feedwater pumps
- Condenser air-removal segment
- Service water pumps
- Auxiliary cooling water pumps
- Auxiliary cooling water booster pumps
- Service and control air system

Analysis Detail

A cursory availability analysis of the solar pilot plant has been conducted using basic techniques of reliability and maintainability analysis which have been used extensively in commercial, military, and space systems. However, the unique nature of the solar pilot plant necessitates that specific groundrules, definitions, operating strategy, and models be established for use in the availability analysis. These are discussed next, in the three subsections that follow.

Analysis Definitions/Groundrules -- The definitions/groundrules presented herein are based, either directly, or with some tailoring to the solar pilot plant, on those established in Ref. 1, Edison Electric Institute (EEI) Availability Report, and/or Ref. 2, Reliability Engineering book.* The EEI availability data collection and analysis system were placed into operation in September 1969. EEI now publishes an annual report of availability and outage statistics for electric generating facilities operating in the United States which includes data on over 2200 generating units. Following are the definitions established:

* See end of this section for complete entries.

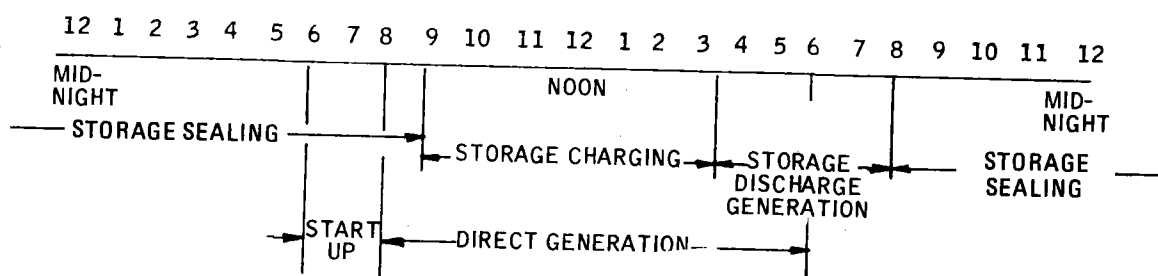
- Availability - of a system or equipment is the probability that it is operating satisfactorily at any point in time when used under stated conditions. As such, availability is a function of the frequency of maintenance and the duration of time to accomplish the maintenance for each maintenance action. Both unscheduled maintenance (forced outages) and scheduled maintenance (planned outages and maintenance outages) are included. (For this analysis, > 98 percent of system capability is considered satisfactory operation.)
- Forced Outage - is the occurrence of a failure or other condition which requires that the load on the system be reduced by 2 percent or more, or that the system be removed from service immediately.
- Planned Outage - is the removal of the system from service for inspection and/or general overhaul. This is work which is usually scheduled well in advance (e. g. , boiler overhaul or turbine overhaul).
- Maintenance Outage - is the removal of the system from service to perform maintenance which could have been postponed for a matter of days but not until the regularly planned outage time. It is maintenance performed to prevent a potential forced outage.
- Noncurtailing Equipment Outage - is the removal of specific equipment(s) from service for repair, which causes no reduction in system output power or a reduction of less than 2 percent. For example, loss of service of an individual heliostat reduces the average daily system output approximately 0.06 percent.
- Free-Time Maintenance - is time during the daily periods of no and unusable insolation during which maintenance can be done which is considered not to degrade system availability.

The following groundrules were assumed:

- Cooling Time - Based on information from Northern States Power, cooling time is generally not considered a significant factor in the maintenance time for fossil-fired power plant equipment.
- Support - In making the mean-time-to-repair (MTTR) predictions, it was assumed that adequate personnel, spare parts and material, tools, test equipment, and facilities will be available to perform scheduled and unscheduled maintenance as required.

Operational Strategy -- The following operational strategy is proposed for use in the availability analysis. Two primary areas which this strategy impacts are allowable equipment failure which constitute a "noncurtailing equipment outage" and the daily "free-time maintenance" for each of the pilot plant subsystems.

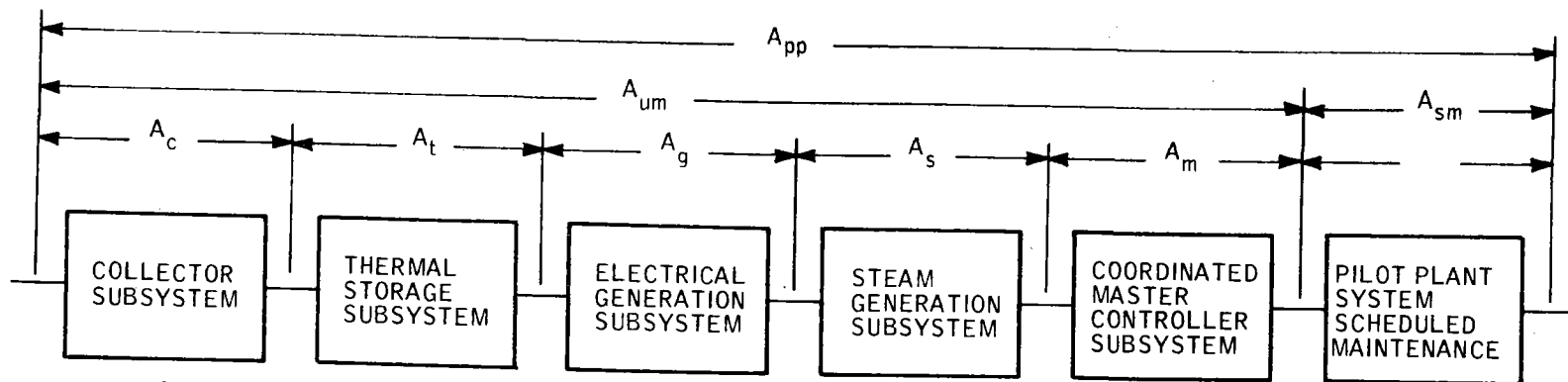
Free-time maintenance is based on the following average daily power generation profile:



Based on this average daily power generation profile, free-time maintenance for each pilot plant subsystem is:

	<u>Free Time Maintenance Daily Hours</u>	<u>Period</u>
● Collector subsystem	12	When not used for startup, storage charging and/or direct generation.
● Steam generation subsystem	12	When not used for startup, storage charging and/or direct generation.
● Electrical generation subsystem	10	When not used for startup, direct generation and/or storage Discharge generation
● Storage subsystem	17.5	When not used for storage charging.
	19.5	When not used for storage discharge generation.

Availability Analysis Models -- At the system level, the solar pilot plant availability is indicated by the model shown in Figure 5-7. The pilot plant availability (A_{pp}) is the product of the availability of each of the five subsystems, considering unscheduled maintenance due to forced outages, and the availability for scheduled maintenance for the entire system (i. e., planned outages and maintenance outages).



$$A_{pp} = A_{um} \times A_{sm}$$

$$= A_c \times A_t \times A_g \times A_s \times A_m \times A_{sm}$$

WHERE

- A_{pp} = SOLAR PILOT PLANT AVAILABILITY
- A_{um} = SOLAR PILOT PLANT AVAILABILITY, UNSCHEDULED MAINTENANCE
- A_c = COLLECTOR SUBSYSTEM AVAILABILITY UNSCHEDULED MAINTENANCE
- A_t = THERMAL STORAGE SUBSYSTEM AVAILABILITY, UNSCHEDULED MAINTENANCE
- A_g = ELECTRICAL GENERATION SUBSYSTEM AVAILABILITY, UNSCHEDULED MAINTENANCE
- A_s = STEAM GENERATION SUBSYSTEM AVAILABILITY, UNSCHEDULED MAINTENANCE
- A_m = COORDINATED MASTER CONTROLLER SUBSYSTEM AVAILABILITY, UNSCHEDULED MAINTENANCE
- A_{sm} = SOLAR PILOT PLANT SYSTEM AVAILABILITY, SCHEDULED MAINTENANCE, i.e., PLANNED OUTAGES AND MAINTENANCE OUTAGES.

Figure 5-7. Solar Pilot Plant System Availability Model

Unscheduled Maintenance -- Unscheduled maintenance is the subsystem availability considering the previously defined forced outages. Subsystem availability is a function of the subsystem hardware items MTBF (mean time between failure) which result in outages and the MTTR or average outage time to get the system back on line considering waiting time, active repair time, administrative time, etc. The basic equation which indicates the availability of a hardware item (A_i) is:

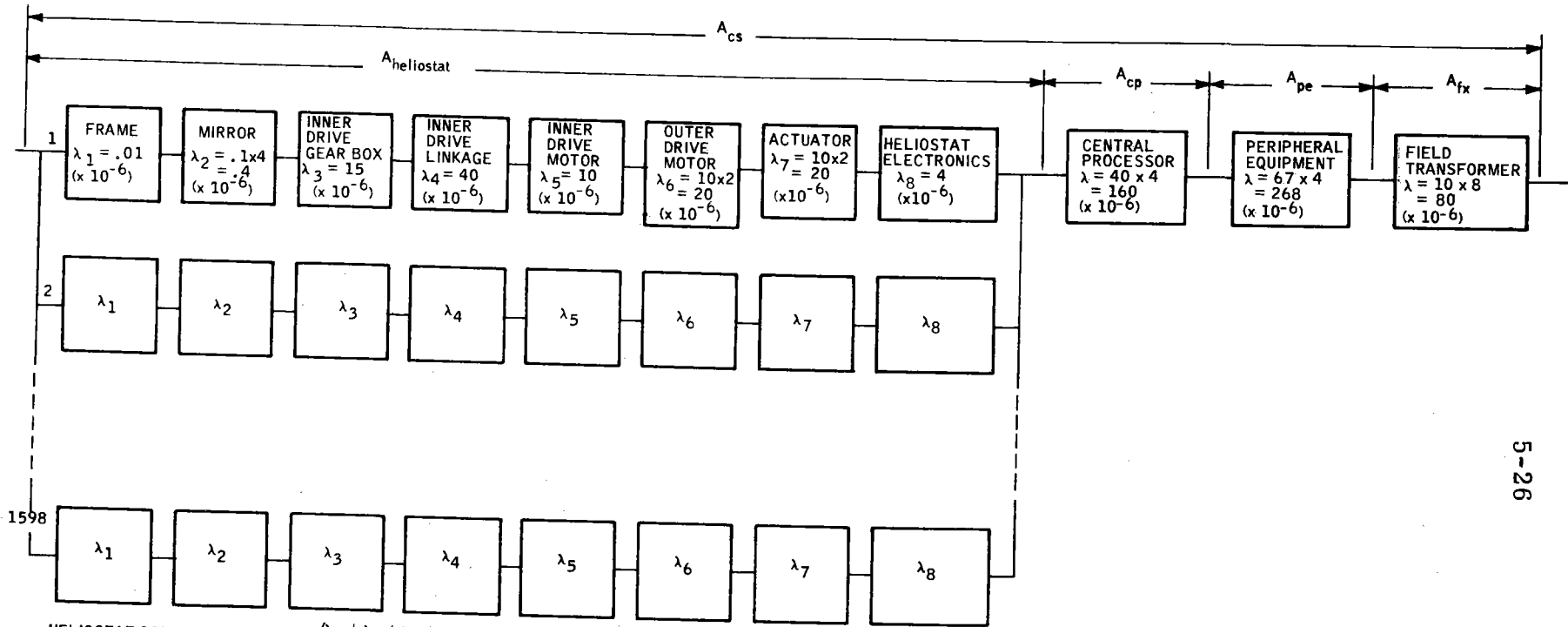
$$A_i = \frac{MTBF}{MTBF + MTTR}$$

The availability of the individual hardware items which comprise each subsystem is combined by an appropriate model which reflects redundancy considerations, e. g., failures which result in noncurtailing outages. Noncurtailing outages which are being included in the subsystem availability models are discussed. As previously defined, noncurtailing outages are hardware item failures or combinations of failures which result in no reduction in system output power or an average daily power reduction of less than 2 percent.

The four availability models are:

- 1) Collector Subsystem Availability Model -- The collector subsystem availability model is as shown in Figure 5-8. As reflected in the model, the items associated with the individual heliostats are treated as one combined item for which 1567 of 1598 are required to achieve 98 percent of the collector subsystem capability, i. e., greater than 98 percent capability will be retained with the loss of any combination of 31 of the following elements:

- Frames
- Four mirrors
- Inner-drive gear boxes



$$\begin{aligned} \text{HELIOSTAT RELIABILITY } (r_1) &= e^{-\lambda_1 + \lambda_2 + \lambda_3 + \lambda_4 + \lambda_5 + \lambda_6 + \lambda_7 + \lambda_8} t \\ &= e^{-126.0001094} \\ &= .99868 \end{aligned}$$

$$\begin{aligned} \text{PROBLEM OF FAILURE OF ONE HELIOSTAT} &= 1 - .99868 \\ &= .00132 \end{aligned}$$

$$\begin{aligned} \text{NO. OF EXPECTED FAILURES IN ONE 12-HR PERIOD} &= 1598 \times .00132 \\ &= 2.11 \end{aligned}$$

IF A POISSON FAILURE DISTRIBUTION IS ASSUMED, THE PROBABILITY OF HAVING 31 OR MORE SIMULTANEOUS HELIOSTAT FAILURES DURING A 12-HR PERIOD IS SO REMOTE AS TO BE NEGLIGIBLE. THEREFORE, $A_{heliostat} \rightarrow 1.0$.

Figure 5-8. Collector Subsystem Availability Model

- Inner-drive linkages
- Inner-drive motors
- Outer-drive motors
- Actuators
- Heliostat electronics

The probability of having 31 or more of the above elements failed within one 12-hour period is so small that it is neglected in availability calculations, assuming that repairs are made promptly. The repairs can be made during "free-time maintenance" without further impacting operation.

Loss of battery backup would impact operation only if such loss occurred when needed for emergency. Here again, 98 percent capability would be retained if as many as 31 backup batteries were lost. The likelihood of sufficient battery power not being available in case of emergency is considered negligible for availability calculations.

Loss of elements of the calibration array does not impact operation, but rather the capability of verifying proper collector alignment. Calibration array repairs must be done during "free-time maintenance" when the receiver is not being heated.

As the collector subsystem is required only during the 12-hour startup or direct-generation cycle, all preventive maintenance can be done during the "free-time maintenance" period. (No preventive maintenance tasks take longer than 6 hours.)

In view of the above, only the central processor, the peripheral equipment, and the field transformer are considered in the collector subsystem availability calculations:

$$MTBF = \frac{10^6}{160 + 268 + 800} = 1970 \text{ hr}$$

$$MTTR = \frac{428 \times 4^{(1)} + 80 \times 10^{(2)}}{508} = 4.9 \text{ hr}$$

$$A_c = \frac{1740}{1744.4} = 0.997$$

- (1) Central Processor or Peripheral Equipment repair time hours.
 (2) Field Transformer repair time hours

- 2) Thermal Storage Subsystem Availability Model -- The thermal storage subsystem availability model is shown in Figure 5-9. The model groups the elements of the thermal storage subsystem in descending order from most used to least to noncritical (depending on the mode) in terms of the daily power generation profile. As reflected in the model, a number of the elements are noncritical; i. e., thermal storage subsystem capability greater than 98 percent will be retained with any one or more of the noncritical elements failed during a 24-hour period.

Loss of any indicator, sensor, or transmitter can be tolerated during the time to repair, without impacting operational capability. Losses are accommodated by deducing necessary information from other readings. All critical indicators, sensors, or transmitters have at least one backup.

Loss of any other portion of the thermal storage subsystem will result in less than 98 percent thermal storage subsystem capability. This reduction doesn't necessarily result in reduction of pilot plant

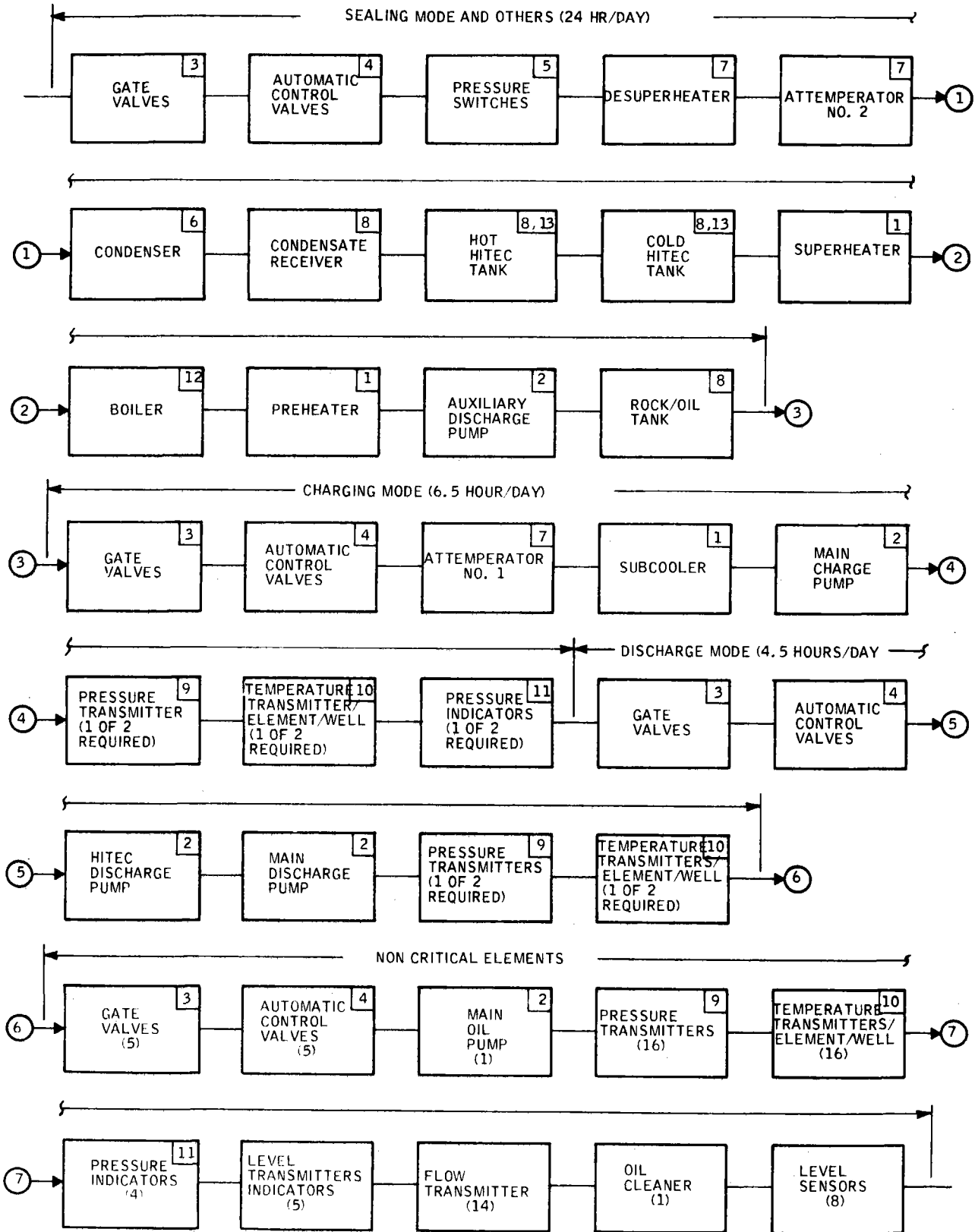


Figure 5-9. Thermal Storage Subsystem Availability Model

capability, as thermal storage subsystem degradation will impact pilot plant capability only during the thermal storage subsystem discharge mode.

Failure rates predicted for the thermal storage subsystem are shown in Table 5-3. Each of the items in the subsystem has been assumed equivalent (for prediction purposes) to one of the items in Table 5-4. Each subsystem item type is identified by a number on the model which corresponds to one of the Table 5-4 items. The order of preference for the failure rates selected from Table 5-4, as data are available, is (1) EEI data for 10 MW(e) units, (2) EEI data for 60 to 89 MW(e) units, or (3) the mean failure rates from Table 18.3 of Ref. 3, "Mechanical Design and Systems Handbook." For those failure rates selected from the handbook, a severity factor (K_f) of 10 has been applied to account for the effect of a ground equipment environment as compared with a laboratory environment (per handbook direction). To account for miscellaneous plumbing, structural items, etc., 10 percent is added to each subsystem predicted failure rate.

The MTTR for each mode is also based on the predicted mode failure rate, the free maintenance time for that mode, and an approximation of the boiler/condenser elements from the 10 MW(e) plant data (14.8 hours) as follows:

- 24-hour cycle - 14.8 hours is the mean.
- 6.5-hour cycle - 14.8 hours requires from -2.7 to 6.5 hours of the load cycle or a weighted average of 2.3 hours; therefore, 2.3 hours of the load cycle would be the normalized mean.

Table 5-3. Thermal Storage Subsystem Component Failure Rates

<u>Time</u>	<u>Item</u>	<u>Failures/10⁶ Hr</u> <u>(λ)</u>	<u>Quantity</u> <u>(η)</u>	<u>ηλ</u>
↑ 24 hr/ day ↓	Gate valves	23.3	7	163
	Automatic control valves	85	4	340
	Pressure switches	35	2	70
	Desuperheater	2.3	1	2.3
	Attemperator No. 2	2.3	1	2.3
	Condensor	23.3	1	23.3
	Condensate receiver	1.5	1	1.5
	Hot Hitec tank	46.5	1	46.5
	Cold Hitec tank	46.5	1	46.5
	Superheater	44	1	44
	Boiler	44	1	44
Preheater	44	1	44	
Aux. discharge pump	2.3	1	2.3	
Rock/oil tank	1.5	1	<u>1.5</u>	
				831 x 1.1 = 914
↑ 6.5 hr/ day ↓	Gate valves	23.3	6	140
	Automatic control valves	85	5	425
	Attemperator No. 1	44	1	44
	Subcooler	44	1	44

Table 5-3. Thermal Storage Subsystem Component Failure Rates
(Continued)

<u>Time</u>	<u>Item</u>	<u>Failures/10⁶ Hr</u> <u>(λ)</u>	<u>Quantity</u> <u>(η)</u>	<u>ηλ</u>
↑ 6.5 hr/ day ↓	Main charge pump	2.3	1	2.3
	Pressure transmitter*	350	1	18
	Temperature trans- mitter/element/well*	150	1	3.2
	Pressure indicator*	40	1	<u>.2</u>
				677 x 1.1 = 745
↑ 4.5 hr/ day ↓	Gate valves	23.3	5	117
	Automatic control valves	85	4	340
	Hitec discharge pump	2.3	1	2.3
	Main discharge pump	2.3	1	2.3
	Pressure transmitter *	350	1	4.4
	Temperature trans- mitter/element/well *	150	1	<u>.8</u>
				467 x 1.1 = 514
↑ Non- Critical ↓	Gate valves		5	-
	Automatic control valves		5	-
	Main oil pump		1	-
	Pressure transmitter		16	-

* These items are redundant only.

* 1 of 2 required during 12-hour cycle, ηλ = frequency of 2 simultaneous failures in 12 hours.

Table 5-3. Thermal Storage Subsystem Component Failure Rates (Concluded)

<u>Time</u>	<u>Item</u>	<u>Failures/10⁶ Hr</u> <u>(λ)</u>	<u>Quantity</u> <u>(n)</u>	<u>nλ</u>
↑ Non- Critical ↓	Temperature trans- mitter/element/well		16	-
	Pressure indicators		4	-
	Level transmitter/ indicators		5	-
	Flow transmitters		14	-
	Oil cleaner		1	-
	Level sensors		8	-

Table 5-4. Typical Power Plant Component Failure Rates

Item No.	Item	Failures/10 ⁶ Hr		
		Per EEI		Per Mechanical Design Handbook
		10 MW(e) Data	60 to 89 MW(e) Data	
1	Superheater (103)	44	76	150
2	Pump, electric drive (905, 922)	-	2.3	135
3	Valves (116, 117)	23.3	18.3	51
4	Control valve	-	-	85
5	Sensor, pressure	-	-	35
6	Condenser (800, 802, 806, 808, 809, 899)	23.3	47	-
7	Attemperator or desuperheater (112)	-	2.3	-
8	Tank	-	-	1.5
9	Pressure transducer	-	-	350
10	Transducer, thermistor	-	-	150
11	Gage, pressure	-	-	40
12	Boiler (101, 102, 114, 115, 116, 117, 118, 126)	180	71	-
13	Heater (104, 105)	-	45	-

- 4.5-hour cycle - 14.8 hours requires from -4.7 to 4.5 hours of the load cycle or a weighted average of 1.1 hours; therefore 1.1 hours of the load cycle would be the normalized means.

Availability of the thermal storage subsystem (A_t) is as follows:

$$A_t = A_t(24 \text{ hr}) \times A_t(6.5 \text{ hr}) \times A_t(4.5 \text{ hr})$$

$$A_t(24 \text{ hr}) = \frac{\text{MTBF}}{\text{MTBF} + \text{MTTR}}$$

where

MTBF = Mean operating time (load cycle hours) between failure in hours = $\frac{10^6}{\lambda}$

MTTR = (as above)

$$A_t(24 \text{ hr}) = \frac{1094}{1094 + 14.8} = 0.987$$

$$A_t(6.5 \text{ hr}) = \frac{1342}{1342 + 2.3} = 0.998$$

$$A_t(4.5 \text{ hr}) = \frac{1945}{1945 + 1.1} = 0.999$$

$$A_t = 0.985$$

Steam Generator Subsystem and Electrical Power Generator Subsystem Availability Model -- The steam generator subsystem is approximated by the boiler element of a 10-MW(e) fossil system for purposes of predicting failure rates and repair rates. The electrical power generation subsystem is approximated by the condenser, turbine, and generator elements of a 10-MW(e) fossil system for prediction purposes. The remainder of the 10-MW(e) fossil system is included as "other" in the tabulation. Forced outage values are listed in Table 5-5 per the EEI data (Ref. 4) for a 10-MW(e) fossil system as approximations of the failure rates.

MTTR values are predicted as follows:

- a) Steam Generator Subsystem - The weighted average repair time for the boiler/condenser elements is 14.8 hours. Based on the 12-hour load/12-hour no-load cycle, 14.8 hours would require from 2.8 to 12 hours of the load cycle on an average of 7.4 hours; therefore, 7.4 hours of the load cycle would be the normalized steam generator subsystem MTTR.
- b) Electrical Power Generation Subsystem - The weighted average repair time for the condenser, turbine/generator elements is 55 hours. Based on the 14-hour load/12-hour no-load cycle, 55 hours would require from 28 to 36 hours of the load cycle or an average of 31.5 hours; therefore, 32 hours of the load cycle would be the normalized electrical generation subsystem MTTR.

Table 5-5. SGS and EGS Forced Outage Predictions

Item	λ , Failures/ 10^6 Hr	Repair Time	MTTR (Normalized)	λ (MTTR)
Boiler	* 19/44,700 = 425	14.8		
SGS	447	14.8	7.4	3145
Condenser	1/44,700 = 22	15		
Turbine	3/44,700 = 67	85		
Generator	2/44,700 = 45	32		
EGS	134	55	31.5	4221
Other	**7/44,700	157	4.8	754
	$\Sigma \lambda = 716/10^6$			$\Sigma \lambda$ (MTTR) = 8120

$$10 \text{ MW Plant MTTR} = \frac{\Sigma \lambda (\text{MTTR})}{\lambda}$$

$$= 11.2 \text{ hr}$$

$$10 \text{ MW Plant MTBF} = \frac{1}{\lambda} = 1397 \text{ hr}$$

$$A_{G,S} = \frac{1397}{1397 + 11.2}$$

$$= .992$$

* Excludes slag and fly ash disposal and fuel handling.
 ** Excludes operating error and external causes.

c) Steam Generator/Electrical Power Generation Subsystems -
Based on the 12-hour load/12-hour no-load cycle, 10.7 hours would require from -1.3 to 10.7 hours of the cycle or a weighted average of 4.8 hours; therefore, 4.8 hours of the load cycle would be the normalized MTTR.

4) Coordinated Master Control Subsystem Availability Model - The coordinated master control subsystem is modeled as shown in Figure 5-10. It is anticipated that redundancy will be incorporated in the subsystem to permit much "on-line" repair or to permit delay of the repair to free-time maintenance without performance degradation. Based on engineering judgment and experience with many other control systems, the following values are predicted:

$$\text{Failure}/10^6 \text{ hours } (\lambda) = 833$$

$$\text{Repair rate (MTTR)} = 4 \text{ hours}$$

$$\text{MTBF} = 1/\lambda = 1200 \text{ hours}$$

$$\begin{aligned} A_m &= \frac{\text{MTBF}}{\text{MTBF} + \text{MTTR}} \\ &= \frac{1200}{1204} \\ &= 0.997 \end{aligned}$$

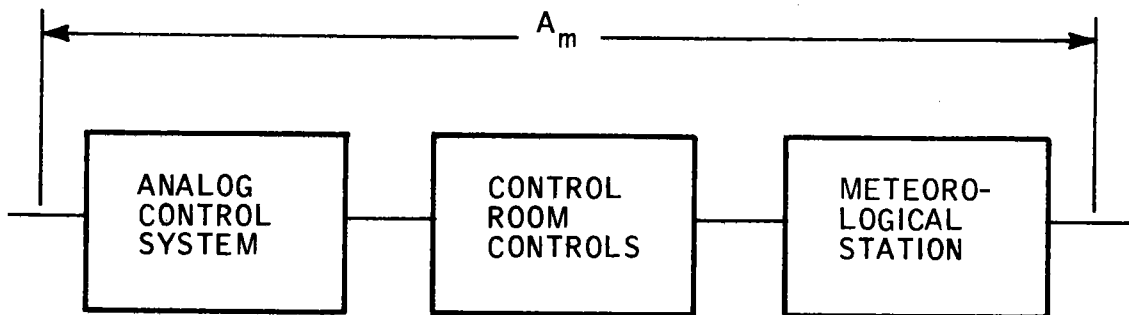


Figure 5-10. Coordinated Master Control Availability Model

Scheduled Maintenance -- The scheduled maintenance requirements of the 10 MW(e) solar pilot plant are based on information obtained by Black & Veatch from power plant operation experience as shown in Table 5-6. It is anticipated that all scheduled maintenance can be performed during diurnal shutdown with the exception of scheduled maintenance performed during the 2-week-long turbine generator annual inspection. This permits effective scheduling of labor shifts.

On most fossil-fired power plants, a thorough inspection of the turbine generator (including removal of the turbine upper shell and inspection of the turbine intervals) takes place at the end of the first year of plant operation. Thereafter, annual inspections usually consist of checking, the seals, stop valve, and a few other items. For the 10 MW(e) solar pilot plant, conducting more thorough annual inspections for an extended period of time may be advisable due to the diurnal cycling of the turbine. System availability which results from scheduled maintenance is calculated as:

Table 5-6. Solar Pilot Plant Scheduled Maintenance Requirements

COMPONENT(S)	MAINTENANCE ACTIVITIES	DOWN TIME PER YEAR*	REQUIRED MANPOWER SKILL CATEGORIES**
Turbine Generator	Annual Inspection and Maintenance	2 Weeks Plant Down Time	ET, MS, EL, MA, PW, RM, IM, L
Condenser	Annual Inspection	2 Days***	ET, MS, RM, L
Cooling Tower	Annual Inspection and Maintenance	4 Days***	ET, MS, EL, MA, RM, L
Condenser Exhauster	Annual Inspection	2 Days***	ET, MS, RM, L
Lubricating Oil Equipment	Annual Inspection, Clean Oil Cooler, Etc.	2 Days***	ET, MS, RM, L
Instrumentation (i.e., Transmitters, Controllers, Switches)	Annual Check	2 Weeks***	ET, MS, EL, IM, RM, L
Deaerator	Annual Inspection	1 Day No Plant Down Time	ET, MS, RM, IM, L

*Down time for component, not plant, unless otherwise noted.

**ET-Engineer/Technician, MS-Maintenance Supervisor, EL-Electrician, MA-Machinist, PW-Pipefitter/Welder, RM-Repairman, IM-Instrument Man, L-Laborer

***Maintenance performed concurrent with annual turbine generator inspection.

Table 5-6. Solar Pilot Plant Scheduled Maintenance Requirements (Continued)

COMPONENT(S)	MAINTENANCE ACTIVITIES	DOWN TIME PER YEAR*	REQUIRED MANPOWER SKILL CATEGORIES**
Feedwater Heaters	Annual Inspection	2 Days No Plant Down Time	ET, MS, RM, IM, L
Pumps	Replace/Repair Seals, Wear Rings, Impellers, Etc.	2 Days Per Pump (Average) No Plant Down Time	ET, MS, MA, RM, L
Heat Exchangers	Annual Inspection	1 Day Per Heat Exchanger (Average) No Plant Down Time	ET, MS, RM, IM, L
Valves, Operators, Positioners	Inspect, Repair Seats, Repack, Lubricate Operators Calibrate Control Valves	1 Day Per Valve (Average) No Plant Down Time	ET, MS, RM, IM, L
Air Compressors	Annual Inspection, Check Valve, Rings, Etc. Clean Cooler, Etc.	6 Days No Plant Down Time	ET, MS, RM, L
Compressed Air Dryers	Check Desiccant, Replace as Necessary	1 Day No Plant Down Time	ET, MS, RM, L
Strainers	Inspect, Repair as Necessary	1/2 Day Per Strainer (Average) No Plant Down Time	ET, MS, RM, L

*Down time for component, not plant, unless otherwise noted.

**ET-Engineer/Technician, MS-Maintenance Supervisor, EL-Electrician, MA-Machinist, PW-Pipefitter/Welder, RM-Repairman, IM-Instrument Man, L-Laborer

***Maintenance performed concurrent with annual turbine generator inspection.

Table 5-6. Solar Pilot Plant Scheduled Maintenance Requirements (Continued)

COMPONENT(S)	MAINTENANCE ACTIVITIES	DOWN TIME PER YEAR*	REQUIRED MANPOWER SKILL CATEGORIES**
Tanks	Annual Inspection	1/2 Day Per Tank No Plant Down Time	ET, MS, RM, L
Diesel Engine for Fire Pump	Annual Inspection, Lubrication, Tune-Up	4 Days No Plant Down Time	ET, MS, MA, RM, IM, L
Motor Control Centers and Separately Mounted Starters	Annual Inspection and Maintenance, Check Contactor Operation, Breaker Trips, OL Trips, Etc.	2 Days No Plant Down Time	ET, MS, EL, IM, L
Motors	Annual Inspection and Maintenance, Check Lubrication, Bearings, Insulation, Temperature Detectors, Etc.	2 Weeks No Plant Down Time	ET, MS, EL, L
Relay Panels	Annual Inspection and Maintenance, Check Operation, Contacts, Connections, Etc.	2 Days No Plant Down Time	ET, MS, EL, L
Batteries	Test Electrolyte Level and Specific Gravity	1 Day Per Month No Plant Down Time	ET, MS, EL, L
Outdoor Oil Circuit Breaker	Annual Inspection and Maintenance, Clean Insulators, Test Oil, Check Mechanism, Contacts, Connections, Etc.	1 Day No Plant Down Time	ET, MS, EL, IM, L

*Down time for component, not plant, unless otherwise noted.

**ET-Engineer/Technician, MS-Maintenance Supervisor, EL-Electrician, MA-Machinist, PW-Pipefitter/Welder, RM-Repairman, IM-Instrument Man, L-Laborer

***Maintenance performed concurrent with annual turbine generator inspection.

Table 5-6. Solar Pilot Plant Scheduled Maintenance Requirements (Concluded)

COMPONENT(S)	MAINTENANCE ACTIVITIES	DOWN TIME PER YEAR*	REQUIRED MANPOWER SKILL CATEGORIES**
Transformers	Annual Inspection and Maintenance, Clean Insulators and Arrestors, Test Oil, Check SPR and All Alarm Mechanisms, Etc.	3 Days No Plant Down Time	ET, MS, EL, IM, L
Metalclad Switchgear	Annual Inspection and Maintenance, Test Protective Relays, Check Breaker Operation, Contacts, Etc.	2 Days No Plant Down Time	ET, MS, EL, IM, L
Metal Enclosed Switchgear	Annual Inspection and Maintenance, Check Breaker Operation, Contacts, Etc.	2 Days No Plant Down Time	ET, MS, EL, IM, L
Battery Chargers	Annual Inspection and Maintenance, Check Operation, Contacts and Connections	1 Day No Plant Down Time	ET, MS, EL, IM, L
Inverters	Bimonthly Inspection and Maintenance, Check Operation of Switches and Relays, by Simulated Failures	2 Days No Plant Down Time	ET, MS, EL, IM, L
Freeze Protection System	Annual Inspection and Maintenance, Check each Circuit and its Controls in Autumn.	2 Days No Plant Down Time	ET, MS, EL, L
Automatic Transfer Switches	Monthly Inspection and Maintenance, Check each Switch with Simulated Signal	1/2 Day No Plant Down Time	ET, MS, EL, L

*Down time for component, not plant, unless otherwise noted.

**ET-Engineer/Technician, MS-Maintenance Supervisor, EL-Electrician, MA-Machinist, PW-Pipefitter/Welder, RM-Repairman, IM-Instrument Man, L-Laborer

***Maintenance performed concurrent with annual turbine generator inspection.

$$A_{sm} = \frac{52 - 2}{52}$$

$$= 0.962$$

Availability Calculations -- From the availability model and the analysis results, the solar pilot plant availability is calculated as follows:

$$A_{pp} = A_{um} \times A_{sm}$$

$$= \left[A_c \times A_t \times (A_g \times A_s) \times A_m \right] \times A_{sm}$$

$$= \left(0.997 \times 0.985 \times 0.992 \times 0.997 \right) \times 0.962$$

$$= 0.971 \times 0.962$$

$$= 0.934$$

PLANT SUPPORT EQUIPMENT

Plant support equipment requirements for the 10 MW solar pilot plant have been reviewed. The majority of the plant construction would be conducted by a general contractor, a mechanical contractor, and an electrical contractor. These contractors would provide their own equipment and erection facilities. The scope of work assigned to these contractors should be as broad as possible to minimize duplication of equipment requirements and work effort. The steam generator, master control system, and the heliostats present their own unique construction requirements and should be erected or installed by separate contractors.

The long-term and short-term equipment required for installation of the heliostats would be provided by the contractor and retained by the utility for support of normal plant operation. Most of this equipment is adaptable to other functions and would be utilized by all subsystems on a shared basis.

The electrical checkout and test equipment would be furnished by the electrical contractor and retained by the utility. Similarly, the equipment required for installation, checkout, and testing of the digital control systems would be provided by the installer and retained by the utility.

Upkeep of the plant site and general plant maintenance will be minimal. Recommendations for support equipment have been included in the report. However, the utility should be consulted since it may have its own preference for maintenance equipment and may prefer to share equipment requirements with its neighboring power plant.

This subsection presents a discussion of support equipment required for the 10 MW solar pilot plant. Support equipment is defined as equipment required for plant operation and maintenance which is not designed into the different plant systems.

Unique equipment and facilities required for construction and continued operation of the following areas and subsystems are presented:

- General Site Area
- Collector Subsystems
- Receiver Subsystem
- Thermal Storage Subsystem
- Electrical Power Generation Subsystem

The majority of the plant construction will be conducted by a general contractor, a mechanical contractor, and an electrical contractor. The equipment these contractors would use as part of their normal construction operations and remove from the site afterwards is not discussed in this report. Unique construction equipment and facilities as well as construction equipment that would be retained for long-term maintenance is identified.

General Site Area

Initial construction activities will include clearing and grading the general site area. This work would be accomplished by a special site preparation contractor who will supply his own equipment.

Field office facilities will be required for the different construction contractors and field engineers. The individual contractors will provide their own mobile trailers. Two additional trailers will be required for the field engineers and the overall project coordination and accounting personnel.

A main water line carrying potable well water runs adjacent to the Barstow plant site. A branch line off this main line will be installed to provide a permanent source of service water and makeup water. During construction the general contractor will provide temporary taps off this branch line for specific construction water requirements.

An electrical power supply capable of providing approximately 3000 kVA will be required during construction. The utility company will probably provide two pad-mounted transformers and wire to the primary side. The electrical contractor will route wire from the secondary side of the transformers and provide various 480 volt and 120 volt distribution panels required for construction power.

The general site area will be relatively free of long-term maintenance requirements. Individual contractors will be engaged as required for major access road repairs. Plant growth control in the heliostat area will be accomplished by a contractor periodically spraying a surface sealer. A small tractor (less than 50 hp) with sickle bar and blade will be required for general site maintenance. A power lawn mower, water hoses and associated grass maintenance equipment will be used for maintaining the lawns around the visitor center and office buildings.

Collector Subsystem

Initial storage and final assembly of the heliostats will require a temporary, weatherproof enclosure. The structure will be a prefabricated metal building providing approximately 5000 square feet of work space. The building will be removed from the site after erection of the heliostats is completed. The metal building would not be required if there are suitable structures within a 5-mile radius of the site where the heliostats could be assembled and transported to the site for installation.

The equipment required for construction of the Collector Subsystem is listed in Tables 5-7 through 5-9. The long-life and short-life equipment included in Tables 5-7 and 5-8 will be provided by the erection contractor and retained by the utility for long-term operation and maintenance. The equipment listed in Table 5-9 will be leased or provided by the erection contractor and removed from the site after erection of the heliostats is completed.

Table 5-7. Collector Subsystem Long-Life Support Equipment

<u>Item</u>	<u>Quantity</u>
Special-Purpose	
Precision-level support/arms	5
Assembly and weld jig (post)	4
General-Purpose	
12-foot rolling scaffold	4
15-foot single gantry	6
20-foot double gantry	1
Truck, 2-1/2 ton with crane	1
Truck, 3/4 ton utility	2
Fork lift (2 ton capacity)	1

Table 5-8. Collector Subsystem Short-Life Support Equipment

<u>Item</u>	<u>Quantity</u>
Special-Purpose	
Trammel tool (actuator pre-set)	1
Trammel tool (34" frame-set)	7
Trammel tool (43.3 frame-set)	4
Precision level	5
Test equipment (heliostat checkout)	2
General-Purpose	
Rolling ladder (5 ft.)	50
Spreader bar	3
Cable sling	2
Small dolly	2
Gas welder	3
Alignment tool (rod ends)	4
Angle indicator (45 degree taper arm)	4

Table 5-9. Collector Subsystem Construction Equipment

<u>Item</u>	<u>Quantity</u>
Trailer for mirror modules	2
Trailer for heliostat frames	2
Tug for trailers	2
Ditcher	4
Back hoe	1
Small tractor w/blade	3
Assembly jig (holds/aligns post during concrete pour/cure)	8
Pneumatic ground rod driver	1
Pneumatic concrete vibrator	1
Air compressor	1
Concrete forms (pair)	3

Receiver Subsystem

The general contractor will provide the slip forms and erect the support tower. Concrete will be transported to the site in a pre-mixed ready condition. The contractor will supply his own erection equipment and remove it from the site after the tower is completed.

The steam generator and receiver equipment on top of the tower will be erected by a separate contractor. Special safety equipment and precautions associated with erecting the boiler and receiver on top of the tower will be furnished by the contractor and removed from the site afterwards. Access platforms and ladders will be provided for routine maintenance and cleaning operations.

Thermal Storage Subsystem

The majority of the erection work associated with the Thermal Storage Subsystem will be performed by the general, mechanical, and electrical contractors. These contractors will provide their own equipment. A 10-ton motorized crane will be required for installation of the heat exchanger tubes and shells. There will be no requirement for retaining this crane at the site on a long-term basis. If future heat exchanger maintenance requires a crane of this size, it can be leased on a short-term basis.

Approximately 8000 to 10,000 tons of 1/2-inch diameter rock will be placed in the oil and rock storage tank. The tank is approximately 60 feet in diameter and 48 feet high with a 12-foot-high dome on top. The rock will be delivered by trucks in a graded and washed condition. Unloading of the rock and placement in the tank will be accomplished in such a manner as to minimize chipping of the rock and creation of fines. A standard construction

crane equipped with a clam shell that would transfer the rock from a stockpile at grade to the tank is preferred. This would require that the tank dome be left off until all the rocks are loaded into the tank.

Periodically, residual oil will be removed from the system and new oil added. This will be accomplished with tank trucks. The necessary transfer equipment has been included in the basic system design and there are no special equipment or provisions required.

Approximately three to four times a year makeup to the salt tanks will be required. Bags of sodium nitrite, sodium nitrate, and potassium nitrate will be stored on pallets in the chemical storage area at the central complex. These chemical salts will be added by hand to the tanks. A small forklift vehicle will be required for transporting the chemicals from the storage area to the tanks.

Electrical Power Generation Subsystem

The equipment and structures associated with the Electrical Power Generation Subsystem will be erected by the general, mechanical, and electrical contractors. These contractors will provide their own equipment.

Prior to initial operation of the unit, the water and steam piping and the steam generator will be flushed and chemically cleaned. The chemical cleaning will be carried out by a separate contractor with special experience and equipment to do a proper job.

There is no special support equipment required for the components of the mechanical systems. Special tools and spare parts will be purchased with the mechanical components based on the manufacturers recommendations.

A 25-ton rail-mounted overhead crane will be used on the central complex operating floor for turbine maintenance. Access hatches will be provided in the operating floor so that the overhead crane can be used for pulling the condensate pump, feedwater heaters, and the turbine lube oil cooler.

Various chemicals will be used during normal operation of the plant. Sulfuric acid and sodium hydroxide will be stored in tanks and metered to the appropriate EPGS systems as required. Tank trucks will periodically deliver new chemicals to the site.

Chlorine gas will be injected into the circulating water system. New cylinders of chlorine gas will be delivered and the empty ones removed as required. Hydrazine, ammonia, sodium phosphate, and organic phosphate will be stored in bulk form in the chemical storage area at the main complex and added to the appropriate mixing tanks as required. The organic phosphate will be fed to the circulating water system at the cooling towers. A forklift truck will be required for transporting the organic phosphate to the cooling tower mixing tank.

Nitrogen gas will be used for shutdown corrosion protection. Cylinders of nitrogen will be connected to a manifold piping system at the main complex. New cylinders of nitrogen gas will be delivered and the empty ones removed as required.

Checkout and test equipment will be required for maintaining the electrical equipment at the site. The recommended electrical support equipment is listed in Table 5-10.

Test equipment will be required for maintaining the main digital control system (computer) and the auxiliary control equipment (actuators, air lines, valves, etc.). This test equipment is listed in Table 5-11.

Table 5-10. Electrical Generation Subsystem Electrical Support Equipment

<u>Item</u>	<u>Quantity</u>
Megger tester (1000 V and 500 V)	1
Vibroground (Associated Research Inc.)	1
Multimeter	1
Millivolt potentiometer	1
Tachometer	1
Relay test set*	1
Transformer oil test set*	1
Variac (variable autotransformer)	1
Phase shifter	1
Phase angle meter	1
High potential tester*	1

* Items are used infrequently and may be borrowed from existing utility when required.

Table 5-11. Electrical Generation Subsystem Control Support Equipment

<u>Item</u>	<u>Quantity</u>
Digital counter	1
Oscilloscope	2
Polaroid camera w/oscilloscope attachment	1
Portable high-speed chart recorder (3 pen)	1
X-Y plotter	1
Digital multimeter	2
Multimeter	5
Pulse signal generator	1
Digital logic tester	3
Analog signal generator (4-20 ma dc)	2
Portable thermocouple/RTD bridge	1
Dead weight tester	2
Hydraulic calibration pump	2
Temperature bath	1
Leak detector solution	2 bottles

Equipment used in the machine shop will primarily be the responsibility of the utility. Major maintenance and specialized machine work will be performed in a completely outfitted machine shop located at the utility's neighboring power plant. The maintenance shop at the pilot plant will provide facilities for equipment dismantling, replacement of spare parts, and minor repair. Typical equipment recommended for the pilot plant is as follows:

Assorted shelves and cabinets

Drill press

Metal cutting band saw

Power hack saw

Radial drill

Pedestal grinder

Double-end grinder

Carbide tool grinder

Threading machine

Metal lathe

A-frame with a 5-ton hoist

Chain hoists

Arc welder

The radial drill may be deleted if one is available at the neighboring power plant.

An assortment of portable welding rings, vices, clamps, and hand tools (wrenches, sockets, screwdrivers, etc.) will also be required.

The general-purpose long-life support equipment previously listed for the Collector Subsystem will be used in the other subsystems and the general plant area on a shared basis.

Recommendations

The information presented in this report has been based on the preliminary design of the 10 MW(e) solar pilot plant.

During the detailed design phase of the project, the quantities of consumable items such as chemicals, oil, and salt will be determined. Once these values are known, the estimated storage and handling equipment requirements should be verified.

The support equipment required by the Collector Subsystem and the Master Control System should be reviewed with potential suppliers. The purchase specifications should then be written to include the recommended support equipment. The final purchase contract should also request operating procedures and a recommended maintenance program from the suppliers.

The support equipment and maintenance programs for the general plant systems should be coordinated with the utility company. Much of the support equipment and some maintenance personnel may be available from the neighboring power plant on a shared basis.

PRELIMINARY SYSTEM TEST AND EVALUATION

A five-phase system test and evaluation program has been developed to determine component, subsystem, and plant performance, as well as operating flexibility characteristics.

The test program was developed on the basis of the following:

- (1) Standard power plant test procedures.
- (2) Subsystem research experiments for the solar-peculiar aspects of the pilot plant.

In addition, tests (e. g. , creep fatigue, seismic) are described which are not being conducted in the subsystem research experiments, but which will provide information concerning the "longer term" effects of plant operation (e. g. , steam generator creep fatigue, thermal cycling).

General

A comprehensive test program is required for the 10 MW(e) solar pilot plant to assure component and construction quality, verify design implementation, demonstrate unit performance, and to establish operating methods.

It is expected that all equipment meets, and is intalled in accordance with, design performance requirements. However, provision is made for performance testing of major components, subsystem, and systems. Test provision and test methods are based on ASME Power Test Codes, ANSI Standards and/or, ASTM Standards.

Five phases are considered in the system test and evaluation program:

- (1) Shop Testing.
- (2) Construction Testing.
- (3) Preoperational Testing.

- (4) Initial Operation Testing.
- (5) Testing after normal operation is achieved.

Shop testing is performed by the material and equipment suppliers at their facilities to ensure that the components being supplied meet or exceed the imposed specifications. Construction testing is performed at the plant site to assure proper installation and erection. Preoperational testing verifies that equipment and systems, short of rolling the turbine, perform in accordance with design criteria. Initial operation testing subjects all equipment, components, instruments, and control loops to actual plant operating conditions. Normal operation testing demonstrates the feasibility of the solar central receiver steam cycle concept under various operating modes and mode transitions.

This report describes the five phases of the test program and identifies special equipment required for the test program.

Shop Testing

Shop tests include nondestructive and performance testing to assure the use of quality material and construction techniques, and to demonstrate equipment performance.

Shop testing is the responsibility of the material and equipment suppliers. It is expected that material and equipment are free from chemical, metallurgical, and mechanical defects; are soundly constructed; and have, as specified, performance characteristics.

To assure acceptable quality and performance, equipment and material are procured in accordance with industry codes and standards. Industry codes and standards specified are included in Table 5-12. These industry codes and

standards represent minimum acceptable quality levels. Further, they establish design and testing requirements to assure that material and equipment are suitable for the intended service.

Table 5-12. Industry Codes and Standards

ASME	American Society of Mechanical Engineers--Boiler and Pressure Vessel Code (a) Section I - Power Boilers (b) Section II - Materials (c) Section V - Nondestructive Examination (d) Section VIII - Pressure Vessels
TEMA	Tubular Exchangers Manufacturer's Association Standards
HEI	Heat Exchange Institute Standards (a) Standards for Closed Feedwater Heaters. (b) Standards for Typical Specifications for Deaerators. (c) Standards for Steam Surface Condenser.
HIS	Hydraulic Institute Standards
ANSI	American National Standard Institute (appropriate standard applied)
AWWA	American Water Works Association (appropriate standard applied)
API	American Petroleum Institute (appropriate standard applied)
NEMA	National Electrical Manufacturers Association (appropriate standard applied)

Construction Testing

Construction testing is described in terms of mechanical tests, control tests, and electrical tests.

General -- All equipment and systems are subjected to tests and checks to the extent necessary (or possible) to assure proper installation and/or erection, and to prove readiness for preoperational testing. These construction tests and checks fall into three general categories: mechanical, control, and electrical.

Mechanical -- Two industry codes are generally applicable to construction testing: ASME Section I - Power Boilers and ANSI B31.1 - Power Piping. All testing associated with field erection of the steam generator is under the jurisdiction of the power boiler code. Other plant pressure piping is tested in accordance with the power piping code. Testing covered by the power piping code is similar to that required by the power boiler code except by specific reference, application, and method.

Field welds in all pressure piping are subject to examination for defects. This examination can be by radiographic, ultrasonic, dye penetrate, magnetic particle, or visual methods. The type of test depends on system design conditions and pipe wall thickness, and is clearly indicated in the applicable code. Circumferential field welds in main steam piping with wall thicknesses greater than 3/4 inch are subject to radiographic examination. Most other field weld examination is visual.

All pressure piping is subject to tests to demonstrate leak tightness. The type of tests include hydrostatic*, pneumatic, mass spectrometer, halide, and initial service leak tests**.

* Test fluid can be water, oil or other suitable fluid.

** ANSI considers 100 percent weld radiography as a substitute for leak testing.

Insofar as possible, piping and equipment are subject to hydrostatic testing, nominally at 1.5 times the system design pressure. When a hydrostatic test is impractical or undesirable, one of the other leak tests can be substituted.

An initial service leak test is normally performed when the other types of leak tests are impractical. This test involves slowly bringing the part to be tested up to design conditions during unit operation and observing areas of possible leakage. This test must be performed after construction is complete.

Table 5-13 lists appropriate leak tightness tests for major plant systems.

All mechanical components are subject to construction tests and checks to assure their operability. Pumps are checked for proper rotation and alignment. Valves are checked for valve stem freedom and seat condition.

Lubricants are checked for conformance to component manufacturer's recommendations. All packings are checked for suitable material, condition, and installation. Other mechanical equipment tests and checks are performed as recommended by the manufacturer to assure that the component is installed and maintained in operating condition.

After system and component cleaning, tests are performed to assure that the systems are clean. Tests associated with cleaning activities include inspection of targets after steam blowing, examinations of flush test filters, testing chemical solution concentrations, and checking flush water conductivity. (Some of these tests may be performed during the preoperational phase.)

Control Tests -- Construction tests and/or checks include instrument calibration, instrument calibration tests, and control loop checks.

Table 5-13. Leak Tightness Tests for Major Systems

<u>System</u>	<u>Leak Test*</u>
High-Pressure Steam System	Hydrotest
Extraction Steam System	
(a) From Turbine to Extraction Isolation Valves	In Service
(b) From Extraction Isolation Valves to Heater	Hydrotest
Feedwater System	Hydrotest
Condensate System	Hydrotest
Auxiliary Cooling Water	Hydrotest
Turbine Lubricating Oil System	Hydrotest with Oil
Service and Control Air System	Pneumatic Test
Fire Protection System	Hydrotest
Service Water System	Hydrotest
Condenser Air Extraction System	In Service

* ANSI B31.1 accepts 100 percent weld joint radiography in lieu of leak testing.

Instrument calibration includes quantitative settings on control and monitoring loop elements, and verification of response characteristics. Also considered is the functional integrity of devices or instruments which are not adjustable by normal means (e. g., thermocouples, resistance temperature detectors, conductivity cells).

Calibrated loop tests are performed to verify instrument loop acceptability in terms of proper interrelationships and expected responsiveness of the loop elements. These tests are performed with all loop components in place and calibrated, and are conducted by applying simulated inputs and observing loop performance.

Electrical Tests -- Electrical construction testing is performed as necessary to confirm that all electrical equipment, materials, and components conform to specifications with respect to construction, composition, identification, rating, connection, installation and wiring. Typical electrical construction checks are listed in Table 5-14.

The most critical tests are of equipment, the failure of which to function properly could result in injury to personnel or severe consequential damage, as well as damage to the equipment which fails to function. Equipment in this category includes that related to phasing, emergency power and lighting, protective relaying, equipment grounding, and abnormal condition alarms and indications.

After installation all conductors are visually checked for apparent termination on the assigned terminals; they are also physically tested for actual termination point. Each conductor is tested for continuity and all conductors are tested to verify grounding or absence of grounding as appropriate.

Table 5-14. Typical Electrical Construction Checks

- (1) Visual and physical check of each cable and each conductor termination to verify apparent correct connection both with regard to location and security.
- (2) Continuity test of each conductor.
- (3) High potential test of each conductor with insulation rated higher than 600 volts. (Check of insulation and terminations.)
- (4) Megger check of each conductor with insulation rated 600 volts or less to verify absence of grounds and absence of shorts between conductors of multiconductor cables.
- (5) Visual routing check to verify that critical cables are in assigned raceway.
- (6) Visual check of conductor and cable shield grounds to verify that shields are grounded at correct locations.
- (7) Visual inspection to verify that all equipment is properly grounded.
- (8) Measurement of ground grid resistance to remote earth from designated locations.
- (9) Visual and physical inspection of grounding system connections.
- (10) Inspection of all breaker, starter, contactor, and relay contacts for proper mating and sequence of operation during manual operation.
- (11) Setting, testing, and adjustment of protective relays with test set.
- (12) Check with test set of motor control center and separately mounted starters for overload tripping at proper current.
- (13) Check with test set of a random sample of motor control center and panelboard breakers for tripping at indicated current.
- (14) Check all relays, coils, motors, and various electrical components for nameplate conformance with regard to voltage, current, and temperature ratings.
- (15) Check each electrical equipment enclosure for environment suitability and conformance to specification.
- (16) Test liquid for dielectric strength in all liquid-filled transformers.
- (17) Check ratio and phase relationship of potential and current transformers. Prior to energization of any current transformer, verify continuity of its secondary circuit with shorting devices removed.

The liquid in all liquid-filled transformers is tested for conformance to standards. ASTM test procedures are employed. Doble* tests are performed on equipment where such tests are applicable.

Preoperational Testing

Preoperational testing is described in terms of functional tests and operational tests.

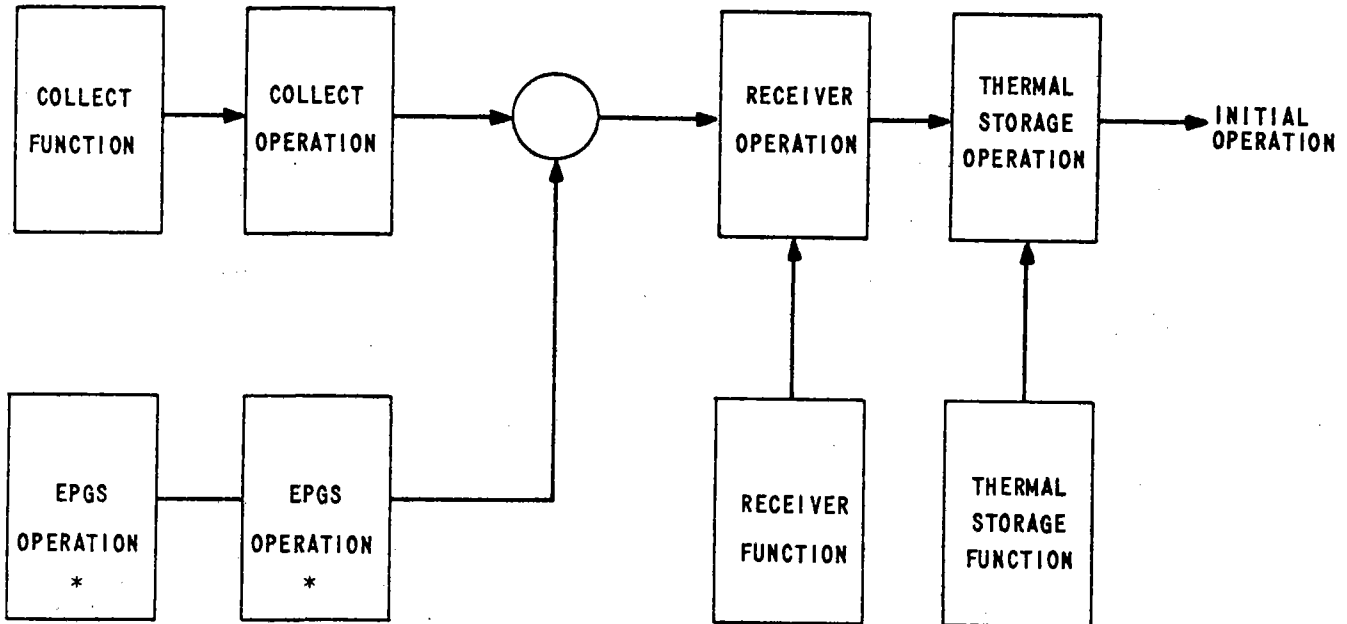
General -- Preoperational testing verifies, insofar as possible, that equipment and systems perform in accordance with design criteria. Included in this phase are functional and operational testing.

Functional preoperational testing includes checks, tests, adjustments, calibration, and system** operation (insofar as possible), to demonstrate that equipment and systems perform intended functions.

After component and system functional testing is complete, subsystem operational tests of the collector subsystem, receiver subsystem, thermal storage subsystem, and electric power generation subsystem are initiated. Preoperational operational testing demonstrates, insofar as possible, the performance of these portions of the station.

Figure 5-11 illustrates the preoperational testing phase sequence. Preoperational testing is completed, and initial operational testing begins, when steam is first admitted to the turbine.

* A series of tests on liquid samples to measure performance characteristics.
** The term "system" is used to represent a division of subsystem units (e. g., feedwater system is part of the Electric Power Generation Subsystem).



* EXCEPT TURBINE GENERATOR

Figure 5-11. Preoperational Function and Operational Testing Sequence

Functional Testing -- Functional preoperational testing includes verifying proper construction and construction testing, control component calibration and checkout, component performance testing (as appropriate), system design verification, and electrical equipment checks.

Verifying proper construction and construction testing includes verifying that required construction tests and checks have been performed, checking that equipment has been set up and maintained as required by equipment manufacturers, verifying adequate system cleanliness, checking proper vent and

drain locations, and other tests and checks to assure that systems and components are in serviceable condition.

Control component calibration and checkout is performed to verify, as nearly as possible, control system performance under actual operating conditions. Where required, simulated signals or inputs are used to verify the performance of the system over its full operating range. Systems, instruments, and control loops are calibrated and aligned at these full range simulated and/or actual operating conditions.

Equipment performance tests are performed to ensure that equipment performance is, as required, within reasonable vibration and noise limits. ASME power test codes are used as a basis for all equipment performance testing.

System design verification involves system operation at conditions as similar as possible to actual operating conditions. Various possible operating modes are checked to assure that the system performs its intended function. Included in these tests is control logic function testing to verify proper system control.

Preoperational electrical equipment testing includes sequential tests to verify that equipment may be safely energized, to verify no load operation of equipment and control systems (interlocks, alarms, and indications), and to verify capability to perform under load (where practical). Typical electrical preoperational checks are listed in Table 5-15. Power circuit breakers which are operated from a separate control power source are operated on a dead bus, and all interlocks are tested for actual performance of their function prior to testing at rated voltage.

Phasing of the generator transformer, auxiliary transformers, and each switch gear bus is performed as each component is energized.

Table 5-15. Typical Electrical Preoperational Checks

- (1) Check phasing of each transformer before it is connected into the pre-operational system and of each switchgear bus immediately upon energization.
- (2) Test performance of inert-gas oil preservation systems.
- (3) Tests to verify that transfer to standby source occurs when loss of normal power to essential equipment is simulated.
- (4) Test operation of each intercommunications system station to verify operation in all modes.
- (5) Check setting and adjustment of all limit switches, pressure switches, level switches, and similar devices and verify that physical operation of each produces the desired control, indication, or alarm function. Setting and adjustment of motor operated valve limit switches and torque switches including verification that torque switch connection and valve operation are coordinated is accomplished by actual valve operation.
- (6) Check oil level of oil lubricated bearings.
- (7) Measure insulation resistance to ground of all motor and transformer windings immediately prior to energization.
- (8) Check rotation of all motors.
- (9) Measure insulation resistance to ground of all switchgear, motor control center, and panelboard power buses immediately prior to energization.
- (10) Verify by test that the local output of each thermocouple corresponds to the indication on the remote indicating device.
- (11) With its power bus de-energized, check each power circuit breaker for proper operation and for correct performance of all interlocks, indications, and alarms.
- (12) With its load disconnected, check each combination starter for proper operation and for correct performance of all interlocks, indications, and alarms.
- (13) Check level and specific gravity of electrolyte in station battery.
- (14) With output breaker open, check operation of inverter transfer switch with simulated loss of normal power.
- (15) With output breaker closed, check operation of inverter upon removal of normal source power.

Ratios and phase relationships of current and potential transformers throughout the system are checked prior to energizing the equipment.

Proper functioning of power transformer liquid preservation systems is verified with regard to leakage control under normal operation.

When functional preoperational testing is complete, systems and components are considered to be operational and able to perform their intended functions within the scope of this testing phase.

Operational Testing -- Operational testing is described in terms of collector, receiver, and thermal storage subsystem tests.

Collector -- Preoperational operational tests and checks assure that the collector subsystem is properly set up, is responding properly to control system demands, and is properly calibrated.

The following preoperational operational tests are considered for the solar collectors:

- 1) Ensure proper performance of all auxiliary instrumentation (tracking photocells, weather station, calibration arrays, etc.). Ensure that all calibrated hardware is within calibration limits. Ensure that each sun tracking equatorial mount is adjusted such that it retains the sun's image at its center all day. Confirm that, with background suppression applied, each photocell of each calibration array reads within ± 2 percent of all others.

- 2) Initial calibration includes the following after installation of the heliostat:
 - a) Precise azimuth and distance to target and azimuth of outer axis bearing center line are determined.
 - b) After leveling of all mirror module frames, the end-to-end scale factors for the linear actuators are determined.
 - c) Initialization switches are set.
 - d) The proper phasing (motor revolutions vs direction command) for each heliostat is determined.
- 3) Monitor performance of selected heliostats for all modes of operation under automatic control.
- 4) Initially perform calibration on each heliostat daily to insure accurate usage of site and calibration parameters.
- 5) Monitor the failure rate (error detections per commands issued) of the wrap-around communication links over at least a week-long, non-stop test.

Receiver -- Operation of the collector and receiver subsystems is initiated and steam is generated for the first time. Feedwater flow is balanced to the boiler panels and superheater desuperheater. All controls and responses are tested for both normal and abnormal operation.

Tests are undertaken to evaluate and prove steam generation performance. Tests are conducted at various rates of steam generation and transient characteristics checked. The following characteristics are determined:

- 1) Capability to regulate steam generation rate.
- 2) Hot and cold startup characteristics and time.
- 3) Steam generation capability at various solar conditions.
- 4) Shutdown characteristics.
- 5) Heat loss characteristics.

Thermal Storage -- Thermal storage performance and capabilities are subjected to testing in this phase. Steam from the solar receiver is admitted at various flow rates and conditions to demonstrate the capability and performance of the thermal storage charging loop. Thermal storage discharge tests are conducted to evaluate subsystem capability and performance under varying load conditions. The following system characteristics are determined:

- 1) Charging characteristics and performance.
- 2) Storage characteristics and performance.
- 3) Discharge characteristics and performance.
- 4) Dynamic response.
- 5) Overall system capability.

Initial Operation Testing

Initial operation testing begins when preoperational testing ends and steam is first admitted to the turbine. Initial operation testing is an extension of preoperational testing. During this phase all equipment, components, instruments, and control loops are subjected to actual unit operating conditions.

Typical electrical initial operation checks are listed in Table 5-16. Initial operation testing of electrical equipment includes checking of all synchronizing equipment for phasing and operation. Actual load currents drawn by motors, transformers, heaters, and similar equipment are measured to confirm that operating conditions are as projected. Overload and breaker trip settings are adjusted to conform with actual operating conditions.

Table 5-16. Typical Electrical Initial Operation Checks

- (1) Check main generator phasing.
- (2) Check operating current of each power load to verify that it is within the predicted range and free of major internal defects.
- (3) Examine each bearing on rotating electrical equipment for unusual heating, noise, or vibration.

This test phase allows evaluation and testing of total plant performance. However, at least initially, specific attention is given to the turbine generator since this is the first time it has been in operation.

The turbine is operated at different loads and steam inlet conditions to prove capability and performance. This testing is similar to that which is performed on a conventional power plant.

Turbine performance is evaluated at various operating conditions in general consideration of ASME PTC 6 Steam Turbine Power Test Code(s), as applicable, to establish base line performance.

Overall station performance and response characteristics to transient conditions are determined. Specifically, the following characteristics are determined:

- 1) Overall unit heat rate or performance at various operational modes.
- 2) Unit cold start-up and hot start-up performance.
- 3) Receiver losses (radiation, convection, etc.).
- 4) Station performance with steam from the solar receiver.
- 5) Station performance with steam from thermal storage.
- 6) Station performance with steam from both the solar receiver and thermal storage.
- 7) Station performance with steam from the solar receiver while charging storage.
- 8) Transient operation performance.
- 9) Plant shutdown performance.

Initial operation testing is complete when unit performance, capabilities, and characteristics have been established. It is likely, however, that solar conditions during initial operational testing represent only a relatively narrow range of anticipated conditions. Performance characteristics may be extrapolated from initial operation tests and verified during normal operation testing.

Normal Operation Testing

Normal operation testing is described in terms of general tests (collector, receiver, thermal storage, and electrical power generation subsystems).

General -- The purpose of the 10 MW(e) solar pilot plant is to demonstrate the feasibility of the central solar receiver concept, and to provide information applicable to future commercial stations. In addition to demonstrating and evaluating novel equipment and concepts, it is intended to determine the following:

- 1) How much energy is available?
- 2) What energy can be captured?
- 3) What energy can be stored?
- 4) What criteria limit potential best performance?
- 5) What are the solar plant operational characteristics?

It is expected that normal operation testing will continue for several years after the plant is considered operational.

During initial operational testing, plant capability and performance were established to a limited degree. The solar conditions during that phase represent only a relatively narrow band of those anticipated. Also, the effects of continued cyclical operation have yet to be considered. During normal operation testing, station performance and capability are completely demonstrated under all operational modes. Tests to establish absolute turbine performance and capability, as well as start-up and shutdown characteristics, would discontinue as this activity becomes a matter of course.

The test plant will include statistical verification of every variable that impacts the net annual energy determination. Furthermore, a study of various plant operating strategies will be conducted. The impacts of cloud cover transients will also be studied.

Collectors -- Normal operational testing of the collector subsystem is performed to evaluate the design and to provide correlation of day to day performance with the following influences.

- 1) Calibration interval
- 2) Communication link wrap-around check failures
- 3) Temperature
- 4) Wind
- 5) Insolation levels
- 6) Shadowing and blocking
- 7) Humidity
- 8) Time of year versus toe-in setting (flux mapping via calibration array)
- 9) Parasitic power
- 10) Control philosophy (how early, and sequence to get on target)
- 11) Whether to stow during short interval rains, etc.
- 12) Receiver efficiency

In addition to providing the required wind velocity and direction, field humidity, barometric pressure, and ambient temperature, weather stations provide information for refraction correction and general performance correlation.

Data are accumulated for each heliostat regarding the magnitude and direction of site constant revision required. This long-term history can be used to evaluate the major contributors to calibration interval requirements and to "flag" individual heliostats which have unique problems.

The following long-term periodic tests allow evaluation of heliostats and associated components.

- 1) At the end of one year and then again at the end of two years, two inner drive gear boxes and two actuator assemblies will be removed and replaced with spares. Prior to removal, lash at each site will be determined and compared with original values. They will be carefully stripped down and fully evaluated with regard to wear, and environmental effects on surface materials (screw, gear teeth) and the change in lash, etc.
- 2) Once each three months, the output levels of all photo-optical pairs on selected heliostats will be recorded to determine long-term degradation characteristics.
- 3) The foundations of several heliostats will be permanently instrumented with precision levels. Monthly night readings will be taken along with the temperature. The levels will be shielded from direct solar insolation. Two outer perimeter, one mid-interval, and one inner heliostat will be instrumented.
- 4) Effects of the Barstow site exposure will be determined periodically on the following:
 - a) Paint wear and thermal reflectivity characteristics.
 - b) Dust erosion upon mirror module reflectivity.

- c) Mirror module and outer axis bearings and stub shaft material degradation.
 - d) Rubber seals for the electronics enclosure and the actuator protective bellows, along with spur gear housing seals.
- 5) Select mirror modules at random and measure the contour at the beginning of the test effort, at the end of one year, and again after two years to determine any long-term effects on the contour shape due to thermal cycles and solar loading.
 - 6) Monitor, on two selected heliostats, the power required per drive mechanism and per total heliostat once per three months to obtain temperature and time influences.
 - 7) Four to six heliostats will be selected and outer axis alignment and toe-in setting reconfirmed with precision measurements twice per year.
 - 8) Sites will be selected and initialization setting stability evaluated (has deadband opened or decreased due to mechanical shifts of adjustments?).

Receiver -- During normal station operation, steady state and transient performance tests are performed to further demonstrate and evaluate the receiver design.

The following predicted performance characteristics are verified both for steady state and transient conditions:

- 1) Metal temperatures and temperature ranges of the boiler, superheater, boiler drum, headers, and interconnecting piping.

- 2) Displacement of headers and heat transfer surfaces.
- 3) Superheater flow required to control steam temperatures.
- 4) Boiler circuit flow stability.

Transient performance tests are conducted by ramping or stepping various inputs to the receiver to determine if the response characteristics match predictions. Also, tests will be conducted to demonstrate the following:

- 1) Start-up and shutdown steam conditions.
- 2) Cloud cycles.
- 3) System shutdown and system runback conditions caused by a receiver, turbine, or storage unit component failure.
- 4) Cavity convection losses at different wind speeds.

In an attempt to determine the extent of any creep fatigue problem, selected superheater tubes are measured periodically for changes in diameter and roundness.

In addition to tests and checks intended to demonstrate and evaluate system concepts and design, the following are measured and recorded.

- 1) Receiver and corbel structure temperature to determine the effects of stray solar radiation.
- 2) Acceleration in the Receiver Support Tower and Receiver to measure amplification effects of seismic accelerations.

Thermal Storage -- Because of its novel design, the thermal storage subsystem is subjected to extensive testing to demonstrate and evaluate the concept and to prove the components. Tests to establish thermal storage characteristics and performance that were begun during preoperational testing are continued to determine changes over time.

The thermal storage subsystem can be divided into two parts: a "Hitec" thermal storage system and an "oil and rock" thermal storage system. "Hitec" thermal storage system components are subjected to the following tests and checks to evaluate the concept and prove the components.

- 1) Tank thermal cycling
 - a) Diurnal
 - b) Deep thermal cycling
- 2) Heat loss
- 3) Pump seal and bearing application
- 4) Salt condition (e. g., decomposition)
- 5) Heat exchanger performance (e. g., fouling)

"Oil and rock" thermal storage system components are subjected to the following tests and checks to evaluate the concept and prove the components:

- 1) Tank thermal cycling
 - a) Diurnal
 - b) Deep thermal cycling
- 2) Heat loss
- 3) Tank flow and pressure distribution
- 4) Temperature distribution in tanks (e. g., thermocline characteristics)

- 5) Rock migration over time
- 6) Oil decomposition rate
 - a) Thermal properties
 - b) Chemical properties
- 7) Interaction of rocks and other oil contaminants
- 8) Heat exchanger performance (e. g. , fouling)

Electric Power Generation Subsystem -- The Electric Power Generation Subsystem (EPGS) is of conventional design. Therefore, extensive testing to demonstrate and evaluate the concept is not required.

However, to allow correlation of testing associated with the other subsystems with net electrical output, turbine performance tests will be periodically performed. This will allow correlations and energy loss assignments to be properly biased.

Performance testing would involve "in-plant" instrumentation (as opposed to a "field" ASME performance test) based generally on the ASME Power Test Code for Steam Turbine.

Special Equipment --

1. Normal surveying equipment to obtain precise azimuth and distance to target measurements.
2. Special-purpose leveling tools and templates, digital counter, and an accurate measuring scale are required to determine end-to-end scale factors for linear actuators.
3. An oscilloscope and special alignment tools are required to set initialization switches.

4. Accelerometers for measuring component responses to seismic activity.
5. Table 5-17 lists collector subsystem instrumentation requirements.

Table 5-17. Preliminary Collector Subsystem Instrumentation List

8	Flux Sensors/Zone x three zones	24 Flux sensors
4	Voltage Transformers and Digitizers Remote	4 Sensors
4	Field Transformers and Controlled Circuit Breaker Sensors	4 Controllers
8	Calibration Arrays each with 224 Sensors	8 Arrays
8	Radiometers	8 Sensors
5	Weather Stations with Electronics	5 Stations
2	WWV Receivers for Time or Timing Generator Subsystem	2 Stations
3	Station Recorders Tape Decks	3 Decks
12	Precise Shaft Encoders with Electronics	12 Shaft encoders
6	Precise Levels (inclinometers)	6 Inclinometers

REFERENCES

- 1) "Report on Equipment Availability for the 10-Year Period, 1964 - 1973," Edison Electric Institute (EEI) Publication 74-57, Dec. 1974.

- 2) "Reliability Engineering," ARINC Research Corporation, 1963.
- 3) Mechanical Design and Systems Handbook, Harold A. Rothbart, 1964.

SECTION 6

SRE TEST SUMMARY

The Subsystem Research Experiments (SREs) are designed to generate data which can establish the technical feasibility of the preliminary pilot plant design. This design, in turn, can be used to demonstrate the potential for solar central receiver commercial power plants.

The intent of this section is to briefly summarize the SRE test results and to evaluate any impact the results may have on the current pilot and commercial plant designs. Originally, we were contracted to design, build, and test three subsystem experiments: the heliostat subsystem, the receiver subsystem, and the storage subsystem. The storage SRE was designed and built; however, testing of that storage device was canceled. Therefore, no discussion of the storage SRE is contained in this section. The heliostat and receiver SREs have also been designed and built, and testing of each has been performed. Unfortunately, the receiver SRE tests are still in progress at the time of the writing of this report. Very little summary test result information is available and we will not attempt to review the progress thus far. Complete heliostat subsystem test data and results are available at this time. Volume III reports all the test details. In this section, we will review the heliostat system level results and compare the experimental results with predicted performance. For the heliostat, predicted performance is computed using the ray trace optical model.

HELIOSTAT TEST SETUP

Basically, Honeywell's SRE collector subsystem consists of four low-profile, tilt-tilt heliostats (one mobile engineering model and three permanent

experimental models) under one central computer control (open-loop tracking), with a 4.88m by 4.27m photocell grid calibration array, as the primary method of detecting heliostat performance. Miscellaneous instrumentation and wiring equipment was also used during performance testing and is described in detail in the Collector Subsystem Test Report.

Figure 6-1 shows the test site layout. Building E-2 contains the central control equipment and mounts the calibration array. The location of the various heliostats with respect to the calibration array is given in Table 6-1.

Table 6-1. Heliostat Location

Heliostat Site	Heliostat Location	
	Line-of-Sight Distance (m)	Azimuth from North (deg)
North	147	10
East	246	90
South	314	163

Figures 6-2 and 6-3 show a typical heliostat in stowed and tracking positions, respectively.

The calibration array consists of 224 analog photodetectors mounted on a rectangular grid 4.9 m (16 ft) wide by 4.3 m (14 ft) high. Grid line spacing is 0.3 m (1 ft). The outputs of the photodetectors are fed to a multiplexer to provide a redirected flux intensity pattern as seen by the calibration array.

Figure 6-4 shows the calibration array with a redirected image on it. The array can be manually repositioned to face any direction to accommodate any of the various test sites.

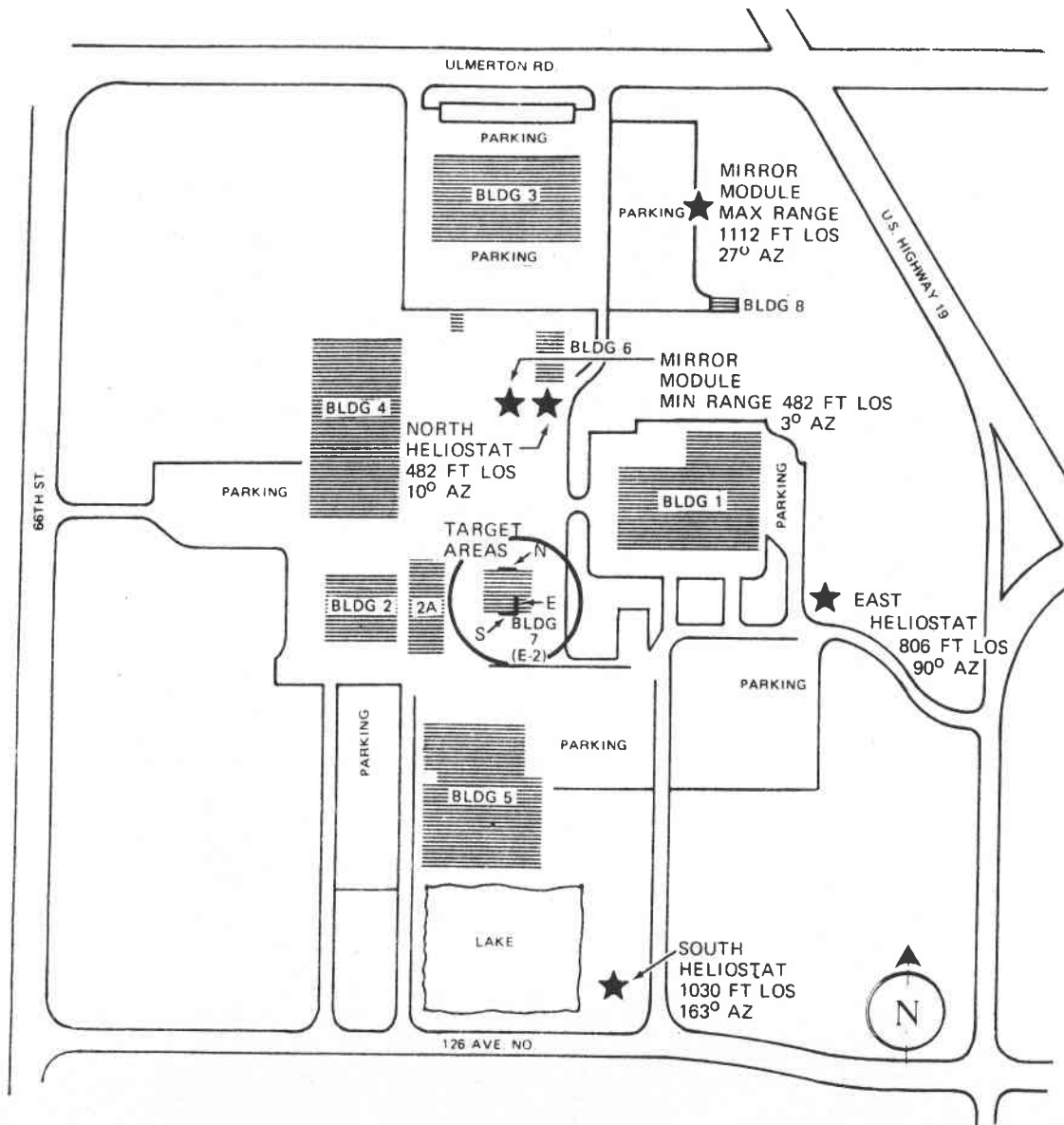


Figure 6-1. Collector SRE Site Plan

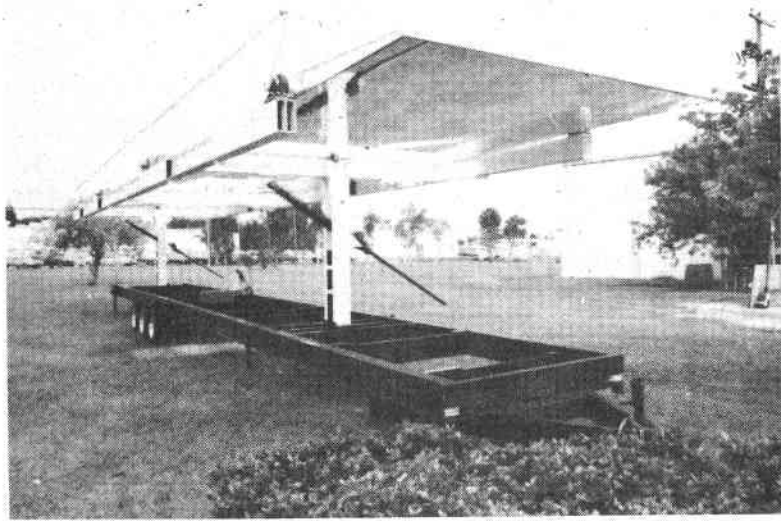


Figure 6-2. Heliostat, Stowed Position

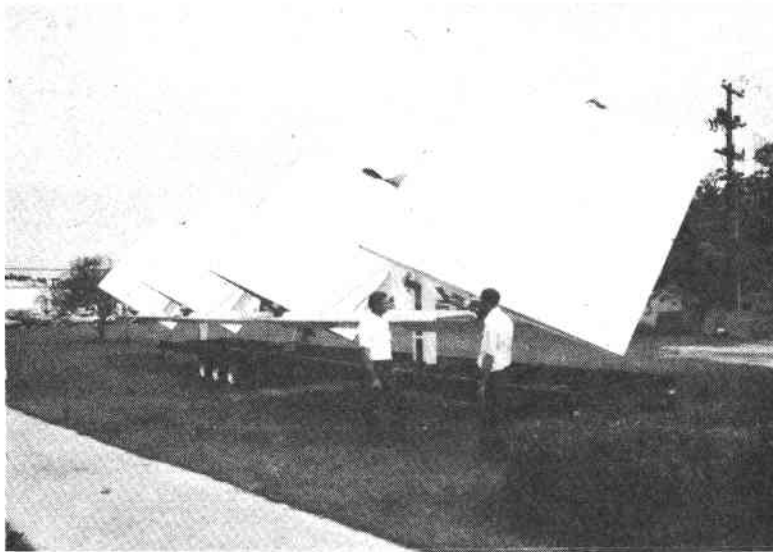


Figure 6-3. Heliostat, Operational Position

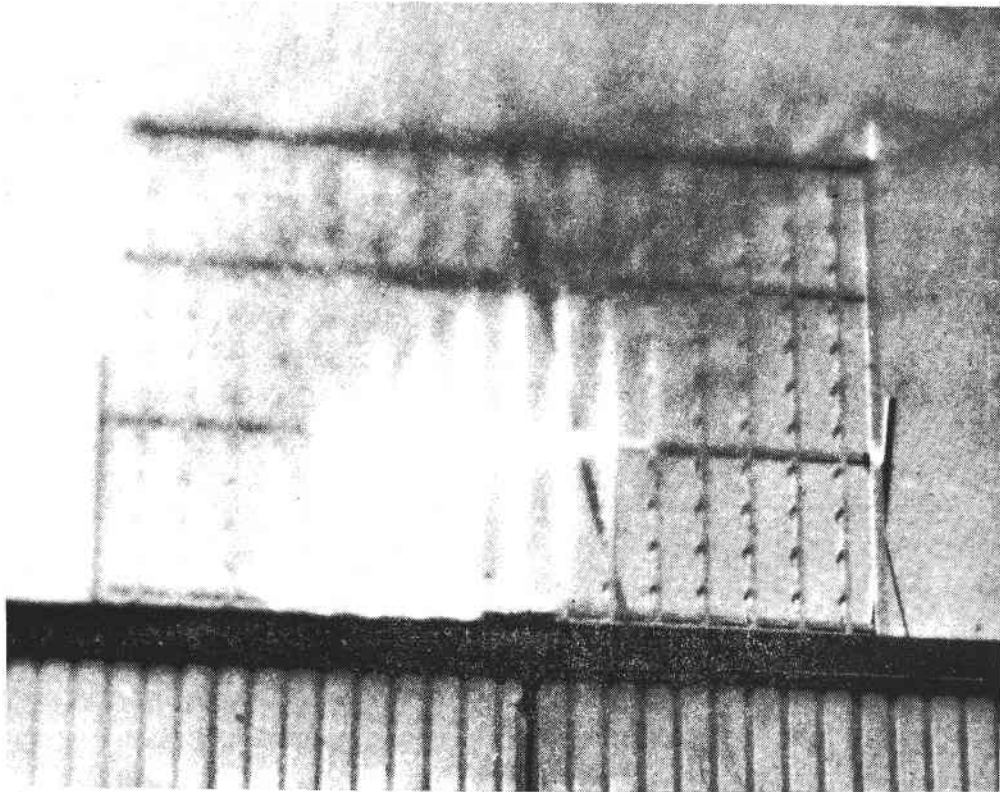


Figure 6-4. Calibration Array Facing North, 9/27/76,
Engineering Model Image

DATA COLLECTION

Figure 6-5 shows a typical output from the test equipment. The output format of the offline data reduction program is shown in the figure. The information at the top of the figure gives the time point, weather, and test equipment conditions and alignment. The main portion of the figure shows the energy distribution on the calibration array. Specifically, the following is recorded:

- Time of day, GMT days, hours, minutes, and seconds
- Operational mode of each heliostat (4)
- Base, height, and azimuth to target for each primary and secondary target associated with each heliostat
- Inner gimbals angle of each heliostat
- Outer gimbals angle of each heliostat
- Outer drive screw length of each heliostat
- Three direction cosines for each heliostat associated with its primary target
- Three direction cosines for each heliostat associated with its secondary target
- Sun's azimuth, elevation, and refraction correction
- Vertical and horizontal location of the centroid of the redirection image upon the photocell array
- 224 photocell readings from the array

40703-II

PHOTOCELL INTENSITY ACROSS 16' x 14' ARRAY.
PHOTOCELLS ARE ACTUALLY ON 1' GRID VERTICAL
AND HORIZONTAL INTERVALS

DAYS RADDYR PRESS	HOURS PAX2MOM TEMP1	MINS SAX2MOM TAMB	DELTA PAXANG TEMP3	DELTA SOF TCELTA	WINDSPD ANGSEVN PYADR	WINDDIR RADGLOBAL	CALMAX	BACKWIG	EM HELIOSTAT AS THIRD HELIOSTAT IN MODE 2				DISTANCE		
DAY	HOURL	MINUTE	SECOND	5	5	5	1000.00	1000.00	521.00	1000.00	55.00	55.00	55.00	55.00	55.00
265.00	13.00	10.00	0.00	5	5	5	1000.00	1000.00	521.00	1000.00	55.00	55.00	55.00	55.00	55.00
1200.00	1000.00	300.00	1000.00	55.00	0.00	176.00	50.00	50.00	55.00	55.00	0.00	0.00	0.00	0.00	0.00
53.00	00.00	55.00	0.00	32.78	0.00	180.00	52.46	52.46	52.46	52.46	0.00	0.00	0.00	0.00	0.00
176.00	00.00	180.00	180.00	0.00	0.00	0.00	0.05	0.05	0.05	0.05	0.00	0.00	0.00	0.00	0.00
52.46	0.00	0.00	-69.35	0.00	1.00	0.00	-0.99	0.00	0.00	0.00	1.00	1.00	1.00	1.00	1.00
0.00	0.00	0.00	0.00	0.00	0.00	0.00	0.00	0.00	0.00	0.00	0.00	0.00	0.00	0.00	0.00
0.05	0.16	0.05	0.00	0.00	0.00	0.07	0.00	0.00	0.00	0.00	1.00	1.00	1.00	1.00	1.00
-0.98	1.00	102.48	23.24	23.27	23.27	0.01	0.28	0.28	0.61	0.61	0.61	0.61	0.61	0.61	0.61
														HORIZ DISTANCE OF CENTROID OF IMAGE FROM CENTER OF ARRAY	
														VERT DIST OF CENTROID FROM CENTER OF ARRAY	
														SUN ELEV CORRECTED FOR REFRACTION	
SUN AZ	SUN ELEV	OUTER AXIS ANGLE	INNER GIMBAL	TGT ELEVATION	VERT DIST OF CENTROID FROM CENTER OF ARRAY		VERT DIST OF CENTROID FROM CENTER OF ARRAY		VERT DIST OF CENTROID FROM CENTER OF ARRAY		VERT DIST OF CENTROID FROM CENTER OF ARRAY		VERT DIST OF CENTROID FROM CENTER OF ARRAY		
2	2	2	2	2	1	2	3	20	21	4	2	2	2	2	
2	1	2	1	2	2	2	8	11	20	13	7	4	0	2	
1	2	2	2	2	3	8	11	20	13	10	7	4	0	2	
2	2	1	2	2	7	13	20	20	26	19	13	6	0	2	
2	1	2	3	4	11	15	31	20	37	30	18	10	4	1	
2	2	2	3	6	14	31	42	21	47	37	24	13	5	2	
2	2	3	3	9	21	35	47	21	56	20	24	14	4	2	
2	2	2	2	0	21	32	47	21	51	40	15	11	4	2	
2	2	2	4	0	17	28	39	20	41	29	17	9	3	2	
2	1	2	7	12	22	22	29	21	28	21	15	5	2	2	
2	2	1	2	3	0	13	13	21	16	13	8	3	2	2	
1	2	0	2	2	0	6	7	21	8	6	3	1	2	2	
2	2	2	2	1	0	2	1	21	2	2	2	2	1	2	
0	2	2	2	2	2	2	2	21	2	2	2	2	2	2	
0	0	0	0	0	0	0	0	0	0	0	0	0	0	0	
265.0	13.00	10.00	0.2849	0.6858	0.0000	0.0000	0.0000	2.196	0.0000	0.0000	0.0000	0.0000	0.0000	0.0000	
4.028	7.175	9.051	0.151	0.0221	50.00	0.0000	0.0000	0.0000	0.0000	0.0000	0.0000	0.0000	0.0000	0.0000	
\$14.0	15.00	-34.00	13.00	-11.00	0.0000	0.0000	0.0000	0.0000	0.0000	0.0000	0.0000	0.0000	0.0000	0.0000	

6-7

WEATHER
CHANNELS
(NOT
OPERATING)

Figure 6-5. Engineering Model Open-Loop Tracking Results

- Five background sensor readings used to compensate the calibration array for background radiation levels
- One background average reading
- Ten weather channels of information to include wind, temperature, pressure, and global, normal incident, and single photocell solar radiation levels.

SUBASSEMBLY TESTS

Various tests were performed on the heliostat subassembly prior to calibration of the heliostat and actual data collection in the open- and closed-loop modes. Only the two most important are summarized here: facet surface contour errors and tracking errors.

Contour Errors

Various mirror modules were evaluated for compliance with contour requirements. Contour measurements were made with the mirror modules horizontally and vertically supported at the axes. A piano wire was used to provide a reference for measurements. Repeatability measurements made indicated the measurements can be repeated within 0.002-inch total error. Measurements were along the various axes of the modules tested. In some cases, measurements were made with no load applied, and in other cases loading was done by applying sandbags over the mirror surface. Figure 6-6 is a typical plot of contour measurements showing the error from the desired theoretical contour. This particular module was measured axially, unloaded, while in horizontal position, as shown by the inset at the top center of the figure.

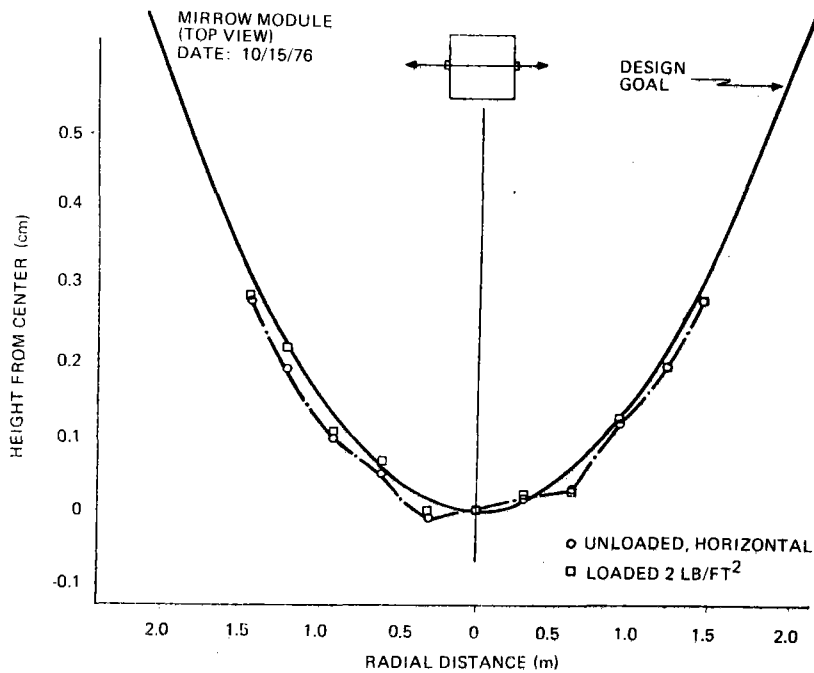


Figure 6-6. Mirror Contour Data

The structural rigidity of all the mirror modules under all simulated environmental loads surpassed the contour control requirements. Under operational wind loading, the outer-axis (vertical image movement) combined deflections did not exceed ± 0.6 mr. Inner-axis deflections under gusts have shown instantaneous extremes of 2.9 mr, but a more nominal average of ± 1.3 mr centroid deflections can be expected across a field average.

Tracking Errors

During a typical day's tracking, vertical and horizontal movement of the image on the calibration array occurs from all sites tested (north, south, and east). These movements are attributed primarily to mechanical linkage of the outer actuator, outer-axis misalignment, inner-drive gearbox, and low target height.

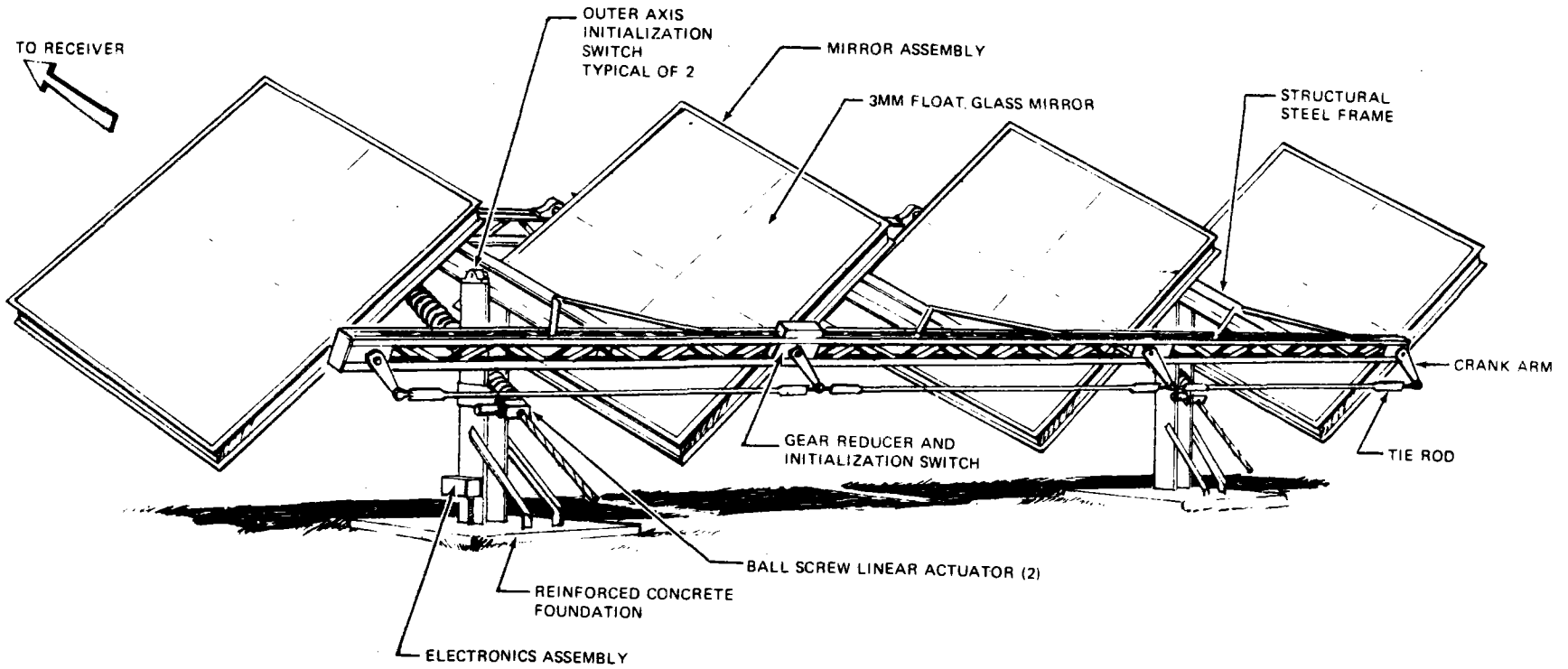
The complete heliostat assembly and primary mechanical components are shown in Figure 6-7. The outer actuator can be seen in the figure. This drive assembly consists of two linear actuators, one at each end of the heliostat. A d-c motor drives a worm gear set which, in turn, drives the bearing support nut. Rotation of this nut causes the screw to translate in and out, depending on the motor's direction. The theoretical effective linear gear ratio of the actuator is 0.01185 inch/motor revolution. Measured values of this gear were 0.70 percent less than theoretical values. Therefore, the total outer-axis gimbale angle is greater than the actual angle after 2000 to 4000 motor revolutions, and the sun's redirected image drifts upward after solar noon. The magnitude of the error induced by the outer actuator is dependent on site location because at different site locations, different gimbale tilts occur.

The inner-drive operation includes a tie rod/crank arm ganging of the four mirror modules (ref. Figure 6-7). Backlash and deflections due to torsional loads contribute to overall errors of the heliostat tracking ability.

The outer-axis misalignment results from the fact that the centerline of the outer-axis pivot is off-perpendicular with the radial vector from target to heliostat. The effect of this misalignment was minimized by compensating for it with program software during tracking.

The low tower height causes centroid movement during tracking due to excessive outer-axis gimbale angle. However, most of the centroid movement occurs early and late in the day when the outer axis is approximately -70 degrees off horizontal. For the pilot plant field layout, this outer-axis tracking envelope would be reduced significantly during hours of useful solar insolation because of the taller tower. The most northern heliostat site location results in a maximum outer-gimbale angle of 18 degrees off horizontal.

40703-II



6-11

Figure 6-7. Heliostat Assembly

The combined effect of these factors results in centroid movement of the image, depending on heliostat location with respect to the target. Figures 6-8 and 6-9 show centroid displacement as a function of time in the horizontal and vertical directions for the south site. The displacements errors for the south site can be translated to milliradians as follows:
 $1 \text{ m} = 3.18 \text{ mr}$.

Table 6-2 summarizes the maximum tracking errors which occur during a typical day's tracking.

Table 6-2. Maximum Tracking Errors

Site Location	Tracking Errors (mr)		Test Date
	Horizontal	Vertical	
South	1.3	1.3	10/25/76
North	0.5	1.3	10/26/76
East	0.5	1.5	11/23/76

This experiment has demonstrated that pointing and tracking accuracies of 2 mr can be obtained with the present four-facet, tilt-tilt, open loop controlled, heliostat configuration. An initial concept of calibration of each heliostat has given way to the need for a two-part calibration scheme: (1) initial site and drive mechanism scale factor calibration, and (2) periodic calibration to make longer-term drift and shift corrections based solely on artificial offset adjustments.

6-13

SOUTH HELIOSTAT
LOS - 314 m
26 OCTOBER 1976

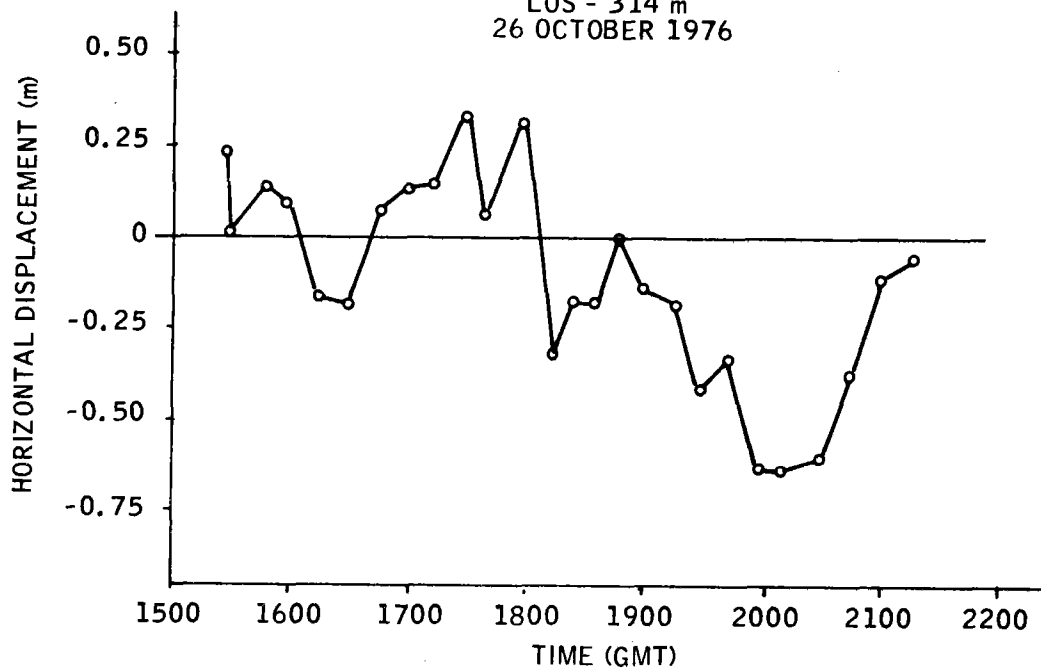


Figure 6-8. Image Horizontal Centroid Track, South Site

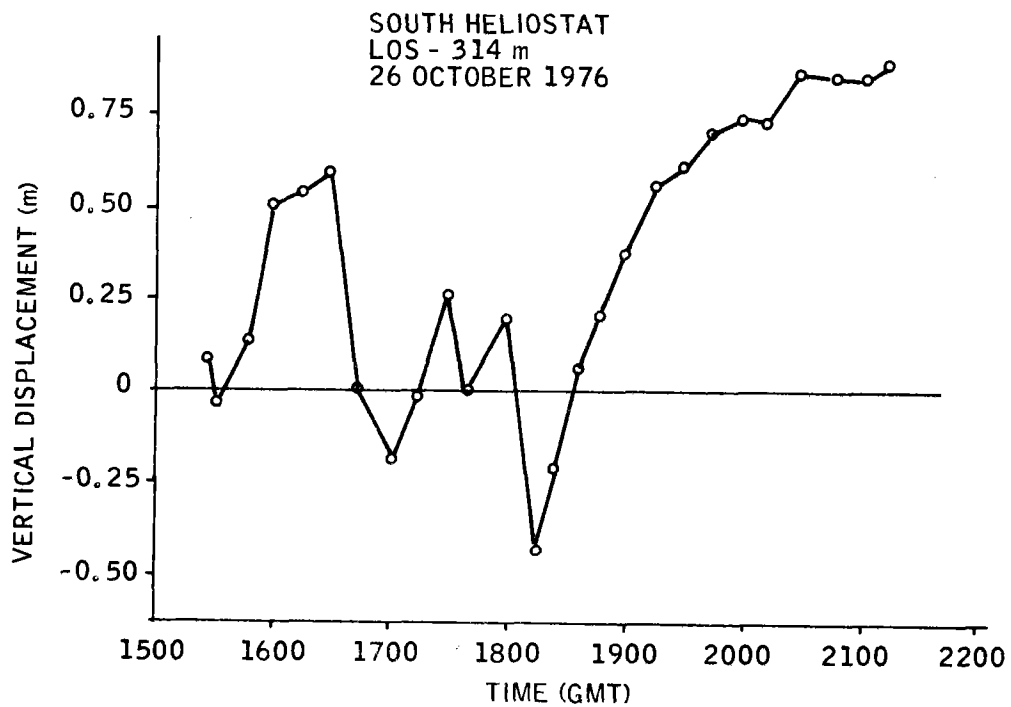


Figure 6-9. Image Vertical Centroid Track, South Site

REFLECTANCE MEASUREMENTS

The spectral reflectance of two samples taken from actual units were measured with a Cary 14 spectrophotometer. A computer program used the output from the Cary 14 to calculate the total solar reflectance. In this program, the solar spectrum is divided into 12 energy bands, and the fraction of the total solar flux in each band is determined. This fraction is then multiplied by the value of the sample reflectance corresponding to the wavelength of each band's center. These values are then summed to obtain the total solar reflectance. Results from these tests are summarized in Table 6-3.

Table 6-3. Reflectances at Various Wavelengths for Two Samples of Mirror Obtained from Honeywell Avionics Division, St. Petersburg, Fla.

Wavelength (microns)	Reflectance	
	Sample A	Sample B
0.40	0.885	0.885
0.45	0.917	0.917
0.50	0.946	0.946
0.60	0.951	0.953
0.65	0.942	0.936
0.70	0.918	0.921
0.90	0.890	0.890
1.10	0.791	0.798
1.10	0.770	0.774
1.30	0.792	0.792
1.50	0.842	0.842
1.90	0.870	0.865
Average	0.870	0.871

Measurements taken at the test site itself consisted of looking directly at incident insolation and then reflected insolation with a calibrated pyrhelimeter. The comparison of the two measurements result directly in the reflectance. The measurements on clean facets showed approximately 87.2 to 89.2 percent reflectance. These reflectance measurements integrates the total spectrum and averages discrete data points on the solar energy profile. A comparison of the results of the two methods shows that the pyrhelimeter method is a reasonable and certainly a quicker way to measure reflectance.

Dirty mirrors exposed to the environment for 1 week with mirrored surface up showed an additional 9.2 percent loss from clean mirrors (i. e., reflectance of 76 to 81.2 percent). This degradation seems to be primarily due to dirt accumulation from humidity and dew. Dirty mirrors exposed to the environment for 1 month show reflectance of 78 to 84.9 percent. Nonstreaking adhering dust is the predominant characteristic. When dusty mirrors were exposed to light rain, the reflectance was further reduced by an additional 24 percent.

POWER BALANCE

Although the calibration array's primary purpose was to determine the re-directed image centroid, it was also used to calculate a power balance. The total power over a given image size is computed with offline computer processing of the calibration array data. As an example of the method, the computer-printed calibration array readings shown in Figure 6-10 can be used. The raw data shown are simply a digital readout for each photocell sensor. The total power striking the array can be computed by summing all photocell readings and applying appropriate calibration constants.

40703-II

6-16

DAYS RADGYR PRESS	HOURS PAX2MOM TEMP1	MINS SAX2MOM TAMB	DELVER PAXANG TEMP3	DELHOP GCF TDELTA	WINDSPD ANGSVN PYNOR	WINDDIR RADGLOBAL	CALMAX RATIO	CALSUMG ENERGY	BACKAVG	HEADINGS FOR DATA AT BOTTOM								
1	1	9	1	1	0	1	0	1	1	1	1	1	0	1	1	CALIBRATION ARRAY OUTPUT		
1	1	1	1	1	1	1	1	1	1	1	1	1	1	1	1		INDIVIDUAL PHOTOCELL SENSOR READINGS	
1	1	1	1	1	2	4	6	5	5	3	2	2	2	2	1			CALIBRATION AND WEATHER DATA
1	1	0	1	1	7	13	17	17	15	12	9	5	3	1	1			
1	1	1	3	7	21	26	49	49	46	36	29	19	7	1	1			
1	1	3	7	17	40	73	99	98	89	69	56	34	17	3	1			
1	1	5	0	30	75	116	150	166	140	57	75	52	28	5	2			
1	1	4	15	34	92	143	183	205	181	143	104	63	33	8	2			
1	1	4	15	22	85	141	188	224	182	151	109	73	35	11	3			
1	1	4	15	40	70	112	148	168	156	133	106	45	31	12	2			
1	1	4	13	20	50	71	67	108	109	92	67	41	23	9	3			
1	1	3	11	15	21	42	49	53	57	51	37	21	11	4	2			
1	1	1	4	7	10	14	18	21	21	14	13	7	3	2	1			
0	1	1	1	3	4	4	5	7	9	6	5	3	2	1	1			
2	2	2	2	2	2	1	218	2	6	0	161	2	6	4	150			
97.00 3.238 015.1	19.00 4.544 0.0000	44.00 5.940 -11.27	-1.100 -82.96 0.0000	0.7567 0.9661 0.0000	0.5767 51.96 951.1	14.21 666.1	0.784 0.7876	6735. 0.2231E-01	0.7843E-01									
(DAY), GREENWICH MEAN TIME	(HR)	(MIN)		RATIO OF PYROHELIOMETER READING TO PHOTOCELL SENSOR READING	PYROHELIOMETER BITS	TOTAL CALIBRATION ARRAY BITS												

Figure 6-10. Calibration Array Output

To accomplish this, the first step is to determine the sun's direct normal intensity at the time of the test. Referring to Figure 6-10, the pyr heliometer reading is shown at the bottom of the figure. The 161 bits shown are multiplied by the calibration constant of $5.596 \text{ W/m}^2/\text{bit}$. A known instrument bias, due entirely to the electronics, of 59.7 W/m^2 is added to this result and we find 960.7 W/m^2 available intensity.

A second calibration factor to be computed is the photocell sensor constant. The silicon solar cells respond to only a portion of the solar wavelength spectrum. Absorption due to water moisture, carbon dioxide, etc., in the atmosphere will have a different and varying effect on the equivalent power sensed by a silicon photocell and the power sensed by a pyr heliometer. A calibration factor is computed by simply tracking the sun with both a silicon solar cell and a pyr heliometer. The ratio between the two readings can be used to deduce the flux measured by the calibration array photocells. In the example of Figure 6-10, the ratio of the photocell reading to the pyr heliometer reading is 218. An additional calibration correction to account for instrument differences shows that the final ratio must be equal to 8.43 divided by the actual measured ratio. The actual total measured power is found by the algorithm below:

$$\text{Power on Array} = \underbrace{20.82 \text{ m}^2}_{\text{Calibration array area}} \times \underbrace{\frac{8.43}{218}}_{\text{Photo-cell calibration}} \times \underbrace{960.7 \frac{\text{W}}{\text{m}^2}}_{\text{Computed sun's DNI}} \times \underbrace{\frac{6735 - 222}{224}}_{\text{Average photo-cell reading}}$$

or

$$\text{Power on Array} = 22,500 \text{ watts}$$

In words, we have summed the calibration array readings, subtracted the background radiation readings, and found the average photocell reading by

dividing by the number of cells (224). This value is multiplied by the total calibration array area, times the DNI, times the photocell calibration constant. One additional modification must be applied to the 22,500-watt value. The photocell sensor itself is mounted horizontally. The actual power which can enter the photocell window is decreased by the cosine of the angle between the nominal redirected beam and the photocell angle (horizontal). Measured values of this reduction in photocell sensor readings as a function of the angle between the incoming beam and the cell orientation show that the readings actually roll off slightly faster than the cosine curve. The glass window at the photocell sensor inlet may account for the difference. Figure 6-11 shows the cosine correction curve.

Using the photocell cosine correction, the measured power is finally calculated as 22,700 watts.

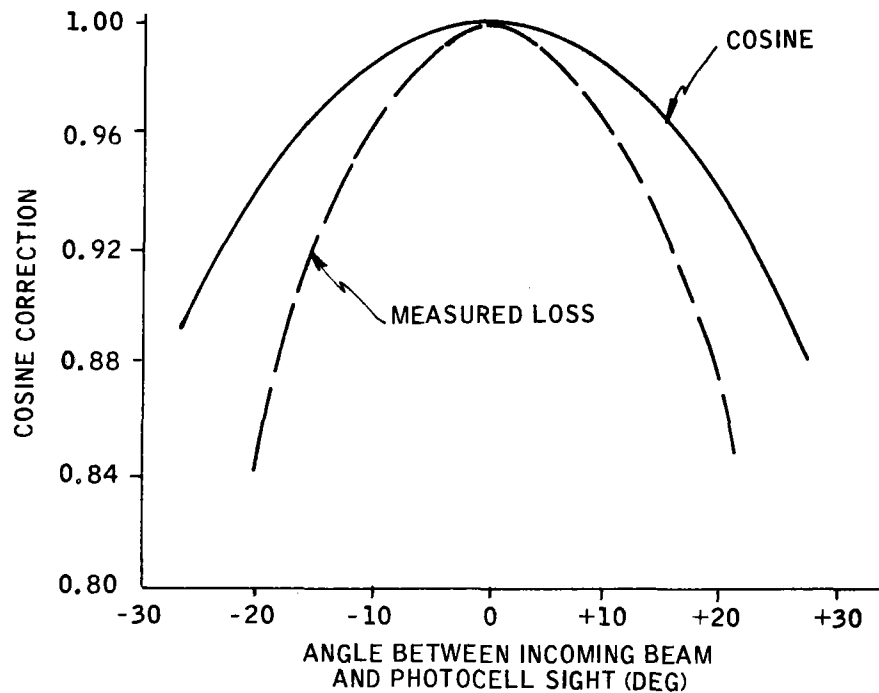


Figure 6-11. Photocell Off-Axis Correction Curve

Measured power levels may be compared with predicted power. We start with the sun's DNI, already calculated to be 960.7 W/m^2 . Since the data in Figure 6-10 is for April 7 at approximately 3 p. m. solar time, the mirror and frame can be shown to introduce negligible shading and blocking losses. The cosine between the mirror normal and the sun vector at this time is calculated as 0.845. The mirrors for this test were somewhat dirty and a mirror reflectance of 0.85 can be used.

The estimated redirected power is found by:

$$\text{Redirected Power} = \text{DNI} \times \text{cosine} \times \text{refl} \times \text{mirror area}$$

where

$$\text{DNI} = 960.7 \text{ W/m}^2$$

$$\text{Cosine} = 0.832$$

$$\text{Refl} = 0.85$$

$$\text{Mirror area} = 9.29 \times 4 \text{ m}^2$$

The result is:

$$\text{Redirected Power} = 25,200 \text{ watts}$$

Thus far, we have not accounted for any atmospheric attenuation losses between the mirror and the calibration array. An atmospheric attenuation loss model was specifically developed to predict pilot and commercial plant losses. This model can be used to predict losses for the SRE tests as well. For the test data of Figure 6-10, the relative humidity was approximately 50 to 55 percent. The temperature was 85°F and the day was relatively clear. Using the atmospheric attenuation loss model, the loss as a function of LOS (line of sight) distance to the target is shown in Figure 6-12. For the north site heliostat, the model predicts an atmospheric attenuation loss of

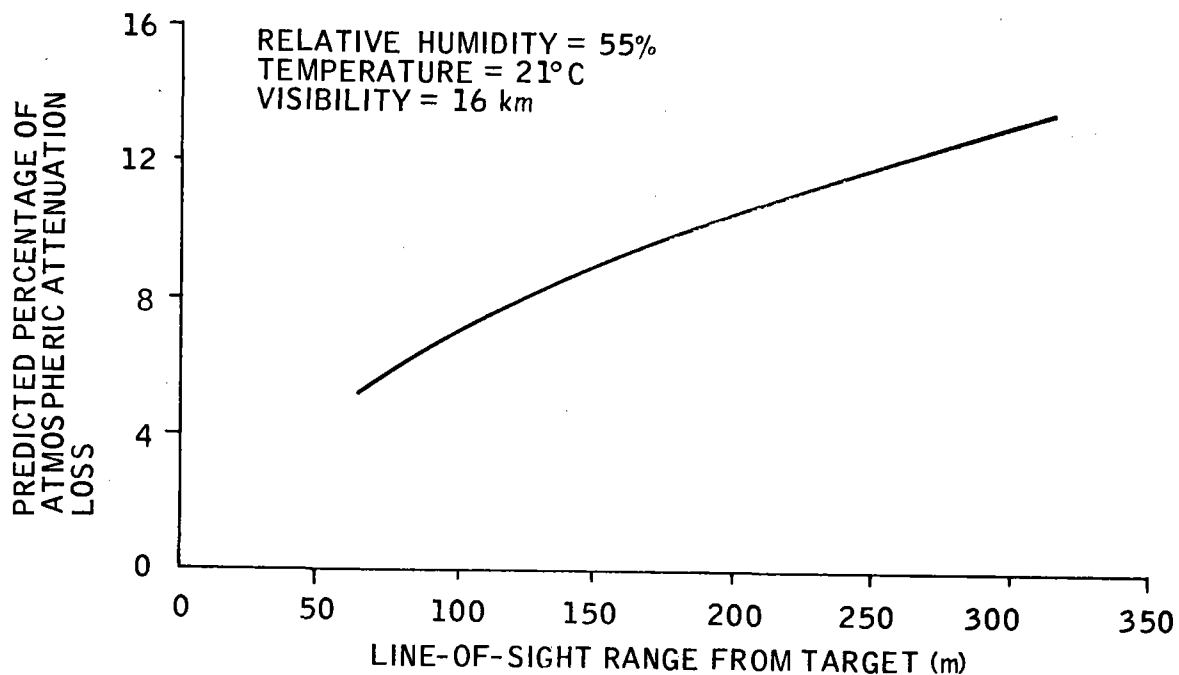


Figure 6-12. Predicted Atmospheric Attenuation Losses versus Range

approximately 9 percent. Applying this to the predicted redirected power, we find a total predicted power of 22,800 watts. This is within 1/2 of 1 percent of the measured power value. Since the calibration array was not originally intended to perform precise power balance calculations, this result is surprisingly accurate. To examine the credibility of these data, a number of different LOS distances to the target were tested. A single mirror module was placed at distances of 81 to 324 m away from the tower. Values of predicted and measured power are shown in Table 6-4. In all cases, the predicted and measured powers are within 2 percent. We find this close correlation to be considerably more accurate than we could have guessed beforehand. However, exactly the same calibration constants and data reduction algorithms were used to calculate the measured power on the array in every case. We cannot say that this type of correlation between the results can be obtained for any test on any day. We can say that the existing data lend credence to the methods we have used to estimate the

Table 6-4. Power Balance Comparison

Distance to Mirror Site (m)	Expected Power (W)	Measured Power (W)	Percent Difference (+ is greater)	Remarks
80.8	55864	5938	+1.3	One mirror module
144.0	5556	5551	-0.8	One mirror module
220.0	5385	5395	+0.2	One mirror module
260.0	5232	5256	+0.5	One mirror module
323.5	5057	4994	-1.2	One mirror module
148.0	22816	22716	-0.4	North heliostat

atmospheric attenuation losses. A continued test of the heliostats and the calibration array under a variety of operating conditions is necessary to confirm findings thus far.

IMAGE CHARACTERISTICS

Magnetic tape and ASR recordings of the image characteristics (flux densities) were obtained throughout the test program. Flux density information was obtained using the calibration array photocells. An example of the raw data obtained from the calibration array is shown in Figure 6-10. The digital readout and appropriate calibration constants can be used to find the flux intensity on the array. The procedure is to take the actual photocell sensor reading minus the residual (or background) reading and multiply by the sun's direct normal intensity and the calibration constant for the photocells. The way in which the direct normal intensity and the calibration constant are obtained was explained previously.

As an example, for a photocell sensor reading of 35, the implied flux density is:

$$\text{Flux} = \underbrace{\frac{8.43}{218}}_{\text{Photo-cell cali-bration}} \times \underbrace{960.7 \frac{\text{W}}{\text{m}^2}}_{\text{Computed sun's DNI}} \underbrace{(35 - 1)}_{\text{Photocell reading}} = 1263 \frac{\text{W}}{\text{m}^2}$$

This calculation was performed for all readings of the calibration array. Flux densities are shown in Figure 6-13. The figure shows some scattering in the results and the scatter is probably accounted for by a combination of actual flux scattering due to optical imperfections and small instrument errors in individual photicell sensors. Isoleths of constant-flux intensity are also shown in the figure. These are drawn to indicate the image size, peak flux, and the image centroid. It is seen that the image is nearly entirely contained within the calibration array boundaries. The peak flux is approximately 8000 W/m^2 and the centroid is displaced from the array center (aimpoint) by approximately 0.3 m. Measured flux densities may be compared with the flux densities predicted by the single-heliostat optical model. The model is described in Section 7 of this volume. For the purpose of comparing with SRE test results, the single-heliostat optical model was run with no tracking error. However, the sun's limb darkening effect and the contour or surface slope errors are modeled. A 1-mr, 1-sigma normal distribution is used for the mirror surface error budget. Figure 6-14 shows the predicted flux map. Flux densities are shown in exactly the same format obtained from the calibration array. That is, the flux densities on 0.3 m (1 ft) centers are plotted. Some scatter in these data can be seen. The scatter is accounted for by both the random draw over the assumed surface error distribution and the scatter due to Monte-Carlo errors. Any Monte-Carlo method can be thought of as a numerical experiment where the error in the results is proportional to the square of

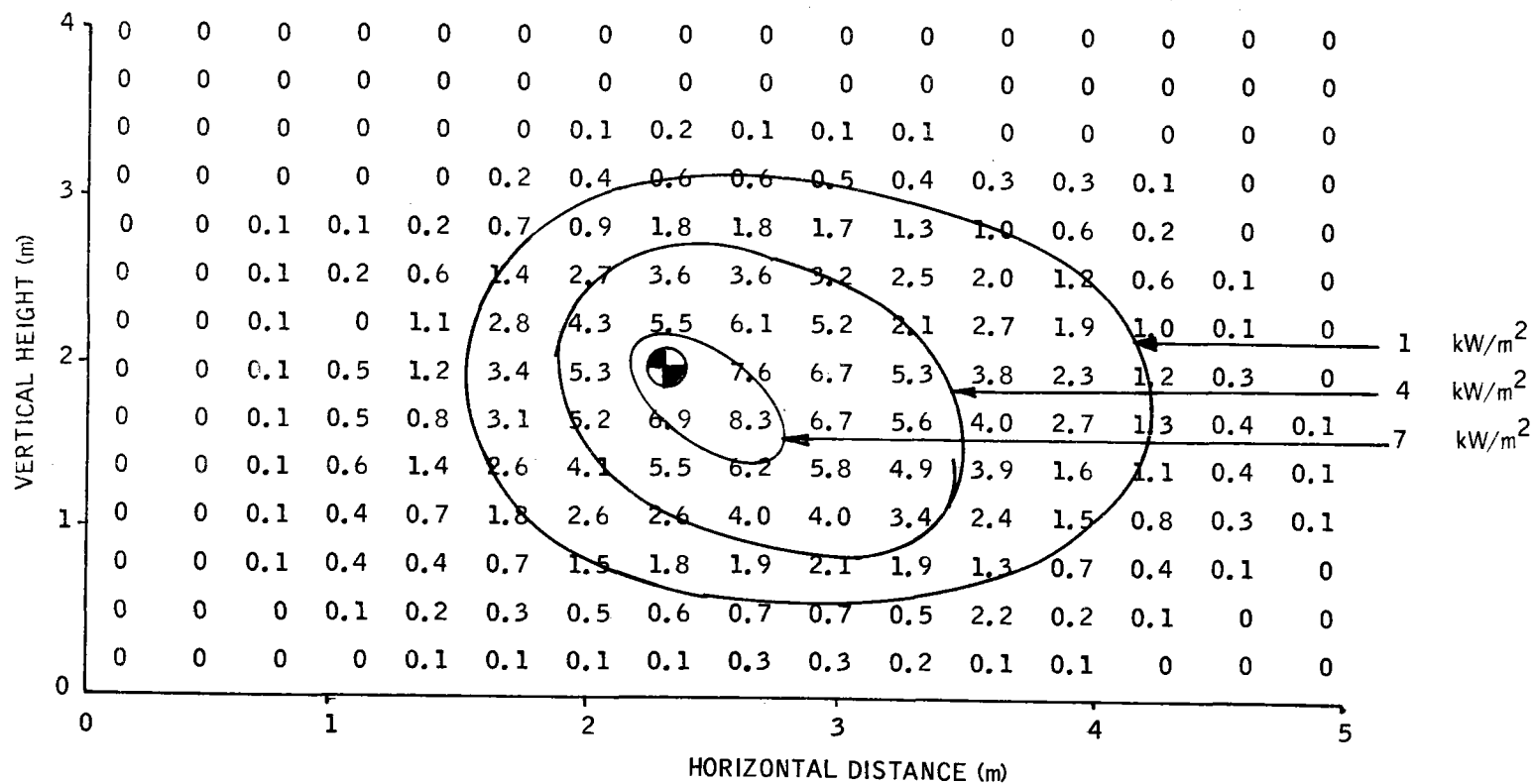


Figure 6-13. Flux Density Measured on the Calibration Array

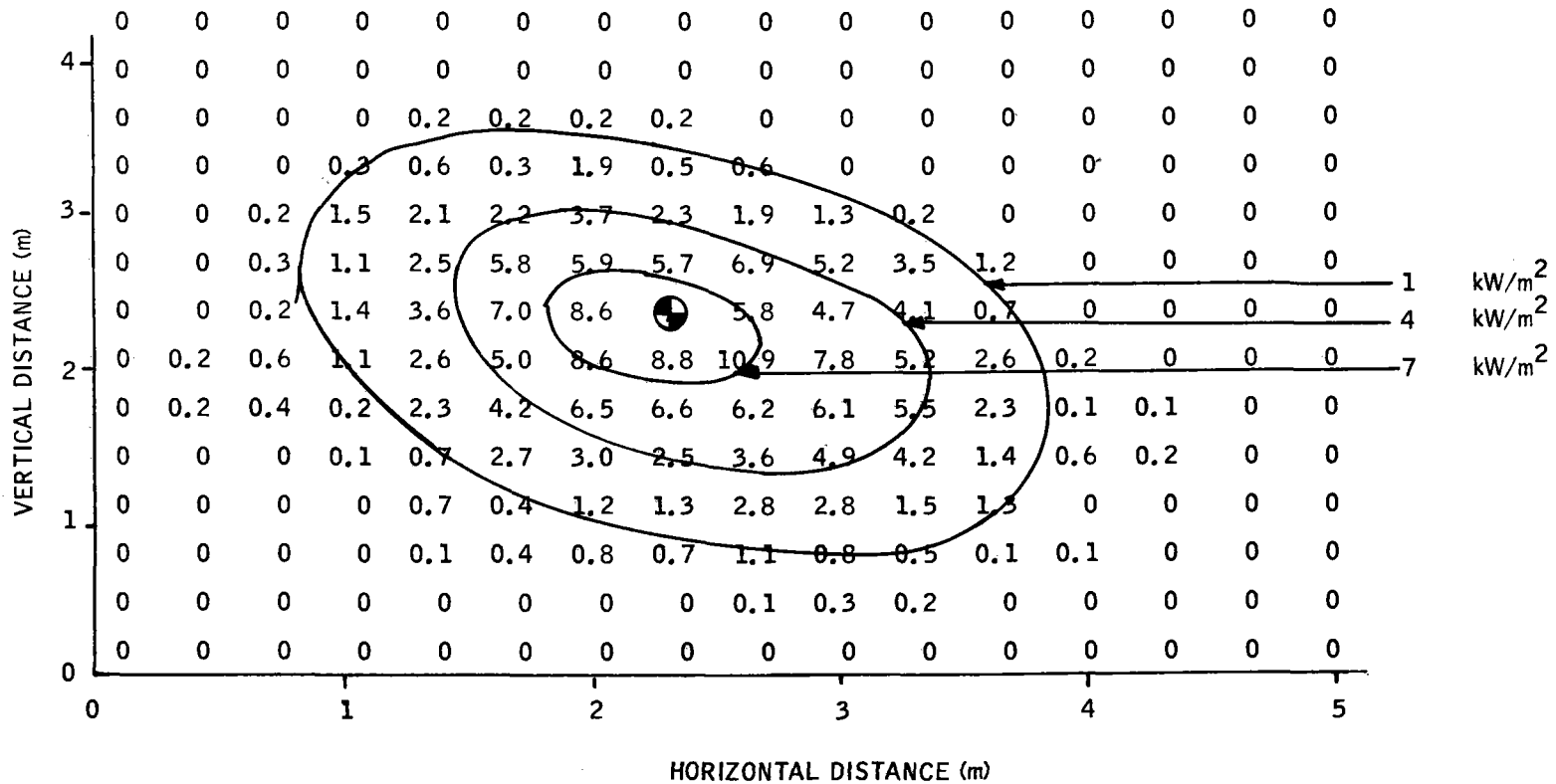


Figure 6-14. Optical Model Predicted Flux Density

the number of experiments. For the data in Figure 6-14, part of the scatter can be thought of as a Monte-Carlo dispersion.

Flux isopleths predicted by the optical model show the image to be slightly elongated and slanted. Two reasons can explain the shape. First the target (calibration array) is positioned vertically and the redirected beam strikes the target at approximately an 8-degree angle with respect to the target normal. Thus, a vertical elongation is expected. The slight slant of the image is accounted for by the off-axis aberrations of the spherical mirror. For this test day and time, the sun is 55 degrees off azimuth from the LOS from the heliostat to the target.

The most important comparison between the measured flux densities and the predicted flux densities is the comparison between the distribution of power over the image (i. e. , the amount of power that is available in a given area). Figure 6-15 compares the flux profiles in two directions. For simplicity, the centroids of both the predicted and measured flux maps are located at the same locations. This simply eliminates the tracking error in the measured data. The flux profiles were estimated as an average flux through the image center. The figure shows quite close agreement between the experimental results, one from SRE tests and one from Monte-Carlo experiments.

In addition to the comparison already shown, we ran the single-heliostat optical model for several other measured flux profiles. SRE test data and optical model data for 12/17/76 are shown in Figures 6-16 through 6-18 for the north, south, and east test sites, respectively. In all cases, good agreement between the measured and predicted results is shown.

We can conclude that the optical model is a fair representation of the actual spherical mirror surfaces and the mirror surfaces optical quality.

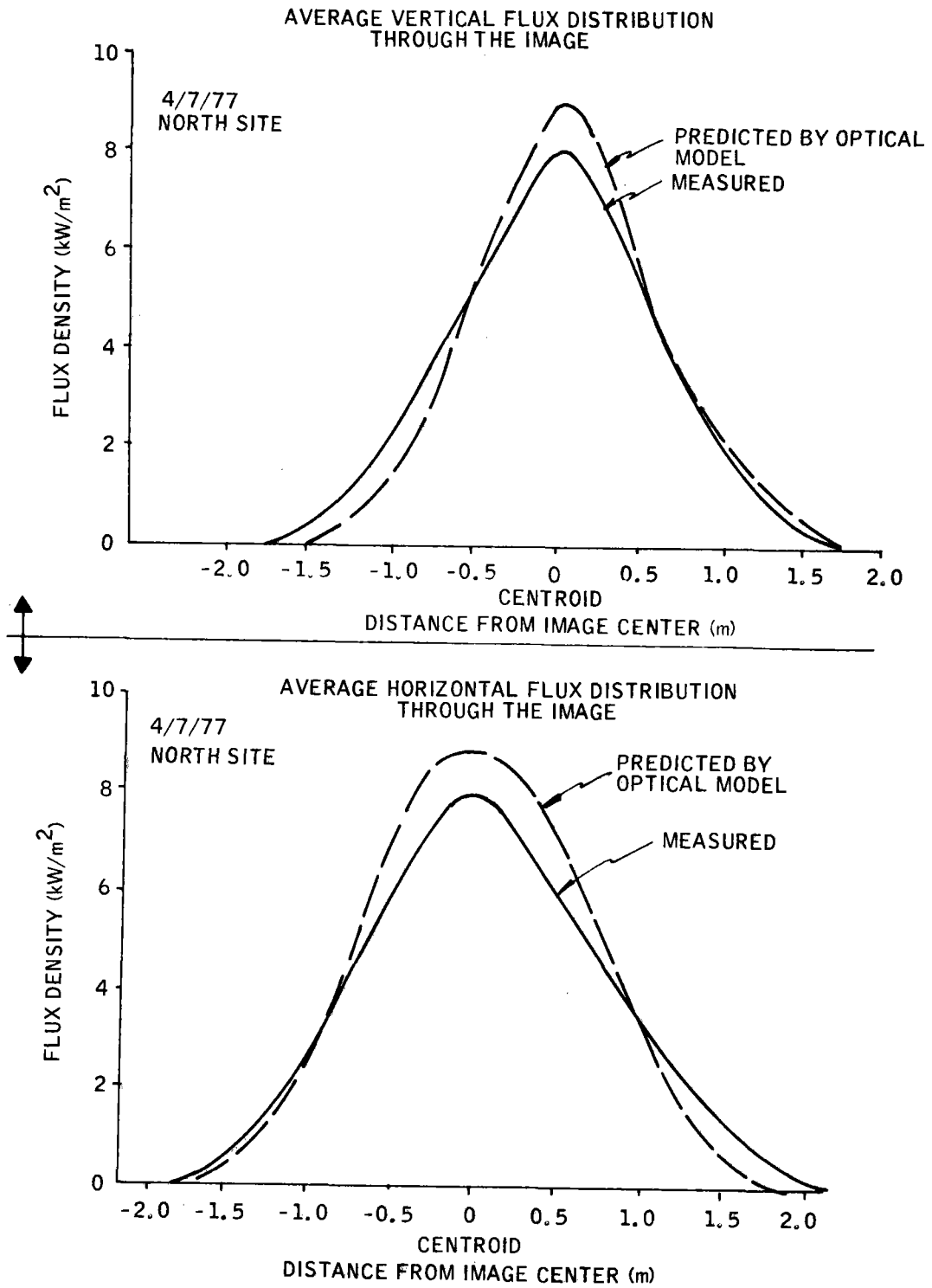


Figure 6-15. Comparison of Predicted and Measured Flux Distribution

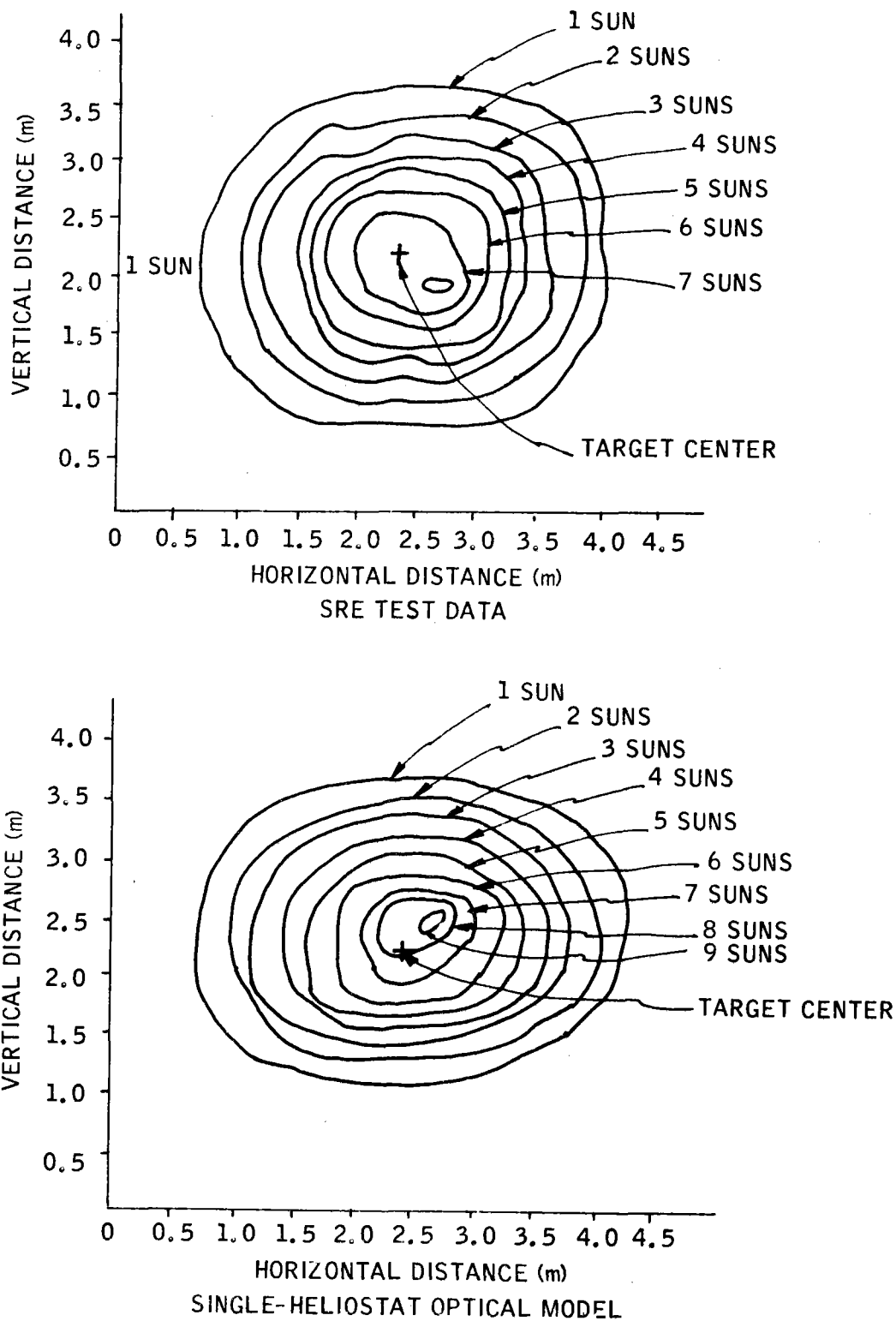


Figure 6-16. Comparison of Test Data with Optical Model - North Site

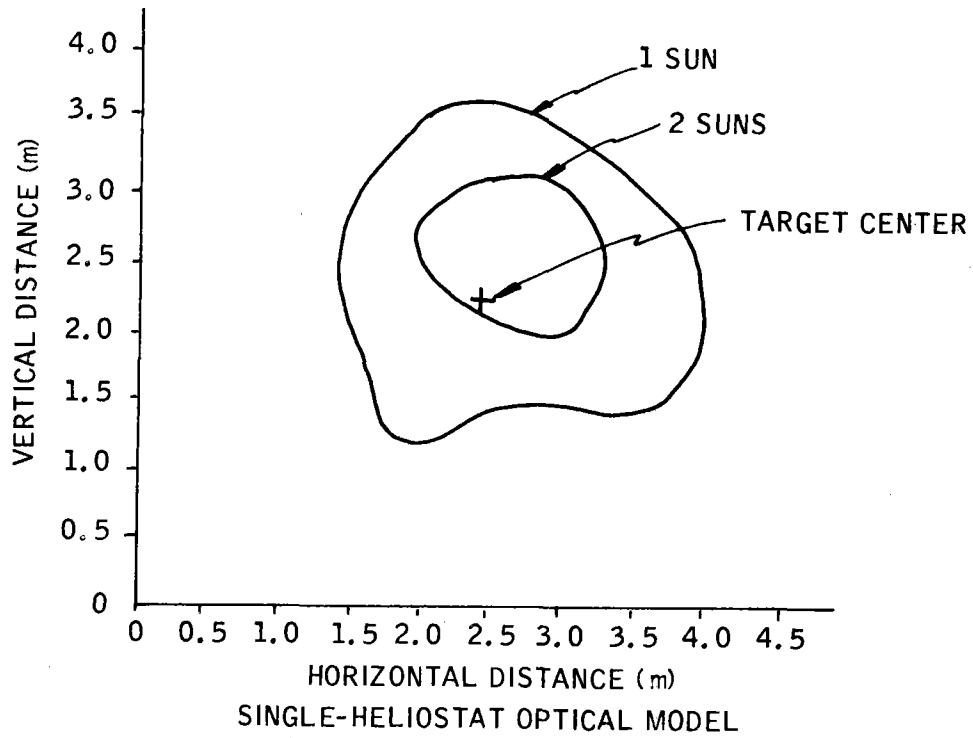
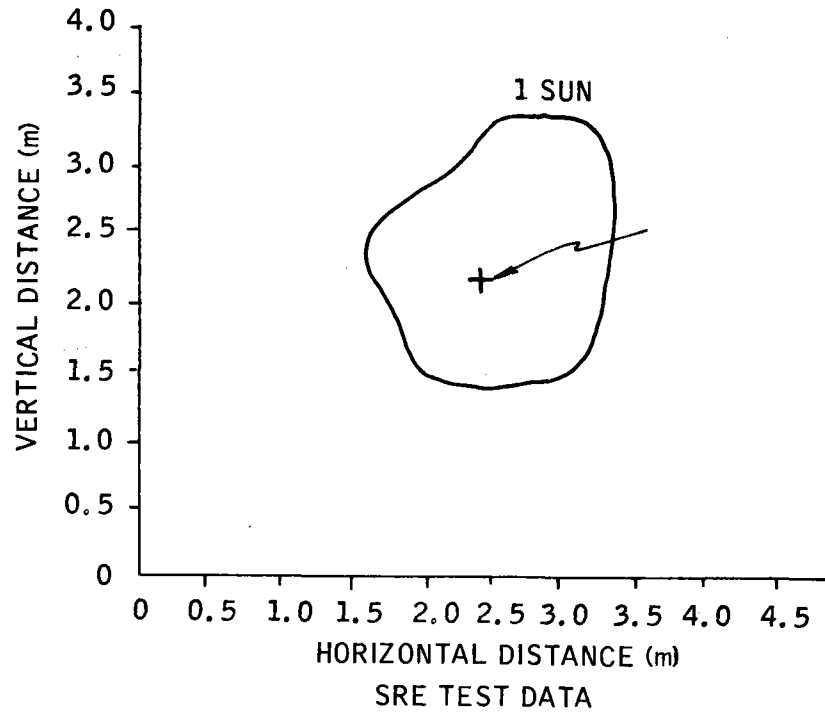


Figure 6-17. Comparison of Test Data with Optical Model - South Site

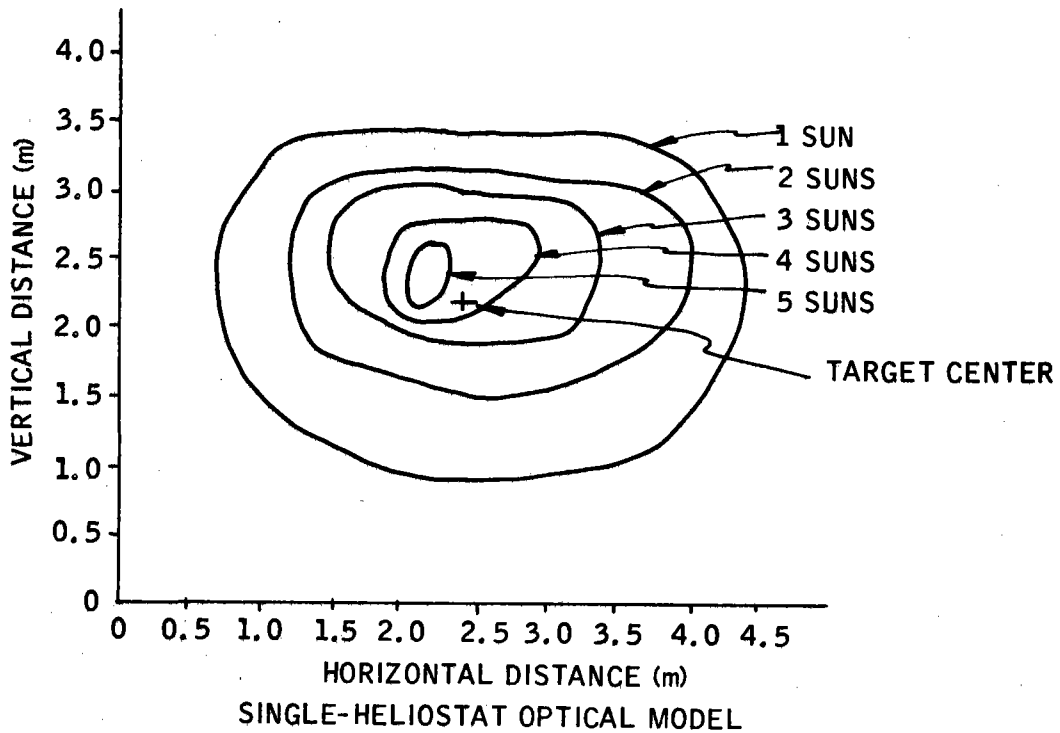
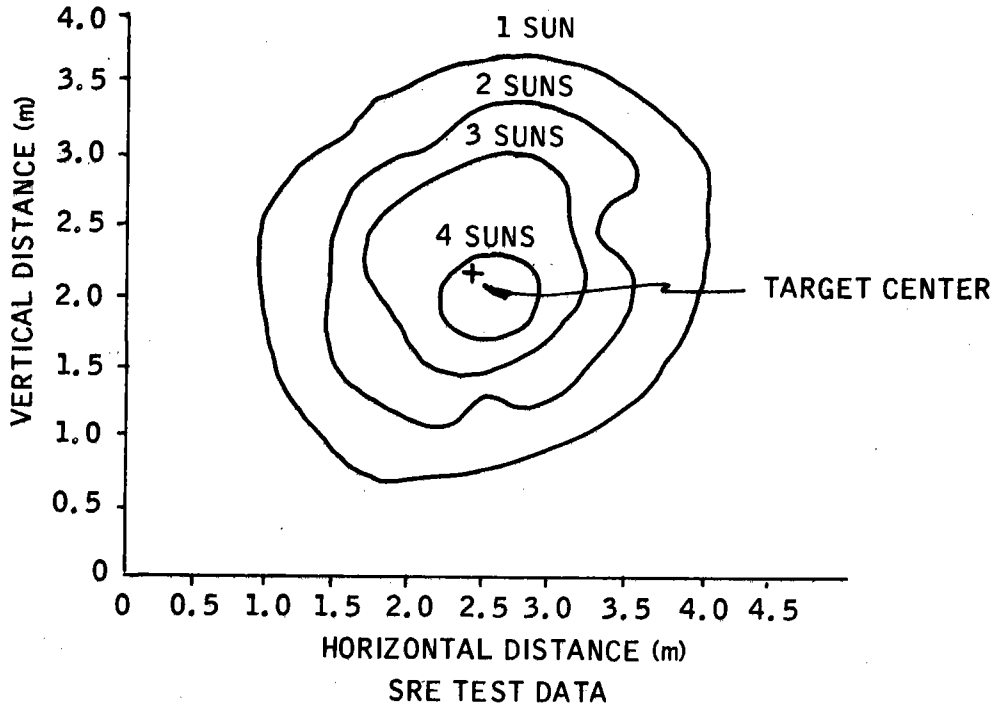


Figure 6-18. Comparison of Test Data with Optical Model - East Site

SECTION 7
ANALYTICAL MODELS

The purpose of this section is to describe the analytical techniques used in calculating the solar plant system performance. The specific models are:

- Central Receiver Optical Model
- Single-Heliostat Optical Model
- Cavity Reradiation Model
- Atmospheric Attenuation Loss Model
- Net Annual Energy Model
- Dynamic Simulation Model

The Central Receiver Optical Model and the Dynamic Simulation Model were designated contract-deliverable items. Both of these models are summarized in this section, and are documented in detail in Books 2 and 3, respectively, of Volume II.

CENTRAL RECEIVER OPTICAL MODEL

The optical model is designed to simulate the optical/thermal performance of the central receiver solar power plant. The plant modeled consists of a field of individually sun-tracking mirror units (heliostats) redirecting the sunlight into a cavity (receiver) mounted atop a tower. The basic plant configuration for this study is shown in Figure 7-1.

The heliostats are arranged in a circular field around the tower. The density of these heliostats within the field (ground cover) is varied by

7-2

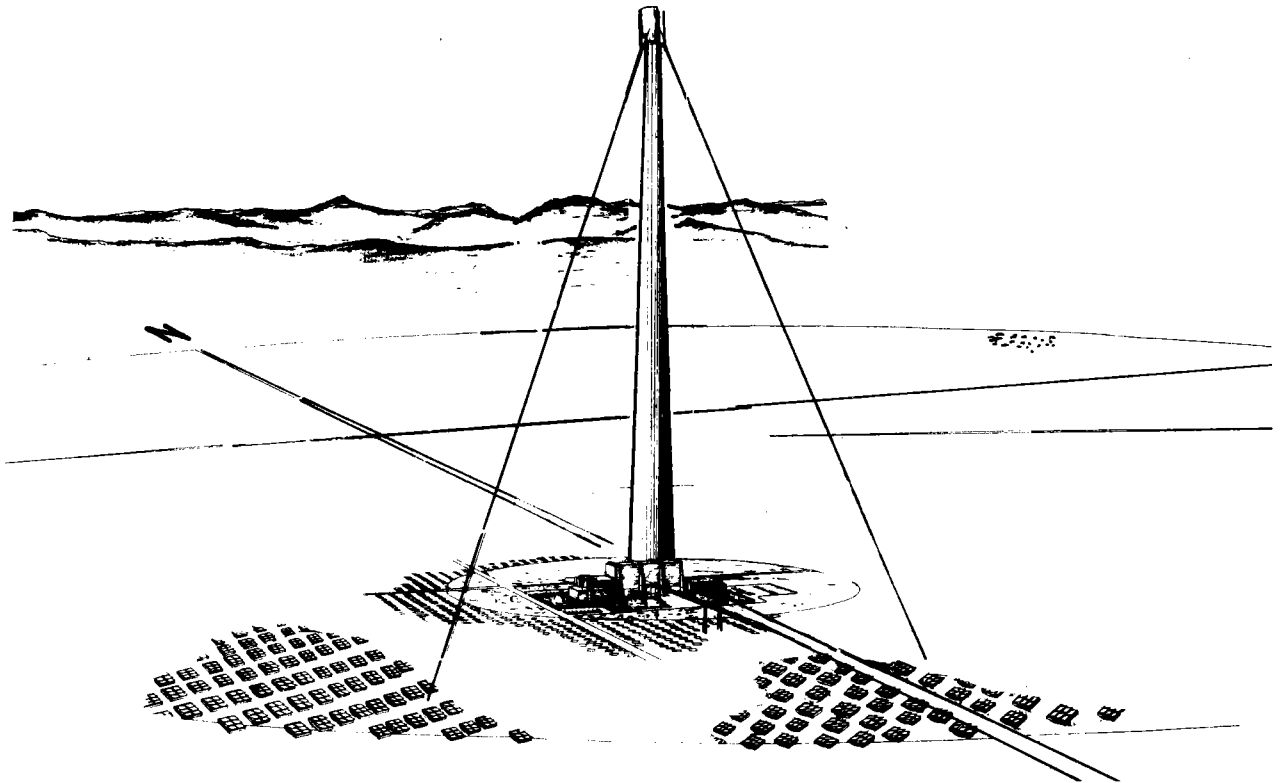


Figure 7-1. Solar Pilot Plant

changing either azimuthal and/or radial spacing. The heliostats are four-facet tilt-tilt type heliostats. Each one consists of four facets mounted between and slightly above two support "I" beams. These beams are, in turn, supported by three "I" beam cross-members. For the SRE heliostat design (Figure 7-2), this arrangement is, in turn, mounted on two pedestals attached to concrete slabs in the ground. This model does not include the pedestals as they do not affect the optical performance of the heliostat except to hold the complete assembly in position. The mirror facets are modeled as a portion of a spherical surface and can be focused at any desirable distance separately or in groups. The facets can be toed-in for any time of the year.

The receiver (Figure 7-3) is an upright circular cylindrical structure with the bottom end open and held in place on the tower by three support struc-

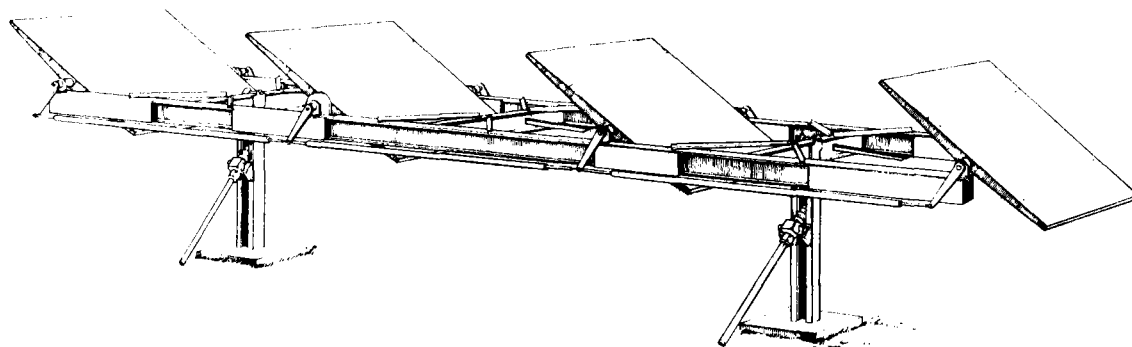


Figure 7-2. Experimental Heliostat Assembly

tures. Sunlight redirected by the heliostats enters the cavity through the receiver aperture between the supports onto the interior surface of the receiver. The tower can be located anywhere in the field within a specified circular cutout area.

The general program software and structure can be applied to a wide variety of designs. In the area of central receivers, the program has been used to model a number of receiver types, including an exposed-surface sphere, cylinder, half-cylinder, star, or cone shape. A variety of aiming strategies has been used for each of these possible configurations. In addition, a planar target has been used for the tower top aperture opening when a cavity-type receiver is used.

For the heliostat, both Az-El and tilt-tilt gimbal sequences have been modeled. A single mirror facet per heliostat or multiple mirror facets can be analyzed with either gimbal sequence. The digital computer code described in Book 2 of this volume has the tilt-tilt heliostat model which is restricted to a four-mirror facet configuration by the modeling of the frame structure.

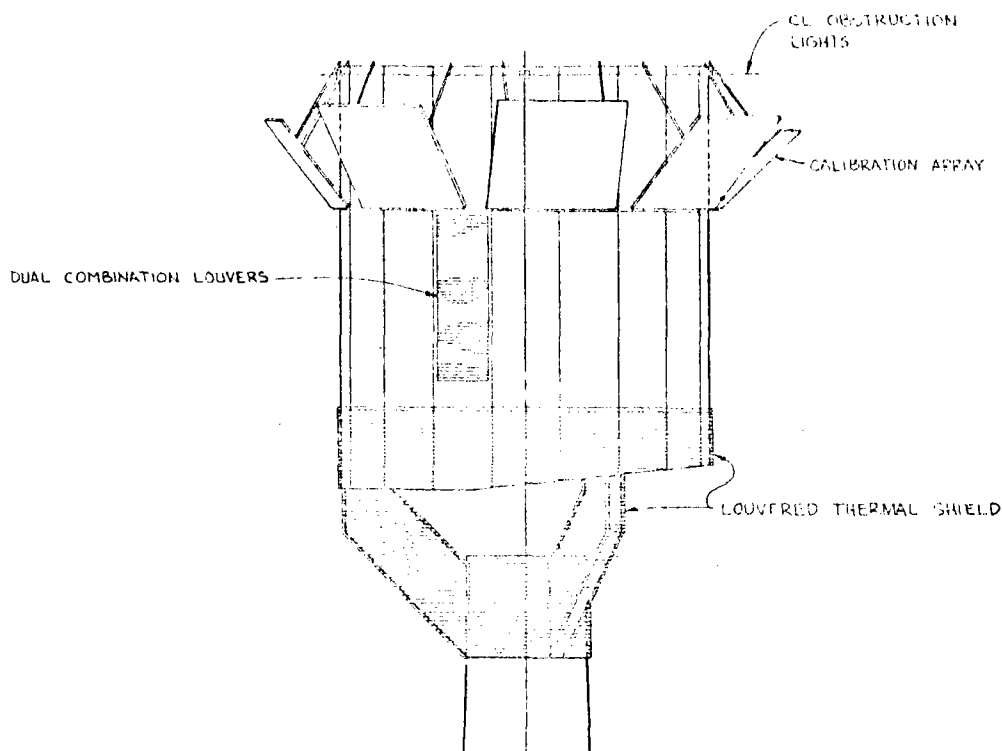


Figure 7-3. Central Receiver

If the specific frame structure were eliminated, the code could be applied to any number of mirror facets, including a single-facet design. The field layout of the heliostats has also been varied with past program versions. Rectilinear, both uniform and nonuniform, heliostat spacing has been modeled, as well as hexagon packing. The version used in the present code orients each heliostat so that the outer tracking axis is normal to a line of sight to the tower. Both uniform and nonuniform field packing densities can be analyzed with the present code.

Other code versions have included options to perform flux mapping on a cavity aperture, a variety of mirror focusing strategies, plant costing algorithms, reflectance analysis by wavelength and incidence angle, and several techniques for analyzing design change impacts on performance. The program documented in book 2 of this volume, however, is limited to the specific design described in this document.

In addition, a single-heliostat ray trace code was written. It models a single heliostat with four square mirror facets of constant focal length redirecting the sun's energy onto a test grid of any orientation. This program was intended to be used to simulate as closely as possible the Florida heliostat test setup. In this way, the optical model used in the Monte-Carlo ray trace codes can be compared with actual experimental data. The program was also used in studies of the heliostat facet toe-in strategy.

Analytic Description

The central receiver solar power plant is simulated by first describing the optical/thermal performance analytically for the redirected and absorbed solar flux.

Given a heliostat position relative to the receiver, the amount of power carried from any point on the sun's surface, monochromatically, at a given instant depends on the path of any sun ray through the system. If the sun's disk coordinates are δ_1 and δ_2 and the impact point on the heliostat is X_1 and X_2 , then the total thermal power over the entire spectrum to the heliostat is:

$$P_H = \underbrace{\int_{\lambda} \int_{x_1} \int_{x_2}}_{\text{Total Spectrum}} \underbrace{\int_{\delta_1} \int_{\delta_2}}_{\text{Sun Disk}} P_H(\lambda, x_1, x_2, \delta_1, \delta_2) d\lambda, dx_1, dx_2, d\delta_1, d\delta_2$$

Further, the redirected ray, in addition to being reflected, is subject to errors in the mirror's surface quality as well as the heliostat's two gimbaled tracking drives. Introducing those errors into the equation, the total

thermal power over the entire spectrum at an instant in time arriving at the receiver becomes:

$$P_{\text{Total}} = \int_{\theta_1} \int_{\theta_2} \int_{\phi_1} \int_{\phi_2} P_T(\theta_1, \theta_2, \phi_1, \phi_2) d\theta_1, d\theta_2, d\phi_1, d\phi_2$$

$\underbrace{\theta_1 \theta_2}_{\text{Tracking Errors}} \quad \underbrace{\phi_1 \phi_2}_{\text{Mirror Imperfections}}$

$$\int_{\lambda} \int_{x_1} \int_{x_2} \int_{\delta_1} \int_{\delta_2} P_H(\lambda, x_1, x_2, \delta_1, \delta_2) d\lambda, dx_1, dx_2, d\delta_1, d\delta_2$$

$\underbrace{\lambda}_{\text{Total Spectrum}} \quad \underbrace{x_1 x_2 \delta_1 \delta_2}_{\text{Mirror Imperfections}}$

where

θ_1, θ_2 = Uncertainties in the angular position of the two gimballed tracking drives on the heliostat

ϕ_1, ϕ_2 = Angular uncertainties in the mirror surface normal due to mirror imperfections

However, this integral does not have a unique solution. Four of the variables, tracking errors (θ_1, θ_2) and mirror imperfections (ϕ_1, ϕ_2), can be known only statistically. For example, a given error in the mirror normal is equally likely to occur anywhere on the mirror surface. The mirror is not known as a continuous surface with smooth waves or ripples but rather as a probability distribution of mirror normals perturbed from the mathematically correct shape by an assumed probability distribution. This reasoning applies also to the gimballed tracking drives. The mirror surface errors will tend to diffuse the light and the tracking drive errors will tend

to misdirect the light. These errors are assumed to be statistically independent of each other or any other design parameter and normally distributed.

Thus, the integral equation is solved by using a Monte-Carlo technique. The simplest Monte-Carlo approach is to observe random numbers, selected in such a way that they directly simulate the physical random processes of the problem at hand, and to deduce the required solution from the behavior of these numbers. For this application, that process involves the ratio of the incident flux on the receiver and the direct solar flux on the heliostat field being equal to the convergent ratio of randomly drawn rays which reach the receiver divided by the total number of rays drawn uniformly over the heliostat field. Appropriate scaling of each ray value for reflectance and absorption losses, tracking and reflective surface anomalies, etc., is included in the Monte-Carlo simulation.

Methodology

The simulation is done by randomly selecting a sufficient number of sun rays to statistically represent the sun's intensity pattern as seen from the earth's surface. Solar limb darkening and atmospheric attenuation losses are accounted for. These same rays are allowed to impinge on the entire heliostat field randomly and are reflected, taking into account minor surface imperfections and heliostat tracking errors, to the receiver if they should strike a properly aligned reflecting surface. The rays drawn must represent the sun's power at that time; thus, each ray is given a relative weighted value as a function of the time and the number of rays drawn. If annual energy is being calculated, then each ray carries the appropriate amount of energy.

Vector analysis is used to trace the rays to avoid complicated coordinate transformations as well as complex trigonometric equations. Vector

analysis requires only one base set of axes. All vector equations are then related to the base axes with vector algebra.

The basic reference vectors in the ray trace code describe local vertical, local north, and local east. Each of these vectors is a unit vector and the set is an orthonormal triad which can be thought of as originating at the tower center. Variations in the direction of these vectors with respect to position on the field are not considered. Thus, the heliostat field is assumed to be a flat plane tangent to the surface of the earth at the tower base.

The sun vector is simply a unit vector along the ray path from the sun's center to the point on the earth's surface at which the tower is located. This sun vector is considered to be the same over the entire plane of the heliostat field. This introduces an error of less than 1 minute of arc per mile of distance from the tower base.

Simplistically, the ray trace methodology is as follows:

- 1) Randomly select an X, Y coordinate position on the field to determine where a sun ray hits.
- 2) Randomly select over the sun's disk whence the ray came and introduce solar limb darkening.
- 3) Randomly determine the amount mirror surface error and tracking error to be introduced into the reflected ray.
- 4) Determine whether that ray enters the receiver cavity.
- 5) Draw as many rays as necessary to obtain accurate results.

A complete description of the basic formulation, methodology, program listing, and sample input/output is given in book 2 of this volume. The basic program flow is described by the chart of Figure 7-4.

Input/Output

The ray trace code requires the following input:

- Field Specification:
 - Outer field radius
 - Inner field radius
 - Ground cover (uniform or nonuniform)

- Heliostat Specification:
 - Facet dimensions
 - Frame dimensions
 - Tracking error statistics
 - Optical error statistics
 - Focusing strategy
 - Toe-in strategy

- Receiver Specification:
 - Tower height
 - Tower location
 - Support size
 - Support location
 - Aperture size and shape
 - Aim height
 - Cavity dimensions

In addition, the user must specify whether a time point or annual energy simulation is requested.

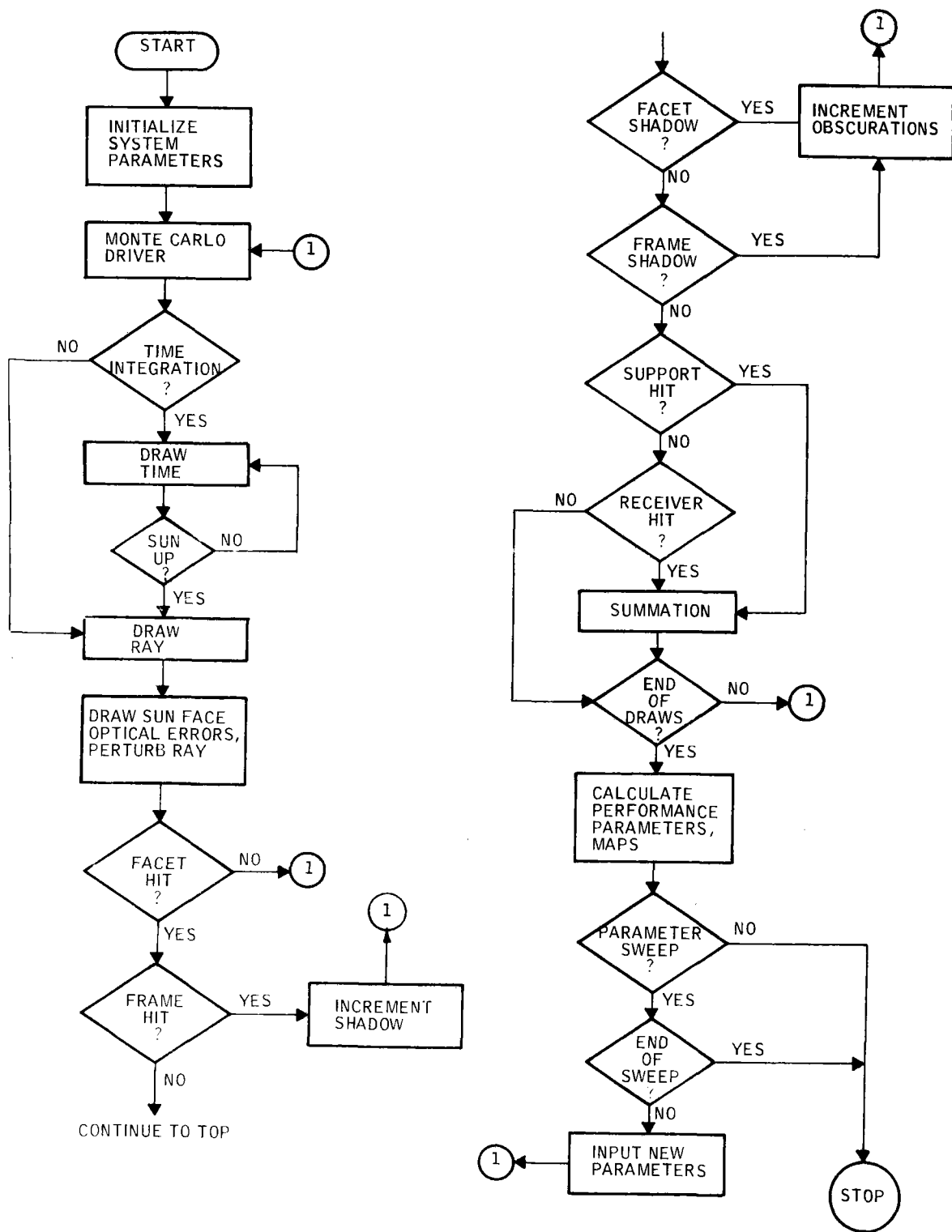


Figure 7-4. Ray Trace Flow Chart

The basic Monte-Carlo output parameters are:

- Of the total rays-drawn, they are divided as follows:
 - Rays drawn before sunrise
 - Rays drawn when the sun was too low on horizon
 - Rays drawn that hit the open field
 - Rays which hit mirror, but were lost in space
 - Rays drawn that were blocked in onblocks
 - Rays that were obscured in offblock
 - Rays which hit walls of the cavity
 - Rays which hit roof of the cavity
 - Rays which missed high
 - Rays which missed across the front
 - Rays which missed low
 - Rays which hit supports
 - Rays which were in the tower shadow
 - Rays which whistled-through the aperture
 - Rays which frame shadowed on same heliostat
 - Rays which frame shadowed on adjacent heliostat
 - Rays which frame blocked on same heliostat
 - Rays which frame blocked on adjacent heliostat

- Power or energy values calculated are:
 - Total available
 - Total on mirrors
 - Total lost in tower shadow
 - Total lost in mirror shadows
 - Total leaving mirrors
 - Total lost to blockage
 - Total on cavity supports
 - Total which whistled through
 - Total which missed aperture

- Flux maps calculated are:
 - Flux on cavity walls
 - Flux on cavity ceiling
 - Redirected flux from field cells
 - Shadow losses in field cells
 - Blockage losses in field cells
 - Aperture misses from field cells
 - Whistles-through from field cells
 - Support hits from field cells

In addition, the distribution of redirected energy over the year is output for annual energy runs.

SINGLE-HELIOSTAT OPTICAL MODEL

The physical layout used for this program model is shown in Figure 7-5. It consists of the sun, a heliostat, and a target array. The sun is represented as a circular disk with limb darkening. The heliostat consists of four mirror facets mounted on an I-beam frame and are gang-driven. The target is a plane of any rectangular shape. Using this model, the solar power reflected from the heliostat to the target array is calculated for a given sun position.

The program uses Monte-Carlo techniques and ray tracing to accomplish this. The optical paths of thousands of individual but randomly selected sun rays are followed through the optical path. Enough rays are drawn to statistically represent the solar intensity which is reflected from the heliostat. This reflected power is directed to the target array and is mapped over the surface to obtain power flux maps.

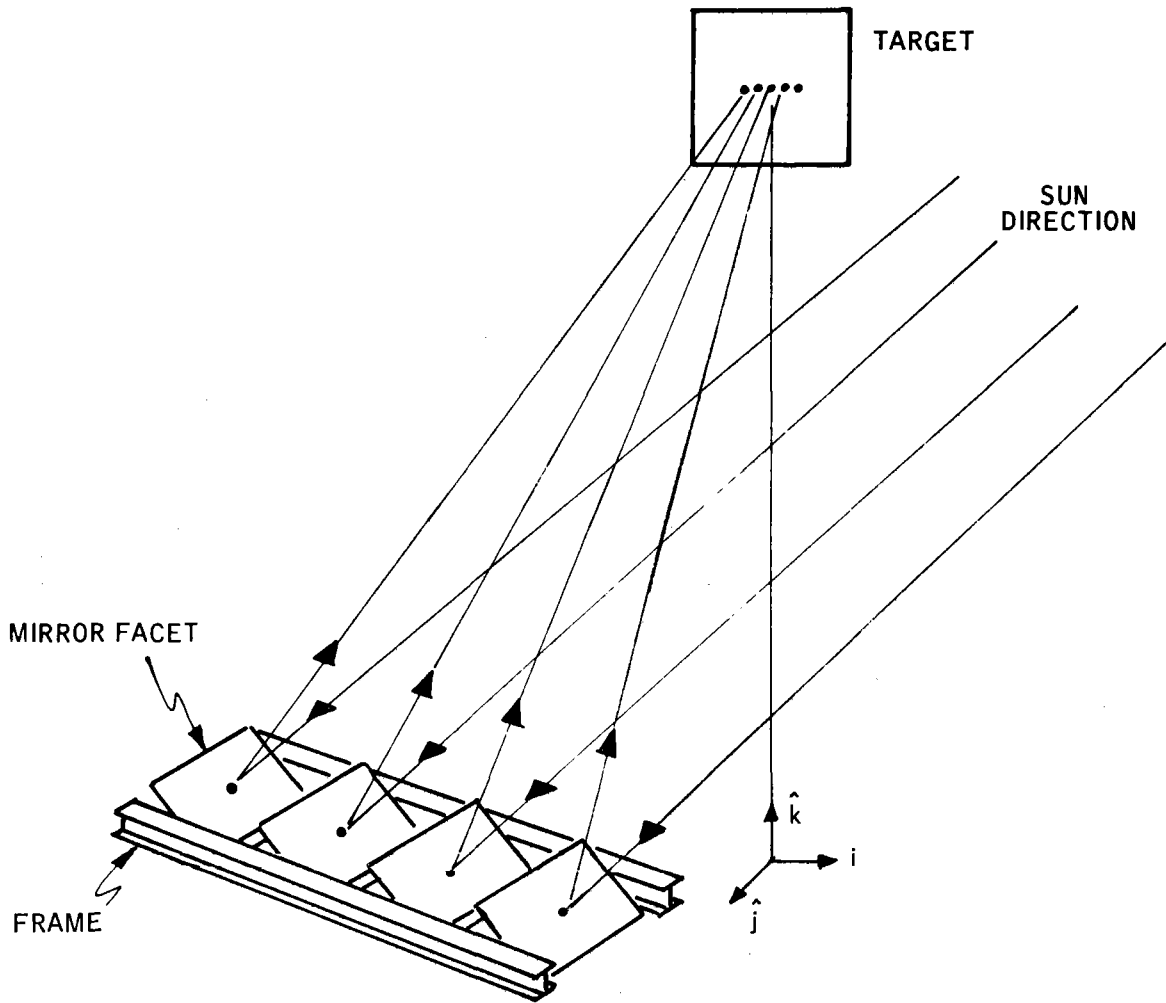


Figure 7-5. Single-Heliostat Model

A basic unit vector triad (local vertical, local east, and local north) is defined. All vector quantities associated with the model are then written in terms of this triad.

What needs to be done to simulate the amount of power reflected onto the target array for a given point in time is to properly align the heliostat and toe-in each facet to focus the reflected power in the right direction. In the process, the limb darkening of the solar surface and the heliostat facet (mirror) surface errors are accounted for. A sufficient number of rays are randomly selected to statistically represent the sun's intensity pattern at the time point chosen. The same rays are allowed to impinge on the heliostat facets randomly and be reflected to the target. The more rays drawn, the more accurate the calculation will be. Each heliostat facet is treated separately and a flux map can be obtained from each one. To do this, several vectors must be determined in terms of the invariant base triad (\hat{i} , \hat{j} , \hat{k}) shown in Figure 7-6. The positions of the sun, heliostat, and target shown in the figure were chosen to make the trigonometry as simple as possible.

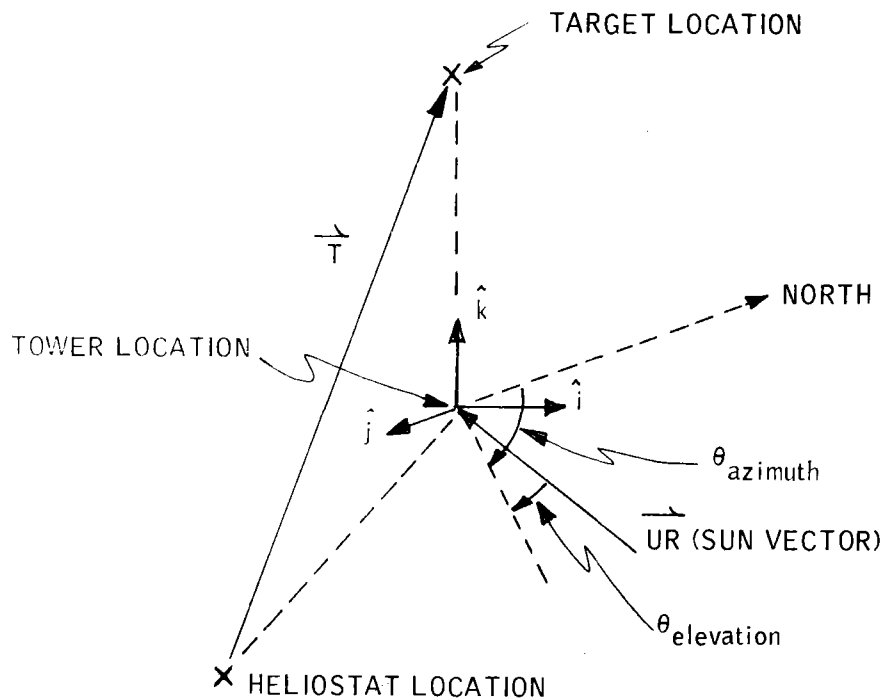


Figure 7-6. Basic Vector Triad (\hat{i} , \hat{j} , \hat{k} with Respect to Tower and Heliostat)

The program is based on the following assumptions:

- Heliostat alignment and toe-in are based on the heliostat center, sun center, and target center.
- Facets are portions of spherical surfaces with constant focal lengths.
- Toe-in is accomplished independent of the time point chosen.
- The target is a plane and can be of any orientation.

Following is a derivation of the primary vector equations used in the program. These equations are used in the calculations indicated by the program flow chart in Figure 7-7.

From Figure 7-6, the sun unit vector (\vec{UR}) and heliostat center-to-target center vector (\vec{T}) can be written as follows:

$$\vec{UR} = (\cos \theta_{az} \hat{j} - \sin \theta_{ay} \hat{i}) \cos \theta_{el} - \sin \theta_{el} \hat{k}$$

and

$$\vec{T} = R_{helio} \sin (\theta_{helio}) \hat{i} + R_{helio} \cos (\theta_{helio}) \hat{j} - H_{target} \hat{k}$$

where:

$(\hat{i}, \hat{j}, \hat{k})$ = Basic unit vector orthonormal triad

θ_{az} = Sun azimuth from north

θ_{el} = Sun elevation from horizontal

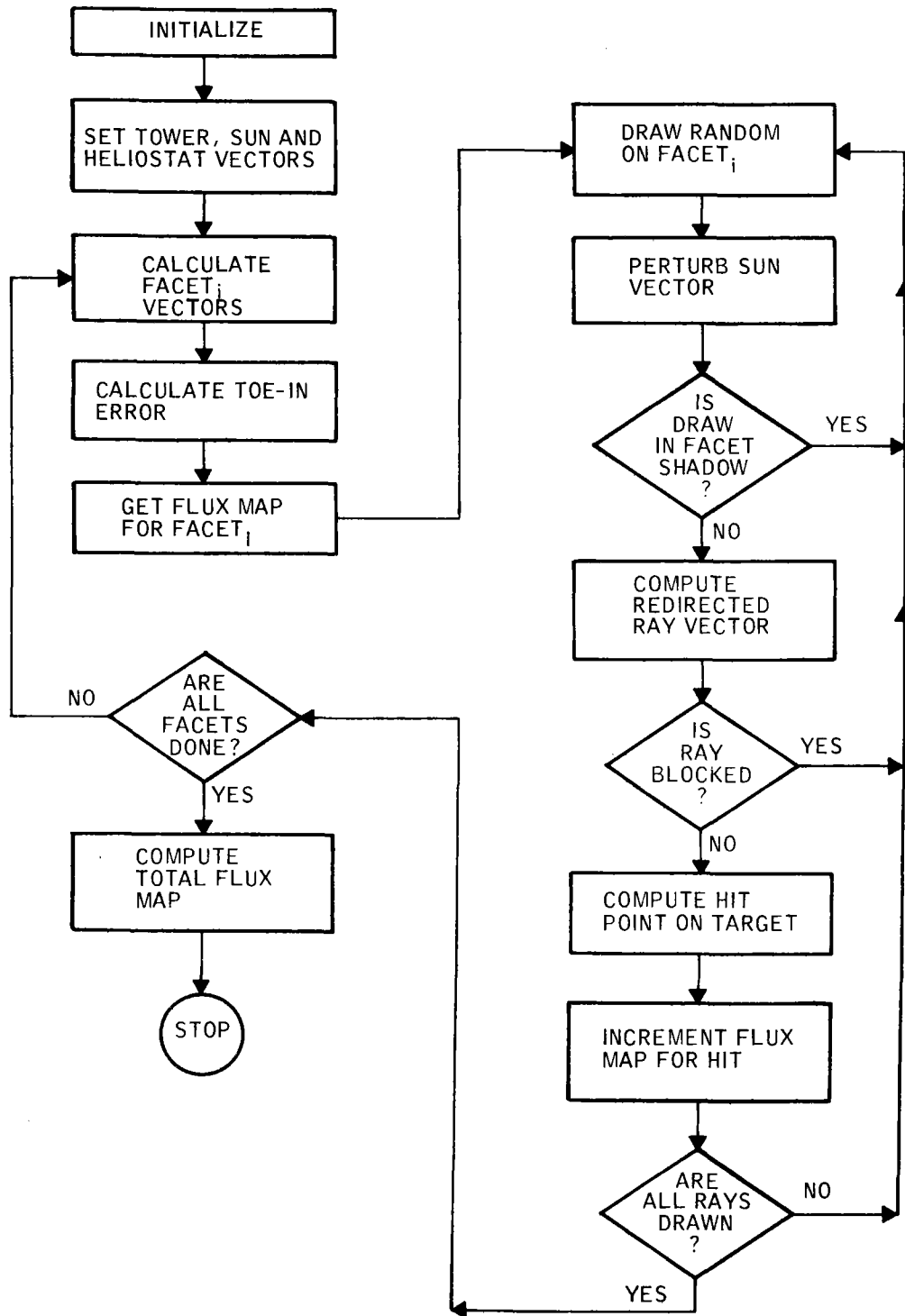


Figure 7-7. Single-Heliostat Model Program Flow Chart

R_{helio} = Horizontal distance from heliostat to target

θ_{helio} = Heliostat azimuth from north

H_{target} = Target height above ground

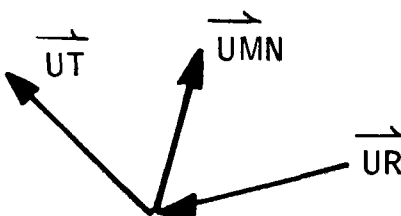
The absolute value of \vec{T} is:

$$|\vec{T}| = \sqrt{R_{\text{helio}}^2 + H_{\text{helio}}^2}$$

and thus the unit vector along \vec{T} is:

$$\vec{UT} = \vec{T} / |\vec{T}|$$

Constructing the following vector diagram, the heliostat nominal unit mirror normal is determined:



$$\vec{UMN} = (\vec{UT} - \vec{UR}) / |\vec{UT} - \vec{UR}|$$

The nominal mirror normal is assumed to be effective at the heliostat center. The mirror normal at any location on any facet i can be constructed using the nominal mirror normal.

To accomplish this, the heliostat position is specified by two vector triads as shown in Figure 7-8. The derivation of these vectors is identical to that

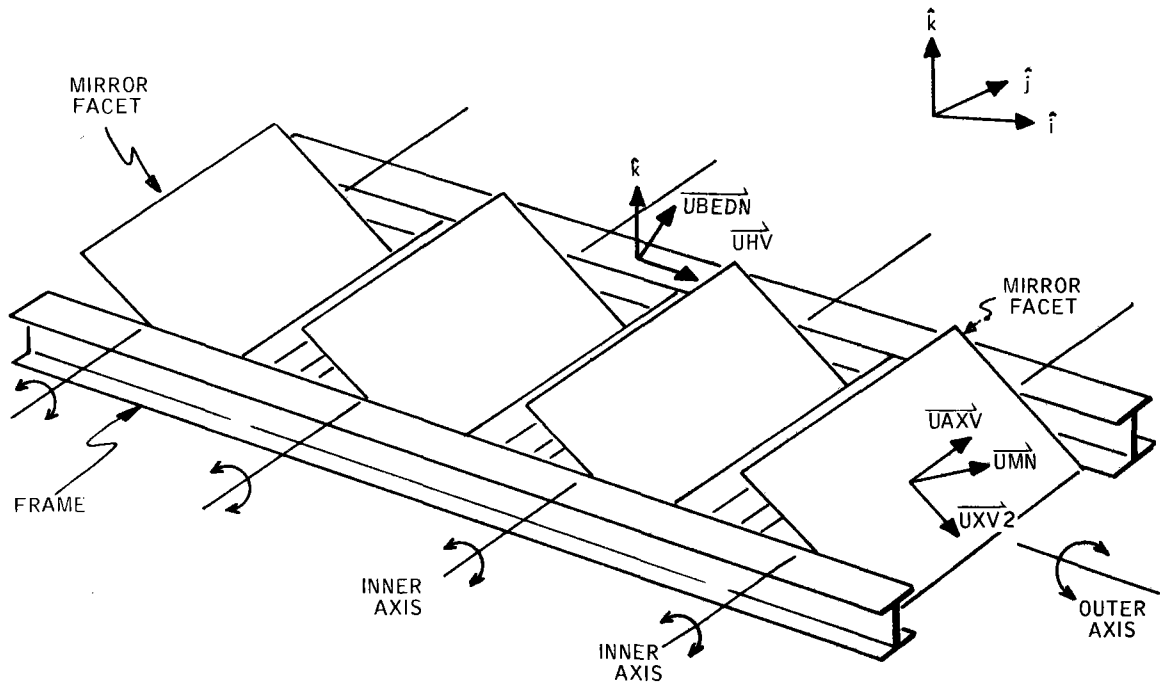


Figure 7-8. Heliostat Vector Triads

used in the full-field ray trace code. A detailed description of this derivation is contained in Book 2 of this volume.

Recall that the derived \vec{UMN} vector is the nominal mirror normal at the optical axis of the heliostat. In other words, it describes the position of an imaginary mirror facet located at the heliostat geometric center. The actual normal for any one of the individual heliostat facets differs slightly from this normal in that each facet may be toed-in, or canted slightly toward the heliostat center to improve the total heliostat focusing ability. A possible toe-in alignment is shown for a side view in Figure 7-9. The program may develop a toe-in angle, θ_t , for each facet of each heliostat in the field (subroutine TOEIN). The toe-in angle is specified by a reference sun position for which all mirror facets in the field are aligned to redirect incoming rays as nearly as possible to a single focal point. Given

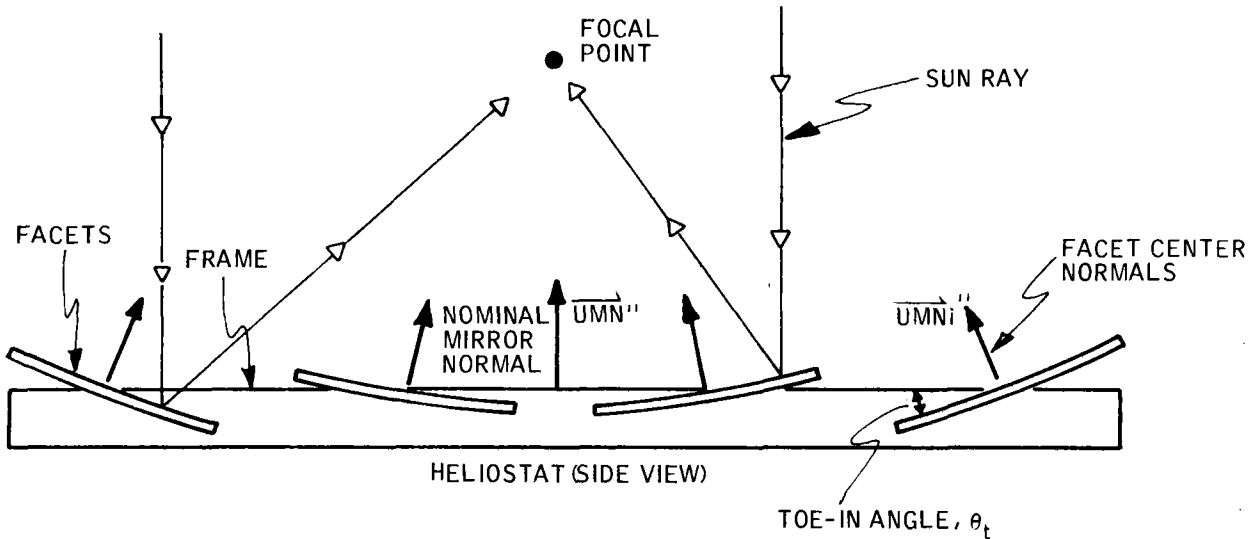


Figure 7-9. Toe-In Strategy

the toe-in angle for a specific mirror facet, the facet center normal and tangent vectors are constructed by:

$$\overrightarrow{UMN}_i = \cos \theta_t \overrightarrow{UMN} + \sin \theta_t \overrightarrow{UXV2}$$

$$\overrightarrow{UXV2}_i = \cos \theta_t \overrightarrow{UXV2} - \sin \theta_t \overrightarrow{UMN}$$

This represents a simple rotation of the mirror facet orientation vectors about the inner axis.

The mirror normal at the hitpoint on the facet surface is found from knowledge of the facet shape. For the baseline tilt-tilt heliostat, each facet has a spherical surface which focuses at a distance F_s . The facet surface and required vectors are shown in Figure 7-10. The vector from the facet center to the hitpoint, \overrightarrow{RHS} , is determined by a random draw over the surface of the mirror. By ignoring the small displacement between the hitpoint indicated by \overrightarrow{RHS} and the actual mirror surface location, the mirror normal at the hitpoint (\overrightarrow{UNN}) can be found by:

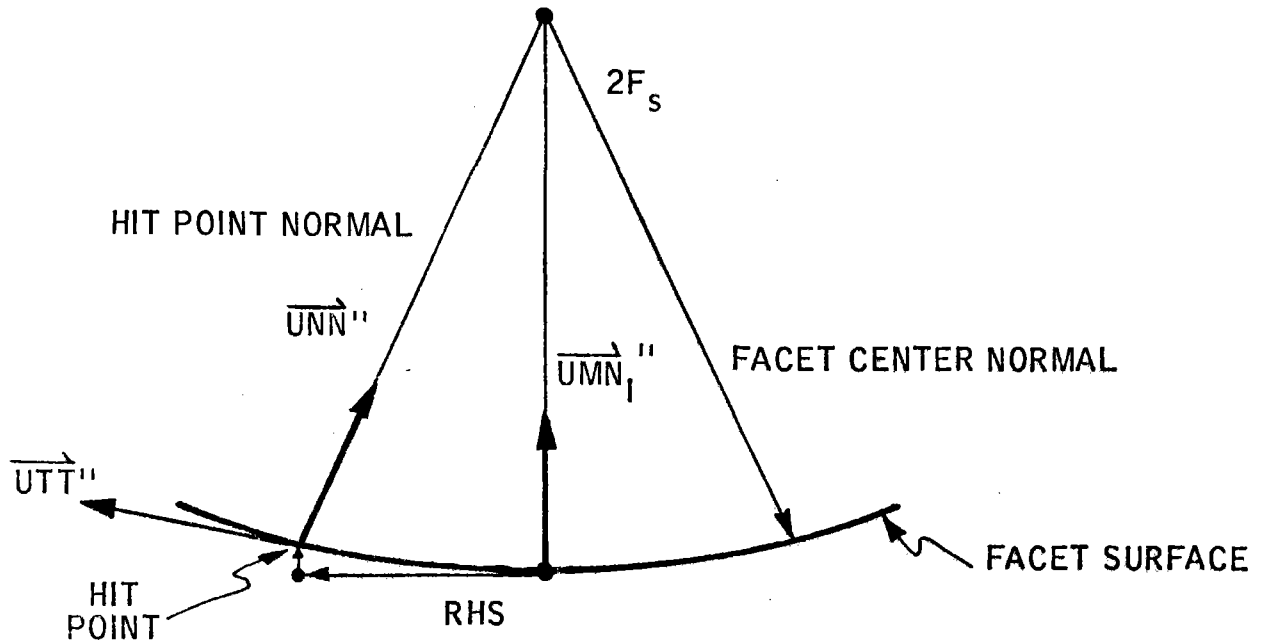


Figure 7-10. Facet Surface Vectors

$$\overrightarrow{UNN} = (-\overrightarrow{RHS} + 2F_s \overrightarrow{UMN}_i) / (\overrightarrow{RHS} + 2F_s \overrightarrow{UMN}_i)$$

Neglecting the small displacement can be thought of as modeling the facet surface as a fresnel mirror so that each element in the mirror is approximately in a single plane normal to the nominal mirror normal.

A local tangent vector is constructed as follows:

$$\overrightarrow{TT} = \overrightarrow{RHS} - (\overrightarrow{RHS} \cdot \overrightarrow{UNN}) \overrightarrow{UNN}$$

and a unit vector tangent to the mirror surface at the hitpoint is:

$$\overrightarrow{UTT} = \overrightarrow{TT} / |\overrightarrow{TT}|$$

To complete a triad at the hitpoint, a second tangent vector is found by:

$$\vec{UT2} = \vec{UTT} \times \vec{UNN}$$

The final perturbation of the heliostat mirror normal is the angular rotation which represents mirror surface irregularity. The sketch of this perturbation is shown in Figure 7-11. The final, fully perturbed mirror normal vector is called \vec{UNNP} and is given by:

$$\vec{UNNP} = \cos\delta_1 \vec{UNN} + \sin\delta_1 (\cos\delta_2 \vec{UTT} + \sin\delta_2 \vec{UT2})$$

where δ_2 is drawn uniformly from 0 to 360 degrees and δ_1 is drawn with a normal distribution having a specified mean and variance. Physically, what this last perturbation means is that the mirror surface normal is locally out of alignment with the average normal by an amount δ_1 . The plane in which the δ_1 rotation occurs is equally likely to occur in any

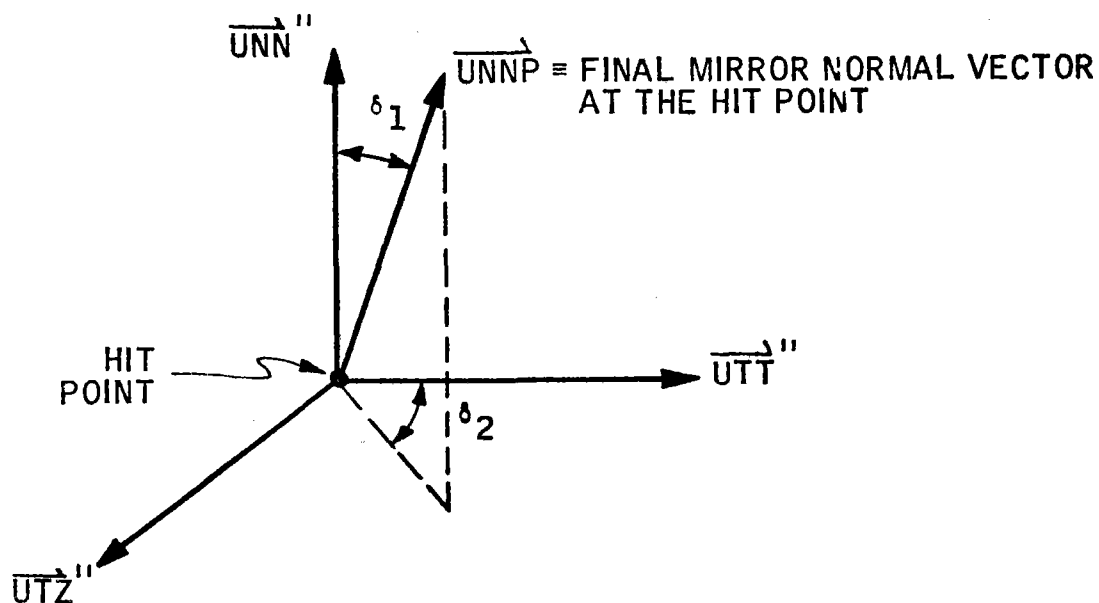


Figure 7-11. Final mirror Normal Perturbation

direction around the local azimuth. Before constructing the reflected ray vector, the sun vector is perturbed for sun limb darkening. This is explained in Book 2 of this volume. The perturbed sun ray is called \overrightarrow{URP} .

The reflected ray vector can now be calculated from the mirror normal \overrightarrow{UNNP} and the sun vector \overrightarrow{URP} . The vector algebra simply obeys Snell's Law and the reflected ray unit vector $\overrightarrow{US1}$ is:

$$\overrightarrow{US1} = -2 (\overrightarrow{URP} \cdot \overrightarrow{UNNP}) \overrightarrow{UNNP} + \overrightarrow{URP}$$

Thus, the $\overrightarrow{US1}$ vector represents a ray path which includes the effects of a finite sun size, a facet toe-in strategy, and mirror surface imperfections.

The target triad is determined from Figure 7-12. A unit vector in vertical

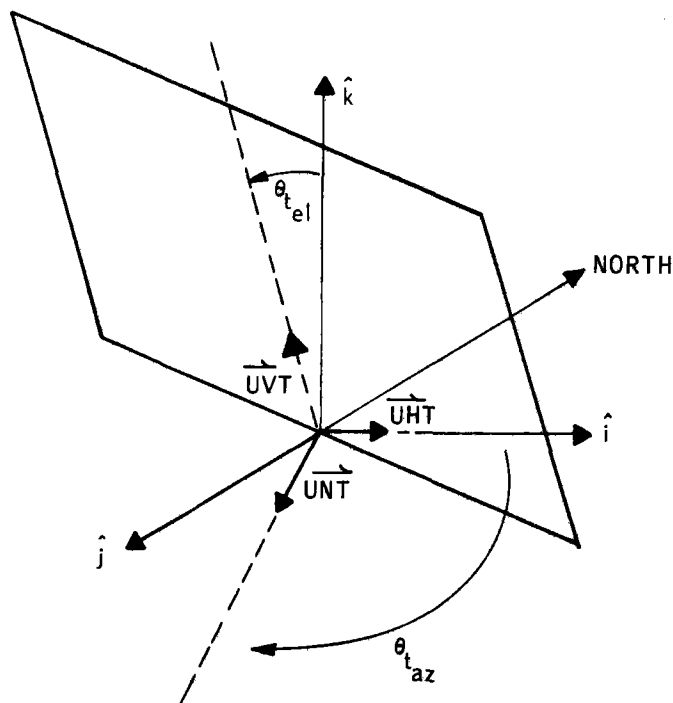


Figure 7-12. Target Triad Definition

direction is:

$$\overrightarrow{UVT} = \cos(\theta_{t_{el}}) \hat{k} + \sin(\theta_{t_{el}}) [-\cos(\theta_{t_{az}}) \hat{j} + \sin(\theta_{t_{az}}) \hat{i}]$$

A unit vector in horizontal direction is:

$$\overrightarrow{UHT} = -\sin(\theta_{t_{az}}) \hat{j} - \cos(\theta_{t_{az}}) \hat{i}$$

and a unit vector normal to target is simply:

$$\overrightarrow{UNT} = -(\overrightarrow{UHT} \times \overrightarrow{UVT})$$

where

$\theta_{t_{el}}$ = Elevation of \overrightarrow{UNT} from horizontal

$\theta_{t_{az}}$ = Azimuth of \overrightarrow{UNT} from north

With the previous information, the x, y coordinate of the ray hit on the target can be calculated. Refer to Figure 7-13; the vector from heliostat center to facet_i center, is:

$$\overrightarrow{XF}_i = [XDF (IFV_i - 1) - ALEN] [\sin(\theta_{helio}) \hat{j} + \cos(\theta_{helio}) \hat{i}]$$

where

XDF = Distance between facet centers

IFV = Facet number

ALEN = Heliostat length

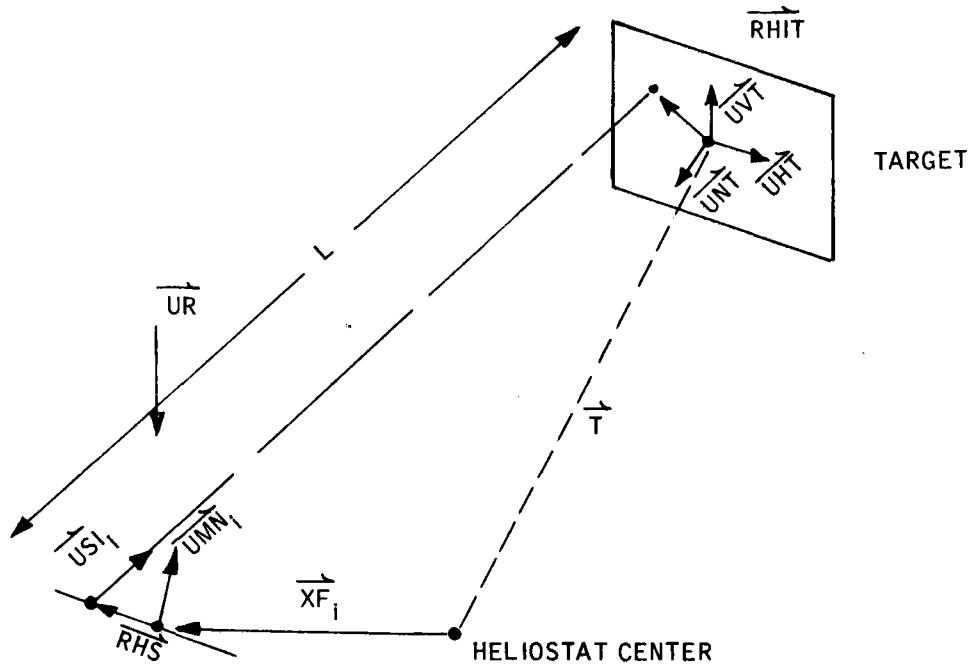


Figure 7-13. Vectors Necessary to Determine Target Hitpoint

Now, the target hit vector is obtained by vector algebra:

$$\vec{R}_{hit} = -\vec{T} + \vec{SF}_i + \vec{RHS} + L \vec{US}_1$$

where

\vec{RHS} = Facet center to ray hit on facet

\vec{US}_1 = Reflected ray unit vector

L = Distance from facet center to target center

and L is determined from the following vector identity:

$$(\vec{T} - \vec{XF} - \vec{RHS}) \cdot \vec{UN}_1 = L \vec{US}_{1_i} \cdot \vec{UN}_1$$

Then the target hitpoint coordinates are found by:

$$Y = \overrightarrow{R}_{hit} \cdot \overrightarrow{UHT}$$

$$Y = \overrightarrow{R}_{hit} \cdot \overrightarrow{UVT}$$

To obtain a flux map, several thousand rays are drawn over each facet. The X and Y coordinates of the hitpoint are used to store the power associated with each ray drawn into appropriate zones on the target. The power into each zone, and consequently the flux on each zone, are outputs of the code.

CAVITY RERADIATION MODEL

The reradiation heat-transfer computations for the pilot plant, commercial plant, and SRE are calculated by dividing the cavity surfaces into a number of constant-temperature nodes. The process can be divided into two separate parts: the calculation of the view factors between the nodes, and the calculation of the heat transfer between the nodes once the view factors are known.

The basic heat transfer analysis is identical for all cavity reradiation calculations. However, the view factor analysis has been done in two ways for the actual plant cavity. We refer to the different view factor calculations as a detailed model and a rubber model. The detailed code is a general canned program which can handle non-axisymmetric nodes within the cavity whereas the rubber model uses axisymmetric cavity nodes. The rubber model is so named because it is relatively inexpensive to run and can calculate view factors for any perturbation of cavity diameter or height.

The view factors for the SRE cavity are calculated as a separate subroutine because of the SRE test setup. In this case, a lamp source is located in the cavity interior. This requires that view factors be modified to account for the energy interaction between the lamp and the cavity walls.

The basic reradiation program uses the view factors to calculate the radiation interchange between all of the nodes inside the cavity wall, the conductive interchange between the metal surface nodes and the fluid nodes, and the conductive interchange between the fluid nodes and some of the metal nodes and the environment. An iterative procedure is used to calculate the temperatures of the metal node so that the net flux to all of the metal surface nodes is zero.

Figure 7-14 is a schematic diagram of the cavity showing the nodal arrangement for the rubber model software. All of the nodes shown are axisymmetric nodes (i. e., they extend in a ring around the cavity wall). Nodes on the inside of the cavity wall are metal surface nodes -- nodes shown on the outside of the cavity wall are fluid surface nodes. Node 20 represents the environment.

Cavity Heat-Transfer Analysis

The heat-transfer analysis is based on dividing the calculations into two regions: a solar region in which solar radiation properties apply, and an IR region in which IR radiation properties apply. The net flux on each cavity surface from the redirected solar power is calculated first, and then the different metal temperatures are calculated by an iterative procedure to give zero net heat flux on all of the metal nodes. The methodology of the solution is outlined below.

Given an enclosure totally defined by N surfaces, we can write a radiosity balance on each of the nodes as:

$$R(I) = D(I) + \rho(I) [F(I,1)R(1) + F(I,2)R(2) + \dots + F(I,N)R(N)] \quad (7-1)$$

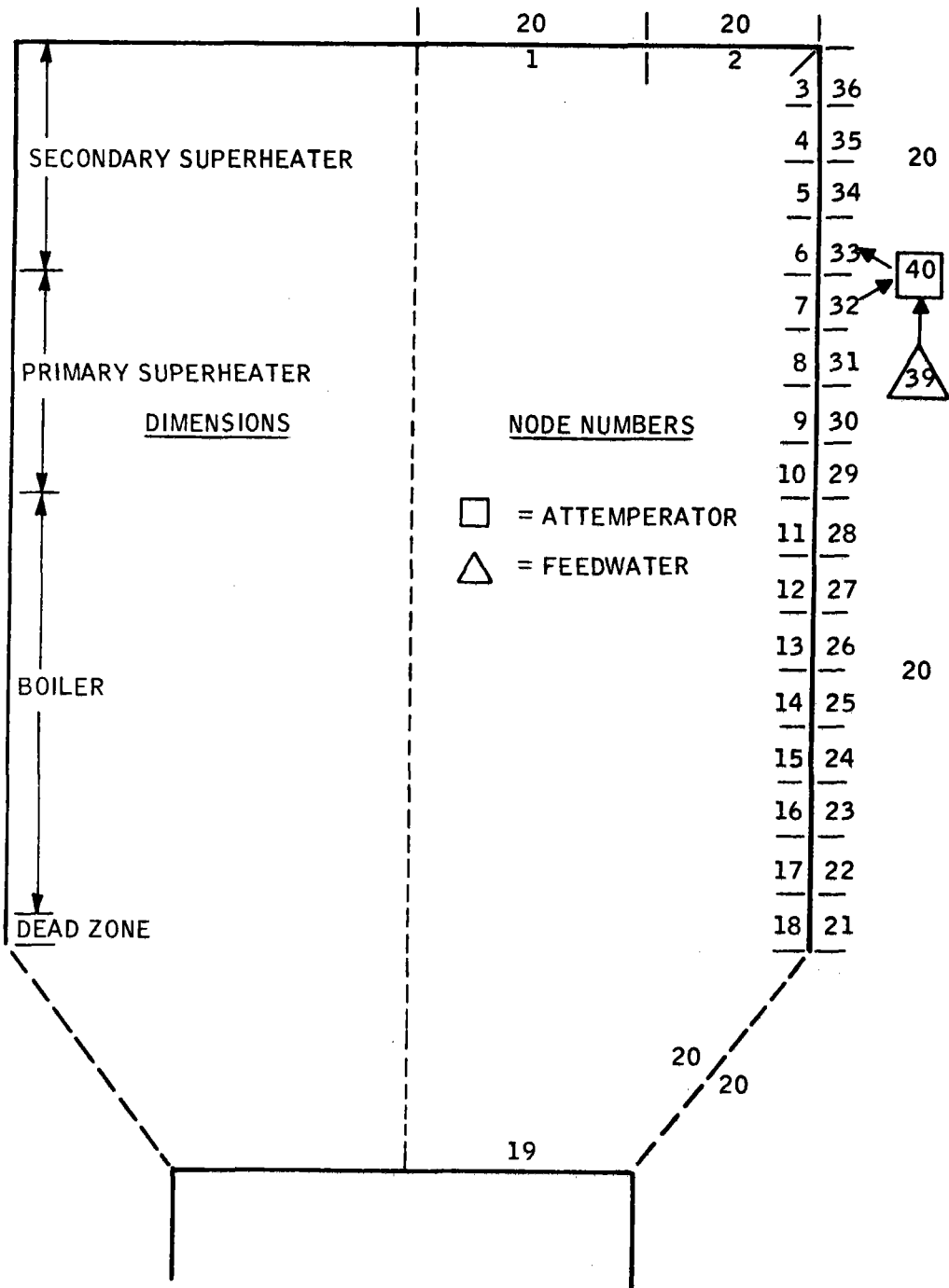


Figure 7-14. Rerad Model Node Numbering

where

$R(I)$ = Radiosity or flux density streaming from $A(I)$ into the enclosure

$D(I)$ = Flux density entering the system at surface $A(I)$ - equal to $EIR(I) + \rho T^4(I)$ for thermal excitation

$\rho(I)$ = Reflectivity of surface $A(I)$ equal to $[1 - EIR(I)]$ or $[1 - ESOL(I)]$

$F(I, N)$ = View factors between two surfaces

This equation can be written as a set of N equations in the N unknowns as follows:

$$\begin{bmatrix} [1-\rho(1)]F(1,1) & -\rho(1)F(1,2) & \dots & -\rho(1)F(1,N) \\ -\rho(2)F(2,1) & [1-\rho(2)]F(2,2) & \dots & -\rho(2)F(2,N) \\ \cdot & \cdot & \cdot & \cdot \\ \cdot & \cdot & \cdot & \cdot \\ -\rho(N)F(N,1) & -\rho(N)F(N,2) & \dots & [1-\rho(N)]F(N,N) \end{bmatrix} \cdot \begin{bmatrix} R(1) \\ R(2) \\ \cdot \\ \cdot \\ \cdot \end{bmatrix} = \begin{bmatrix} D(1) \\ D(2) \\ \cdot \\ \cdot \\ \cdot \end{bmatrix} \quad (7-2)$$

Transfer Matrice
Response Vector
Excitation Vector

Equation 7-2 may be multiplied by the inverse of the transfer matrice to produce:

$$\begin{bmatrix} R(1) \\ R(2) \\ \cdot \\ \cdot \\ \cdot \\ R(N) \end{bmatrix} = \begin{bmatrix} B(1,1)B(1,2) \dots B(1,N) \\ B(2,1)B(2,2) \dots B(2,N) \\ \cdot \\ \cdot \\ \cdot \\ B(N,1)B(N,2) \dots B(N,N) \end{bmatrix} \cdot \begin{bmatrix} D(1) \\ D(2) \\ \cdot \\ \cdot \\ \cdot \\ D(N) \end{bmatrix} \quad (7-3)$$

Response Vector
Inverse of the Transfer Matrice
Excitation Vector

A heat balance at every node area $A(I)$ can be written as:

$$\frac{QS(I, \text{net})}{A(I)} = \left[\begin{array}{l} \text{Total flux density} \\ \text{streaming from } A(I) \end{array} \right] - \left[\begin{array}{l} \text{Total flux density} \\ \text{incident at } A(I) \end{array} \right] \quad (7-4)$$

where

$QS(I, \text{net})$ = Net rate of energy exchange at node I due to solar power input

$A(I)$ = Area of node I

The second term on the right side of this equation can be written as:

$$\left[\begin{array}{l} \text{Total flux density} \\ \text{incident at } A(I) \end{array} \right] = \left[\begin{array}{l} \text{Flux originally} \\ \text{incident at } A(I) \end{array} \right] + \left[\begin{array}{l} \text{Flux incident at} \\ \text{A(I) due to mul-} \\ \text{tiple reflections} \end{array} \right] \quad (7-5)$$

The flux originally incident on $A(I)$ is equal to $SOLCON(I)$, while the flux incident at $A(I)$ due to multiple reflections is $[F(I, 1)R(1) + F(I, 2)R(2) \dots F(I, N)R(N)]$. Equation 7-4 can then be written:

$$\frac{QS(I, \text{net})}{A(I)} = R(I) - [F(I, 1)R(1) - F(I, 2)R(2) \dots F(I, N)R(N)] - \text{SOLCON}(I) \quad (7-6)$$

The $R(I)$'s are the response vector due to multiple reflections. The excitation vector for this case, defined as the radiosity entering the system at area $A(I)$, is:

$$D(I) = \text{SOLCON}(I) * [1 - \text{ESOL}(1)] \quad (7-7)$$

Using Equation 7-7, Equation 7-3 can be solved for the various $R(I)$ values, and Equation 7-6 can be solved for the $QS(I)$ vector, which is independent of the temperature surface I .

For the heat exchange due to the infrared reradiation, the values of the excitation matrix is a function of the temperature of the surface. In this case, it would save computing time if the values of $QR(I, \text{net})/A(I)$ could be computed as a function of these temperatures, as well as simplify the iterative procedure.

We can write radiosity and heat balances on area $A(I)$:

$$\frac{QR(I, \text{net})}{A(I)} = R(I) - \text{Incident IR flux} \quad (7-8)$$

and

$$\frac{QR(I, \text{net})}{A(I)} = \text{EIR}(I)\theta T(I)^4 - \text{EIR}(I) \text{ (Incident IR flux)} \quad (7-9)$$

Cancelling the incident IR flux between these two equations gives the result:

$$\frac{QR(I, \text{net})}{A(I)} = \frac{EIR(I)}{1-EIR(I)} [\theta T(I)^4 - R(I)] \quad (7-10)$$

Subbing R(I) from Equation 7-3 into Equation 7-10 gives the result:

$$\frac{QR(I, \text{net})}{A(I)} = \frac{EIR(I)}{1-EIR(I)} \left[\theta T(I)^4 - \sum_{j=1}^n B(I, J) D(J) \right] \quad (7-11)$$

Noting that, for IR radiation, $D(J) = EIR(J)\theta T(J)^4$, we get the:

$$\frac{QR(I, \text{net})}{A(I)} = \frac{EIR(I)}{1-EIR(I)} \left[\theta T(I)^4 - \sum_{J=1}^n B(I, J) EIR(J) \theta T(J)^4 \right] \quad (7-12)$$

Adding and subtracting the term:

$$\frac{EIR(I)}{1-EIR(I)} \left[\sum_{j=1}^n B(I, J) EIR(J) \theta T(I)^4 \right] \quad (7-13)$$

We get the result:

$$\begin{aligned} \frac{QR(I, \text{net})}{A(I)} = & \frac{EIR(I)}{1-EIR(I)} \left[\theta T(I)^4 - \sum_{j=1}^n \theta B(I, J) EIR(J) T(I)^4 \right. \\ & \left. + \sum_{j=1}^n \theta B(I, J) EIR(J) (T(I)^4 - T(J)^4) \right] \quad (7-14) \end{aligned}$$

It can be shown that

$$\sum_{J=1}^n B(I, J) EIR(J) = 1$$

Therefore, the above Equation 7-14 becomes:

$$\frac{QR(I, net)}{A(I)} = \frac{EIR(I)}{1-EIR(I)} \sum_{j=1}^n (1-\delta_{ij}) B(I, J)EIR(J) (T(I)^4 - T(J)^4) \quad (7-15)$$

where δ_{ij} is the Kronecker delta.

This can be expressed in terms of the script F factor;

$$\frac{QR(I, net)}{A(I)} = \sum_{J=1}^n SF(I, J) [\theta T(I)^4 - \theta T(J)^4] \quad (7-16)$$

Therefore, we can write the final IR heat balance as:

$$\begin{bmatrix} \frac{QR(I)}{A(I)} \\ \cdot \\ \cdot \\ \cdot \end{bmatrix} = \theta \begin{bmatrix} SF(I, J) \dots \dots \dots \\ \cdot \\ \cdot \\ \cdot \end{bmatrix} \begin{bmatrix} [T(I)^4 - T(J)^4] \dots \dots \dots \\ \cdot \\ \cdot \\ \cdot \end{bmatrix} \quad (7-17)$$

IR Heat Input Vector
Script F Matrice
Radiation Temperature Matrice

Finally, the conductance between any two nodes is given by:

$$\left[\frac{QC(I, J)}{A(I)} \right] = [C(I, J)] [T(I) - T(J)] \quad (7-18)$$

where $C(I, J)$ is the conductance from node J to node I.

The program tries to solve the matrix equations for the temperature of each node so that the net heat transfer to each node is zero. Combining the conduction, IR radiation, and solar radiation, we get:

$$\frac{QT\theta T(J)}{A(I)} = \frac{QS(I)}{A(I)} + \frac{QC(I)}{A(I)} + \frac{QR(I)}{A(I)} \quad (7-19)$$

or writing in terms of the N temperatures of the nodes,

$$\begin{aligned} \frac{QT\theta T(I)}{A(I)} &= \frac{QS(I)}{A(I)} + \sum_{J=1}^n C(I, J)[T(I) - T(J)] \\ &+ \sum_{J=1}^n SF(I, J) [T(I)^4 - T(J)^4] \end{aligned} \quad (7-20)$$

A series expansion to the first-order terms for a function of N independent variables can be written:

$$f(x_{01}, x_{02}, x_{on}) = f(x_1, x_2, \dots, x_n) + \sum_{j=1}^n \frac{\partial f(x_1, x_2, \dots, x_n)}{\partial x_j} (x_{0j} - x_j) \quad (7-21)$$

We want $f(x_{01}, x_{02}, x_{on})$ to be equal to zero. Therefore, solving the Equation 7-21 for the value of $x_{0j} - x_j$ gives the result in matrix form for a set of N equations of the form of Equation 7-21 in the N variables;

$$\begin{bmatrix} \frac{\partial f_1}{\partial x_1} & \frac{\partial f_1}{\partial x_2} & \dots & \frac{\partial f_1}{\partial x_n} \\ \frac{\partial f_2}{\partial x_1} & \frac{\partial f_2}{\partial x_2} & \dots & \frac{\partial f_2}{\partial x_n} \\ \vdots & \vdots & \ddots & \vdots \\ \frac{\partial f_n}{\partial x_1} & \frac{\partial f_n}{\partial x_2} & \dots & \frac{\partial f_n}{\partial x_n} \end{bmatrix} \cdot \begin{bmatrix} \Delta x_1 \\ \Delta x_2 \\ \vdots \\ \Delta x_n \end{bmatrix} = \begin{bmatrix} -f_1 \\ -f_2 \\ \vdots \\ -f_n \end{bmatrix} \quad (7-22)$$

where all of the above functions and partial derivatives are evaluated at the present assumed values of the x_j . Equation 7-22 can be rewritten in a form to give the new guesses x_{0j} directly. Doing this gives the result:

$$\begin{bmatrix} \frac{\partial f_1}{\partial x_1} & \frac{\partial f_1}{\partial x_2} & \dots & \frac{\partial f_1}{\partial x_n} \\ \vdots & \vdots & \ddots & \vdots \\ \frac{\partial f_n}{\partial x_1} & \dots & \dots & \frac{\partial f_n}{\partial x_n} \end{bmatrix} \cdot \begin{bmatrix} x_{01} \\ x_{02} \\ \vdots \\ x_{0n} \end{bmatrix} = \begin{bmatrix} -f_1 + \sum_{j=1}^n \frac{\partial f_1}{\partial x_j} \cdot x_j \\ -f_2 \\ \vdots \\ -f_n + \sum_{j=1}^n \frac{\partial f_n}{\partial x_j} \cdot x_j \end{bmatrix} \quad (7-23)$$

By using matrix Equation 7-23, the new values x_{oj} can be solved directly from the various functions and the old values x_j .

We first set

$$f_1(x_1, x_2, \dots, x_n) = \frac{QTOT(J)}{A(I)} [T(1), T(2) \dots T(N)]$$

$$x_j = T(I)$$

The solution is then found by solving Equation 7-20 for all of the nodes for the assumed values of the $T(I)$ and $T(J)$. If the values of the $QTOT(I)/A(I)$ are all within the prescribed limits, the iteration is terminated. If it is not within the required limits, Equation 7-23 is solved for the new values of $T(I)$ and the procedure is repeated.

For some nodes, the temperature is assumed consistent and the heat rate is allowed to float. In these cases, the iteration at a constant-temperature node becomes $T_{oj} = T_j$ for $j = c$. In addition, the values of

$$\frac{\partial f_1}{\partial x_c} ; \quad \begin{matrix} j = 1, n \\ j = c \end{matrix}$$

are also zero. Matrix Equation 7-23 then becomes matrix Equation 7-24 for node c being a constant-temperature node at constant-temperature x_c :

$$\begin{bmatrix} \frac{\partial f_1}{\partial x_1} & \dots & 0 & \dots & \frac{\partial f_1}{\partial x_n} \\ \vdots & & & & \vdots \\ 0 & \dots & 1 & \dots & 0 \\ \vdots & & & & \vdots \\ \frac{\partial f_n}{\partial x_1} & \dots & 0 & \dots & \frac{\partial f_n}{\partial x_n} \end{bmatrix} \cdot \begin{bmatrix} x_{01} \\ \vdots \\ x_c \\ \vdots \\ x_{on} \end{bmatrix} = \begin{bmatrix} -f_1 + \sum_{\substack{J=1 \\ J \neq c}}^n \frac{\partial f_1}{\partial x_j} \cdot x_j \\ \vdots \\ -f_n + \sum_{\substack{J=1 \\ J \neq c}}^n \frac{\partial f_n}{\partial x_j} \cdot x_j \end{bmatrix} \quad (7-24)$$

Essentially, the problem is simplified to one of $N - R$ equations in $N - R$ unknowns, where R is the number of constant-temperature nodes.

In the program, the aperture and all of the fluid nodes are constant-temperature nodes. The values of the temperatures of the constant-temperature fluid nodes are evaluated at each iteration: This allows us to incorporate the STEAMTABLE routine into the program.

View Factor Analysis

The nodes used in the rubber model heat-transfer analysis for both the pilot plant and commercial plant are axisymmetric nodes. This choice of nodes simplifies the calculation of the view factors in the cavity considerably. Known closed-form solutions for the view factor between two coaxial discs were in combination with various known arithmetic and reciprocity relations between view factors. Use of these equations allowed the calculation

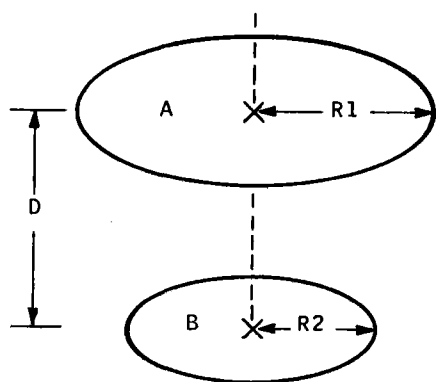
of all view factors in the cavity with axisymmetric nodes. Figure 7-15 lists the basic equations and relations necessary in the view factor analysis.

Cavities with a slanted bottom were modeled by use of a single semicylindrical node at the bottom of the cavity. Figure 7-16 illustrates the geometry which was modeled. In this case, it was necessary to add the concept of symmetry to those relations defined in Figure 7-15.

Calculation of the view factors for the case of nonaxisymmetric nodes requires the use of costly numerical solution methods. Considerable cost savings exist when running variable-cavity geometries by running the axisymmetric node model. Figure 7-17 details the relative costs of the two models. The added cost of the heat balance routine due to use of the nonaxisymmetric model is due to the larger number of nodes required with the nonaxisymmetric model.

The heat balance routine assumes that all nodes are maintained at a constant temperature. The axisymmetric node model will only be correct, therefore, when the temperature distribution in the cavity is axisymmetric (or when the incident flux distribution is axisymmetric). However, the error in net cavity efficiency generated by using the axisymmetric model in place of the nonaxisymmetric model is less than 1 percent. This can be shown by dividing the losses into three types: solar reradiation, IR radiation, and conduction losses.

It can be shown from symmetry and reciprocity relationships between view factors that view factor from any node (or point) in the cavity to an axisymmetric node (in this case the aperture) is a function only of the paraxial distance between the two nodes and does not depend on the angular position of the nonaxisymmetric node. Figure 7-18 outlines the proof. Since the solar rereflection is a function only of the radiation properties and aperture view factors of the given node, there are no errors generated



$$1) \sum_{J=1}^n F(i,J) = 1 \quad i = 1, 2, \dots, N$$

FOR AN ENCLOSURE TOTALLY DEFINED BY N SURFACES

$$2) A(i) F(i,J) = A(j) F(j,i)$$

$$3) F(i,J_1) + F(i,J_2) = F(i,J_1 + J_2)$$

$$4) A(i_1) F(i_1,J) + A(i_2) F(i_2,J) = A(i_1 + i_2) F(i_1 + i_2,J)$$

$$F(A,B) = 0.5 \left(z - \sqrt{z^2 - 4x^2y^2} \right)$$

WHERE

$$X = R2/D$$

$$Y = D/R1$$

$$Z = 1 + (1 + X^2) Y^2$$

Figure 7-15. Rubber Model View Factor Algebra

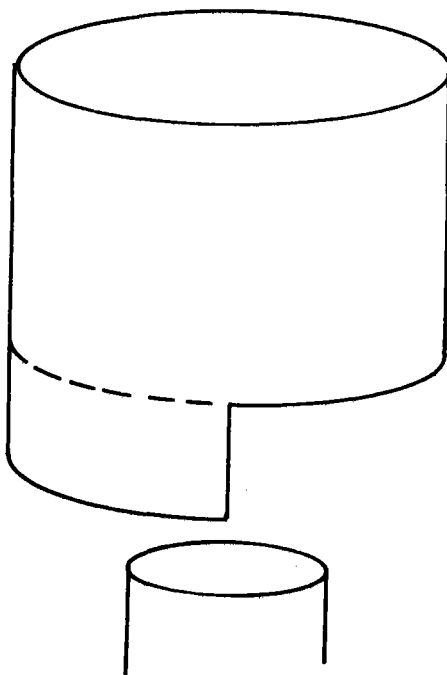


Figure 7-16. Cavity Geometry for Shielded Cavity Case

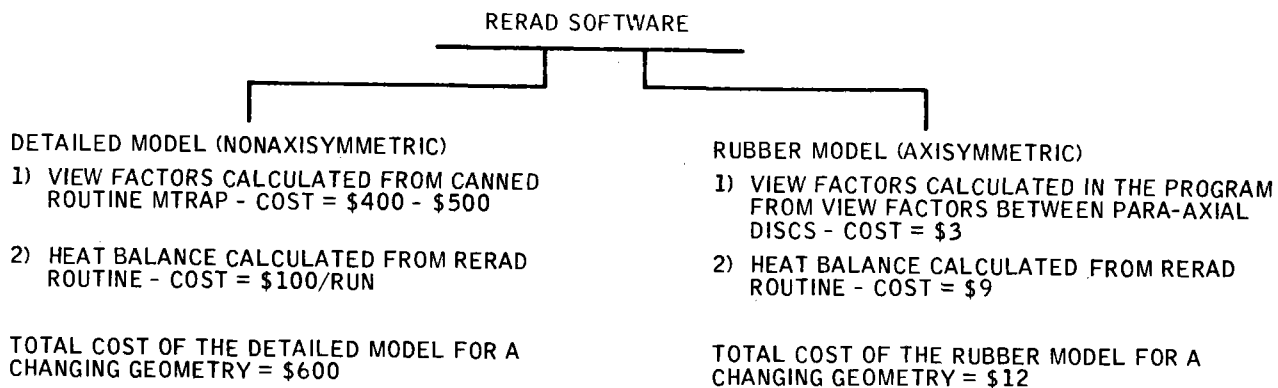


Figure 7-17. Rerad Model Software Costs

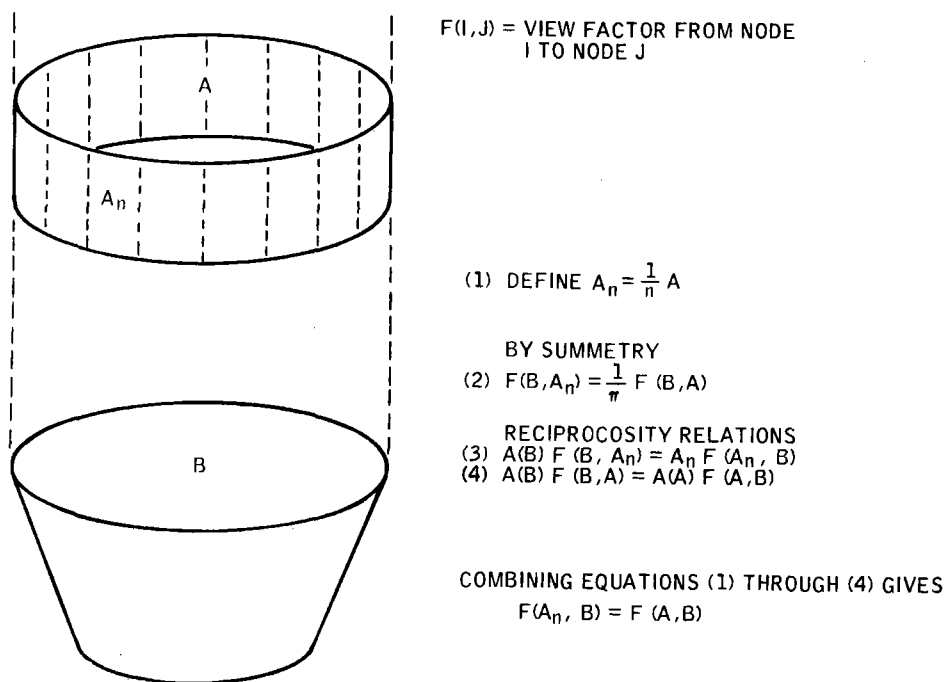


Figure 7-18. Proof of Relationship Between View Factors

in the estimation of solar rereflected power by using the axisymmetric node model rather than a nonaxisymmetric node model for a cavity with an axisymmetric aperture.

The IR reradiation losses are a function of metal surface temperature. Metal temperature depends on the incident flux and the temperature of the fluid in the receiver tubes. Doubling the incident flux will have the effect of approximately doubling the temperature difference across the receiver tubes for a constant heat-transfer coefficient, since it would then be necessary to dissipate twice as much flux from a given metal surface node. The fluid temperatures can be assumed to be held constant by the boiling temperature of the water and the attemperator. However, we know that:

$$\text{Flux} = U(T_m - T_f) \quad (7-25)$$

where

Flux = Heat transfer flux through a given area

U = Overall heat transfer coefficient

T_m = Metal surface temperature

T_f = Fluid temperature (constant)

Therefore, the effect of doubling the flux with a constant U on tube metal surface temperatures is identical to the effect of halving the value of U at constant flux on metal surface temperatures.

If T_m in Equation 7-25 is interpreted as the effective average metal surface temperature of an axisymmetric node, the value of T_m will be a function of the incident flux distribution on that node. We can simulate the effect of

this nonaxisymmetric flux distributions on T_m at constant power level input to a given node by varying the U value in our axisymmetric model.

Examination of the ray trace runs showed that the maximum flux on any given node in the cavity is not more than three times the average flux of all of the nodes at that height in the cavity. As a worst-case analysis, therefore, the value of U was decreased by a factor of three to simulate the IR losses if the entire axisymmetric metal node temperature were at the maximum temperature likely to be encountered in that node. Conduction losses are analyzed in a similar way.

Table 7-1 presents the results of this analysis. The "Percent of Losses" column is the percent of total cavity losses the term listed on the left is in the average run. The total loss error of 9.5 is a weighted average of the three types of losses. Since the losses are only about 10 percent of the total power into the cavity, the net error is absorbed power and cavity

Table 7-1. Error* In Net Cavity Efficiency Due to the Rubber Model (3/21 Noon)

<u>Loss Factor</u>	<u>Percent of Losses</u>	<u>Percent Error</u>
Solar reradiation	29	None
IR reradiation	67	10.7
Conduction losses	4	58.0

* Total weighted losses error due to modeling nonaxisymmetric flux distribution as axisymmetric flux distribution for a right-circular cylinder is:

$$\text{Total loss error} = 0.29(0) + 0.67(0.107) + (0.04)(0.58) = 9.5\%$$

efficiency made by using the axisymmetric model in the worst-case analysis is less than 1 percent. The actual error due to the use of the axisymmetric model is much less than this worst-case maximum. Hence, we used the rubber model software almost exclusively in analyzing the pilot and commercial plant cavity performance.

The SRE cavity view factors from the lamp nodes to the cavity nodes were obtained by use of the Monte-Carlo method in a routine called FLUXSUM. View factors calculated by the FLUXSUM routine are combined with the view factors calculated by the coaxial disc method by use of the view factor algebra defined in Figure 7-15 to get all view factors for the SRE cavity.

Program FLUXSUM was written to determine the performance of the SRE light column and to determine if the light column would be capable of approximating the expected pilot plant flux profile on the SRE receiver. As in other ray trace codes, conclusions are based on the assumption that if many random rays are drawn, the results converge to a statistically accurate flux. The more rays that are drawn, the more accurate are the results.

Program FLUXSUM draws random rays over the surface of the simulator lamp. The path of every ray is then traced and the code calculates the position at which the ray hits one of the cavity walls. The specification of a given random ray requires four random number draws: 1) the height of the plane of the origination point of the ray relative to the base of the cavity; 2) the azimuth angle of the origination point of the ray in the given height plane relative to a base axis; 3) the elevation angle of the direction of the drawn ray relative to a tangent plane to the lamp at the origination point of the ray; and 4) the azimuth angle of the direction of the drawn ray relative to a reference axis in the tangent plane to the lamps surface.

The first two draws determine where the random ray originates from on the lamp. These are uniform drawn and they generate a uniform distribution of ray origination points over the surface of the lamp.

The intensity of light from a given point on the lamp surface is dependent on the elevation angle by Lambert's Cosine Law. The third random number drawn for the elevation angle of the drawn ray must be made to reflect this distribution. This is done by drawing uniformly over the sine of the elevation angle. The fourth draw, which gives the azimuth angle of the direction of the drawn ray, is again a uniform draw.

When all of the hits have been sorted and summed, the code outputs a nodal summary of where the rays hit the cavity walls versus where the rays originated from. These results are then used to calculate the view of factors from one node to another by the assumption that the number of rays which originated from Node A and struck Node B is proportional to the view factor from Node A to Node B.

Sensitivity Analysis

A large number of input parameters are necessary to run the rerad rubber model. In order to investigate the effect of errors made in estimating the values of these variables on overall cavity efficiency, a sensitivity analysis was performed over the set of input parameters.

Table 7-2 is a list of the input parameters which were varied in the sensitivity analysis. The base value listed is the value which is assumed to hold in all of our performance runs. The range is the lowest and highest values of the given parameter which were run in the sensitivity analysis.

Table 7-2. Sensitivity Analysis Variables

Variable	Definition	Base Value	Range
Solar emissivity	Emittance of inside cavity surfaces in solar spectrum	0.9	0.8 to 0.95
Pressure drops	Pressure drops through boiler and boiler and two superheaters in psia	Superheater: 1 to 43 Superheater: 2 to 28 Boiler: 8	22 to 66 14 to 42 4 to 12
Boiler inside HTC	Film heat-transfer coefficient in boiler, Btu/hr-ft ² °F	10,000	6000 to 14,000
Superheater inside HTCs	Film heat-transfer coefficients in the superheaters, Btu/hr-ft ² °F	Superheater: 1 to 811.5 Superheater: 2 to 663	611.5 to 1011.5 463 to 863
Environmental temperature	Assumed temperature of outside environment, °F	100	70 to 130
IR emissivity	Emittance of inside cavity surfaces in IR spectrum	0.9	0.8 to 0.95
Heat loss coefficient	Heat-transfer coefficient between nodes adjacent to outside environment and environment, Btu/hr-ft ² °F	0.0003157 (8 in. fiberglass)	0.000157 to 0.000394
Frac - Assumed node temperature point	Fluid node temperature - Inlet fluid temperature + Frac* (Outlet fluid temperature - Inlet fluid temperature)	0.5	0.2 to 0.8

Table 7-3 gives the results of the sensitivity analysis. Each variable was varied through the range given in Table 7-2, while all of the other variables were held at their base values. The positive and negative $\Delta\%$ are the maximum and minimum percent change in cavity efficiency from the base value noted in the range of the variable listed on Table 7-2. The RUN ALL LIMITS case is the result of running all the values of those variables together which, when run singly, result in the maximum increase in the value of the cavity efficiency over its baseline value, and doing the same for all of those values which decrease the cavity efficiency.

The RUN ALL LIMITS case is a worst-case analysis. It can be concluded, therefore, that the maximum error in our cavity efficiency due to errors in the base value of our input parameters is 3.4 percent in the worst case

Table 7-3. Sensitivity Analysis Results for
3/21 Noon

Variable	Positive Δ %	Negative Δ %
Solar emissivity	1.20	2.70
Pressure drops	0.01	0.02
Frac	0.09	0.10
Boiler inside HTC	0.01	0.02
Superheater inside HTC	0.02	0.04
Environment temperature	0.04	0.05
IR emissivity	0.11	0.26
Heat loss coefficient	0.20	0.11
RUN ALL LIMITS	1.68	3.39

throughout the range of values of input parameters we are likely to actually see. The probable error due to errors in the input parameters is much less than the maximum of 3.4 percent.

ATMOSPHERIC ATTENUATION LOSS MODEL

The energy radiated by the sun is a function of wavelength and can fluctuate somewhat depending on the presence of solar flares, sun spots, etc. This radiation is substantially modified by absorption and scattering in the earth's atmosphere. Absorption is due to water vapor, ozone, nitrogen, some uniformly mixed gases (CO_2 , CO , O_2 , NO_2 , and CH_4), and water vapor continuum. Scattering is primarily due to aerosols and molecular scattering.

Figure 7-19 shows typical spectral distribution curves related to the sun. The various atmospheric constituents mentioned in the previous paragraph provide the wavelength selective absorption and scattering shown in the figure. This figure shows what arrives at the outer fringes of the earth's atmosphere as well as what arrives at the earth's surface.

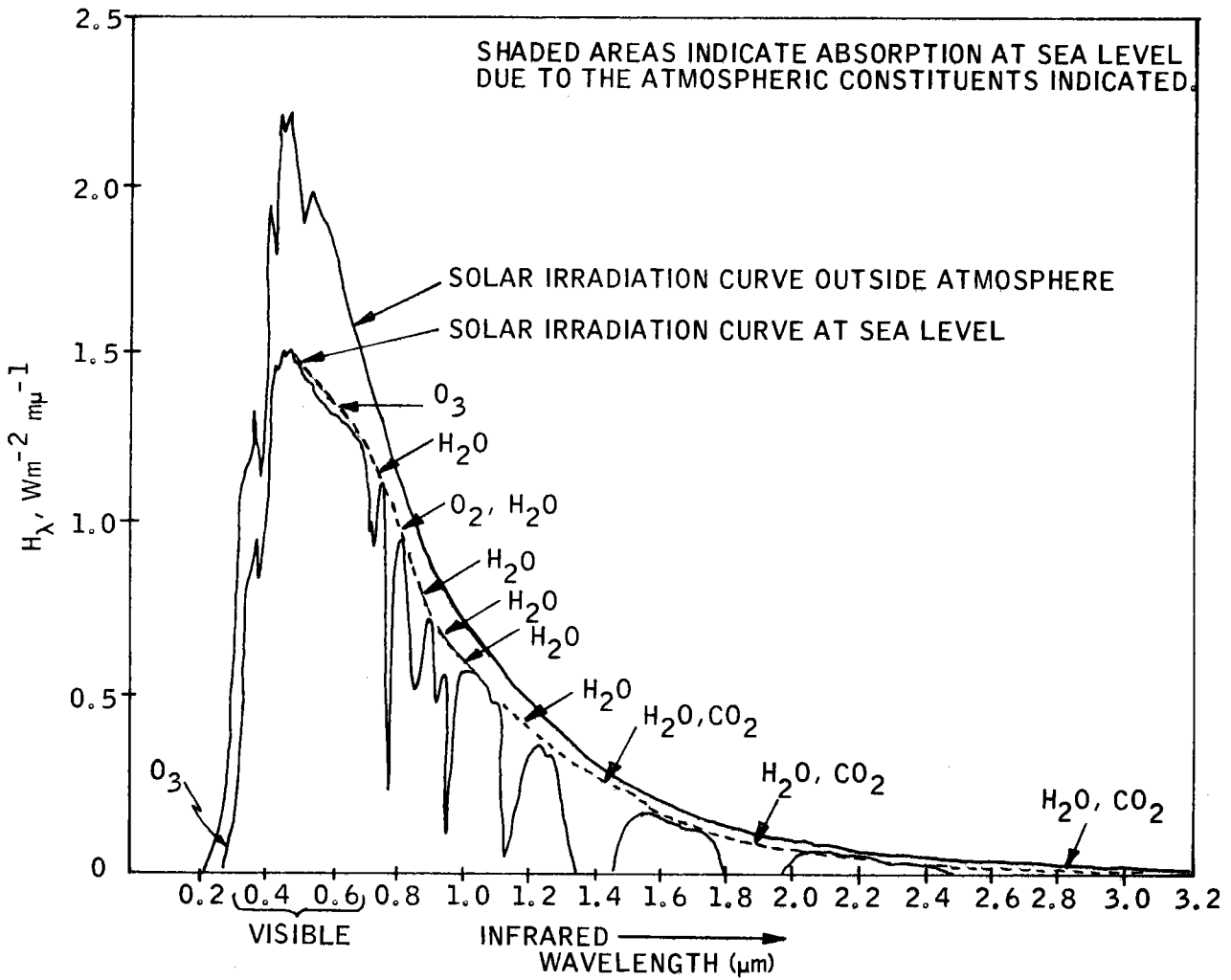


Figure 7-19. Spectral Distribution Curves Related to Sun

As shown in the figure, energy is lost over the entire sun's spectrum. Most of the losses in the visible region (0.2 to 0.75 μm) occurs due to scattering, while the losses in the infrared are primarily due to absorption. The figure indicates typical spectral distribution curves. Actual distributions vary widely depending on atmospheric dust concentration, air mass, water vapor concentration, and other atmospheric factors.

Much has been written concerning the atmospheric attenuation of the sun's energy. This subject has become increasingly important to solar energy programs and most important to those programs in which solar central receiver power plants are being developed. In the case of the solar central receiver, we are interested in the atmospheric attenuation losses which occur between the reflecting surface of the heliostat and the receiver surface. All solar conversion systems must use whatever spectral distribution of energy is available at the earth's surface. However, the central receiver reflects this energy back through the lower atmosphere to a single target. For long enough path lengths, an additional attenuation loss of energy must be accounted for in the performance evaluation.

As the distance the redirected sun's energy must travel is increased, as in the central receiver solar power plant, the attenuated bands broaden as more absorption and scattering takes place. Since the atmosphere is most dense near the earth's surface, the effects of absorption and scattering are the most prominent here. This becomes especially important when attenuation over horizontal or slant paths near the surface must be accounted for. Figure 7-20 is a schematic depicting the energy losses for the pilot plant central receiver system. The percentage losses shown were obtained using an atmospheric attenuation model based on past empirical work. The atmospheric conditions of visibility (20 to 60 km) and relative humidity (10 to 30 percent) are typical for desert sites. Solar irradiation available at the ground (720 to 1020 W/m^2) are in agreement with measured values. Losses from scattering and absorption were calculated to be 24 to 49 percent

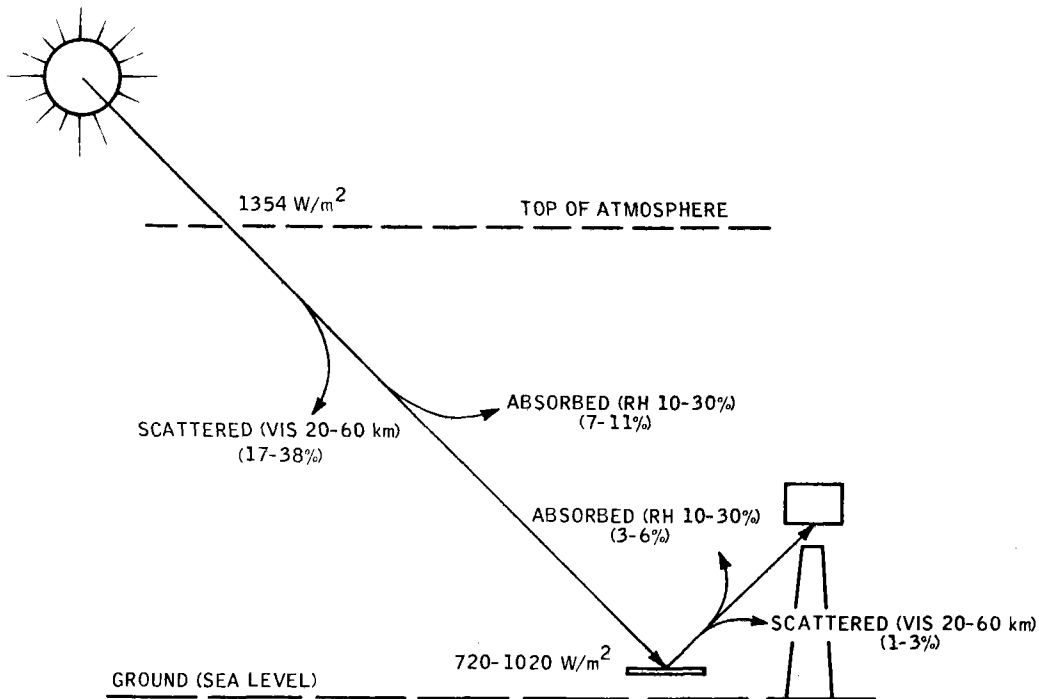


Figure 7-20. Pilot Plant Design Time Atmospheric Attenuation Losses

from the top of the atmosphere to the ground and 4 to 9 percent from the reflecting surfaces to the receiver. We believe these losses to be representative of what can be expected. However, we caution that there are no known precise methods for predicting these losses. The method we have used, and other methods we are aware of, can be quite accurate in predicting the losses in energy from the top of the atmosphere to the earth's surface. On the other hand, the predicted losses from reflecting surfaces to a central receiver are normally smaller and thus subject to more error. In developing a model for the solar central receiver atmospheric attenuation losses, it is our intent to provide insight in the factors which will influence these losses. We also wish to provide an estimate of the expected losses which should be interpreted as a mean value and not an absolute.

Analysis Model

The model used in this program is based on work reported in Elements of Infrared Technology, by Kruse, McGlauchin, and McQuistan, Wiley 1962, Ch. 5. This work is particularly applicable since it deals specifically with those aspects of the earth's atmosphere which affect the transmittance in the infrared region where most wavelength band broadening occurs. It provides a means of relating atmospheric transmission to a parameter which is readily measureable -- humidity. This is done by dividing the spectrum into nine "windows" or regions of high transmissions between absorption bands and factoring the transmission into two terms. The terms are τ_a , the transmittance affected by the selective or molecular absorption, and τ_s , the transmittance affected by scattering, a form of attenuation much less strongly dependent on wavelength.

The radiation intensity which remains in some wavelength interval λ_1 to λ_2 after the sun's radiation has traveled through a specified path length is given by:

$$I_{d\lambda} = \int_{\lambda_1}^{\lambda_2} H_{\lambda}(\lambda) \tau(\lambda) d\lambda$$

where

$I_{d\lambda}$ = Radiation intensity at end of path (W/m^2)

H = Irradiance at path start ($W/m^2 \mu m$)

λ = Wavelength (μm)

τ = Transmittance over path

The integration is performed over all wavelengths from λ_1 to λ_n . The method used to calculate losses models the solar spectral distribution in

wavelength windows from λ_1 to λ_2 and λ_2 to λ_3 , etc., up to λ_n which is λ_{10} for the nine-window model. Figure 7-21 shows the wavelength windows used in relation to the solar spectrum. The last two windows are seen to be relatively unimportant in the loss calculation.

The model follows the Elder-Strong window approximation method (Elder, T. and Strong, J., J., Franklin Institute 255, 189 (1953)) so that the radiation intensity which remains after traveling through some part of the atmosphere may be rewritten as:

$$I_{d\lambda} = \sum_i H\lambda_i \tau_i \Delta\lambda_i$$

where

$H\lambda_i$ = Irradiance available in window i

τ_i = Total transmittance in window i

λ_i = Wavelength range of window i

Further, the total transmittance in any window is the product of the absorption and scattering transmittance terms:

$$\tau_i = \tau_{ai} \tau_{si}$$

It still remains to determine expressions for τ_{ai} and τ_{si} . They will be stated here without development but can be found in a report by Langer, R. M., Report on Sig. Corps Contract Number DA-36-039-SC-7235 (May 1957).

These two expressions are:

$$\tau_{ai} = \begin{cases} \exp(-A_i w^{1/2}) & w < w_i \\ k_i \left(\frac{w_i}{w}\right)^{\beta_i} & w > w_i \end{cases}$$

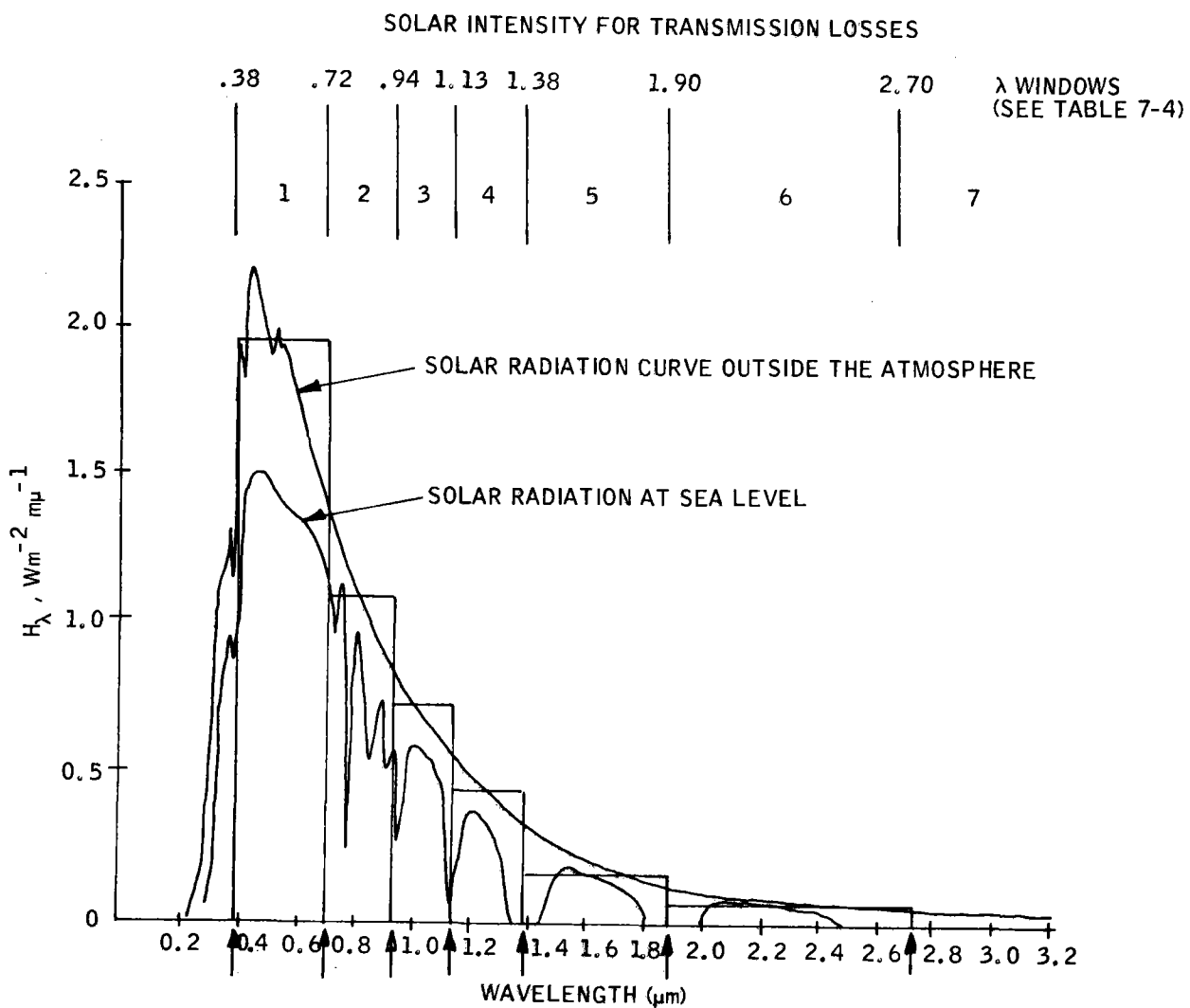


Figure 7-21. Wavelength Windows Relative to Solar Spectrum

and

$$\tau_{si} = \exp \left\{ - \frac{3.91 \ell}{v} \left(\frac{0.55}{\lambda_i} \right)^q \right\}$$

where

$$q = 0.585 (v)^{1/3} \text{ for } (v \leq 6 \text{ km})$$

i = Atmospheric window number

τ_{ai} = Absorption component of τ for window i

τ_{si} = Scattering component of τ for window i

w = Visibility range (km)

l = Path length (km)

$$\left. \begin{array}{l} A_i, w_i \\ k_i, \beta_i \end{array} \right\} = \text{Empirical window constants (Table 7-4)}$$

The radiation intensity attenuation is simply the difference between that available at the path start and end points:

$$\text{Loss} = \sum_i H \lambda_i \Delta \lambda_i - I_{d\lambda}$$

Note that the constants used in the equation for the absorption component of transmittance will give a τ_{ai} equal to 1.0 in the first window. Thus, the model will show no absorption losses in the first window, which covers the visible region. The model ignores all energy in the ultraviolet region. The absorption component of transmittance for all other windows is plotted

Table 7-4. Window Limits and Constants

Window No.	Wavelength Limits (μm)	Central λ_i (μm)	A_i	k_i	β_i	w_i
1	0.38 to 0.72	0.55	0	1	0	-
2	0.72 to 0.94	0.83	0.031	0.800	0.112	54.0
3	0.94 to 1.13	1.04	0.036	0.865	0.154	54.0
4	1.13 to 1.38	1.26	0.130	0.830	0.093	2.0
5	1.38 to 1.90	1.64	0.211	0.802	0.111	1.1
6	1.90 to 2.70	2.30	0.350	0.814	0.104	0.35
7	2.70 to 4.30	3.50	0.373	0.827	0.095	0.26
8	4.30 to 6.0	5.15	0.913	0.679	0.194	0.18
9	6.0 to 15.0	10.5	0.598	0.784	0.122	0.17

as a function of precipitable water in the energy path in Figure 7-22. The model assumes that precipitable water vapor per unit horizontal distance decreases exponentially with altitude with a scale height of 2 km. The total precipitable water vapor in any path is found by integrating along the path lengths.

Example Calculations

Table 7-5 illustrates a transmittance calculation by the window method outlined above. The sun is assumed to be at a 45-degree elevation angle. For example purposes, a single heliostat is assumed to be 1.68 km from the receiver, with an angle from horizontal to the redirected energy path of 17.5 degrees. Assumed meteorological conditions are that the air temperature is 60°F, relative humidity is 60 percent, and seeing is good (visibility = 30 km).

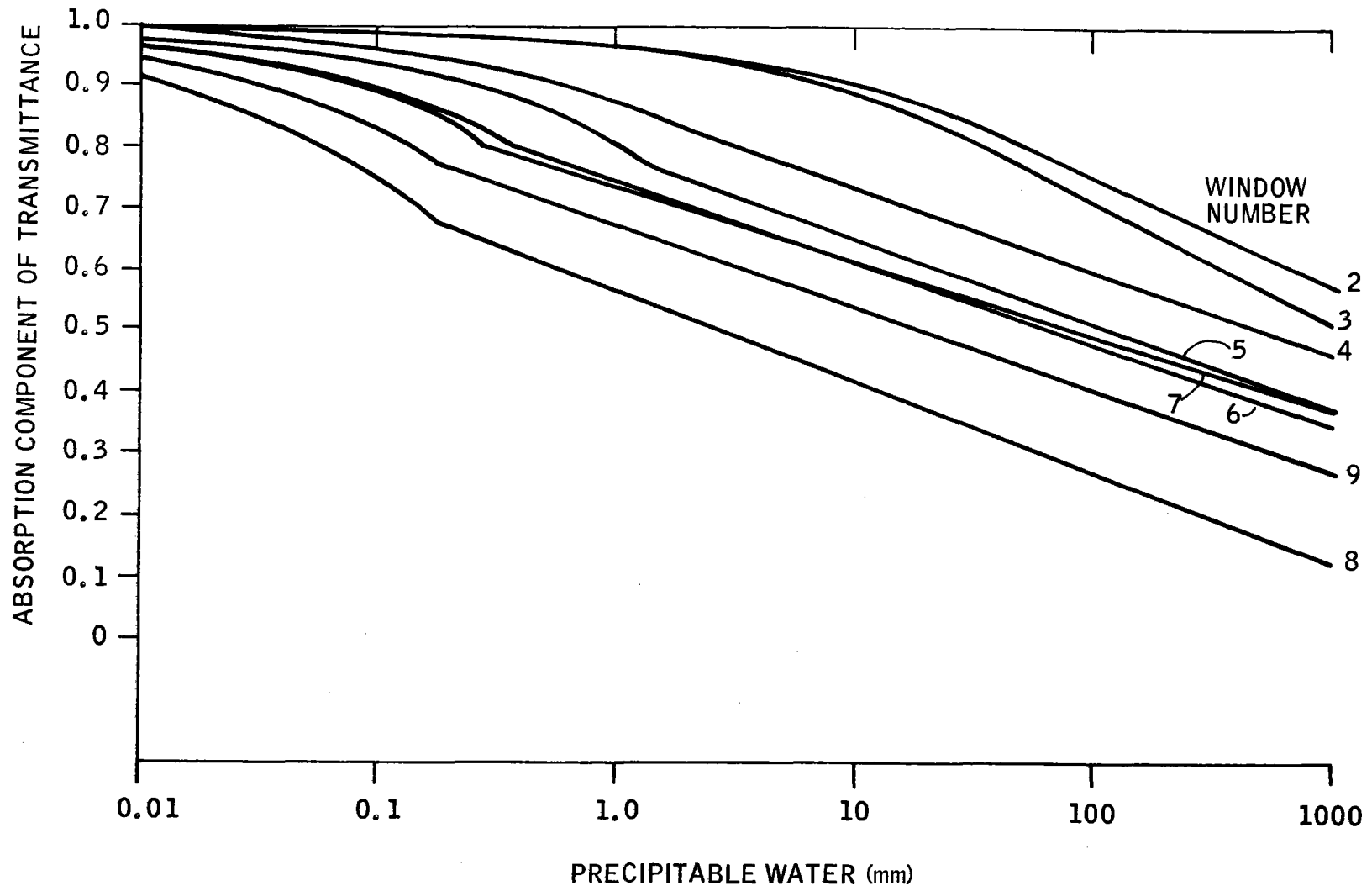


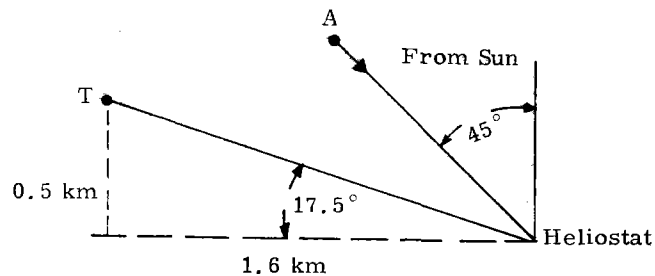
Figure 7-22. Water Vapor Transmission

Table 7-5. Atmospheric Transmission Calculation

Window No. (i)	Window λ Limits (μm)	Midpoints λ_i (μm)	I_A Sun (W/m^2)	Path A to M		$\tau_i =$ $\tau_{ai} \quad \tau_{si}$	I_m (W/m^2)	Path M to T		τ_i $\tau_{ai} \quad \tau_{si}$	I_T (W/m^2)
				τ_{ai}	τ_{si}			τ_{ai}	τ_{si}		
1	0.38 - 0.72	0.55	580.4	1.0	0.69	0.69	402	1.0	0.79	0.79	318
2	0.72 - 0.94	0.83	235.3	0.86	0.84	0.72	170	0.90	0.90	0.81	137
3	0.94 - 1.13	1.04	124.3	0.83	0.89	0.74	92	0.87	0.93	0.81	74
4	1.13 - 1.38	1.26	100.5	0.68	0.92	0.63	63	0.72	0.95	0.68	43
5	1.38 - 1.90	1.64	99.2	0.60	0.95	0.57	57	0.64	0.97	0.62	35
6	1.90 - 2.70	2.30	51.6	0.57	0.97	0.55	27	0.60	0.98	0.59	16
7	2.70 - 4.30	3.50	23.8	0.57	0.99	0.56	13	0.60	0.99	0.60	8
8	4.30 - 6.0	5.15	6.6	0.36	0.99	0.36	2	0.40	1.0	0.40	1
9	6.0 - 15.0	10.5	~2.0	0.49	1.0	0.49	1	0.52	1.0	0.52	1

40703-II

7-54



$$\tau_{AM} = \frac{\sum I_M}{\sum I_A} = 0.68 \text{ (Total transmittance from sun to heliostat)}$$

$$\tau_{MT} = \frac{\sum I_T}{\sum I_M} = 0.77 \text{ (Total transmittance from heliostat to target)}$$

$$\tau_{AMT} = \frac{\sum I_T}{\sum I_A} = 0.52 \text{ (Total transmittance from sun to heliostat to target)}$$

In Table 7-5, I_A is solar intensity outside the atmosphere for each window. I_M and I_T are subsequent mirror and tower irradiances (unity mirror reflectance). The entries in the three I-columns permit calculation of total transmittances for selected wavelength intervals. Transmittances for the span from 0.38 to 15.0 μm are shown in the table.

For this example, the table shows that the losses from the top of the atmosphere to the mirror are 32 percent and from the mirror to the receiver the losses are 23 percent.

To evaluate the losses for a field of heliostats, we perform a calculation as shown in the example for each of 100 representative field cells as shown in Figure 7-23. The power redirected from each cell is that power calculated as reaching the earth times the mirror area in the cell times the cosine factor for the cell:

$$\text{Power}_{\text{cell } j} = \sum_i I_M * \text{Area}_{\text{mirrors};} * \text{Cosine};$$

Thus, the total redirected power is weighted by cell effectiveness. Transmittance losses by each cell is then calculated along its path to the receiver. Total loss from the heliostat field to the receiver is simply the sum of the losses from each cell.

Figure 7-24 shows the predicted atmospheric attenuation losses between the heliostat field and the receiver for the preliminary pilot plant design. The sun position was selected as that occurring at the pilot plant design time, December 21. The figure shows the percentage loss versus the relative humidity at two different visibilities. The range of relative humidity was selected by interrogating the 1963 Inyokern weather tape. For clear days in December, the relative humidity during afternoon hours varies from 6 to 15 percent. On days when clouds are present, relative humidity was as high

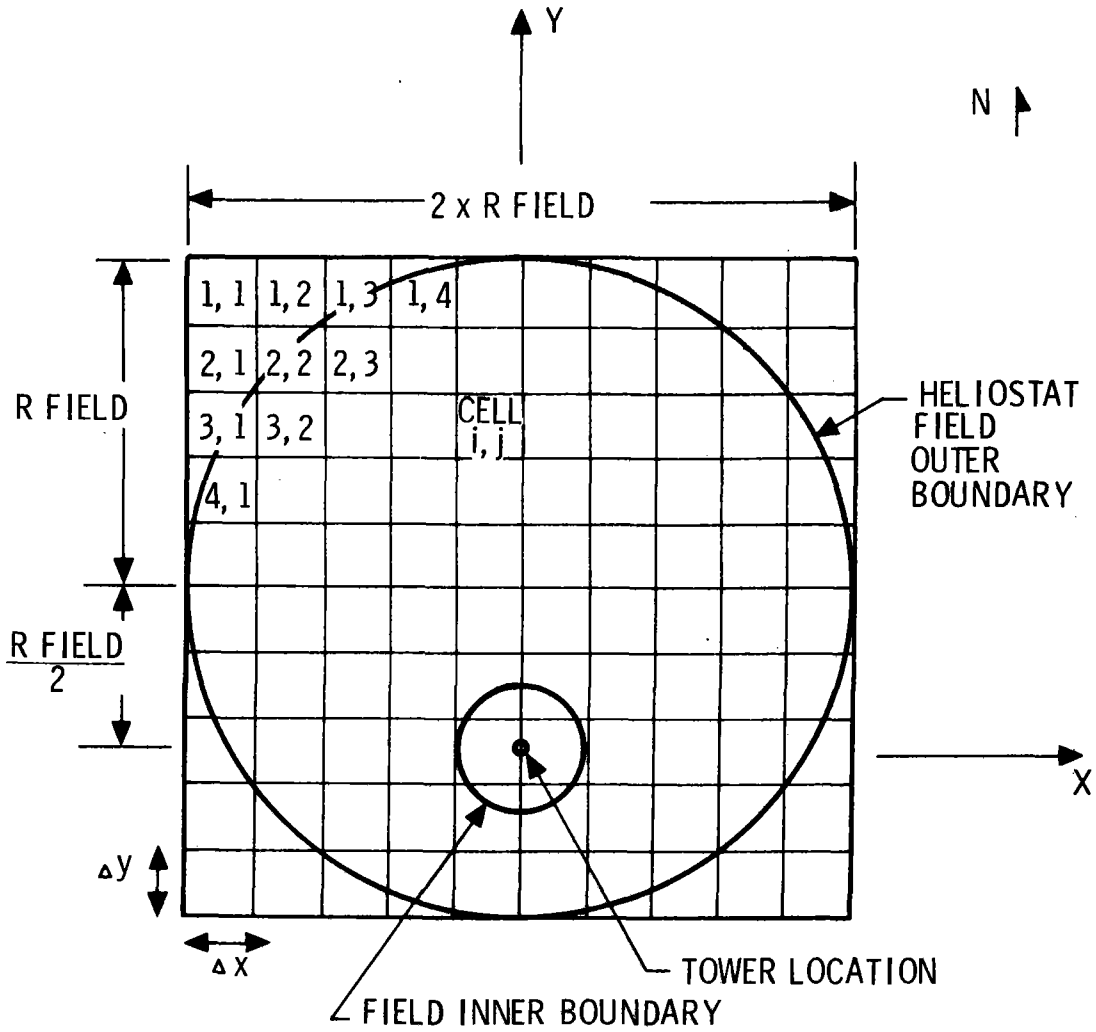


Figure 7-23. Heliostat Field Cells

as 29 percent. A temperature of 57°F was typical of December afternoons. No data on visibility were readily available. However, values between 24 and 60 km seem reasonable. It can be pointed out that the model predicted solar intensity reaching the earth varied from 710 W/m² to 740 W/m² for the 24-km visibility curve, and 980 W/m² to 1020 W/m² for the 60-km visibility curve. Weather tape data indicate that the available solar intensity at 2 p. m. on clear days varies from 810 W/m² to 880 W/m². A curve lying between the 24-km and 60-km visibility curves would best represent these conditions. Referring to Figure 7-24, at relative humidities in the 6 to 15 percent range, the model predicts that 4 to 5 percent of the redirected energy will be lost due to atmospheric attenuation.

Other results obtained from the model show that:

- The greater the average path length from the heliostat to the receiver, the greater the losses
- If humidity and visibility are held constant, the percentage losses from the field to the receiver increase as sun elevation angle increases.

The first result is expected. The second is not so obvious. As the sun gets higher in the sky, the path from the top of the atmosphere to the earth's surface is shortened. Thus, losses from the top of the atmosphere to the earth's surface will be less. Referring to Figure 7-19, the absorption of the energy is wavelength specific so that the losses per unit path length as a function of path length will decrease. This is shown in Figure 7-25, where constant humidity along a path is assumed. In other words, the more available energy that is absorbed, the less energy available that is left to be absorbed. This is somewhat mitigated by absorption band broadening. The model takes this factor into account. Thus, for high sun elevations there will be more energy available at the ground to be later absorbed on the way to the receiver.

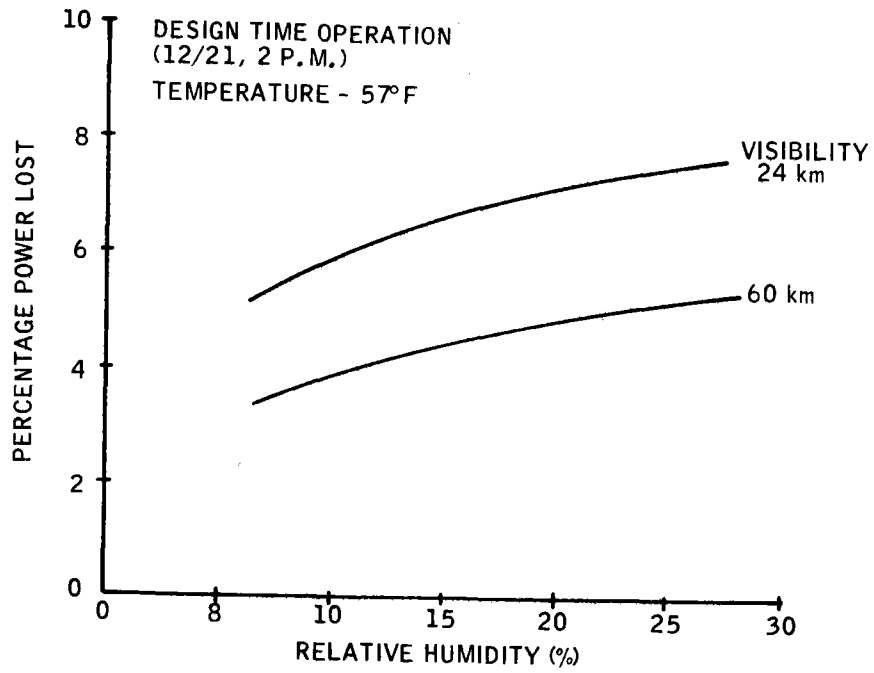


Figure 7-24. Atmospheric Attenuation Losses for the Pilot Plant

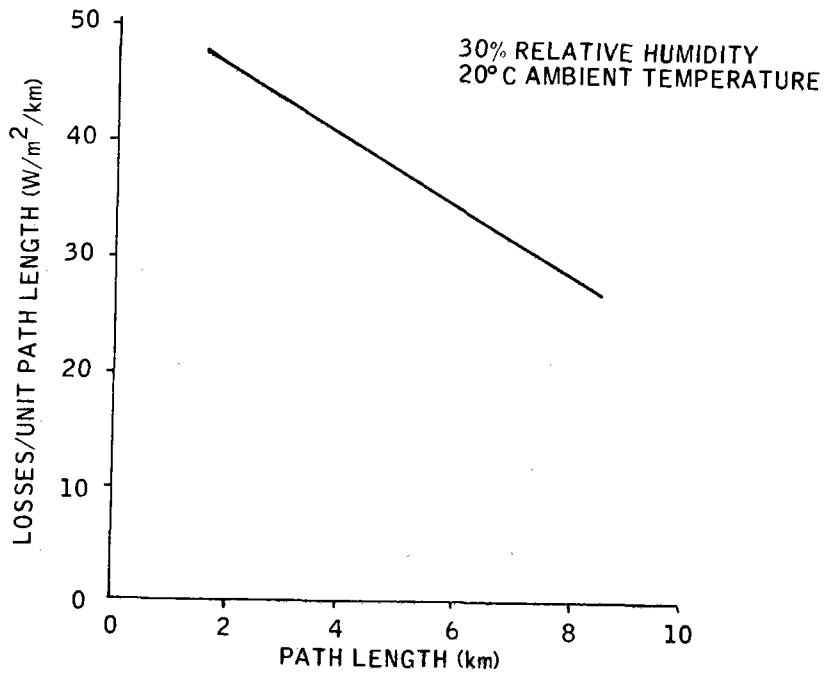


Figure 7-25. Radiation Intensity Attenuation from Mirror to Target

The atmospheric attenuation loss model was used to estimate the losses for the pilot plant and commercial plant concepts, as well as the losses for the SRE heliostats. Selected results for each of these can be found in appropriate sections of this volume.

NET ANNUAL ENERGY MODEL

The net annual energy calculation model interrogates the Inyokern weather tape for hourly insolation, ambient temperature, dew point temperature, wind speed, and the sun's azimuth and elevation angles. These inputs are the driving force for a yearly analysis of pilot plant operational characteristics.

The following basic model assumptions are made in the net annual energy calculations:

- The Inyokern weather tape represents the average year.
- The analysis is quasi-steady-state at any increment of time. The time step is chosen as 1 hour, which coincides with weather tape data sample time.
- Transients other than receiver startup and shutdown are ignored (i. e., cloud effects and control lags are ignored).
- Calculation hierarchy during simultaneous storage charge and discharge will be to charge first then discharge.
- Auxiliary energy requirements include overnight usage.

Figure 7-26 shows a simplified calculation flow chart of the pilot plant net annual energy model using receiver-only operation.

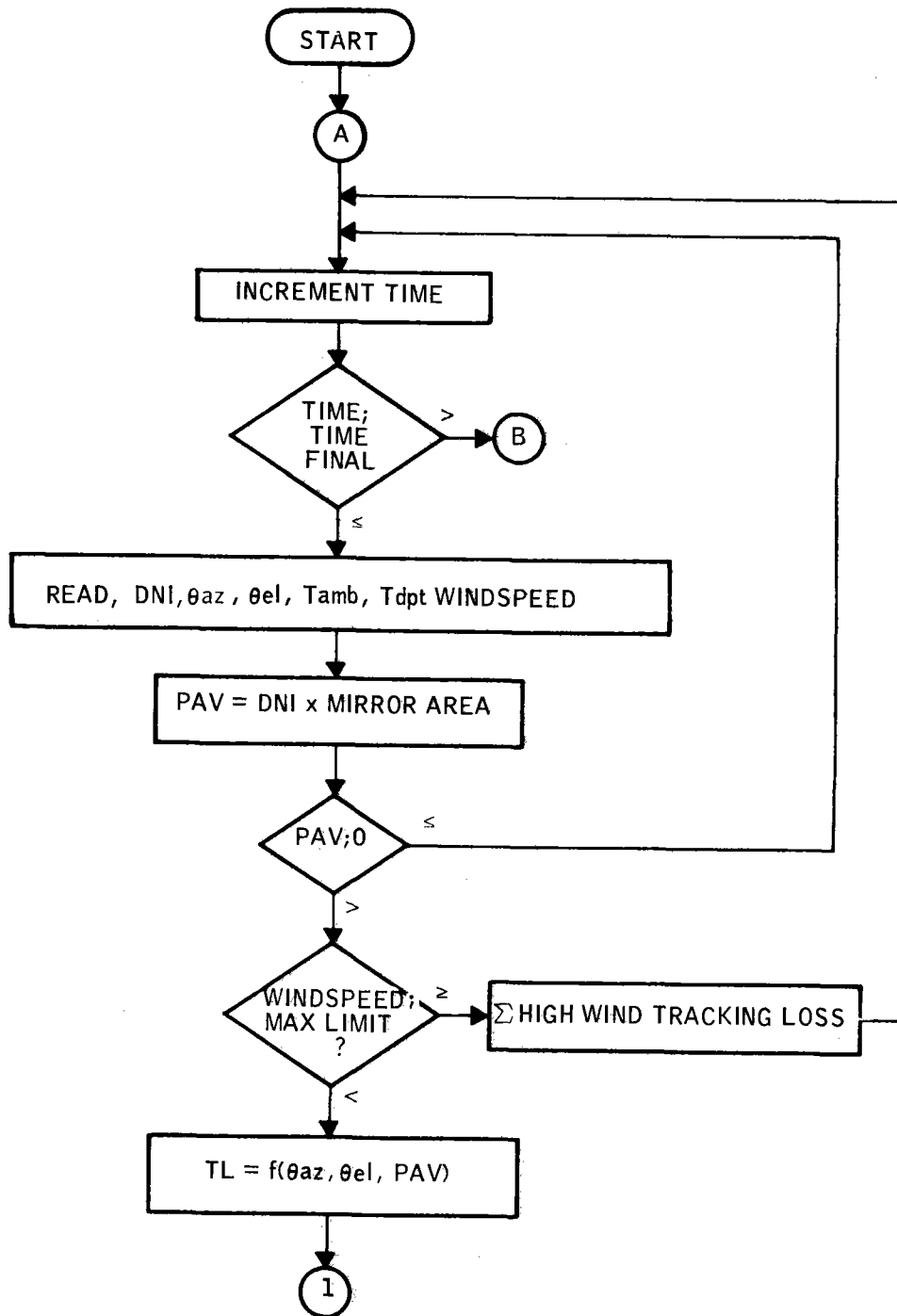


Figure 7-26. Pilot Plant Model Flow Chart

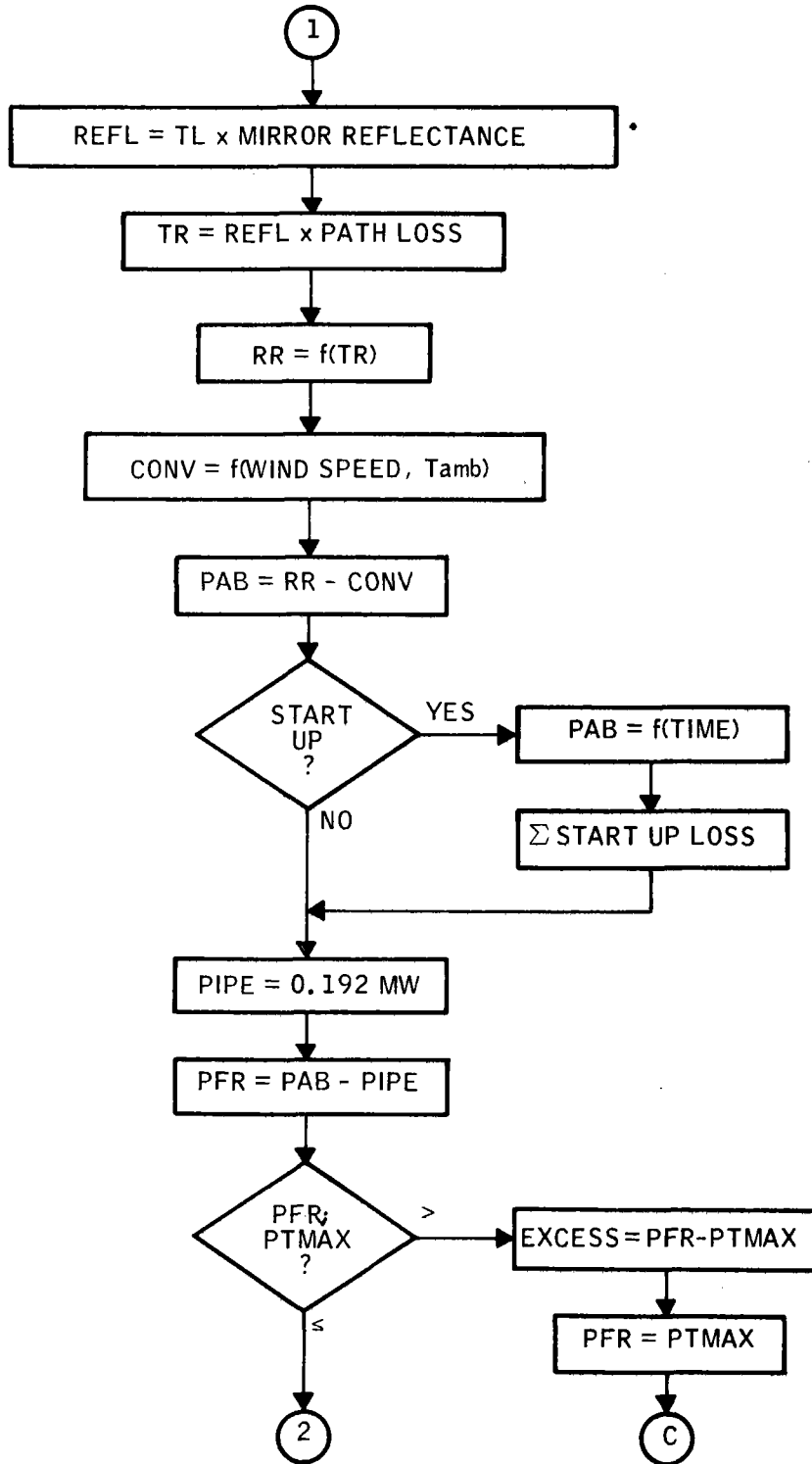


Figure 7-26. Pilot Plant Model Flow Chart
(Continued)

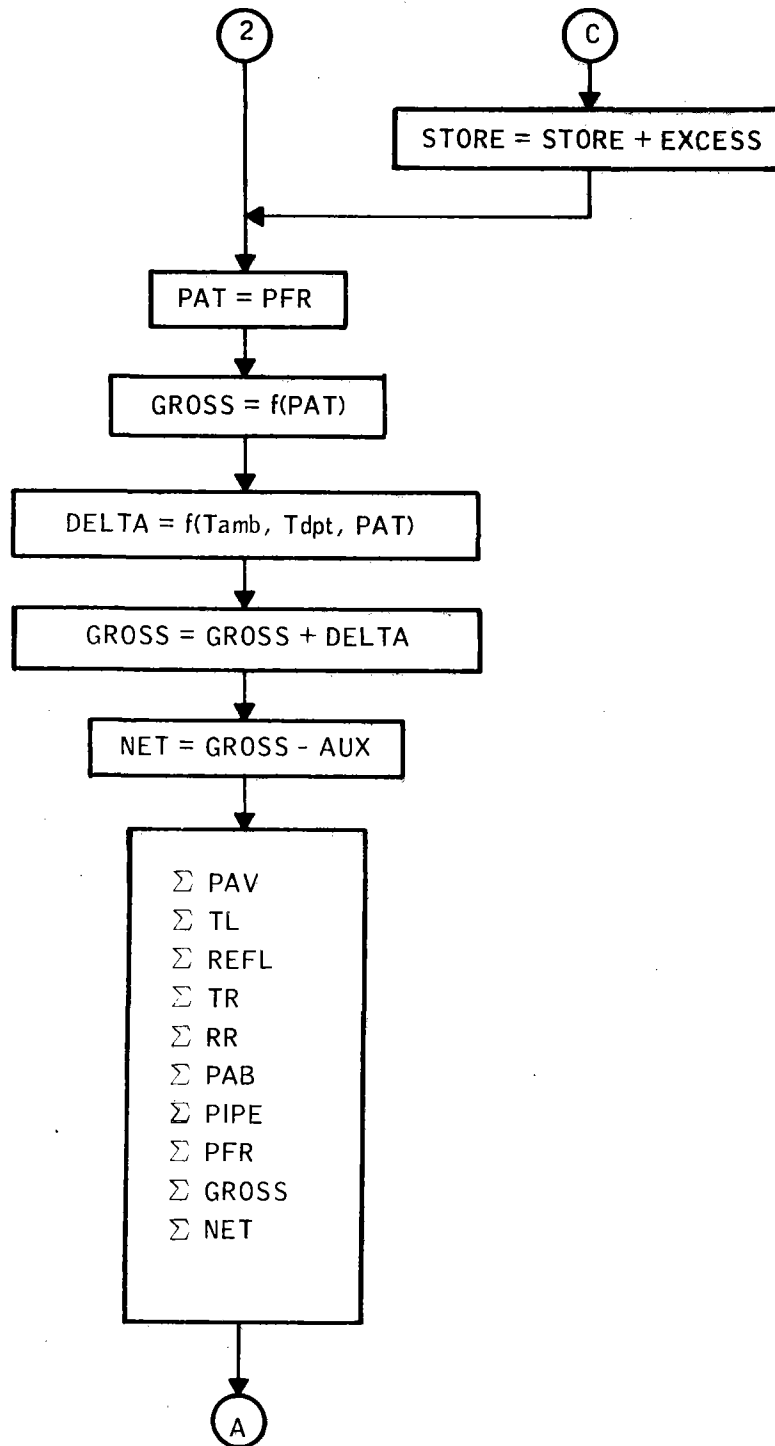
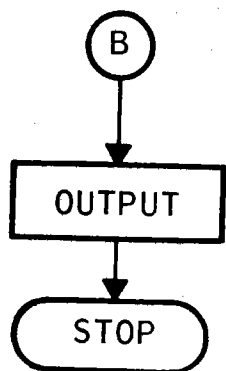


Figure 7-26. Pilot Plant Model Flow Chart
(Continued)



PAV	=	POWER AVAILABLE
TL	=	TRACKING LOSS
REFL	=	REFLECTANCE LOSS
TR	=	TRANSMITTANCE LOSS
RR	=	RERADIATION AND CONDUCTION LOSS
CONV	=	CONVECTION LOSS
PAB	=	POWER ABSORBED
PIPE	=	PIPING THERMAL LOSS
PFR	=	POWER FROM RECEIVER
PAT	=	POWER AT TURBINE
STORE	=	STORAGE ENERGY
GROSS	=	GROSS ELECTRICAL OUTPUT
DELTA	=	BACK PRESSURE CORRECTION
NET	=	NET ELECTRICAL OUTPUT
AUX	=	AUXILIARY POWER

Figure 7-26. Pilot Plant Model Flow Chart (Concluded)

Hourly data are read from the Inyokern weather tape. Insolation values are multiplied by the mirror area to give the total available power each hour. If the wind speed is greater than the allowable limit, the available energy is also designated as high-wind tracking loss. Heliostat tracking losses are calculated from the tracking efficiency which is a function of the sun's azimuth and elevation angles. Mirror reflectance losses and atmospheric attenuation are subtracted from the power left after tracking losses to give the power into the cavity.

The absorbed power is equal to the power into the cavity multiplied by the cavity efficiency, which is a function of the power into the cavity, minus the convection losses, which are a function of the ambient temperature and wind speed.

During morning startup, absorbed power is allocated as startup loss. The power into the turbine is the absorbed power minus any piping thermal losses. Gross electrical output is calculated from the gross turbine efficiency, which is a function of the power into the turbine. The gross electrical output is corrected for variant turbine backpressures as a function of ambient wet-bulb temperature and the power into the turbine. Pilot plant net electrical output power is the gross output minus the auxiliary power losses.

The net annual energy model integrates the hourly power quantities over the year and outputs the integrated energy quantities associated with each of the losses of pilot plant operation. Results obtained from the model, as well as the specific model assumptions, are reported in Section 2 of this volume.

DYNAMIC SIMULATION MODEL

Basically, the pilot plant operates as a time-dependent solar power conversion device for the sun, converting solar into electrical power. From a practical standpoint, the ultimate ability to effectively and efficiently use the pilot plant as a power conversion device depends upon the capability to coordinate the various time-varying plant functions in response to changing environmental or electrical load demand situations. Figure 7-27 illustrates these various power flow paths between the sun and the ultimate users.

As shown, the heliostats act to convert available direct normal solar intensity at the earth's surface into redirected solar power into the receiver cavity. Here, the steam generator acts as the means to convert the redirected solar power into steam power for flow to either of two plant subsystems. First, the primary recipient of steam power is the turbine/generator (part of the electrical generator subsystem), which operates to provide direct conversion to electrical power. Second, steam power can be channeled to the thermal storage subsystem, where steam energy is extracted and stored for later useage. The thermal storage system can, in turn, retrieve this stored energy and reconvert it back to steam power to drive the turbine/generator.

The primary objective of modeling the pilot plant is to account for the interdependent time-varying effects of the various power flows shown in Figure 7-27. Figure 7-28 identifies a number of the more-significant effects which ultimately interact to affect the amount of electrical power that can be derived from available solar intensity at any instant of time.

Starting at the top of the figure, solar power available at the earth's surface obviously varies with time of day and year. In addition, cloud passages and other atmospheric disturbances can degrade or completely interrupt the flow of solar power to the heliostat surfaces.

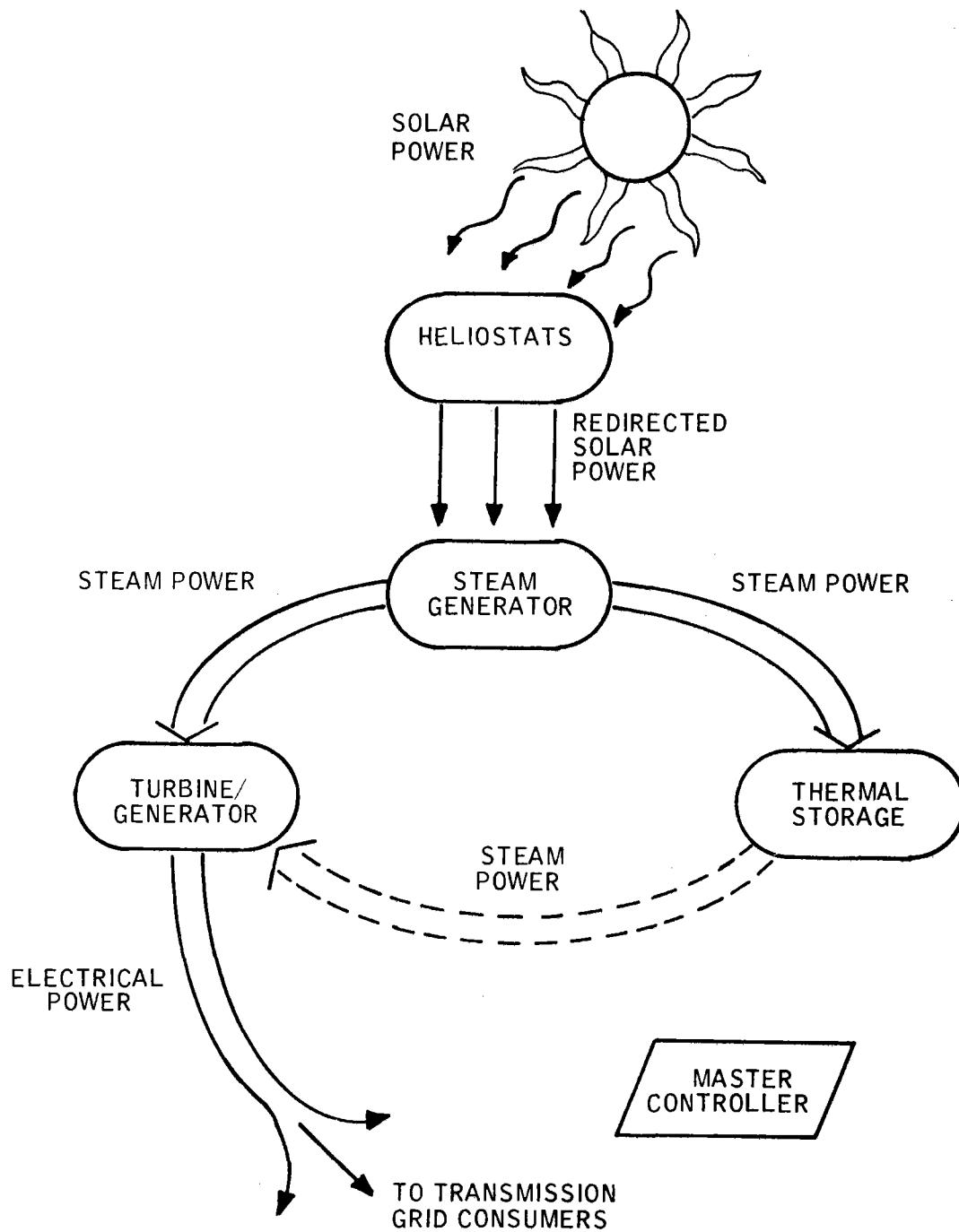


Figure 7-27. Pilot Plant Distribution Flows for Transient Analysis Studies

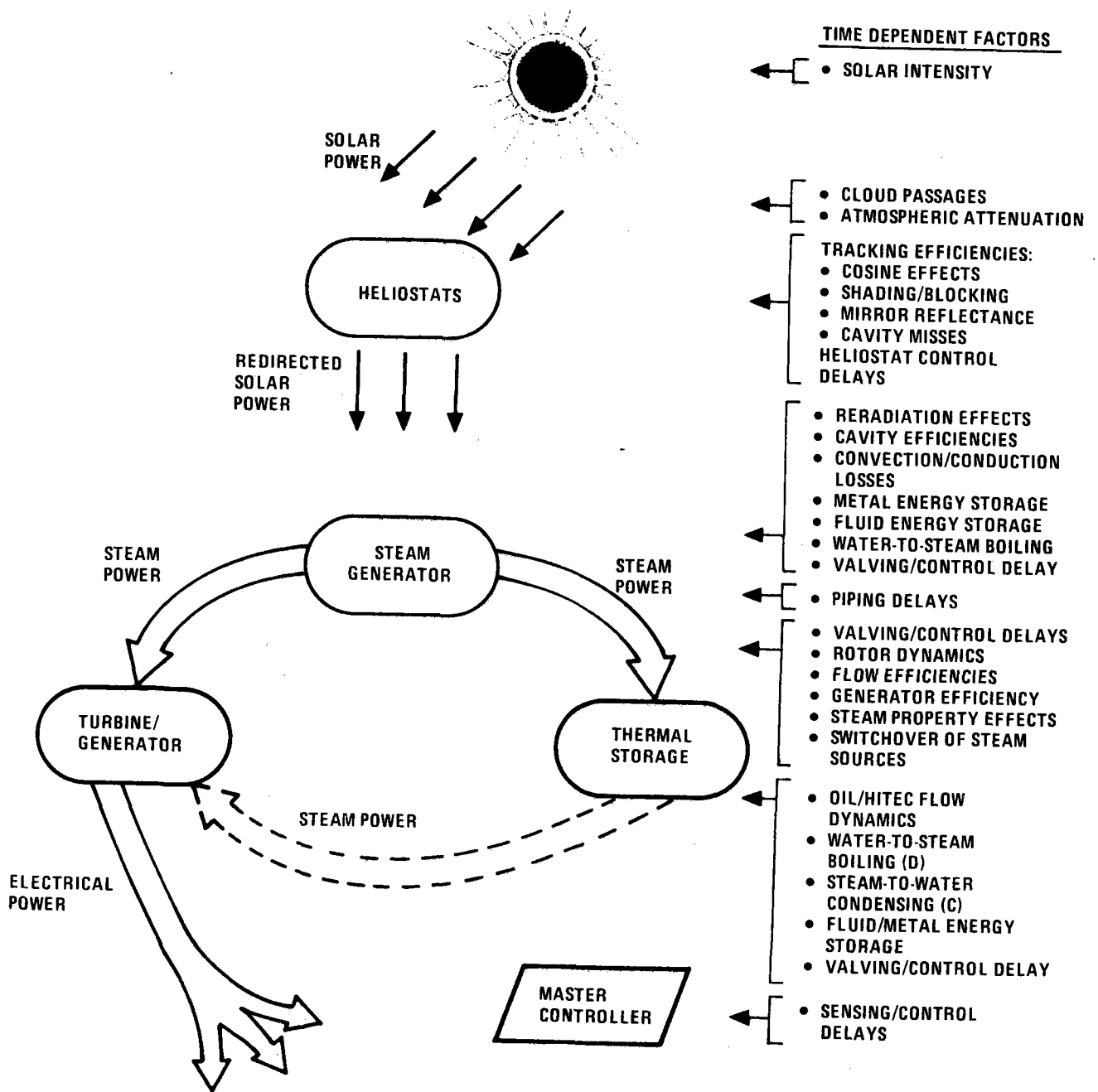


Figure 7-28. Time-Dependent Factors in Pilot Plant Operations

A number of time-dependent tracking efficiency terms effect the amount of redirected solar power entering the receiver cavity. These efficiencies include cosine effects, heliostat shading and blocking, mirror reflectance, and cavity misses. In addition, heliostat control system delays and time-dependent inaccuracies affect the ability of the heliostats to efficiently redirect solar power.

Once the redirected power enters the receiver cavity, most will be incident upon the steam generator active metal surfaces (e. g. , boiler, primary and secondary superheater surfaces). In addition, solar power will be incident upon the cavity ceiling. The total amount of absorbed energy into the steam generator metal surfaces will be the sum of this solar incident power plus reradiated power due to cavity temperature differences and absorptivities, all of which will vary with time.

The absorbed power into the steam generator is used to increase both the fluid and metal energy levels. Eventually, water boiling within the steam generator produces usable steam flow. The dynamics of metal temperatures changing with time, and the fluid (water or steam) energy level changing with time, ultimately affects the quality and amount of steam flowing from the steam generator. Valving and control system dynamics will also significantly affect the ability of the steam generator to produce steam power over time.

After steam exists in the steam generator, it must flow through a substantial length of piping (148 m) from the top of the receiver tower to the turbine/generator at ground level. This long piping distance results in energy loss and pressure drop effects dependent on steam mass flow rate.

Once steam flow has entered the turbine, dynamics of the governor system, throttle valving, rotor dynamics, and condenser exhaust system must be considered as the amount of instantaneous mechanical power which can be

extracted is dependent on all of these factors. In addition, turbine power conversion efficiencies, which vary with flow rate, must be considered. Finally, since the turbine is of the dual-admission type, switchover dynamics (valves opening and closing, etc.) between alternate sources of steam supply must be considered.

The thermal storage system itself represents an energy conversion device with a variety of valves, flow paths, metal masses, and water/steam fluid masses. Dynamic effects of these factors must also be considered in properly evaluating the pilot plant's ability to generate electrical power in response to load demand.

Finally, the master controller represents an overall plant control element which inherently contains control delays. These delays must be examined to determine their compatibility with overall plant response characteristics.

All of these time-dependent effects are incorporated in a performance evaluation tool - a computerized model of the pilot plant called the solar pilot plant dynamic simulation. This simulation is briefly described below.

Solar Pilot Plant Dynamic Simulation Description

The basic solar pilot plant dynamic simulation model is illustrated schematically in Figure 7-29. As indicated, models of each of the principle subsystems have been developed:

- Collector subsystem
- Steam generator subsystem
- Electrical generation subsystem

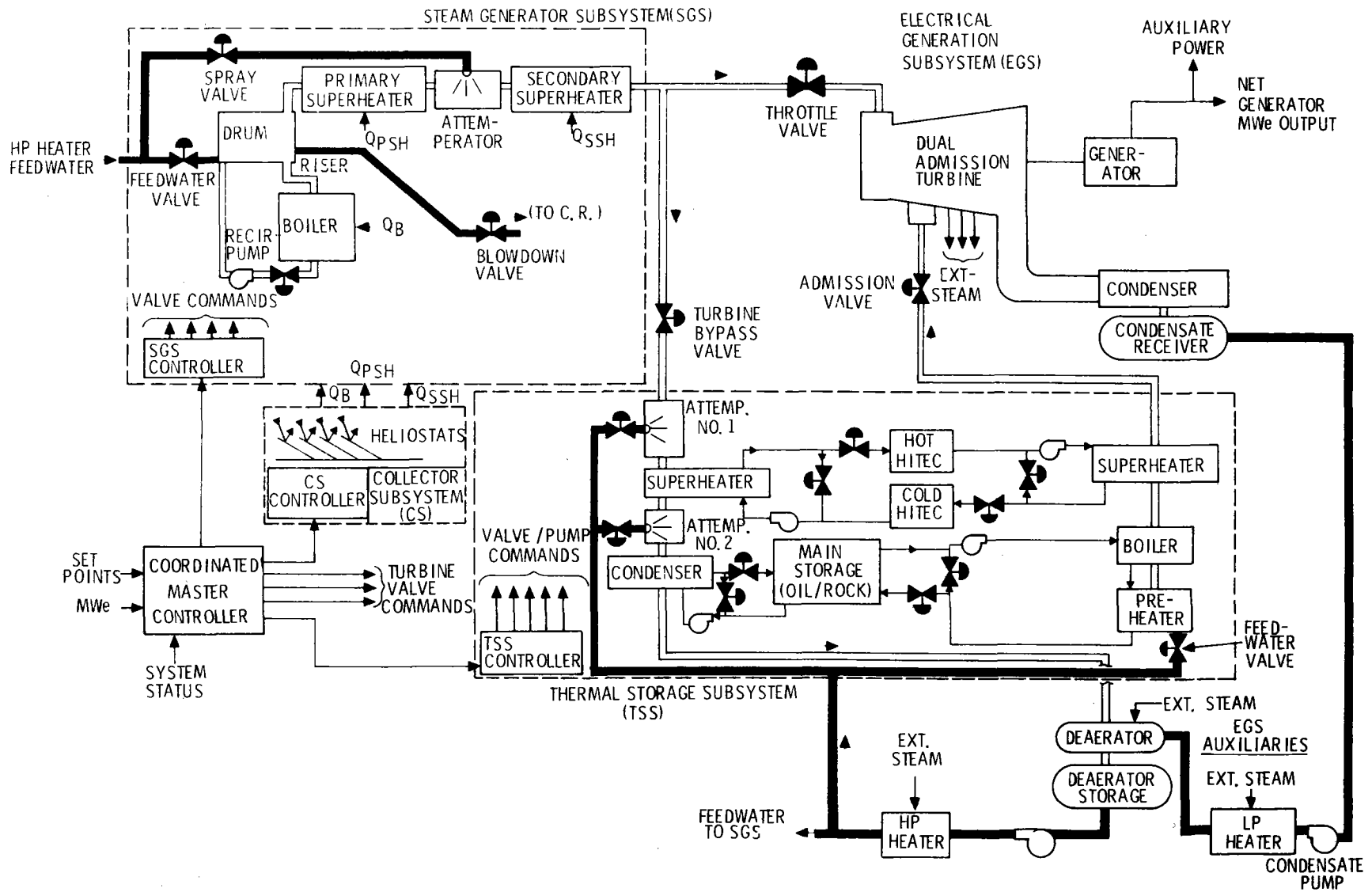


Figure 7-29. Solar Pilot Plant Dynamic Simulation Functional Diagram

- Thermal storage subsystem
- Master controller subsystem

Each of these models may be run individually or collectively as the complete solar pilot plant model.

A detailed description of each of the models is contained in Book 3 of this volume. This description includes all assumptions and derivations of the methods used to generate the models.

The following discussion summarizes the principal features of each of these models to acquaint the reader with the background for better understanding the transient analysis results.

Collector Subsystem Model Overview

Figure 7-30 illustrates the time-dependent computational flow characteristics of the collector subsystem model. As shown, the primary elements of the collector subsystem model are solar intensity generation functions, a simulated cloud model, tracking efficiency corrections, and a cavity reradiation model.

A number of different solar intensity conditions representative of entire days or portions of a day are optionally available on solar pilot plant dynamic simulation data files. Figure 7-31 and 7-32 illustrate four complete days of varying cloud interference patterns typical of Southwestern United States. Generally, the cloud interference becomes increasingly more prevalent for each of the four numbered days. Data are stored on a data file in 10-minute increments for use in the solar pilot plant dynamic simulation. The computer program then interpolates between points.

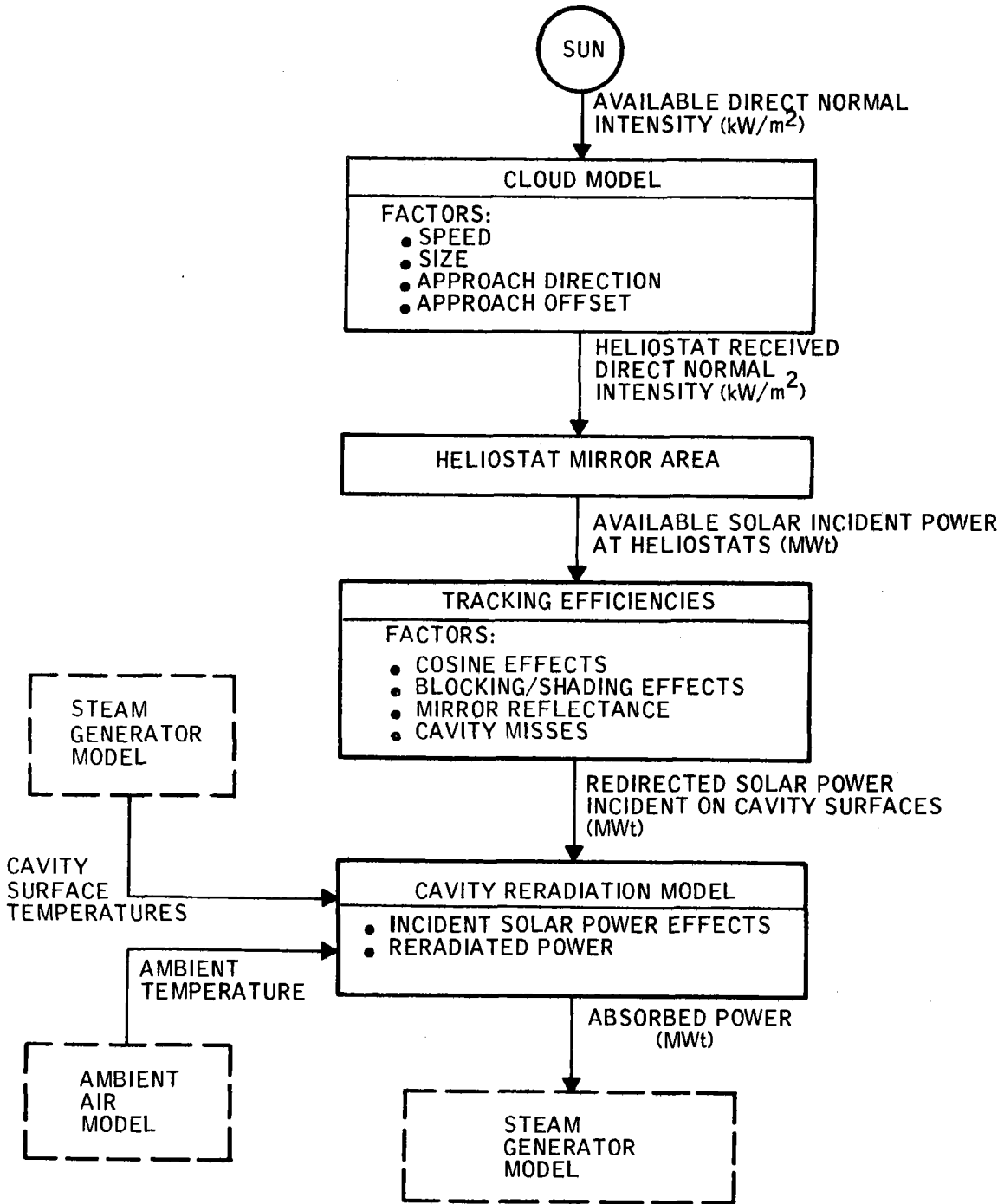
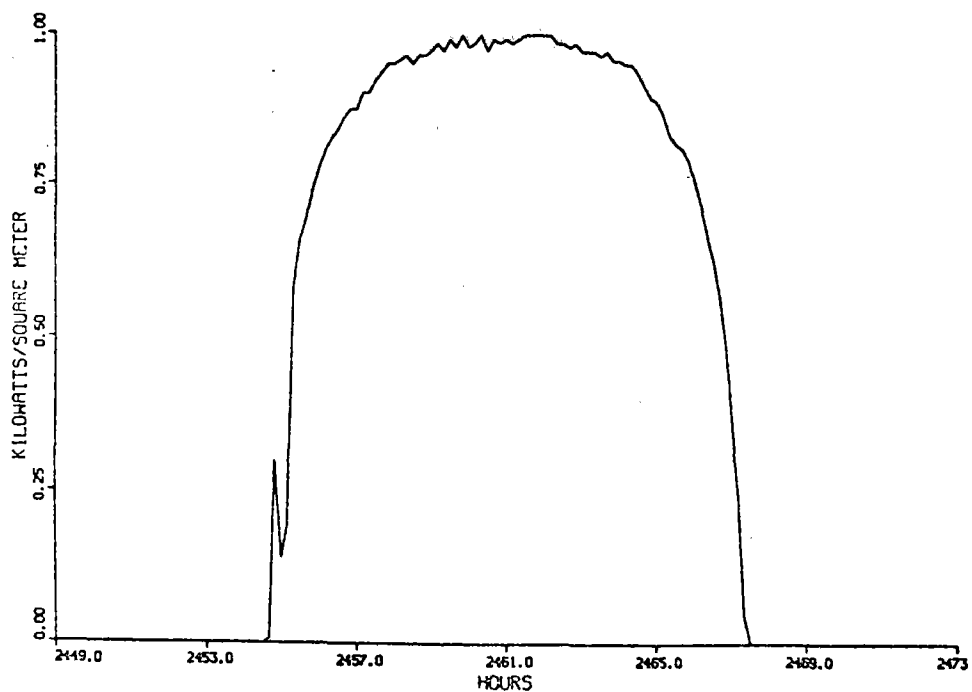
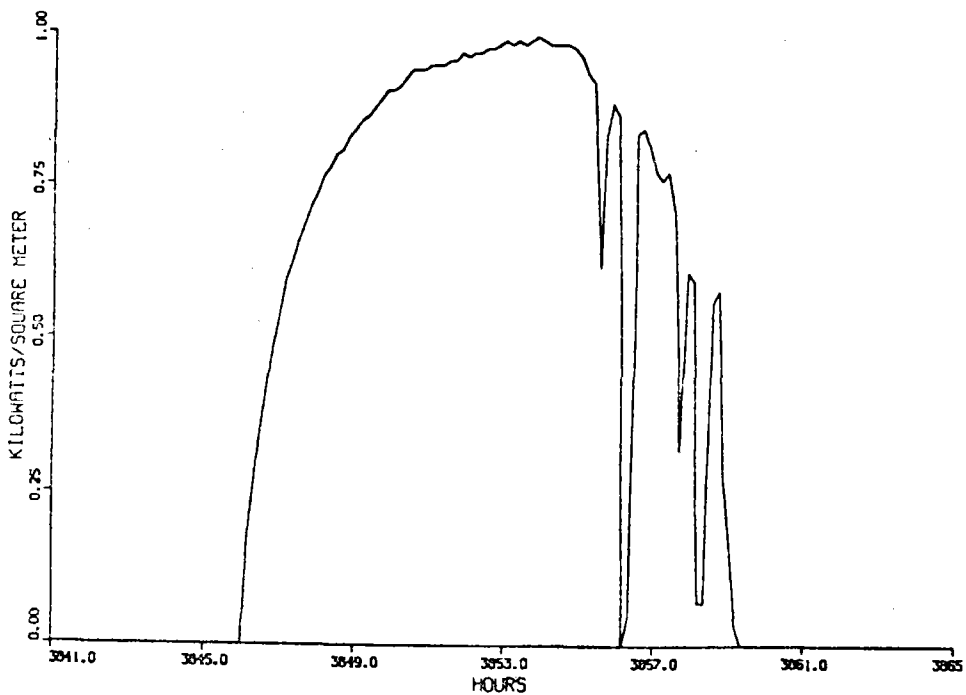


Figure 7-30. Collector Subsystem Model Flow Relationships

7-72



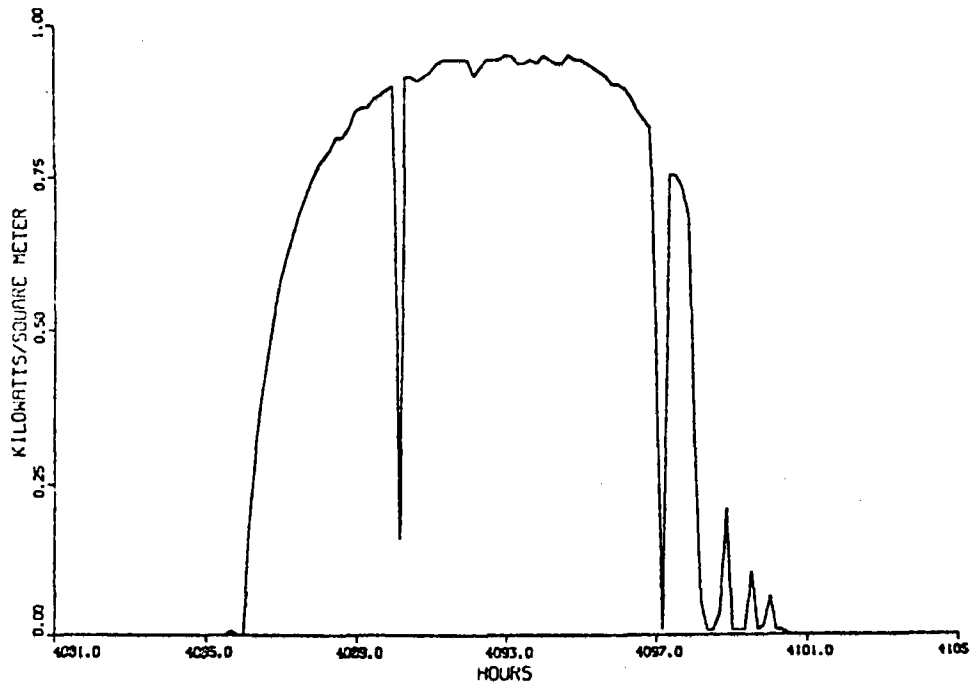
a) Day No. 1



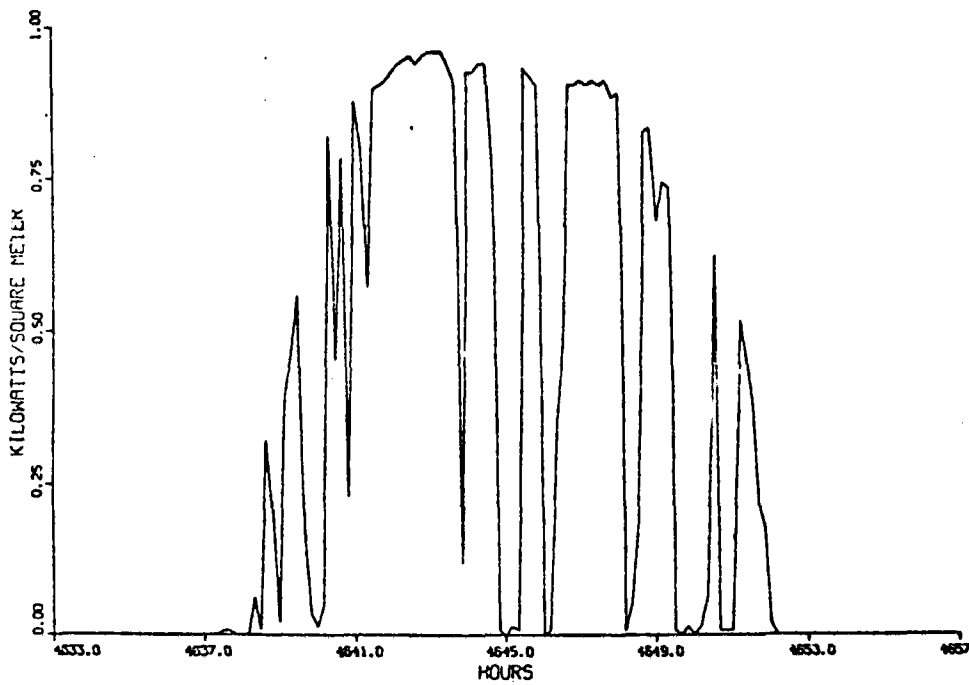
b) Day No. 2

Figure 7-31. Solar Intensity versus Time Plots for Days 1 and 2 for Collector Subsystem Model

7-73



c) Day No. 3



d) Day No. 4

Figure 7-32. Solar Intensity versus Time Plots for Days 3 and 4 for Collector Subsystem Model

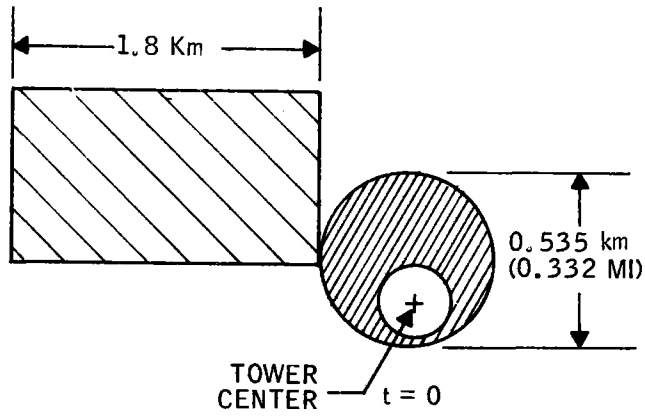
Reductions in solar intensity due to cloud passages are used to represent instantaneous coverages of the entire collector field.

For more detailed investigations of cloud disturbances, another data file is also available. This alternative set of data contains short time intervals of simulated cloud passages for which cloud speed, length, direction of approach, and amount of heliostat field coverage may be varied.

Figure 7-33 illustrates a view from above the field of a simulated rectangular cloud passing through the north half of the collector field moving from the west to east. The simulated cloud is rectangular in shape, 1.8-km (51.12 miles) long, and moving at a speed of 11.4 km/hr (7.1 mph). These size, speed, and approach conditions, as noted in the detailed Collector Subsystem model description in Book 3 of this volume, are believed to be most representative of those occurring in the Southwestern United States.

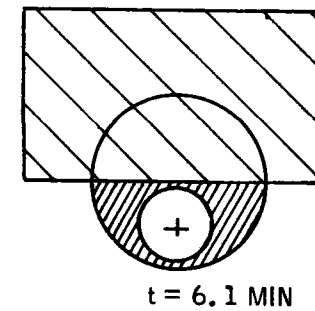
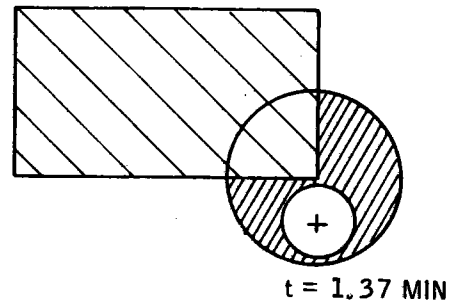
The collector subsystem model portion of the solar pilot plant dynamic simulation contains cloud data with combinations of the following parameter variations:

- Speed: 11.4 km/hr (10.4 ft/sec = 7.1 mph)
21.9 km/hr (20.0 ft/sec = 13.6 mph)
32.9 km/hr (30.0 ft/sec = 20.4 mph)
- Length: 0.67 km (2200 ft = 0.42 mi)
1.8 km (5900 ft = 1.12 mi)
4.88 km (16,000 ft = 3.03 mi)
- Direction of Approach: North, east, south, west
- Field Coverage: Entire field, or either half of field relative to direction of approach



CLOUD

DIRECTION : W → E
 SPEED : 11.4 km/HR (7.1 MPH)
 LENGTH: 1.8 km (1.12 MI)
 COVERAGE: NORTH 1/2



40703-II

7-75

Figure 7-33. Typical Scenario for Transient Analysis Studies

As shown in Figure 7-30, the collector subsystem model also incorporates time-dependent tracking efficiency functions to modulate the amount of redirected solar power into the receiver cavity. These efficiency computations include cosine effects, blocking and shading effects of individual heliostats, mirror reflectance, and cavity misses. For the results presented in this report, a constant mirror reflectance of 0.9 was assumed.

To compute the amount of time-dependent steam generator absorbed power into the respective metal surfaces, a transient reradiation model was developed. The basis for this model is detailed in the ray trace code program based upon Monte-Carlo statistical evaluation of cavity performance. The transient reradiation model operates more efficiently from a computer time requirement than the ray trace code, and is therefore more conducive to economic computer plant performance evaluation.

Steam Generator Subsystem Model Overview

The steam generator subsystem simulates the solar pilot plant steam generator. Figure 7-34 illustrates the principal functional elements of the steam generator subsystem. Its principle of operation is described as follows.

High-pressure saturated feedwater enters the drum through the feedwater valve. The drum, containing saturated water and steam, provides the means to separate dry steam from the water. Saturated water is circulated in the drum/boiler portion of the steam generator subsystem with a recirculating pump. Water flows from the bottom of the drum through downcomer lines, through the recirculating pump and valve, and into the boiler section. Here, the water is heated by radiant energy.

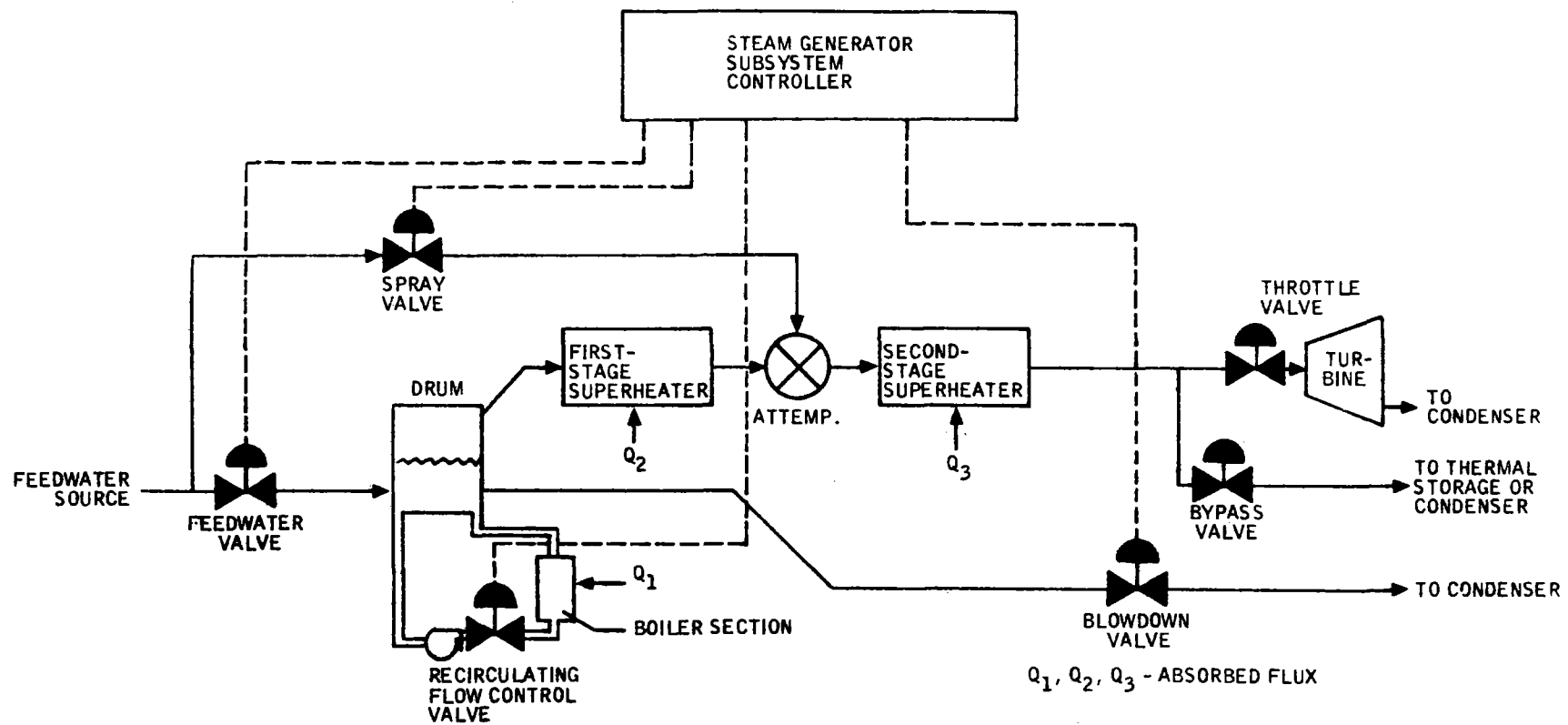


Figure 7-34. Steam Generator Subsystem Concept Model Elements

The mixture of water/vapor then returns to the drum through risers. Dry steam, obtained through a cyclone separator in the drum, then flows to a first-stage (or primary) superheater section. Here, additional radiant energy is added to superheat the steam. Steam exits the primary superheater, is mixed with feedwater (for temperature control) in the attemperator, and enters the second-stage (or secondary) superheater for further superheating. At the exit point of the secondary superheater, the superheated steam has been approximately conditioned for flow to either the turbine or thermal storage.

The steam generator subsystem uses a three-node representation (boiler, primary, and secondary superheaters) of the metal heat-absorbing surfaces. Consequently, absorbed heat flux on each of the three generator surfaces is averaged azimuthally first, and then with generator height. Complete steam property values over the range of steam generator subsystem operating conditions (i. e. , cold startup to design operating conditions) is incorporated. The model provides for boiler tube boiling onset dynamics, and tracks steam quality parameters throughout the subsystem.

Figure 7-35 illustrates the steam generator subsystem control subsystem. Steam flow existing in the secondary superheater is controlled by outlet pressure. Feedwater flow is controlled by a three-element controller (drum level, steam outlet flow, feedwater flow). Temperature measurement at the secondary superheater exit is used to control the attemperator feedwater flow. Proportional-plus-integral control is used on all control elements. Bias hand-control valves are provided for all valving.

At the time the performance results were generated utilizing the solar pilot plant dynamic simulation, model parameter values for the pilot plant steam generator design were unavailable. Consequently, parameter values reflecting those of the SRE (Subsystem Research Experiment) were used, with the radiant heat inputs and inlet/output mass flow variables scaled to

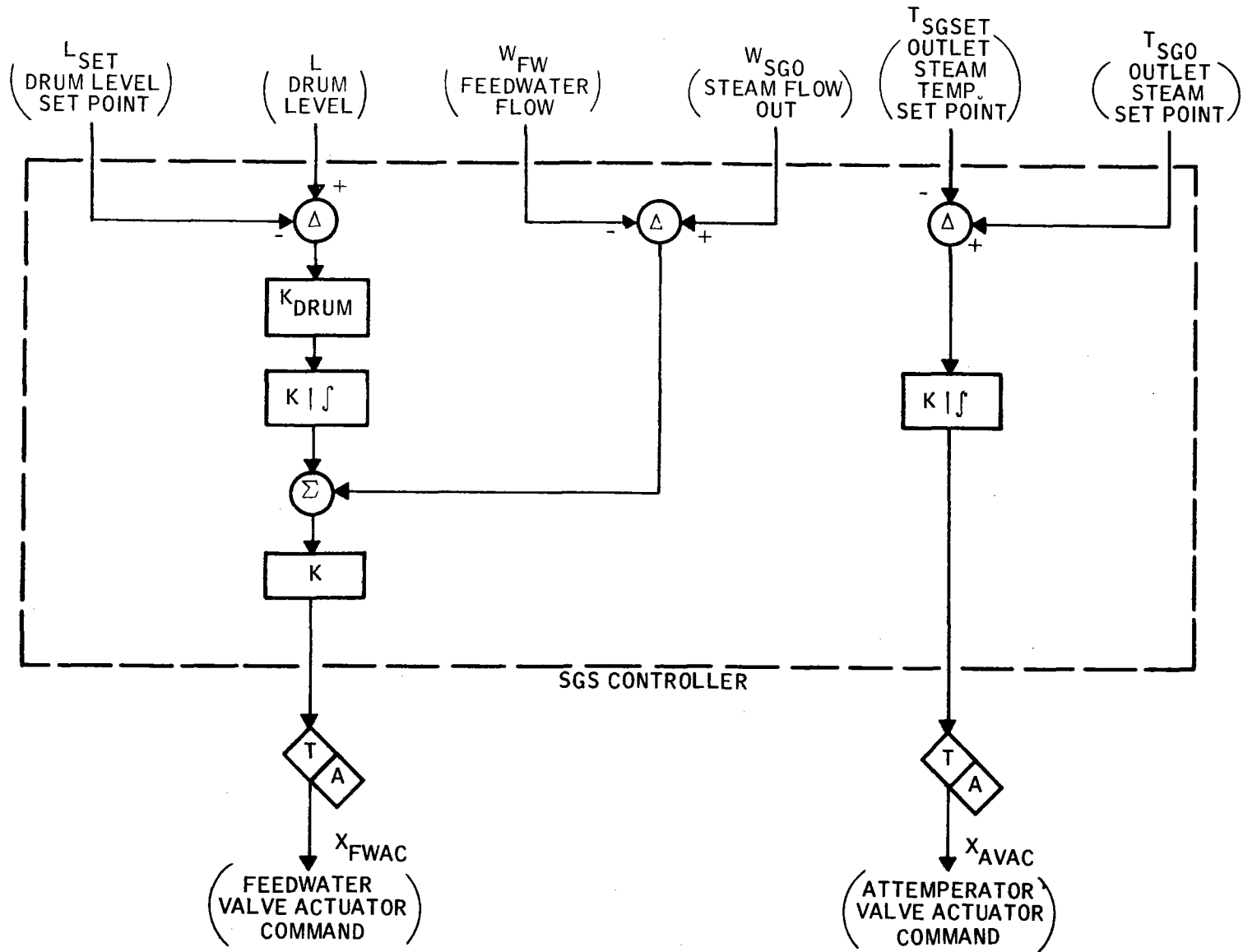


Figure 7-35. Steam Generator Subsystem Controller Block Diagram

reflect the respective differences in rated outputs. Since the SRE unit was designed to be dynamically similar to the pilot plant steam generator, this method of scaling is judged appropriate and should yield representative time-varying response characteristics.

Electrical Power Generation Subsystem Model Overview

Figure 7-36 illustrates the overall Electrical Power Generation Subsystem model.

The turbine model simulates the dual-admission feature of the solar pilot plant system. Receiver steam passes through a main stop valve, then a governor (or throttle) valve, to provide steam power to the turbine. The governor valve controls rotor speed and responds to load demand changes (from the coordinated master controller) to provide the correct governor valve area opening.

Similarly, steam from thermal storage may be admitted through a downstream admission port. An admission stop valve and throttle valve are provided for steam flow control. In this case, rotor speed and load are also controlled by modulating the admission valve opening area. The turbine may operate either from receiver or storage steam, or from combination of steam flow from these two sources.

For both the admission and throttle valving systems, servomotor dynamics are incorporated. Most importantly, this includes response time lags, and rate and position limits of the valve.

Within the turbine, time-delay effects of steam chest mass flow storage and rotor inertia are modeled. Efficiency relationships relating electrical output power to thermodynamic power input are incorporated as functions of

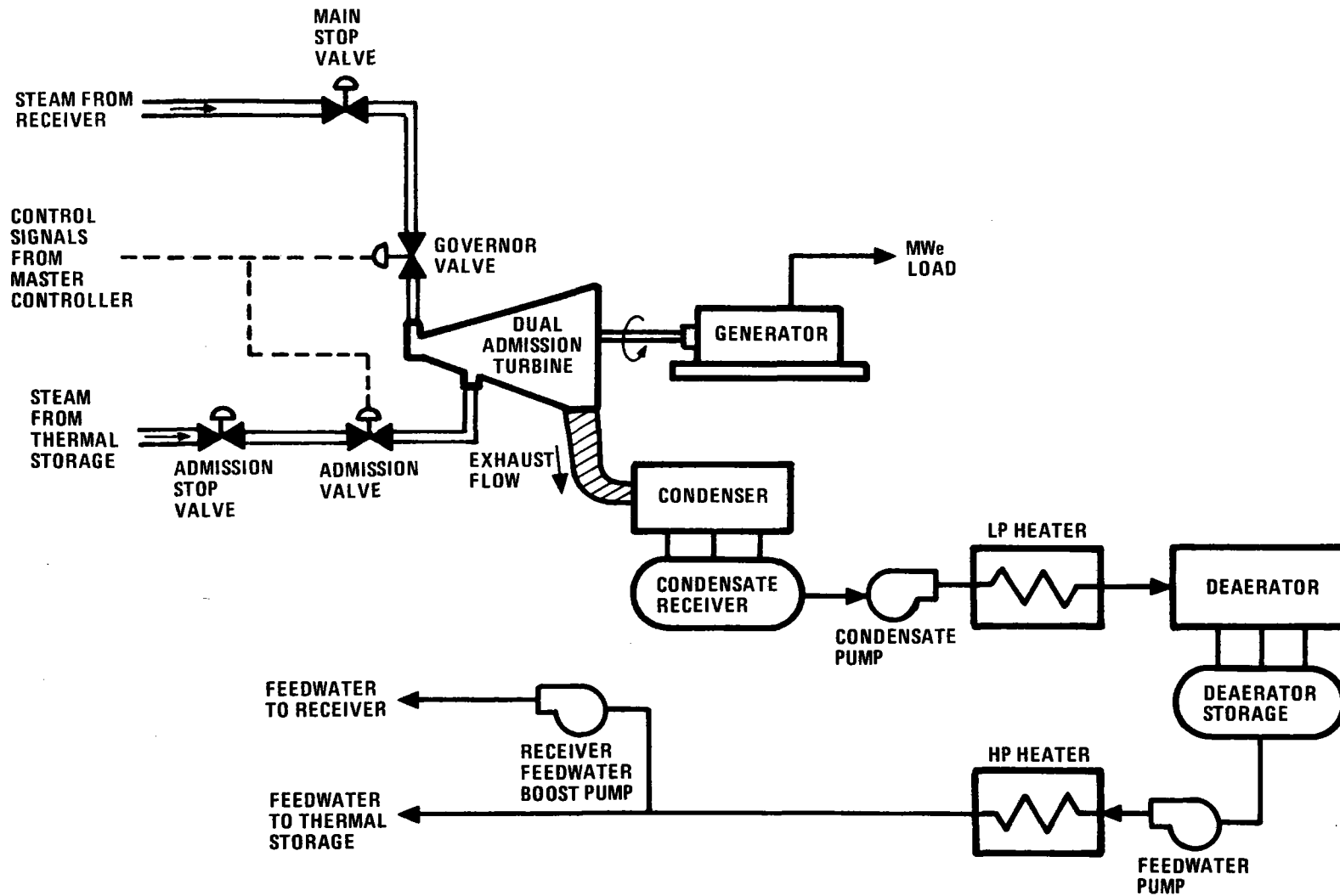


Figure 7-36. Functional Schematic of Electrical Generation Subsystem

steam flow. These curves account for differences in relative efficiencies between receiver, admission, and admission/receiver steam flow. Variations in incoming and exhaust steam enthalpies are also taken into account in the load calculation.

Electrical load characteristics, as derived from basic synchronous generator equations, are incorporated. These equations provide the information necessary to calculate electrical load torque angles as functions of power factor and load.

The steady-state characteristics of the feedwater temperature to turbine steam flow are incorporated in the simulation. In addition, time-lag dynamics representative of the relative responsibilities of the various heat-exchanging devices in the feedwater return circuits have been incorporated.

Finally, the Electrical Power Generation Subsystem model includes all significant piping dynamics between subsystems which interface with the electrical generation subsystem. This includes the steam lines from the receiver and storage, and feedwater return lines to the receiver.

Thermal Storage Subsystem Model Overview

The thermal storage subsystem is modeled using a multi-node representation of the preheater, boiler, and superheater portions of storage discharge. Figure 7-37 shows the discharge design configuration upon which the model is based. Due to lack of time, an equivalent model for the attemperator, desuperheater, and condenser charge-side portions of the storage subsystem were not developed. Instead, a simplified lag function believed representative of the charge steam flow buildup was used.

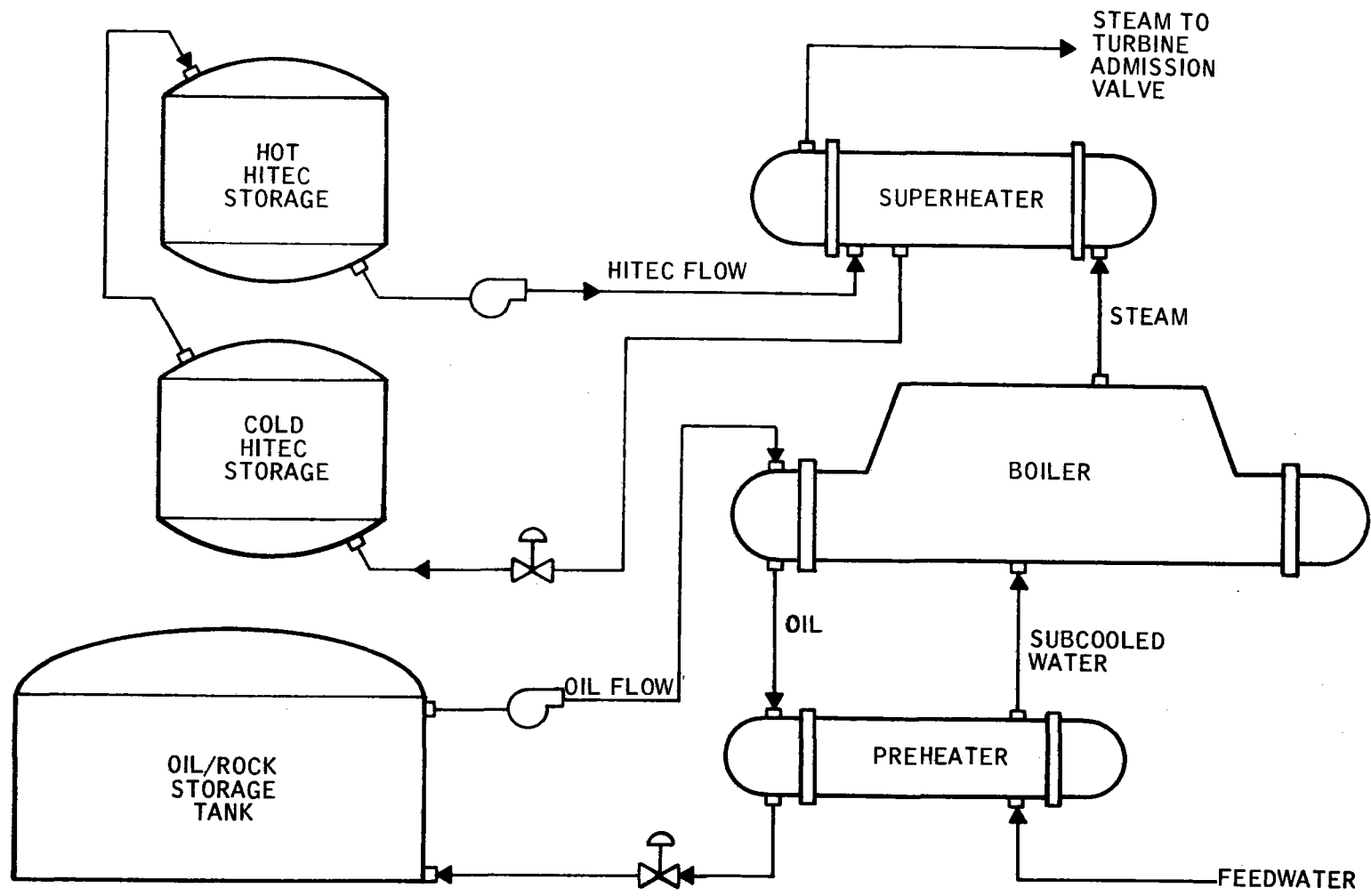


Figure 7-37. Thermal Storage Subsystem Discharge Configuration

The storage model contains all parameter data relative to metal masses, heat-exchanger surface areas, and heat-transfer coefficients, fluid volumes, valve dynamic, and storage control system. Upon command from the master controller, the storage system model is capable of delivering or accepting steam flow with dynamics similar to those anticipated from the storage hardware.

Master Controller Subsystem Model Overview

The model for the coordinated master controller subsystem is shown in Figure 7-38. The principal of operation has been previously described in Section 4, "Operation, Instrumentation, and Control."

One way to view the role of the master controller subsystem in the pilot plant operation is to use the power flow method of Figure 7-39. Fundamentally, the master controller subsystem responds to load demand signals derived from load dispatcher coordination. The master controller subsystem then determines the best means to satisfy this load demand through combinations of steam generator or storage steam.

Steam flow production capability of the steam generator will be dependent in time on the amount of incoming absorbed power. If the entire amount of steam flow production is required to satisfy load demand, steam flow will be admitted to the turbine on a first-priority basis. If an excess production capability exists, the steam generator pressure will begin to rise, indicating a buildup of thermodynamic energy within the device. The master controller subsystem senses this pressure rise and responds by admitting steam to storage in a quantity sufficient to bring the pressure back to nominal.

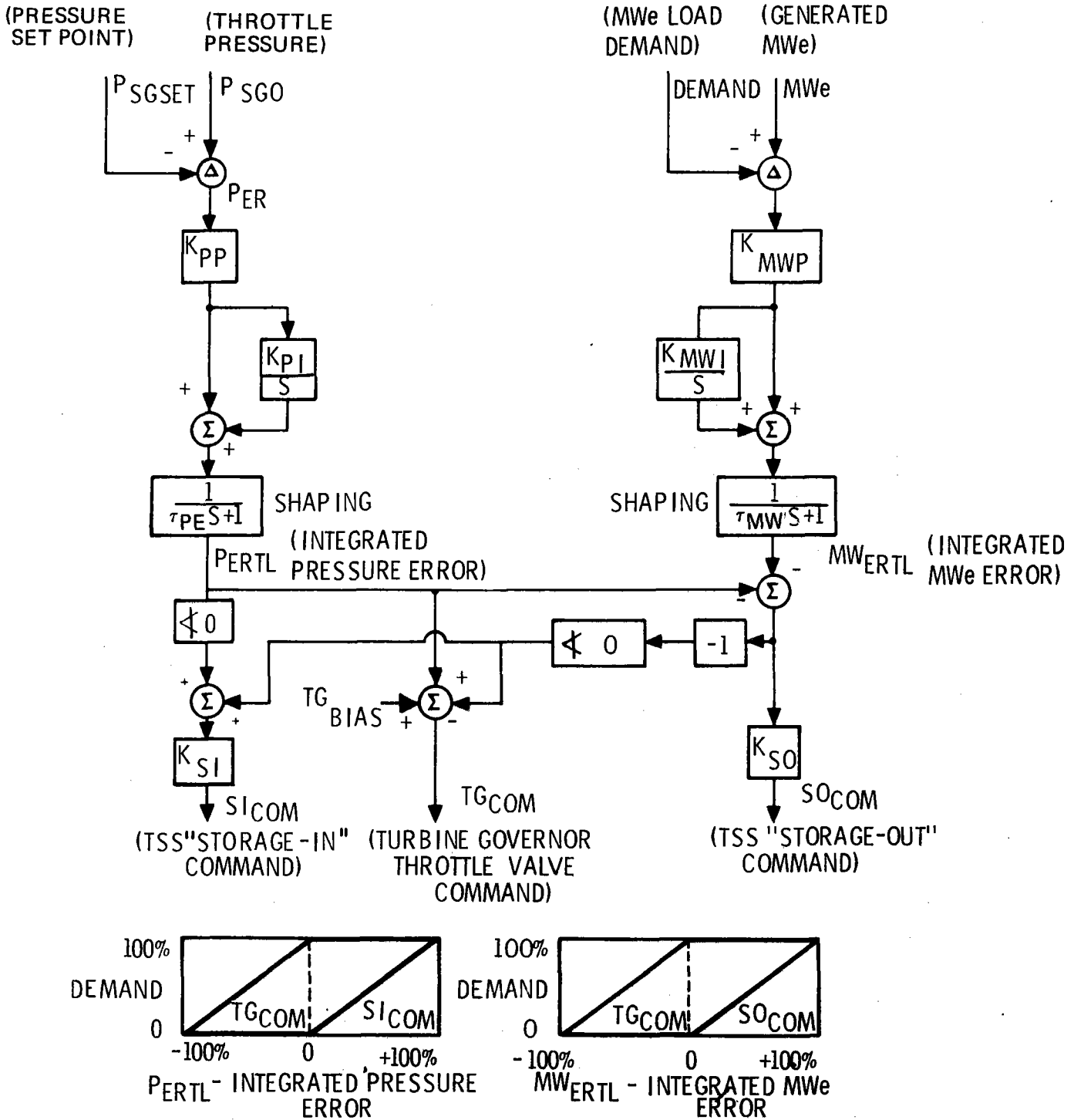


Figure 7-38. Master Control Subsystem Block Diagram

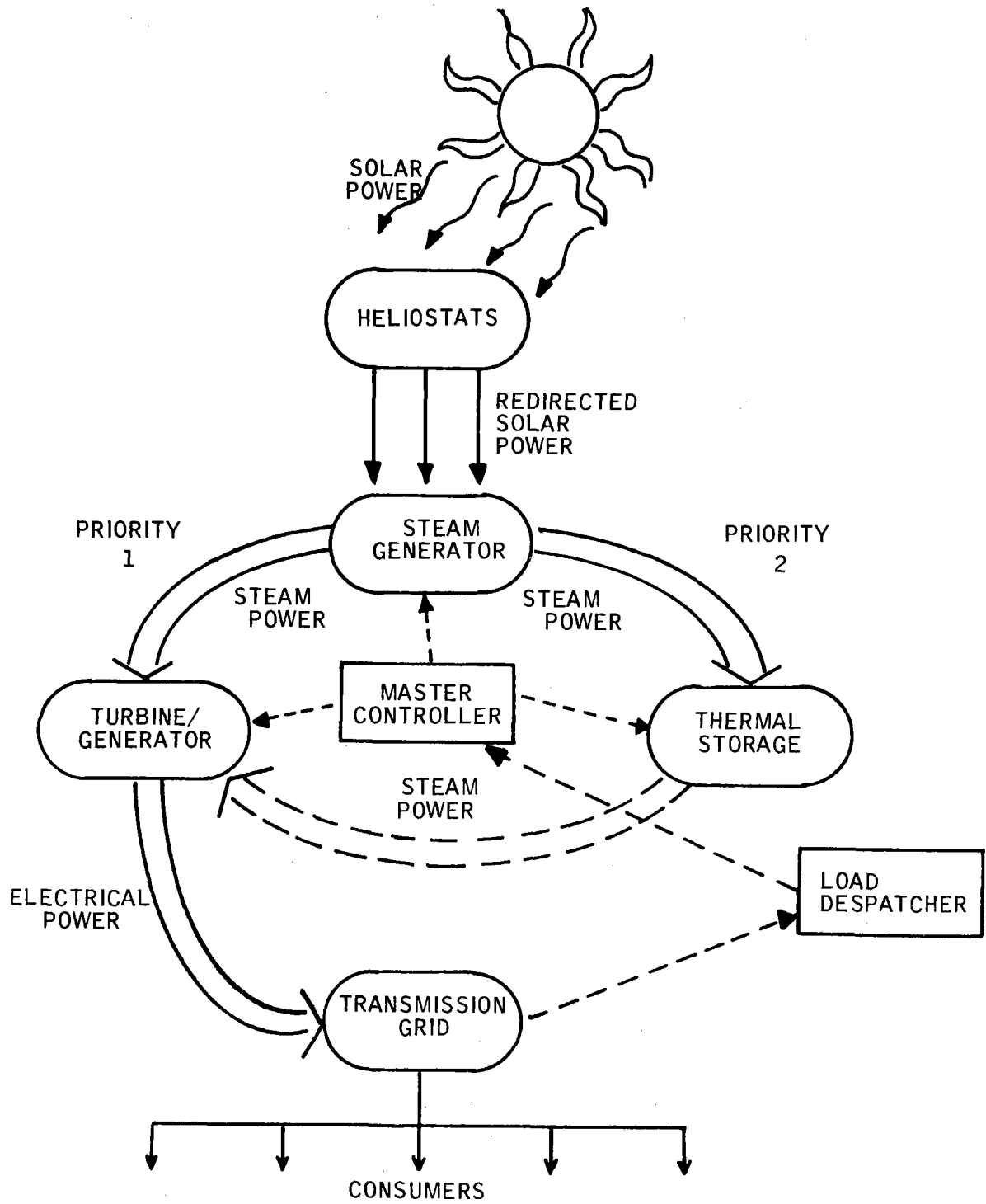


Figure 7-39. Power Flows Under Master Controller Direction

On the other hand, if the steam generator pressure begins to fall below its nominal set point, the master controller subsystem will respond by reducing the amount of steam flow required from the steam generator. This reduction in flow will occur by the master controller subsystem first reducing flow to storage, and then reducing the flow to the turbine generator. Since this reduction in steam flow to the turbine also causes electrical power generation to fall below the load demand level, the master controller subsystem must also then command the thermal storage system to begin admitting steam to the admission port of the turbine. Consequently, the master controller subsystem acts to maintain rated pressure of the steam generator under all load demand and incoming absorbed power conditions.

APPENDIX A

IDENTIFICATION OF DATA

Information requested by Sandia Corporation and included in Volume II, System Descriptions and System Analysis, is identified and the reference location within the text is given in the following:

A. Plant Design Characteristics:

1. Schematics and flow diagrams for all modes of plant operation - Appendix B
2. Physical characteristics - Appendix B
3. Design point and annual energy balance - Section 2
4. Nominal subsystem characteristics - Appendix B
5. Subsystem efficiencies - Design point and annual energy calculations - Section 2
6. Auxiliary power requirements - Appendix B

B. Design rationale and evolution - Section 3

C. Net annual energy calculations - Section 2 and Section 7

D. Transient plant analysis and models - Section 4 and Volume II, Book 3

E. Plant control system - Section 2 and Volume IV

F. Plant safety considerations - Section 5

B-1

APPENDIX B
SYSTEM CHARACTERISTICS
AND REQUIREMENT COMPLIANCE

CONTENTS

SECTION 1	SPECIFICATION AND REQUIREMENT IDENTIFICATION
SECTION 2	SOLAR PILOT PLANT SYSTEM
SECTION 3	COLLECTOR SUBSYSTEM
SECTION 4	RECEIVER SUBSYSTEM
SECTION 5	THERMAL STORAGE SUBSYSTEM
SECTION 6	ELECTRICAL GENERATION SUBSYSTEM

SECTION 1

SPECIFICATION AND REQUIREMENT IDENTIFICATION

This appendix contains the basic requirements which were used to design the pilot and commercial solar plants. Distinction has been made between ERDA-specified requirements and internally-derived requirements by noting in the appropriate specification column of each subsystem characteristic the ERDA Document in which the requirement was specified.

<u>Code</u>	<u>Identification</u>
A Annex 1,	Customer Specification, RFP
B Appendix 1,	Customer Specification RFP
C Appendix 2,	Customer Specification, RFP
D Appendix 3,	Customer Specification, RFP
E Appendix 4,	Customer Specification, RFP
F ERDA Letter, 11-3-76,	Pilot Plant Site Parameters
G Skinrod TWX, 12-24-76,	Pilot Plant Site Parameters
H Skinrod Letter, 1-14-77,	Site Parameter Clarifications
I Skinrod Letter, 11-8-76,	Specification Clarification
J Skinrod Letter, 12-15-76,	Cost and Performance Data
K Brune Letter, 2-3-77,	Cost and Performance Data Changes

B-5

SECTION 2
SOLAR PILOT PLANT SYSTEM

40703-II

SYSTEM CHARACTERISTICS

Item No.	Characteristic	Spec (1)		Current Baseline		Spec. Var.
		PP	Com.	Pilot Plant	Commercial	
1	Basic Performance	I	J	10 MW(e) net output at 12-21, 2 p. m., rec. only. 7 MW(e) net output storage only. 3 hr storage after 20 hr hold. .95 kw/m ² insolation. 2 3°C wet bulb, 28°C dry bulb. Wet cooling.	100 MW(e) net output at 3-21 noon, rec. only. 210 MW(e) net output storage only. 3 hrs storage after 20 hrs hold. .95 kw/m ² insolation. 23°C wet bulb. 28°C dry bulb. Wet cooling.	
2	Start-up Time - Cold	I		180 min. from sun rise and 21°C (70°F) to full rated power. 131 min. to power available to grid.	Same as PP	
	Diurnal	I		180 min. from sun rise and 21°C (70°F) to full rated power Note (2) 131 min. to power available to grid.	Same as PP	
3	Emergency Shutdown	I		Instantaneous	Same as PP	
4	Dynamic Load Variation			4% min. ramp and/or ±10% instantaneous step between 20% and 100% load	Same as PP	
5	Annual Net Output	I		21,350 MW h	TBD	
6	Environmental Wind	G	G	Operating - 3.5 M/S at 10 M alt. $V_h = V_{ref} (h/h_{ref})^{.15}$	Same as PP	

NOTE: (1) See Section 1 for specification and requirement source identification.

(2) The increased Electrical Generation developed during diurnal startup over a cold start-up is approximately 6.4 MWh.

SYSTEM CHARACTERISTICS

Item No.	Characteristic	Spec (1)		Current Baseline		Spec. Var.
		PP	Com.	Pilot Plant	Commercial	
7	Temperature	G	G	Survival w/o damage 40 M/S (Ref Alt.) Operating -30°C to +50°C (-20°F to 120°F) Performance, TBD TBD	Same as PP Same as PP TBD TBD	

NOTE: (1) See Section 1 for specification and requirement source identification.

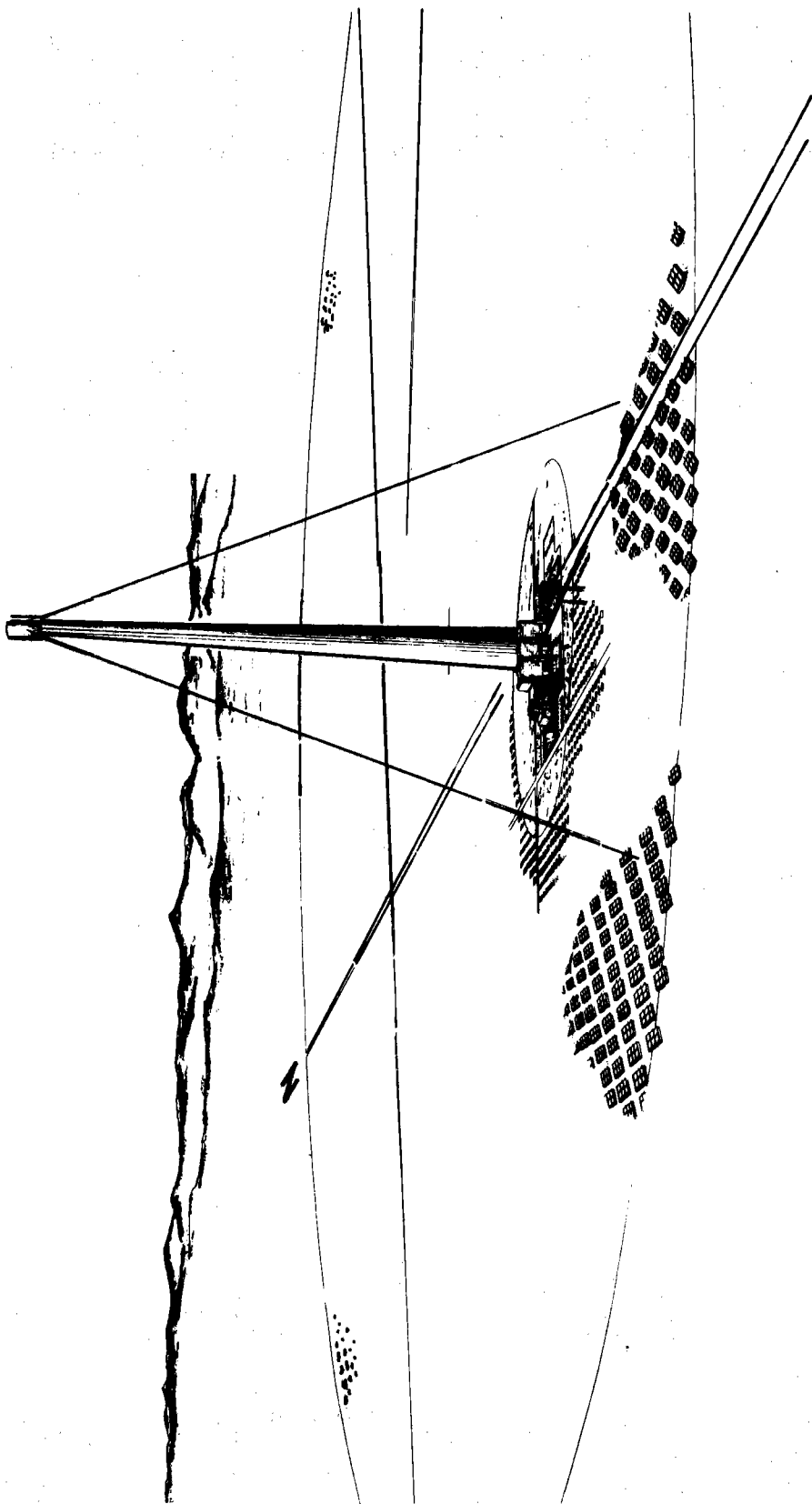
SYSTEM CHARACTERISTICS

Item No.	Characteristic	Spec (1)		Current Baseline		Spec. Var.
		PP	Com.	Pilot Plant	Commercial	
1	Environment (Cont)					
	Humidity	I		Operation with no permanent degradation.	Same as PP	
	Dust	I		Operation with no permanent degradation.	Same as PP	
	Hail	G		Survival w/o damage - 25mm dia at 23 M/s.	Same as PP	
	Lightning	I		Survival with repairable damage.	Same as PP	
	Earthquake	F		UBC zone 3, NRC Reg. Guide 1.60. 0.25 g horizontal, 0.25 g vertical SSE.	Same as PP	
	Rain	G H		100mm annual, 75mm max. 24 hr rate operation with no permanent damage.	Same as PP	
	Snow	G		Design snow load - 250 Pa (5.0 psf). Operation with no permanent damage.	Same as PP	
2	Peak Auxiliary Power			2.3 MW(e)**	18.0 MW(e)**	
3	Site Location	H		Barstow, California	TBD	

NOTE: (1) See Section 1 for specification and requirement source identification.

**Simultaneous storage and receiver.

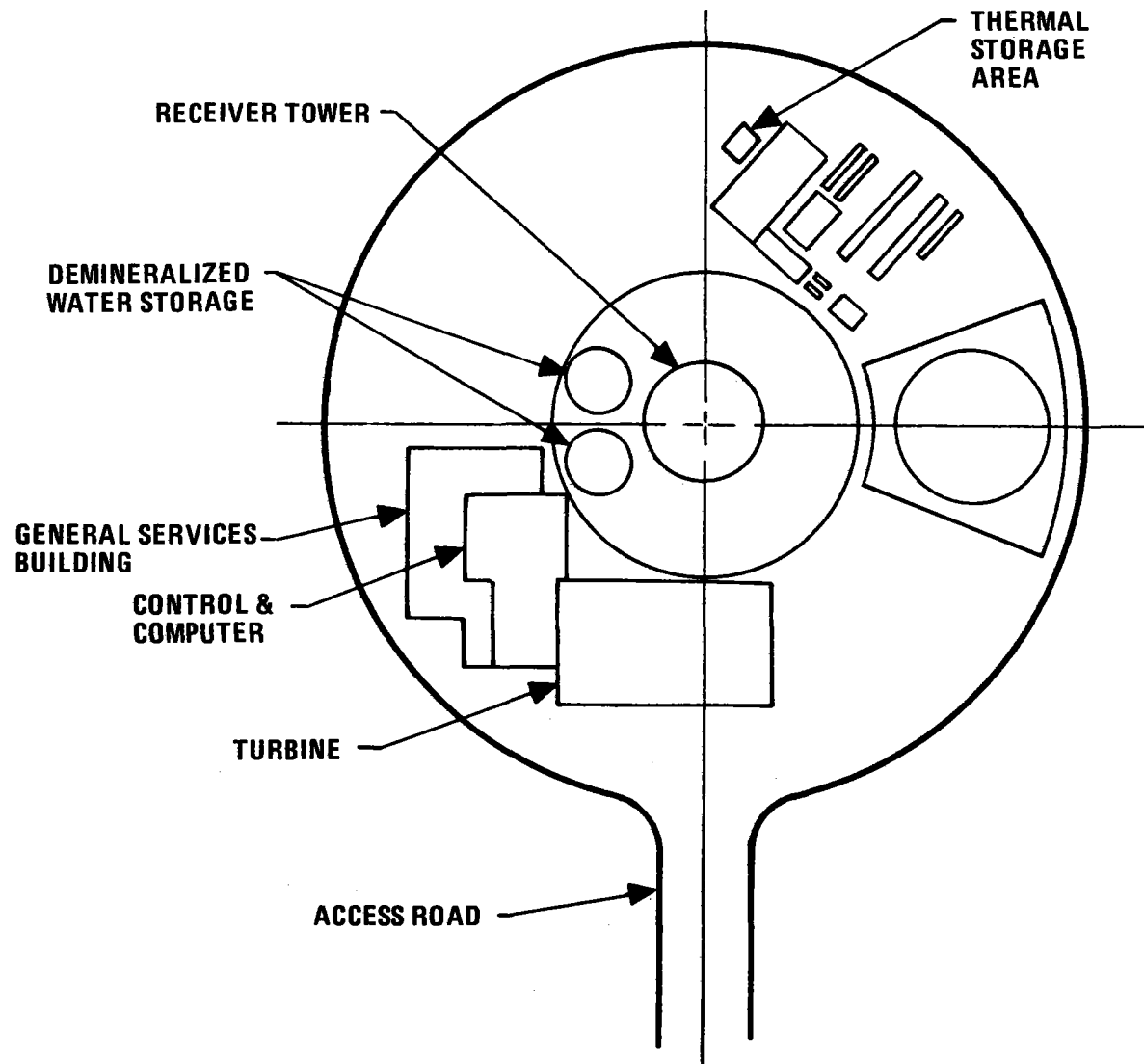
B-9



Solar Power Plant

40703-II

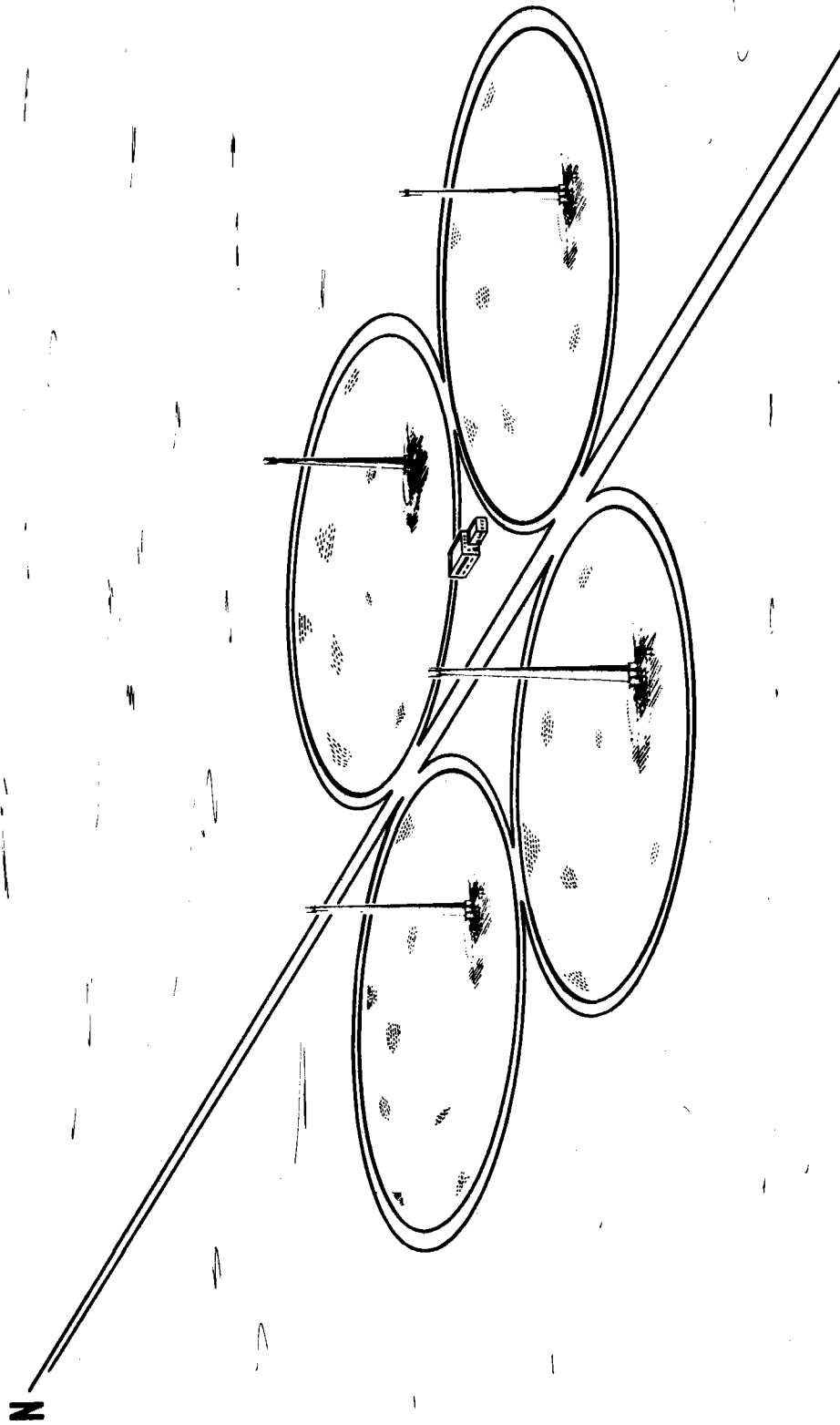
10 MW SOLAR PILOT PLANT - CENTRAL PLANT COMPLEX



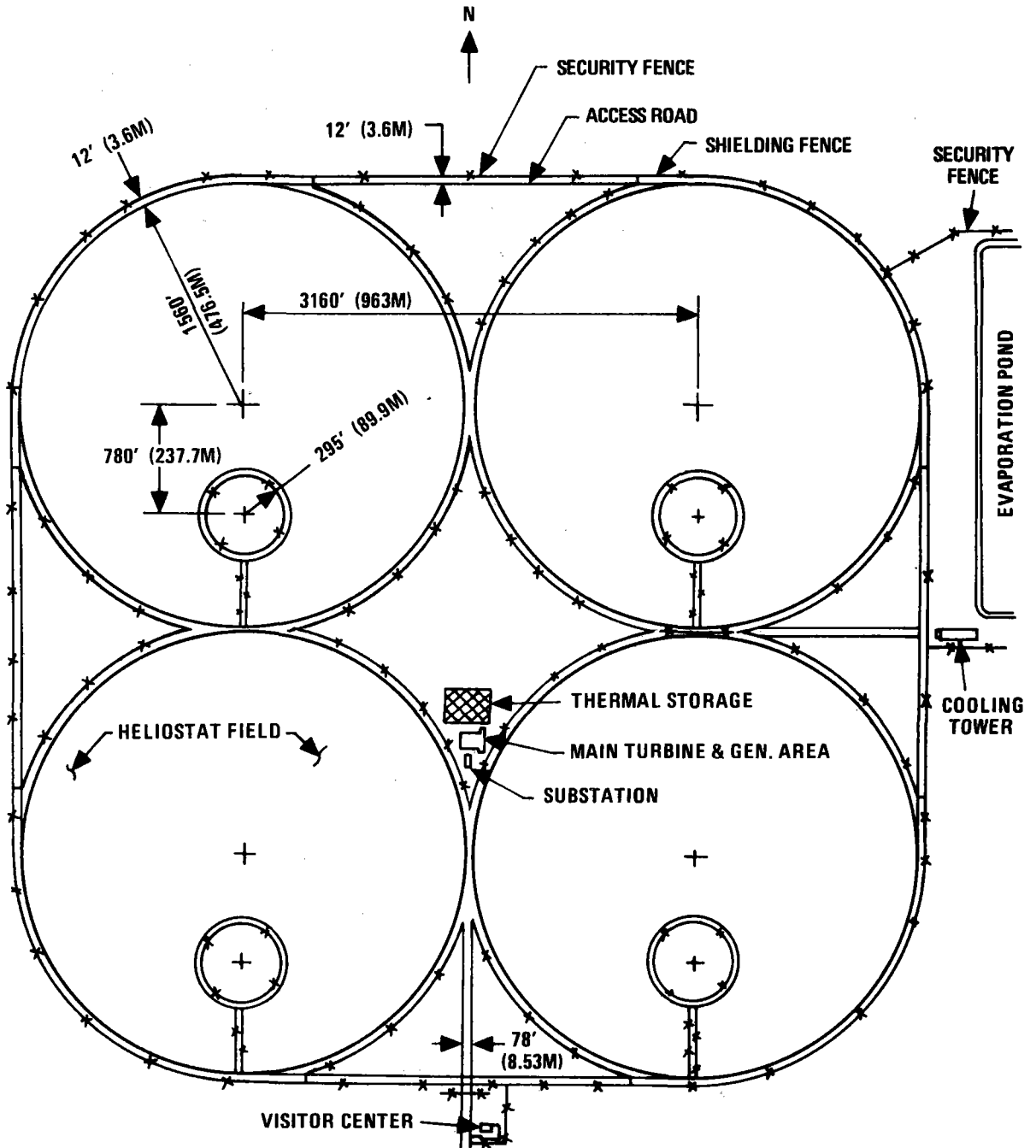
40703-II

B-11

COMMERCIAL PLANT CONCEPTUAL DESIGN



100 MW(e) SOLAR PLANT CONCEPTUAL SITE ARRANGEMENT



B-15

SECTION 3
COLLECTOR SUBSYSTEM

40703-II

COLLECTOR SUBSYSTEM CHARACTERISTICS

Item No.	Characteristic	Spec (1)		Current Baseline		Spec. Var.
		PP	Com.	Pilot Plant	Commercial	
1	Direct Solar Radiation (Design Point)	I	J	0.95 kw/m ² , 12-21, 2 pm, 35.70°N. Lat.	0.95 kw/m ² , 3-21, noon, 35.7°N. Lat.	
2	Ground Cover			Non-uniform, 0.29 mirror/field ratio (avg.)	Same as PP	
3	Field Layout			Polar, Tower 1/2 field radius south of center. One Tower/Field	Same as PP - Four Fields	
4	Heliostat Orientation			Outer axis normal to radial	Same as PP	
5	Facet Size			10m ² , 3.048m x 3.281m	Same as PP	
6	Facet Spacing			5.08m (16 ft 8 in.)	Same as PP	
7	Gimbal Sequence			Tilt/tilt	Same as PP	
8	Gimbal Limits			Frame +30°, -75° Mirror module ±180°	Same as PP	
9	Heliostat Weight			6348 kg (14,077 lbs)	Same as PP	
10	Facets per Heliostat			4	Same as PP	
11	No. of Heliostats			1598	20,220 (Total Four Fields)	
12	Field Outer Radius			267.5m (878 ft) see Fig. 3-9	475.5m (1,560 ft) see Fig. 3-10	
13	Field Inner Radius (Plant Radius)			50.3m (165 ft) see Fig. 3-9	89.9m (295 ft) see Fig. 3-10	

NOTE: (1) See Section VII for specification and requirement source identification.

COLLECTOR SUBSYSTEM CHARACTERISTICS

Item No.	Characteristic	Spec (1)		Current Baseline		Spec. Var.
		PP	Com.	Pilot Plant	Commercial	
1	Reflectivity			0.90 clean	Same as PP	
2	Total Mirror Area			63,920 M ² (688,029 ft ²)	808,800 M ² (8,706,136 ft ²)	
3	Wind	G		Survival w/o damage -40 M/S (90 MPH)* Operational - 13.5 M/S (30 MPH max)	Same as PP* Same as PP	
4	Temperature	G		Operational TBD to TBD Operational (degraded and safe) -30°C to 50°C.	TBD	
5	Environmental Degradation			80% Avg. Reflectivity Value between weekly washing.	Same as PP	
6	Start-up Sequence			See page 3-11	Same as PP	
7	Redirected Flux (Focus)			Fixed focal length 418 M (1372 ft)	Fixed Focal Length 749.8 M (2460 ft)	
8	Optical Quality			1 mrad, 1 σ optics		
9	Tracking Accuracy			2 mrad, 1 σ per axis		
10	Tracking Efficiency			See page 3-5.		

NOTE: (1) See Section VII for specification and requirement source identification.

* 3-deg max. effective angle of attack.

40703-II

B-17

COLLECTOR SUBSYSTEM CHARACTERISTICS

Item No.	Characteristic	Spec (1)		Current Baseline		Spec. Var.
		PP	Com.	Pilot Plant	Commercial	
11	Tracking Rate			23°/h normal max.	Same as PP	
12	Slew Rate			1080°/h calibration and emergency.	Same as PP	
13	Return to Storage Time			< 15 min.	Same as PP	
14	Peak Thermal Power into Aperture			43 MW (TH) (3/21, 9/21 noon)	582,924 kW (TH) (3/21, 9/21 noon)	
15	Annual Thermal Energy into Cavity Aperture			121,650 MW h (TH)	TBD	

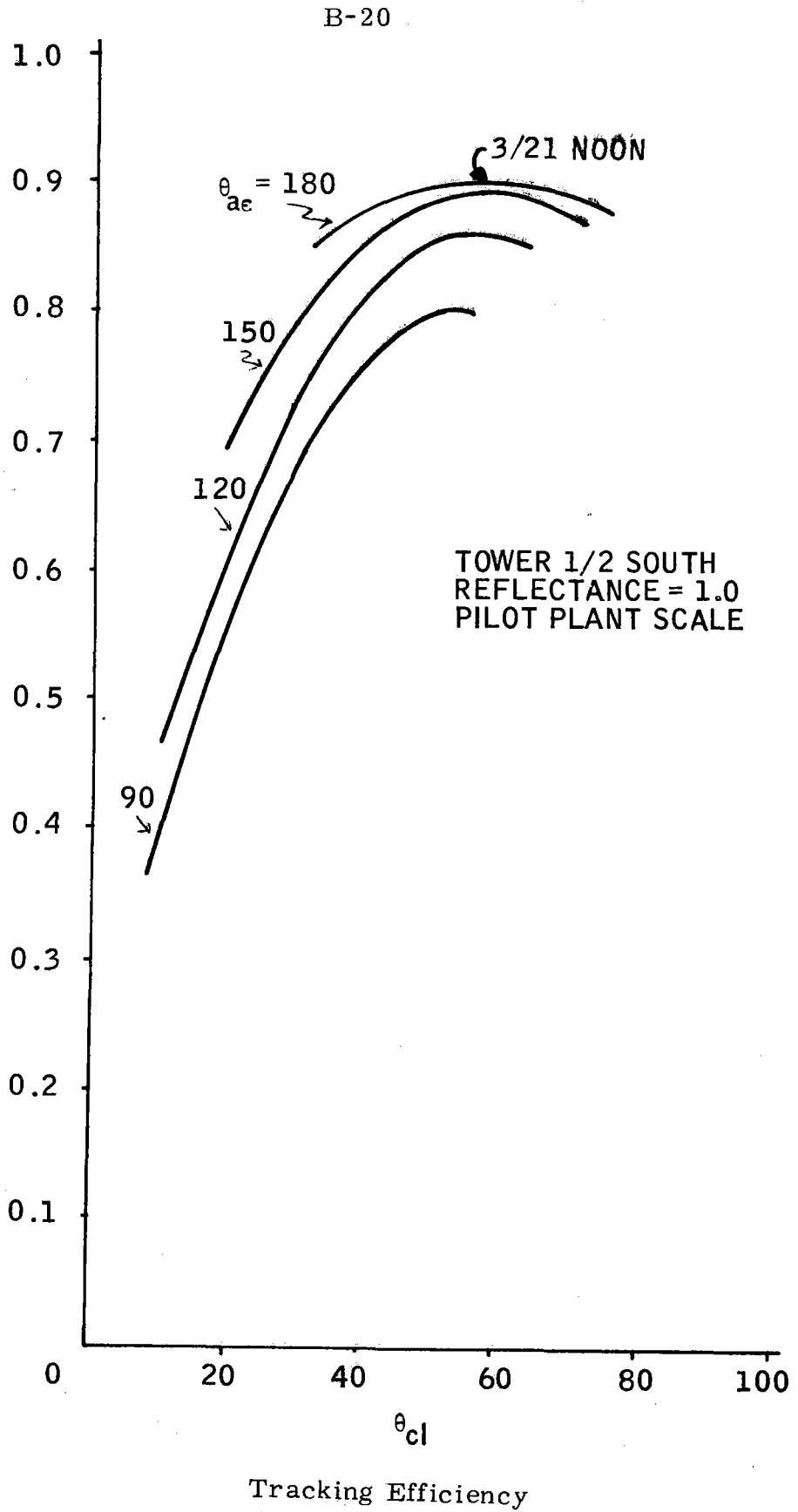
NOTE: (1) See Section 1 for specification and requirement source identification.

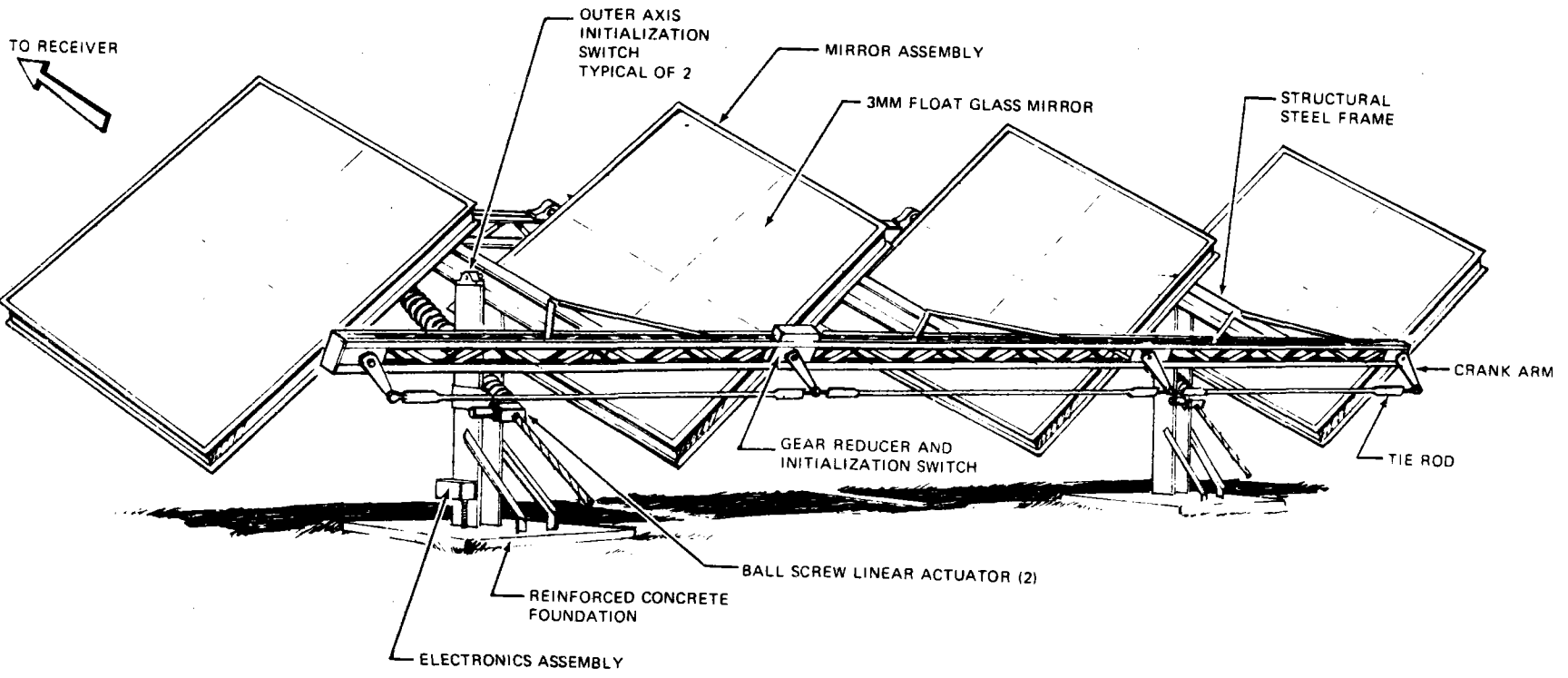
COLLECTOR SUBSYSTEM CHARACTERISTICS

Item No.	Characteristic	Spec (1)		Current Baseline		Spec. Var.
		PP	Com.	Pilot Plant	Commercial	
1	Net Annual Thermal Energy per Unit Mirror Area, Absorbed			1.60 MWh(TH)/M ²	1.84 MWh(TH)/M ²	
2	Net Peak Power into Aperture per Unit Mirror Area (Thermal)			673 W(TH)/M ²	TBD	
3	Auxiliary Power Input			Computer Subsystem 38.5 kW C2 Array - 0.8 kW	Total 661.85 kW	
4	No. of Field Transformers			8	TBD	
5	Transformer - Size Avg. Power Voltage In Voltage Out			17 kW Secondary Rating 7 kW per Octant 9.34 kVrms, 60 Hz, 1φ 115 Vrms, 60 Hz, 1φ	TBD	
6	No. of Calibration Arrays			8	TBD	
7	Size of Calibration Array			8.53m wide x 7.31m high (28 ft x 24 ft)	TBD	
8	Calibration Array Location on Tower			22m (71 ft) above aperture, aimpoint to aimpoint.	TBD	
9	Control Computers Model and Quantity			L6/43, 5 ea.	TBD	
10	No. of Control Sectors			8	TBD	
11	Battery Size and Quantity			1 per heliostat, 20A hr @ 1 hr rate	Same as PP	

NOTE: (1) See Section 1 for specification and requirement source identification.

OVERALL TRACKING EFFICIENCY = $\frac{\text{POWER INTO CAVITY}}{\text{DNI} \times \text{MIRROR AREA}}$



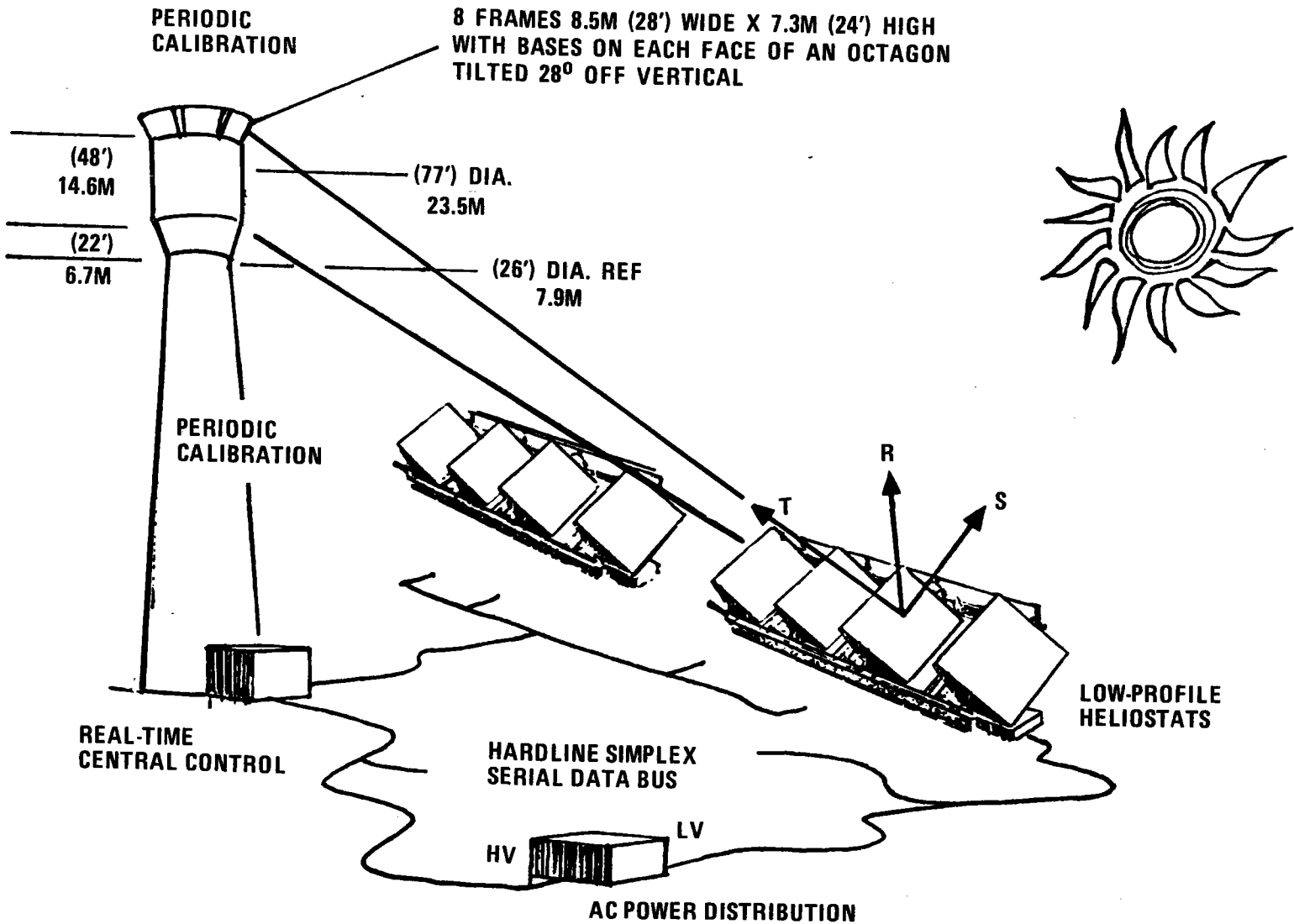


Tilt-Tilt Heliostat

40703-II

B-21

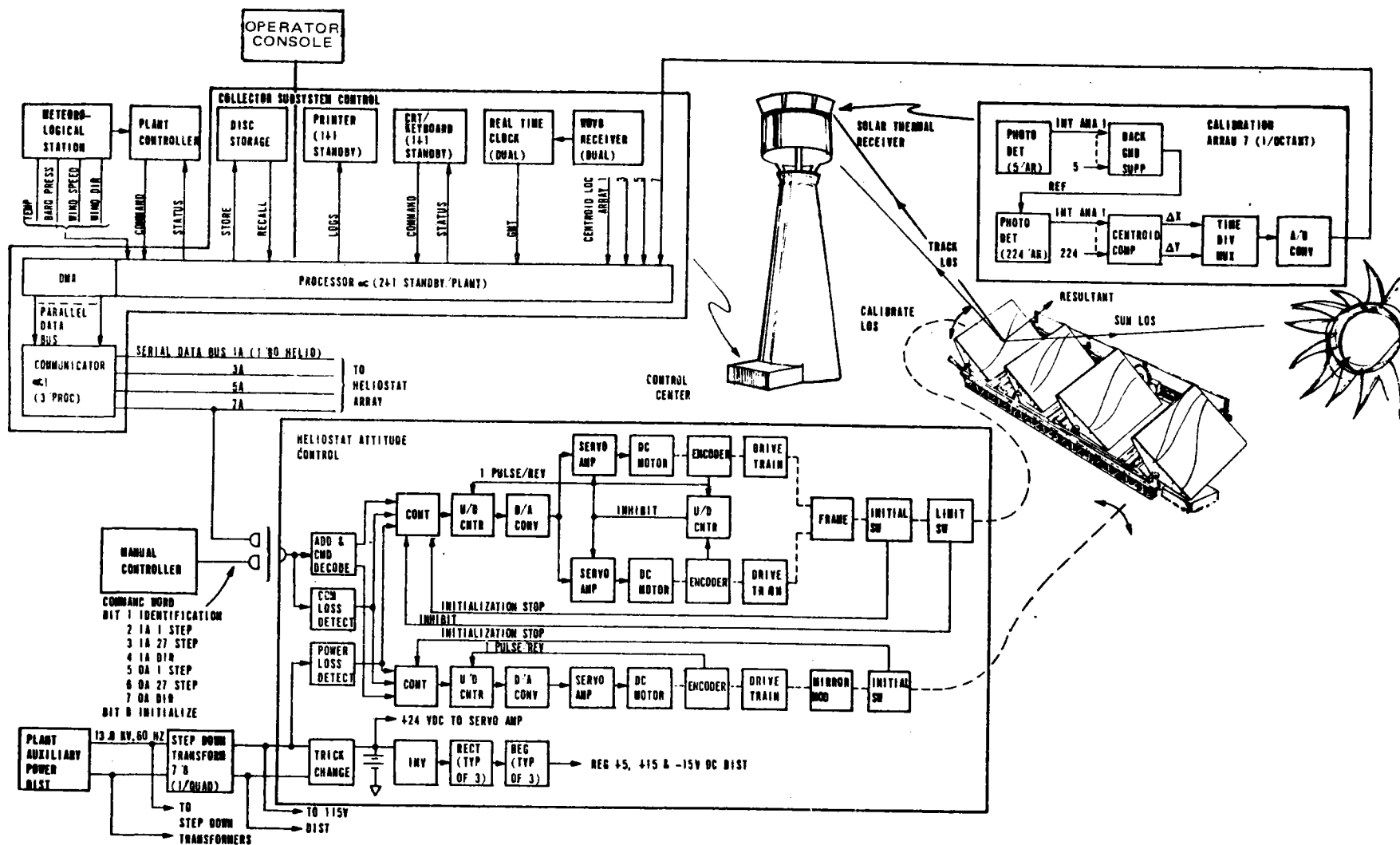
COLLECTOR CONCEPT

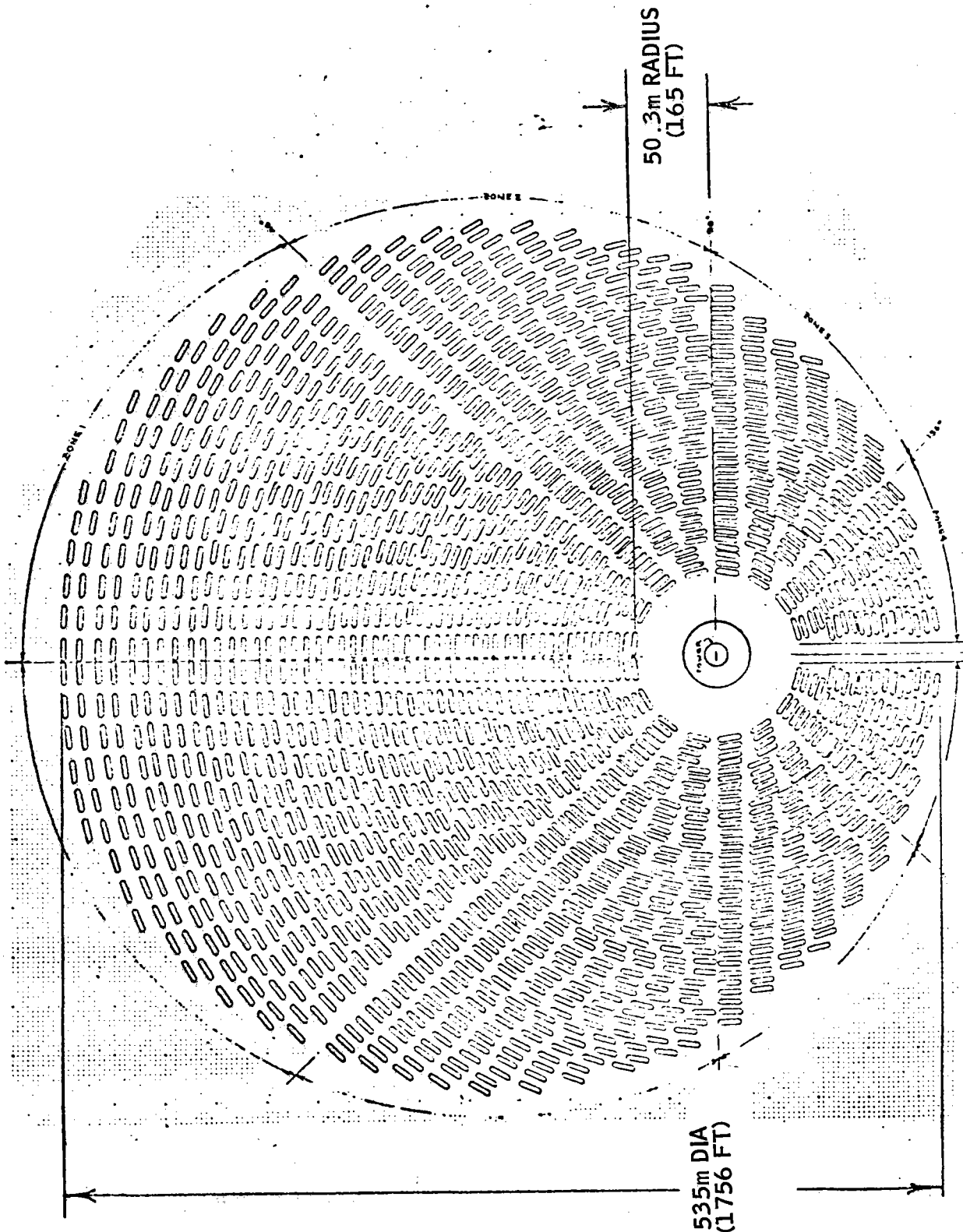


40703-II

B-22

PILOT PLANT COLLECTOR SUBSYSTEM FUNCTIONAL DIAGRAM





50.3m RADIUS
(165 FT)

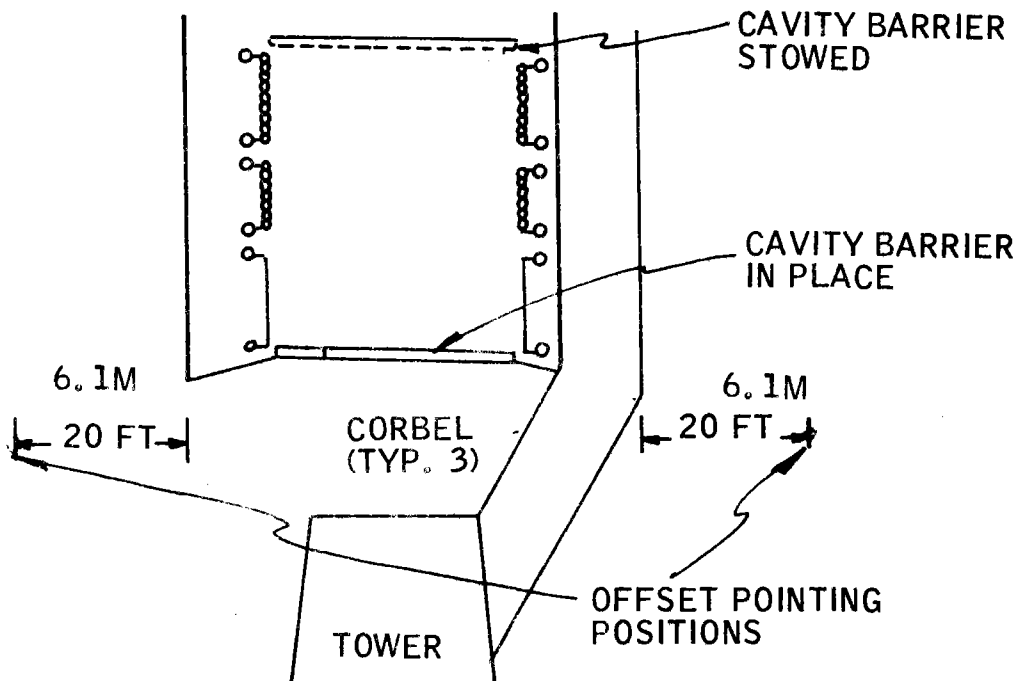
535m DIA
(1756 FT)

Pilot Plant Collector Field Heliostat Arrangement
SK 107131

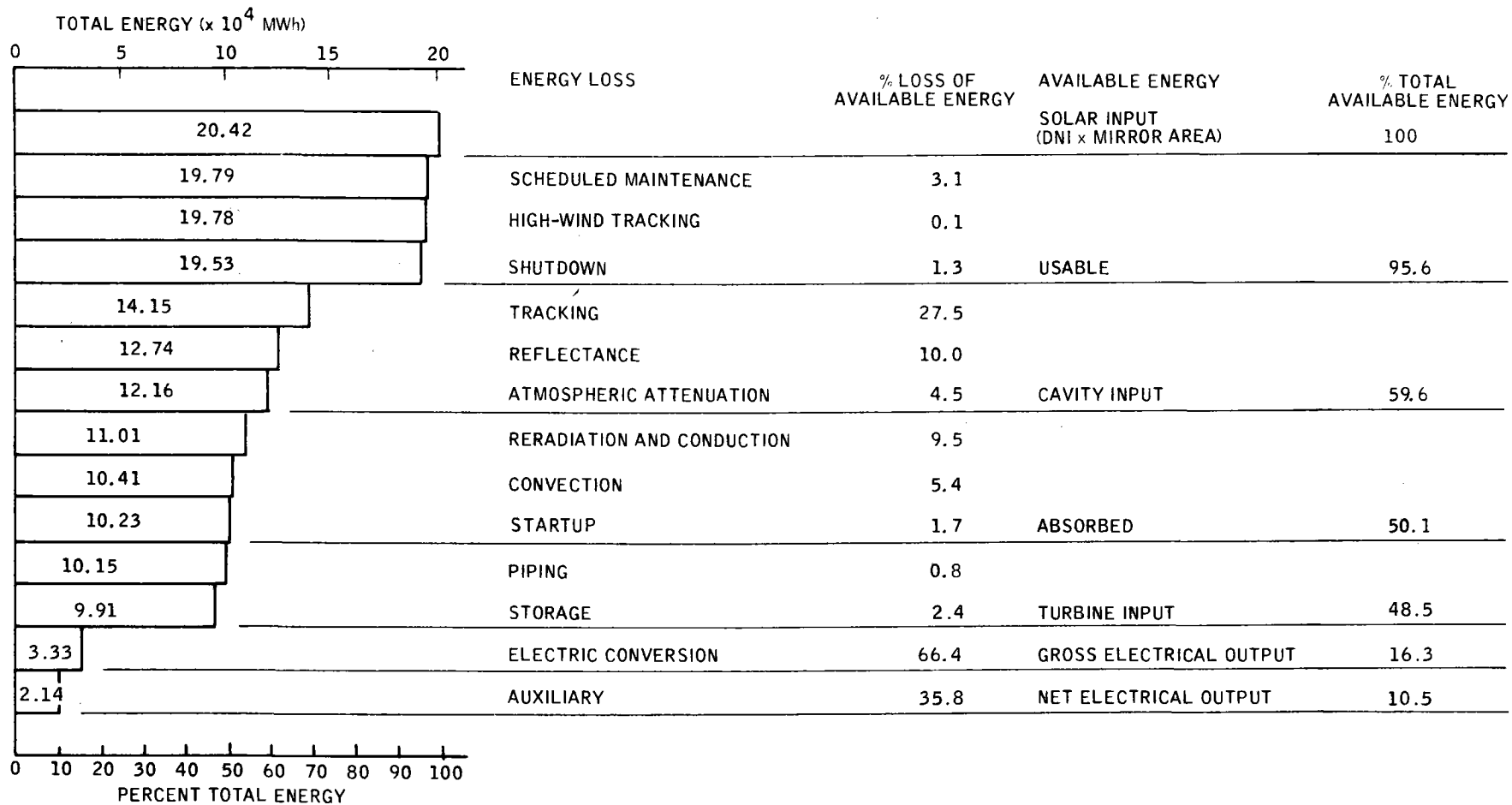
START-UP SEQUENCE

The following sequence is defined for the plant collector start-up:

1. Bring up computer - on line (15 min)
2. Prepare and perform computer self-check diagnostics (15 min)
3. Check that transformers are operable and are energized. Check that winds are acceptable (5min)
4. Check that flux density in the field is adequate for start-up (5 min)
5. Command via the computer for all heliostats to initialize (15 min)
6. Command via the computer for each heliostats to point at its offset pointing position. The locus of these offset pointing positions in-scribes a circle about the tower as hown in Figure 1. The positions are established so that no ray hits the tower when the heliostats are directed at the offset positions (5 min)
7. Upon command from the receiver operator enable the boiler heliostats to heat the boiler (5 sec)
8. Upon command from the receiver operator enable the first stage superheater (S/H-¹) heliostats to beam energy to the S/H-¹ (5 sec)
9. Upon command from the receiver operator enable the second stage superheater (S/H-²) heliostats to beam energy to the S/H-² (5 sec)
10. After all heliostats are beaming energy to the receiver change to track and cal while track modes (1 min/H/S)



40703-II



B-26

Annual Energy Budget

RECEIVER SUBSYSTEM CHARACTERISTICS

Item No.	Characteristic	Spec (1)		Current Baseline		Spec. Var.
		PP	Com.	Pilot Plant	Commercial	
1	Tower Height			126.5m (415 ft)	228.6m (750 ft)	
2	Tower Diameter			7.9 m (26 ft) outside concrete	14.02 m (46 ft)	
3	Corbel Size			1.22m (4.0 ft) wide	1.68m (5.5 ft) wide	
4	Corbel Spacing			3 equally spaced	Same at PP	
5	Corbel Orientation			1 true south	Same as PP	
6	Cavity Diameter			14.9m (49 ft)	26.1m (85.6 ft)	
7	Cavity Height			Major - 16.6m (54 ft) Minor - 14.6m (48 ft)	Major - 28.3m (93.0 ft) Minor - 25.3m (83.0 ft)	
8	Boiler Height			Major - 8m (26 ft 3 in) Minor - 6.17m (20 ft 3 in)	TBD	
9	Boiler Heating Surface Area			344.4m ² (3707 ft ²)	TBD	
10	Superheater Height (Total)			8m (26 ft 3 in)	TBD	
11	Superheater Heating Surface Area			150.1m ² (1616 ft ²) 225.8m ² (2425 ft ²)	TBD TBD	
12	Steam Gen. Housing Height			25.8 - 27.6m (84.5 ft - 90.5 ft)	38.7 - 40.5m (127 ft - 133 ft)	
13	Steam Gen. Housing Diameter			24.4m (80 ft)	36.5m (119.6 ft)	
14	Ceiling Configuration			Bare (Refractory)	Same as PP	

NOTE: (1) See Section 1 for specification and requirement source identification.

RECEIVER SUBSYSTEM CHARACTERISTICS (CONTINUED)

Item No.	Characteristic	Spec (1)		Current Baseline		Spec. Var.
		PP	Com.	Pilot Plant	Commercial	
1	Steam Generator Weight Dry Wet			265.1x10 ³ kg (584,000 lb) 289.2x10 ³ kg (637,000 lb)	TBD	
2	Aperture Area (annulus)			218.3m ² (2350 ft ²)	650.8m ² (7005 ft ²)	
3	Net Corbel Area			29.0m ² (312.4 ft ²)	76.9m ² (827.8 ft ²)	
4	Net Aperture Area			189.3m ² (1419 ft ²)	573.9m ² (6177.6 ft ²)	
5	Aperture Slant Height Major Minor			7.6m (25 ft) 5.5m (18 ft)	TBD TBD	
6	Aperture Lower Dia.			7.9m (26 ft)	TBD	
7	Aperture Upper Dia.			14.9m (49 ft)	TBD	
8	Peak Absorbed Thermal Power			42.95 MW(th)	510.1 MW(th)	
9	Design Point Absorbed Thermal Power			34.92 MW(th)	TBD	
10	Peak Wall Incident Flux			300 kW/m ² (95,100 btu/h/ft ²)	TBD	
11	Vertical Separation Tower to Cavity			6.7m (22 ft) major	TBD	
12	Annual Thermal Energy Absorbed by working Fluid			102,310 MWh	TBD	
13	Efficiency (Annual Average)			84.1%	TBD	

NOTE: (1) See Section 1 for specification and requirement source identification.

RECEIVER SUBSYSTEM CHARACTERISTICS (CONTINUED)

Item No.	Characteristic	Spec (1)		Current Baseline		Spec. Var.
		PP	Com.	Pilot Plant	Commercial	
1	Aux. Power Required			Recirculation Pumps 300 HP at 440V	TBD	
2	Wind Load			13.5 m/sec operating 60 m/sec nonoperating	Same as PP	
3	Seismic Load			Design basis earth quake from NRC Reg. Guide 1.60 UBC seismic zone III 0.25g Vertical and 0.25g horizontal accel.	Same as PP	
4	Flux Level-Incident, Absorbed			See PP	TBD	
5	Flux Distribution Incident, Absorbed			See PP	TBD	
6	Steam Flow - Design Maximum			49,593 kg/h (109,332 lbs/h) 61,000 kg/h (134,779 lbs/h)	411,206 kg/h (906,555 lb/h)* 699,051 kg/h (1,541 (1,541,144 lb/h)**	
7	Steam Pressure at 2nd Stage S.H. outlet			10.6 MPa (1540 psia) Design 11.0 MPa (1600 psia) Max.	10.7 MPa (1546 psia)* 11.4 MPa (1649 psia)**	
8	Steam Temp at 2nd Stage S.H. Outlet			516°C (960°F)	518°C (965°F)**	
9	Feedwater Temp at Drum Inlet			204°C (399°F) Design 215°C (419°F) Maximum	206°C (402°F)	
10	Feedwater Temp at Spray Attenuator Inlet			204°C (399°F) Design 215°C (419°F) Maximum	TBD 206°C (402°F)	

NOTE: (1) See Section 1 for specification and requirement source identification.

* 100 MW(e) Net Receiver Steam Driving Turbine

RECEIVER SUBSYSTEM CHARACTERISTICS (CONTINUED)

Item No.	Characteristic	Spec (1)		Current Baseline		Spec. Var.
		PP	Com.	Pilot Plant	Commercial	
1	Feedwater Line Velocity Boiler Feed Pump to Receiver Drum			2.4 m/s (472 ft/min)*	4.2 m/s (13.8 ft/s)	
				2.3 m/s (450 ft/min)**	Common Header*** 2.3 m/s (7.7 ft/s) Each Rec. Branch*** 2.5 m/s (8.1 ft/s) Common Header**** 1.5 m/s (4.8 ft/s) Each Rec. Branch****	
2	Feedwater Line Pressure Dr. Boiler Feed Pump to Recr. Dr. Friction			0.655 MPa (95 psi)*	0.793 MPa (115 psi)***	
				0.510 MPa (74 psi)**	0.379 MPa (55 psi)****	
				Elevation	0.931 MPa (135 psi)	
3	Steam Line Velocity 2 ST. SH Outlet to Turbine Throttle			19.4 m/s (3813 ft/min)*	29 m/s (96 ft/s) Each Rec. Branch*** 47 m/s (153 ft/s) Common Header*** 43 m/s (141 ft/s) Turbine Branch*** *****	
				Valve	18.4 m/s (3627 ft/min)**	

NOTE: (1) See Section 1 for specification and requirement source identification.

* Receiver Design Point

** Simultaneous Storage and Receiver Storage Design Point

*** 100 MW(e) Net Receiver Steam Driving Turbine

**** 1.7 Times 100 MW(e) Net Steam Flow

RECEIVER SUBSYSTEM CHARACTERISTICS (CONTINUED)

Item No.	Characteristic	Spec (1)		Current Baseline		Spec. Var.
		PP	Com.	Pilot Plant	Commercial	
4	Steam Line Pressure Drop Rcvr. 2 St. SH Outlet to Turbine Throttle Valve			0.517 MPa (75 psi)* 0.421 MPa (61 psi)**	1.378 MPa (200 psi)** 0.724 MPa (105 psi)**	
5	Boiler Des. Pressure			13.03 MPa (1875 psig)		
6	Recirculation Pumps Number Type Size Des. Flow Rate Des. Total Discharge Head			3 Vertical, in-line, centrifugal 8x8x15/150 HP 0.126m ³ /s (2000 gpm) 53.3m (175 ft)		

NOTE: (1) See Section VII for specification and requirement source identification.

* Receiver Design Point

** Simultaneous Storage and Receiver Storage Design Point

*** 100 MW(e) Net Receiver Steam Driving Turbine

RECEIVER SUBSYSTEM CHARACTERISTICS (CONCLUDED)

Item No.	Characteristic	Spec (1)		Current Baseline		Spec. Var.
		PP	Com.	Pilot Plant	Commercial	
1	No. of Spray Attemperator Nozzles			1		
2	Drum Safety Valves Number Type Size			1 Crosby HC-75 2" Set Pressure: 1875 psig Cap: 111787 16m/h Temp: Sat.		
3	Super Heater Safety Valve Number Type Size			1 Crosby HCA-78 1 1/2"/G/3" Set Pressure: 1675 psig Cap: 30819 16 m/h Temp: 515.6°C (960°F)		

NOTE: (1) See Section 1 for specification and requirement source identification.

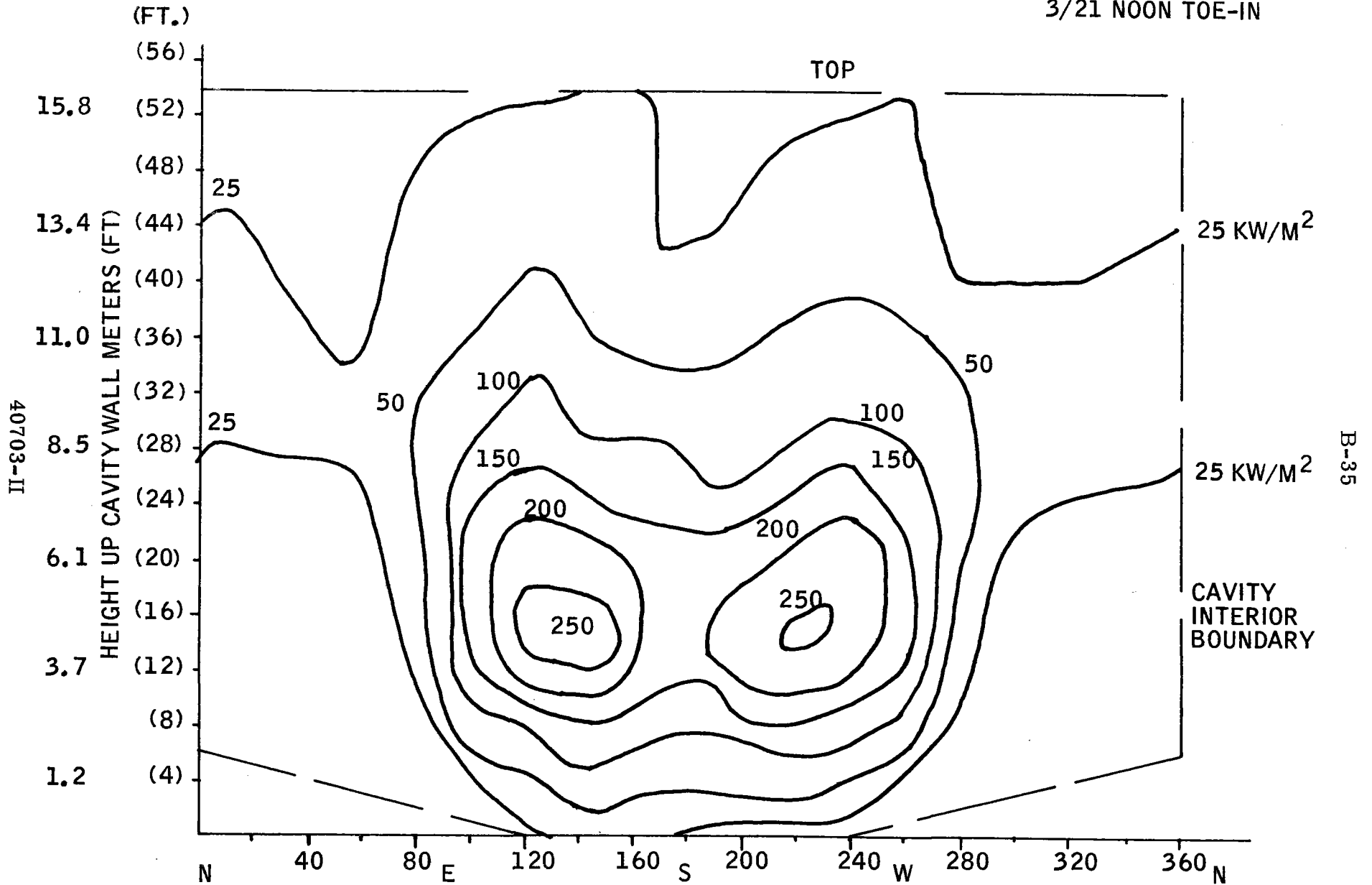
FEED WATER SPECIFICATIONS

Item	Pilot Plant PDBR Spec
pH	9.3 → 9.5*
Oxygen, O ₂ , ppm	< 0.007
Iron, Fe, ppm	0.01 max
Copper, Cu, ppm	0.005 max
SiO ₂ , ppm	0.02 max
Total Hardness, ppm	0.0**
Organics, ppm	0.0**
Total Solids, ppm	0.05 max
Ammoniz, N H ₃	As Required
Hydrazine, N ₂ H ₄	As Required

*With carbon-steel feedwater heaters.

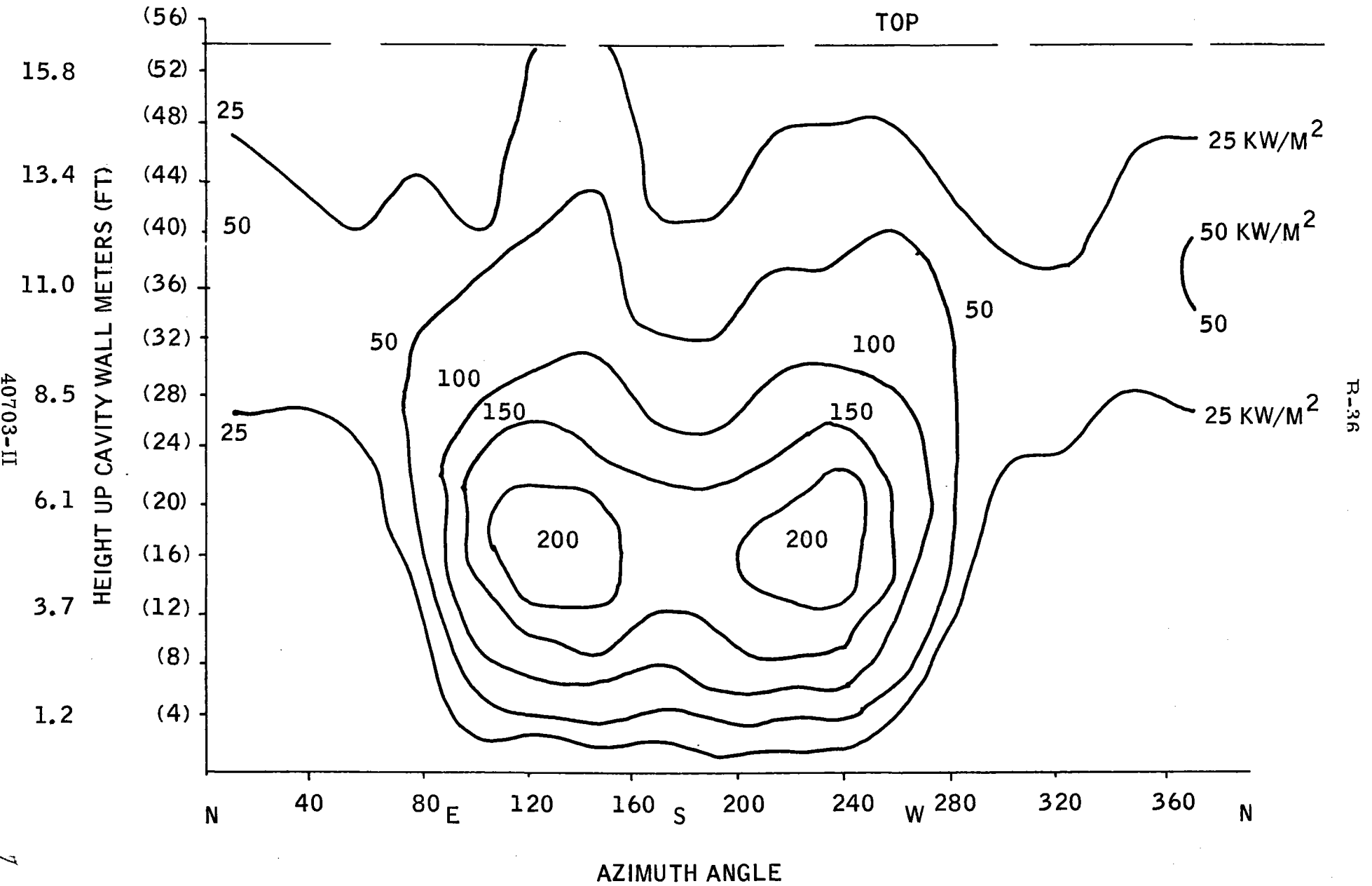
**The specification of 0 ppm is given as a recommendation to keep these contaminants completely out of the feedwater. Special analyses for these contaminants are available. Detection limits using these special analyses are 2.0 ppm for total hardness and 0.05 ppm for organics.

3/21 NOON
TOWER 1/2 SOUTH
CORBEL SOUTH
3/21 NOON TOE-IN



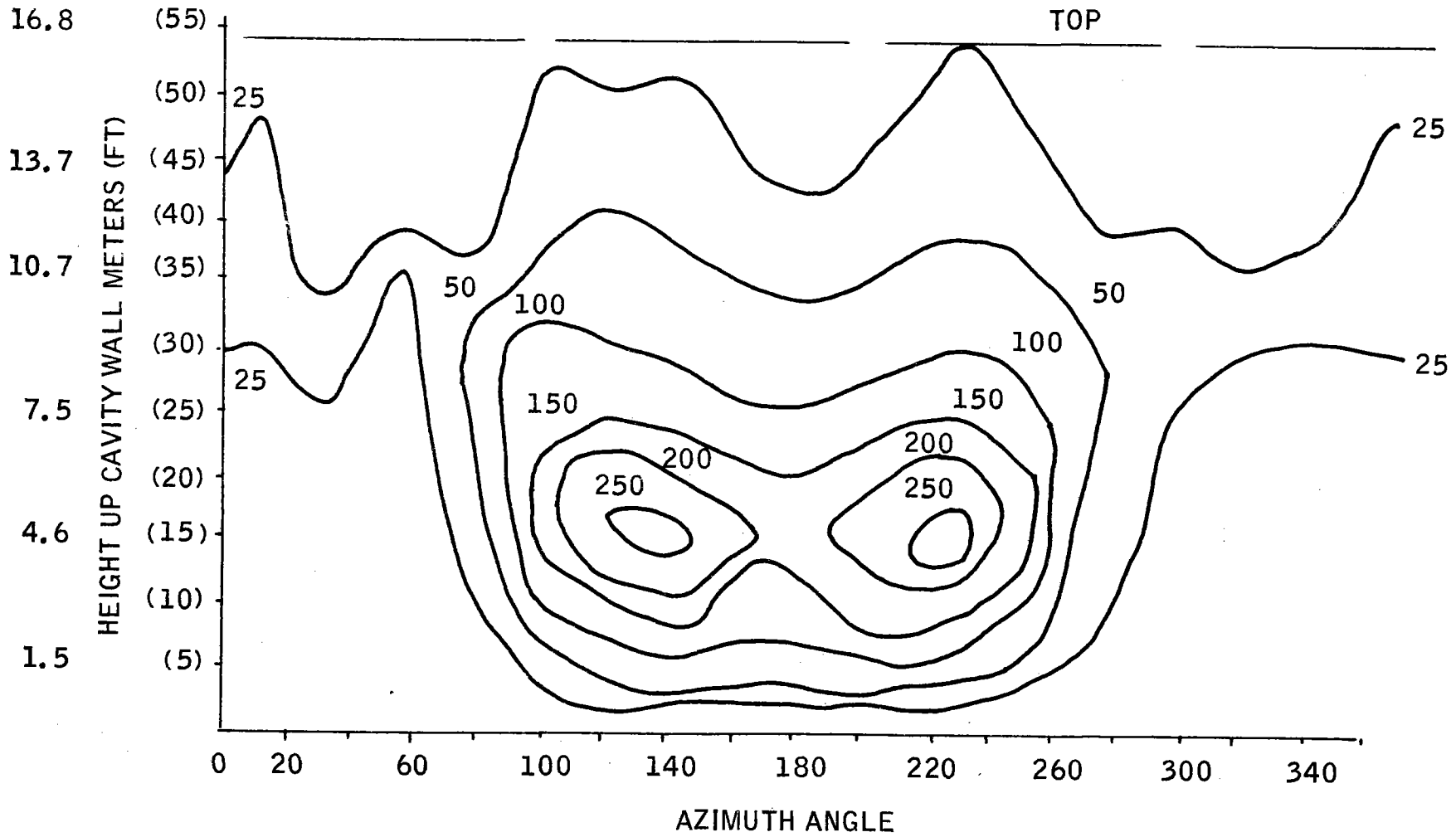
Cavity Wall Incident Flux Map for 3/21 Noon

6/21 NOON



Cavity Wall Incident Flat Map for 6/21 Noon

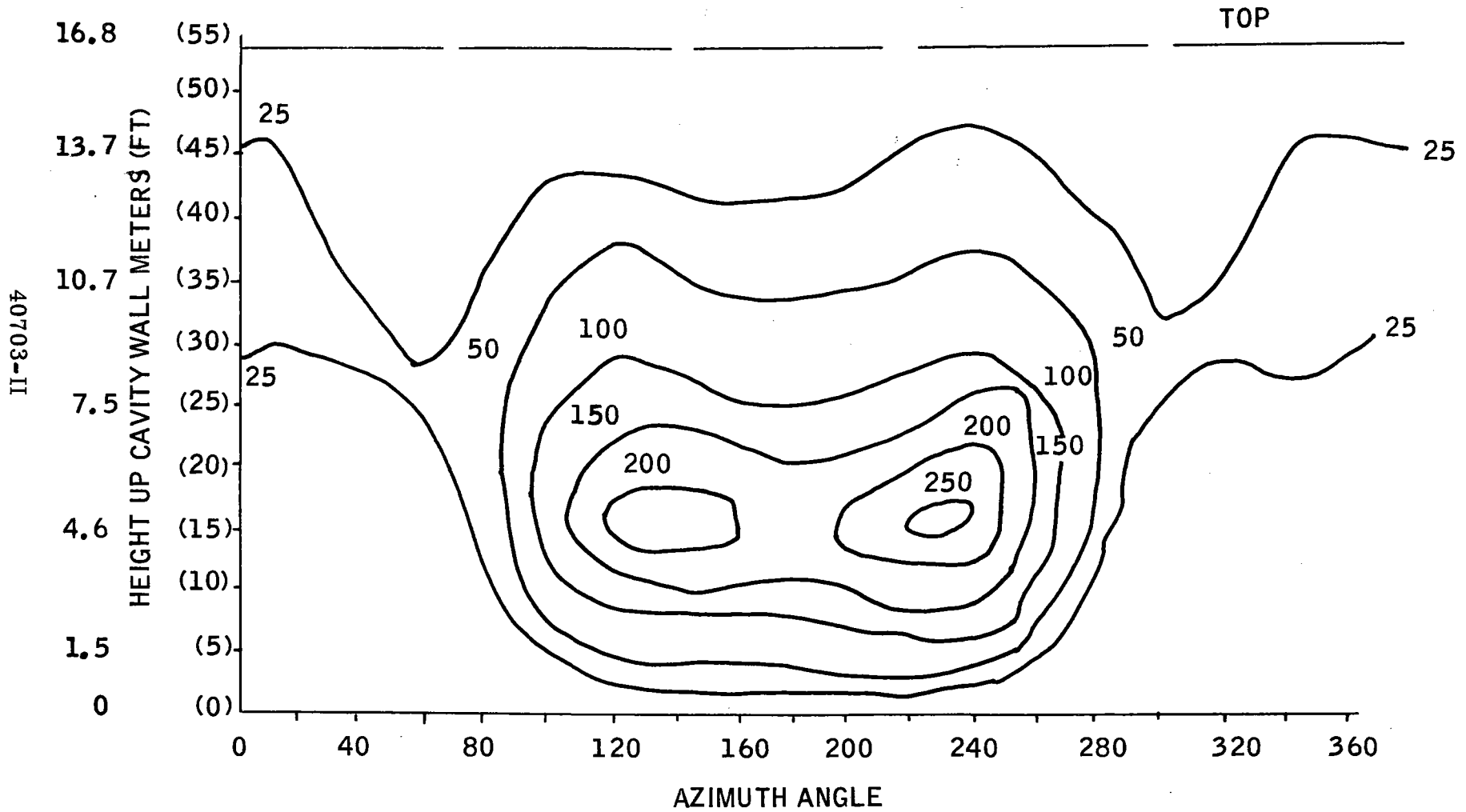
12/21 1200



B-37

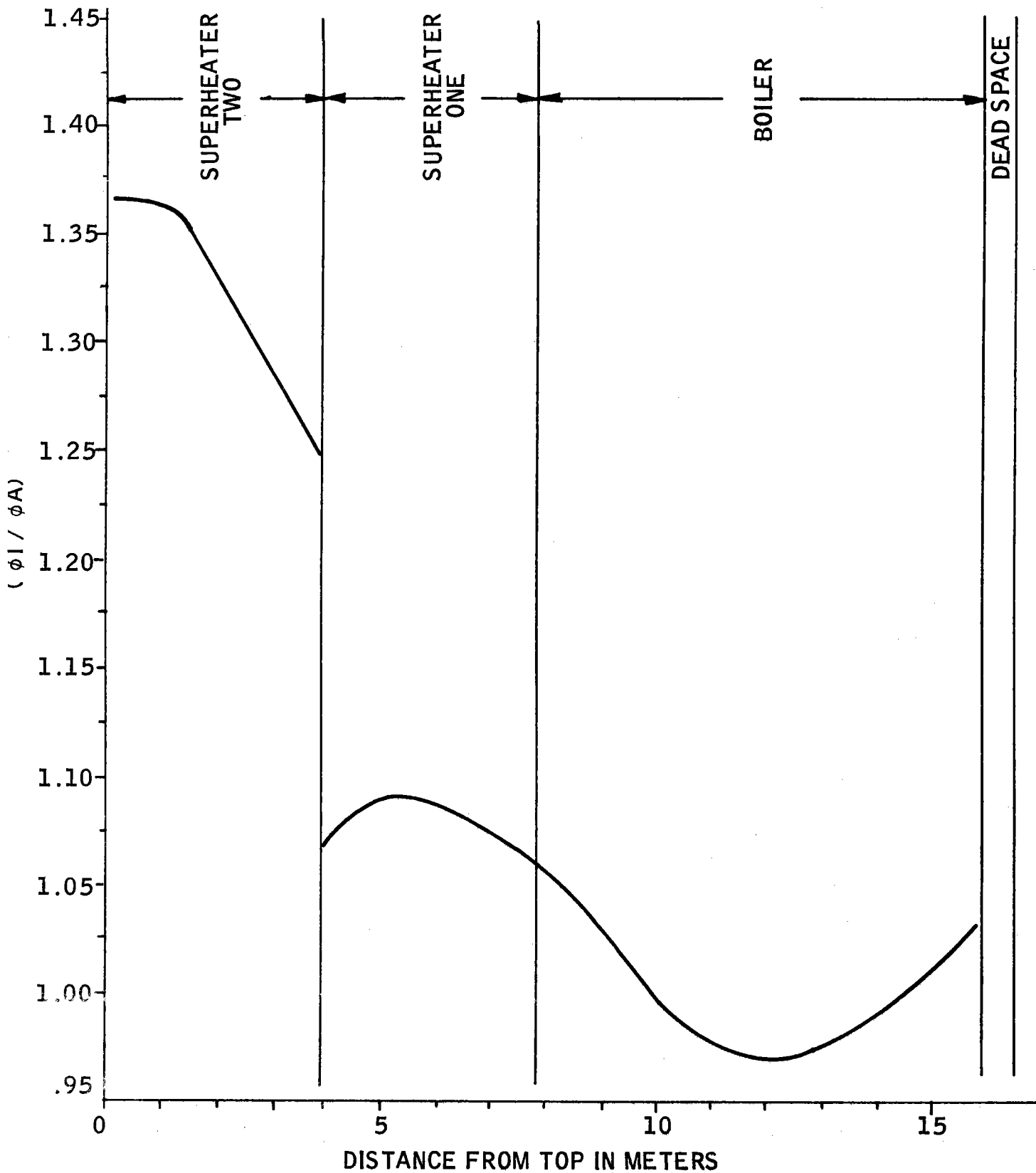
Cavity Wall Incident Flat Map for 12/21 Noon

12/21 1400

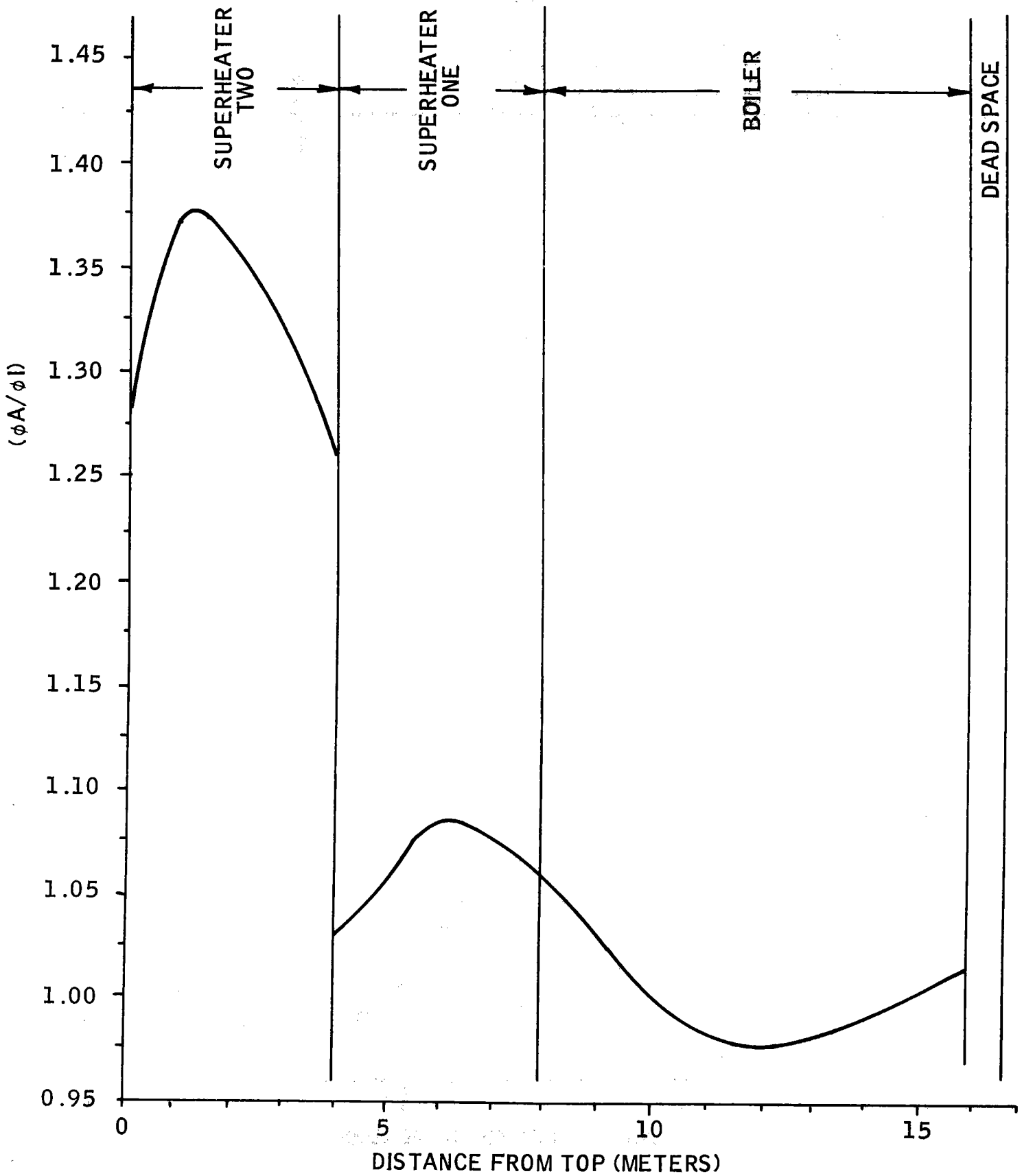


Cavity Wall Incident Flat Map for 12/21 2 P.M.

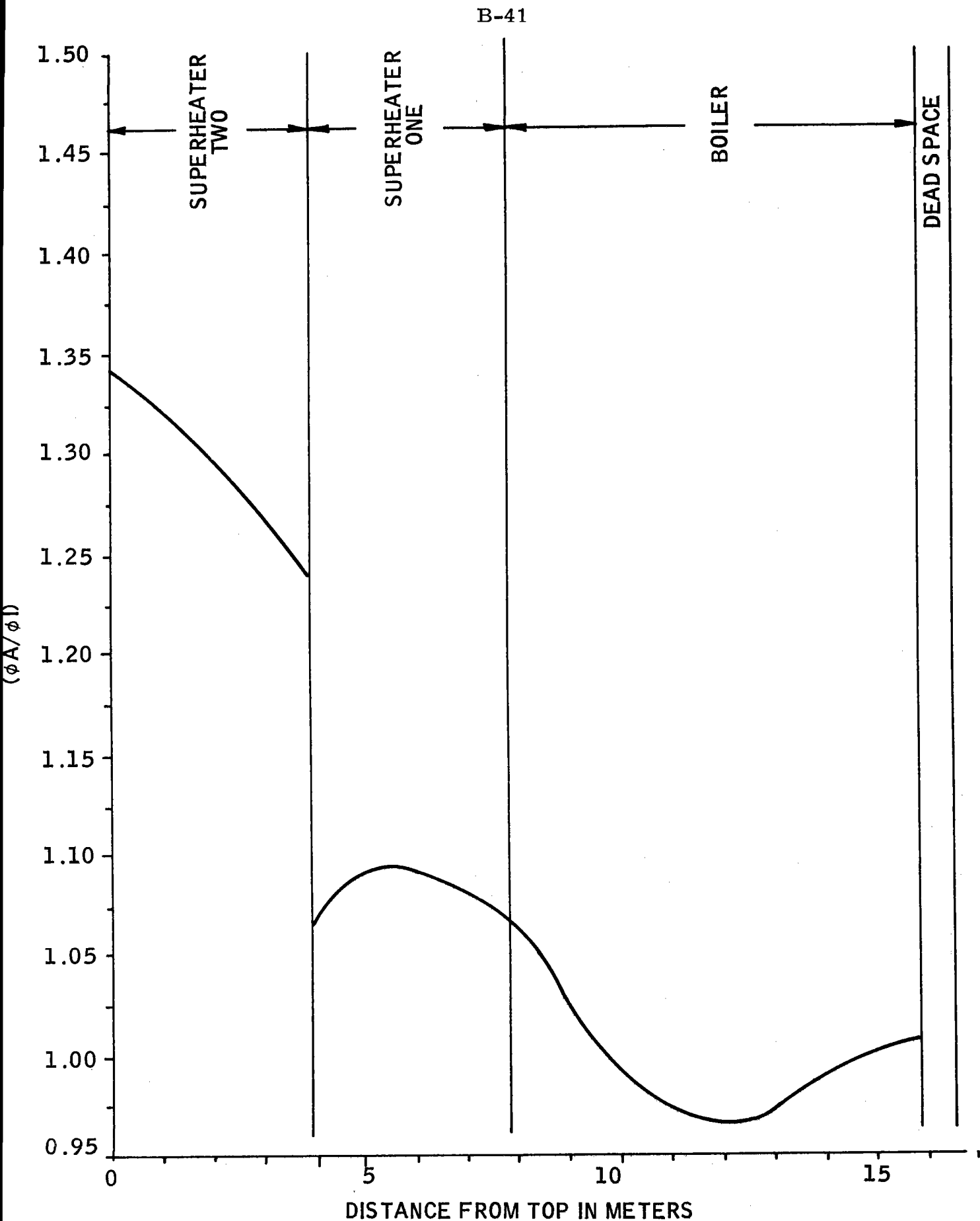
B-39



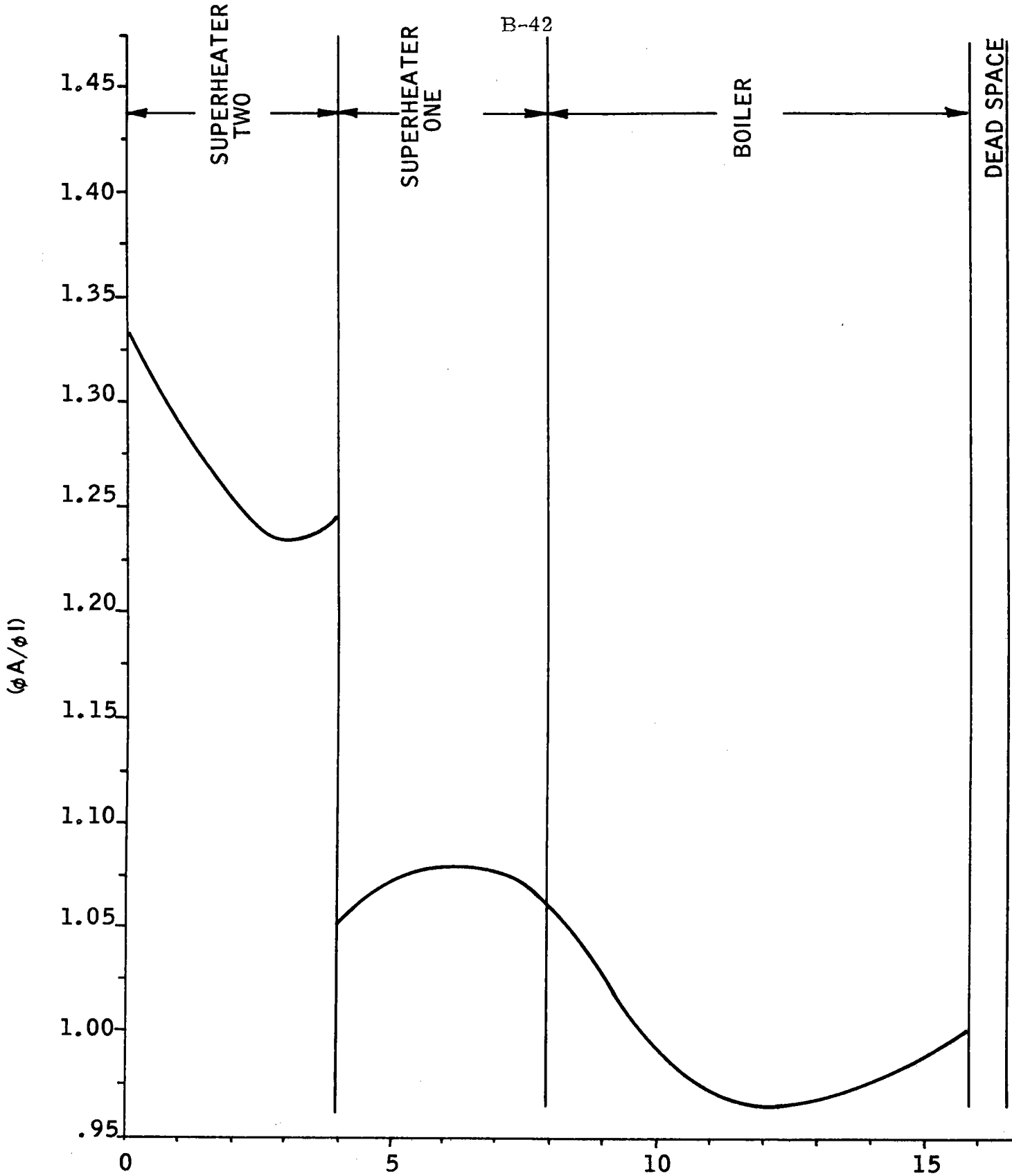
Circumferential Average $\phi A / \phi I$ Versus Cavity Position for 3/21 Noon



Circumferential Average ($\phi A / \phi I$) Versus Cavity Position for 6/21 Noon



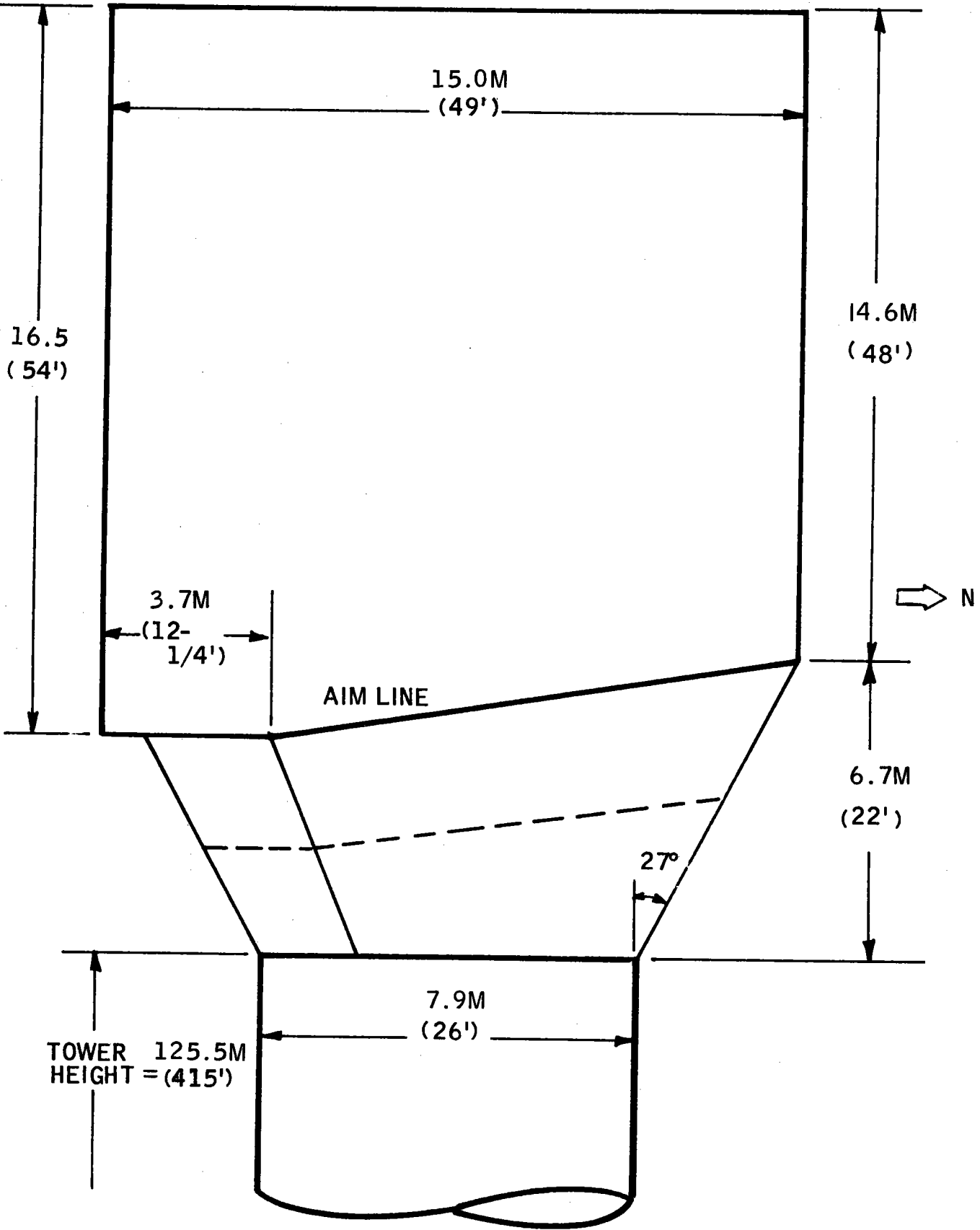
Circumferential Average $\phi A / \phi I$ Versus Cavity Position for 12/21 Noon



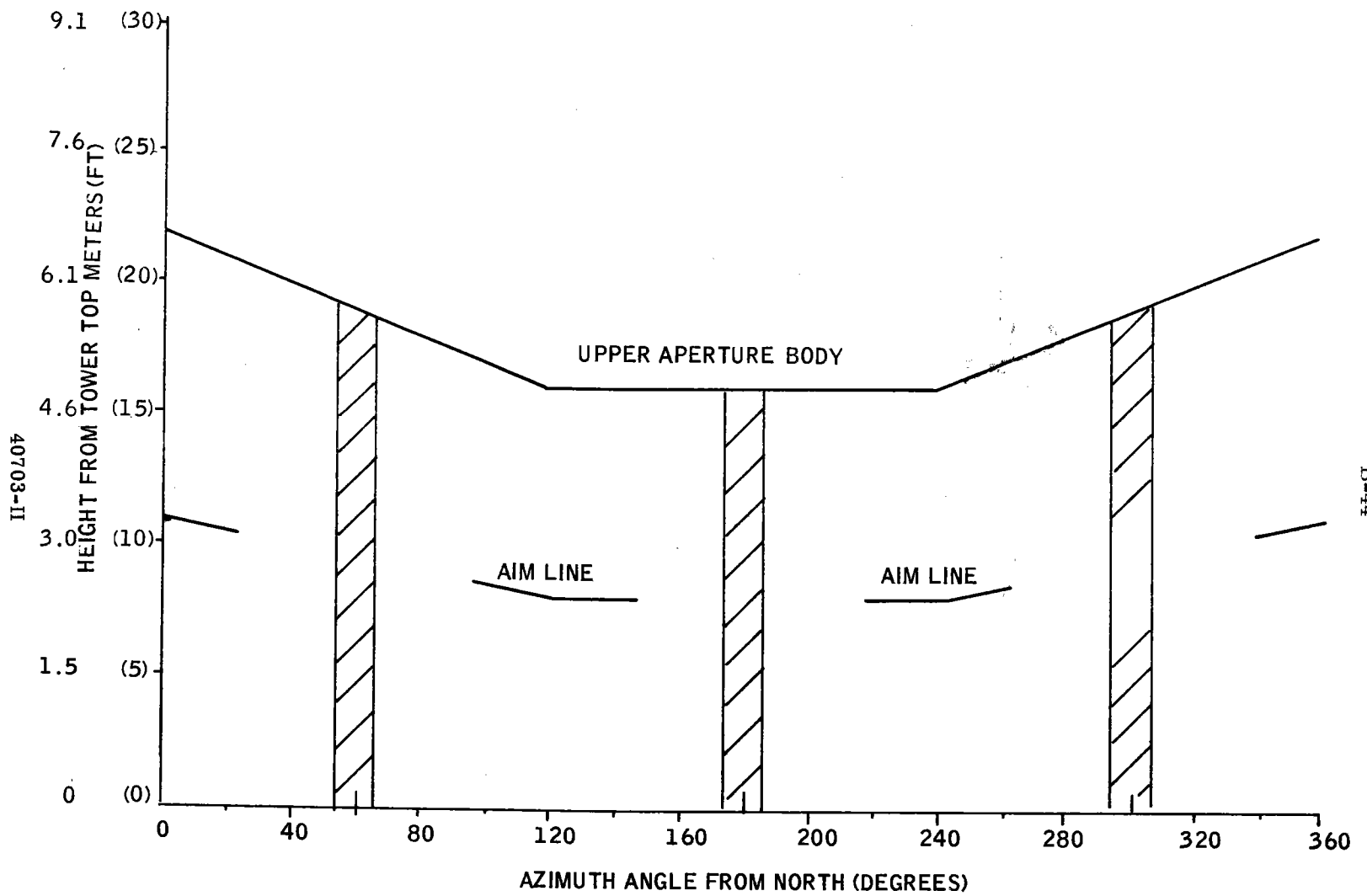
Circumferential Average ϕ_A/ϕ_I Versus Wall Position for 12/21 2 P. M.

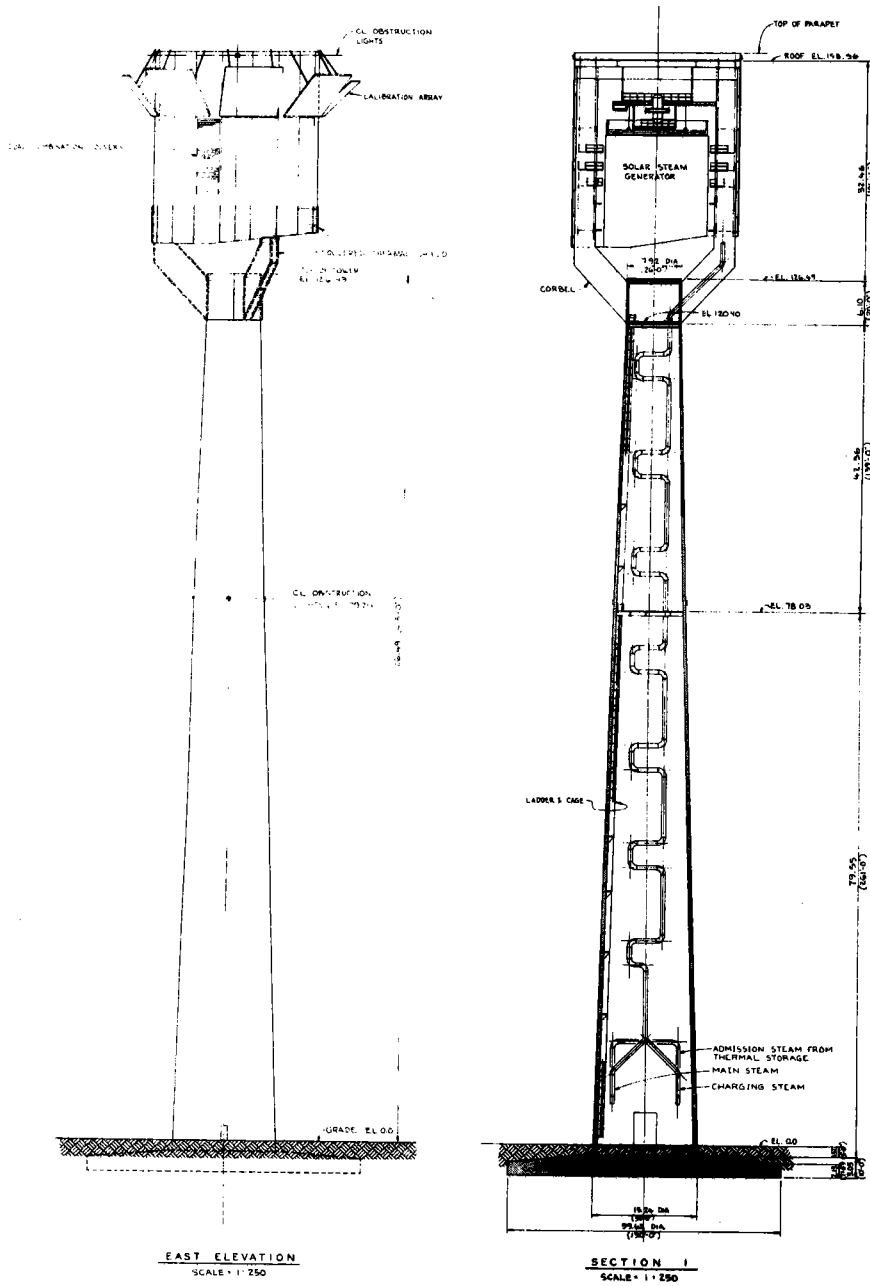
B-43

N



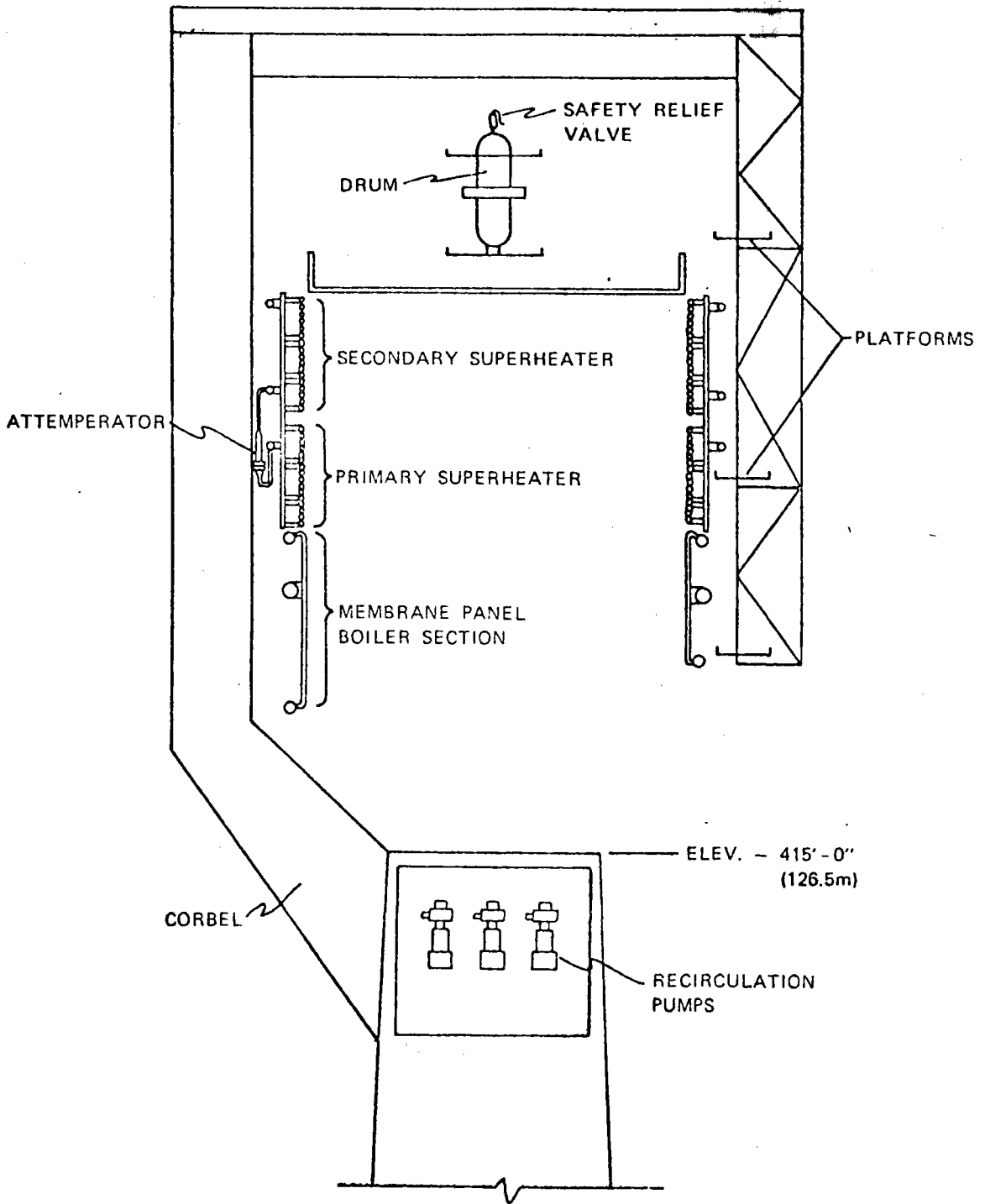
Receiver - Cavity Configuration



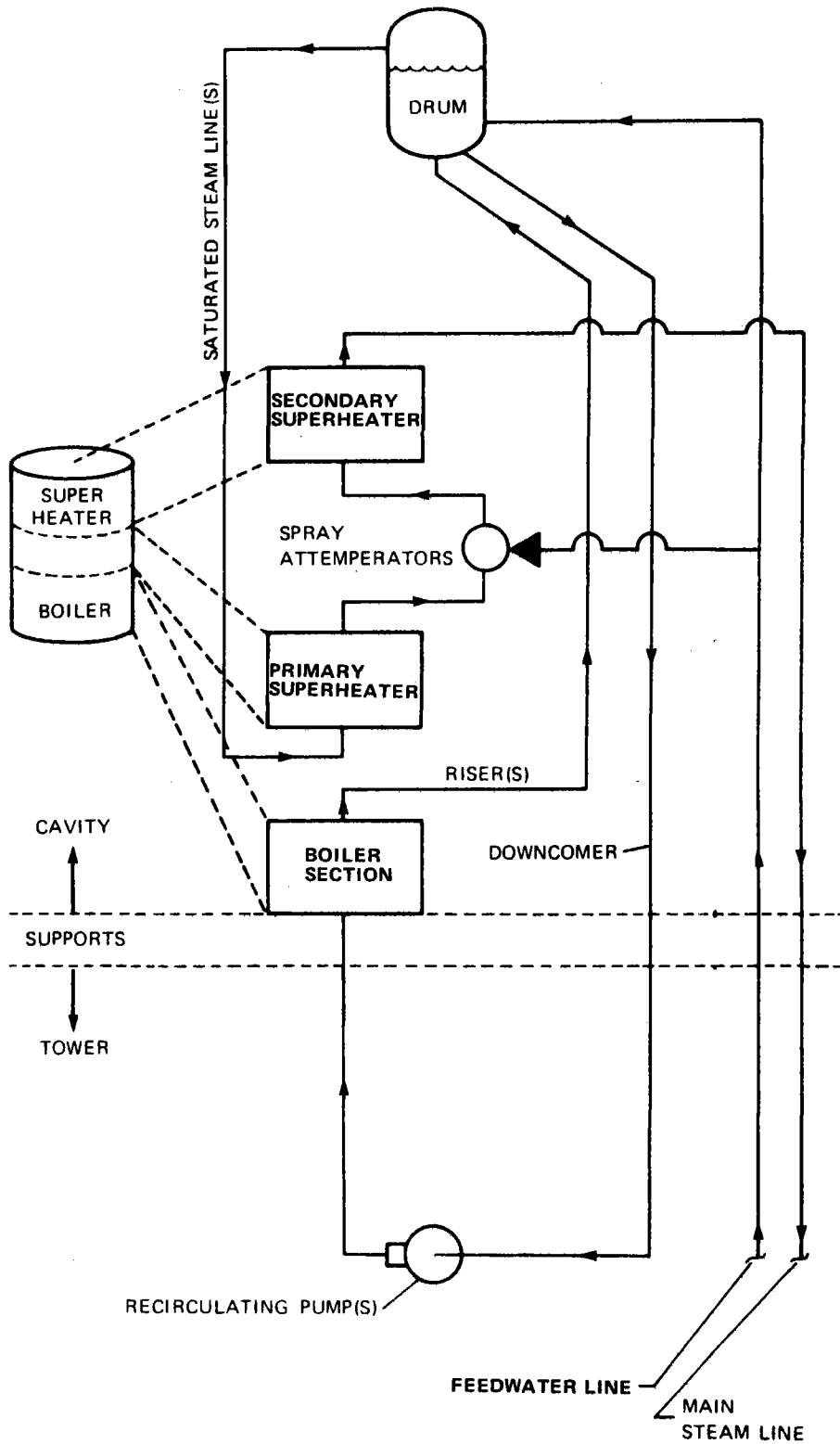


Receiver and Tower

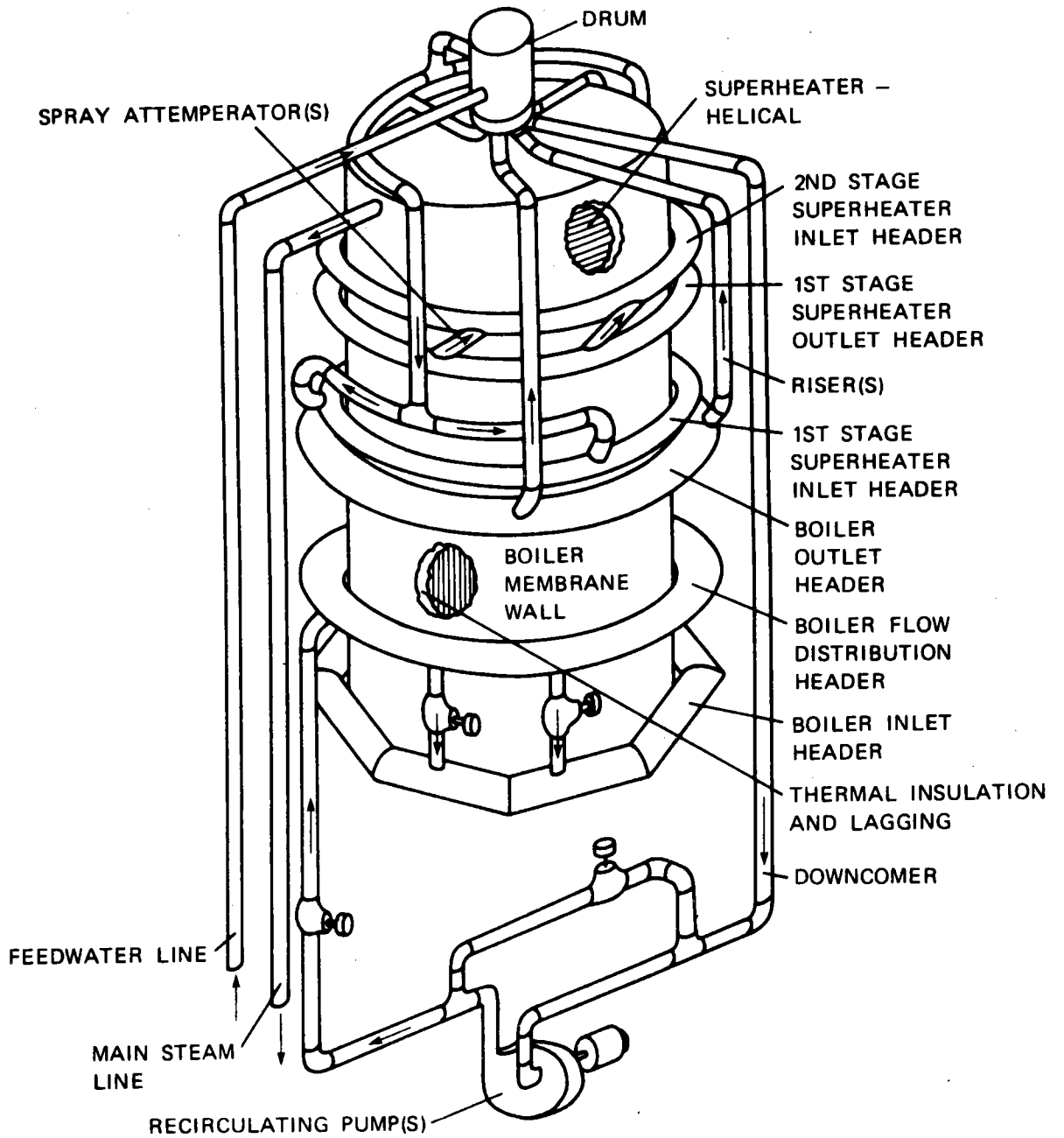
B-46



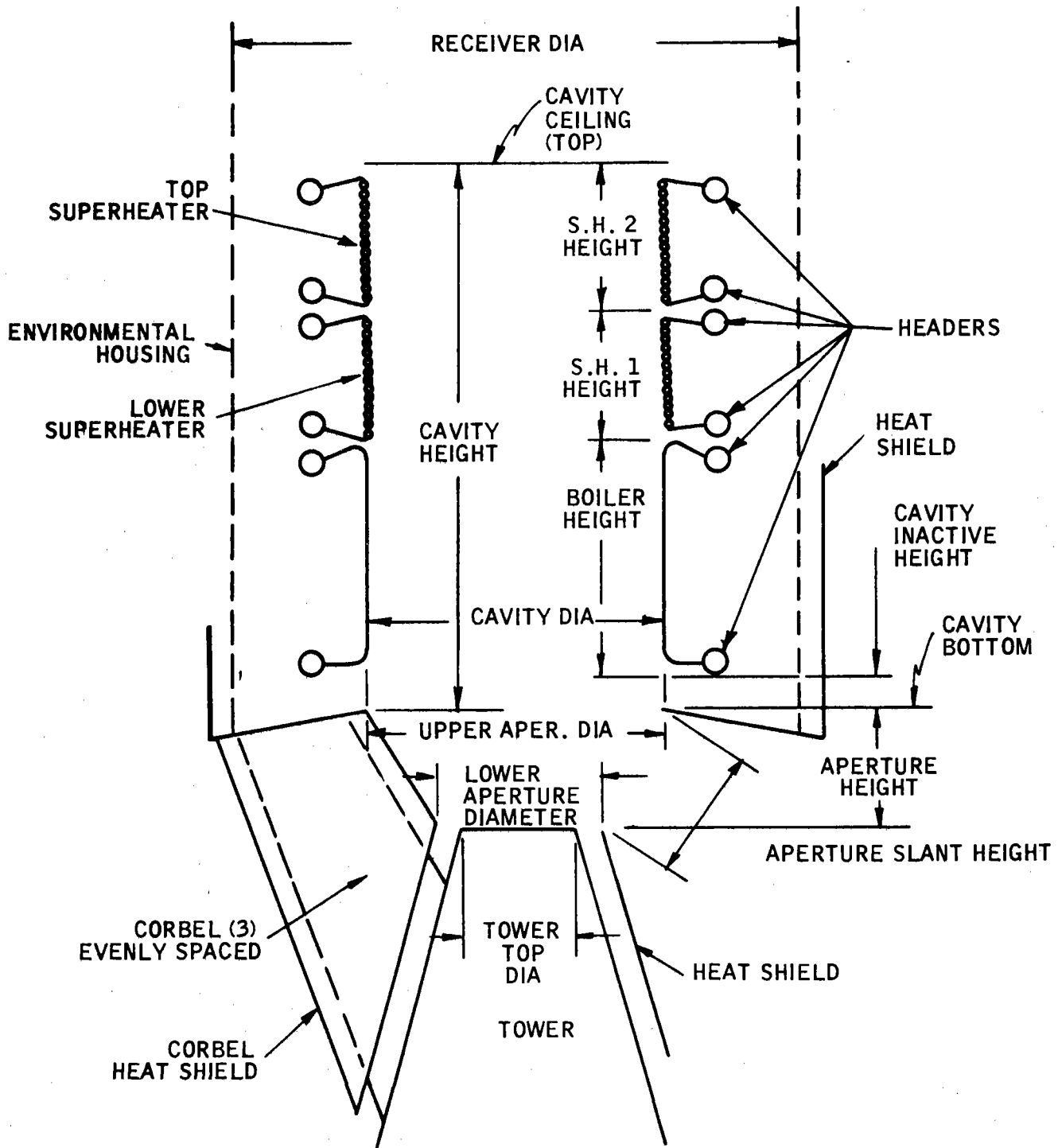
Steam Generator Housing



Solar Steam Generator - Flow Schematic



SRE Design Arrangement



Receiver Terminology

B-51

SECTION 5
THERMAL STORAGE SUBSYSTEM

40703-II

STORAGE SUBSYSTEM CHARACTERISTICS

Item No.	Characteristic	Spec (1)		Current Baseline		Spec. Var.
		PP	Com.	Pilot Plant	Commercial	
1	Total Storage Capacity (including heat loss for 23 hr)			133.1 MWh (th)	961 MWh (th)	
2	Superheater Storage					
	No. of Tanks			2	Same as PP	
	Tankage Capacity			155.1 m ³ (5476.7 ft ³)	1240.85 m ³ (43,815.3 ft ³)	
	Tank Size			7 m x 4.3 m (20 ft dia x 16 ft high at wall)	12.2 m x 9.8 m (40 ft x 32 ft high at wall)	
	Tank Material			SS 304	Same as PP	
	Storage Material			HITEC	Same as PP	
	Storage Material Qty.			253,558 Kg (558,990 #)	1,927,768 Kg (4,249,929 #)	
	Capacity (including 23 hr heat loss)			17.1 MWh (th)	130 MWh (th)	
3	Main Storage					
	No. of Tanks			1	2	
	Tank Capacity			3418 m ³ (120,700 ft ³)	26,970 m ³ (952,335 ft ³)	
	Tank Size			18.3 m dia x 14.6 m (60 ft dia x 48 ft high at the wall)	34.8 dia x 14.63 m high (114 ft dia x 48 ft high at the wall)	
	Tank Material			Low Alloy Steel	Same as PP	

NOTE: (1) See Section I for specification and requirement source identification.

40703-II

B-52

STORAGE SUBSYSTEM CHARACTERISTICS

Item No.	Characteristic	Spec (1)		Current Baseline		Spec. Var.
		PP	Com.	Pilot Plant	Commercial	
	Main Storage (Cont)					
	Storage Material			Granite 13mm (0.5 in.) ASTM Grade 6 Oil-Caloria HT-43	Same as PP	
	Material Quantity			Granite 7161t (7894 Tons) Oil 827,882 l (218,727 gal)	Same as PP Granite 51,312t (56,561 Tons) Oil 6,141,672 l (1,622,635 gal)	
	Storage Capacity (incl. heat loss after 23 hr)			116 MWh (th)	831 MWh (th)	
4	Heat Loss Rate			5%/Day	Same as PP	
5	Gross Turbine Heat Rate From Storage Only			3.512 kWh (th)/kWh(e) (11,985 Btu/kWh)	3.145kWh (th)/kWh(e) (10,733 Btu/kWh)	

40703-II

B-53

NOTE: (1) See Section I for specification and requirement source identification.

STORAGE SUBSYSTEM CHARACTERISTICS

Item No.	Characteristic	Spec (1)		Current Baseline		Spec. Var.
		PP	Com.	Pilot Plant	Commercial	
1	Total Auxiliary Power					
	Charge			337 kW(e)	2920 kW(e)	
	Discharge			207 kW(e)	1984 kW(e)	
	Hold			44 kW(e)	351 kW(e)	
2	Total Noninterruptible Pwr.					
	Charge			30 kW(e)	269 kW(e)	
	Discharge			30 kW(e)	269 kW(e)	
	Hold			30 kW(e)	269 kW(e)	
3	Charging (Design)					
	Steam Inlet Pressure			10.1 MPa (1465 psia)	Same as PP	
	Temperature			510°C (950°F)	Same as PP	
	Flow			13.96 kg/s (110,782 lb/h)	95.76kg/s (760,000 lb/h)	
	Attemperator Pressure			10.2 MPa (1480 psia)	Same as PP	
	Temperature			205°C(461°F)	Same as PP	
	Flow			203°C (397°F) - Turbine on 1.42 kg/s (11,237 lb/h)	9.71 kg/s (77,059 lb/h)	
	Condensate Pressure			9.8 MPa (1423 psia)	Same as PP	
Temperature			256°C (492°F)	Same as PP		
Flow			15.37 kg/s (122,013 lb/h)	105.5 kg/s (837,059 lb/h)		

NOTE: (1) See Section I for specification and requirement source identification.

40703-II

B-54

STORAGE SUBSYSTEM CHARACTERISTICS

Item No.	Characteristic	Spec (1)		Current Baseline		Spec. Var.
		PP	Com.	Pilot Plant	Commercial	
1	Discharging (Design)					
	SH Outlet Pressure			3.62 MPa (532 psia)	Same as PP	
	Temperature			391°C (735°F)	Same as PP	
2	Flow			13.61 kg/s (108,080 lb/h)	114.0 kg/s (904,497 lb/h)	
	FW Preheater					
	Input Pressure			3.79 MPa (550 psia)	Same as PP	
3	Temperature			205°C (401°F)	Same as PP	
	Flow			13.61 kg/s (108,080 lb/h)	114.0 kg/s (904,497 lb/h)	
	Desuperheater HITEC Pump					
4	Quantity			1	3	
	Type			Centrifugal, constant speed	Same as PP	
	Flow			12.91/s (205 gpm)	Same as PP	
5	Input Power			11 kW (15 HP)	Same as PP	
	Condenser Oil Pump					
	Quantity			1	3	
6	Type			Centrifugal, two speed	Same as PP	
	Flow			2651/s (4200 gpm)	Same as PP	
	Input Power			112 kW (150 HP)	Same as PP	

NOTE: (1) See Section I for specification and requirement source identification.

40703-II

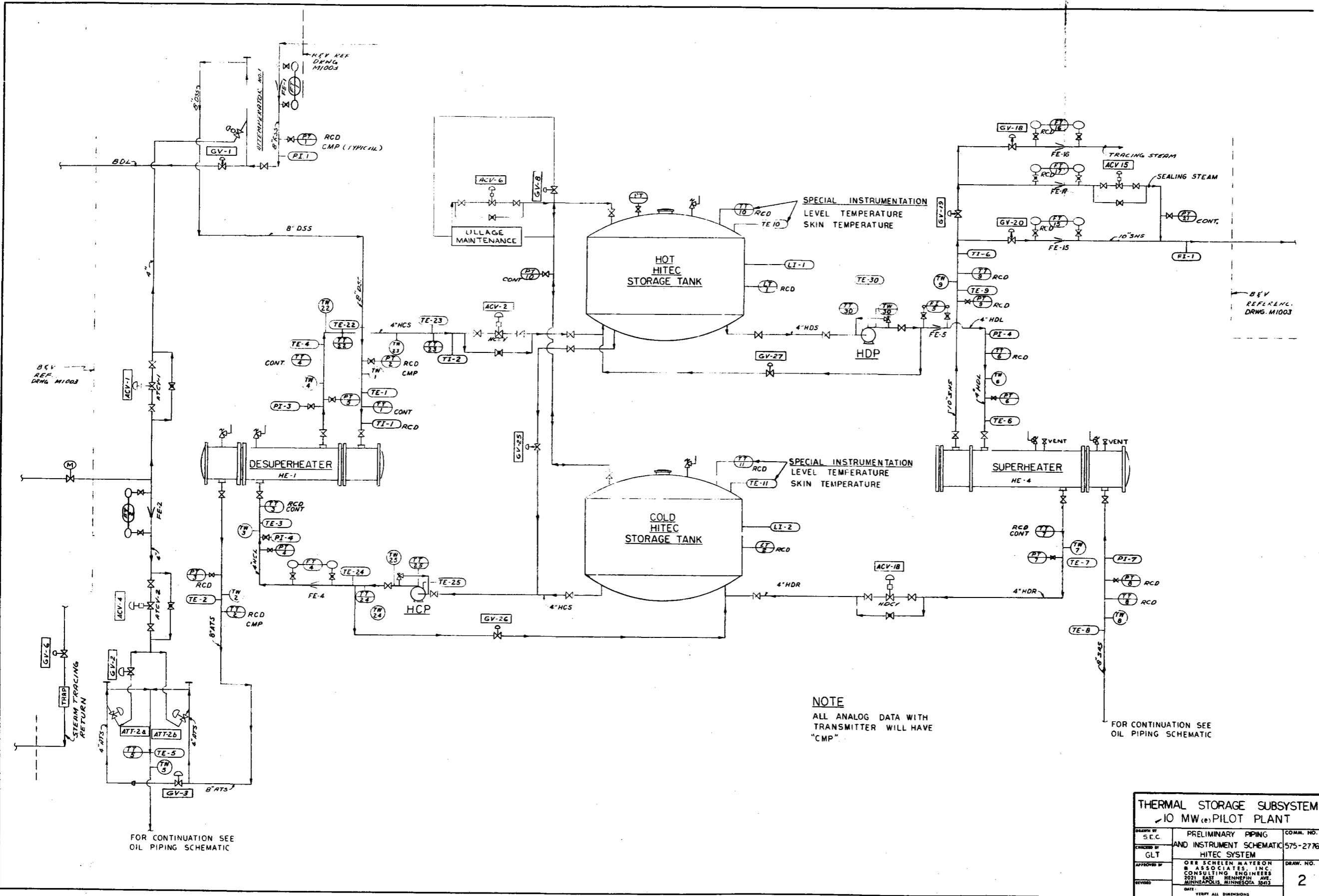
B-55

Item No.	Characteristic	Spec (1)		Current Baseline		Spec. Var.
		PP	Com.	Pilot Plant	Commercial	
1	SH HITEC Pump Quantity Type Flow Input Power			1 Centrifugal 12.9 l/s (205 gpm) 11 kW (15 HP)	4 Same as PP Same as PP Same as PP	
2	Boiler Oil Pump Quantity Type Flow Input Power			1 Centrifugal, two speed 265 l/s (4200 gpm) 112 kW (150 HP)	8 Same as PP Same as PP Same as PP	
3	Feedwater Line Velocity BFP to Storage PH Inlet			1.98 m/s (6.5 ft/s)	Same as PP	
4	Feedwater Line Pressure Drop BFP to Storage PH Inlet Friction Elevation			0.014 MPa (2 psi) 0	Same as PP Same as PP	
5	Steamline Velocity Storage SH Outlet to TAV			44.6 m/s (8788 ft/min) (Des)	Same as PP	
6	Steamline Pressure Drop Storage SH Outlet to TAV			0.345 MPa (50 psi) (Des)	Same as PP	

40703-II

B-56

NOTE: (1) See Section I for specification and requirement source identification.

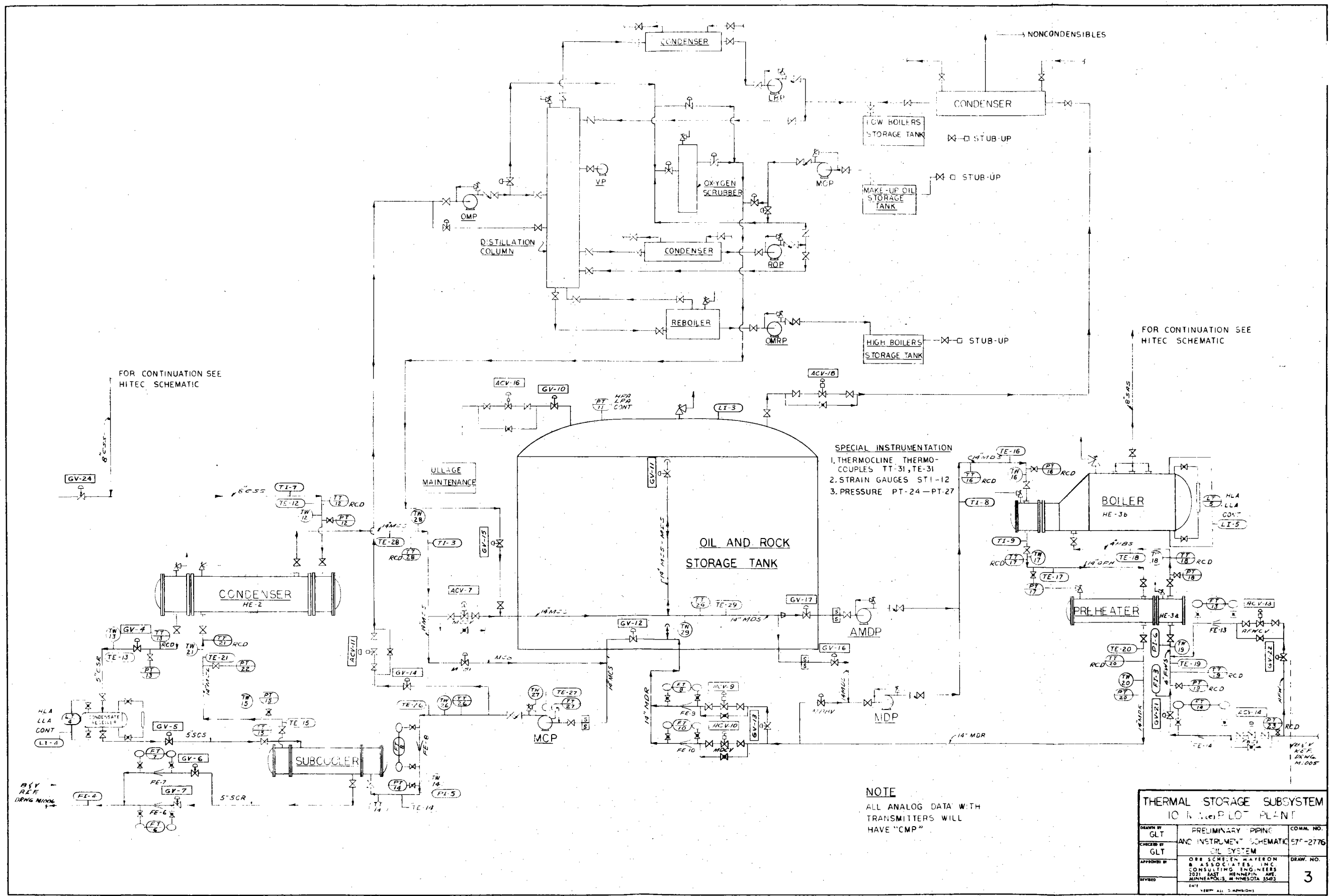


NOTE
 ALL ANALOG DATA WITH TRANSMITTER WILL HAVE "CMP".

FOR CONTINUATION SEE OIL PIPING SCHEMATIC

FOR CONTINUATION SEE OIL PIPING SCHEMATIC

THERMAL STORAGE SUBSYSTEM 10 MW(e) PILOT PLANT		
DRAWN BY S.E.C.	PRELIMINARY PIPING AND INSTRUMENT SCHEMATIC	COMM. NO. 575-2776
CHECKED BY GLT	HITEC SYSTEM	
APPROVED BY	ORE SCHELEN MAYERON & ASSOCIATES, INC. CONSULTING ENGINEERS 2021 EAST HENNEPIN AVE. MINNEAPOLIS, MINNESOTA 55413	DRAW. NO. 2
REVISED	DATE	VERIFY ALL DIMENSIONS



FOR CONTINUATION SEE HITEC SCHEMATIC

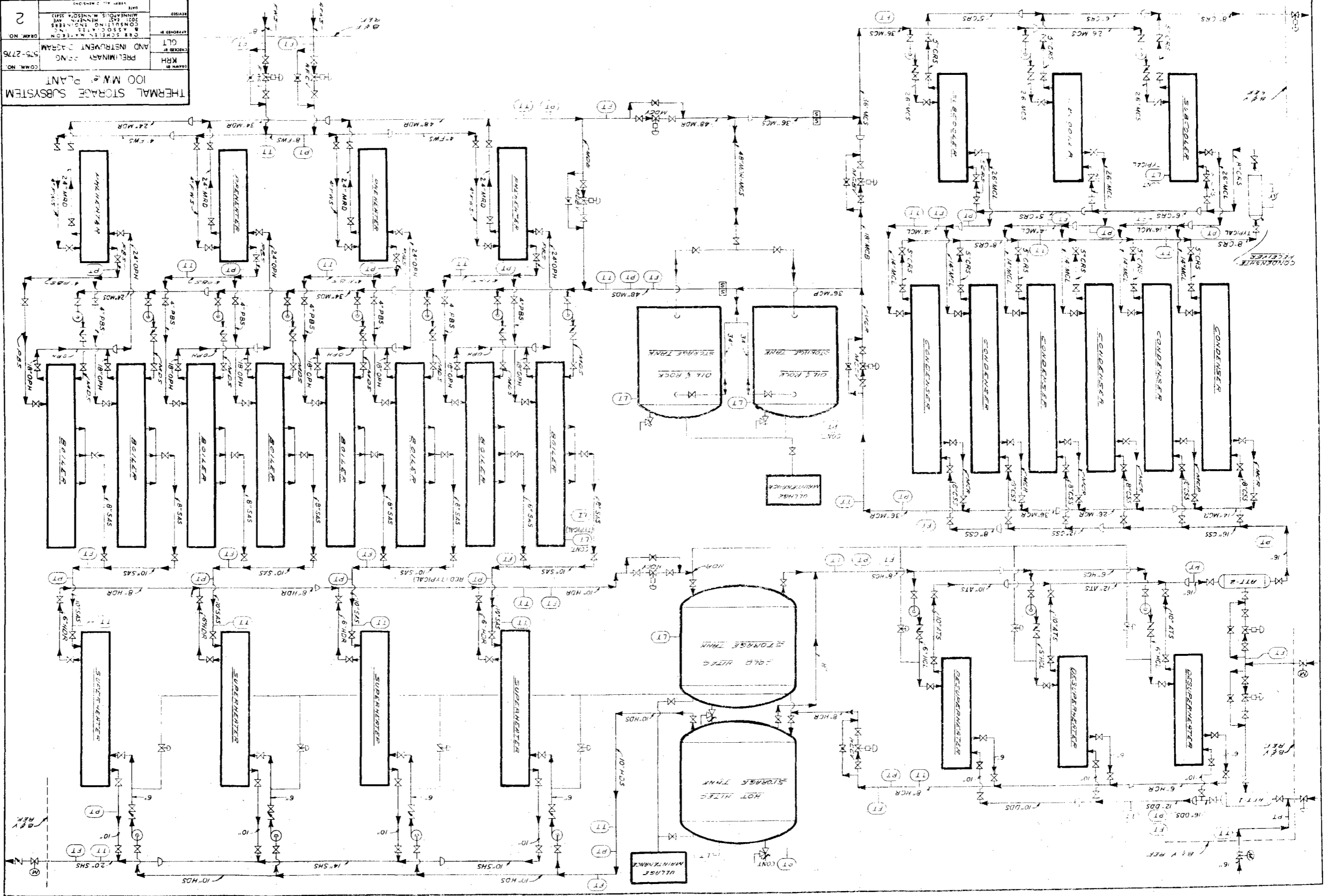
FOR CONTINUATION SEE HITEC SCHEMATIC

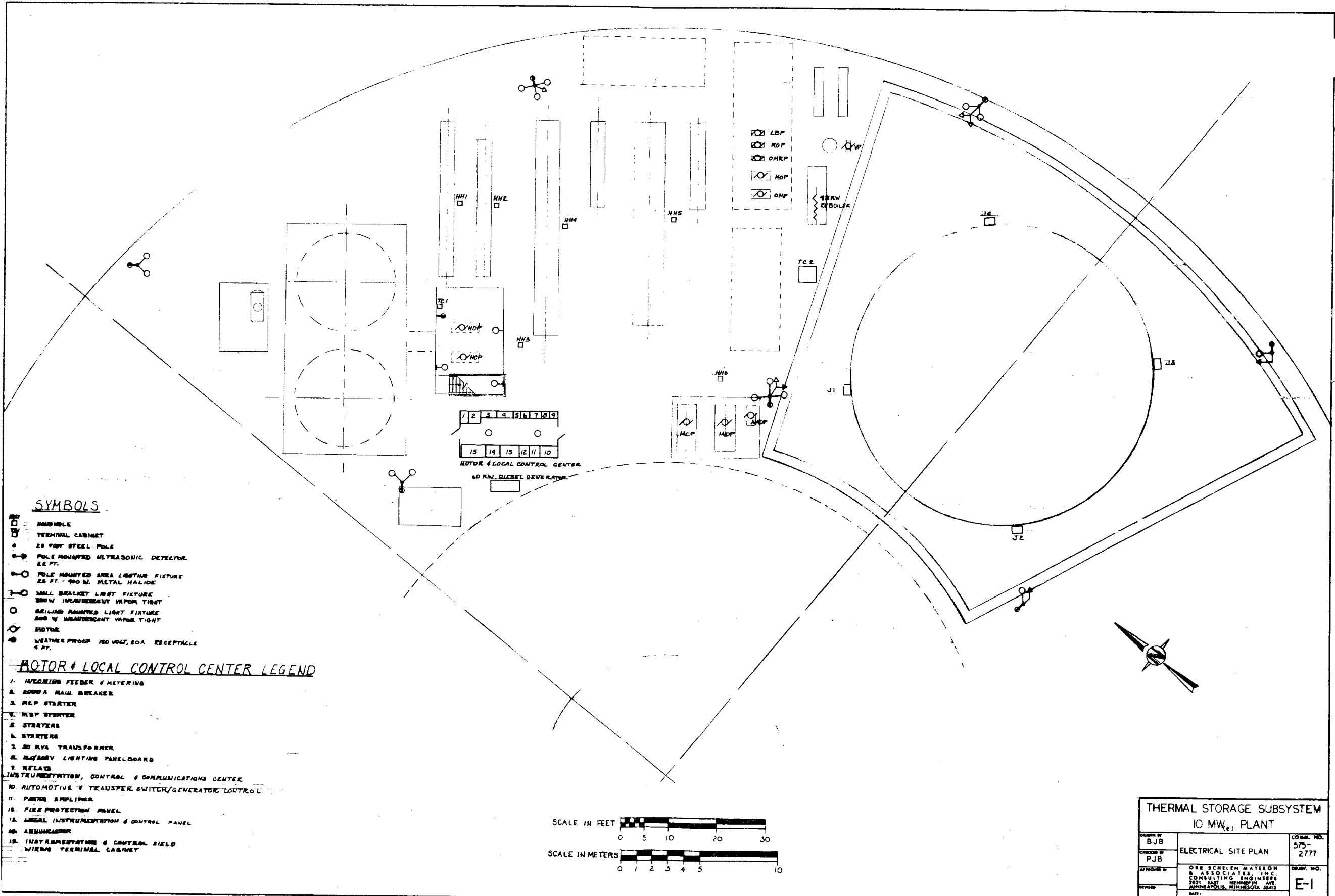
SPECIAL INSTRUMENTATION
 1. THERMOCLINE THERMO-COUPLES TT-31, TE-31
 2. STRAIN GAUGES ST-1-12
 3. PRESSURE PT-24-PT-27

NOTE
 ALL ANALOG DATA WITH TRANSMITTERS WILL HAVE "CMP"

THERMAL STORAGE SUBSYSTEM 10 MW PILOT PLANT		
DRAWN BY	PRELIMINARY PIPING AND INSTRUMENT SCHEMATIC	COMM. NO.
CHECKED BY	OIL SYSTEM	57-2776
APPROVED BY	ORR SCHEMEN WAYERSON & ASSOCIATES, INC. CONSULTING ENGINEERS 2021 EAST WENDELL AVE. MINNEAPOLIS, MINNESOTA 55413	DRAW. NO.
REVISED		3

THERMAL STORAGE SUBSYSTEM
 100 MW PLANT
 PRELIMINARY Piping AND INSTRUMENT DIAGRAM
 575-2776
 COM. NO.
 KPH
 CHECKED BY
 CLT
 APPROVED BY
 DATE
 REVISION
 2



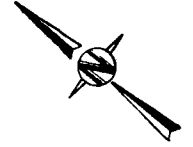
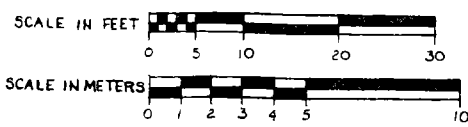


SYMBOLS

- MACHINABLE
- TERMINAL CABINET
- 25 FOOT STEEL POLE
- POLE MOUNTED ULTRASONIC DETECTOR 22 FT.
- POLE MOUNTED AREA LIGHTING FIXTURE 25 FT. - 400 W. METAL HALIDE
- SMALL BRACKET LIGHT FIXTURE 250W INCANDESCENT VAPOR TIGHT
- CEILING MOUNTED LIGHT FIXTURE 400 W INCANDESCENT VAPOR TIGHT
- MOTOR
- WEATHER PROOF 120 VOLT, 20A RECEPTACLE 4 FT.

MOTOR & LOCAL CONTROL CENTER LEGEND

- 1. INCOMING FEEDER & METERING
- 2. 600VA MAIN BREAKER
- 3. MCP STARTER
- 4. MDP STARTER
- 5. STARTERS
- 6. STARTERS
- 7. 25 KVA TRANSFORMER
- 8. 120/240V LIGHTING PANELBOARD
- 9. RELAYS
- 10. INSTRUMENTATION, CONTROL & COMMUNICATIONS CENTER
- 11. AUTOMOTIVE T TRANSFER SWITCH/GENERATOR CONTROL
- 12. PAPER AMPLIFIER
- 13. FIRE PROTECTION PANEL
- 14. LOCAL INSTRUMENTATION & CONTROL PANEL
- 15. ASSEMBLY
- 16. INSTRUMENTATION & CONTROL FIELD
- 17. WIRING TERMINAL CABINET

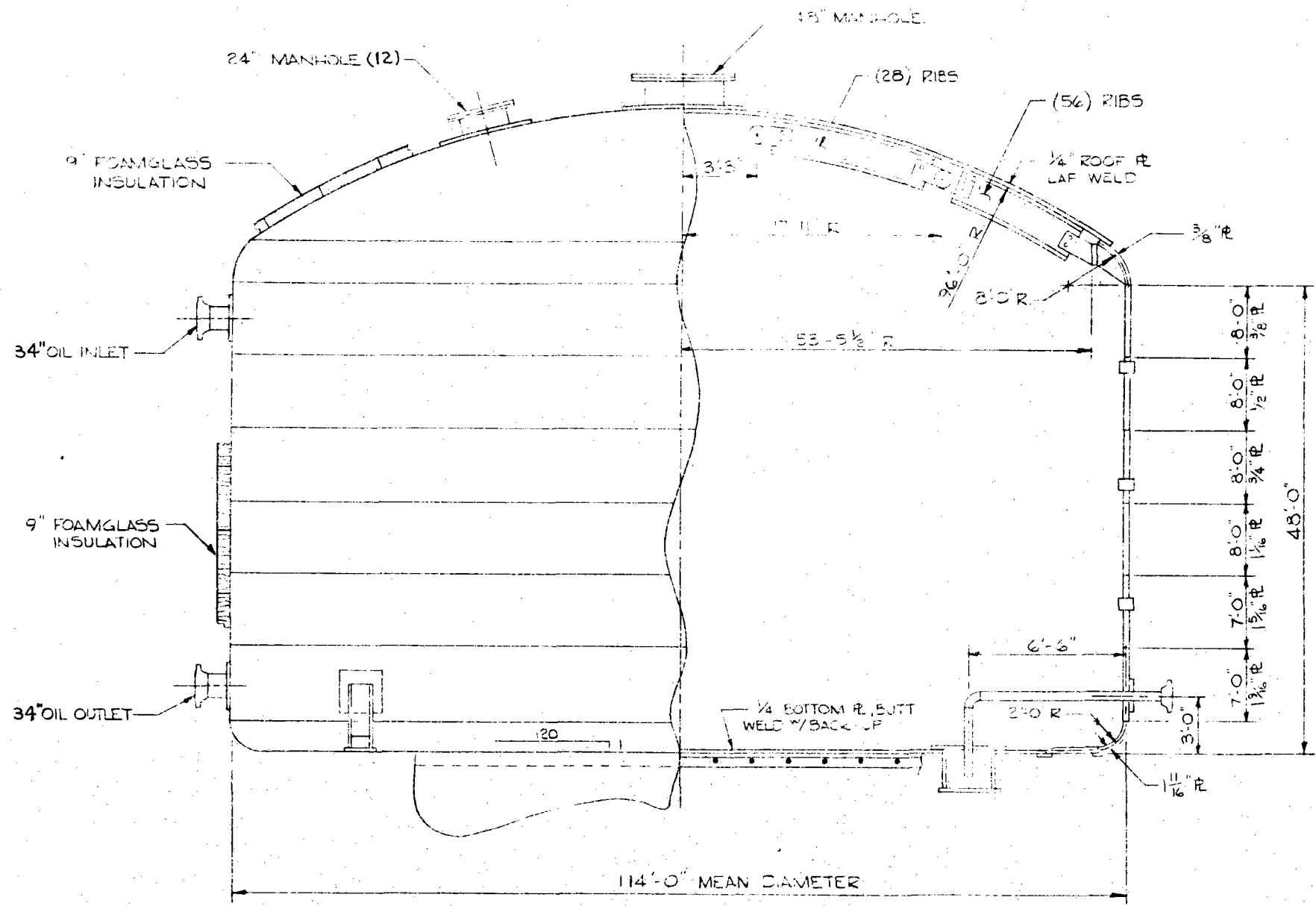


THERMAL STORAGE SUBSYSTEM 10 MW_e PLANT		
DESIGNED BY BJB	ELECTRICAL SITE PLAN	CONTRACT NO. 575-2777
CHECKED BY PJB		DRAWING NO. E-1
APPROVED BY	ORE SCHELEN MAYERSON & ASSOCIATES, INC. CONSULTING ENGINEERS 2021 EAST HENNINGSON AVE. MINNEAPOLIS, MINNESOTA 55417	
REVISED	DATE: 1987 ALL DIMENSIONS	

B 1 7 1 6 1 5 4 1 3 1 2 1 1

B-69

D
C
3



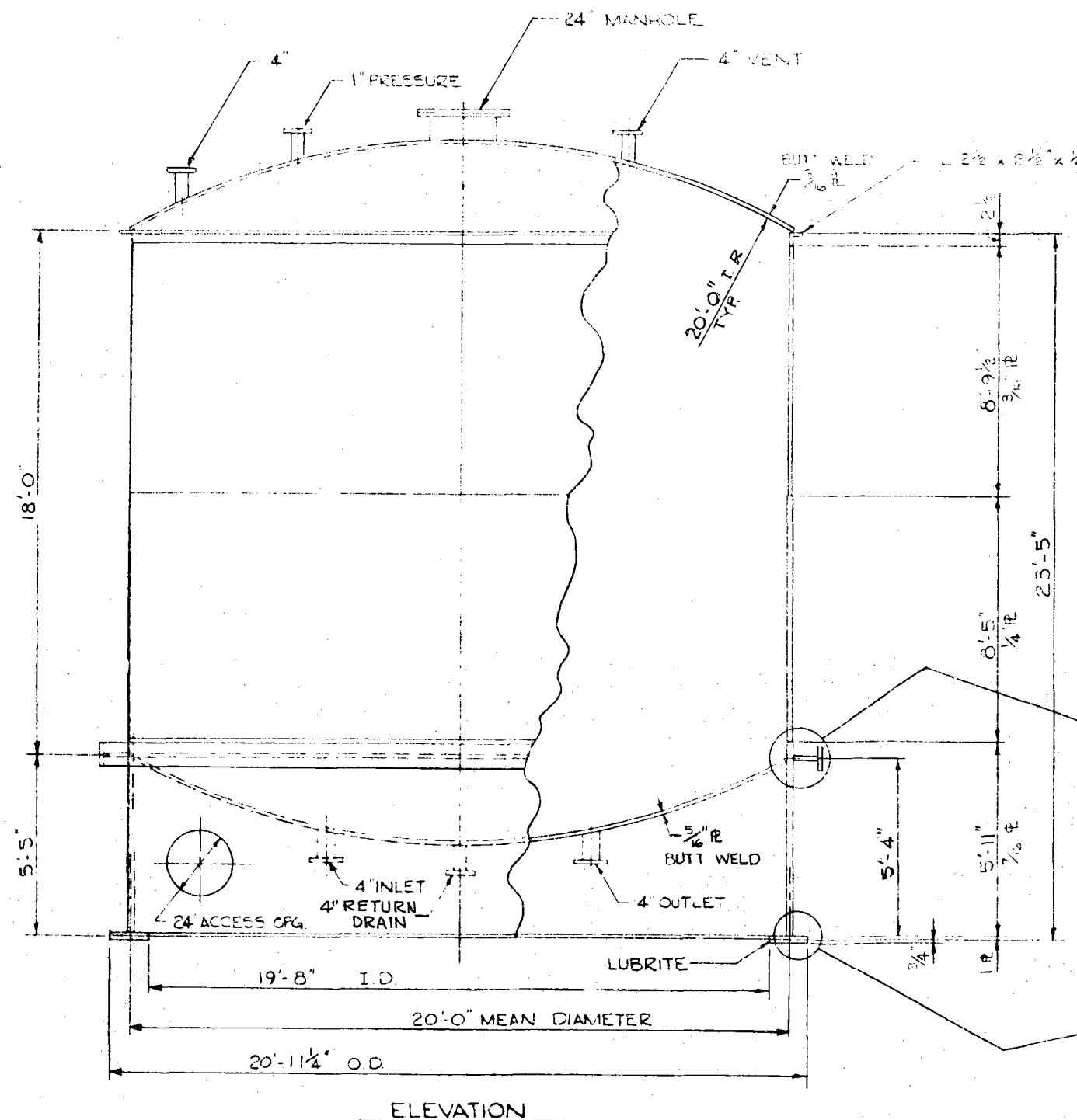
ELEVATION

DESIGN DATA	
DESCRIPTION	114" DIA. OIL/ROCK TANK FOR HONEYWELL
NUMBER REQUIRED	2
CAPACITY	43,000 GALLONS
DESIGN PRESSURE	1.5 PSI
OPERATING PRESSURE	1.5 PSI
TEST PRESSURE	1.625 PSI
DESIGN TEMPERATURE	600 ST. IN. COLLAPSE
TEST TEMPERATURE	AMBIENT
JOINT EFFICIENCY	NO SHELL
CORROSION ALLOWANCE	NONE
CODE & STAMP	SEE NOTE # 2
CUSTOMER SPECIFICATION	EXHIBIT A
MATERIALS	
SHELL & BOT. KNUCKLE	A 533 CLASS 2 GRADE A
TOPE TOP KNUCKLE	A 516-60
HEADS	NONE
NOZZLE	NECK A 516
MANWAY	A 516-60 FLANGE A 516-60 COVER A 516-60
REINFORCING PADS	A 533 CLASS 2 GRADE A
PIPE	A 516
COUPLINGS	A 516
STIFFENER RINGS	A 516
INTERNAL	A 516
BOLTING	BOLTS A 533 NUTS A 516 STUDS A 516
GASKETS	COMPRESSION ASBESTOS
STRUCTURAL	A 516
ELECTRODES	A 516
STRESS RELIEF	REQUIRED PWHT PER ASME SECTION VIII
CLEANING	BROOM CLEAN AFTER ERECTION
SURFACE PREPARATION	NONE
CONSTRUCTION	
INTERNAL PAINTING	NONE
EXTERNAL PAINTING	NONE
LINING	NONE
INSULATION	REQUIRED, 9" OF FOAMGLASS & 5" ROCK WOOL
LADDERS & PLATFORMS	NONE & ANCHOR CHAIRS
CATHODIC PROTECTION	NONE
FOUNDATIONS	3000 PSI CONCRETE & 4" DIA. REBAR PER DRAWING
QUALITY ASSURANCE	
QA MANUAL	NOT APPLICABLE
MILL CERTIFICATIONS	ALL PRESSURE RETAINING MATERIAL
WELDERS	ASME SECTION 9 QUALIFIED
WELDING	PER A.P.I. STD. 650 APP. D
NONDESTRUCTIVE TESTING	RADIOGRAPH SHELL & BOTTOM KNUCKLE
SPECIAL TESTING	PER A.P.I. STD. 650 APP. D
TESTING	NONE
SHELL	HYDROTEST + 1.625 PSI
BOTTOM	VACUUM BOX PER A.P.I. STD. 650
ROOF	VACUUM BOX PER A.P.I. STD. 650

NOTES: 1. FLANGE BOLT HOLES STRADDLE TANK VERTICAL & RADIAL CENTER LINES UNLESS OTHERWISE SPECIFIED.
 2. A.P.I. STD. 650 APP. D, FOR FABRICATION, ERECTION, TESTING & EXAMINATION. A.P.I. STD. 650 APP. D, DESIGN MODIFIED FOR THERMAL LOADS.

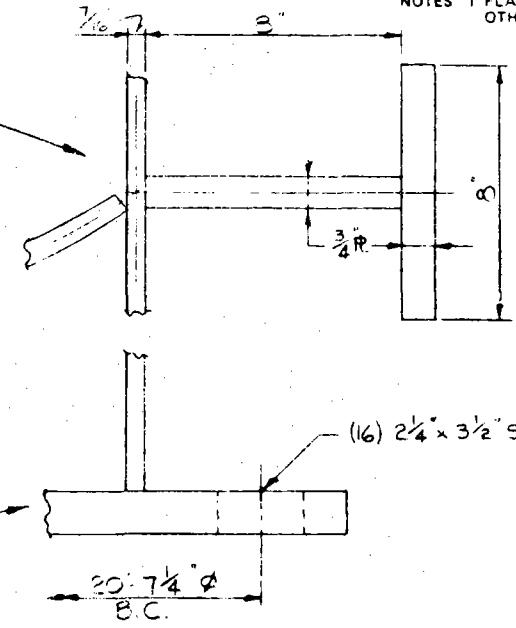
PROJECT ENGINEER APPROVAL & DATE X/11/4-5-77	CHECKED BY & DATE X/11/4-5-77	DRAWN BY & DATE X/11/4-5-77	NO.	REVISION
			<p>BROWN-MINNEAPOLIS TANK</p> <p>THIS DRAWING IS THE PROPERTY OF BROWN-MINNEAPOLIS TANK AND IS TO BE USED ONLY IN CONNECTION WITH WORK PERFORMED BY BROWN-MINNEAPOLIS TANK. THE DRAWING IS NOT TO BE COPIED IN WHOLE OR IN PART AND MUST BE RETURNED UPON REQUEST.</p> <p>PURCHASER'S NO.</p>	
DESCRIPTION			114" φ x 48' HIGH OIL/ROCK TANK FOR HONEYWELL	
DRAWING NUMBER			77-D441103	
ORDER NUMBER			SHEET	

1 2 3 4 5 6 7 8 9 10 11 12 13 14 15 16 17 18 19 20 21 22 23 24 25 26 27 28 29 30 31 32 33 34 35 36 37 38 39 40 41 42 43 44 45 46 47 48 49 50 51 52 53 54 55 56 57 58 59 60 61 62 63 64 65 66 67 68 69 70 71 72 73 74 75 76 77 78 79 80 81 82 83 84 85 86 87 88 89 90 91 92 93 94 95 96 97 98 99 100



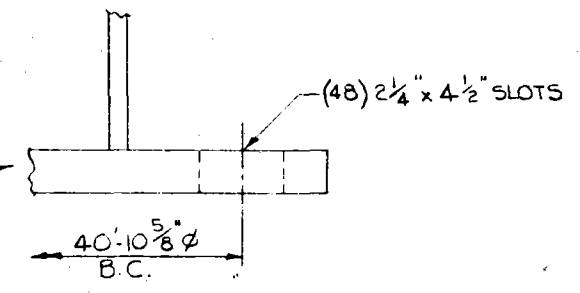
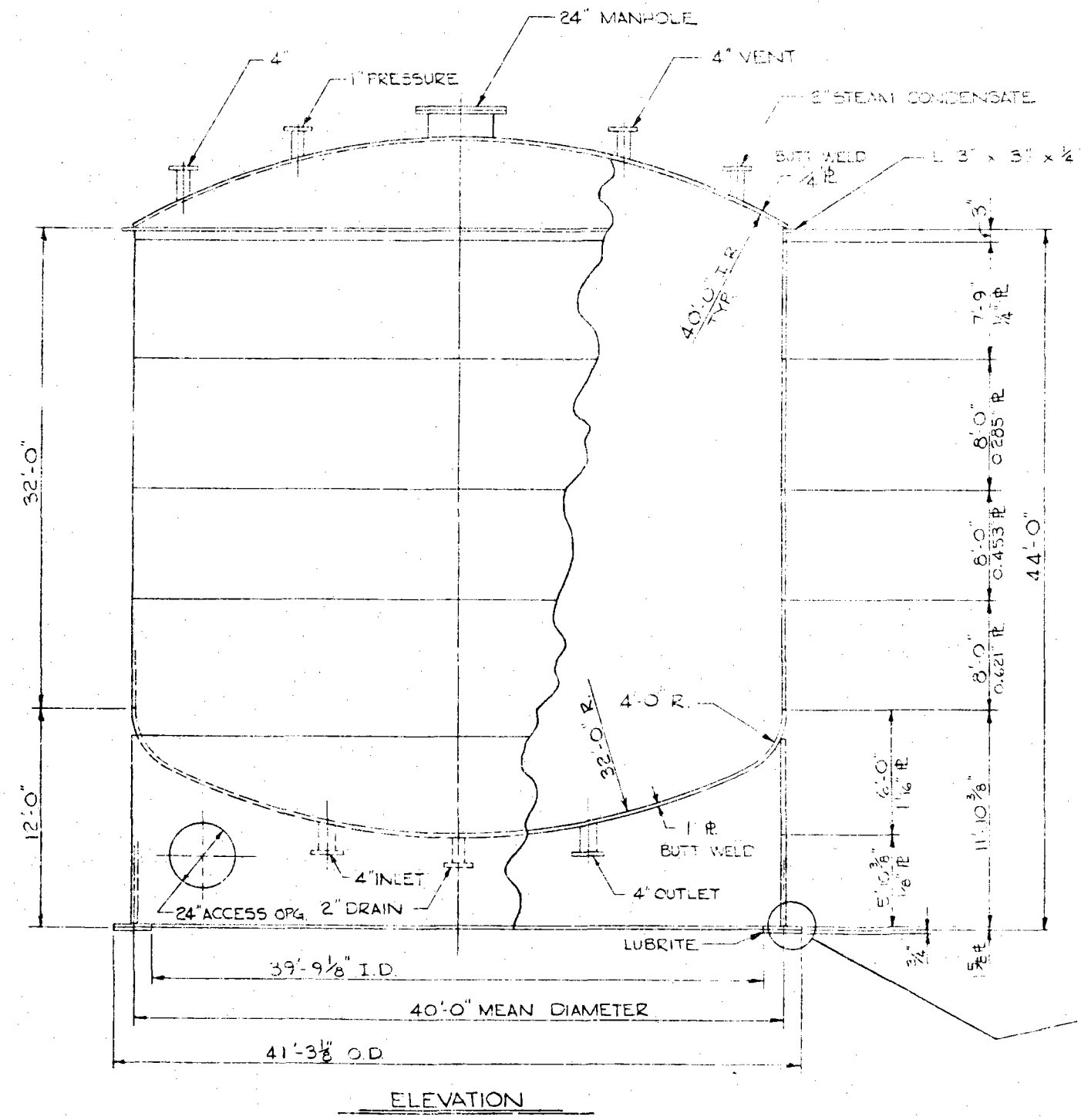
DATA SHEET		B-71
DESCRIPTION	20' x 18' HITEC TANK	
NUMBER REQUIRED	1	
CAPACITY	PROD. HEAD 150' OF 6" DIA.	
DESIGN PRESSURE	PROD. HEAD 150' OF 6" DIA.	
OPERATING PRESSURE	PROD. HEAD 150' OF 6" DIA.	
TEST PRESSURE	HYDROSTATIC HEAD 400' PSIG	
DESIGN TEMPERATURE	AMBIENT	
TEST TEMPERATURE	AMBIENT	
JOINT EFFICIENCY	1.0	
CORROSION ALLOWANCE	AP 101 220 1R 5/16"	
CODE & STAMP	AP 101 220 1R 5/16"	
CUSTOMER SPECIFICATION	EXHIBIT A	
SHELL	A 240-304	
TOP/BOTTOM	NONE	
HEADS	A 240-304	
NOZZLE	NECK A 240-304	FLANGE A 150' 20A
MANWAY	NECK A 240-304	FLANGE A 150' 20A COVER A 150' 20A
REINFORCING PADS	A 240-304	
PIPING	NONE	
COUPLINGS	NONE	
STIFFENER RINGS	A 240-304	
INTERNAL	NONE	
BOLTING	BOLTS A 150' 20A NUTS A 150' 20A	STUCCO WANE
GASKETS	COMP. GASKETS	
STRUCTURAL	A 240-304	
ELECTRODES	F 308	
STRESS RELIEF	N/A	
CLEANING	N/A	
SURFACE PREPARATION	N/A	
INTERNAL PAINTING	N/A	
EXTERNAL PAINTING	N/A	
LINING	N/A	
INSULATION	N/A	
LADDERS & PLATFORMS	N/A	
CATHODIC PROTECTION	N/A	
FOUNDATIONS	N/A	
Q.A. MANUAL	NOT APPLICABLE	
MILL CERTIFICATIONS	RECORD ON ALL PRESS. RETAINING PARTS	
WELDERS	DETERM. BY TEST ONLY IN QUAL. FILE	
WELDING	N/A	
NONDESTRUCTIVE TESTING	N/A	
SPECIAL TESTING	NONE	
SHELL TESTING	HYDROTEST + 0.25 PSIG	
BOTTOM TESTING	0.125 PSIG w/ SOAP SUDS	
ROOF TESTING	0.125 PSIG w/ SOAP SUDS	

NOTES 1 FLANGE BOLT HOLES STRADDLE TANK VERTICAL & RADIAL CENTER LINES - UNLESS OTHERWISE SPECIFIED.



PROJECT ENGINEER APPROVAL & DATE	CHECKED BY & DATE	DRAWN BY & DATE 4-4-77	NO.	REVISION
			THIS DRAWING IS THE PROPERTY OF BROWN-MINNEAPOLIS TANK AND IS TO BE USED ONLY IN CONNECTION WITH WORK PERFORMED BY BROWN-MINNEAPOLIS TANK. THE DRAWING IS NOT TO BE COPIED IN WHOLE OR IN PART AND MUST BE RETURNED UPON REQUEST.	
			PURCHASER'S NO.	
			DESCRIPTION 20' x 18' HIGH HITEC TANK FOR HONEYWELL	
			DRAWING NUMBER 77-044102	
			ORDER NUMBER	

D
C
B
A



DATA SHEET	
DESCRIPTION	40' x 32' HITEC TANK
NUMBER REQUIRED	1
CAPACITY	100 TONS
DESIGN PRESSURE	HYDROSTATIC HEAD + 0.125 PSI
OPERATING PRESSURE	HYDROSTATIC HEAD + 0.125 PSI
TEST PRESSURE	HYDROSTATIC HEAD + 0.125 PSI
DESIGN TEMPERATURE	AMBIENT
TEST TEMPERATURE	AMBIENT
JOINT EFFICIENCY	AS PER SHELL & BOTTOM HEAD
CORROSION ALLOWANCE	AS PER WELDED JOINTS
CODE & STAMP	API STD 620 NO. 1
CUSTOMER SPECIFICATION	EXHIBIT A
SHELL	A 240-304
TOP, BOTTOM	NONE
HEADS	A 240-304
NOZZLE	NECK A 32-304 FLANGE A 307-304
MANWAY	NECK A 240-304 FLANGE A 240-304
REINFORCING PADS	A 240-304
PIPING	NONE
COUPLINGS	NONE
STIFFENER RINGS	A 240-304
INTERNALS	NONE
BOLTING	BOLTS A 193-B NUTS A 193-B
GASKETS	COMB. ASBESTOS
STRUCTURAL ELECTRODES	A 240-304 E 308
STRESS RELIEF	N.A.
CLEANING	N.A.
SURFACE PREPARATION	N.A.
INTERNAL PAINTING	N.A.
EXTERNAL PAINTING	N.A.
LINING	N.A.
INSULATION	N.A.
LADDERS & PLATFORMS	N.A.
CATHODIC PROTECTION	N.A.
FOUNDATIONS	N.A.
O.A. MANUAL	NOT APPLICABLE
MILL CERTIFICATIONS	READ ON ALL PRESSURE RETAINING PARTS
WELDERS	AS PER SECTION IX QUALIFIED
WELDING	PER API STD 620
NONDESTRUCTIVE TESTING	RADIOGRAPH SHELL & BOTTOM HEAD PER API STD 620
SPECIAL TESTING	NONE
SHELL	HYDROTEST + 0.125 PSI
BOTTOM	
ROOF	0.125 PSI W/ SOAP BUBS

NOTES: 1. FLANGE BOLT HOLES STRADDLE TANK VERTICAL & RADIAL CENTER LINES - UNLESS OTHERWISE SPECIFIED.

PROJECT ENGINEER APPROVAL & DATE	CHECKED BY & DATE	DRAWN BY & DATE 4-5-77	NO. _____	REVISION _____
			<p>BROWN-MINNEAPOLIS TANK</p> <p>THIS DRAWING IS THE PROPERTY OF BROWN-MINNEAPOLIS TANK AND IS TO BE USED ONLY IN CONNECTION WITH WORK PERFORMED BY BROWN-MINNEAPOLIS TANK. THE DRAWING IS NOT TO BE COPIED IN WHOLE OR IN PART AND MUST BE RETURNED UPON REQUEST.</p> <p>PURCHASER'S NO. _____</p>	
DESCRIPTION 40' x 32' HIGH HITEC TANK FOR HONEYWELL			DRAWING NUMBER 17-D44104	
ORDER NUMBER			SHEET	

B-75

SECTION 6
ELECTRICAL GENERATION SUBSYSTEM

40703-II

ELECTRICAL GENERATION SUBSYSTEM CHARACTERISTICS

Item No.	Characteristic	Spec (1)		Current Baseline		Spec. Var.
		PP	Com.	Pilot Plant	Commercial	
1	Gross Capacity			12 MW(e)*	110.62 MW(e)	
2	Output Frequency			60 Hz	Same as PP	
3	Output Voltage			13,800 Volts	Same as PP	
4	Gross Turbine Efficiency			0.345* 0.285*	0.385* 0.318*	
5	Auxiliary Power Need***			See Table A	See Table B	
6	Net Capacity - Receiver			10 MW(e)*	97.8 MW(e)	
7	Net Capacity - Storage			7.5 MW(e)*	74.4 MW(e)	
8	Gross Capacity - Storage			9 MW(e)*	89.9 MW(e)	
9	Gross Cycle Heat Rate			10,428 kJ/kWh (9884 Btu/kWh)*	9353 kJ/kWh (8865 Btu/kWh) ⁺	
10	Net Cycle Heat Rate			10,995 kJ/kWh (10,422 Btu/kWh)*	9671 kJ/kWh (9167 Btu/kWh) ⁺	
11	Gross Plant Heat Rate			11,626 kJ/kWh (11,020 Btu/kWh)*	10,361 kJ/kWh (9821 Btu/kWh) ⁺	
12	Net Plant Heat Rate			13,933 kJ/kWh (13,207 Btu/kWh)*	11,721 kJ/kWh (11,110 Btu/kWh) ⁺	
13	Steam H. P. Header Size			20.3 cm (8 in.) nominal	30.5 cm (12 in.) Nominal each Rec Branch 50.8 cm (20 in.) Nominal Common Header	
14	Receiver Superheater			10.6 MPa (1540 psia)	11.48 MPa (1665 psia) [⊕] 10.83 MPa (1570 psia) ⁺	

40703-II

B-76

NOTE: (1) See Section I for specification and requirement source identification.

* Receiver Design Point.

+ 100 MW(e) net receiver steam driving turbine

* Storage Design Point

⊕ 1.7 times 100 MW(e) net steam flow

** Simultaneous Storage and Receiver

*** At receiver design point

ELECTRICAL GENERATION SUBSYSTEM CHARACTERISTICS

Item No.	Characteristic	Spec (1)		Current Baseline		Spec. Var.
		PP	Com.	Pilot Plant	Commercial	
15	Receiver Superheater Outlet Temperature			516°C (960°F)	518°C (965°F)	

NOTE: (1) See Section I for specification and requirement source identification.

40703-II

B-77

ELECTRICAL GENERATION SUBSYSTEM CHARACTERISTICS

Item No.	Characteristic	Spec (1)		Current Baseline		Spec. Var.
		PP	Com.	Pilot Plant	Commercial	
1	Turbine Design H. P. Throttle Steam Pressure			10.1 MPa (1465 psia)	Same as PP	
2	Turbine Design H. P. Throttle Steam Temperature			510 °C (950 °F)	Same as PP	
3	Steam Line Pressure Drop due to Friction-Receiver SH Outlet to Turbine Throttle Valve			517 kPa (75 psi)*	1379 kPa (200 psi) [⊕] 724 kPa (105 psi) ⁺	
4	Turbine Throttle H. P. Design Flow			49,592 kg/h (109,332 lbs/h)*	411,206 kg/h (906,555 lb/h)*	
5	Steam Line Temperature Drop Receiver SH Outlet to Turbine Throttle Valve			6 °C (10 °F)	8 °C (15 °F)	
6	Storage Superheater Outlet Pressure			3.6 MPa (532 psia) [⊙] *	Same as PP	
7	Storage Superheater Outlet Temperature			391 °C (735 °F) [⊙] *	Same as PP	
8	Turbine L. P. Design Steam Pressure			3.275 MPa (475 psia)	Same as PP	
9	Turbine L. P. Design Steam Temperature			388 °C (730 °F)	Same as PP	

40703-II

E-78

NOTE: (1) See Section I for specification and requirement source identification.

* Receiver Design Point.

+ 100 MW(e) net receiver steam driving turbine.

⊙ Storage Design Point.

⊕ 1.7 times 100 MW(e) net steam flow.

ELECTRICAL GENERATION SUBSYSTEM CHARACTERISTICS

Item No.	Characteristic	Spec (1)		Current Baseline		Spec. Var.
		PP	Com.	Pilot Plant	Commercial	
10	Steam Line Pressure Drop due to Friction - Storage SH Outlet to Turbine Throttle Valve			845 kPa (50 psi)⊛*	Same as PP	
11	Steam Line Temperature Drop - Storage SH Outlet to Turbine Throttle Valve			3°C (5°F)⊛*	Same as PP	

NOTE: (1) See Section I for specification and requirement source identification.

* Simultaneous Storage and Receiver.

⊛ Storage Design Pt.

ELECTRICAL GENERATION SUBSYSTEM CHARACTERISTICS

Item No.	Characteristic	Spec (1)		Current Baseline		Spec. Var.
		PP	Com.	Pilot Plant	Commercial	
1	Turbine to HPFWH Outlet Pressure			2.03 MPa (294 psia)*	Same as PP for Heater #5	
2	Turbine to HPFWH Outlet Temperature			338°C (641°F)*	Same as PP for Heater #5	
3	Turbine to LPFWH Outlet Pressure			86.9 kPa (12.6 psia)*	Same as PP for Heater #1	
4	Turbine to LPFWH Outlet Temperature			96°C (204°F)*	Same as PP for Heater #1	
5	Max. Receiver Steam Outlet - Flow			61,000 kg/h (134,479 lbs/h)	411.2 Mg/h (906,555 lb/h) ⁺ 699.1 Mg/h (1,541,144 lb/h) [⊕]	
	Pressure			11.0 MPa (1600 psia)	10.8 MPa (1570 psia) [⊕] 11.5 MPa (1665 psia) [⊕]	
	Temperature			515.5°C (960°F)	518°C (965°F) ⁺ [⊕]	
6	Friction Loss at Max. Receiver Steam Flow			655 kPa (95 psi)	1379 kPa (200 psi) [⊕]	
7	Temperature Loss at Max. Receiver Steam Flow			6°C (10°F)	8°C (15°F)	
8	HPFWH Outlet Pressure at Maximum Flow			4620 kPa (670 PSI)	Same as PP	
9	HPFWH Outlet Temperature at Maximum Flow			215°C (419°F)	207°C (404°F)	
10	Condenser Back Pressure			6.76 kPa (2 in. HgA)*	Same as PP	
11	Condensate Temperature			38.3°C (101°F)*	Same as PP	
12	Condenser Power Required			448 kW(e)	4213 kW(e)	

NOTE: (1) See Section I for specification and requirement source identification.

* Receiver Design Point.

+ 100 MW(e) net receiver steam driving turbine.

* Storage Design Point.

⊕ 1.7 times 100 MW(e) net steam flow.

** Simultaneous Steam...

ELECTRICAL GENERATOR SUBSYSTEM CHARACTERISTICS

Item No.	Characteristic	Spec (1)		Current Baseline		Spec. Var.
		PP	Com.	Pilot Plant	Commercial	
1	BFP No. Operating			1 Booster, 1 Main	Same as PP	
2	BVP Flow			49,592 kg/h (109,332 lbs/h)*	411,206 kg/h (906,555 lbs/h)*	
3	Feedwater Booster Pump Sunction Temperature			155°C (311.5°F)		
4	BFP Developer Head (ea.)			Booster - 575 m (1737 ft) Main - 1211 m (3973 ft)		
5	BFP Power Req (ea.)			Booster - 148 kW(e) Main - 409 kW(e)	Booster - 727 kW(e) Main - 2549 kW(e)	
6	Condensate Pump No. Operating			1	1	
7	Condensate Pump Developer Head (ea.)			172 m (565 ft)	Same as PP	
8	Condensate Pump Power Req (ea.)			20 kW(e)	250 kW(e)	
9	HPFWH Steam Inlet Pressure			1889 kPa (273.9 psia)	Same as PP ⁺	
10	HPFWH Steam Inlet Temperature			338°C (641°F)*	Same as PP ⁺	
11	HPFWH Steam Inlet Flow			4116 kg/h (9075 lb/h)	20,568 kg/h (45,345 lb/h) ⁺	
12	HPFWH Feedwater Inlet Temperature			158°C (316.5°F)*	181°C (357.6°F) ⁺	
13	HPFWH Feedwater Outlet			204°C (399.1°F)* (Allow 1°F line loss)	207°C (404.1°F) ⁺ (Allow 2°F line loss)	

NOTE: (1) Section I for specification and requirement source identification.

* Receiver Design Point.

+ 100 MW(e) Net Receiver Steam Driving Turbine.

ELECTRICAL GENERATION SUBSYSTEM CHARACTERISTICS

Item No.	Characteristic	Spec (1)		Current Baseline		Spec. Var.
		PP	Com.	Pilot Plant		
1	Deaerator Steam Inlet Pressure			547 kPa	(79.37 psi)*	Same as PP +
2	Deaerator Steam Inlet Temperature			357°C	(674°F)*	Same as PP +
3	Deaerator Steam Inlet Flow			4541 kg/h	(10,011 lb/h)*	22.51 Mg/h (49,627 lb/h) +
4	Deaerator Feedwater Inlet Temperature			88°C	(191°F)*	121°C (250°F) +
5	Deaerator Feedwater Outlet Flow			49,592 kg/h	(109,332 lb/hr)*	411.21 Mg/h (906,555 lb/h) +
6	Deaerator Feedwater Outlet Temperature			155°C	(311.5°F)*	Same as PP +
7	LPFWH Steam Inlet Pressure			80.6 kPa	(11.69 psi)*	Same as PP +

NOTE: (1) See Section I for specification and requirement source identification.

* Receiver Design Point.

+ 100 MW(e) Net Receiver Steam Driving Turbine.

ELECTRICAL GENERATION SUBSYSTEM CHARACTERISTICS

Item No.	Characteristic	Spec (1)		Current Baseline		Spec. Var.
		PP	Com.	Pilot Plant	Commercial	
1	LPFWH Steam Inlet Temperature			96°C (204.2°F)*	Same as PP ⁺	
2	LPFWH Steam Inlet Flow			3540 kg/h (7804 lb/hr)*	30,107 kg/h (66,374 lbs/h) ⁺	
3	LPFWH Feedwater Inlet Temperature			39°C (101.5°F)	Same as PP	
4	LPFWH Feedwater Outlet Temperature			88°C (190.7°F)	91°C (195.7°F) ⁺	
5	Turbine Name Plate Capacity Type Speed No. of Extractions			15000 kW(e) Automatic Admission, Non-reheat, condensing, Bottom exhaust, single shell 3600 rpm 3 plus automatic admission	120,000 kW(e) Same as PP 5 plus automatic admission	

40703-II

B-83

NOTE: (1) See Section I for specification and requirement source identification.

+ 100 MW(e) Net Receiver Steam Driving Turbine.

ELECTRICAL GENERATION SUBSYSTEM CHARACTERISTICS

Item No.	Characteristic	Spec (1)		Current Baseline		Spec. Var.
		PP	Com.	Pilot Plant	Commercial	
1	Generator Type			Rotating Field, Synchronous Totally enclosed, air cooled	Rotating Field, Synchronous, Totally enclosed, hydrogen cooled,	
	Capacity			18,750 kVA	135,000 kV	
2	Condenser Type			Surface Condenser with water cooled tower	Same as PP	
	Surface Area			1598 m ² (17,200 ft ²)	11,184 m ² (120,000 ft ²)	
	Tube Material			304 SS	Same as PP	
	Design Steam Load			37,395 kg/h (82,442 lb/h)*	350,611 kg/h (772,966 lb/h)	
	Design ITD Design Temp (ambient)			4°C (7.2°F) 23°C (73°F) wet bulb	5.7°C (10.2°F) Same as PP	
3	Main Feedwater Pump Number			2	2	
	Type			Single Stage, High Speed Centrifugal	Multistage Centrifugal	
	Design Flow			1.23 m ³ /min (350 gpm)	13.6 m ³ /min (3600 gpm)	
	Design Total Dynamic Head			1211 m (3973 ft)	1410 m (4627 ft)	
	Motor Size			800 HP	6000 HP	
4	Feedwater Booster Pump Number			2	2	
	Type			Single Stage, High Speed Centrifugal	Centrifugal	
	Design Flow			1.23 m ³ /min (327 gpm)	13.1 m ³ /min (3450 gpm)	
	Design Total Dynamic Head Motor Size			545 m (1789 ft) 350 HP	Same as PP 2000 HP	

NOTE: (1) See Section I for specification and requirement source identification.

ELECTRICAL GENERATION SUBSYSTEM CHARACTERISTICS (CONCLUDED)

Item No.	Characteristic	Spec (1)		Current Baseline		Spec. Var.
		PP	Com.	Pilot Plant	Commercial	
1	Deaerator					
	Type			Direct Contact, Tray	Same as PP	
	Design Pressure			862 kPa (125 psia)	Same as PP	
	Design Temperature			204°C (400°F)	Same as PP	
	Design Delivered Capacity			60,999 Kg/h (134,479 lb/h)	699,051 kg/h (1,541,144 lb/h)	
2	Storage Capacity			8.4 m ³ (2,220 gal)	61 m ³ (16,000 gal)	
	Air Compressor					
	Number			2	Same as PP	
	Type			Oil Free Reciprocating	Same as PP	
	Capacity (ea.)			125 scfm	200 scfm	
	Discharge Pressure			125 psi	Same as PP	

40703-II

B-85

NOTE: (1) See Section I for specification and requirement source identification.

Table A. Auxiliary Power Requirements
10 MWe Pilot Plant

Thermal Storage EPGS Turbine	Charge*	Simultaneous Charge and Discharge*	Discharge*	Hold
Throttle	C 78 R 124 S 337 E 1741 T 2280			C 78 R 124 S 44 E 1741 T 1987
Admission		C 78 R 124 S 401 E 1271 T 1874	C 0 R 0 S 207 E 1271 T 1478	
Simultaneous Throttle and Admission +		C 78 R 124 S 401 E 1459 T 2062	R/S DP C 78 R 124 S 207 E 1459 T 1868	
Seal		C 78 R 124 S 370 E 1747 T 2319	C 0 R 0 s 98 E 854 T 952	

* Assumes storage oil maintenance unit consumes 48 kW at an efficiency of 0.90. If new value, X, is obtained, entry in each block should be changed as follows:

$$S' = S - \frac{48}{0.9} + \frac{X}{0.9} = S - 53.3 + \frac{X}{0.9}$$

+ Based on 50% from receiver and 50% from thermal storage.

Table B. Auxiliary Power Requirements at Generator Terminals, 100 MWe Commercial Plant*

Thermal Storage EPGS Turbine	Charge	Simultaneous Charge and Discharge	Discharge	Hold
Throttle	Peak Rec Flow C 708 R 1377 S 2820 E 12983 T 17988			C 708 R 1377 S 351 E 10404 T 12840
Admission		C R S E T	SDP C 0 R 0 S 1984 E 7522 T 9506	
Simultaneous Throttle and Admission		C R S E T	C R S E T	
Seal		C R S E T	C R S E T	

* Assumes Thermal Storage Auxiliary Power Requirements listed in BCD (March 2, 1977) with oil maintenance unit power of (48 kW) (7.9) / 0.9 = 379 kW.

1 2 3 4 5 6 7 8

PIPING AND INSTRUMENT DIAGRAM LEGEND

ABBREVIATIONS	
AT	ANALYZER TRANSMITTER
CC	CONDUCTIVITY CELL
CD	CONTROL DRIVE
CP	CONTROL PANEL
EH	EXHAUST HEAD
EJ	EXPANSION JOINT
FC	FLOW CONTROLLER
FE	FLOW ELEMENT
FH	FLEXIBLE HOSE
FI	FLOW INDICATOR
FS	FLOW SWITCH
FT	FLOW TRANSMITTER
GG	GAUGE GLASS
GP	GAUGE PANEL
HFI	HIGH FLOW INTERLOCK
HLA	HIGH LEVEL ALARM
HLI	HIGH LEVEL INTERLOCK
HPA	HIGH PRESSURE ALARM
HPI	HIGH PRESSURE INTERLOCK
HTA	HIGH TEMPERATURE ALARM
HTI	HIGH TEMPERATURE INTERLOCK
L	LEVEL
LC	LEVEL CONTROLLER
LFA	LOW FLOW ALARM
LFI	LOW FLOW INTERLOCK
LI	LEVEL INDICATOR
LLA	LOW LEVEL ALARM
LLI	LOW LEVEL INTERLOCK
LPA	LOW PRESSURE ALARM
LPI	LOW PRESSURE INTERLOCK
LS	LEVEL SWITCH
LT	LEVEL TRANSMITTER
LTA	LOW TEMPERATURE ALARM
LTI	LOW TEMPERATURE INTERLOCK
PC	PRESSURE CONTROLLER
PI	PRESSURE INDICATOR
PH	PH
PS	PRESSURE SWITCH
PT	PRESSURE TRANSMITTER
RD	RUPTURE DISC
SC	SAMPLE COIL
SJ	SHIVEL JOINT
SS	STAINLESS STEEL
ST	STRAINER OR FILTER
TC	TEMPERATURE CONTROLLER
TE	TEMPERATURE ELEMENT
TI	TEMPERATURE INDICATOR
TR	TRAP
TS	TEMPERATURE SWITCH
TT	TEMPERATURE TRANSMITTER
TH	TEMPERATURE WELL
UH	UNIT HEATER
VT	VACUUM PRESSURE TRANSMITTER
VS	RELIEF VALVE VENT SEAL
ZS	LIMIT SWITCH
PREFIX H, HIGH	
PREFIX L, LOW	
FLOW DIAGRAM CONNECTION NUMBERING SYSTEM:	
XXX-XX-XXX	
TERMINATING FLOW DIAGRAM NUMBER	
CONNECTION NUMBER	
ORIGINATING FLOW DIAGRAM NUMBER	
THE FLOW DIAGRAM PREFIX "M1" WILL NOT BE INCLUDED.	

VALVES	
	GATE
	GLOBE
	PLUG
	BALL
	NEEDLE
	CHECK
	STOP CHECK
	AIR OPERATED CHECK
	AIR OPERATED CHECK WITH CLOSING HANDWHEEL
	BUTTERFLY
	VALVE BYPASS
	SAFETY OR RELIEF
	DIAPHRAGM
	IN-LINE SAFETY OR BACK PRESSURE
	ANGLE
	THREE WAY
	FOUR WAY
	MOTOR OPERATED
	SOLENOID OPERATED
	PISTON OPERATED WITH POSITIONER
	DIAPHRAGM OPERATED WITH POSITIONER
	PISTON OPERATED
	SELF CONTAINED CONTROL
	DIAPHRAGM OPERATED SPRING CLOSING
	DIAPHRAGM OPERATED SPRING OPENING
	DIRECT FLOAT OPERATED
	AUTOMATIC RECIRCULATION CONTROL

ACCESSORIES	
	RATE OF FLOW METER
	DISPLACEMENT METER
	SIGHT FLOW INDICATOR
	STRAINER, Y-TYPE
	STRAINER, CONE OR PLATE TYPE
	STRAINER, BASKET TYPE
	FILTER, CARTRIDGE
	STRAINER, DUPLEX BASKET TYPE
	EXPANSION JOINT
	TRAP
	GAUGE GLASS
	ORIFICE
	FLOW NOZZLE
	PITOT TUBE, ANNUBAR
	FLOW TUBE
	OPEN DRAIN FUNNEL
	FLEXIBLE HOSE
	ROOF OR FLOOR DRAIN
	CLOSURE, SCREWED
	CLOSURE, WELDED CAP
	HEAD CHAMBER
	EXHAUST HEAD
	SAFETY VALVE DRIP PAN
	VENT SEAL
	LINE SIZE CHANGE
	INSULATING FLANGE OR BUSHING
	PRESSURE BREAKDOWN ELEMENT
	BLIND FLANGE
	DETECTOR

INSTRUMENTS	
	LOCAL INSTRUMENT
	LOCAL ELECTRICAL DEVICE
	ELECTRONIC TRANSMITTER OR CONTROLLER
FIRST LINE - TRANSMITTER DESIGNATION	
SECOND LINE - TRANSMITTER DESIGNATION OR SERVICE	
THIRD LINE - DESIGN SET POINT (FOR LOCAL CONTROL)	
	PNEUMATIC TRANSMITTER OR CONTROLLER
FIRST LINE - TRANSMITTER DESIGNATION	
SECOND LINE - RECEIVER DESIGNATION	
THIRD LINE - DESIGN SET POINT (FOR LOCAL CONTROL)	
INSTRUMENT FUNCTIONS	
CMP - COMPUTER (DATA LOGGING)	
CNT - CONTROL	
EHC - TURBINE CONTROL	
IND - INDICATOR	
RCD - RECORDER	
LCNT - LOCAL CONTROL	
LIND - LOCAL INDICATION	

PIPING	
	PIPING 2-1/2" AND LARGER
	PIPING 2" AND SMALLER
	TEMPORARY PIPING
	PIPING FURNISHED WITH EQUIPMENT
	EXISTING PIPING
	FUTURE PIPING

NOT TO BE USED FOR CONSTRUCTION

BLACK & VEATCH
CONSULTING ENGINEERS

ENERGY RESEARCH AND DEVELOPMENT ADMINISTRATION
10 MW SOLAR PULSED PLANT

PIPING AND INSTRUMENT DIAGRAM LEGEND

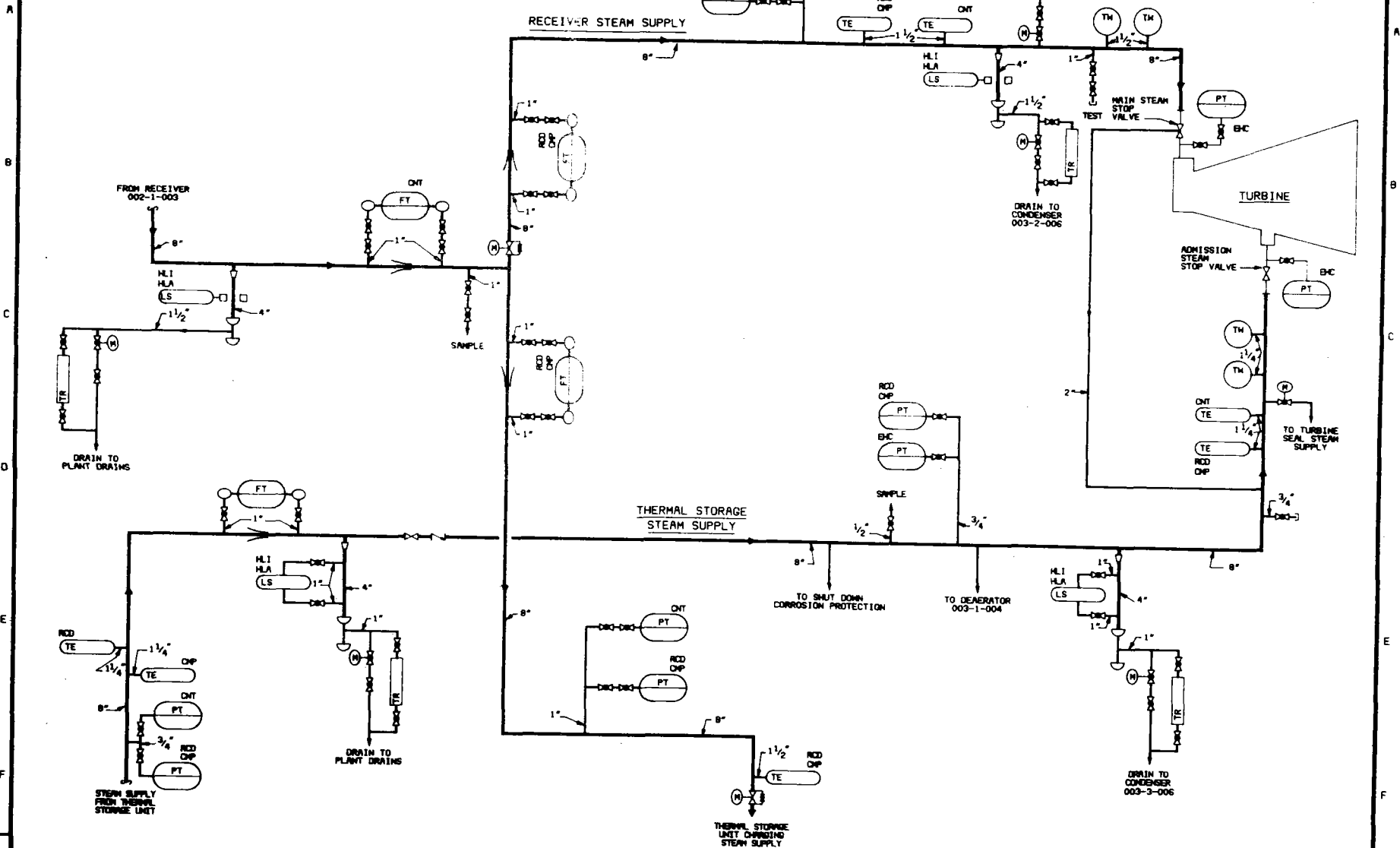
REV. NO. REV.
M1001

40703-II

B-91

NO.	DATE	REVISIONS	ENR	CK	REC	APP	DATE

1 2 3 4 5 6 7 8



40703-II

13-53

NO	DATE	REVISIONS	DES	CK	REC	APP

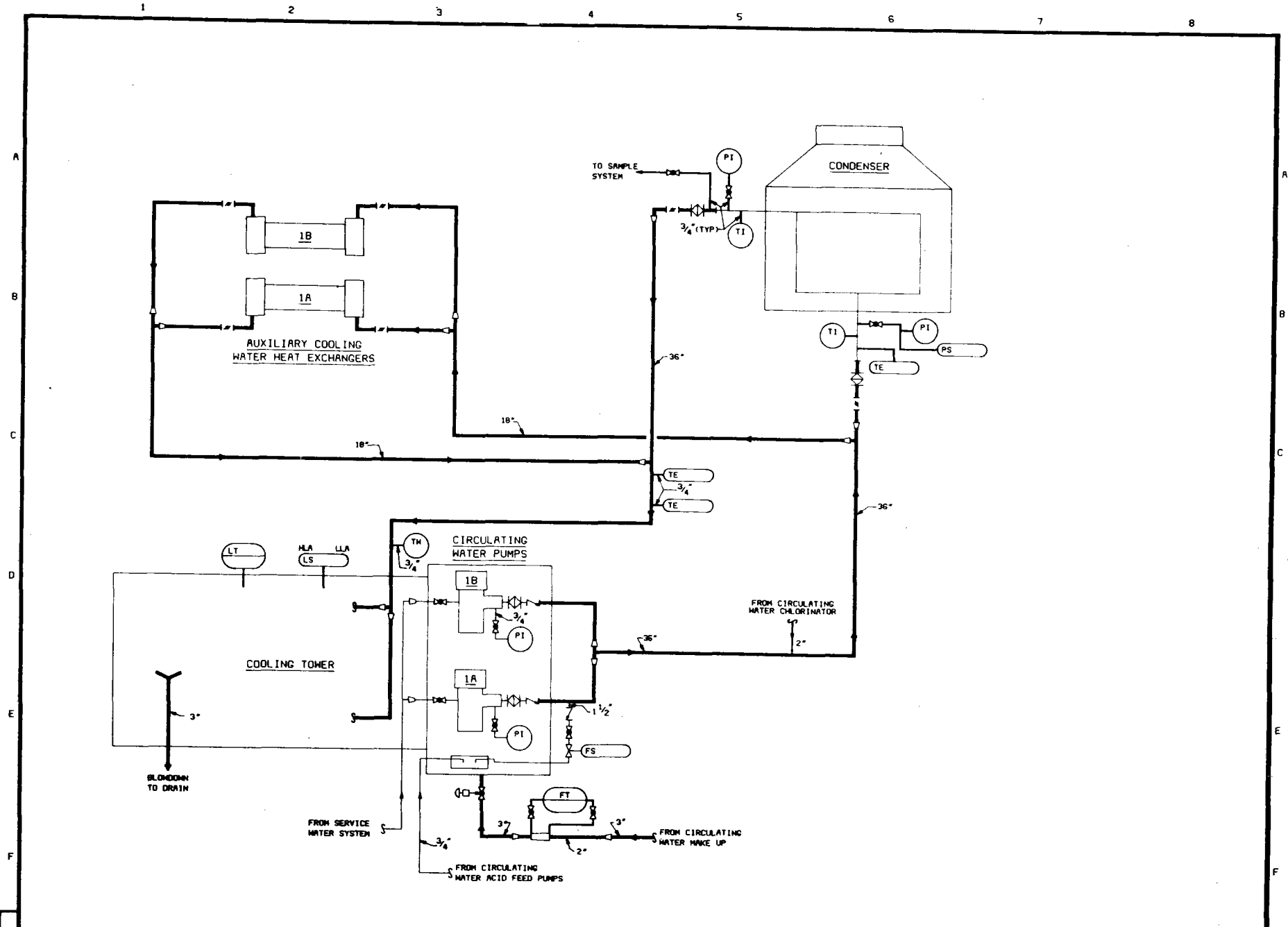
NOT TO BE USED FOR CONSTRUCTION

BLACK & VEATCH
CONSULTING ENGINEERS
PROJECT 7021

ENERGY RESEARCH AND DEVELOPMENT ADMINISTRATION
10 MW SOLAR PLANT
PIPING AND INSTRUMENT DIAGRAM
HIGH PRESSURE STEAM

REV. 01
M1003

40703-II



B-97

NO	DATE	REVISIONS	DESIGN	CHECK	REVISION	DATE

NOT TO BE USED FOR CONSTRUCTION

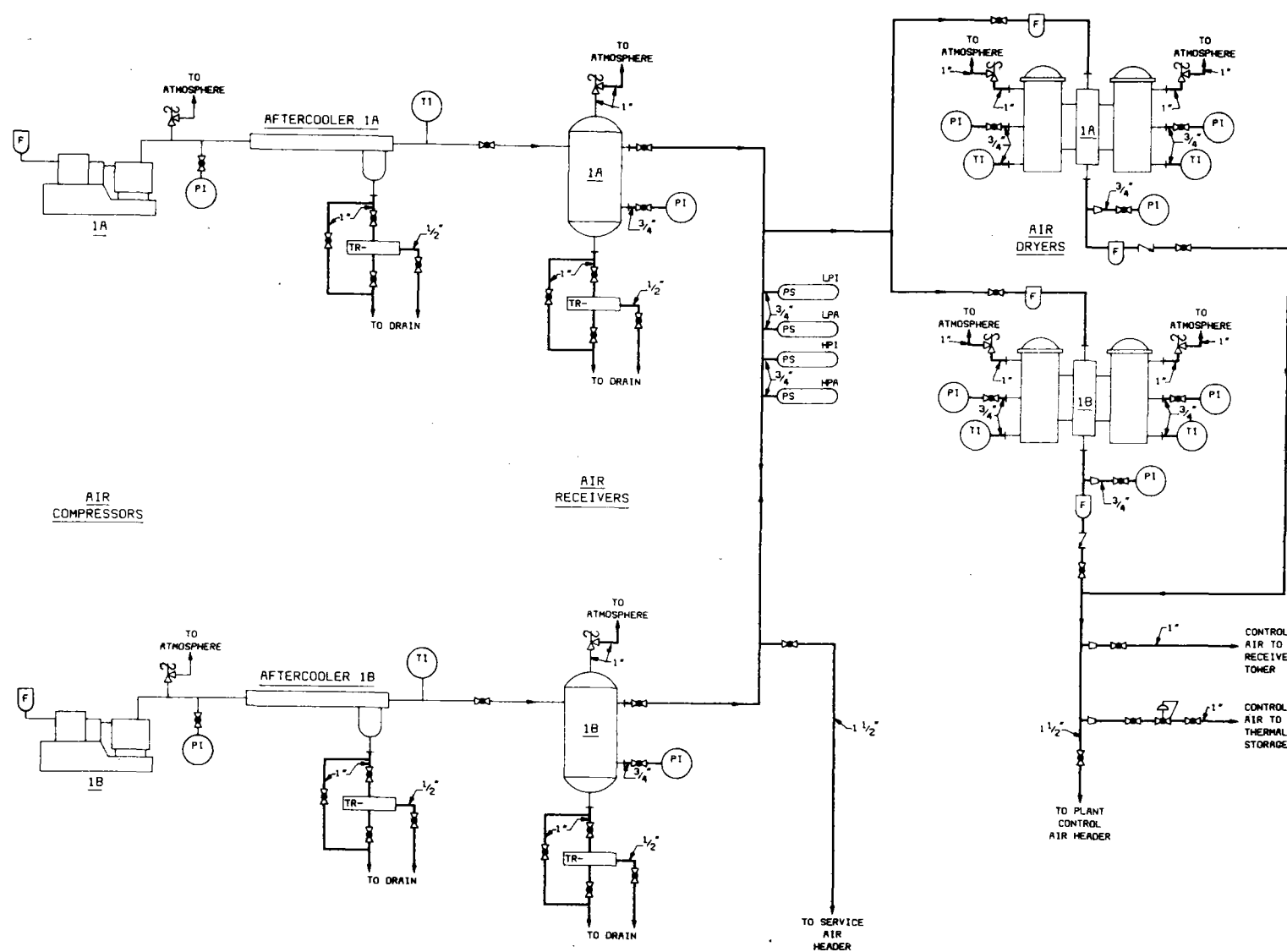
BLACK & VEATCH
CONSULTING ENGINEERS
PROJECT 7021

ENERGY RESEARCH AND DEVELOPMENT ADMINISTRATION
10 MW SOLAR PILOT PLANT
PIPING AND INSTRUMENT DIAGRAM
CIRCULATING WATER

REV. DATE NO. REV.
M1007

A
B
C
D
E
F

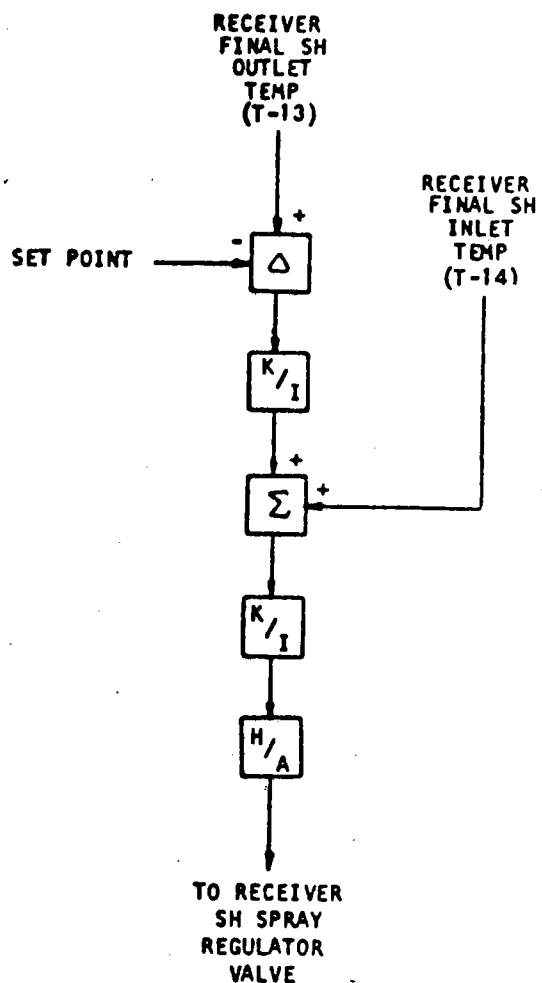
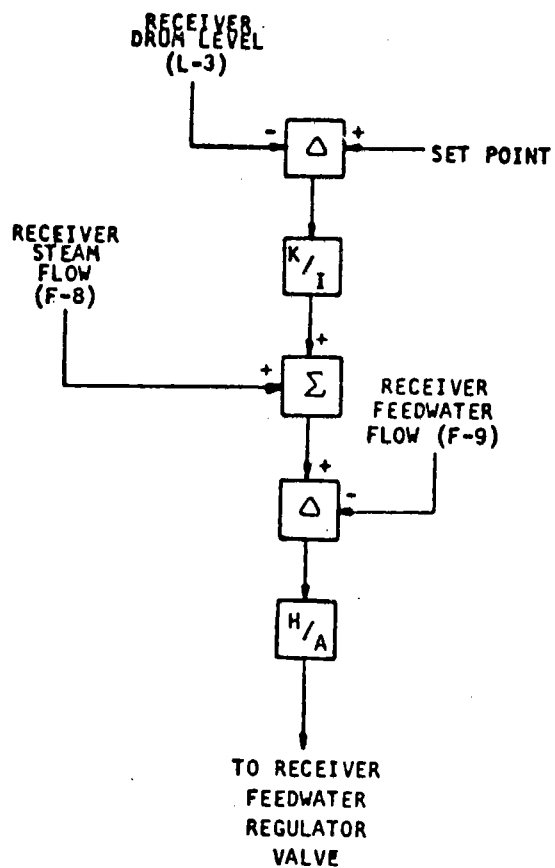
A
B
C
D
E
F



40703-II

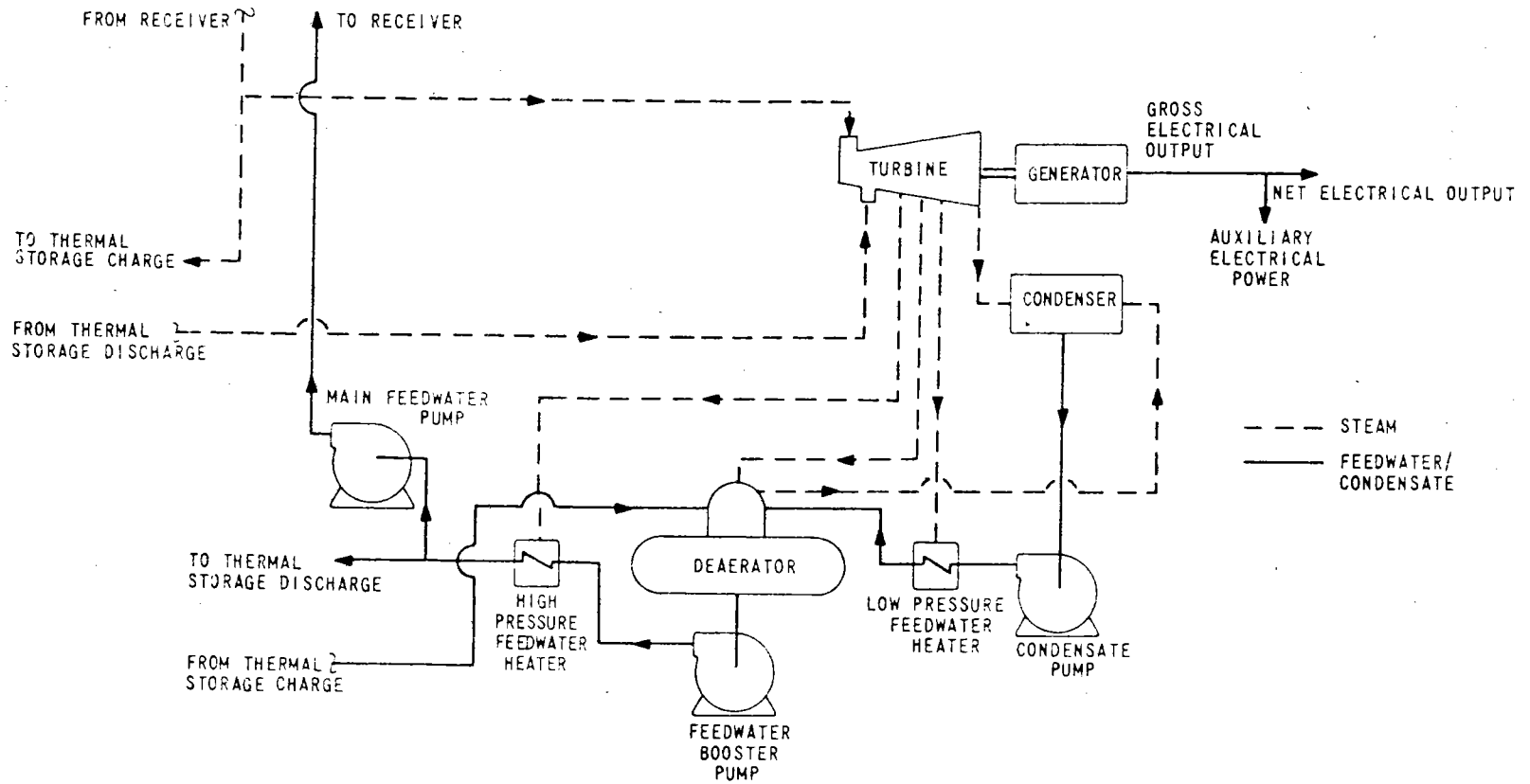
B-100

NO. IN. 000758 DATE REVISIONS DWN CK PCC RPP DATE OF ISSUE	NOT TO BE USED FOR CONSTRUCTION		BLACK & VEATCH CONSULTING ENGINEERS		ENERGY RESEARCH AND DEVELOPMENT ADMINISTRATION 10 MW SOLAR PILOT PLANT		BAY (NO. REV.)
			PROJECT 7021		PIPING AND INSTRUMENT DIAGRAM SERVICE AND CONTROL AIR SYSTEM		M1010



Feedwater and Steam Temperature Controls

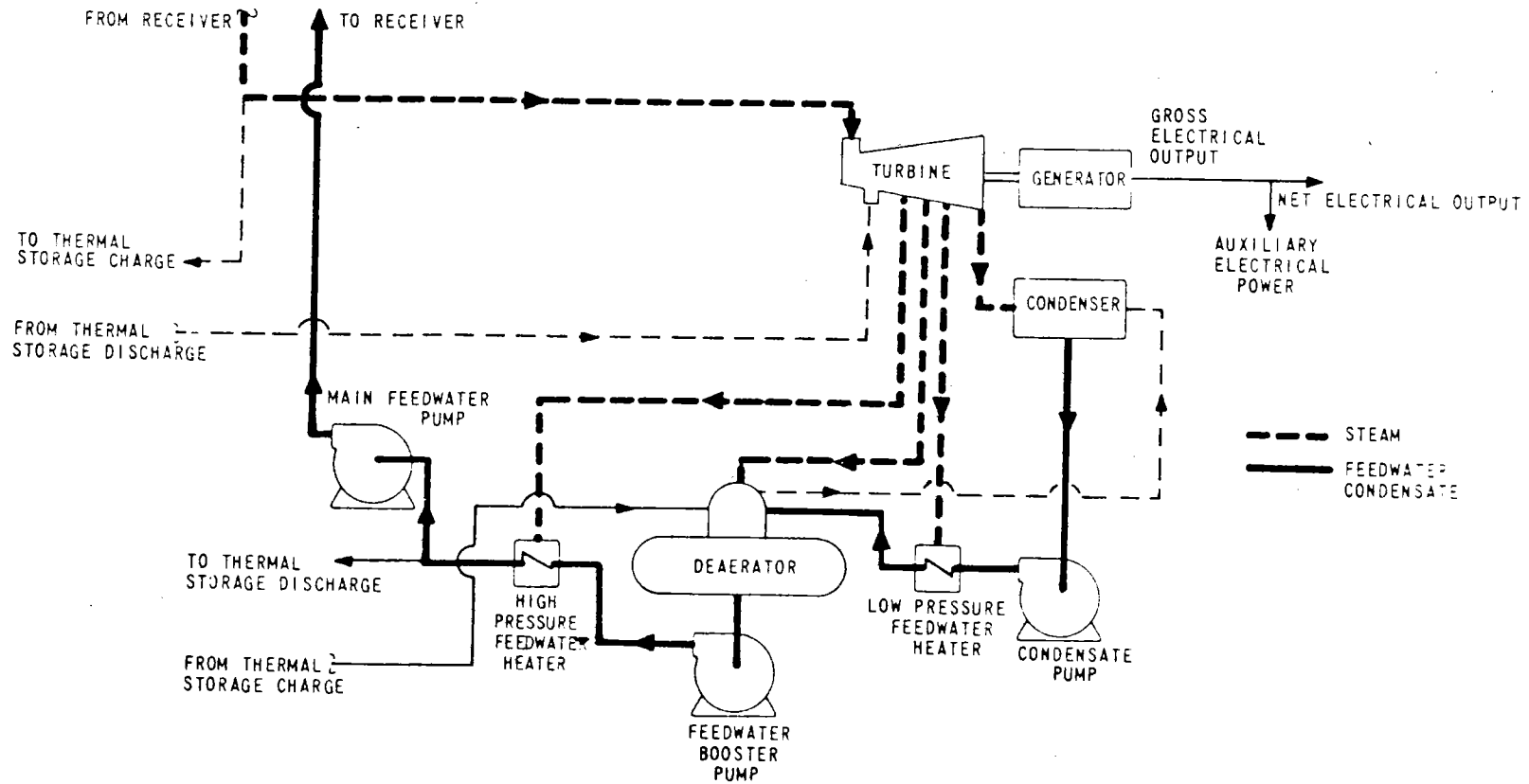
40703-II



ELECTRICAL POWER GENERATION SUBSYSTEM

B-104

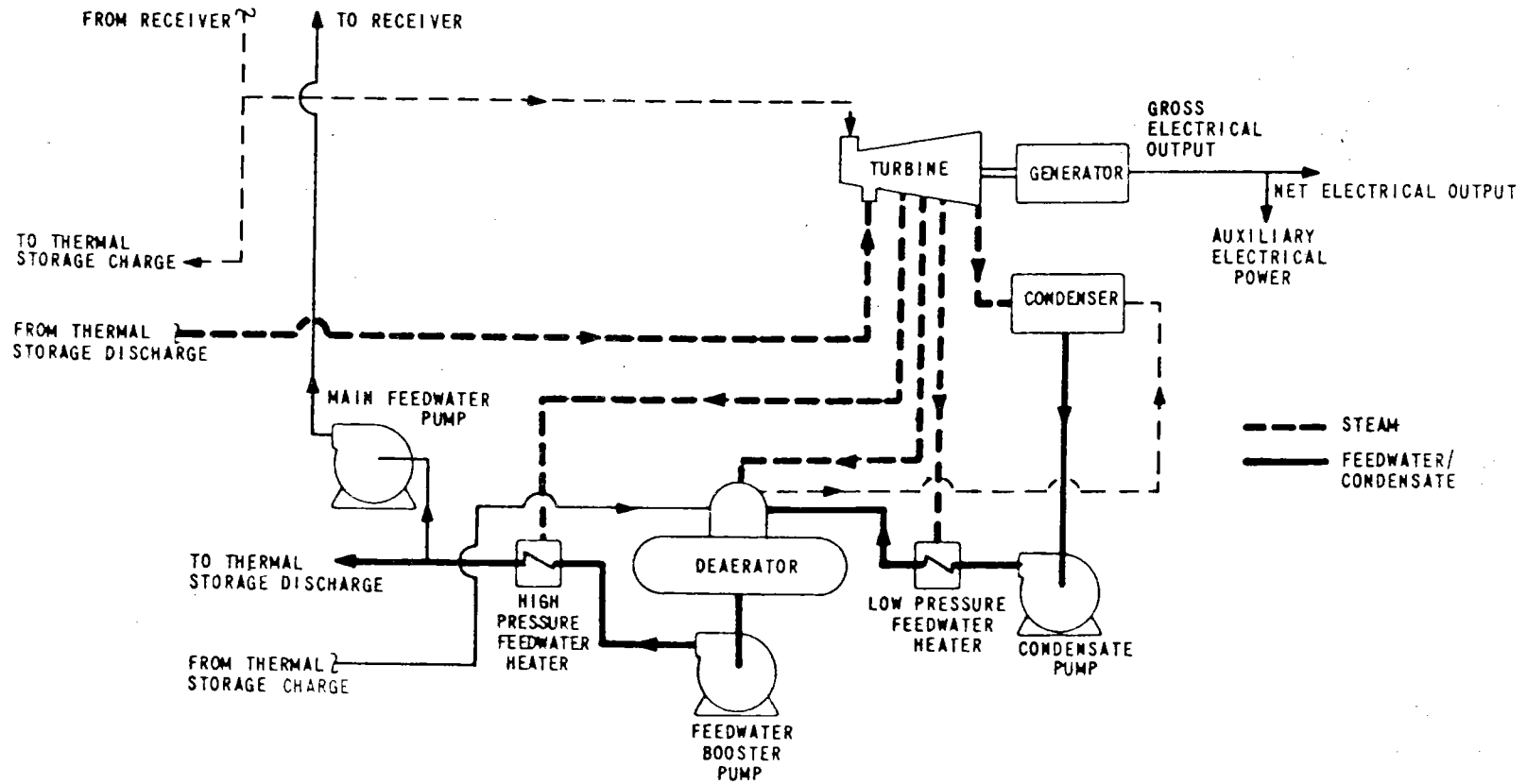
40703-II



ELECTRICAL POWER GENERATION SUBSYSTEM
MODE A-RECEIVER DRIVING TURBINE, THERMAL
STORAGE HOLDING

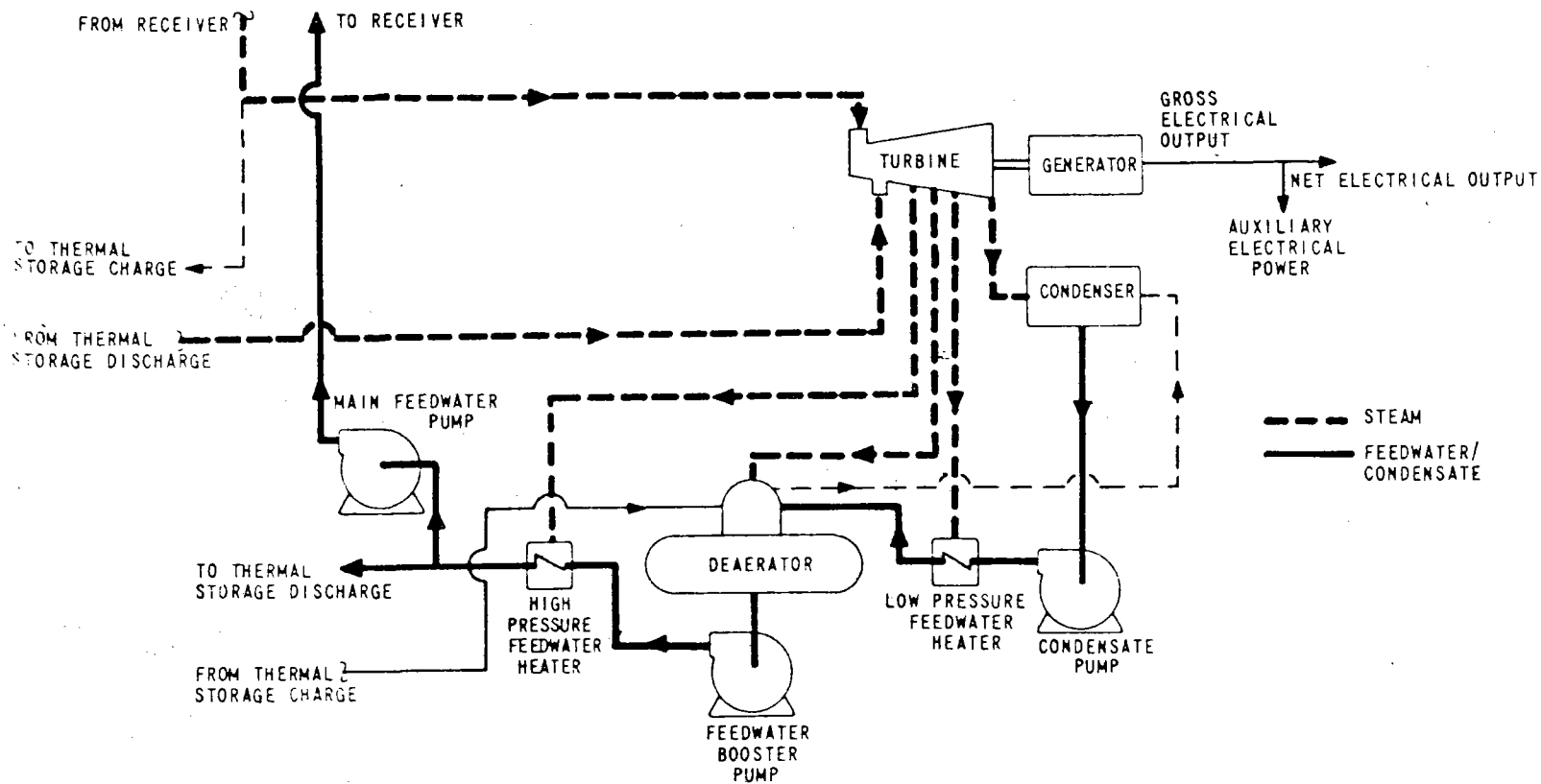
B-105

40703-II



ELECTRICAL POWER GENERATION SUBSYSTEM
MODE B-THERMAL STORAGE DRIVING TURBINE
RECEIVER OFF

B-106

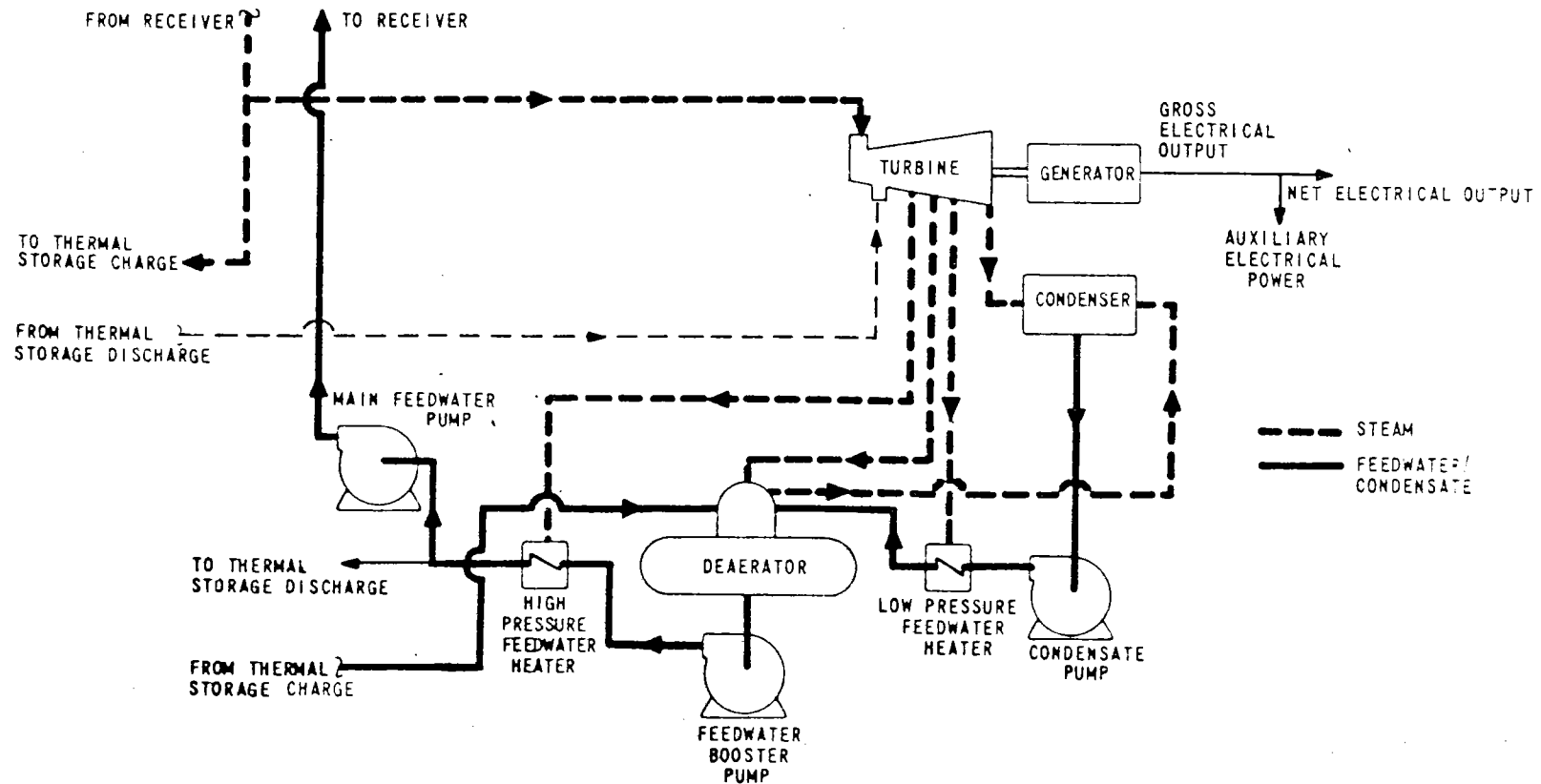


ELECTRICAL POWER GENERATION SUBSYSTEM
 MODE C-RECEIVER AND THERMAL STORAGE
 DRIVING TUBINE SIMULTANEOUSLY

40703-II

B-107

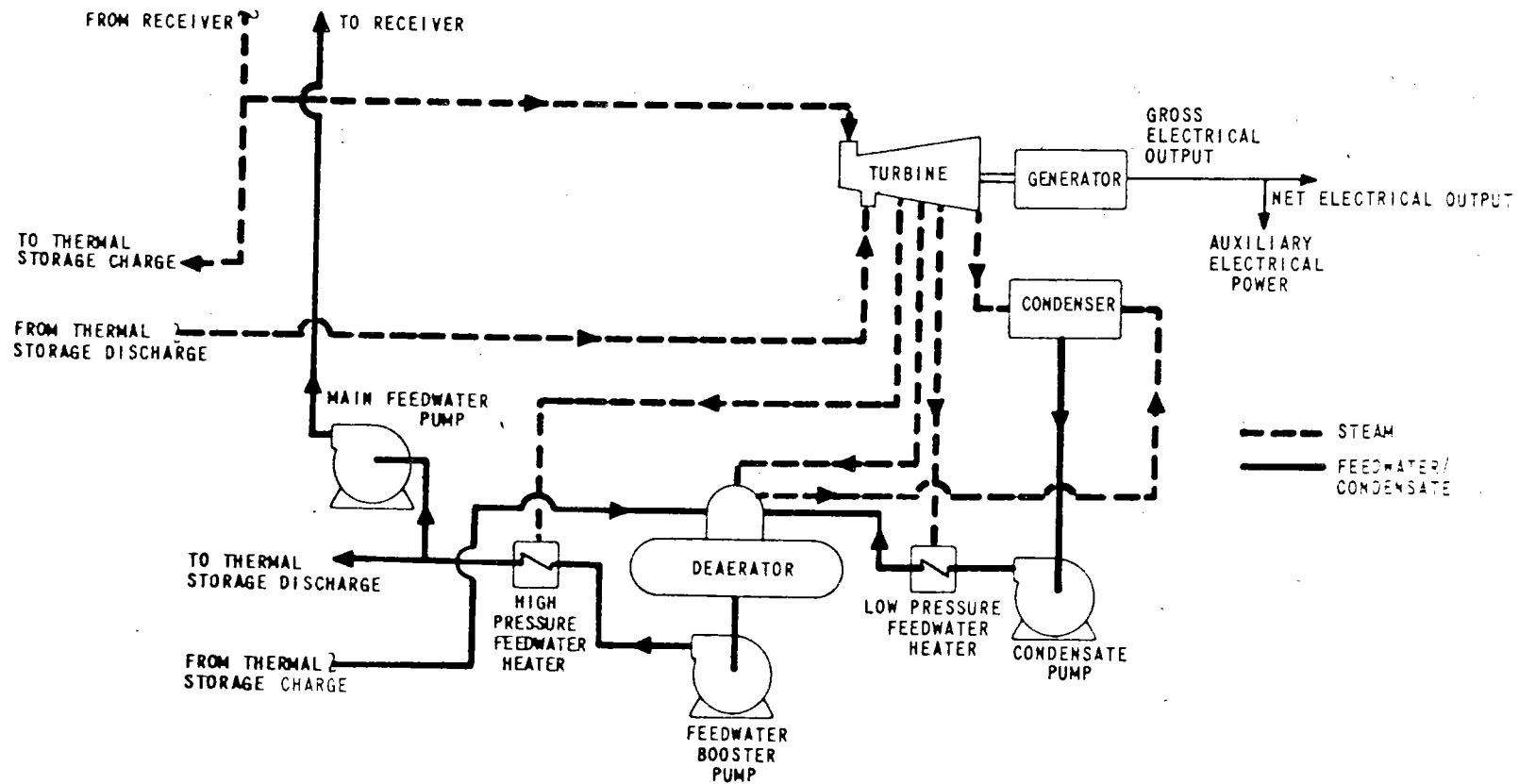
40703-II



B-109

ELECTRICAL POWER GENERATION SUBSYSTEM
MODE E-RECEIVER DRIVING TURBINE AND
CHARGING THERMAL STORAGE

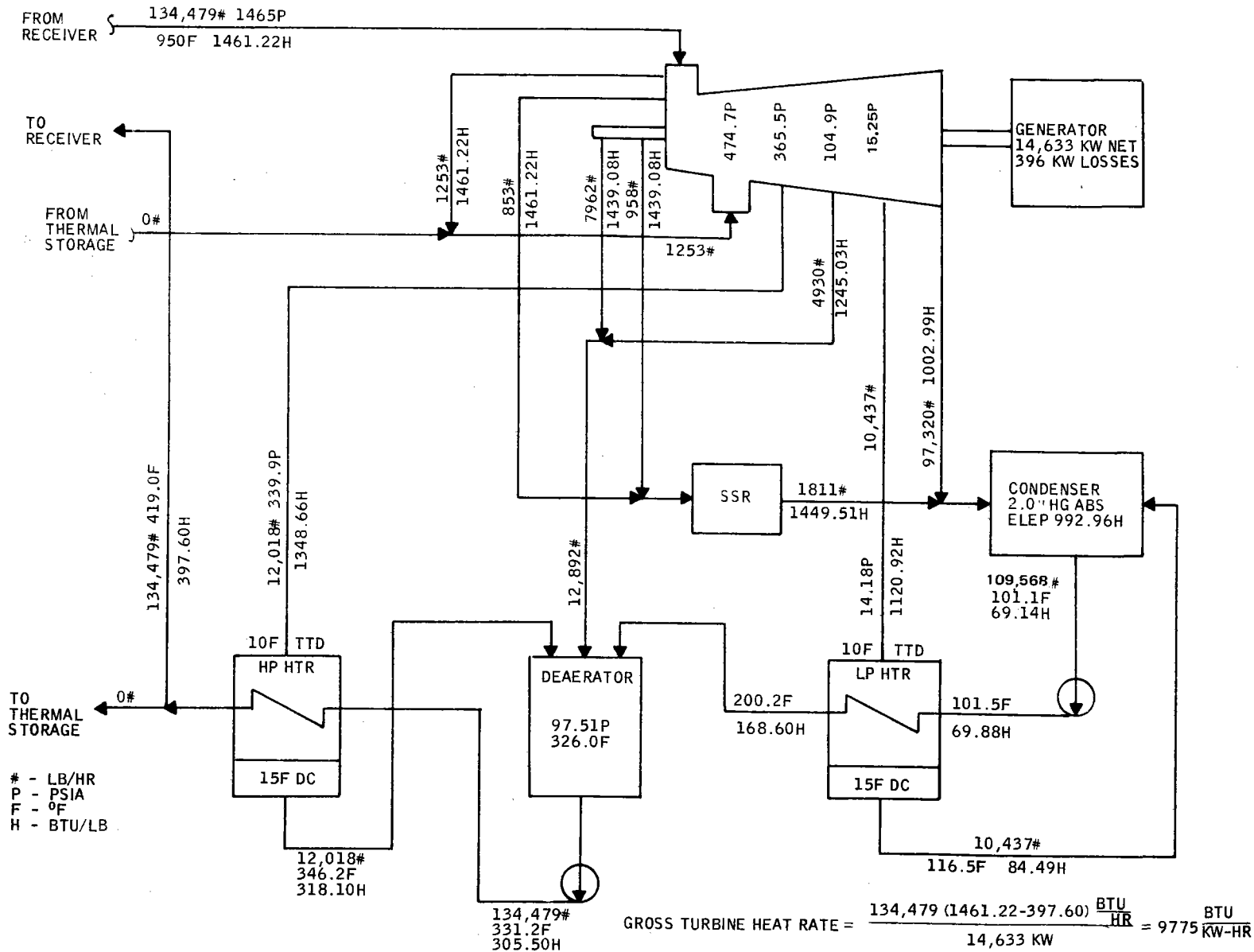
40703-II



B-110

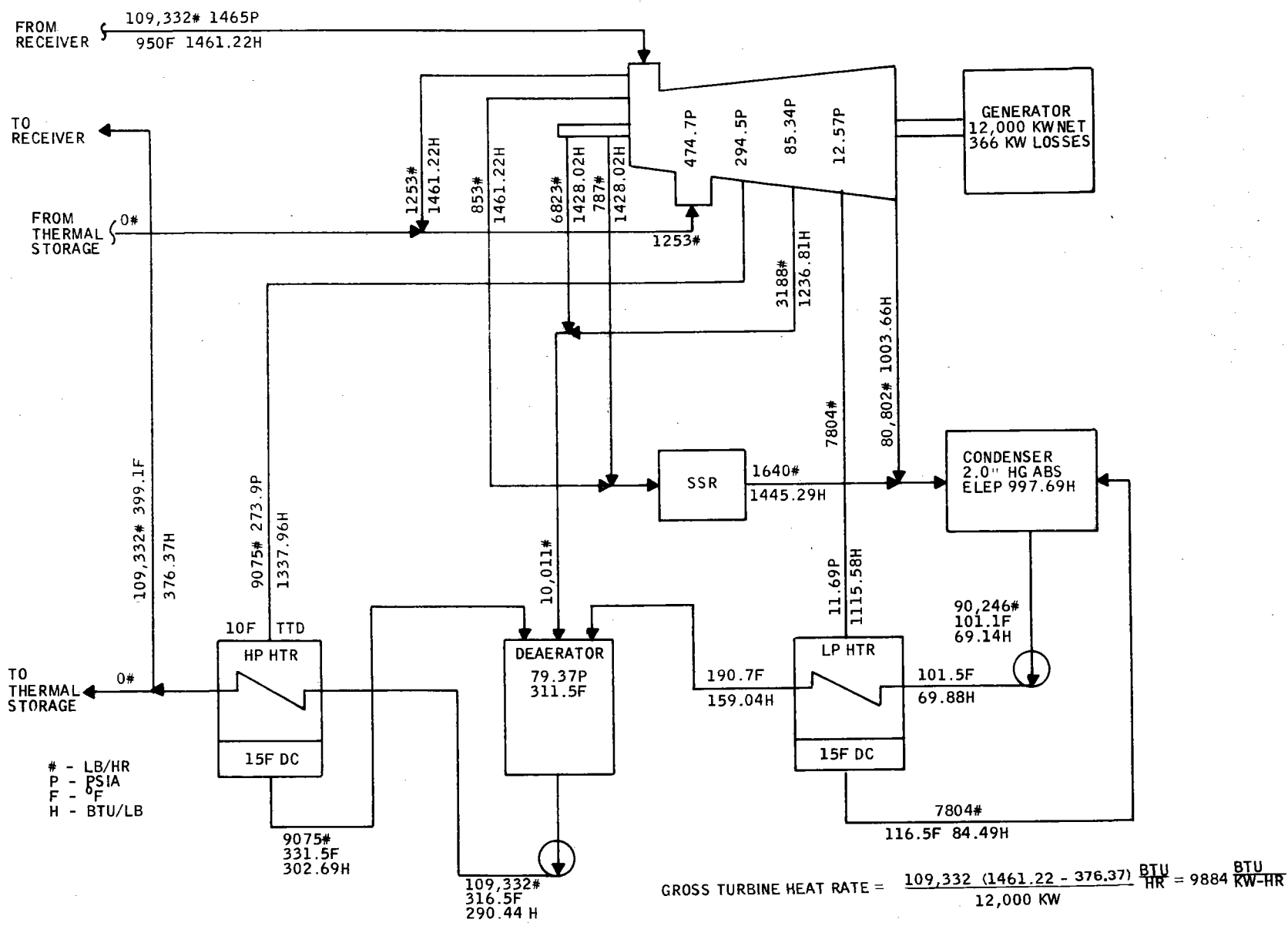
ELECTRICAL POWER GENERATION SUBSYSTEM
MODE F-RECEIVER AND THERMAL STORAGE
DRIVING TURBINE SIMULTANEOUSLY, WHILE
RECEIVER CHARGING THERMAL STORAGE

40703-II



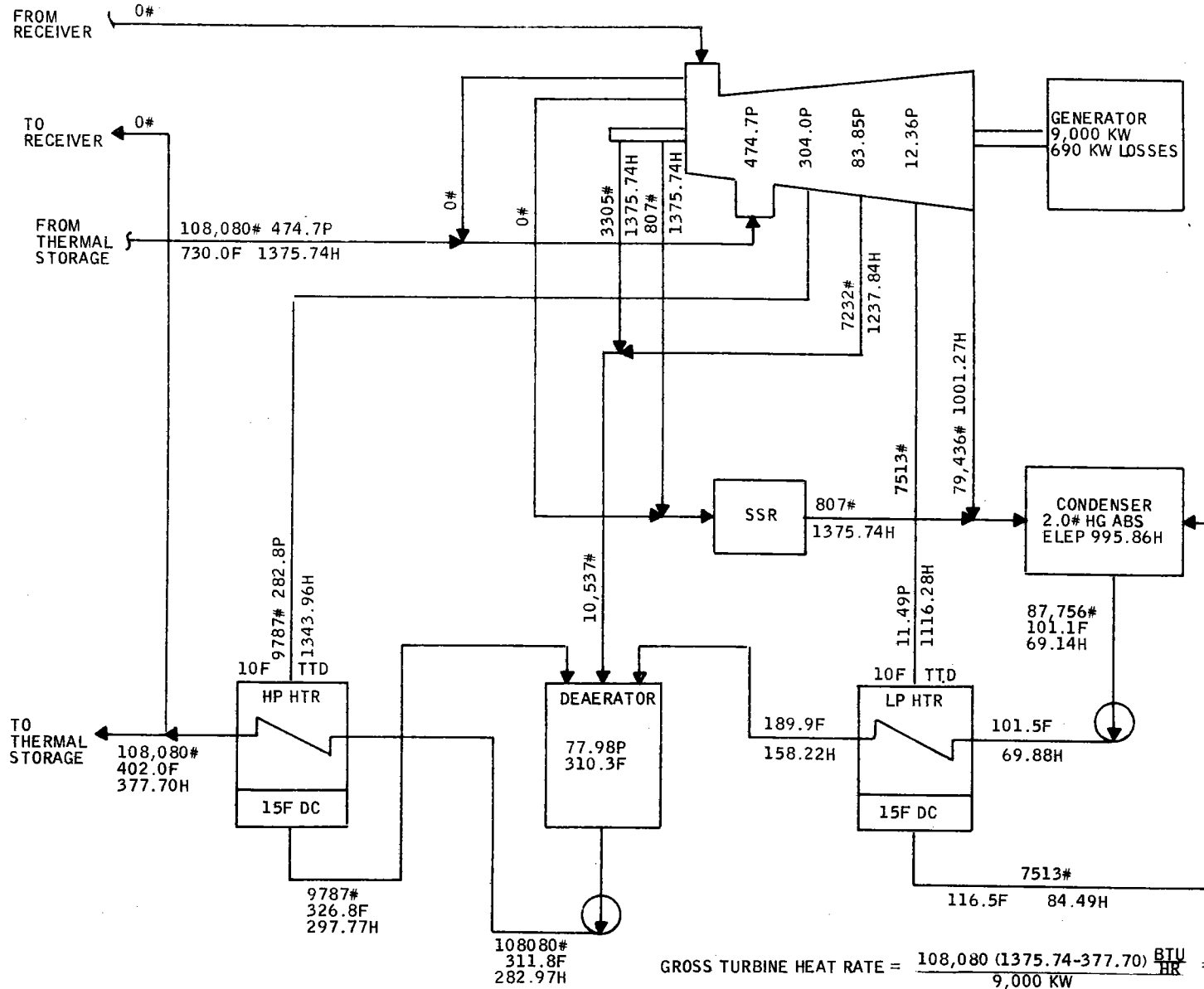
B-111

Maximum Input (3/21, Noon - Receiver)



Design Point Heat Balance (12/21 2 PM - Receiver)

40703-II



B-113

Design Point Heat Balance (Storage)

Heat Rate Equations

$$1. \text{ Gross (Turbine or Cycle) Heat Rate} = \frac{W_1 h_1 - W_2 h_2}{\text{generator output in kw}}$$

where: W_1 = steam entering the cycle, lb per hr

W_2 = feedwater leaving the cycle from the highest pressure heater, lb per hr

h_1 = enthalpy of steam entering the cycle, Btu per lb

h_2 = enthalpy of feedwater leaving the cycle, Btu per lb

$$2. \text{ Net (Turbine or Cycle) Heat Rate} =$$

$$\frac{W_1 h_1 - W_2 h_2}{\text{generator output in kw} - \text{boiler feedpump power in kw}}$$

Note: This simplified "Net" heat rate is commonly used to compare cycles since the remaining plant auxiliary loads will vary greatly for a given situation.

$$3. \text{ Gross (Station or Plant) Heat Rate} =$$

$$\frac{(W_1 + W_3) h_1 + W_4 h_4 - W_2 h_2}{(\text{boiler efficiency}) (\text{generator output in kw})}$$

where: W_3 = steam lost between the boiler and turbine, lb per hr

W_4 = water lost as boiler blowdown, lb per hr

h_4 = enthalpy of blowdown, saturated liquid at boiler pressure, BTU per lb

Note: The heat rate included in the attached letter assumed:

$$W_3 = 0 \text{ lb per hr}$$

$$W_4 = 0 \text{ lb per hr}$$

$$\text{Boiler Efficiency} = \text{Receiver Efficiency} = 90\%$$

Heat Rate Equations (Cont)

4. Net (Station or Plant) Heat Rate =

$$\frac{(W_1 + W_3)h_1 + W_4h_4 - W_2h_2}{(\text{boiler efficiency})(\text{generator output in kw} - \text{auxiliary power in kw})}$$





Note: The auxiliary power was first assumed to be the design value of 2,000 kw. The second "Net Station Heat Rate" listed was calculated using an auxiliary load of 1,654 kw, which is the present estimate of auxiliary power requirements when operating at 12 Mw.

To calculate efficiency, divide 3413 Btu/kwh by the heat rate.

MEASURING/READOUT LETTERS

PROCESS VARIABLE	FUNCTION
A = Analysis**	R = Recording
C = Conductivity	I = Indicating
D = Density	T = Transmitter
F = Flow	RT = Recording Transmitter
L = Level	IT = Indicating Transmitter
M = Moisture	
P = Pressure	
S = Speed	
T = Temperature	
V = Viscosity	
W = Weight	
Z = Position	

ENCLOSURE SYMBOLS

FUNCTION	SYMBOL
Measuring Or Readout	
Manual Signal Processing	
Automatic Signal Processing	
Final Controlling	

Analog Diagramming Symbols